OPTICAL SCIENCES

Friedrich Bachmann
Peter Loosen
Reinhart Poprawe
(Eds.)

High Power Diode Lasers

Technology and Applications

Springer

Springer Series in
OPTICAL SCIENCES 128

Founded by H.K.V. Lotsch

Editor-in-Chief: W.T. Rhodes, Atlanta

Editorial Board: A. Adibi, Atlanta
T. Asakura, Sapporo
T.W. Hänsch, Garching
T. Kamiya, Tokyo
F. Krausz, Garching
B. Monemar, Linköping
M. Ohtsu, Tokyo
H. Venghaus, Berlin
H. Weber, Berlin
H. Weinfurter, Munich

Springer Series in OPTICAL SCIENCES

The Springer Series in Optical Sciences, under the leadership of Editor-in-Chief *William T. Rhodes*, Georgia Institute of Technology, USA, provides an expanding selection of research monographs in all major areas of optics: lasers and quantum optics, ultrafast phenomena, optical spectroscopy techniques, optoelectronics, quantum information, information optics, applied laser technology, industrial applications, and other topics of contemporary interest.

With this broad coverage of topics, the series is of use to all research scientists and engineers who need up-to-date reference books.

The editors encourage prospective authors to correspond with them in advance of submitting a manuscript. Submission of manuscripts should be made to the Editor-in-Chief or one of the Editors. See also www.springer.com/series/624

Editor-in-Chief

William T. Rhodes
Georgia Institute of Technology
School of Electrical and
Computer Engineering
Atlanta, GA 30332-0250, USA
E-mail: bill.rhodes@ece.gatech.edu

Editorial Board

Ali Adibi
School of Electrical and
Computer Engineering
Van Leer Electrical Engineering Building
Georgia Institute of Technology
777 Atlantic Drive NW
Atlanta, GA 30332-0250, USA
E-mail: adibi@ece.gatech.edu

Toshimitsu Asakura
Hokkai-Gakuen University
Faculty of Engineering
1-1, Minami-26, Nishi 11, Chuo-ku
Sapporo, Hokkaido 064-0926, Japan
E-mail: asakura@eli.hokkai-s-u.ac.jp

Theodor W. Hänsch
Max-Planck-Institut für Quantenoptik
Hans-Kopfermann-Strasse 1
85748 Garching, Germany
E-mail: t.w.haensch@physik.uni-muenchen.de

Takeshi Kamiya
Ministry of Education, Culture, Sports
Science and Technology
National Institution for Academic Degrees
3-29-1 Otsuka, Bunkyo-ku
Tokyo 112-0012, Japan
E-mail: kamiyatk@niad.ac.jp

Ferenc Krausz
Ludwig-Maximilians-Universität München
Lehrstuhl für Experimentelle Physik
Am Coulombwall 1
85748 Garching, Germany
and
Max-Planck-Institut für Quantenoptik
Hans-Kopfermann-Strasse 1
85748 Garching, Germany
E-mail: ferenc.krausz@mpq.mpg.de

Bo Monemar
Department of Physics
and Measurement Technology
Materials Science Division
Linköping University
58183 Linköping, Sweden
E-mail: bom@ifm.liu.se

Motoichi Ohtsu
University of Tokyo
Department of Electronic Engineering
7-3-1 Hongo, Bunkyo-ku
Tokyo 113-8959, Japan
E-mail: ohtsu@ee.t.u-tokyo.ac.jp

Herbert Venghaus
Heinrich-Hertz-Institut
für Nachrichtentechnik Berlin GmbH
Einsteinufer 37,
10587 Berlin, Germany
E-mail: venghaus@hhi.de

Horst Weber
Technische Universität Berlin
Optisches Institut
Strasse des 17. Juni 135
10623 Berlin, Germany
E-mail: weber@physik.tu-berlin.de

Harald Weinfurter
Ludwig-Maximilians-Universität München
Sektion Physik
Schellingstrasse 4/III
80799 München, Germany
E-mail: harald.weinfurter@physik.
uni-muenchen.de

Friedrich Bachmann Peter Loosen
Reinhart Poprawe
Editors

High Power Diode Lasers

Technology and Applications

Springer

Dr. Friedrich Bachmann
ROFIN-SINAR Laser GmbH
Berzeliusstr. 83
D-22113 Hamburg
Germany

Prof. Dr. Peter Loosen
Fraunhofer-Institut for Laser Technology
Steinbachstr. 15
D-52074 Aachen
Germany

Prof. Dr. Reinhart Poprawe
Fraunhofer-Institut for Laser Technology
Steinbachstr. 15
D-52074 Aachen
Germany

Library of Congress Control Number: 2006931196

ISBN-10: 0-387-34453-5 e-ISBN-10: 0-387-34729-1
ISBN-13: 978-0-387-34453-9 e-ISBN-13: 978-0-387-34729-5

Printed on acid-free paper.

© 2007 Springer Science+Business Media, LLC
All rights reserved. This work may not be translated or copied in whole or in part without the written permission of the publisher (Springer Science+Business Media, LLC, 233 Spring Street, New York, NY 10013, USA), except for brief excerpts in connection with reviews or scholarly analysis. Use in connection with any form of information storage and retrieval, electronic adaptation, computer software, or by similar or dissimilar methodology now known or hereafter developed is forbidden.
The use in this publication of trade names, trademarks, service marks, and similar terms, even if they are not identified as such, is not to be taken as an expression of opinion as to whether or not they are subject to proprietary rights.

9 8 7 6 5 4 3 2 1

springer.com

Contents

1 Introduction **1**
Reinhart Poprawe

2 High-Power Diode Laser Technology and Characteristics **5**
Martin Behringer
2.1. Principles of Diode Laser Operation 5
2.2. Manufacturing Technology 25
2.3. Chip Characterization Methods and Measurements 33
2.4. Broad Area Emitters and Arrays 47
2.5. High-Brightness Emitters and Arrays 55

3 Packaging of Diode Laser Bars **75**
Konstantin Boucke
3.1. Introduction 75
3.2. Mounting of Diode Laser Bars 77
3.3. Cooling 83
3.4. Expansion-Matched Packages 104
3.5. Mounting of Micro-Optics 117

4 Incoherent Beam Superposition and Stacking **121**
Peter Loosen, Alexander Knitsch
4.1. Introduction and Survey 121
4.2. Beam Collimation 128
4.3. Techniques for Beam Combination 142
4.4. Stacking Techniques 150
4.5. Beam Symmetrization and Fiber Coupling 162
4.6. Beam Quality Limits and Comparison to Coherent Coupling 175

5 Laser Systems Beam Characteristics, Metrology, and Standards **181**
Bert John Neubert, Wolf-Dieter Scharfe
5.1. Introduction 181
5.2. Theoretical Background of Beam Propagation 183
5.3. Power Density Distribution 186
5.4. Propagation of the Beam Widths 188
5.5. Measurement of the Beam Power 196
5.6. Measurement of the Power Density Distribution and the Beam Propagation Ratio, M^2 196

5.7. Beam Positional Stability 204
5.8. Wavefront of a Laser Beam 205
5.9. Lifetime 206
5.10. Laser Safety 209
5.11. Table of International Standards related to Laser Metrology 210
5.12. Practical Hints for Measurements 211

6 Diode Laser Systems 215
Friedrich Bachmann
6.1. Introduction 215
6.2. Multi-Purpose Diode Laser Systems 215
6.3. Modular Diode Laser Systems 245

7 Applications 285
D. Petring, R. Polzin, M. Becker
7.1. Joining Technologies 285
7.2. Cutting and Laser-Assisted Machining Technologies 387
7.3. Surface Treatment 425

8 Summary and Outlook 535
Reinhart Poprawe

Index 539

1
Introduction

Reinhart Poprawe

The motivation for writing this book is at least threefold: the extremely promising laser characteristics of high-power diode lasers; their vast application potential in production processes like welding, soldering, polymer joining, cutting, and surface treatment; and last but not least, a 5-year project called "Modular Diode Laser Tools" funded by the German Federal Ministry of Education and Research, which this book summarizes in terms of results and future outlook.

TEM_{00} mode diode lasers in the power range of several milliwatts have been around for many decades and their application in fiber-based telecommunications, CD-DVD devices and bar code scanners is well established. High-power diode lasers in the range of tens of watts were introduced in the late 1990s and their extremely promising characteristics exceeded our expectations for future industrial applications in production. Power levels of 50 W per 1 cm bar at efficiencies around and over 50% were demonstrated, the first applications in polymer welding were shown in the laboratory, and the first large-scale introductions to industrial applications were also realized at that time. The question arose whether – and if so how – those lasers could someday complement classical CO_2 and solid-state lasers, possibly even in the near future. Modular concepts like combining single bars in stacks of up to 25 had already lead to the development of cup-sized kilowatt lasers. The possibility of extrapolation to multi-kilowatt, shoebox-sized systems was obvious.

In terms of application, not only were the extreme improvements expected from efficiency and maintenance-free operation promising, but also, the possibility of tailoring the beam profile to the geometry of the work piece to be processed opened up totally new horizons for laser materials processing. The example of joining demonstrates the idea best. The classical serial approach brings energy and thus heat to the process path and allows the material to expand and distort during the process, leading to a continuous buildup of misalignment of the process path. This could be significantly reduced if not eliminated by simultaneous processing with a beam geometry matching the process path, leading to timely parallel fusion of the components to be joined.

The limiting factor on the state of the art at that time was the beam quality, i.e., the beam parameter product, finally defining on the focusability and thus the

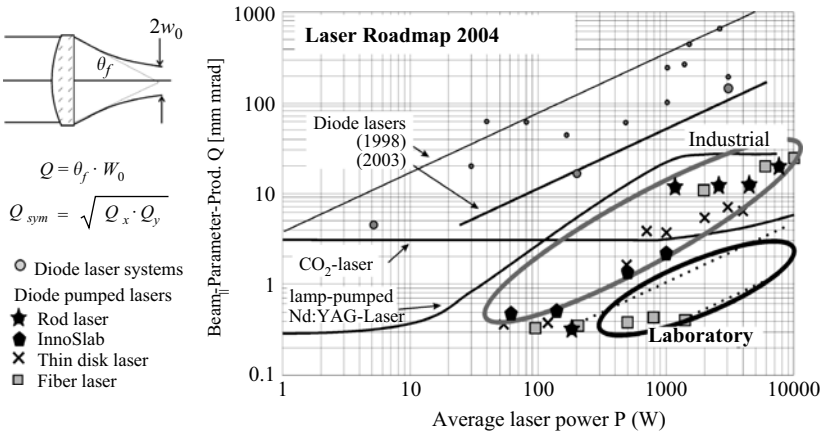

FIGURE 1.1. Comparison of different laser sources in a beam quality versus power diagram

applicability to a large number of processes demanding high intensities in the range of and above 10^6 W/cm^2. Values in the 1990s were around 400 mm mrad at 1-kW laser power. Figure 1.1 shows the status and development in that respect of high-power diode laser systems, starting in 1998, in comparison to other high-power systems like CO_2, solid-state, and fiber lasers.

The lifetime of such sources – in the range of a few hundred to a thousand hours – was totally unacceptable for industrial applications. To meet the incredibly challenging research and development goals of extreme, compact, high-power, high-beam-quality modular diode laser systems, a roadmap with quantitative milestones was generated.

A proposal on "Modular Diode Laser Tools" was formulated in 1997, in the form of a competition among five nationally funded highlight projects designed to lead toward growth of future technologies and markets for German industry. Seventeen industrial companies and seven R&D institutes designed and won the project on the development of future high-power diode laser technology. The project, which was finally started in mid-1998, was divided into three main divisions:

- Semiconductor Technology
- System Technology
- Application Technology.

This book summarizes the results of this ambitious endeavor in scientific and technological terms. It does not reflect any of the incredible group efforts that are inevitably a part of a project of this size. Even in the very beginning, the project plan had more than 1,500 entries, most of them interrelated with more than one other, leading to an extremely challenging structure.

All participants deserve the greatest respect and thanks for their ongoing activity, their belief in the technology, and their trust in the partner they are supplying or relying on for supplies. This project was a true challenge in every sense.

Aachen, October 2006

Dr. Friedrich Bachmann
Prof. Dr. Peter Loosen
Prof. Dr. Reinhart Poprawe

Acknowledgments. The editors, authors, and co-authors express their deep gratitude for the funding and support provided by the German Ministry of Education and Research (BMBF), especially Dr. Rainer Röhrig, and to the Verein Deutscher Ingenieure Technologiezentrum (VDI-TZ) for project control and guidance, especially Dr. Holger Junge, Dr. Siegfried Schubert, and Dr. Peter Soldan.

2
High-Power Diode Laser Technology and Characteristics

Martin Behringer

2.1. Principles of Diode Laser Operation

Götz Erbert and Reinhard März

Laser operation relies on two conditions, stimulated emission of the amplifying medium and feedback by an optical resonator. The threshold of laser operation is obtained if the gain in the resonator compensates for the overall losses, i.e., the propagation losses and the apparent losses due to the extraction of light [2.1]. Both common laser conditions are satisfied in diode lasers in another way than in typical gas or solid-state lasers. The resonator is given by the semiconductor structure itself using the crystal facets as mirrors. The gain in diode lasers involves a whole crystal structure and not only excited single atoms, ions, or molecules. Modern semiconductor lasers restrict the excited volume to reduce the threshold current by applying quantum wells or quantum dots. Technically, this is achieved by growing very thin layers consisting of different crystal compositions for quantum wells or by applying two-dimensional growth for quantum dots. A scheme of a diode laser is shown in Fig. 2.1. The following chapter takes a short tour through the excitation of high-power semiconductor lasers by examining the current injection of carriers, the optical gain, and appropriate resonator structures. More detailed descriptions of several aspects can be found in several textbooks [2.2, 2.3].

The electronic states of crystals form energy bands (Fig. 2.2). At zero temperature, Pauli's principle results in band filling up to a certain level, the Fermi energy level. The status at finite temperatures is described by the Fermi function [2.4]. In semiconductor crystals, the Fermi level is always between two energy bands, the valence band and the conduction band. The minimum gap between both energy bands is called band gap. Semiconductors without impurities and distortions exhibit no allowed states in the band gap. For optoelectronics, direct semiconductors are normally used where the minimum energy of the conduction band and the maximum energy of the valence band are at the Γ-point, i.e., at the center of the Brillouin zone.

If an electron is lifted into the conduction band, e.g., by absorption of a photon, it will leave a hole in the valence band. The optical gain within a semiconductor laser

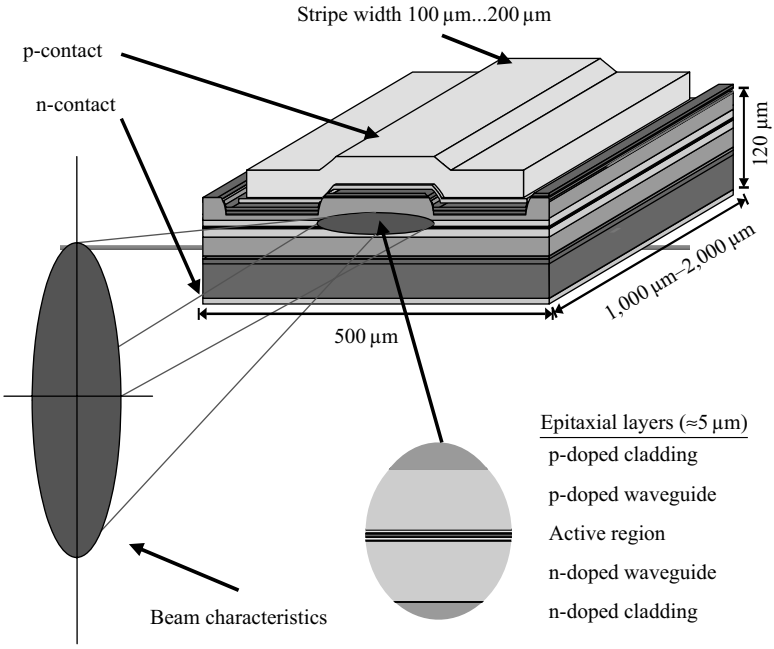

FIGURE 2.1. Schematic of a semiconductor diode stripe laser

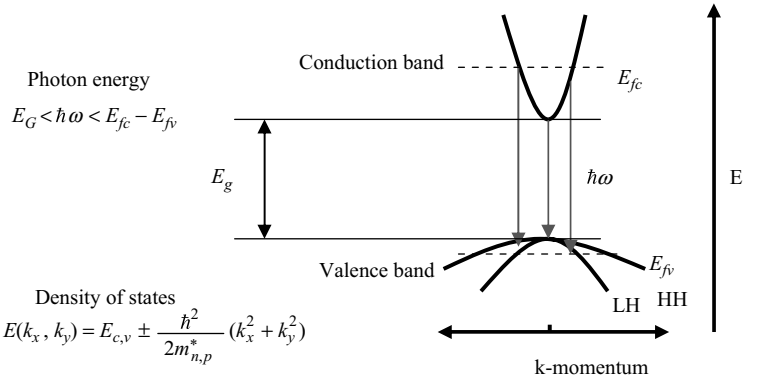

FIGURE 2.2. Band structure of a direct semiconductor crystal close to the Γ-point. The valence band is split into bands for light and heavy holes. E_g is the energy difference between valence and conduction band respectively. In unpumped material, the Fermi level is in the band gap, inversion pumped material can be described by so called quasi Fermi levels E_{fc} and E_{fv}

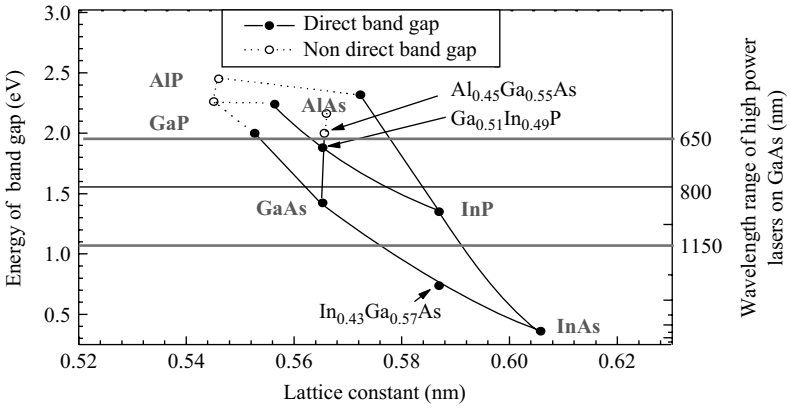

FIGURE 2.3. "Landscape" for laser design band gap of III/V compound semiconductors versus lattice constant

is then generated by radiative recombination of those electron–hole pairs. Direct semiconductors allow for the emission of a photon in a quantum-mechanical first-order process. Most III/V compound semiconductors exhibit direct band gaps, semiconductors such as silicon and germanium exhibit an indirect band structure and are therefore not suited for light-emitting optoelectronic components. The energy of the generated photon corresponds to the difference of the two energy levels. The wavelength of the semiconductor lasers is determined by the size of the band gap and in turn by the composition of the crystal. High-power semiconductor lasers emitting in the 0.7–1.0-μm-wavelength region are typically realized on GaAs and alloys lattice-matched to GaAs. Figure 2.3 shows the energy corresponding band gap versus the lattice constant.

Three crucial questions lead to a deeper understanding of stimulated emission in semiconductor lasers.

- How can a semiconductor crystal be most effectively pumped to generate optical gain?
- How can an excited semiconductor crystal be embedded in an optical resonator?
- How many electron-hole pairs are required to generate optical gain?

2.1.1. Optical Gain in Semiconductors

The first question concerns the generation of optical gain. Like gas and solid-state lasers, semiconductor lasers can be excited by photons of sufficient energy or by electron beams. However, the option to pump semiconductor diode lasers by applying an electrical current represents the main advantage of those devices compared to the competing technologies. Diode lasers make use of the conductivity of semiconductors by doping, i.e., by embedding impurity atoms with a higher or lower number of electrons in the outer shell. These atoms create new quantum-mechanical states within the band gap. If the new states are close to the edge of the

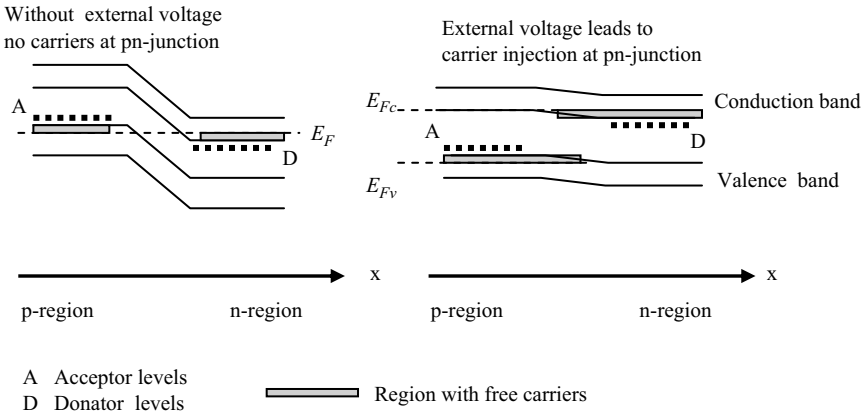

FIGURE 2.4. Recombination at the pn-junction of a semiconductor diode laser

valence band, the electrons will occupy these states, leaving holes in the valence band. This case is called p-doping, due to the fact that positively charged carriers are generated in the valence band which can carry a current. If, in contrast, the new states are close to the conduction band, electrons will be thermally excited to the conduction band. This case is called n-doping, because the negatively charged electrons will carry the current if a potential difference is applied. A diode laser, just like a normal diode, always consists of a p-doped part and an n-doped part (see Fig. 2.1). When a positive electrical potential is applied at the p-doped region, the holes will move to the n-doped region. A negative electrical potential at the n-doped region will drive the electrons to the p-doped part. The optical gain is generated at the pn-junction. At the junction an electron and a hole will recombine, creating one photon, i.e., the energy will be converted to light (see Fig. 2.4). To achieve a substantial current flow, the potential difference must be at least slightly above potential difference given by the band gap. If the injection level – typically at carrier density 10^{18} to 10^{19} cm^{-3} – is high enough, the generated photons exceed the loss.

First semiconductor diode lasers produced in the 1960s were simple homo-junction devices consisting of GaAs. The thickness of the active region was determined by the diffusion length, typically 2 μm. In modern semiconductor diode lasers, due to development of modern epitaxial growth methods, the active region is a quantum well; that means, a thin layer of about 10 nm is surrounded by material with a larger band gap. The injected carriers can now be captured in a very thin layer by the potential barriers of the larger band gap material. In Fig. 2.5, the distribution of the band gaps is shown for a typical modern semiconductor laser. The quantum well consists of InGaAs. The well is embedded in AlGaAs, a ternary alloy with larger band gap but nearly the same lattice constants as GaAs. The band gap offsets must deliver high enough barriers, typically >100 meV, for electrons and holes to have negligible leakage of carriers by thermal excitation (about 24 meV at room temperature).

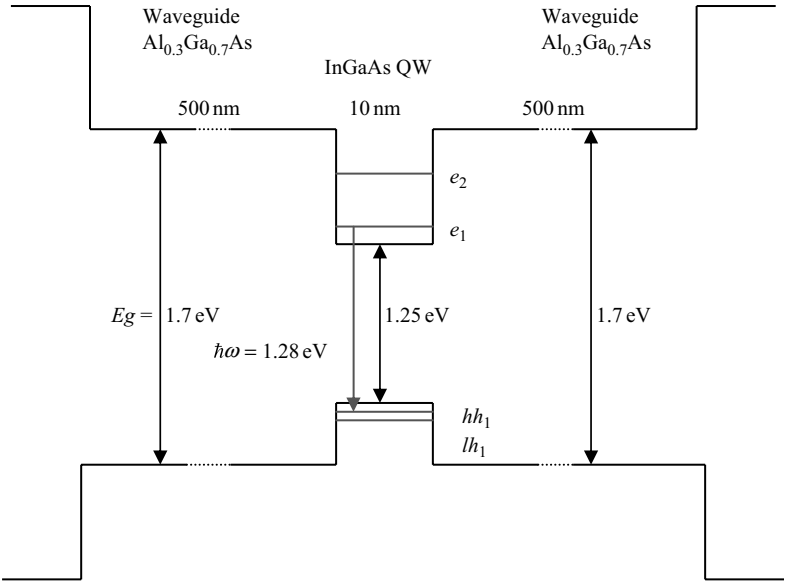

FIGURE 2.5. Band gap distribution and relevant energy levels of an InGaAs-QW embedded in a AlGaAs waveguide layers

Using a quantum well as active region has several advantages:

- First, since the band gap increases outside the quantum well (QW), only the QW-region has to be pumped to generate inversion. Since this volume is very small, the injection current density is reduced by about three orders of magnitude in comparison to homo-junction lasers.
- Second, the carriers are efficiently captured by the QW's barrier making it unnecessary to dope the regions close to the junction. The efficiency of radiative recombination reaches more than 90% in modern standard devices, material of highest quality allows for efficiencies of nearly 100%. On the other hand, the low doping results in laser structures with very low internal loss. As a consequence, QW's opened a way to long lasers of high external efficiency. The reduction of thermal and series resistance by lengthening the lasers up to 4 mm for single emitters and 2 mm for bars allows the high power of about 4 W of 100-μm stripe-single emitters and more than 50 W of laser bars, respectively.
- Third, the quantum well is a layer of about 10-nm thickness. Such thin layers allow for material compositions with lattice constant not fully matching that of GaAs. By replacing gallium partly (typically a few percent) with indium, the addressable wavelength range can be extended up to 1,100 nm. The introduced strain improves the distribution of density of states further and allows threshold current densities of typically 200 A/cm^2 for high-power semiconductor lasers. By replacing Arsenic with Phosphorous, the wavelength range can be extended down to 730 nm.

Table 2.1. Composition of QW and barrier layers for diode lasers emitting between 780 nm and 1060 nm

Wavelength	QW-material	QW thickness	Lattice mismatch	Polarisation	Barriers
780 nm	GaAsP	14 nm	0.8%	TM	$Al_{0.45}Ga_{0.55}As$
810 nm	GaAsP	15 nm	0.5%	TM	$Al_{0.45}Ga_{0.55}As$
810 nm	AlInGaAs	8 nm	1%	TE	$Al_{0.35}Ga_{0.65}As$
880 nm	$In_{0.08}Ga_{0.92}As$	7 nm	1%	TE	$Al_{0.45}Ga_{0.55}As$
940 nm	$In_{0.10}Ga_{0.90}As$	8 nm	1.2%	TE	$Al_{0.35}Ga_{0.65}As$
980 nm	$In_{0.12}Ga_{0.88}As$	10 nm	1.3%	TE	$Al_{0.35}Ga_{0.65}As$
1,060 nm	$In_{0.15}Ga_{0.85}As$	8 nm	1.5%	TE	$Al_{0.25}Ga_{0.75}As$

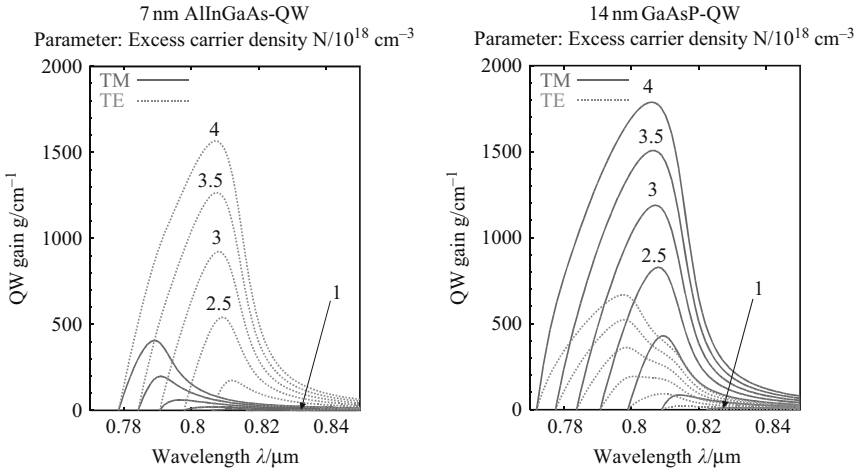

Figure 2.6. Calculated optical gain versus wavelength at different excitation levels for a compressively strained AlInGaAs-QW and a tensile-strained GaAsP-QW at 810 nm

For example, devices emitting at 808 nm, which are important for optical pumping of Nd–based solid-state lasers, can be produced by using compressively strained InAlGaAs or tensile-strained GaAsP-QWs. Table 2.1 shows compositions of QWs for the most interesting wavelengths.

Figure 2.6 shows the optical gain at different excitation levels versus wavelength at 810 nm for an AlInGaAs and GaAsP QW embedded in AlGaAs layers with higher band gap. The gain is calculated from the band structure.

The optical gain in the active material can reach values of more than 1,000 cm^{-1}. Since only a small part of the guided mode is confined in the QW (see next paragraph) the modal optical gain is much smaller, about 10 to 30 cm^{-1}. Despite this reduction the gain is still much higher than that of other lasers, especially that of typical solid-state lasers. The large gain allows for high mirror losses, i.e., light extraction of up to 95% even for extremely short resonator lengths of 1 to 2 mm.

From the figures it is seen that the optical gain increases sublinearly with carrier density. The density of states in a QW geometry increases in a step-like manner. The gain saturates at a given wavelength due to the limited number of states.

In laser design for practical estimations the gain g can be described by the following formula:

$$\text{Material gain in QW } g = g_0 \cdot \ln \frac{j}{j_{tr}} \tag{2.1}$$

where j stands for the current density applied to the devices. The reference gain g_0 and the transparency current j_{tr} are material constants depending on composition, thickness and strain value of the QW and barrier material, respectively. The current density is correlated with the carrier density by injection efficiency and carrier lifetime. Their values are in most practical cases near 100% and around 1 ns, respectively. Compressively strained In(Al)GaAs exhibits transparency currents between 50 and 100 A/cm^2 in the wavelength range 800 to 1060 nm. The values for tensile-strained GaAsP QWs at 800 nm are between 100 and 150 A/cm^2. On the other hand, the g_0 values for tensile-strained QWs are higher. The threshold current densities of tensile-strained or compressively strained QW lasers are similar.

The values of the optical gain g resulting from Eq. (2.1) describe only the material gain within the quantum well. The important value for the amplification of the optical wave within the resonator, the modal gain g_m, depends on the degree of overlap of the optical wave with the QW.

2.1.2. Optical Resonators

The optical resonator of a semiconductor diode laser consists of a waveguide structure between the mirrors build by crystal facet (Fig. 2.7).

These facets are coated to achieve the optimum reflectivity. In the vertical dimension, perpendicular to the pn-junction, the modal intensity distribution and the number of modes are determined by the thickness and composition of the grown layers. Waveguiding is supported for modes with two polarizations, one nearly transverse electric (TE) and one nearly transverse magnetic (TM). For

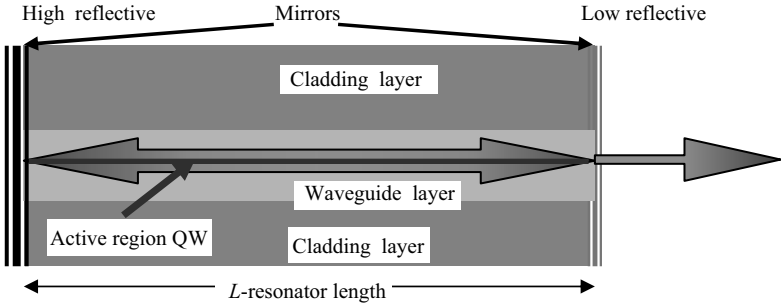

Figure 2.7. Schematic of diode laser optical resonator

the TE case, the electrical field vector oscillates parallel to the epitaxial layers; for the TM case the magnetic field vector. The polarization of the diode laser beam is determined by the kind of QW. Tensile-strained QWs yield more gain for TM modes, compressively strained QWs for TE-modes (see Fig. 2.6).

In the lateral direction the mode distribution is determined by geometrical aspects of the current injection and/or by lateral waveguide for example due to the etched waveguide structure. A broad contact stripe represents the most elementary structure from a fabrication point of view. "Broad" means that the lateral dimensions are large compared to both wavelengths and carrier diffusion length. Broad-Area (BA) diode lasers exhibit widths of around 100 μm corresponding to about 400 wavelengths and about 50 diffusion lengths, respectively. This broad lateral waveguide supports many guided modes resulting in the typical multimode beam characteristics of semiconductor diode lasers. Since nearly all recombination processes can contribute to the modal gain, the efficiency of such devices is very high. Measures to improve the lateral beam characteristics by mode selecting structures and the properties of such kind of diode lasers will be discussed in section 2.5.

2.1.2.1. Vertical Waveguide Structures

The vertical structure, an epitaxial layer structure, defines both an optical waveguide and a pn-junction by using the quantum well. The design of waveguide takes advantage of the increase of refractive index n with increasing band gap. This is illustrated in Fig. 2.8. AlAs exhibits $n = 2.9$ and GaAs 3.5. In comparison AlAs has a band gap energy of 2.9 eV and GaAs 1.4 eV. The active region has the highest refractive index and lowest band gap and allows thus for waveguiding. A single QW with a thickness of 10 nm is too thin to produce a good waveguide. As a consequence, the QW is embedded in a core region with material of higher refractive index and so-called cladding layers which have a lower refractive index.

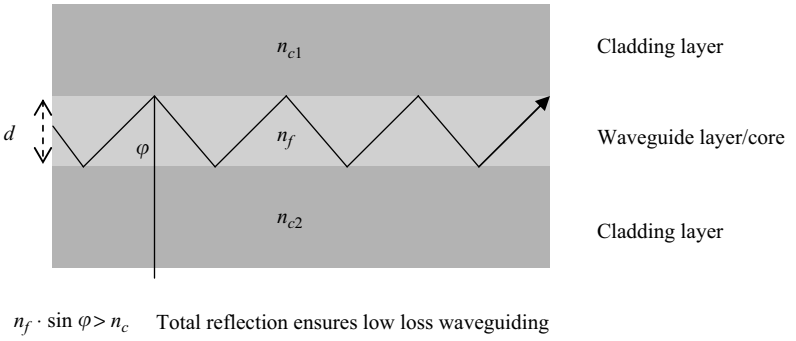

FIGURE 2.8. Schematic of a three layer waveguide: basic structure for diode lasers

These type of structures are designated as separate confinement heterostructures (SCH).

The thickness of the core and the refractive index difference between core and cladding layers determine the number of possible vertical modes and their distribution. For the core layer with a typical thickness between 0.5 μm to 2 μm the laser designer has the choice of different compositions of AlGaAs or AlInGaAsP, which must be lattice-matched to GaAs. The core layer is surrounded by cladding layers with a lower refractive index with a higher content of Al or P, respectively.

The waveguide design is an optimization to satisfy several partly detrimental demands for high-power, high-efficiency diode lasers. For TE-modes, the confinement factor Γ

$$\Gamma = \frac{\int_0^d E(x) \cdot E^*(x)dx}{\int_{-\infty}^{\infty} E(x) \cdot E^*(x)dx} \tag{2.2}$$

with thickness d of the quantum well and the local electrical field E describes the portion of the power of the propagating mode guided in the QW. For TM polarization, the formula is similar but slightly more complicated. Obviously, a high confinement factor ensures a high modal gain g_m. required for efficient laser operation. In fact, the modal gain $g_m = \Gamma \cdot g$ is given by the product of material gain and the confinement factor.

However, a very strong confinement of the light results in a high facet load and large beam divergence. For high-power diode lasers these parameters are critical with respect to reliability. As a rule of thumb, it is much easier to create lasers that withstand 5 to 10 MW/cm^2 on the facet for a short time than lasers that exhibit lifetimes of more than 10,000 h. In addition, a large beam divergence makes highly efficient, low-cost beam shaping nearly impossible.

Third, the layer structure is responsible for the series and thermal resistances. A high wall plug efficiency and good thermal stability requires a strong confinement of the optical wave in a thin layer structure.

Currently, a variety of waveguide structures are used to deal with these requirements. The optimal compositions and layer thickness depend on wavelength, the desired power, divergence, and wall plug efficiency. Figure 2.9 shows a layer structure for a high-power diode lasers emitting at 800 nm. The active region is a tensile-strained GaAsP-QW with a relatively large thickness of 15 nm. The core layer consists of $Al_{0.45}Ga_{0.65}As$. The cladding layers have an AlAs content of 70%. A small core thickness of 0.5 μm results in a smaller spot size and a larger confinement factor and, in turn, in a lower threshold current. On the other hand, the beam divergence and facet load can be reduced drastically by enlarging the core thickness. Higher-order modes will also exist for a core thickness above 1 μm. Due to their lower modal gain, these modes will never pass the threshold. Using a long resonator of about 2 mm and a thick GaAsP-QW delivering a high gain, lasers with core thickness upto 2 μm can be realized at high efficiency (LOC = large optical cavity).

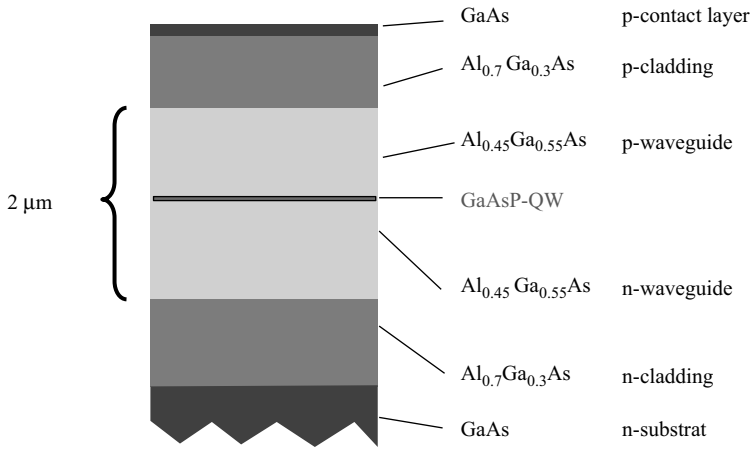

FIGURE 2.9. Schematic of layer structure of high-power 810-nm diode laser

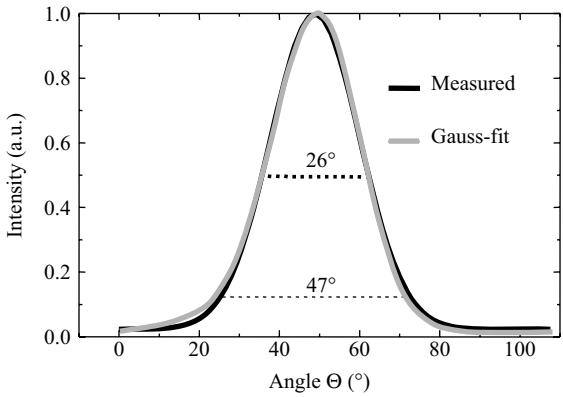

FIGURE 2.10. Intensity distribution of vertical beam of large optical cavity (LOC) diode laser

The distribution of optical intensity of the lowest-order mode inside the waveguide and the resulting intensity distribution for the far field are depicted in Fig. 2.10.

Waveguides with a large core diameter offer low-facet load and low numerical aperture (NA). Typically, 95% of the optical power is fed at an angle $<50°$, which in turn allows for the use of cost-efficient optical systems for collimation.

On the other hand, if a high wall plug efficiency of the diodes themselves represents the crucial requirement specification, e.g., for pumping solid-state lasers, the core thickness is reduced to obtain higher modal gain and reduced threshold current.

2.1.2.2. Lateral Waveguide Structures

In comparison to vertical optical waveguiding determined by the epitaxial layer system the optimization of lateral waveguiding is significantly more challenging. Generally, the effective refractive index is given by the layer structure. The value is typically close to the value of the refractive index of the core layer. Any impact on refractive index of one layer of the waveguide structure will change the effective refractive index. For mathematical description in a first and usually sufficient approximation, the impact on one layer must be multiplied with the confinement factor of this layer get the impact on the effective index. The waveguiding can be described like that of to the vertical structure if we assume that this effective index varies in lateral dimension, resulting in a "core" and "cladding" similar to usual waveguides. For high-power diode lasers the main interest is having only a weak waveguiding. Weak waveguiding allows larger dimensions for the fundamental mode and therefore lower facet load and higher output power. In the multimode case, the divergence will be smaller. In comparison to vertical waveguiding, the change in refractive index of the lateral waveguide core to the cladding is a magnitude lower that means typical around 10^{-3}.

In the case of broad-area lasers, the layer structure does not change in the lateral direction. The impact on effective index is given by the injection current only. The injection current causes the accumulation of carriers in the QW. The higher carrier density depresses the refractive index. Filling the higher band level by carriers leads to lower absorption and of course at the lasing wavelength to optical gain. Due to the common Kramers–Kronig relation this results in a reduction of the refractive index. A second effect is described by the Drude formula that free carriers due to plasma effects reduce the refractive index.

On the other hand, due to the series resistance, and non-radiative recombination, the temperature of the layer structure is rising up by several kelvin in dependence of thermal resistance. The refractive index increases with temperature roughly by 3.10^{-4}.

Both effects change the effective index by 10^{-4} to 10^{-3} but work against each other. So the behavior of broad area devices is not clearly predictable and changes especially with operating conditions. At threshold the carrier effect dominates typically. We have gain but "anti-guiding" caused by the index depression. In general we speak of "gain-guided" devices. The "anti-guiding" leads to optical loss and results in a slight drop in efficiency near the threshold.

Since the carrier density is clamped at threshold the heating effect dominates at operation levels high above threshold. The index depression is overbalanced and we have "normal" index guiding by the higher refractive index in the region of current injection. The efficiency increases slightly but the lateral divergence in general too.

Changing the layer structure in lateral direction a fixed effective index step can be created. One of the easiest ways is to etch the p-side cladding and partly the waveguide layer away. If we replace it by a material with lower index, typically Al_2O_3 or Si_3N_4 are used, the effective index is reduced. A schematic view is given in Fig. 2.11.

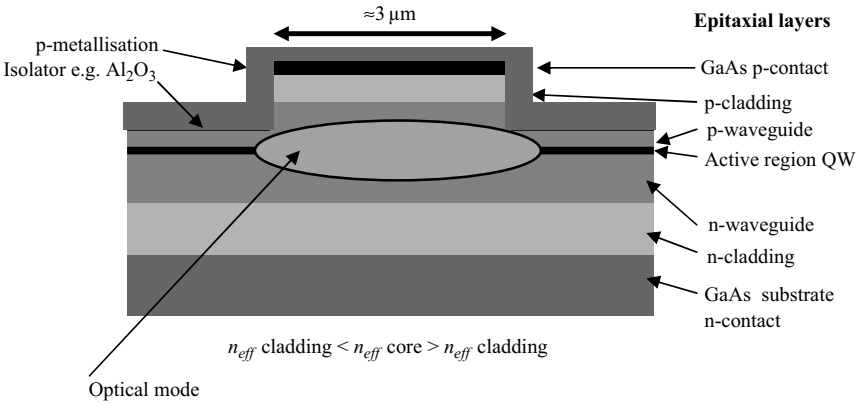

FIGURE 2.11. Schematic of a ridge waveguide structure

The refractive index difference is determined by the etching depth. It should be high enough that the impact on index under operating conditions can be neglected, but on the other hand small enough to achieve at least a few microns for the width of the fundamental mode. In high-power devices such structures were mainly used as mode selection filters in so called tapered lasers described in Chapter 2.5.

2.1.2.3. Longitudinal Modes and Spectral Behavior

The mirrors of a diode laser are fabricated by cleaving the semiconductor crystal perpendicular to stripes and coating the facets. This process delivers nearly ideal plane mirrors and ensures a high crystalline quality. As a consequence, high-power diode lasers are embedded in nearly perfect Fabry–Perot resonators with a highly reflecting mirror on the rear side and a low reflecting mirror on the front side for light extraction. The high material gain allows for a large light extraction. Currently, typical front mirrors exhibit reflectivities of ≈10% for devices with a length of 1 mm, 5% for 2 mm, and even 2% for devices with a length of 4 mm. The low reflectivity of the output mirror ensures a high wall plug efficiency at the expense of an increased sensitivity to optical feedback. Optical feedback may degrade the beam characteristics and modify the spectral behavior.

The resonator length defines the longitudinal mode spacing, adjacent modes are typically of 0.05 nm apart from each other. The spectral width of diode lasers is mainly determined by the gain spectrum. In addition, the gain spectrum is homogeneously broadened due to the high relaxation velocity within the conduction and valence band. Ridge waveguide lasers and partly tapered lasers (see Chapter 2.5) can be operated in a single longitudinal mode. However, the stability of this operating point is poor since the thresholds of adjacent modes are close to each other and upon weak changes in current, temperature or feedback mode hopping will appear. An additional mode filter is required to stabilize the single longitudinal mode regime. Such filters rely on more sophisticated chip technologies and/or additional external cavities. The additional fabrication costs prevent up to now

their use in commercial high-power diode lasers for material processing. Due to the large number of excited modes in broad area devices their spectral width is typically 1 to 2 nm.

2.1.3. Overview – Laser Basics

In the following a set of useful formulas for the description of high-power semiconductor lasers will be given. These formulas are based on relatively simple approximations, but they can give quick hints for understanding and optimization. For detailed descriptions there are several review articles and textbooks available.

Important formulas start with the equation for the lasing threshold in diode lasers with a Fabry–Perot resonator. At threshold the current density must be high enough so that the gain can compensate the internal loss α_i and mirror losses α_m.

$$g_{th} = \Gamma \cdot g_0 \cdot \ln\left(\frac{j_{th}}{j_T}\right) = \alpha_i + \alpha_m = \alpha_i + \frac{1}{L} \ln \frac{1}{R_f \cdot R_r} \tag{2.3}$$

R_f and R_r are the reflectivities of the front and the rear coupling mirrors, respectively. α_i is the value of internal losses, which stems mainly from free carrier absorption. Free carriers are necessary for the current flow. There is a trade off between series resistance and internal loss. It is an optimization process for doping level and light distribution to get a low internal loss. High-power devices achieve losses below $2\,\mathrm{cm}^{-1}$ down to $0.5\,\mathrm{cm}^{-1}$. L is the resonator length. From the equation it can be calculated straightforwardly that with gain values of about $10\,\mathrm{cm}^{-1}$ a threshold with very low values of R_f using a resonator length of 2 mm and longer can be reached. For 2-mm-long devices typical threshold current densities are between $100\,\mathrm{A/cm}^2$ and $200\,\mathrm{A/cm}^2$ at 900 nm and longer wavelengths and between $200\,\mathrm{A/cm}^2$ and $300\,\mathrm{A/cm}^2$ at around 800 nm.

The dependence of output power on pumping current above threshold can be described by a linear relation (2.4).

$$P_{opt} = \eta_d \cdot \frac{\hbar \cdot \omega}{q} \cdot (I_{op} - I_{th}) \tag{2.4}$$

$$\eta_d U = \eta_i \cdot \frac{\alpha_m}{\alpha_m + \alpha_i} \tag{2.5}$$

η_d is the so-called slope efficiency (Eq. (2.5)). To compare diode lasers at different wavelengths it is given by a dimensionless figure. It depends as usual for lasers on the relation between out coupling loss (mirror loss) α_m to the sum of internal losses α_i and out coupling losses multiplied by the efficiency of pumping, the so called internal efficiency η_i. For example if one has a gain of $10\,\mathrm{cm}^{-1}$ available and an internal loss of $2\,\mathrm{cm}^{-1}$ the laser can have mirror loss of $8\,\mathrm{cm}^{-1}$. Such configuration will result in a slope efficiency of 80%. The second factor in Eq. (2.4) gives the wavelength dependent normalization (photon energy divided by elementary charge).

An important factor in getting high-power from the small foot print of a semiconductor laser is the wall plug or better conversion efficiency η_c, the quotient of optical output power to electrical input power.

$$\eta_c = \frac{P_{opt}}{I_{op} \cdot U} = \eta_d \cdot \frac{\hbar \cdot \omega}{q} \cdot \frac{(I_{op} - I_{th})}{I_{op} \cdot (U_d + I_{op} \cdot R_s)}$$

$$= \eta_i \cdot \frac{\alpha_m}{(\alpha_m + \alpha_i)} \cdot \frac{\hbar\omega}{q \cdot (U_d + I_{op} \cdot R_s)} \cdot \frac{(I_{op} - I_{th})}{I_{op}} \tag{2.6}$$

To get a clear view of the physical background this relation can be split in four factors (last part of Eq. (2.6)).

The first factor η_i describes the pumping efficiency. The second gives the relation of output coupling to the total resonator losses. The third factor stands for the relation between the necessary voltage to get current injection to the real voltage of the device. This value includes the additional voltage due to the series resistance inside and outside of the chip. The last factor describes how far above threshold the laser works. Whereas the first factor is near one, that means nearly 100% of injected carriers will create lasing photons inside the resonator, for the other three we have values around 80% which results in a conversion efficiency of typically 50% for high-power diode lasers. Due to the fact that the ohmic loss grows quadratic with current, there exists a maximum for the conversion efficiencies at a certain operating current or equivalent output power. Therefore the development of optimized high-power diode lasers is coupled to the output power target.

Up to now thermal properties of diode lasers were not included. Temperature has an impact on threshold and differential efficiency mainly. The influence on thermal and electrical conductance is not so strong and normally neglected.

Phenomenologically the temperature dependence of threshold current and slope efficiency can be described with the help of exponential functions and two specific constants, T_0 and T_1 – see Eqs. (2.7) and (2.8).

$$I_{th}(T_{j2}) = I_{th}(T_{j1}) \cdot e^{\frac{T_{j2} - T_{j1}}{T_0}} \tag{2.7}$$

$$\eta_d(T_{j2}) = \eta_d(T_{j1}) \cdot e^{\frac{T_{j2} - T_{j1}}{T_1}} \tag{2.8}$$

Here, I_{th} and η_d are measured at the different junction temperatures T_{j1} and T_{j2}. It is very difficult to get values for T_0 and T_1 from first principles, but relatively simple to extract them from measurements. For practical use these constants are determined for every type of diode lasers. There are some common design rules, that high barriers and lower threshold current densities will increase both values, giving lasers with better temperature stability. Typical values are 100 K to 150 K for T_0 and 500 K and more for T_1.

This temperature dependence and the thermal resistance have to be included for an optimization of laser design for high efficiency at high-power output. A simulation process is introduced in the next subsection.

2.1.4. Modeling of Semiconductor Lasers

The efficiency model presented here is primarily designed for optimizing a laser diode, which is based on a given waveguide cross section by adapting the length of its resonator and the reflectance of its front facet and by applying an appropriate operating current. The model is formulated in terms of the differential quantities, i.e., gain, loss, currents, resistances, and power densities are related to infinitely thin slices of the laser resonator. Within the framework of such a theory, it is straightforward to formulate also the wall plug efficiency

$$\eta_W(\Delta T,\ \alpha_m,\ j) = p_{opt}(\Delta T,\ \alpha_m,\ j)/p_{el}(j) \tag{2.9}$$

in terms of the emitted optical power density $p_{opt}(\Delta T,\ \alpha_m,\ j)$ and the applied electrical power density $p_{el}(j)$. Three external parameters are used within the model. ΔT describes the temperature difference between heat sink and active region. For the case of a perfectly reflecting rear facet of the resonator, the loss coefficient is given as $\alpha_m = -\ln(R)/(2L)$, where R stands for the reflectance of the front facet and L for the length of the resonator. The line current density j applied to the laser forms the third external parameter. The electric model

$$p_{el}(j) = U_o j + \rho_s j^2 \tag{2.10}$$

relates the applied electrical power density to the voltage U_o at the pn-junction and to the series resistance ρ_s of the laser diode. The optical model [2.5] consists of three equations

$$p_{opt}(\Delta T,\ \alpha_m,\ j) = \eta_d(\Delta T,\ \alpha_m) \cdot [j - j_l - j_{th}(\Delta T,\ \alpha_m)] \tag{2.11}$$

$$\eta_d(\Delta T,\ \alpha_m) = \eta_i(\Delta T)\alpha_m/[\alpha_i(\Delta T) + \alpha_m] \tag{2.12}$$

$$j_{th}(\Delta T,\ \alpha_m) = j_{tr}(\Delta T) \cdot \exp\{[\alpha_i(\Delta T) + \alpha_m]/g_o(\Delta T)\} \tag{2.13}$$

relating the density of the emitted optical power to the differential quantum efficiency $\eta_d(\Delta T,\ \alpha_m)$ and the threshold current density $j_{th}(\Delta T,\ \alpha_m)$. The fixed parameters of the model – the transparency current density $j_{tr}(\Delta T)$, the internal quantum efficiency $\eta_i(\Delta T)$, the modal loss and gain coefficients $\alpha_i(\Delta T)$ and $g_o(\Delta T)$ – which are not subject to the optimization process, are given by $j_{tr}(\Delta T) = j_{tr}(0)\exp(\Delta T/T_{tr})$, $\eta_i(\Delta T) = \eta_i(0)\exp(-\Delta T/T_\eta)$, $\alpha_i(\Delta T) = \alpha_i(0)\exp(\Delta T/T_\alpha)$ and $g_o(\Delta T) = g_o(0)\exp(-\Delta T/T_g)$, where the T_{tr}, T_η, T_α, T_g represent the corresponding characteristic temperatures [2.6]. In Eq. (2.11), the leakage current density j_l acts as a simple offset. The thermal model describes the power dissipation

$$p_{el}(j) = p_{opt}(\Delta T,\ \alpha_m, j) + \Delta T/\rho_T \tag{2.14}$$

caused by the heat transfer to the heat sink. It allows to compute the thermal rollover of the laser diode and the temperature increase of the active region of the laser diode in comparison to the heat sink [2.7]–[2.10].

The computation of the optimum wall plug efficiency $\eta_W^{(max)}$ is equivalent to searching zeros in a four-dimensional ($\Delta T,\ \alpha_m,\ j,\ \chi$) parameter space, i.e.,

$$\frac{\partial p_{opt}}{\partial \Delta T}[1 + \chi \rho_T p_{el}] + \chi p_{el} = 0 \tag{2.15}$$

$$\frac{\partial p_{opt}}{\partial \alpha_m}[1 + \chi \rho_T p_{el}] = 0 \tag{2.16}$$

$$\frac{\partial p_{opt}}{\partial j}[1 + \chi \rho_T p_{el}] - \frac{\partial p_{el}}{\partial j}[n_W + \chi \rho_T p_{el}] = 0 \tag{2.17}$$

$$p_{el} - p_{opt} - \Delta T/\rho_T = 0 \tag{2.18}$$

where χ represents a Lagrange multiplier introduced to account for the power conservation (Eq. (2.15)). Equations (2.15) and (2.16) both include a term $[1 + \chi \rho_T p_{el}(j)]$. It can easily be shown that this term can never vanish i.e., Eq. (2.16) can be simplified to $\delta P_{opt}/\delta \alpha_m = 0$ and used to express the line current density in terms of ΔT and α_m. It is now straightforward to eliminate the Lagrange multiplier χ by using Eq. (2.15). The final expressions for these quantities are:

$$j = j_{th} - \eta_d \frac{\partial j_{th}}{\partial \alpha_m} \Bigg/ \frac{\partial (1/\eta_d)}{\partial \alpha_m} \tag{2.19}$$

$$\chi = -\eta_W / \left\{ \left[\frac{\partial \ln(p_{opt})}{\partial \Delta T} \right]^{-1} + \rho_T p_{opt} \right\}. \tag{2.20}$$

The zeros in the remaining two-dimensional ($\Delta T,\ \alpha_m$) parameter space must be computed by solving the remaining Eqs. (2.17) and (2.18) numerically.

2.1.5. Laser Characteristic

The computation of the laser characteristic yields a deeper insight into the optimization process. Figure 2.12 shows these characteristics for a high-power laser emitting at 808 nm (see Table 2.3 for the device parameters). The loss coefficient $\alpha_m = 0.30\,\mathrm{mm}^{-1}$ of the device as well as the temperature difference $\Delta T = 9.4\,\mathrm{K}$ between heat sink and active region and the line current density at the optimum operating point (oop) $j_{oop} = 1.57\,\mathrm{A/mm}$ is obtained from the optimization process described above. Along the laser characteristic, the temperature difference ΔT vs. current density is computed by using Eq. (2.18).

Figure 2.12 shows the optical power density p_{opt} as well as the wall plug efficiency η_W and the temperature difference ΔT between heat sink and active region as a function of the current density j applied to the laser. It becomes apparent that the optimum wall plug efficiency is obtained far away from the rollover (ro) $j_{ro} = 7.7\,\mathrm{A/mm}$. Furthermore, the wall plug efficiency drops sharply for current densities below the optimum $j < j_{oop}$ and the temperature difference increases dramatically up to $\Delta T_{ro} = 89.2\,\mathrm{K}$ at the rollover. These results indicate that the operation of the device close to the efficiency optimum helps

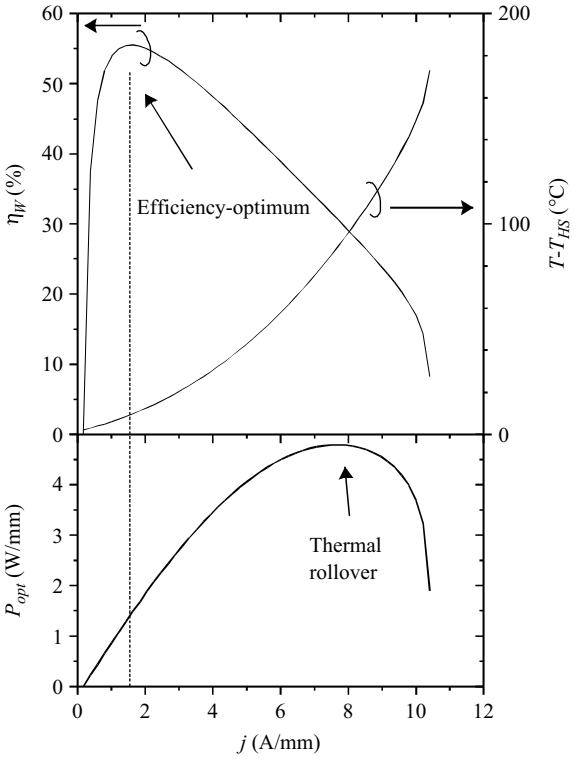

FIGURE 2.12. Optical power density p_{opt}, wall plug efficiency η_W and the temperature difference ΔT between heat sink and active region as a function of the current density j applied to a high-power laser operated at 808 nm

to prevent the devices from thermal stress which in turn results in device degradation.

The change of the wall plug efficiency caused by a varying operating current density j (at constant device length) is given by

$$\left[\frac{\delta\eta_W}{\delta j}\right]^{(N)} = \frac{j_l + j_{th}}{j - (j_l + j_{th})} - \frac{\rho_s j}{U_o + \rho_s j} \tag{2.21}$$

$$\left[\frac{d\eta_W}{dj}\right]^{(N)} = \left[\frac{\delta\eta_W}{\delta j}\right]^{(N)} - \frac{\rho_T j(U_o + 2\rho_s j - \eta_d)}{p_{opt}\left(\rho_T + \left[\frac{\delta p_{opt}}{\delta\Delta T}\right]^{-1}\right)}. \tag{2.22}$$

Equation (2.21) shows that the normalized derivative $[\delta\eta_W/\delta j]^{(N)}$ contains one positive and one negative term. Obviously, the positive term dominates for line current densities close to the threshold. The second, negative term which is driven by the series resistance increases with increasing line current density. The change of the device temperature along the laser characteristic, yields a second, decreasing

contribution which also gains importance with an increasing line current density. This contribution is driven by the thermal resistance.

2.1.6. Measurement of Parameters

To study the properties of real lasers, it is necessary to measure the model parameters. The intrinsic optical parameters, i.e., $\alpha_i(\Delta T = 0)$, T_α, $\eta_i(\Delta T = 0)$, T_η, $j_{tr}(\Delta T = 0)$, T_{tr}, $g_o(\Delta T = 0)$, T_g can be extracted by measuring threshold current and differential efficiency of equivalent uncoated (uc) laser diodes $\alpha_m(L_n) = -\ln(R_{uc})/L_n = \gamma_R/L_n$ differing only in lengths L_n. For these measurements, it is crucial to ensure that heat sink temperatures T_{HS} and corresponding device temperatures coincide. Therefore, the parameters have to be determined using the pulsed measurement with sufficiently short pulses at a sufficiently low repetition rate. The parameter extraction itself relies for the intrinsic optical parameters always on linear functions $Y = mX + b$ with slopes m and offsets b in order to gain accuracy by applying linear regression. Table 2.2. shows the procedure for parameter extraction in more detail. Based on Eq. (2.13), $1/\eta_i(T_{HS})$ and $\alpha(T_{HS})/(\gamma_R \eta_i(T_{HS}))$, i.e., α_i are extracted from offset and slope from $1/\eta_d$ versus L_n plots for different heat sink temperatures T_{HS}.

In a second step, the slope and offset from $\ln(j_{th}(T_{HS}))$ versus $1/L_n$ plots yield $\gamma_R/g_o(T_{HS})$ and $\ln[j_{tr}(T_{HS})] + \alpha_i(T_{HS})/g_o(T_{HS})$ based on Eq. (2.14). By using the already extracted parameter α_i, g_o and $\ln[j_{tr}(T_{HS})]$ can now be extracted. By using the equations for the coefficients, the characteristic temperatures T_α, T_η, T_{tr}, and T_g are finally computed by using the slopes of the corresponding $\ln(\chi)$ versus T_{HS} plots, where χ equals to α_i, η_i, j_{tr} and g_o, respectively.

The line series resistance ρ_S is extracted from measurements of the serial resistance for devices of various length which allows to eliminate the series resistance of the feeding circuitry. The voltage

$$U_o = \frac{hc}{e\lambda} \tag{2.23}$$

Table 2.2. Extraction of the intrinsic optical parameters from pulsed measured j_{th} and η_d at samples of various lengths L_n and heat sink temperatures T_{HS}

Input		Extracted Parameter	
X	Y	Slope	Offset
L_n	$1/\eta_d(T_{HS})$	$\frac{\alpha_i(T_{HS})}{\eta_i(T_{HS})\gamma_R}$	$\frac{1}{\eta_i(T_{HS})}$
$1/L_n$	$\ln(j_{th}(T_{HS}))$	$\frac{\gamma_R}{g_o(T_{HS})}$	$\ln[j_{tr}(T_{HS})] + \frac{\alpha_i(T_{HS})}{g_o(T_{HS})}$
T_m	$\ln(\alpha_i)$	T_α	
T_m	$-\ln(\eta_i)$	T_η	
T_m	$\ln(j_{tr})$	T_{tr}	
T_m	$-\ln(g_o)$	T_g	

can be at best extracted from the measured emission wavelength λ. Finally, the thermal resistance ρ_T which is significantly affected by the assembly of the laser, can be obtained by measuring p_{opt}, p_{el} and the emission wavelength λ at an operating point above threshold under pulsed and continuous-wave (cw) operation. The temperature difference between heat sink and active region under cw operation can be extracted from the difference between the emission wavelengths of pulsed and cw operation. The thermal resistance ρ_T is finally determined by using Eq. (2.18).

2.1.7. Optimizing High-Power Lasers

There is an increasing interest in applying high-power laser diodes for material processing. The increase of wall plug efficiency forms one of the most convincing arguments for their use. Within this context, the optimization of wall plug efficiency represents a generic task to maximize the wall plug efficiency but also to reduce the aging of the diodes.

Table 2.3. shows the parameters extracted for a high-power laser diode emitting at 808 nm and 940 nm. All temperatures are related to a heat sink temperature of 25°C.

TABLE 2.3. Extracted parameters, optimized external parameters result and several characteristic parameters after optimization for a high-power laser diode operating at 808 nm and 940 nm in the AlGaAs/GaAs material system

	808 nm	940 nm	
Extracted parameters			
$\alpha_i(T_{HS})$	0.02	0.01	1/nm
T_α	>300	300	K
$\eta_i(T_{HS})$	1.15	1.08	W/A
T_η	194	>500	K
$j_{tr}(T_{HS})$	0.1	0.13	A/mm
T_{tr}	350	85	K
$g_o(T_{HS})$	0.64	0.18	1/mm
T_g	90	>500	K
U_o	1.53	1.32	V
ρ_S	0.065	0.04	Ω mm
ρ_T	8.2	9.0	K mm/W
Optimization results			
ΔT	9.4	11.1	K
α_m	0.30	0.10	1/mm
j	1.57	2.01	A/mm
Related features			
ΔT_{th}	2.1	3.0	K
J_{th}	0.18	0.25	A/mm
P_{opt}	1.43	1.58	W/mm
η_W	55.5	56.2	%

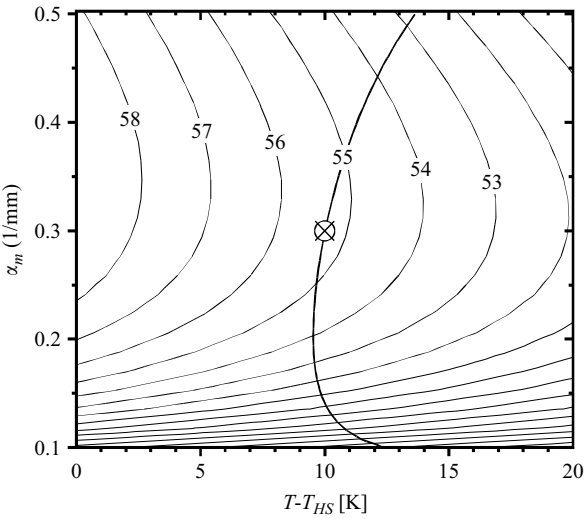

FIGURE 2.13. Contours of wall plug efficiency within the α_m -ΔT plane at constant line current density. The computed optimum and the curve of conserved power are included to illustrate the optimization result

Figure 2.13 shows contours of constant wall plug efficiency (unit: %), computed using Eq. (2.10), for a window in the α_m-ΔT plane close to the optimum. The thick solid line shows the trace of conserved power, i.e., the trace of realistic operating points in the α_m-ΔT plane. The optimum operation point computed using the Eq. (2.15) to (2.18) is also shown. It becomes obvious that the wall plug efficiency drops rapidly, if α_m drops, i.e., if the reflectance of the output facet becomes larger than its optimum value. A decreased reflectance, in contrast, seems to reduce the wall plug efficiency less. As a second result, better thermal connections of the heat sink leading to a lower temperature difference seem to result in a moderately increasing wall plug efficiency.

For a more detailed discussion, it is useful to examine the case of a front facet exhibiting the minimum reflectance accepted by the underlying application. For a front facet with e.g., $R = 3\%$, the optimized laser emits 8.47 W at a length of $L = 5.94$ mm. Starting from this point, the optical power can be further increased by increasing the device length and/or the applied current. Based on these results, it turns out to be useful to optimize the wall plug efficiency under the modified boundary conditions. Figure 2.14 shows the results of the wall plug efficiency and the emitted optical power as functions of the resonator length. Obviously, the wall plug efficiency drops rapidly if the length of resonator is smaller than the optimum length. But it becomes also apparent that the length of the resonator can be increased by another 5 mm at the expense of a moderate decrease $< 2\%$ of the wall plug efficiency. The reduction of the device length to 2 mm, in contrast, leads to a drastic reduction down to 10% of the wall plug efficiency. The wall

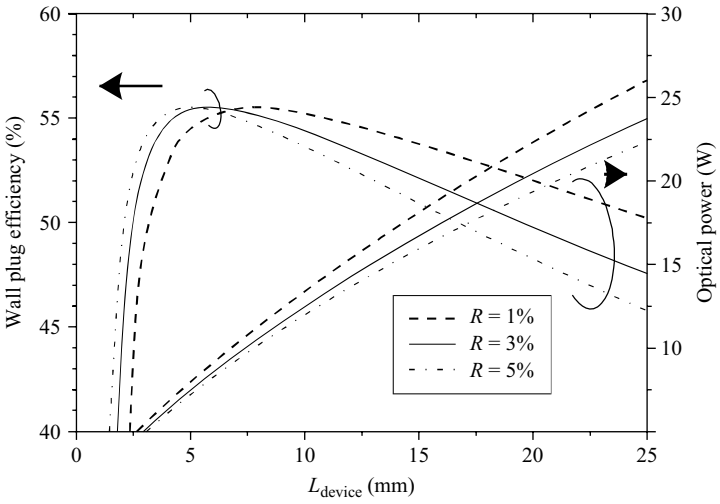

FIGURE 2.14. Optimized wall plug efficiency and corresponding output power as a function of the resonator length of the laser

plug efficiency versus $\log(L)$ drops nearly symmetrically close to its optimum, i.e., doubling and halving of the device length result approximately in the same reduction of the wall plug efficiency. Figure 2.14 shows also that the efficient use of the chip area with respect to the emitted optical power described by the figure of merit FOM $= [P(L)/P(L_{opt})]/[L/L_{opt}]$ drops, i.e., lengthy lasers use the chip area increasingly inefficient. The analysis of the second example in Table 2.3 shows, that a high-power laser diode emitting at 940 nm leads to similar results.

2.2. Manufacturing Technology

Martin Behringer

The most elementary semiconductor laser diode consists only of an optical active medium on a crystalline substrate having metal contacts for electrical current injection and two crystal facets to form an optical resonator. Such a device requires only few fabrication steps, namely, epitaxy, evaporation of the metal layer, cleaving the cavity facet, and cutting the chips out of the wafer. Sophisticated designs increasingly optimize the optical waveguiding as well as the light generation. For all devices, the fabrication starts with a crystalline substrate, the wafer, and continues with the epitaxial growth of the crystalline layers. Then, the surface is patterned into conducting and isolating areas. Finally, the end facets forming the resonator have to be manufactured. This section gives a brief description of state of the art epitaxial techniques and semiconductor technologies in respect of processing laser diodes.

2.2.1. MOVPE and MBE

A variety of epitaxial techniques for crystal growth have been developed during the last decades. For high-power laser diodes, epitaxial growth of III-V semiconductors, especially GaAs, plays a crucial role. Liquid phase epitaxy, growing the layers out of a melt, was used for a long time due to advantages of easy growing of very thick layers and parallel growth on many wafers at the same time. Today, crystalline growth out of the gas phase is preferred. Among these techniques, MOVPE and MBE are most commonly applied since they offer a good control of composition and thickness of the deposited layers and thus allow for the fabrication of complicated laser structures.

The principles of MOVPE (metal-organic vapor phase epitaxy) are often attributed to Manasevit et al., who worked during the 1960s [2.11, 2.12]. However, earlier activities in the field of MOVPE have been reported [2.13].

Figure 2.15 shows a typical MOVPE reactor. For growth, the substrates are moved from the loading position (a) to the growth position (b). During the growth, metal-organic precursors and hydrides are lead into a reactor, where they are decomposed and deposited on the heated substrate. This deposition usually takes place at temperatures in the range from 600°C to 800°C [2.14, 2.15]. Homogeneity, smoothness, and good electro-optical data form the main quality criteria of epitaxial layers which in turn determine performance parameters of the high-power lasers.

MOVPE has experienced a dramatic development during the last few years. The design of MOVPE reactors became more sophisticated, allowing better control of the composition and thickness (down to only a few monolayers) of the epitaxial layers. The list of improvements starts with the quality of the substrates (etch pit densities $<1{,}000\,\mathrm{cm}^{-2}$), continues with the homogeneity of the growth on the wafer, and ends with the reduction of contaminants in precursors used for growth. As a result, epitaxial layers of higher electron and hole mobility and less optical absorption at higher homogeneity and reproducibility became available. In parallel, a basic modeling of the MOVPE process has been established [2.14–2.17]. However, due to the complexity of these processes, the models suffer still from certain deficiencies. During the last years, in situ measurement allowed

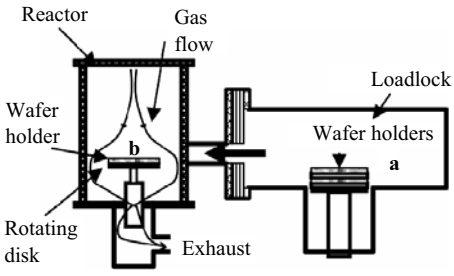

FIGURE 2.15. Schematic diagram of an MOVPE growth reactor and process

for an exact control of MOVPE parameters, such as the temperature of the wafers, the deposition rate and the composition of the deposited layers [2.18]. For the next years, these tools will enable the automated control of highly sophisticated MOVPE processes.

The option of large-scale production of highly advanced devices as well as their versatility are the main advantages of MOVPE over other epitaxial techniques. The use of hazardous materials and the complexity of the processes are its main disadvantages. However, today, industry learned to handle these processes well and therefore MOVPE is a widespread tool in III-V semiconductor industry. Due to the increasing size of the substrates and reactors, the cost of the devices could be significantly reduced. Whereas some years ago only a maximum of three 2-inch wafers could be processed at a time, current production reactors can process up to a hundred 2-inch wafers, or an equivalent number of 3- or 4-inch wafers [2.19, 2.20].

MBE (molecular-beam epitaxy) offers another option to fabricate similarly complicated devices. In contrast to MOVPE, MBE uses molecular beams of the different elements, without using a carrier gas or a precursor. Therefore, besides the good control over composition, doping, and layer thickness, MBE offers a further increase of the purity of the epitaxial layers. The main disadvantages of the MBE are the further increasing equipment cost and the interdependency between homogeneity of the layers and the homogeneity of the molecular beam which limits its use for large-scale production. Nevertheless, today both epitaxial growth techniques are well established. World records concerning efficiency, emitted power, device lifetime, and electro-optical characteristics have been achieved by using both techniques. Against this background, the decision in favor of the techniques is usually driven by secondary arguments like intellectual property and fabrication experience.

To summarize, today's high-power semiconductor lasers require:

- precise control of doping levels,
- precise control of layer composition,
- exact limitation of impurities in the layers,
- the ability to grow thin layers (fractions of a monolayer) and also thick layers up to a few micrometers,
- the ability to change composition and doping conditions during growth,
- high crystalline quality,
- good reproducibility and homogeneity.

Both growth techniques satisfy these requirements and are being used today.

2.2.2. Laser Processing

After epitaxial layer deposition, laser processing of the wafers can be carried out. Here the electrical contacts for current injection and the laser facets forming an optical cavity are realized. Figure 2.16 shows a typical broad area diode laser which consists of a substrate, epitaxial layers, grooves in the semiconductor

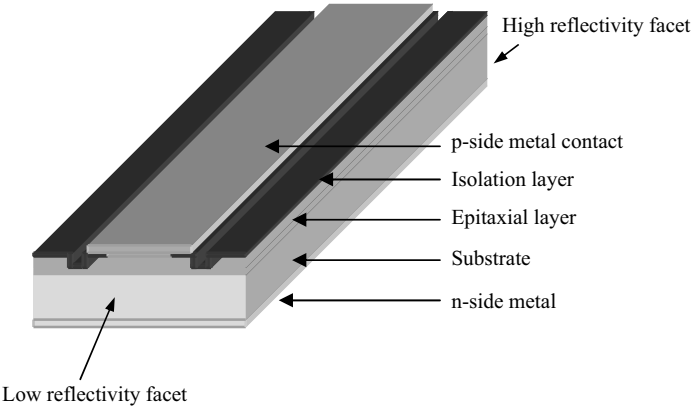

FIGURE 2.16. Typical design of a semiconductor diode laser

layers limiting the current spreading and preventing lasing perpendicular to the intended direction, isolating layers defining the region for current injection, metallic p- and n-contacts of the diode and the mirrors, forming a resonator. The following section describes the processing sequence from the semiconductor wafer to the final device.

In the first lithographic step, the active area is defined and transferred into the semiconductor epitaxial layers by using an etching step.

2.2.2.1. Photolithography and Patterning

As depicted in Fig. 2.17a, patterning of semiconductors starts with depositing a thin photo resist layer. This layer changes its physical and chemical characteristics when exposed to light. Illumination can be done either by direct writing with, e.g., a laser beam or an electron beam into the resist or by exposure with a master pattern. This master pattern can be 1:1 when contact of the wafer with the photo mask exists, or 1:4 or 1:5 when projection illumination is performed, using a reticle. Masks are, roughly spoken, transparent substrates with an opaque, usually metallic pattern that allows to illuminate certain areas and prevent illumination in other areas on the wafer. As shown in Fig. 2.17a, the photo mask is placed above the photoresist coated wafer and uniformly illuminated. Depending on the type of resist, the illuminated or the not illuminated fraction of the resist is washed out during the development process (see Fig. 2.17b). The resist pattern is transferred into the epitaxial layers by a subsequent etching process, e.g., wet chemical etching with an acid (see Fig. 2.17c), which ideally leaves regions covered by the resist unaffected.

Photoresists have to meet the following requirements:

- sensitivity at the wavelength used for lithography,
- chemical resistance against wet chemical solvents and dry chemical processes,
- complete stripping of the remaining resist at the end of patterning.

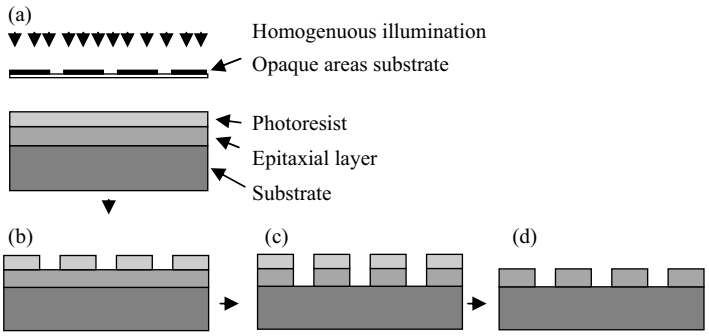

FIGURE 2.17. Photolithography: process sequence: (a) illumination of photoresist coated wafer, (b) developing and transfer of pattern into photoresist, (c) structuring of semiconductor layer, (d) removal of photoresist after patterning of wafer

The best photolithography process is selected by using the following arguments:

- shapes and sizes (dimensions) to be patterned,
- number of layers to be positioned on top of each other,
- required precision of overlay alignment needed for the device,
- wafer size and throughput in production.

Mask exposure offers the advantages of massive parallel processing, good pattern overlay, high resolution, high flexibility in defining patterns, high degree of automation, and almost unlimited possibility for rework on errors. It is one of the most important tools in semiconductor technologies today. Further information about this topic can be found in the literature [2.21–2.23].

Patterning can be done using wet chemical etching or dry chemical and/or physical etching techniques. Wet chemical etching represents a cost-effective, well established process for parallel processing of large areas and/or many wafers at a time. The solvents are chosen depending on the material. For wet chemical etching, also the crystal orientation can massively influence the etching speed and the vertical profile of the etched semiconductor surface. However, semiconductors of certain compositions cannot be etched by wet etching. Another possibility is etching from a gas phase or a plasma. For further details, see [2.24].

After etching, the resist is removed and the pattern that was once designed on the photomask has been transferred into the semiconductor (Fig. 2.17d). For defining the current injection area, an insulating layer is deposited onto the wafer surface, as can be seen in Fig. 2.18b.

2.2.2.2. Deposition of Dielectrics

Dielectrics are commonly deposited using plasma-enhanced chemical vapor deposition (PECVD), sputter deposition or evaporation. PECVD is also known as glow discharge chemical vapor deposition. It uses electron energy (plasma) as the activation method to enable deposition at low temperatures ($T < 500°C$) and

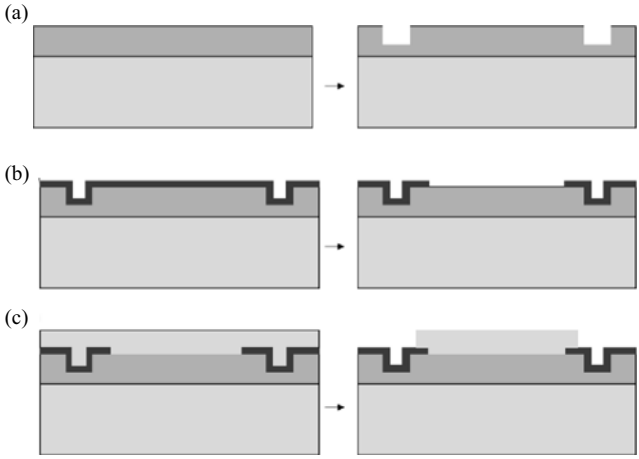

FIGURE 2.18. Process sequence in device technology: (a) structuring of semiconductor, (b) deposition of isolating layer and patterning, (c) metallization and patterning

at reasonable deposition rates. Supplying electrical power at a sufficiently high voltage to a gas at reduced pressures (<1.3 kPa), results in the breaking down of the gas and generates a glow discharge plasma consisting of electrons, ions and electronically excited species. The vapor reactants are ionized and dissociated by electron impact, hence generating chemically active ions and radicals that undergo the heterogeneous chemical reaction at or near the heated substrate surface and deposit the thin film. The versatility of PECVD has led to rapid growth, and this technology has become a very important processing method for the deposition of thin films and coatings for a wide range of applications, including dielectrics (e.g., SiO_2, Si_3N_4, AlN) for microelectronics and optoelectronics; refractory ceramic materials (e.g., SiC, TiN, TaN, Al_2O_3) used for hard coatings, protection against corrosion, oxidation, or as diffusion barriers; and metal films (e.g., W, Mo, Al, Au, Cu) for micro-electronics and for protective coatings. Compared to other deposition methods, PECVD has the following advantages:

- low operating temperature,
- fast processing time,
- good adhesion,
- controllability of the mechanical strain
- low pinhole density,
- very good step coverage,
- compatibility with pattern transfer processes, and
- adequate electrical properties.

In Fig. 2.19 a schematic of a PECVD rector is depicted. The wafers are carried on top of a carrier plate. Between the plate and an electrode, a plasma is generated and the dielectric is deposited onto the wafer.

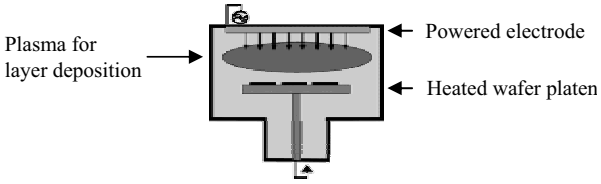

FIGURE 2.19. Schematic diagram of an PECVD reactor for dielectric layer deposition

After depositing the layer on the whole wafer area, the insulation is removed again from those areas of the chip, where the electrical current has to be injected, as shown in Fig. 2.18b. This can be achieved using photo techniques and etching in the same way as described above. Finally, a metal contact is deposited onto the wafer, as can be seen in Fig. 2.18c. The metal is deposited on the whole wafer again and removed after photolithographic definition of the contact structure and etching.

2.2.2.3. Metallization

The metal layer or layer stack is deposited either by evaporation or by sputtering. The metal area has to allow for:

- efficient current injection into the semiconductor,
- good current spreading over the whole contact area,
- good removal of waste heat, that is generated in the device and
- stable mechanical contact to the surrounding package.

Metal contacts are applied to both sides (p- and n-side) of the diode. Depending on the semiconductor and the doping different metals are chosen. The most commonly used materials on p-type doped GaAs are platinum (Pt), titanium (Ti), chromium (Cr), and gold (Au), on n-type doped GaAs germanium (Ge), titanium (Ti), nickel (Ni), and gold (Au) are used. For further details on what metal to chose and how to form ohmic or Schottky like contacts, please consult [2.25, 2.26].

2.2.3. Mirror Coating

For the definition of the laser resonator, the wafer is finally cleaved into bars whose facets are to be coated with dielectric mirrors. For realizing very precise facets, the crystalline structure of the semiconductor is of great advantage. As many compound semiconductors used for optoelectronics have a cubic lattice, the crystal can be cleaved in a way that the facets are perfectly parallel toward each other automatically. For mirror deposition, the cleaved bars are stacked on top of each other as shown in Fig. 2.20. The bars are stacked into special specimen holders for homogenous layer deposition. The design of the bar holders varies from about 50 to more than 500 bars. The special design of theses holders often is proprietary and is normally not published. The coatings are deposited in a vacuum

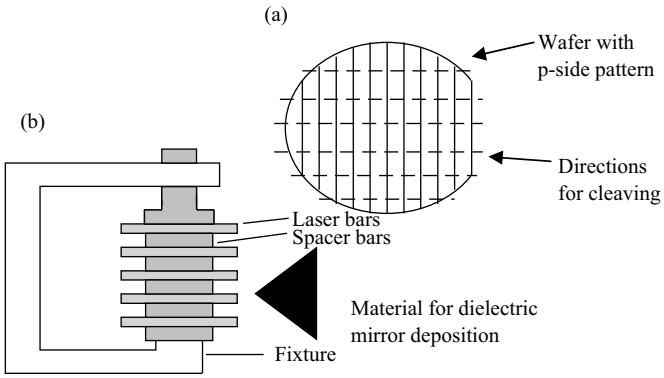

FIGURE 2.20. Mirror preparation: (a) cleaving a wafer and preparing laser bars, (b) stacking of laser bars for mirror deposition

system. While the mirror on the rear side has a reflectivity of almost 98% (high reflectivity side, HR), the front mirror allowing for light extraction has a much lower reflectivity (anti reflection side, AR). Therefore, the mirrors have to be deposited in subsequent fabrication steps.

The coatings for the facets have to provide the following properties:

- chemical and mechanical stability,
- good adhesion,
- low mechanical stress,
- high transparency at the laser wavelength and
- tunable optical properties.

These properties are crucial to obtain excellent behavior with respect to device lifetime and catastrophic optical mirror damage. Today, several different technologies for mirror processing are being used. The differences lie in the facet preparation and in the coating materials. The cleaving can be done either in vacuum or in normal atmosphere and the native oxide on the bars can be removed or transformed into some other material like AlN. For infrared high-power diode lasers, typical material combinations to obtain high reflectivity are: SiO/TiO or AlO and Si. Low reflectivity is normally realized using AlO or SiON. As the mirror has to sustain high optical field densities, only minimal deviations of this fabrication step can be accepted. Depending on what technology is being used, estimates on the costs for mirror deposition vary between $ 100 and only a few dollars per laser bar. For further information see [2.27–2.30].

2.2.4. Production and Processes

Today, high-power lasers are mainly made in the arsenic or phosphorus containing III/V-material system. In the future, power lasers based on (AlInGa)N will also be

available. Besides the pure manufacturability of lasers, costs play an increasingly important role. Production with little problems and high yield has to be considered when choosing the design of the laser chip, the technology of production, and the size of the individual unit. Therefore, after defining the requirements for the laser diode, the most simple design using the most simple processes that can fulfill the requirements for the laser diode sufficiently have to be chosen for a "production friendly" development. A less complicated design often results in lower rework rates; a well-established technology results in a higher uptime of machinery, and a smaller chip is more tolerant of manufacturing and handling errors than bigger laser bars. Also the degree of automation plays a crucial role in manufacturing costs. Normally, a higher degree of automation results in higher yield due to reduced mishandling, leading to lower production costs per unit on one side; but it results in higher costs of ownership on the other side. Therefore, depending on the volume, one has to choose the right equipment for production. A further factor is the lot size and the wafer size. Normally, not all areas of a semiconductor wafer can be used for diode laser production. For example, the outer parts or each wafer normally have higher defect densities and are consequently neglected in production. Therefore, it is more efficient to produce on a larger wafer scale if the handling does not cause additional new problems. One always has to consider:

- needs,
- volume,
- design,
- technologies available and
- expertise at hand

when designing the manufacturing process for an optoelectronic device.

2.3. Chip Characterization Methods and Measurements

Konstantin Boucke and Jens W. Tomm

2.3.1. Standard Characterization Methods

The reliable measurement of electrical, optical, and thermal properties is an essential tool during development and qualification of diode laser devices, but it is also necessary to supervise the quality of laser devices and mounting processes during production. Especially those parameters that are either of principal importance for the laser performance – such as output power and efficiency – or those that are indicators for reduced device reliability – such as burn-in and lifetime test results – have to be measured with high reproducibility and on a broad statistical basis, making it necessary to integrate these measurements into the production chain. This distinguishes these "standard" characterization methods from more advanced measurements which aim at a deeper understanding of diode laser devices in research and development.

2.3.1.1. Electro-Optical Characterization

The electro-optical characteristics determine the basic performance of the laser bar in terms of optical output power and electrical power consumption as a function of the driving current. Therefore, each laser bar undergoes an electro-optical characterization; some laser bar manufacturers perform an electro-optical characterization of the laser bars *before* mounting, and all manufacturers perform these measurements on the mounted bars before and after an initial device burn-in.

The results of a specific electro-optical characterization determines whether the measured laser bar meets its basic specifications, while the homogeneity and statistics of the characterization results over a number of identical bars yields information about the quality and stability of the production process. In many cases, specific problems in the production chain can be identified by analyzing abnormal electro-optical characterization results. Therefore, electro-optical characterization – although being a comparably simple measurement – is one of the most powerful tools for quality control in the production of laser bars.

For electro-optical characterization, the mounted laser bar is electrically contacted and connected to an appropriate cooling structure. For measuring the optical output power, typically an integrating sphere with attached photo diode is used instead of a thermal measuring head, because this measurement method is significantly faster and shows fewer deviations due to different beam divergence angles for uncollimated beams. Additionally, a spectrometer may be attached to the integrating sphere to simultaneously measure the spectral intensity distribution of the laser bar.

By increasing the driving current in a stepwise fashion from zero to a device-specific maximum current, the characteristic curves, optical power versus current $P_{opt}(I)$, voltage versus current $U(I)$, and peak wavelength versus current $\lambda_0(I)$ are measured, and the efficiency as a function of current is calculated.

$$\eta(I) = \frac{P_{opt}(I)}{I \cdot U(I)} \tag{2.24}$$

From the characteristic curves, further parameters are derived, such as the series resistance, the threshold current, and the slope efficiency:

$$\text{Series resistance } R_s[\Omega] \qquad R_S = dU(I)/dI \tag{2.25}$$

$$\text{Threshold current } I_{th}[\text{A}] \qquad I_{th} : d^2P_{opt}(I)/dI^2 = \max \tag{2.26}$$

$$\text{Slope efficiency } \eta_s[\text{W/A}] \qquad \eta_s = dP_{opt}(I)/dI \quad (I > I_{th}) \tag{2.27}$$

A detailed analysis of the characteristic curves gives information on the acceptable operation range and the load limits of the measured laser bar in conjunction with the chosen mounting technology and package type (Fig. 2.21). Ideally, the operating point of the laser bar should be close to the point of maximum efficiency. The pump current at which the maximum efficiency is reached can be adjusted, e.g., by changing the resonator length or the reflection coefficient of the front facet.

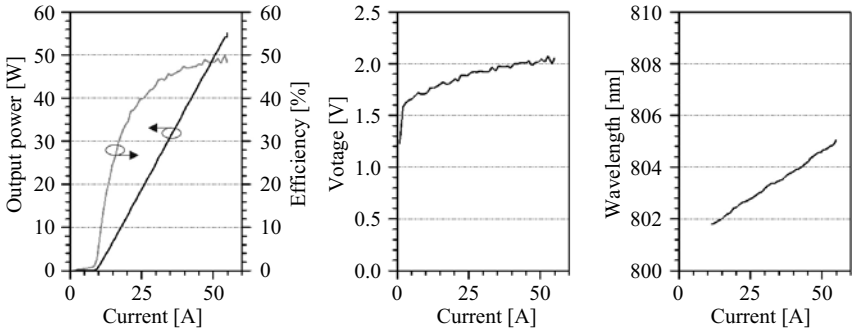

FIGURE 2.21. Sample characteristic curves, measured using an 808-nm broad-area laser bar with 19 emitters, 150 μm emitter width, 500 μm pitch

Critical for long-term operation of the laser bar is excessive thermal load. As a rule of thumb the operation temperature should not exceed 60°C, measured at the pn-junction. A measure for the temperature rise at the pn-junction is the emission wavelength of the laser. Typically, for GaAs laser devices the emission wavelength shifts with 0.27 to 0.29 nm/K toward longer wavelengths; therefore a temperature rise of 35°C from a base temperature of 25°C to 60°C corresponds to a wavelength shift of approximately 10 nm.

Increased operation temperatures lead to an increased threshold current and a reduced slope efficiency of the laser (see Chapter 2.1.3.), thus reducing the overall efficiency. This also takes place when the pump current is increased. Then the thermal degrading efficiency leads to the "thermal rollover" of the laser, indicated by a bowing of the P-I curve. Thermal rollover is a secure indicator of thermally overstressing the bar, resulting in a strongly reduced lifetime.

Different definitions are used for a quantitative determination C_{TRO} of the thermal rollover, either being based on the curvature of the P-I curve or the deviation of the P-I curve from an ideal straight line, measured at a given current level I_{TRO}:

$$C_{TRO} \sim \left.\frac{d^2P(I)}{dI^2}\right|_{I=I_{TRO}} \quad \text{or} \quad C_{TRO} \sim [\eta_S \cdot (I - I_{th}) - P(I)]_{I=I_{TRO}} \qquad (2.28)$$

Besides the characteristic curves also the wavelength spectrum of the laser bar is of importance when judging the quality of a laser bar and it's packaging. A narrow Lorentzian-shaped spectrum without additional peaks is a positive indicator, while spectral broadening or a second peak in the spectrum can indicate defects or strong inhomogeneities in the chip material as well as packaging induced stress or defects. Typically, the spectral width of a state of the art broad area laser bar is between 1.5 and 2 nm (FWHM).

The following table summarizes typical electro-optical data of state of the art broad area laser bars with different emitter structures and different wavelengths.

TABLE 2.4. Typical electro-optical data for state of the art power laser bars

	808 nm 25 emitters	808 nm 19 emitters	980 nm 25 emitters
Cavity length	1.2 mm	1.2 mm	1.5 mm
Emitter width/pitch	200 µm/400 µm	150 µm/500 µm	200 µm/400 µm
Fill factor	50%	30%	50%
Max. current	65 A	50 A	70 A
Max. output power	60 W	50 W	55 W
Max. voltage	2.0 V	2.1 V	1.8 V
Max. efficiency	55%	55%	65%
Threshold current	14 A	9 A	12 A
Slope efficiency	1.15 W/A	1.15 W/A	1.05 W/A
Fast axis divergency[1]	60°	60°	65°
Slow axis divergency[1]	8°	8°	8°
Spectral width (FWHM)	2 nm	2 nm	2.5 nm
Degree of polarisation	>90%	>90%	>95%

The thermal operation conditions of the laser bar are mainly governed by the thermal resistance R_{th} of the laser package,

$$R_{th} = \frac{\Delta T}{P_{therm}} \tag{2.29}$$

where ΔT is the temperature rise in the pn-junction caused by the thermal power P_{therm} dissipated by the laser bar during operation (see Chapter 3.3). The thermal resistance is a function of the laser bar structure as well as of the package type and structure. Since the thermal resistance – and the resulting operating temperature as a function of the current – is the main factor limiting the average output power of the laser bar, and because a typically high values of the thermal resistance are a good indicator for failures in the packaging process, the measurement of the thermal resistance is also of great importance for design and diagnostic purposes.

A very accurate and easy method to obtain the thermal resistance makes use of the temperature dependence of the laser wavelength to measure the temperature rise in the pn-junction. To determine the precise thermal wavelength drift factor $\Delta\lambda_{th} = d\lambda/dT$ of a given laser structure, the emission wavelength of the laser has to be measured at different temperatures and in the "power-free" limit, $P_{therm} = 0$, meaning with very short pulse durations (<1 µs) and a low duty cycle (<0.1%). With knowledge of the drift factor $\Delta\lambda_{th}$ and the emission wavelength in the "power-free" limit, $\lambda(P_{therm} = 0)$, the thermal resistance can be directly calculated

[1] Full angle, 95% enclosed power.

from the electro-optical characterization data:

$$P_{therm} = U(I) \cdot I - P_{opt},$$
$$\Delta T(P_{therm}) = \frac{\lambda(P_{therm}) - \lambda(P_{therm} = 0)}{\Delta\lambda_{th}}$$
$$\Rightarrow R_{th} = \frac{\Delta T(P_{therm})}{P_{therm}} \tag{2.30}$$

2.3.1.2. Far-Field and Beam Divergence Angles

For the proper design of optics, such as fast-axis and slow-axis collimators (see Chapter 4.2), the knowledge of the angular beam distribution, equivalent to the far-field of the laser bar, is required. In fast-axis, perpendicular to the epitaxial layers of the laser, the laser beam can be well approximated by a Gaussian beam: The thickness of the waveguide layers is small enough to support only the fundamental mode. An important information for the optics design is the beam divergence angle, because it dictates the required numerical aperture of the collimation optics and yields the beam width in fast direction after collimation, as a function of the focal length of the optics.

In slow-axis direction, the beam profile is dominated by the presence of higher-order modes, and the detailed profile depends on the laser structure and type. However, also in slow-axis typically only the beam divergence angle is required as a design parameter.

The measurement of the far-field intensity distribution of a laser bar is performed by rotating the bar around its vertical and horizontal axes, with the turnpoint in the center of the front facet. The intensity as a function of the angular position is detected by a photo diode behind a pinhole. To avoid distortions of the measured far-field, the distance between laser bar and the pinhole has to be large enough: Due to the lateral extension of the laser bar in slow-axis direction, the detector receives beams under different angles from the left-most and right-most emitters of the bar, resulting in a limited angular resolution of the measurement (Fig. 2.22). As seen from the detector, in the center position, the angle between the edges of the laser bar is given by

$$\tan\left(\frac{\Delta\alpha}{2}\right) = \frac{b}{2d} \quad \Rightarrow \quad \Delta\alpha = 2\arctan\left(\frac{b}{2d}\right) \tag{2.31}$$

For all other detector positions on a circle with radius d the angle $\Delta\alpha$ is smaller. For a 10 mm bar, the calculation shows that a distance d of approximate 1 m is required to achieve an angular resolution of $\Delta\alpha < 0.5°$.

By rotating the laser bar around fast and slow axes, a two-dimensional scan of the far-field intensity distribution $I_{FF}(\varphi, \theta)$ can be generated. Under the assumption that the fast-axis and slow-axis are precisely aligned to the rotational axes of the measurement set-up, the axes are independent of each other and it is sufficient to

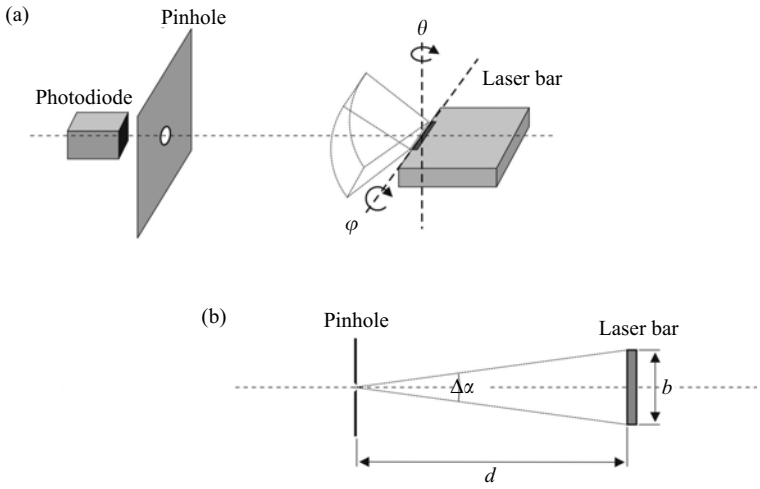

FIGURE 2.22. (a) Schematic set-up for the far-field measurement of a laser bar. (b) Determination of the minimum required distance between laser bar and detector

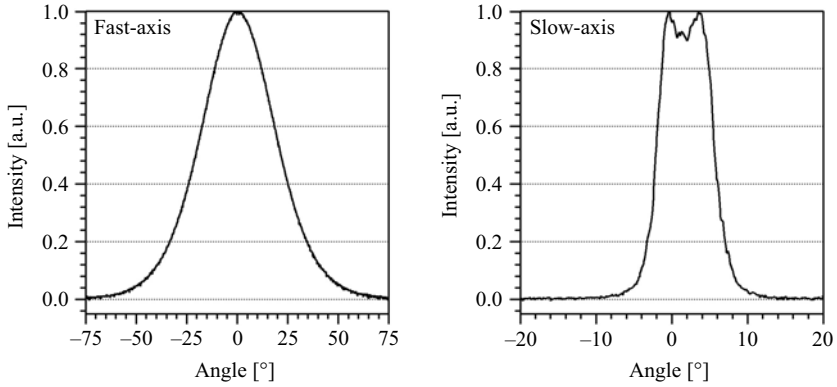

FIGURE 2.23. Fast-axis and slow-axis far-field intensity distributions of a standard broad area laser bar

measure only one-dimensional profiles along fast and slow axes (Fig. 2.23). From these profiles, the fast- and slow-axis divergence angles can be calculated.

For the divergence angles different definitions are in use: The definition of the beam radius and divergence angle by the decrease of the intensity to $1/e^2$ of the maximum intensity is derived from the theory of Gaussian beams. A general parameter to characterize the width of a distribution is the "full width at half-maximum" (FWHM) criterion. Finally, motivated by the practical need of achieving a certain transmission efficiency through optics with limited aperture,

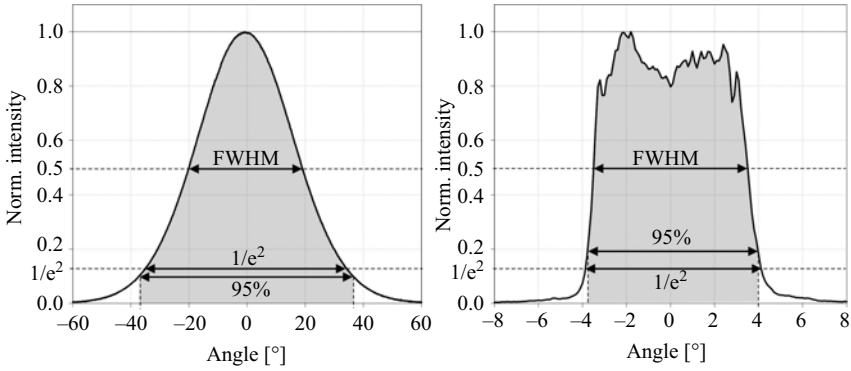

FIGURE 2.24. Determination of divergence angles according to different definitions

the criterion of 95% power inclusion is defined.[2] Figure 2.24 shows the different definitions for the divergence angle with typical fast-axis and slow-axis far-field intensity distributions.

In fast-axis, all commercially available high-power diode lasers show an approximately Gaussian far-field intensity distribution.[3] Varying values of the divergence angle result from differences in the epitaxial layer structure of the laser: so-called LOC (large-optical-cavity) structures are now widely used to reduce the fast-axis divergence angle. The reduction of the fast-axis divergence angle is important in order to enable the use of fast-axis collimation optics with smaller numerical aperture, being less expensive and less sensitive against aberrations and misalignment. During recent years, optimized laser designs led to a reduction of the fast-axis divergence angle from 80° down to 60° or even 45° for some laser types (see Fig. 2.25).

Also, in slow-axis different far-field patterns can be observed, depending on the lateral laser structure. Standard broad area lasers show a top-hat-like far-field, while especially the so-called "multi-stripe" geometry tends to a double-lobed far-field. By optimization of the laser structure, material parameters, and processing, a reduction of the divergence angle has also been achieved in slow-axis . However, while the reduction of fast-axis divergence mainly serves the simplification of the collimation optics, the divergence reduction in slow-axis directly indicates

[2] As a matter of fact, this criterion is not based on "enclosed power" but on "enclosed linear power density," because the two-dimensional, angular intensity distribution is only integrated along one axis (fast-axis or slow-axis) to obtain the divergence angle for fast-axis or slow-axis. Combined for both axes, this criterion corresponds to a rectangular aperture with dimensions in fast- and slow-axis chosen appropriately to transmit $(95\%)^2 \cong 90\%$ of the total power.

[3] Slight deviations from the Gaussian shape arise from the fact that the zero-order mode of a planar waveguide is not precisely a Gauss mode.

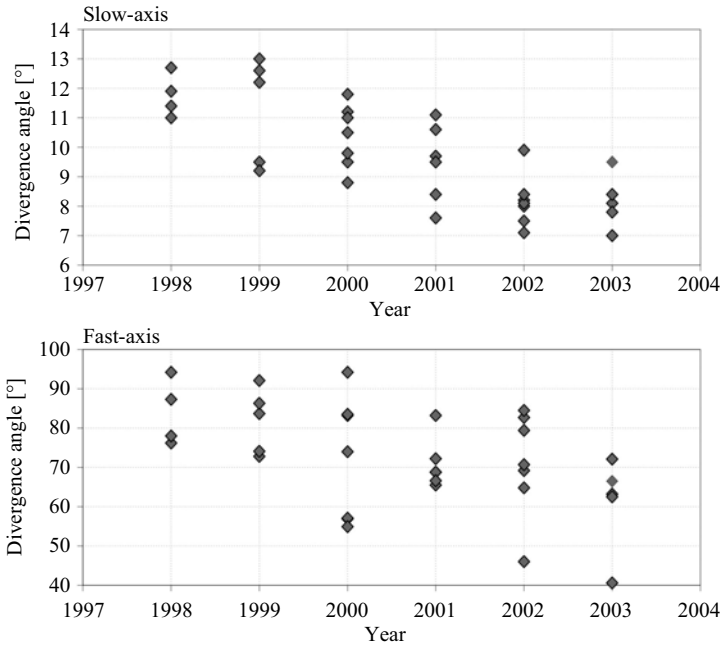

FIGURE 2.25. Development of the fast-axis and slow-axis divergence angles (full angle, 95% enclosed power) during the last years, according to measurements on commercial and R& D laser bars of different types and from different sources. In spite of the large variation of the values between different laser bar types, a general trend to reduced divergence angles in both axes can be seen (Measurements performed at the Fraunhofer Institute for Laser Technology)

an improvement in beam quality when comparing laser structures with the same stripe width.

While the fast-axis far-field typically shows no dependence on the operation current when above the threshold, in slow-axis most high-power diode lasers show some increase of the divergence angle with increasing current (Fig. 2.26). Different mechanisms contribute to this effect: The increased current leads to a stronger current spreading and higher temperature gradients between the center and the edges of each emitter, resulting in a widening of the far-field pattern. Additionally, at higher operation currents, the filamentation of the intensity distribution is amplified, reducing the beam quality and thus enlarging the divergence angle.

2.3.2. Advanced Characterization

This section deals with several analytical tools and techniques which can be applied to “cm-bars” *additionally* in order to learn more details about their performance and reliability limits as well as to identify weak points of the device design or the

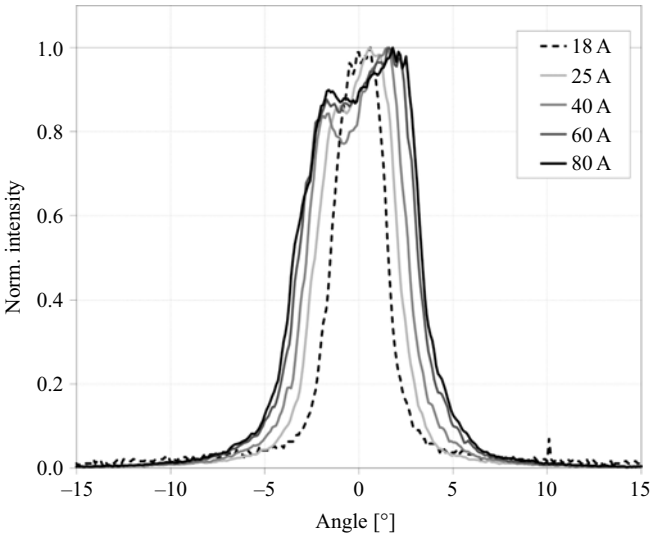

FIGURE 2.26. Change of the slow-axis far-field intensity distribution with increased operation current, measured on an 808-nm laser bar

technology applied. The application of these techniques offers additional chances to locate sources of degradation and for obtaining insight into the microscopic processes that affect the devices during operation.

2.3.2.1. "By-Emitter" Analysis of Standard Parameters

Emission wavelength, power, line width, and thermal tuning rate are standard device parameters (see section 2.3.1). In some cases it is useful to measure these parameters separately for each single emitter of a "cm-bar," since knowledge of standard parameters on a "by-emitter-scale" provides information about bar uniformity. Thus "by-emitter analysis" allows us to identify defective emitters, but it also provides information about packaging-induced stresses and defects [2.31, 2.32]. Figure 2.27 shows the emission pattern of a "cm-bar" array consisting of 19 emitters at 22°C and 58.5°C heat sink temperature. The pattern is detected by a CCD-camera mounted to the exit of a monochromator. As expected for increasing temperature, the emission wavelength is shifted toward the infrared according to the temperature dependence of the energetically lowest quantum-well transition, which is responsible for lasing. In addition, the wavelength homogeneity across the array is substantially changed. The "bow-like" behavior (top) is replaced by an almost uniform distribution (bottom). From such pattern one can easily determine "thermal" tuning rates for single emitters which differ substantially. These tuning rates are influenced by a variety of effects, among others (a) local temperature, (b) packaging-induced strain, and (c) all kinds of non-homogeneities, which are built into the device during wafer fabrication or epitaxy.

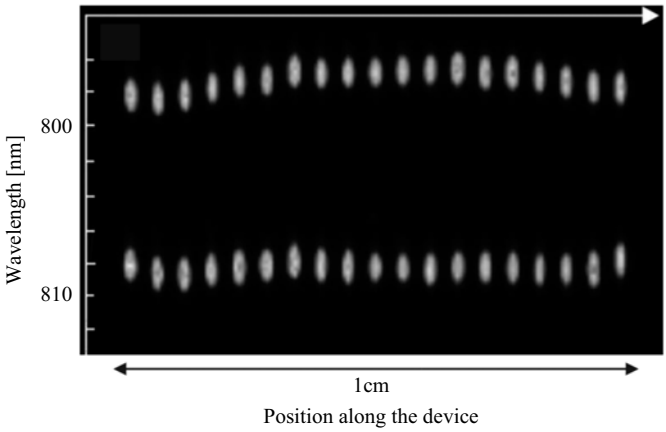

FIGURE 2.27. Emission pattern of a "cm-bar" array consisting of 19 emitters at 22°C (top line of emission spots) and 58.5°C (bottom line of emission spots) base heat sink temperature measured by a thermistor that is located about 3 mm off the actively cooled heat sink of the array. This pattern is detected by a CCD-camera

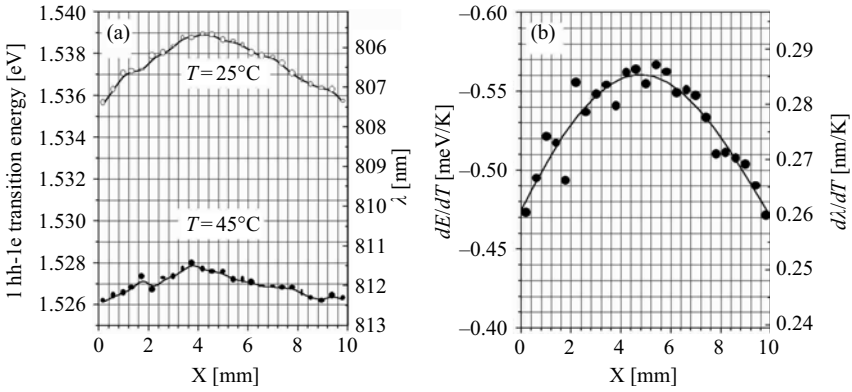

FIGURE 2.28. (a) Position of the energetically lowest optical transition in the QW versus local position along the "cm-bar" array consisting of 25 emitters. Measuring temperatures are 25 (open circles) and 45°C (full circles). Thermal tuning rate of the lasing transition versus local position along a "cm-bar" array consisting of 25 emitters. (b) The result presented in this figure is determined from the data shown in Fig. 2.28(a) by subtracting the positions for both temperatures and dividing them by the temperature difference

In order to eliminate the uncertainty of the temperature distribution within the device thermal tuning rates are determined by Fourier-transform (FT) photocurrent spectroscopy (PC) see [2.32, 2.33]. In Fig. 2.28a the energetically lowest optical transition in the quantum well is plotted versus local position along the device. From these raw data we determine "by-emitter" tuning rates (compare Fig. 2.28b).

These "by-emitter" tuning rates are free of any thermal non-uniformity effects and reflect the genuine change of the semiconductor band structure along the array, namely, the modification of the packaging-induced stress along the bar for two different temperatures. Now we recall our earlier experimental finding that the packaging-induced strain in In-packaged "cm-bar" arrays vanishes toward the bar edges, i.e., at $x = 0$ and 10 mm [2.32]. Thus we can use these locations as "zero-reference" and are now able to give absolute numbers for the packaging-induced strain. Using the strain sensitivity of -2.1 eV (cf. [2.34]), we obtain from the 3.1- and 1.8-meV "bowings" for 25°C and 45°C (see Fig. 2.28b), center-of-bar-strains of about -0.15% and -0.09% , respectively. In other words, in our example, about 40% of the packaging-induced strain vanishes when the device is heated up by 20°C. It is possible to take benefit from the knowledge about the packaging-induced strain and to separate the tuning rates into two parts, namely, into the pure *thermal* tuning contribution ($-0.48\,\mathrm{meVK^{-1}}$) and *mechanical pressure* tuning contribution of $-0.56\,\mathrm{meVK^{-1}} - (-0.48\,\mathrm{meVK^{-1}}) = -0.08\,\mathrm{meVK^{-1}}$. The latter one is, of course *indirectly*, also a thermal one, because the mechanical deformation is caused by the temperature increase. Nevertheless, we can state that about 15% of the "thermal tuning rate" of the central emitters in this "cm-bar" array is actually caused by pressure tuning. The use of "by-emitter" tuning rates (see [2.34]), allows for the statement of more accurate local temperatures along arrays. Thus a systematic error of about 15% that is potentially involved in temperature data that are derived from the emission wavelength by using one constant "integral" tuning rate can be ruled out by the "by-emitter" approach. The investigation of the polarization of the device emission on a by-emitter scale also offers useful information.

Figure 2.29 shows electroluminescence scans along a 25 emitter InGaAlAs-"cm-bar." Figure 2.30 gives the spatial variation of the degree of polarization of Fig. 2.29. The degree of polarization provides *qualitative* information about the spatial variation of the packaging-induced strain. The increase toward the

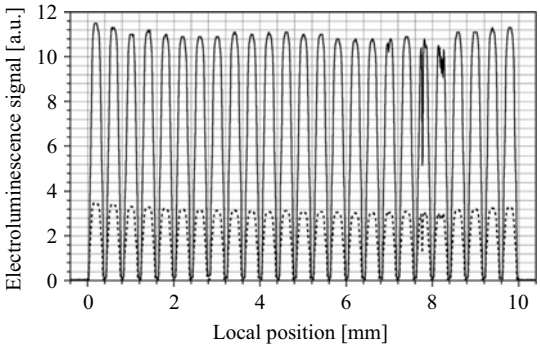

FIGURE 2.29. Electroluminescence scans along an InGaAlAs-"cm-bar." The operation current is 0.5 A, i.e., about 5% of the laser threshold for this kind of devices. By using a polarization filter TE- (full line) and TM-scans (dotted line) are monitored separately

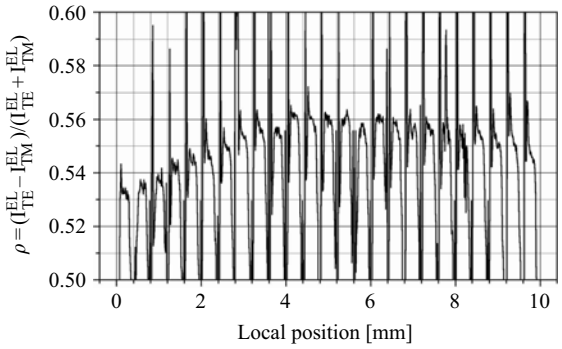

FIGURE 2.30. Degree of polarization (ρ) of the electroluminescence versus local position. The result presented in this figure is determined from the data shown in Fig. 2.29

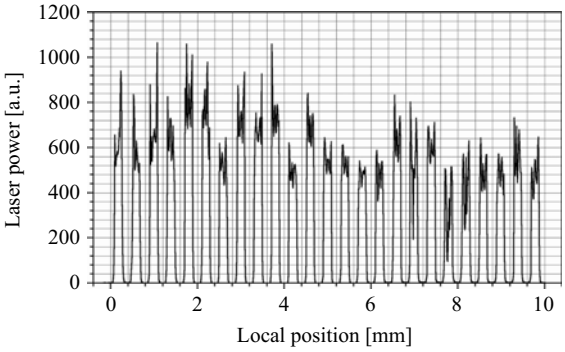

FIGURE 2.31. Laser emission at I = 20 A along the same InGaAlAs-"cm-bar," which data are already presented in Fig. 2.29 and Fig. 2.30

center of the bar is caused by decreased TM-emission due to the increased split between heavy-hole and light-hole-valence-band in the quantum well of the laser structure. This leads to a reduced hole population of states in the light-hole band. Thus Fig. 2.30 *qualitatively* confirms the quantitative result that is presented in Fig. 2.27 and Fig. 2.28. Consideration of the electroluminescence pattern without using of the parameter "polarization" allows at least the identification of defective emitters at 7.0, 7.8, and 8.2 mm in Fig. 2.29. Information about laser power for this particular 25 emitter containing InGaAlAs-"cm-bar" completes our discussion.

Figure 2.31 shows that the emitters at 7.8 and 8.2 mm, which are affected by dark-line defects, show poorer lasing, whereas the emitter at 7.0 mm shows surprisingly more emission than other emitters which are nominally "defect-free," e.g., the emitter at 9 mm. This apparent contradiction becomes clarified if one takes into account that the electroluminescence pattern provides information about the region about one diffusion length deep into the device (i.e., several microns from the mirror), whereas the lasing is affected by device properties along the whole

cavity length. Furthermore, for electroluminescence (I = 0.5 A) an almost uniform thermal distribution can be presumed, whereas for the case of lasing (I = 20 A), this is definitely not guaranteed any longer. Furthermore, power redistributions between the emitters represent an important issue.

It is noteworthy that only the "by-emitter" parameters, which are based on *spectral* information (see Fig. 2.28), are genuine parameters that refer nearly exclusively to individual emitter properties. For those parameters that rely on *intensities* (see Fig. 2.29 and Fig. 2.30) it must be conceded that non-uniform current distributions through the emitters, which are connected all in parallel, represent an additional parameter of uncertainty. This limitation, however, does not prohibit the conclusion that by-emitter analysis, i.e., the measurement of local device parameters along a device, represents a useful tool for identifying defective emitters as well as for the quantification of packaging-induced stresses.

2.3.2.2. Facet Temperatures: Raman Analysis

The micro-Raman technique is an established spectroscopic method for *surface temperature* measurements [2.35–2.39]. Thus micro-Raman represents a complementary technique to the measurement of the *averaged cavity temperature* from the laser emission wavelength. Since the laser facets are part of the laser cavity, their temperature is determined by both, the averaged cavity temperature plus the temperature increase caused by extra heat sources at the surface. Thus facet temperatures are higher than averaged bulk temperatures. The facet temperature measurements presented here are performed by micro-Raman spectroscopy. A DILOR x-y-Raman-spectrometer equipped with a microscope (spatial resolution of about 1 μm corresponds to the waveguide thickness) and a liquid-Nitrogen-cooled CCD-camera that allows for synchronous signal pick-up of the Stokes and anti-Stokes GaAs-or AlAs-like TO-phonon peaks generated at the device waveguide serves as a surface-temperature micro-probe. As excitation source we use the 514.5-nm line of Ar^+-ion laser creating a temperature probe with a depth-resolution of about 100 nm. Temperature calibration is done quite straightforwardly by measurements with reference devices that were heated upto more than 300°C. The device itself is mounted on a temperature-stabilized heat sink (typically stabilized at 25°C) that allows for active alignment of the device waveguide with respect to the microscope objective by using x-y-z-piezo translation stages.

We measure surface temperatures for both pulsed and cw operation. In case of pulsed operation we apply 5 μs pulses at repetition rates between 10 and 50 kHz. In this case the Ar^+-ion laser is modulated by an electro-optical modulator triggered by the laser pulse power supply. Such pulsed μ-Raman facet temperature measurements are described in detail by Kranz et al. [2.38].

Information on the local temperature in the surface layer was derived in two ways; from the ratio of the anti-Stokes and Stokes line intensities and – independently – from the spectral positions of those lines. Test experiments revealed that the lattice heating caused by the cw excitation laser does not exceed 10 degrees

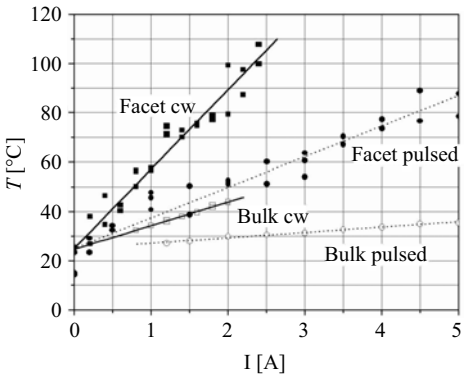

FIGURE 2.32. Facet (full symbols) and bulk (open symbols) temperatures in a 808-nm InAlGaAs/AlGaAs/GaAs high-power diode laser "single-chip" versus operation current. Squares mark cw data, whereas circles represent data obtained in pulsed operation. The heat sink temperature is stabilized at 25°C

if the excitation power is kept below 850 μW. Furthermore, we always subtract from the actual spectrum a spectrum that is monitored without the presence of excitation laser light. The experimental setup as well as methodology has been described more in detail in [2.39].

Figure 2.32 shows facet temperatures determined by micro-Raman spectroscopy and bulk temperatures derived from the emission wavelength of an 808 nm emitting InAlGaAs high-power diode laser "single-chip" device versus operation current for cw-operation as well as for pulsed excitation. For the bulk temperatures the expected result, a significant reduction of the thermal load, is visible when switching from cw to pulsed operation. This reduction is also the main motivation for using this operation mode in our experiments. At 2 A the cw facet temperature amounts to about 90°C, i.e., well below the 120–140°C that are considered critical for facets of lasers made of the AlGaAs-system (cf. [2.37]). Figure 2.32 demonstrates the significant reduction of both bulk and facet temperatures when switching from cw to pulsed. The reduction of the facet overheating (factor of about 2) is significantly weaker than the bulk temperature reduction (factor of about 5). This effect is understood by taking into account the different thermal relaxation behavior of facet and bulk, cf. also [2.38]. Deeper insight into the quantities, however, requires accurate thermal modeling (see [2.40]). The discussed effect is mainly used to reduce the bulk heating contribution to the facet temperature as well as for being able to perform measurements at operation currents higher than the nominal ones.

Results from 940-nm-emitting high-power "single chip" devices with and without current blocking layer at the front facet show interesting differences (see also [2.41]). Threshold and slope efficiency for both are found to be almost similar. This is not surprising since a 30 μm current blocking layer at 2 mm long laser cavity should not substantially affect their amplification properties. A striking

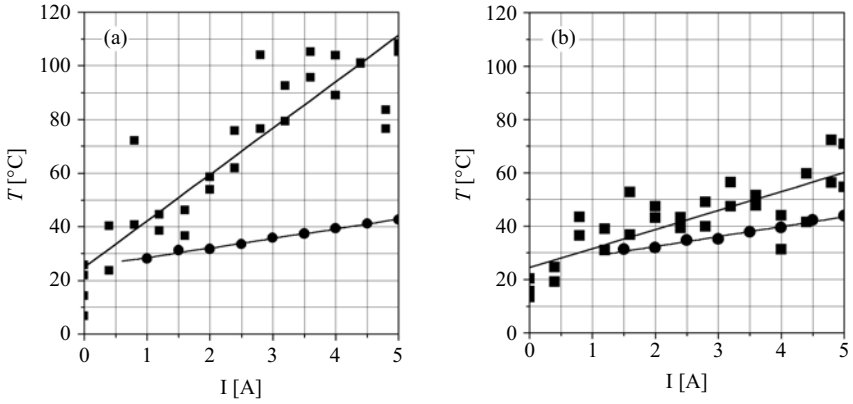

FIGURE 2.33. (a) Facet (full squares) and averaged bulk (full circles) temperatures for a 940 nm InGaAs/AlGaAs/GaAs high-power "single-chip" lasers without current blocking layer versus cw operation current. (b) Facet (full squares) and averaged bulk (full circles) temperatures for a 940 nm InGaAs/AlGaAs/GaAs high-power "single-chip" lasers with a 30 μm current blocking layer versus cw operation current

difference, however, is seen for the facet temperatures, where a reduction of the facet overheating by a factor of 4 is observed (see Fig. 2.33). Reproducibility tests with other sets of lasers provide reductions by a factor between 3 and 4. Regardless of this impressive evidence of the success of a technological measure another very important conclusion may be drawn from this experiment. Since the optical load for the facets of both lasers is almost similar it is clear that the *facet heating is not caused by reabsorption* of laser light. This important finding is in excellent agreement with former results obtained by other authors for QW lasers (cf. [2.37] and [2.42]). Facet heating by surface currents is considered a likely explanation.

2.4. Broad Area Emitters and Arrays

Martin Behringer

In the previous chapters, it was mentioned that diode lasers for direct laser processing mainly convince through the excellent wall plug efficiencies (up to 70% in comparison to 5% for lamp pumped solid-state lasers [SSL], 10% for diode pumped SSL, and 20% for disk laser). High optical power is always correlated with:

- high operating current,
- high optical power load at the chip end facets,
- high heat load (also for highly efficient devices).

The successful operation and required stability against the induced stress requires consideration of a number of design aspects.

- As a rule of thumb, it is necessary to apply a current of ≈1 A to obtain an optical output of 1 W (at a wavelength of ≈1 μm). For laser bars emitting 50 W this results in a total electric load of ≈50 A. Therefore, large contact areas and a large pn-junction area for the optical emission must be applied to minimize the local current densities.
- The increase of wall plug efficiency represents the best way to reduce the heat load. Current efforts aim to increase this figure from 40% (standard a few years ago) upto 80%. Besides these attempts, it is still necessary to dissipate the generated heat through the contact area more efficiently, e.g., by using larger heat transfer areas.
- Minimizing electrical losses, especially at high current densities, requires low series resistances, which can be reduced by enlarging the contacts, increasing the doping levels, and improving the electron and hole mobility inside the epitaxial layers.
- Efficient emission and low scattering or absorption losses can be achieved by optimizing the quality of the epitaxial layers and by improving the waveguide and quantum well design.
- Catastrophic optical mirror damage (COMD) can be avoided by using a large optical cavity (LOC) in order to reduce the local optical power density at the end facets.

Current high-power diode lasers consider all these aspects. Since the requirements are partly contradictory, it is impossible to fulfill them all at the same time. Nevertheless, modern high-power diode lasers exhibit the following typical characteristics: long resonator, wide contacts, and large optical cavity, as can be seen in Fig. 2.34.

Besides the operation conditions for the diode itself, the emission pattern has to be considered, when the radiated power needs to be redirected using systems of optical elements.

In the following section, the design of today's high-power diode lasers is briefly discussed and typical data are presented.

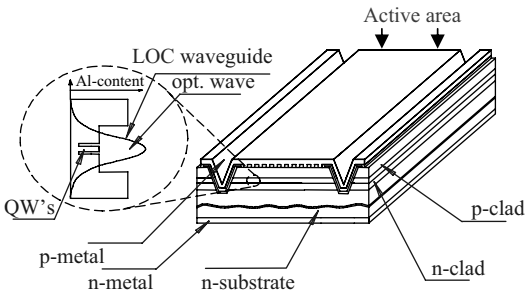

FIGURE 2.34. Schematic of a diode laser

2.4.1. Design and Material Parameters

As mentioned above, it is desirable to increase the width of the optical wave over a larger area. Some designs confine the optical wave in horizontal direction by incorporating a sharp index step using layers with different refractive indices. Some designs increase the loss for higher-order modes and thus support the desired optical wave in comparison to undesired modes. Large optical cavities (LOC) were first described by Garbusov et al. [2.43], who used a 1.2-μm-wide AlGaAs (40% aluminum) waveguide and AlGaAs (60% aluminum) cladding layers. Commercially available high-power diode lasers today expand the wave's height to 1 μm to 2 μm and upto 400 μm in the horizontal direction per emitter. New attempts to widen the optical wave further use a kind of photonic band gap structure. With this, the fundamental mode is spread out over a height of upto 20 μm, resulting in both, a low optical intensity at the mirror facet and a narrow far-field pattern in vertical direction. In Fig. 2.34 a typical emitter for high-power emission is depicted. It shows a wide contact, a long resonator, and a high epitaxial layer structure for a large optical waveguide. The main parameters for the design are summarized in section 2.1.

2.4.2. Electric and Optical Characteristics

2.4.2.1. PI Characteristics and Wall Plug Efficiency

The most important advantages for the application of high-power diode lasers include the high wall plug efficiency and the direct tunability of the output power by controlling the electric current through the device. Figure 2.35 shows an optical power versus current and operating voltage versus current characteristic of a high-power laser emitting at 940 nm. Upto the threshold current of $I_{th} \approx 10$ A, only spontaneously emitted photons, i.e., at very low optical power, can be observed. Above the threshold, the output power increases linearly with the driving current. The slope efficiency depends on internal quantum efficiency, the reflectivities of rear and front facets and absorption within the semiconductor material and on the frequency of the emitted photons. Here, the slope efficiency is $\eta \approx 1.2$ W/A for currents between 11 A and 80 A.

When the current is switched on, the voltage over the pn-junction increases rapidly to a value of U ≈ 1.4 V, which corresponds to a photon energy of ≈1.4 eV. Above this value, the voltage increases slowly with increasing current due to the series resistance. Due to the low series resistances, this increase is small in state-of-the-art high-power laser diodes. As a second consequence of the low series resistances, the wall plug efficiencies attain typically maximum values of 50% to 60%. It becomes obvious from the left part of Fig. 2.35 that the wall plug efficiency of the examined laser is <1% below threshold and about 65% at an operating current $I_{op} \approx 80$ A (80 W). At very high operating currents ($I_{op} > 100$ A), the wall plug efficiency drops slowly due to the series resistance and resulting heat

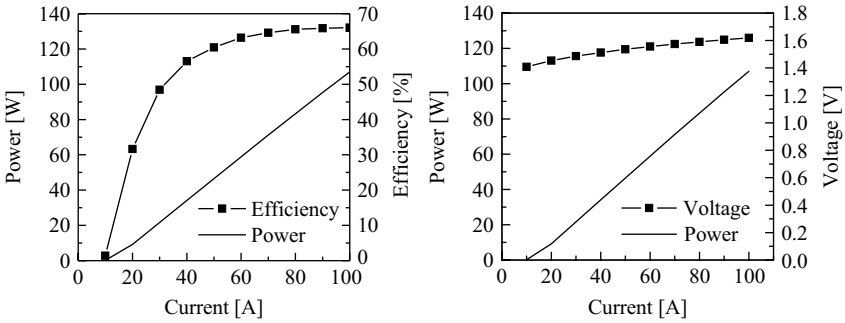

FIGURE 2.35. Light-current; efficiency-current (left) and light-current; voltage-current (right) diagram of a diode laser bar for 940-nm emission

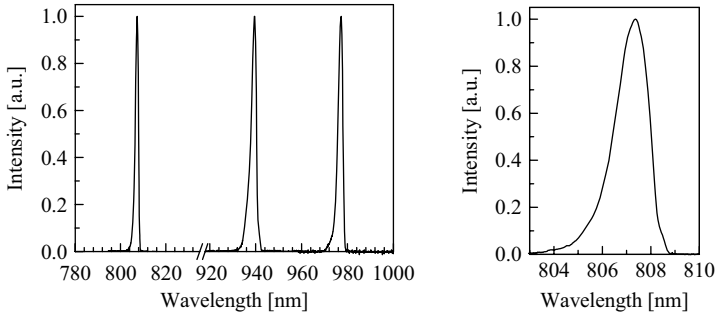

FIGURE 2.36. Emission spectrum of 808-, 940-, and 980-nm 1-cm laser bar

generation in the device. Typical values for state of the art high-power diode lasers in the different spectral regions are given in section 2.3.1.

2.4.2.2. Emission Spectrum

Wavelength multiplexing (cf. Chapter 4.3.2) represents a promising technology to increase the local power density for direct laser processing. The ability to narrow the emission spectrum and to actively determine the wavelength of a fabricated laser structure are two necessary conditions for the use of this technique. Figure 2.36 depicts the spectra of diode lasers emitting in the 808-, 940-, and 980-nm-wavelength range.

All spectra were measured using cw operation on bars which were mounted on actively cooled heat sinks. Obviously, all devices emitted within a spectral window of $\Delta\lambda < 5$ nm. The zoomed part of the spectra demonstrate that the full width at half-maximum (FWHM) is typically 2 to 2.5 nm irrespective of the emission wavelength. As has already been pointed out, the homogeneity over the wafer production as well as wafer-to-wafer reproducibility are indispensable for successful control of the wavelength on a commercial basis. Figure 2.37 shows the measured peak wavelengths of 600 diodes located on two 4-inch wafers out of a common

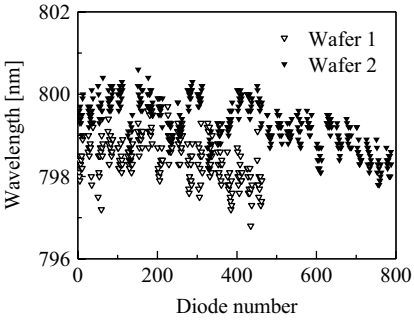

FIGURE 2.37. Peak wavelength distribution over one production lot

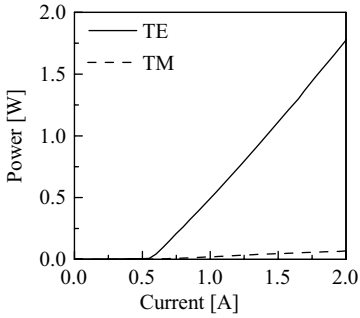

FIGURE 2.38. Light-current curve for TE and TM polarization

production lot. The wavelengths vary only by ± 1.5 nm. Therefore, the spectral emission of all bars fit into a window of only 4 nm. Based on this behavior, it is theoretically feasible to combine the power of upto $\approx$50 lasers with different wavelength in the 0.8–1.0 μm window by multiplexing and enhance the power in a laser beam for future applications. Practical designers have to consider the bandwidth of lasers and filters and therefore combinations of about six wavelengths are possible. Current systems rely on the few wavelength windows available today. Most often bars with 808-, 880-, 915-, 940-, and 980-nm are used.

2.4.2.3. Polarization

Polarization multiplexing (cf. Chapter 4.3.1) allows us to double the local power density in a laser beam further at an unchanged beam parameter product. The use of this technique requires a high degree of polarization in laser emission. Figure 2.38 shows the linear PI-characteristics for TE and TM polarization of an 808-nm AlInGaAs laser diode. It becomes evident that the optical power is mainly emitted in TE polarization, since the threshold for TM polarised laser emission is significantly higher and, as a consequence, the power emitted (at the operating point) in TE polarization exceeds TM polarized power by more than one order

of magnitude. The preferred polarization and the degree of polarization depend mainly on the strain in the device itself and especially in the QWs. For AlInGaAs QWs grown on a GaAs substrate, the QW material is compressively strained.

For QWs containing phosphorous, the strain is tensile and the band diagram is changed in a different way. As a result, the emission from aluminum-free QWs containing phosphorous is TM polarized. For practical applications, the degree of polarization and not the mode distribution represents the crucial figure.

2.4.2.4. Spatial Emission Pattern

To combine the emission from several diode lasers out of one bar into a single nearly circular spot, and/or, in a second step, to combine beams from different stacks, and to finally feed the emitted light into a glass fiber (for further details see Chapter 4.5), it is necessary to collimate the emitted light using optical elements such as lenses or lens-like structures. The design of efficient optical systems takes care of the far-field pattern. Current diode lasers exhibit asymmetrical far fields. Figure 2.39, shows the horizontal (a) and vertical (b) emission pattern of a laser. As the focusability of the light must not change during operation, it is important to have a narrow far-field during the whole operating time. The data were measured in cw-operation after a total operating time of 9,000 h for the device. In the horizontal direction (a), it exhibits a modulated far-field with a typical FWHM of about 10° due to multiple horizontal modes supported by the device. The pattern in the vertical direction, in contrast, has a FWHM of ≈35° at a near Gaussian shape. This Gaussian shape indicates that only the fundamental mode is emitted. The exact shape of the far-field pattern depends on the underlying layer structure, the contact design, the packaging and the operating conditions. For illustration, Fig. 2.40 depicts the far-field pattern for currents of 20 A (just above threshold) and 80 A (above the maximum specified operating current).

At low current densities, the FWHM is 4° and 34° in horizontal and vertical direction, respectively. At higher currents slow-axis FWHM rises to 5.9°, whereas the fast-axis FWHM remains stable as a consequence of the vertical single mode

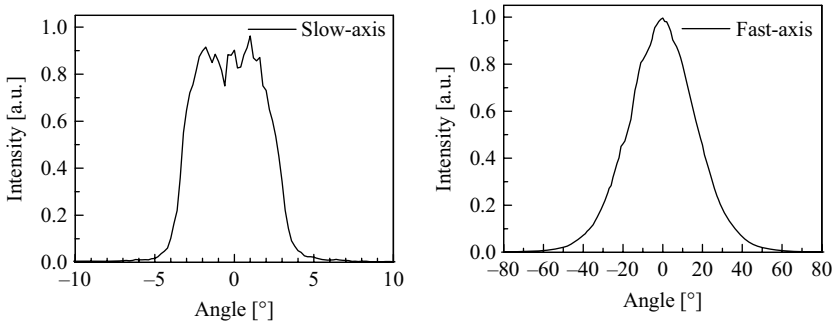

FIGURE 2.39. Far-field emission pattern for a 980-nm high-power diode laser bar after 9,000 h of continuous operation

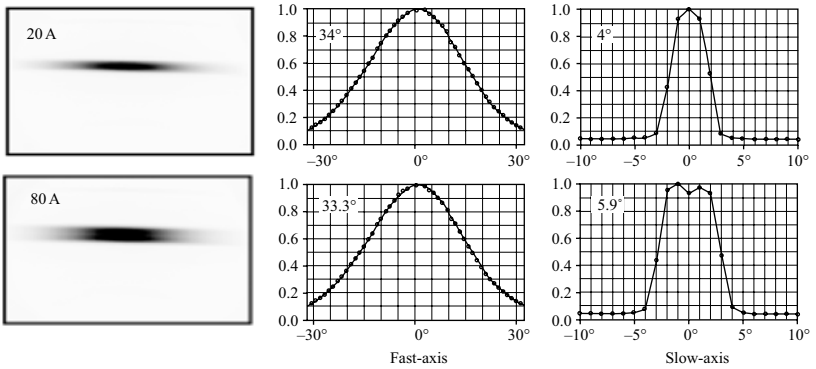

FIGURE 2.40. Far-field pattern at different operation currents. The last axis hardly changes between just above threshold (20 A) and at high current levels (80 A), while the slow-axis gradually widens: The FWHM increases from 4° to almost 6°

operation. The slow-axis, however, can emit higher-order modes whose mixture shows rather chaotic behavior caused by little changes of current, feedback from outside the laser back into the diode, and temperature distribution. Section 2.5 discusses developments which target at improved control of this spatial emission in the horizontal direction.

2.4.3. Lifetime and Reliability

The lifetime of semiconductor lasers depends on the operating conditions, in particular the applied current, the temperature within the active region, and the optical output power at the chip end facets. The temperature has a great impact on the aging behavior. As can be seen in section 2.1, the temperature increases the threshold current and reduces the slope efficiency simultaneously. Therefore it reduces the wall plug efficiency of the device and increases parasitic heat. Diffusion processes, the increased growth of defects, and their increased mobility at higher temperatures further promote the degradation of diodes. Figure 2.41 (left) compares the degradation of lasers bars of the same structure but operated at two different heat sink temperatures by displaying the output power versus time at a constant driving current. Obviously, the emitted power of the laser bars running at room temperature degrade only 0.5% during the first 500 h. In contrast, the bars operated at a heat sink temperature of 50°C degrade by about 5% of the original power after the same time.

The acceleration of degradation with increasing device temperature can be described by

$$AF_{th} \approx \exp\left[\frac{E_a}{k}\left(\frac{1}{T_1} - \frac{1}{T_2}\right)\right] \tag{2.32}$$

an exponential dependence of the acceleration factor (AF). When depicted in a semi-logarithmic plot, the lifetime versus temperature shows a linear relationship.

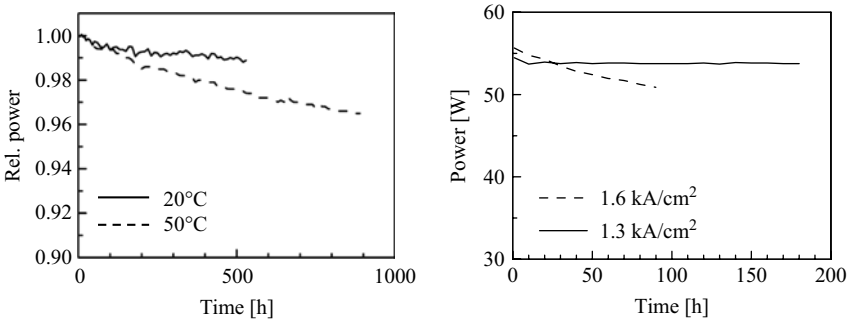

FIGURE 2.41. Output power over time: Left part: at 20°C and 50°C sub-mount temperature. Right part: for different current densities

The slope of the corresponding straight line is designated as the activation energy E_a. Typical values for high-power diode lasers in the InAlGaAs material system for an emission wavelength between 780 and 1,000 nm are between 0.3 and 0.5 eV.

In addition, the current density and the density of the optical power at the mirror facet have impact on the lifetime of the device. While the optical power density mainly enhances degradation in the mirror or in the region close to the mirror, the density of the applied current mainly affects the degradation of the semiconductor bulk material. In addition, the influence of current and optical power are interdependent, since the optical power is increased by an increasing current. Furthermore, a high optical power density can also interact with defects located inside the laser structure. To compute the total expected lifetime, one has to form the product of the different acceleration factors for temperature, current, and power. Nevertheless, the validity of this acceleration factors is limited only to a certain range of operation conditions without catastrophic degradation. Extreme current densities yield new degradation mechanisms that do not play a significant role under normal circumstances. Figure 2.41 (right part) depicts such degradation for laser structures operated at different current densities. While one structure quickly degrades to about 90% of the initial output power, the other structure remains almost stable during the first 200 h. The power density and the temperature of both structures were almost identical, but the current density differed by 30% . The different current density alone cannot explain the different degradation of the devices.

The lifetimes and output powers of diode lasers have been steadily increased over the last decades. Figure 2.42 (left part) shows the emitted output power per package or per laser bar over the last 40 years. The available cw power was increased from $P \approx 2.4$ W in 1984 to over $P \approx 20$ W in 1998 to 70–80 W in 2002. This steady increase was made possible by improvements in packaging technology and device efficiency. Figure 2.42 (right part) displays the emitted power at a constant driving current over lifetime. The data were taken from five laser bars with a fill factor

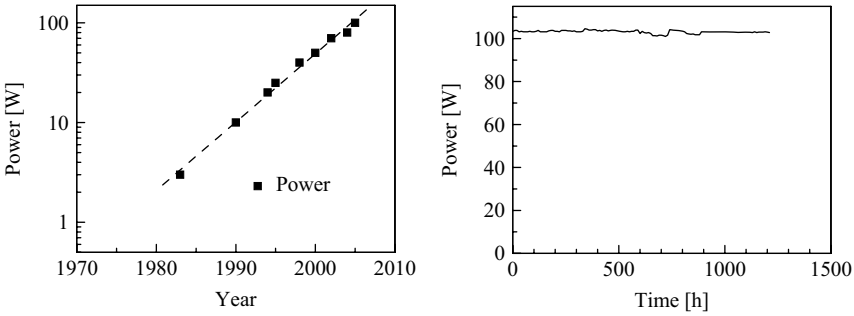

FIGURE 2.42. Development of output power per package during the last 40 years (left), and current test of 100 W/laser bar (right)

of 50% at a wavelength of 940 nm. At the beginning of the test the power level was at slightly above 100 W per bar. It can be seen that the output power changes little over the first 1,200 h with a degradation rate of less than 1% per kh. It becomes obvious, that today's power laser can be used upto 100 W and it has to be stated that the power is produced and emitted with an efficiency of more then 65%.

Recently, different operating conditions for power lasers became more important. Instead of a continuous-wave operation, a pulsed mode with a frequency of only a few Hertz and a duty cycle of upto 50% became more relevant for practical applications, e.g., welding or soldering in an industrial environment. This operating mode leads in addition to increased temperature, current, and power to increased thermo-mechanical stress cycles, enhancing the degradation. This stress is caused by the different thermal expansion coefficients of semiconductor and the commonly used copper heat sinks (see Chapter 3). The periodic heating or cooling of the device turns out to be equivalent to periodically changing the strain in the laser bar. It triggers other degradation mechanisms and leads to shorter lifetimes or even to spontaneous failures. To overcome this phenomenon, packaging as well as diode laser and operating conditions have to be designed to match the mutual needs. Today, laser bars that can survive more than 70 million cycles with a failure rate $<2\%$ can be designed.

2.5. High-Brightness Emitters and Arrays

Marc Kelemen

High-power high-brightness diode lasers are attracting more and more interest for applications previously dominated by expensive and inefficient solid-state lasers due to their better efficiency, compactness, and reliability. The significant fact about conventional high-brightness optical sources is that they exhibit about an

order-of-magnitude higher brightness than semiconductor lasers. The brightness is defined as

$$B = \frac{P}{A\Omega} \tag{2.33}$$

where P is the optical output power, A the emitting area, and Ω the solid angle into which the power is emitted. For a tapered diode laser this definition leads approximately to [2.44]

$$B = \frac{P}{\lambda_0^2 M_\perp^2 M_\parallel^2} \tag{2.34}$$

where λ_0 is the vacuum wavelength and M^2 the beam propagation parameter perpendicular ($M_\perp^2$) and in the plane ($M_\parallel^2$) of the epitaxial layer.

Today broad-area diode lasers are used to achieve high outputs. But standard broad-area waveguide designs are susceptible to modal instabilities, filamentation, and catastrophic optical mirror damage (COMD) failure [2.45]. This results in low beam qualities and values for the brightness limited to around $1 \times 10^7\,\mathrm{Wcm^{-2}sr^{-1}}$. On the other hand, high beam qualities are realized with ridge lasers emitting in a diffraction limited optical beam. The reliable output power of these lasers is mainly limited by the onset of facet degradation, which depends on the power density on the facet. Due to the small stripe width of a few microns, the output power is typically limited to about 700 mW, resulting in a brightness of less than $7 \times 10^7\,\mathrm{Wcm^{-2}sr^{-1}}$ [2.46].

A lot of different solutions have been proposed in the last few years to overcome these problems and to achieve high output power together with high beam quality. The main effort has been directed to develop broad-area structures that support only one lateral mode. Tapered devices [2.47, 2.48], distributed-feedback (DFB) lasers [2.49, 2.50], and monolithically integrated master-oscillator power amplifiers (MOPAs) [2.51] have been demonstrated, and all of them are able to produce output powers well above 1 W together with a high beam quality.

Among these, devices based on laterally tapered gain sections in combination with ridge-waveguide sections as depicted in Fig. 2.43 seem to be the most promising candidates when reproducible and low-cost fabrication is required. For the other concepts a costly epitaxial regrowth step or the fabrication of a holographically defined reflection grating is necessary, lowering the manufacturing yield. Tapered diode lasers produce diffraction limited output powers upto several watts in cw operation. The value of the brightness for a 1 W laser emitting a diffraction-limited beam at 1 µm wavelength is $10^8\,\mathrm{Wcm^{-2}sr^{-1}}$ according to Eq. (2.34). Hence tapered diode lasers provide a brightness upto a few times $10^8\,\mathrm{Wcm^{-2}sr^{-1}}$ in comparison to the few $10^7\,\mathrm{Wcm^{-2}sr^{-1}}$ of conventional semiconductor lasers.

This chapter is focused on the design and the performance of high-power diode lasers comprising ridge and tapered sections for near diffraction limited output power in the multiwatt regime optimized for the GaAs-based wavelength ranges between 880 and 1040 nm. It gives an overview of experimental work that has been

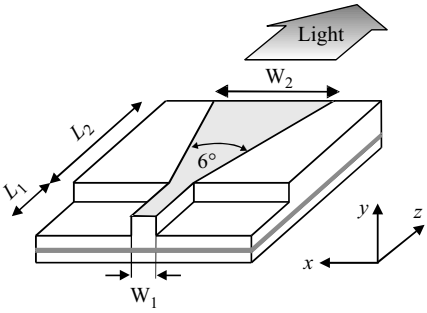

FIGURE 2.43. Schematic of a tapered diode laser with a ridge waveguide for mode filtering. The length L_1 of the ridge section is 500 μm. A taper angle of 6° together with a taper section length L_2 of 2 mm leads to an emitting aperture W_2 of about 200 μm

carried out in order to improve the beam quality as well as to enhance the output power of these devices. In the next section some theoretical background concerning the beam filamentation process and the far-field of devices with tapered gain regions is presented. The second section contains a description of the typical layer structure and fabrication process of the tapered diode lasers. The following sections contain an extensive review of experimental data, including output power, lifetime, beam quality, and astigmatism. The chapter concludes with a short description of tapered diode laser arrays comprising 19 tapered laser diodes.

2.5.1. Theoretical Background

2.5.1.1. Causes of Filamentation Processes

In broad-area devices, beam filamentation is the main physical effect that limits the device performance when high beam quality is required. With increasing power levels, spatial-hole burning occurs due to the interaction between the amplified optical field and the carrier density in the active region. Therefore, the complex optical index becomes inhomogeneous and leads to self-focusing of the optical wave. This results in filament formation, which severely deteriorates the beam quality [2.52].

The dependence of the complex optical index n on the carrier density n_c of the active layer is given by the following [2.53]:

$$n(n_c) = n_0 - \frac{1}{2k_0} g_m(n_c) \cdot \alpha_H + \frac{i}{2k_0} [g_m(n_c) - \alpha_i] \tag{2.35}$$

In this equation, $g_m(n_c) = \Gamma g(n_c)$ is the modal optical gain given by the product of the material gain $g(n_c)$ and the optical confinement factor Γ. The optical confinement factor is determined by the overlap between the vertical mode profile in the waveguide structure and the active layer. α_H is the linewidth enhancement factor, k_0 the vacuum wavenumber, n_0 the carrier independent part of the optical index, and α_{opt} are the total optical losses, respectively.

In order to achieve lateral coherence and to suppress filament formation in semiconductor lasers to reach high brightness, three principles are crucial:

- The differential optical index $\delta n(n_c)$ is proportional to the linewidth enhancement factor α_H. By finding ways to lower α_H, it is therefore possible to reduce the sensitivity against self-focusing and filamentation. For example, diode lasers based on quantum dot structures have been shown to possess an inherently low linewidth enhancement factor. Especially for tapered diode lasers, an increase of the ridge and taper section length further lowers the linewidth enhancement factor [2.54].
- Minimizing the optical losses α_{opt}. Using different lengths of the ridge and the taper sections of a tapered diode laser can change the optical losses. In addition the anti-reflection coating can be varied. In the case of a tapered diode laser the optical losses consist of the internal optical losses α_i, the resonator losses α_R and additionally a geometrical part (as additional resonator losses) due to the tapered resonator design which is well described in [2.53]:

$$\alpha_{opt} = \alpha_i + \alpha_R - \frac{1}{2(L_1 + L_2)} \ln\left(\frac{W_1^2 n_{eff}}{4\lambda_0 L_2}\right) \tag{2.36}$$

- As has been theoretically and experimentally analyzed in [2.55, 2.56], the differential optical index $\delta n(n_c)$ is proportional to the square of the confinement factor. So, a reduced confinement factor also reduces the variation of the optical index due to spatial-hole burning. This can be realized through epitaxial design, as described in the next section.

2.5.1.2. Astigmatism and Corrected Far Field

In order to determine whether the beam quality is diffraction limited, the measurement of interest is not the angular width of the output beam (far field) as normally used for broad-area diode lasers, but rather a measurement that is more sensitive to beam quality, a measurement of the beam at a waist called "corrected far-field" [2.44, 2.47].

At the output facet the curved wavefronts of tapered diode lasers diffract according to Snell's law and the beam will propagate with a width that is approximately n_{eff} times the internal full taper angle. With a taper angle of 6° this product yields a beam about 20° wide. The beam is astigmatic, since in the direction perpendicular to the quantum well it diverges from the output facet, but in the plane of the quantum well it diverges from a virtual source that is approximately L_2/n_{eff} behind the output facet inside the device. Because n_{eff} is dependent on the carrier density and the temperature, distortions of the carrier distribution or different thermal management concepts have a remarkable influence on n_{eff} and on the position of the virtual source [2.57].

For the measurements, a spherical lens is used to collimate the beam in the fast-axis direction (vertically) as shown in Fig. 2.44. Because of the astigmatism, the beam is focused in the lateral plane resulting in a waist w_{ff}, called corrected

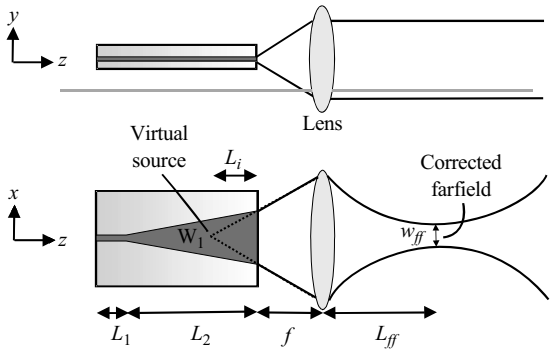

FIGURE 2.44. Schematic of an astigmatism measurement. A lens is used to collimate the beam in the fast-axis direction (vertically). Because of the astigmatism, the beam is focused in the lateral plane resulting in a waist, called corrected far field

far field. The distance L_{ff} between lens and corrected far field provides a direct measure of the astigmatism using the lens equation and the known focal length f of the measurement lens. Similarly, the width w_{ff} of the waist is a measure of the width of the virtual source.

It can also be shown that a lateral scan of the power distribution at this waist is exactly the same as the power distribution that would be found at a focal length beyond the measurement lens if an ideal thin cylindrical lens had been placed at the output facet to collimate the beam in the lateral plane; (removal of the quadratic phase curvature due to the divergence of the beam). Hence, the relative power density measured at the waist as a function of the lateral distance x is a direct measure of the far-field pattern with the quadratic phase curvature removed, if one interprets ϕ as:

$$\phi = \arctan(x/f) \tag{2.37}$$

This ideal beam is convenient to be used as a benchmark for the beam quality of real beams. For an ideal top hat distribution the full width half-maximum angle ϕ_{FWHM} for the far-field distribution of the power density is [2.44]:

$$\phi_{FWHM} \approx 0.84\lambda_0/\mathrm{W}_2 \tag{2.38}$$

If the near-field profile is not top hat but rather Gaussian (if gain saturation plays no role), the far-field distribution as Fourier transformation of the Gaussian near-field distribution has a factor of 1.5 instead of 0.84 for the full width half maximum angle in Eq. (2.37).

2.5.2. *Fabrication of Tapered Devices*

The fabrication of high brightness lasers with high conversion efficiency requires an epitaxial layer sequence with low internal losses ($<2\mathrm{cm}^{-1}$), low confinement

factor (<1.5%) and high internal conversion efficiency (>0.9). The reduction of the internal losses and of the confinement factor can be achieved by broadening the waveguide layers [2.58]. This reduces the overlap of the optical mode with the highly doped cladding layers. Generally the laser structures were grown by molecular beam epitaxy (MBE). As an example the typical fabrication process of a tapered diode laser emitting at 940 nm is described in detail in the following.

1. The active region consists of a single InGaAs-quantum well embedded in an 880 nm thick AlGaAs core region with 20% Al content. For 940 nm the quantum well is 7 nm thick with a nominal Indium content of 12% . The optical waveguide is formed by 1 μm thick AlGaAs claddings with 40% Al. Si and Be are used for n- and p-type doping, respectively. The doping concentrations start at a level of $5 \times 10^{17}\,\mathrm{cm}^{-3}$ near the core and increase to a level of $2 \times 10^{18}\,\mathrm{cm}^{-3}$ in the outer cladding regions. The GaAs cap layer is highly p-doped ($6 \times 10^{19}\,\mathrm{cm}^{-3}$) in order to reduce the contact resistance. The layer design exhibits an overlap of the fundamental optical mode with the quantum well of 1.3% at 940 nm. It has been shown previously that this low modal gain epitaxial layer structure suppresses beam filamentation in tapered laser oscillators and tapered laser amplifiers [2.56]. As a further advantage of this layer sequence, 95% of the optical power is concentrated in the undoped core layers and the overlap of the fundamental mode with the doped cladding layers is only 5% . As a result, low internal losses of $1.5\,\mathrm{cm}^{-1}$ are obtained, measured on Fabry-Perot laser diodes of different lengths. The high material quality of the MBE-grown laser structures yields a high internal efficiency of more than 90%. The use of high-band-gap ($E_g = 1.68$ eV) AlGaAs core layers with 20% of Al content leads to a strong carrier confinement. This results in laser diodes with relatively temperature insensitive characteristics. Experimentally, a characteristic temperature of $T_0 = 160$ K is observed for broad area diode lasers in the temperature range between 15°C and 80°C.
2. From this material diode lasers comprising a ridge section as well as a tapered section have been fabricated in a standard process [2.53]. Figure 2.43 shows a schematic of the device. A typical structure for tapered diode lasers consists of a taper angle of 6° together with a taper section length of 2 mm. This leads to an emitting aperture of about 210 μm width. The length of the ridge section is $L_1 = 500$ μm, resulting in a total device length of 2.5 mm.
3. After thinning and cleaving a highly reflective double-stack of Si and SiO_2 (95% reflectivity) is deposited on the back facet by reactive magnetron sputtering. Two different anti-reflection coatings are used for the front-facet: (i) a single layer of SiN (<1% reflectivity) and (ii) a single layer of SiON (<0.01% reflectivity). In principle this device can function as either an amplifier [2.47] or a laser depending on the rear facet coating.
4. Finally the devices are mounted p-side down on copper mounts (C-mounts) with indium solder. Uniform pumping of the laser medium is achieved by current injection via bond wires.

The epitaxial layer sequences and fabrication processes of the GaAs based tapered diode lasers emitting between 880 nm and 1040 nm are similar and reported in [2.56].

2.5.3. Characterization and Results of Single Emitters

2.5.3.1. Electro-Optical Characterization

Figure 2.45 shows a typical P-I-characteristic together with the wall plug efficiency of a tapered diode laser emitting at 940 nm at a heat sink temperature of 20°C [2.59]. The length of the taper section is 2 mm and the length of the ridge section is 0.5 mm. The anti-reflection coating is provided by SiON resulting in a reflectivity of less than 0.01% . The device shows a comparatively low threshold current of 0.78 A corresponding to a threshold current density of 400 A/cm^2. The maximum slope efficiency of 0.88 W/A together with the low series resistance of 30 mΩ results in a high conversion efficiency. At 4 W of output power a maximum wall plug efficiency of 45% is achieved.

The emission spectra of the devices have a spectral width (FWHM) of 3 nm at 4 A. From the shift of the peak emission wavelength with driving current a total thermal resistance of 7 K/W can be deduced for the complete experimental setup including the thermoelectric cooling of the C-mount heat sink.

For tapered diode lasers emitting at other wavelengths similar results have been reached [2.59–2.61]. Figure 2.46 summarizes typical P-I-characteristics for

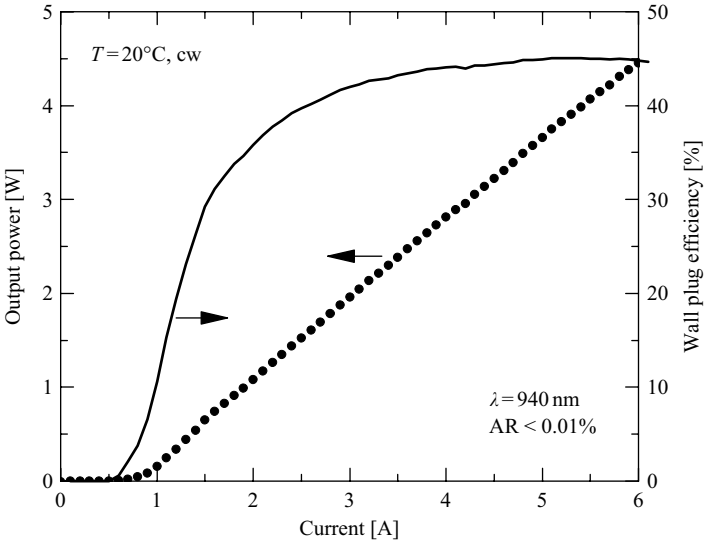

FIGURE 2.45. Typical current-power characteristic and wall plug efficiency of a tapered diode laser emitting at 940 nm. The measurements have been done at a heat sink temperature of 20°C and in continuous-wave mode

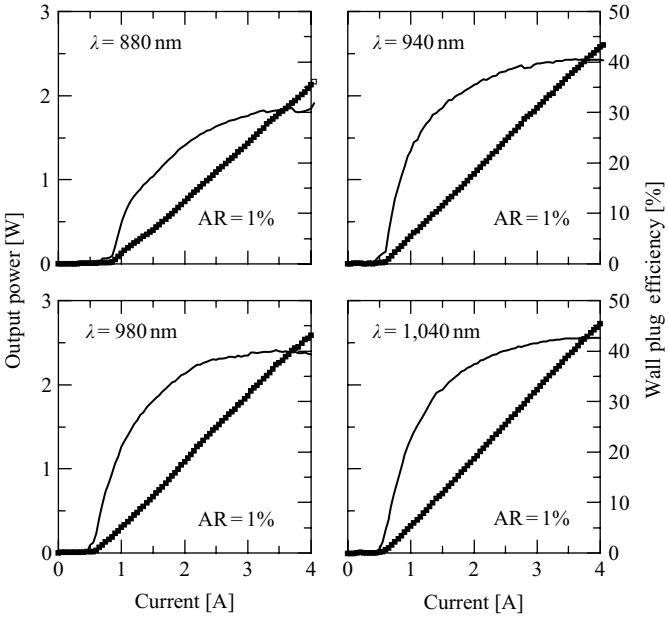

FIGURE 2.46. Typical current-power characteristics and wall plug efficiencies of tapered diode lasers emitting at different wavelengths. The measurements have been done at a heat sink temperature of 20°C and in continuous-wave mode

TABLE 2.5. Electro-optical characteristics of tapered lasers with different emission wavelengths

λ (nm)	880	940	940	980	1040
AR(%)	1	1	0.01	1	1
I_{th} (A)	0.85	0.60	0.78	0.64	0.62
J_{th} (A/cm^2)	440	310	400	330	320
s.e. (W/A)	0.66	0.77	0.88	0.80	0.81
P_{4A} (W)	2.1	2.6	2.8	2.6	2.7
η_{4A}(%)	30	40	44	39	43

tapered diode lasers emitting between 880 nm and 1040 nm. In contrast to Fig. 2.45 the anti-reflection coating in this figure is provided by SiN resulting in a reflectivity of 1% in order to reduce the threshold current. For all wavelengths output powers of more than 2 W have been reached at a current of 4 A. The threshold currents are between 0.6 A for 1040 nm and 0.85 A for 880 nm. Slope efficiencies (*s.e.*) between 0.81 W/A and 0.66 W/A have been measured together with corresponding wall-plug efficiencies between 30% for 880 nm and 43% for 1040 nm. Table 2.5 summarizes the main results of the electro-optical characterization for the tapered diode lasers emitting between 880 nm and 1040 nm.

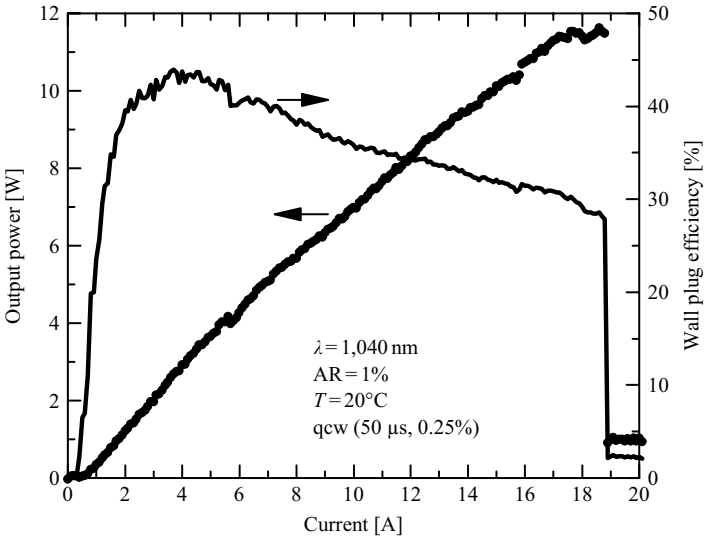

FIGURE 2.47. Typical current-power characteristic and wall plug efficiency of a tapered diode laser emitting at 1040 nm. The measurements have been done at a heat sink temperature of 20°C and in quasi-continuous-wave mode (50-µs pulse time, 0.25% duty cycle)

In order to investigate the limitation on the output power and the stability of the output facet, the driving current can be ramped up in quasi-continuous-wave (qcw) mode to the point of sudden failure. In Fig. 2.47 the qcw mode was realized by a pulse time of 50 µs and a duty cycle of 0.25%. A record of 11.6 W output power for single tapered diode lasers was achieved at a driving current of 18.5 A. At 18.8 A catastrophic optical mirror damage occurred at the front facet. The power density at the emitting facet is estimated to be about 6 MW/cm^2, which is comparable to broad-area diode-lasers [2.61].

As an example the long-term reliability of the tapered diode lasers emitting at 1040 nm has been tested by aging a batch of six devices at a heat sink temperature of 50°C [2.61]. Under constant current condition at 4 A (Fig. 2.48) the output power is 2 W. All devices show only gradual degradation within the first 1,100 h without sudden failure. Defining a 20% decrease of the output power as a criterion for the lifetime, an extrapolated lifetime of more than 10,000 h can be deduced for a heat sink temperature of 50°C. Under a cautious assumption of 0.2 eV for the activation energy, a lifetime of more than 20,000 h at room temperature can be deduced from these data. The beam quality parameter M^2 remains unchanged after the accelerated aging. In addition lifetimes of more than 10,000 h have been demonstrated for tapered diode lasers emitting at 940 nm and 980 nm.

2.5.3.2. Beam Quality and Brightness

The useful output power of tapered devices is limited by the deterioration of the beam quality with increasing power. For this it is instructive to look at the

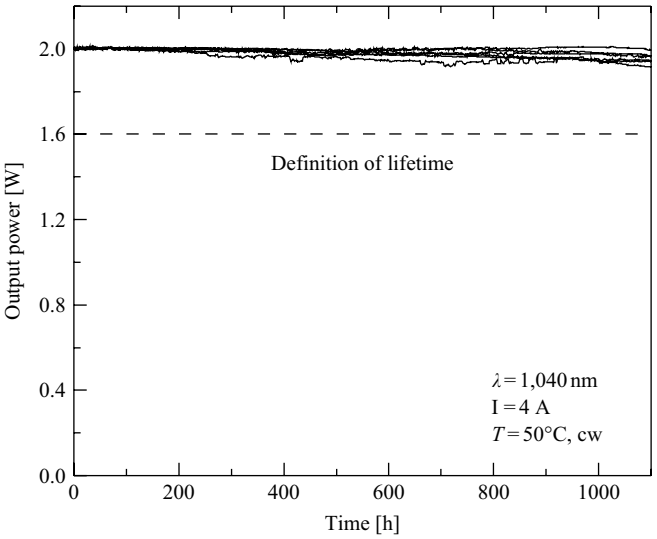

FIGURE 2.48. Reliability test of a batch of six tapered diode lasers at an output power of 2 W and a heat sink temperature of 50°C. A lifetime of more than 20,000 h can be deduced from these data at 20°C

illumination patterns at the output facet, often called near-field patterns. The structure observed in the near-field is mostly closely related to the effects inside the tapered gain region that degrade the beam quality. These patterns simply show the relative power density at the facet and do not provide a measure of the phase, which to first order one expects to vary quadratically across the facet [2.44]. Figure 2.49 shows the dependence of the beam profile at the facet (near-field) on the output power for a tapered diode laser emitting at 1040 nm. Upto 3 W the near field profiles can be described with Gaussian curves demonstrating the diffraction limited behavior. For higher output powers slight filamentation effects occur.

In order to investigate the beam quality of tapered laser oscillators, the beam quality parameter M^2 was measured after ISO 11146 with a commercial beam analyzing system (DataRay Beam Scope).

The dependence of the beam quality parameter M^2 on the output power is shown in Fig. 2.50 for tapered diode lasers emitting at different wavelengths [2.54, 2.60, 2.62]. All diodes consist of a taper section length of 2,000 μm and a ridge section length of 500 μm. A beam quality parameter as low as $M^2 = 2$ or less is achieved at an output power of 2 W for all wavelengths except 880 nm. At 1040 nm the beam quality remains nearly diffraction limited upto output powers of 3 W due to the lowest confinement factor ($\Gamma = 1.1\%$) of all tapered diode lasers investigated.

In good accordance to the predictions given in section 2.5.1 the experimental results further show that the length of the ridge and the taper sections have a strong impact on the beam quality at high output powers. In Fig. 2.51 tapered diode lasers

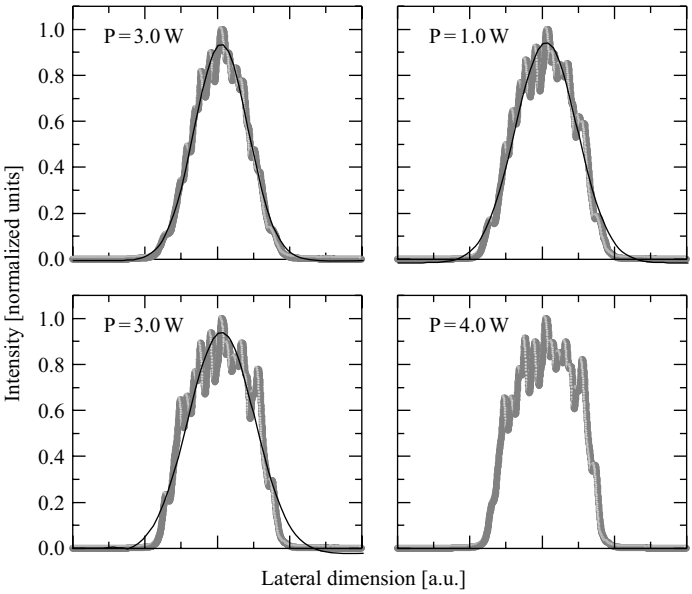

FIGURE 2.49. Dependence of the near-field profiles of tapered diode lasers emitting at 1040 nm on the output power at a heat sink temperature of 20°C (cw). The Gaussian-like fit curves demonstrate the nearly diffraction limited behavior of the tapered diode lasers up to 3 W

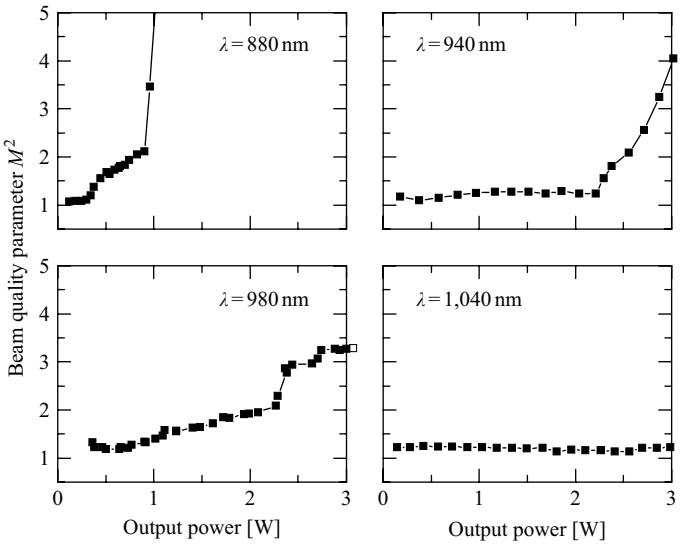

FIGURE 2.50. Typical M^2 characteristics of tapered diode lasers emitting at different wavelengths in dependence on the output power. The measurements have been done at a heat sink temperature of 20°C and in continuous-wave mode

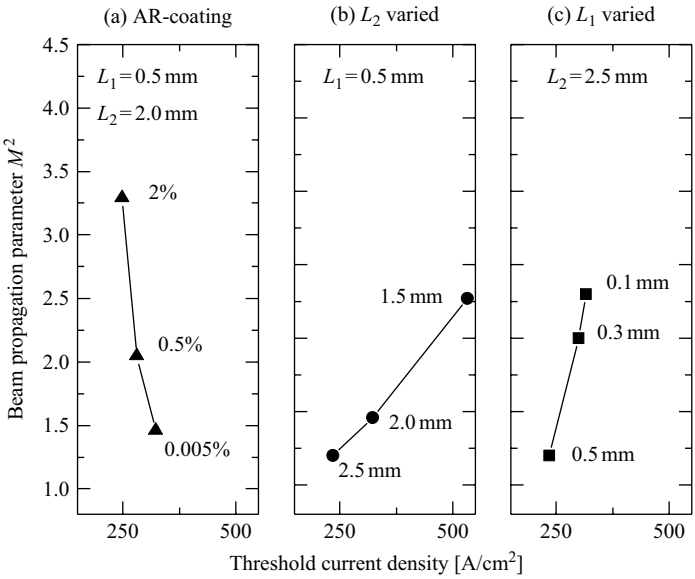

FIGURE 2.51. Typical M^2 characteristics of tapered diode lasers emitting at 940 nm in dependence on the (a) anti-reflection coating (b) taper section length L_2, and (c) ridge section length L_1. The measurements have been done at a heat sink temperature of 20°C and in continuous-wave mode at a power level of 1 W

emitting at 940 nm are shown for different lengths of the ridge and the taper section as an example. For a ridge length of 100 μm the beam quality starts to decrease rapidly at a power level of $P = 1$ W. In contrast to this result, the beam quality of the devices with ridge lengths of $L_1 = 500$ μm remain in the range of $M^2 < 1.5$ upto more than 2 W of output power. In addition, a longer taper section length also enhances the beam quality. Whereas the beam quality of devices having a taper length of 2,000 μm remains nearly diffraction limited upto about 2.2 W with an M^2-value of 1.3, a taper section length of 1,500 μm causes M^2 to increase rapidly above a lower power level of about 0.4 W. It has been shown that the increase of the length of one or both sections lowers the linewidth enhancement factor and leads to a lower tendency of filamentation and hence to a better beam quality [2.54].

With increasing output facet reflectivity, an increasing percentage of the optical field is reflected into the resonator enhancing the formation of dynamically varying longitudinal and transverse structures in the intensity distribution [2.47]. Therefore it is reasonable to reduce the facet reflectivities as far as possible to avoid such a phenomenon. In Fig. 2.51 anti-reflection coatings down to 0.005% have been used to further improve the beam quality. But it may be advantageous to accept higher facet reflectivities to reduce backward reflections from optical components like lenses and fibers. So for practical reasons an anti-reflection coating of 1% is frequently used today.

2.5.3.3. Corrected Far-Field and Astigmatism

Far-field profiles of the devices were measured after correcting for the quadratic phase front divergence by using a cylindrical lens (corrected far field) according to section 2.5.1. An example for the evolution of the lateral far-field profiles of tapered diode lasers with increasing output power can be seen in Fig. 2.52. A power independent far field angle of 0.24° (FWHM) is obtained for the full range of cw output powers [2.59]. This value is equal to 1.06 times the value predicted by Eq. (2.5). The fraction of power at 3 W contained inside the central lobe is 93% (2.8 W). To estimate the brightness (P/λ^2) of this source, one can use the power in the central lobe divided by ($1.06 \cdot \lambda^2$), where the factor 1.06 has been added to the denominator to account for the increase in the far-field angle above the diffraction limit. The result is a brightness value of $3.0 \cdot 10^8\,\mathrm{Wcm^{-2}sr^{-1}}$.

The measured M^2-parameters in Fig. 2.52 range between 1.1 at 1 W and 4.1 at 3 W of output power. The growth of side lobes at higher output powers is responsible for the increase of the beam quality parameter M^2. Conventionally beam diameters have been measured at the $1/e^2$ intensity point; i.e., at 13.5% of the maximum intensity. ISO 11146 requires the use of a "Second Moment" definition of beam diameter. For this reason the side lobes also increase the calculated beam quality factor M^2.

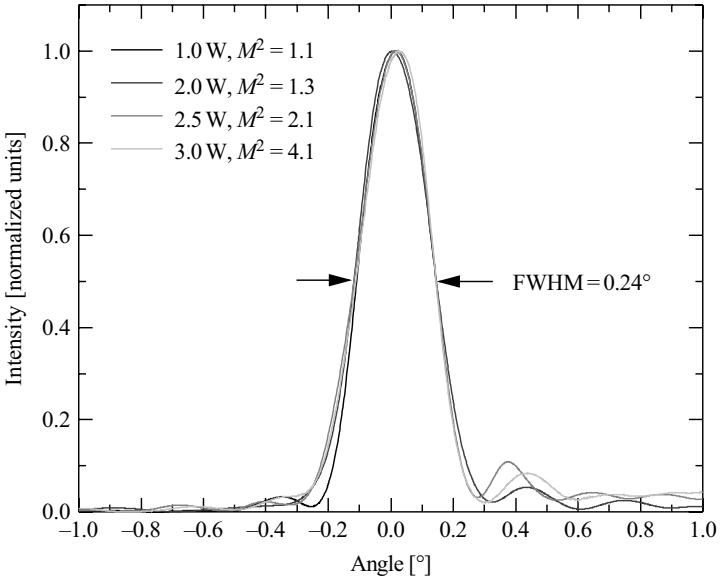

FIGURE 2.52. Dependence of the lateral far-field profiles of tapered high-power diode lasers on the output power after removal of the quadratic phase curvature by a cylindrical lens at a heat sink temperature of 20°C (cw). Additionally the measured values of M^2 are given corresponding to the output power

For the diodes emitting at 980 nm similar values for the corrected far field have been obtained [2.60]. For 1040 nm the far field distribution is more Gaussian like. In this case the measured values of 0.43° upto 4 W must be compared to the theoretical value of 0.40° for a Gaussian near field distribution. This value is equal to 1.03 at an output power of 4 W and results in a brightness of $3.6 \cdot 10^8$ $\mathrm{Wcm^{-2}sr^{-1}}$ [2.61].

In [2.62] the astigmatism curves (distance between virtual source and facet) in dependence on the current have been investigated for different design parameters. It has been shown experimentally that in the low current regime ($I < 3I_{th}$) the ridge and the taper section length have a significant influence on the position of the virtual source, visible in a change of the astigmatism. There is a weaker influence of the design on the astigmatism in the higher current regime ($I > 3I_{th}$).

The astigmatism of tapered diode lasers is mainly temperature driven, as shown in Fig. 2.53. A lower thermal resistance, leading to a better heat flow, results in a fast cross over into a flat curve. In contrast to this, higher values of the thermal resistance lead to a gradual change over to a flat behavior. As a result, the astigmatism remains nearly constant in the higher current regime respectively higher output regime. The same effect takes place by making the tapered section length longer. Here for longer tapered section lengths the power losses per area decrease, there is a better heat flow, and the astigmatism reaches saturation faster [2.62].

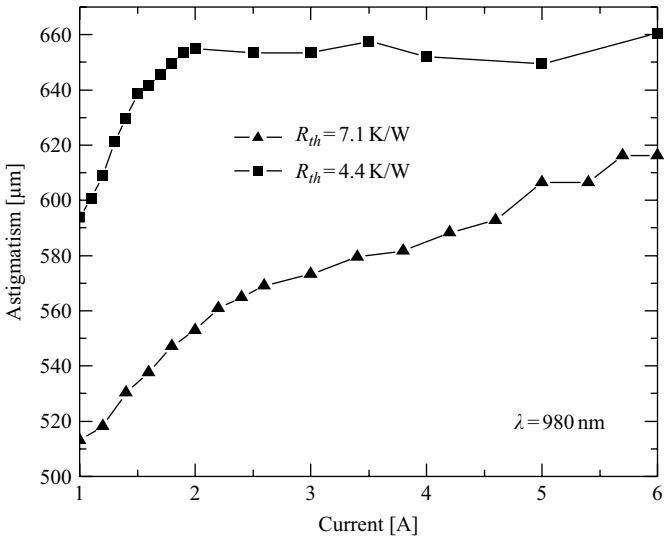

Figure 2.53. Astigmatism of tapered diode lasers emitting at 980 nm in dependence on the current for different thermal resistances. All measurements have been done at a heat sink temperature of 20°C in cw mode. The thermal resistance has been changed by using different heat sinks

2.5.4. Characterization and Results of High-Brightness Arrays

Depending on heat sink and facet preparation the available and reliable output power of a single tapered diode laser is restricted to a few Watts only. Therefore, it is straightforward to fabricate monolithically integrated diode laser arrays in order to achieve higher output powers and higher optical power densities. A diode laser bar with tapered lasers instead of broad area devices comprises 19 single emitters with 210 μm wide apertures and a pitch of 500 μm from laser to laser.

Figure 2.54 shows the P-I-characteristic of a tapered diode laser array together with its wall-plug efficiency. The device has a slope efficiency of 0.74 W/A, a threshold current of 10.5 A and a threshold current density of 380 A/cm^2. The array delivers nearly 30 W of optical output power under cw-operation and a driving current of 50 A which is limited by the current source. The output power is distributed fairly uniformly among the 19 emitters with an average of 1.54 W in very good agreement with the results of the single emitters shown in Fig. 2.45. No rollover occurs and the wall-plug efficiency does not reach its maximum in the observed current range, 38% is achieved at the highest output power. All measurements are performed at a heat sink temperature of 25°C.

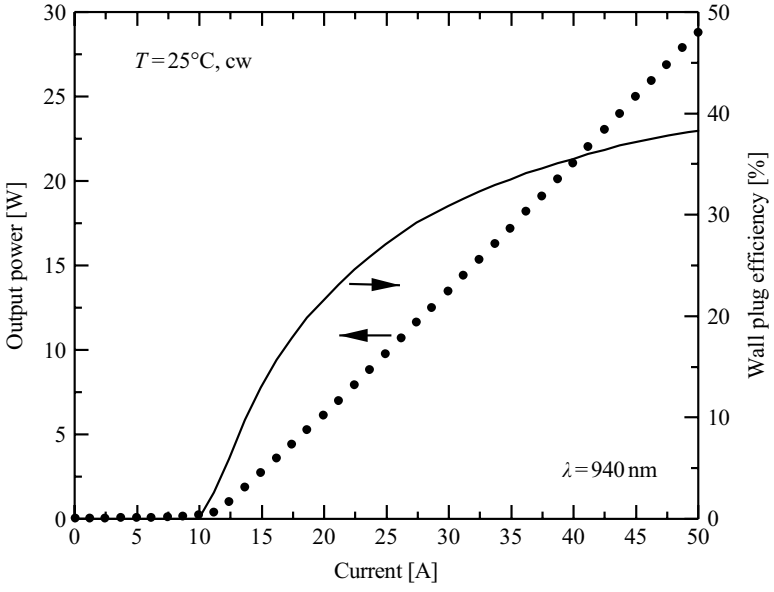

Figure 2.54. P-I-characteristic and wall plug efficiency of a tapered laser array emitting at 940 nm comprising 19 individual emitters. The measurements have been done at a heat sink temperature of 25°C and in continuous-wave mode

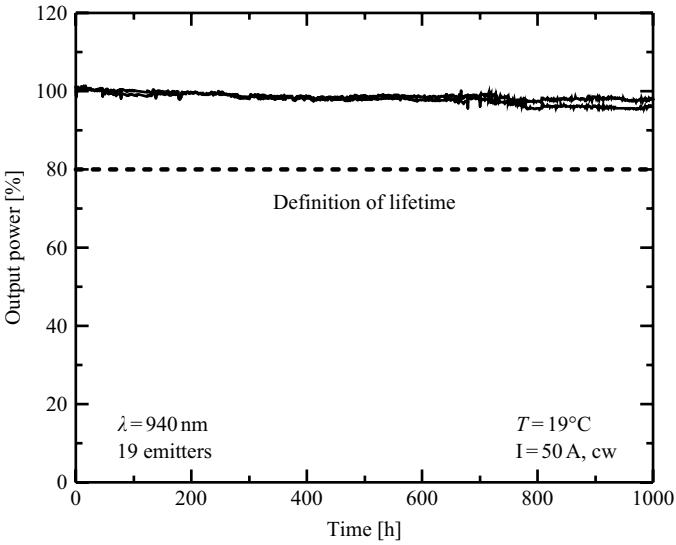

FIGURE 2.55. Reliability test of tapered laser arrays emitting at 940 nm at a current of 50 A and a heat sink temperature of 19°C in continuous-wave mode

The long-term reliability of the tapered laser array has been tested by aging two devices emitting at 940 nm at a heat sink temperature of 50°C (Fig. 2.55). Both devices show only gradual degradation within the first 1,000 h without sudden failure. Defining a 20% decrease of the output power as a criterion for the lifetime, an extrapolated lifetime of more than 5,000 h can be deduced for a heat sink temperature of 50°C.

List of Symbols

B	brightness
f	focal length of lens
g	material gain
g_m	modal optical gain
I_{th}	threshold current
J_{th}	threshold current density
k_0	vacuum wavenumber
L_1	length of ridge section
L_2	length of taper section
M^2	beam propagation parameter
n	complex optical index
n_c	carrier density
n_0	carrier-independent part of the optical index

n_{eff}	effective index of refraction
P	output power
$s.e.$	slope efficiency
W_1	width of the ridge waveguide
W_2	width of output facet
a	astigmatism
α_i	internal losses
α_R	resonator losses
α_{opt}	total optical losses
Γ	confinement factor
η	wall plug efficiency
η_i	internal efficiency
λ_0	vacuum wavelength
ϕ_{FWHM}	full-width half-maximum (FWHM) angle

References

[2.1] Koechner W (1966) Solid State Laser Engineering. Springer-Verlag, Berlin, Heidelberg, p. 82ff.

[2.2] Diehl R (ed.) (2000) High-Power Diode Lasers. Springer-Verlag, Berlin, Heidelberg.

[2.3] Carlsson NW (ed.) (1994) Monolithic Diode-Laser Arrays. Springer-Verlag, Berlin, Heidelberg.

[2.4] Suhura T (2004) Semiconductor Lasers Fundamentals. Marcel Dekker, Inc., New York, Basel.

[2.5] Tansu N, Mawst LJ (2002) Temperature sensitivity of 1300-nm InGaAsN quantum-well lasers. IEEE Photonic Technology Letters 14, 1052–1054.

[2.6] Haug A (1987) Relations between the T_0 values of bulk and quantum-well GaAs. Journal of Applied Physics B44, 151–153.

[2.7] Garbuzov D, Shiau GJ, Bulovic V, Boroditsky M, Chao CP, Forrest SR (1995) Photoluminescence study of excess carrier spillover in 1.3 μm wavelength strained multi-quantum-well InGaAsP/InP laser structures. Applied Physics Letters 66, 1307–1309.

[2.8] Lu H, Blaauw C, Makino T (1995) High-temperature single-mode operation of 1.3 μm strained MQW gain-coupled DFB lasers. IEEE Photonic Technology Letters 7, 611–613.

[2.9] Evans JD, Simmons JG, Makino T (1997) On the temperature sensitivity of strained multiple quantum well, long wavelength semiconductor lasers: Root cause analysis and the effects of varying device structures. Proceedings of the SPIE 3001, 218–234.

[2.10] Ishikawa M, Shiozawa H, Itaya K, Hatakoshi G, Uematsu Y (1991) Temperature dependence of threshold current for InGaAlP visible laser diodes. IEEE Journal of Quantum Electronics 27, 23–29.

[2.11] Manasevit HM (1969) The use of metal-organics in the preparation of semiconductor materials I. Epitaxial gallium-V compounds. Applied Physics Letters 116, 1725.

[2.12] Manasevit HM (1972) The use of metal-organics in the preparation of semiconductor materials: Growth on insulation substrates. Journal of Crystal Growth 13–14, 306.

[2.13] Miederer W, Ziegler G, Dotzer R (1962) German Patent 1,176,102.

[2.14] Shaw DW (1972) Kinetic aspects in the vapor phase epitaxy of III–V-compounds. Journal of Crystal Growth 31, 130.
[2.15] Reep DH, Ghandi SK (1983) Deposition of GaAs epitaxial layers by organometallic CVD. Temperature and orientation dependence. Journal of Electrochemical Society. 130, 675.
[2.16] Leys MR, Veenvliet H (1981) A study of the growth mechanism of epitaxial GaAs as grown by the technique of metalorganic vapor phase epitaxy. Journal of Crystal Growth 55, 145.
[2.17] Stringfellow G (1999) Organometallic vapor-phase epitaxy: Theory and Practice, 2nd Edition. Academic Press, San Diego.
[2.18] Richter W, Zettler JT (1996) Real-time analysis of III–V-semiconductor epitaxial growth. Applied Surface Science 100/101, 465.
[2.19] http://www.aixtron.com/.
[2.20] http://www.veeco.com/.
[2.21] Grovenor CRM (1992) Microelectronic Materials. Institute of Physics publishing, Bristol and Philadelphia, ISBN 0-85274-270-3.
[2.22] Thompson LF, Willson CG, Bowden MJ (1994) Introduction to Microlithography, 2nd Edition. American Chemical Society.
[2.23] Beneking H (1991) Halbleiter-Technologie, B.G. Teubner, Stuttgart.
[2.24] Adachi S, Oe K (1983) Journal of Electrochemical Society 130 and 12, 2427.
[2.25] Mattox DM (1998) Handbook of Physical Vapor Deposition (PVD) Processing. Noyes Publications.
[2.26] Sze SM (1981) Physics of Semiconductor Devices. John Wiley & Sons.
[2.27] Gasser M, Latta EE (1992) Method for mirror passivation of semiconductor laser diodes. US Patent No. 5144634.
[2.28] Tu L, Schubert E, Hong M, Zydzik G (1996) In-vacuum cleaving and coating of semiconductor laser facets using thin silicon and a dielectric. Journal Applied Physics 80(11), 6448.
[2.29] Collot P, Delalande S, Olivier J (1999) Sulphur passivation of dry-etched AlGaAs laser facets. Electronics Letters 35(6), 506.
[2.30] Ueda O (1996) Reliability and Degradation of III–V optical devices. Artech House.
[2.31] Xia R, Larkins EC, Harrison I, Dods SRA, Andrianov AV, Morgan J, Landesman JP (2002) Mounting induced strain threshold for the degradation of high power AlGaAs laser bars. Photonics Technology Letters 14, 893.
[2.32] Tomm JW, Gerhardt A, Elsaesser T, Lorenzen D, Hennig P (2002) Simultaneous quantification of strain and defects in high power diode laser devices. Applied Physics Letters 81, 3269.
[2.33] Tomm, JW, Gerhardt A, Müller R, Malyarchuk V, Sainte-Marie Y, Galtier P, Nagle J, Landesman JP (2003) Spatially-resolved spectroscopic strain measurements on high-power laser diode bars. Journal of Applied Physics 93, 1848.
[2.34] Gerhardt A, Weik F, Quoc Tran T, Tomm JW, Elsaesser T, Biesenbach J, Müntz H, Seibold G, Biermann ML (2004) Device deformation during low frequency pulsed operation of high power diode bars, Applied Physics Letters 84, 3525.
[2.35] Todoroki S, Sawai M, Aiki K (1985) Temperature distribution along the striped active region in hig-power GaAlAs visible lasers. Journal of Applied Physics 58, 1124.
[2.36] Brugger H, Epperlein PW (1990) Mapping of local temperature distributions on mirrors of GaAs/AlGaAs laser diodes. Applied Physics Letters 56, 1049.

[2.37] Tang WC, Rosen HH, Vettinger P, Webb DJ (1991) Raman microprobe study of the time development of AlGaAs single quantum well laser facet temperature on route to catastrophic breakdown. Applied Physics Letters 58, 557.
[2.38] Kranz MC, Rosen HJ, Lenth W (1990) Localized temperature dynamics of GaAlAs laser facets investigated by Raman microprobe measurements. El. Letters 26, 990.
[2.39] Tomm JW, Thamm E, Bärwolff A, Elsaesser T, Luft J, Baeumler M, Mueller S, Jantz W, Rechenberg I, Erbert G (2000) Facet degradation of high power diode laser arrays. Applied Physics A 70, 377.
[2.40] Puchert R, Tomm JW, Jaeger A, Bärwolff A, Luft J, Späth W (1998) Emitter failure and thermal facet load in high-power laser diode arrays. Applied Physics A 66, 483.
[2.41] Rinner F, Rogg J, Konstanzer H, Mikulla M, Weimann G, Tomm JW, Thamm E, Poprawe R (2003) Facet temperature reduction a current blocking layer at the front facets of high power InGaAs/AlGaAs lasers. Journal of Applied Physics 93, 1354.
[2.42] Herrmann FU, Beeck S, Abstreiter G, Hanke C, Hoyler C, Korte L (1991) Reduction of mirror temperature in GaAs/AlGaAs quantum well laser diodes with segmented contacts. Applied Physics Letters 58, 1007.
[2.43] Garbusov DZ, Abeles J, Morris NA, Gardner PD, Triano AR, Harvey MG, Gilbert DB, Conolly JC (1996) High power separate confinement heterostructure AlGaAs/GaAs laser diodes with broadened waveguide, SPIE Proceedings 2682, 20.
[2.44] Walpole JN (1996) Semiconductor amplifiers and lasers with tapered gain regions. Optical and Quantum Electronics 28, 623.
[2.45] Moser A, Latta EE (1992) Arrhenius parameters for the rate process leading to catastrophic damage of AlGaAs-GaAs laser facets. Journal of Applied Physics, 71, 4848–4853.
[2.46] Pawlik S, Traut S, Thies A, Sverdlov B, Schmidt B (2002) Ultra-high power RWG laser diodes with lateral absorber region. 18th IEEE International Semiconductors Laser Conference, Garmisch, Germany, 163.
[2.47] Kintzer ES, Walpole JN, Chinn SR, Wang CA, Missaggia LJ (1993) High power strained-layer amplifiers and lasers with tapered gain regions. IEEE Photon Technological Letters 5, 605.
[2.48] O'Brien S, Schönfelder A, Lang RJ (1997) 5W CW diffraction-limited InGaAs broad-area flared amplifier at 970 nm. IEEE Photon Technolgical Letters 9, 1217.
[2.49] de Mars SD, Dzurko KM, Lang RJ, Welch DF, Scifres DR, Hardy A (1996) Angles grating distributed-feedback laser with 1 W single-mode, diffraction-limited output at 980 nm. Technical Digest CLEO 96, 77.
[2.50] Paschke K, Bogatov A, Bugge F, Drakin AE, Fricke J, Guther R, Stratonikov AA, Wenzel H, Erbert G, Tränkle G (2003) Properties of ion-implanted hig-power angled-grating distributed-feedback lasers, IEEE Journal of Selected Topics in Quantum Electronics 9, 1172.
[2.51] O'Brien S, Welch DF, Parke RA, Mehuys D, Dzurko K, Lang RJ, Waarts R, Scifres D (1993) Operating characteristics of a high-power monolithically integrated flared amplifier master oscillator power amplifier. IEEE Journal of Quantum Electronics 29, 2052.
[2.52] Stohs J, Bossert DJ, Gallant DJ, Brueck SRJ (2001) Gain, refractive index change and linewidth enhancement factor in broad-area GaAs and InGaAs quantum-well lasers. IEEE Journal of Quantum Electronics 37(11), 1449.
[2.53] Mikulla M (2000) Tapered high-power, high-brightness diode lasers Topics of Applied Physics 78, 265.

[2.54] Kelemen MT, Weber J, Rogg J, Rinner F, Mikulla M, Weimann G (2002) Beam quality and linewidth enhancement factor of ridge-waveguide tapered diode lasers. 18th IEEE International Semiconductor Laser Conference, Garmisch, Germany, 81.
[2.55] Dente GC (2001) Low confinement factors for suppressed filaments in semiconductor lasers. IEEE Journal of Quantum Electronics 37(12), 1650.
[2.56] Mikulla M, Chazan P, Schmitt A, Morgott S, Wetzel A, Walther M, Kiefer R, Pletschen W, Braunstein J, Weimann G (1998) High-brightness tapered semiconductor laser-oszillators and amplifiers with low modal gain epilayer-structures. IEEE Photonic Technological Letters 10(5), 654.
[2.57] Lang RJ, Hardy A, Parke R, Mehuys D, O'Brien S, Major J, Welch D (1993) Numerical analysis of flared semiconductor laser amplifiers. IEEE Journal of Quantum Electronics 29, 2044.
[2.58] Al-Muhanna A, Mawst LJ,Botez D, Garbuzov DZ, Martinalli RU, Connolly CJ (1997) 14.3 W quasi-continuous wave front-facet power from broad-waveguide Al-free 970 nm diode lasers. Applied Physics Letters 71, 1142.
[2.59] Kelemen MT, Rinner F, Rogg J, Wiedmann N, Kiefer R, Walther M, Mikulla M, Weimann G (2002) High-power, high-brightness ridge-waveguide tapered diode lasers at 940 nm. SPIE Proceedings 4648, 75.
[2.60] Mikulla M, Kelemen MT, Walther M, Kiefer R, Moritz R, Weimann G (2001) High-power 980 nm laser diodes by MBE. SPIE Proceedings 4580, 11.
[2.61] Kelemen MT, Weber J, Rinner F, Rogg J, Mikulla M, Weimann G (2003) High-brightness 1040 nm tapered diode lasers. SPIE Proceedings 4947, 252.
[2.62] Kelemen MT, Weber J, Kallenbach S, Pfahler C, Mikulla M, Weimann G (2004) Astigmatism and beam quality of high-brightness tapered diode lasers. SPIE Proceedings 5452, 233.

3
Packaging of Diode Laser Bars

Konstantin Boucke

3.1. Introduction

Konstantin Boucke

The packaging process is of decisive importance for the applicability of high-power diode laser bars – not only technically but also economically.

Technically, the laser bar is not operable without being packaged, and the quality of the package critically influences major characteristics of the laser bar, such as achievable output power, wavelength, lifetime, and even the polarization properties.

From an economical point of view, the packaging process – including testing and quality control measures – contributes strongly to the production costs of a high-power diode laser. Due to the higher standards that have to be met in terms of alignment precision, subcomponent preparation, and soldering-process control, highly specialized equipment and well-experienced operators are needed. This leads to the fact that the packaging process accounts for more than 50% of the total production costs of a packaged diode laser bar.

As for other electronic or opto-electronic devices, the package of a high-power laser bar has to provide the following basic features:

- mechanical stability for mounting and handling,
- electrical contacts both on the n-side and the p-side of the device,
- cooling to remove the waste heat generated by the diode laser.

Due to the large power turnover and the comparably small size of a diode laser bar, the cooling capabilities of the package are of especially great importance: With a typical efficiency of 50%, a laser bar producing an optical output power of 50 W equally generates 50 W of waste heat [3.1,3.2]. Taking into consideration a typical size of 10×1 mm, this results in an extremely high heat flux density of 500 W/cm^2. To maintain it's high efficiency and a long lifetime, the operation temperature of the laser bar should be kept as low as possible, typically below 60°C. This requires very effective cooling, resulting in the fact that the package design is dominated by the cooling aspect (Fig. 3.1).

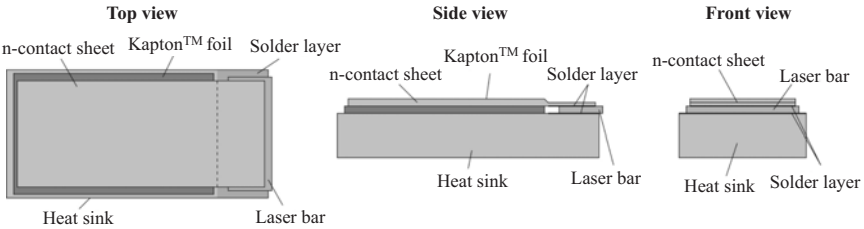

FIGURE 3.1. Schematic drawing of a typical diode laser bar package

Depending on the specific requirements, different cooling techniques may be used. For high-average-power applications active cooling with water-cooled, microchannel heat sinks is necessary. For reduced average power levels, passive cooling using massive copper heat sinks mounted on thermo-electric coolers may be used. In either case, the standard heat sink material in nearly all commercially available packages is copper, because of its excellent thermal conductivity (approx. 380 $Wm^{-1} K^{-1}$), its good mechanical machining properties, and its comparatively low price.

Alternative materials and material combinations are investigated mainly for three reasons:

1. to achieve thermal expansion-matching between the heat sink and the laser bar, believed to result in an increased device reliability and lifetime;
2. to improve the cooling capabilities of the package, e.g., by using diamond heat spreaders;
3. to isolate the cooling water circuit electrically from the laser bar, reducing the requirements on the cooling liquid quality and preventing voltage-driven corrosion in the cooling circuit.

The first two of these points are addressed in sections 3.3.5 and 3.4, respectively.

The mismatch in thermal expansion between the laser bar and the (copper) heat sink – the coefficient of thermal expansion (CTE) of copper is 17 ppm/K while it is approximately 6.8 ppm/K for GaAs-based laser bars – has a major influence on the mounting technique used for laser bars. To compensate the different expansion behavior without inducing a severe amount of stress into the laser bar, a weak and deformable solder interface between the laser bar and the heat sink has to be formed. For this reason, high-power laser bars are – in most commercially available packages – mounted with indium soft solder instead of the in photonics packaging widely used AuSn solder. Therefore, the indium soldering of high-power opto-electronic devices is one of the key technologies for the packaging of laser bars.

3.2. Mounting of Diode Laser Bars

Jens Bisenbach

3.2.1. Mounting Principle

Mounting of diode laser bars demands precise positioning, superior thermal and electrical contact, and reliable contact junctions between all involved materials during the operated lifetime.

For the mounting process diverse technologies are known and established. Some of them are only suitable in combination with certain operational conditions – e.g., operation in quasi-continuous wave (pulsed) – or can only be applied in conjunction with a coefficient of thermal expansion (CTE)-matching submount material. The most used processes are listed in order of frequency of application:

- soft soldering with ductile solder, like indium, to a copper heat sink on the p-side (see Fig. 3.2);
- soldering with harder solder, like AuSn alloys, to CTE-adapted submounts on the p-side, made, e.g., of copper/tungsten (see Fig. 3.3);
- soft soldering with ductile solder, such as indium or a comparable solder, to a ceramic block which is nearly expansion matched to GaAs with separate grooves for each bar;
- clamping the p- and n-side between two very precisely lapped and possibly thick Au-plated, stiff copper heat sinks, by applying a very uniform pressure over the

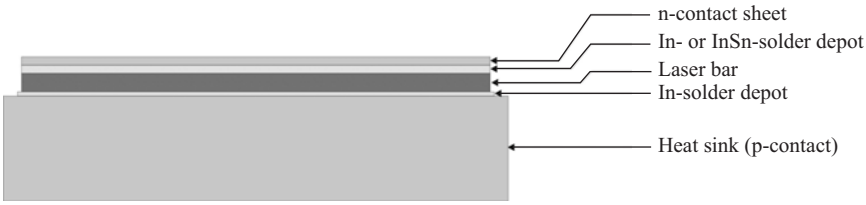

Figure 3.2. Direct laser bar mounting to heat sink using soft solder (front view)

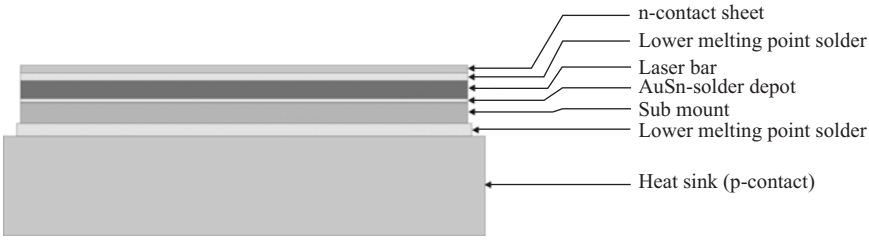

Figure 3.3. Submount setup for laser bar mounting with hard solder (front view)

Table 3.1. Overview of the physical properties of different solder alloys (compiled from references [3.5–3.13])

Type of solder	λ [W/mK]	Max. allowed elongation [%]	Yield strength [N/mm^2]	Liquidus temperature [°C]
InBi22	–	85	14.5	93–108
PbSn40Bi20	–	120–150	25–35	95–156
PbBi40Sn20	–	50–100	25–35	95–117
InAg2	–	20–25	4–6	114–148
InSn48	–	16–34	43	117
InPb15Ag2	–	–	–	142–149
SnPb29In17.5Zn0.5	25.5	–	–	149
In	71–87	41	0.4–2.4	156
Sn70Pb18In12	–	–	–	164
PbSn36Ag2	59	25–30	30	178
PbIn50	22	14–18	40–45	178–210
SnPb40	60–70	27	42–51	183
PbSn40	–	30	30	183–235
SnZn9In5	–	–	62	188
AuSn90	–	6	77	217
SnAg3.5	57–78	20–30	25–35	221
SnCu1	–	8–15	28–32	227
Sn	63	28	10–15	232
Bi	9	–	–	271
AuSn20	46	1	275	280
PbSn5Ag2.5	44	20–30	25–35	280
SnSb8	–	50–55	40–45	280
PbIn5Ag2.5	42	28–34	35–40	307
Pb	37–42	17	21–36	327
SnAu5	–	–	–	519

bar contact surface and so providing a homogeneous contact without any filler material.

Already well known from mounting other high power semiconductors to heat sinks, the widely used mounting technology is soldering. In most cases a ductile solder is used to fix the 10-mm laser bar to the heat sink. There are certain requirements that define the choice of solder suitable for laser bars (see also Table 3.1).

- Ability to compensate for the stress due to the mismatch between the thermal expansion of the laser bar and the heat sink material. For non-matching CTE materials, ductile solder is used.
- Wetting behavior to the metallization surfaces applied to the mounting partners.
- Suitable melting point and process temperature to allow a step-soldering process if the n-contact sheet is also soldered after mounting the bar, or a submount is used.

Besides the metallurgical design, the technology used to align and join the bar to the heat sink is also important for high-quality results. Two different processes are

used for soldering laser bars: (1) an individual pick, place, and join (PPJ) process with an integrated reflow oven which is not sealed, but uses shielding gas that can also include flux components, and (2) a pick and place to clamping tools plus an additional batch reflow process. Both are reflow-like processes, where first the solder is applied, then the components are brought into position, and afterward the reflow process is run. The main difference of the two processes is the alignment method, the component handling, and the ambient control.

The PPJ process uses multi-axis alignment stages and an optical control with adapted image-processing software to control the position of the laser bar, which is picked up by a very precise and flat vacuum tool. When the position is adjusted, the tool will hold the bar during the following soldering process. This guarantees a very low "smile" (see Chapter 4.2.2, Fig. 4.19) of the laser bar after mounting, as the vacuum tool keeps the bar in the planar position. Precise pick and place units are commercially available, whereas the integrated oven which has to fulfill requirements regarding shielding gas, process gas guiding, and tightness as well as optical access for alignment is usually a custom design and the key to successful soldering. Depending on the degree of automation of this process, especially for the laser bar positioning procedure, this process can be strongly operator dependent. One major advantage of this kind of process is the remaining smile of less than 1 μm on a 10-mm laser bar, which allows a very efficient fast-axis beam shaping by means of micro-optics.

The batch process, on the other hand, uses pick and place units to adjust the bar to the heat sink, or even mechanical stops are used. This part of the process can be fully automated, avoiding operator dependence. During and after this alignment process, bar and heat sink are fixed in a clamping tool, which preserves especially the lateral positions (i.e., bar overhang) of the components during the next steps (Fig. 3.4).

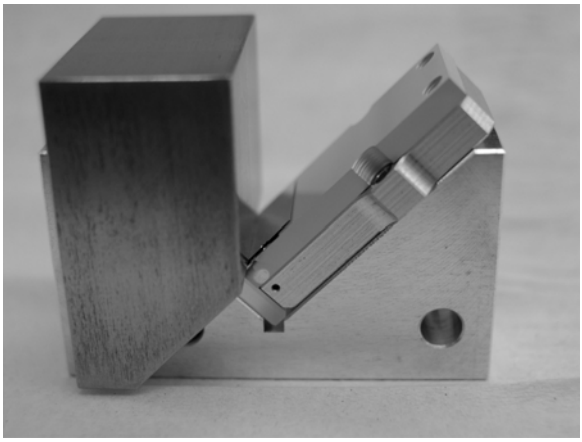

Figure 3.4. Clamping tool and process weight with metallized heat sink, laser bar and contact sheet

This tool holding the adjusted parts will now be transferred to a reflow oven, which can handle usually up to 100 parts in one process run and allows, due to the closed oven chamber, very controlled ambient and gas conditions and the application of vacuum to reduce voids in the solder junction. However, "smile" cannot be controlled as well as in the PPJ process; using very sophisticated clamping tools, a smile of 2–4 μm can be achieved with high yield. Another advantage of this process is the possibility to solder n-contact sheets or further additional elements directly to the diode laser device in the same process step. Therefore, from the economical point of view, the batch process is the more advantageous in terms of throughput and costs, the more components have to be mounted to the diode laser device.

3.2.2. State of the Art

Today, there are mainly two soldering techniques used for the manufacturing of commercial diode laser bars:

- indium technology
- AuSn technology

Indium technology allows to compensate for the thermal expansion mismatch between heat sink materials and the GaAs material of the laser bar during the mounting process (cool-down phase) as well as during operation, since indium is very soft and ductile. At only 1.5 N/mm^2 indium starts yielding, so the solder material itself limits the maximum mechanical load to the laser bar. Also the ductility of indium is very high, so that indium can equalize the displacement between bar and heat sink due to thermal expansion without forming cracks and voids between bar and heat sink. The wetting characteristics are excellent for indium combined with the standard Au metallization used for laser bars. A disadvantage is the limited operation temperature if mechanical or thermo-mechanical cycling with high plastical deformation rates for the indium interface is applied.

In contrast, AuSn joints are comparably stiff, so they allow no stress and strain compensation (Fig. 3.5). All forces that result from a mismatch between heat sink material (usually CTE-matched submounts) and the GaAs laser bar are transferred directly to the laser bar. The reliability of AuSn joints is very good; AuSn is well suited for high-temperature applications as generally requested for military lasers. It also does not degrade during mechanical cycling, when the device design is laid out not to exceed the elastic deformation of the solder interface. The endurance limit for high electrical current causing electromigration or cycle stress causing voids and cracks is very high. But without a heat sink material very close to a thermal expansion coefficient of $6.5 \times 10^{-6}\,\mathrm{K}^{-1}$, AuSn can cause very high stress in the laser bar, which initiates fast degradation. If AuSn would be used to directly solder bars to common copper heat sinks, the bar would even crack during the cool down from process temperature to ambient temperature. Using AuSn, there is to consider a trade-off between superior thermal cycling characteristics on one side and the increase of the thermal resistance on the other side, which is caused

by the lower thermal conductivity of the CTE-matched submount materials and an additional joint between submount and heat sink.

For both techniques, indium and AuSn soldering, the solder can be applied by using preforms or by direct evaporation of the solder material to the heat sink or submount, respectively. Preforms of AuSn solder are available with a thicknesses of less than 20 μm, whereas the thinnest indium preforms are 20 μm in thickness. To avoid excess solder junction resistance and also the discharge of molten solder during the mounting process, a thickness of below 15 μm is required. This means, for indium, physical vapor deposited (PVD) solder depots are best suited, whereas AuSn can be used as a preform (Fig. 3.6).

The purity of the deposited indium solder can be controlled by the PVD parameters, primarily the remaining pressure during deposition ($<10^{-6}$ mbar). In case of the use of preforms, precautions depending on the supplied quality have to be considered, like mechanical surface preparation and cleaning.

3.2.3. Residual Stress

A laser bar mounted to a heat sink is mechanically stressed. This results from the unequal thermal expansion behavior of GaAs as basic bar material and the

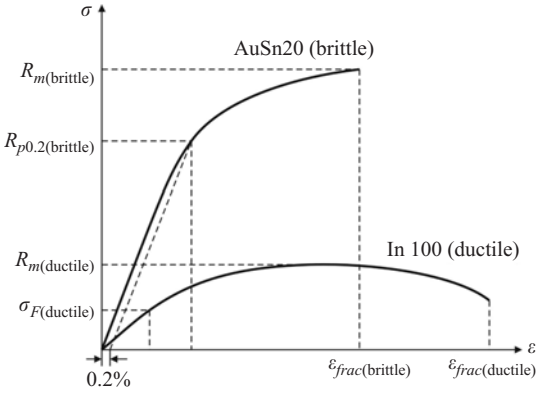

FIGURE 3.5. Schematic illustration of stress strain characteristics of soft and hard solder

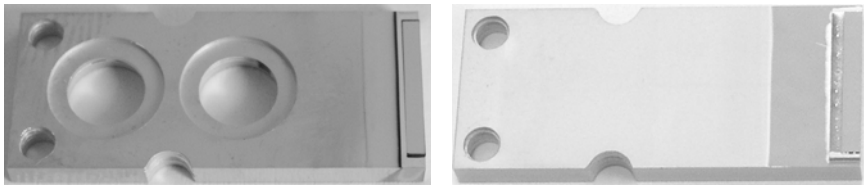

FIGURE 3.6. Laser bar mounted with indium directly on a heat sink (left) and with AuSn using an additional submount (right)

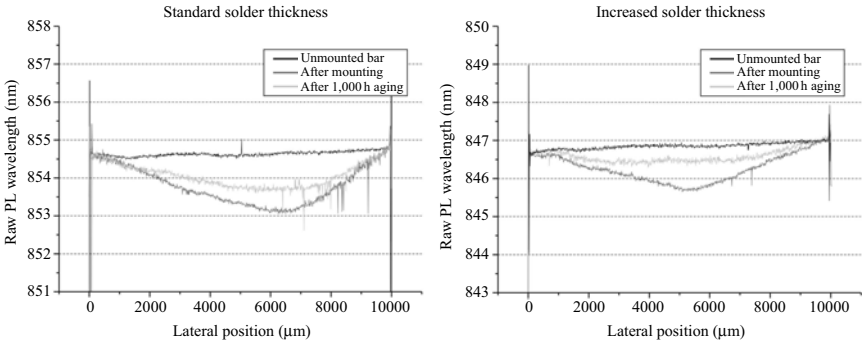

FIGURE 3.7. Change of mounting induced stress with original solder junction thickness (left) and with increased solder junction thickness (right), indicated by the photoluminescence (PL) wavelength. In both cases a stress relaxation after aging can be seen

heat sink material, usually copper. By means of soft solder this stress will be partly compensated for by the plastic deformation of the solder during a thermal cycle. But even with very soft material, like indium, which is among the lowest-yield-strength solder materials, an accumulation of infinite small stress-loaded areas over the entire bar area results in a stress concentration in the center of the laser bar. In this model the bar edges are at zero stress level. Taking into account that an increased stress level leads to stronger degradation of the laser bar during operation [3.4], a stress reduction is necessary. The level of maximum stress can be decreased by increasing the thickness of the stress-relieving layer, that is, the soft solder junction thickness. But as the solder passes through the liquid phase during the soldering process, the original solder thickness – e.g., the preform thickness – is not what matters, but the residual thickness of the solder interface after solidification; applied forces during the soldering process will squeeze out the liquid solder. The remaining solder thickness is a function mainly of applied forces and wetting behavior. In experiments, the maximum stress level could be reduced by 35% by increasing the solder interface thickness by a factor of 1.5 (Fig. 3.7).

Using material with adapted CTE, the maximum stress level resulting from the cool-down phase of the soldering process can also be reduced. But even in this case, the maximum resulting stress level is not negligible. Finally, there is stress introduced during operation cycles, because the thermal gradient in the device also causes stress.

3.2.4. Packaging Parameters Influencing Lifetime and Reliability

There is a wide set of parameters that influence the solder interface between bar and submount/heat sink like the temperature/time regime, pressing/clamping forces,

surface metallizations and their purity, geometrical misalignment, ambient conditions during soldering, etc. These parameters have to be adapted and optimized for the individual process concept and the equipment used. Besides general parameters, consider that the laser bar is a very fragile device, which requires certain precautions during handling and the manufacturing process to prevent defects. For example, for some bars, cleaning of the front facet is not possible without causing damage, due to the mirror-coating process applied by the diode laser bar manufacturer. Therefore, contamination or defects caused by touching these surfaces with tools, by out-gassing of residues from the solder surfaces or wetting by means of fluxes has to be strictly avoided (Figs. 3.8, 3.9).

Inhomogeneities of the solder interface, such as bubbles and voids are a further failure source (Fig. 3.10) or non-parallelism between the laser bar and the heat sink mounting surface. This leads not only to a variation in thermal resistance, it also can cause localized brittle areas in the solder junction due to the formation of intermetallics between the solder material and the metallization layers, eventually resulting in a lack of pure solder material. This kind of solder interface defects will induce inhomogeneous stress to the laser bar, leading to accelerated degradation.

3.3. Cooling

3.3.1. Introduction

Dirk Lorenzen

Cooling is a technical process that keeps a heat source (diode laser bar) at a desired temperature. The cooling process accomplishes the stationary dissipation of heat,

Figure 3.8. Sample illustration of solder discharge and wetting of the front facet

which is created by that amount of electrical power P_{el} maintaining diode laser operation, that is not converted into optical power P_{opt}, but into thermal power $P_{th} = P_{el} - P_{opt}$.

The thermal resistance R_{th} of a heat dissipating region (heat source + heat sink) is defined as the temperature difference ΔT between the hottest and the coldest point within this region that is created by 1 W of thermal power:

$$R_{th} = \frac{\Delta T}{P_{th}}. \tag{3.1}$$

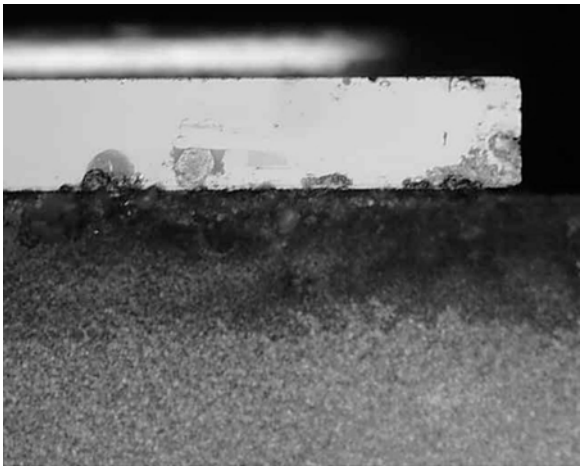

FIGURE 3.9. Sample illustration of flux residue

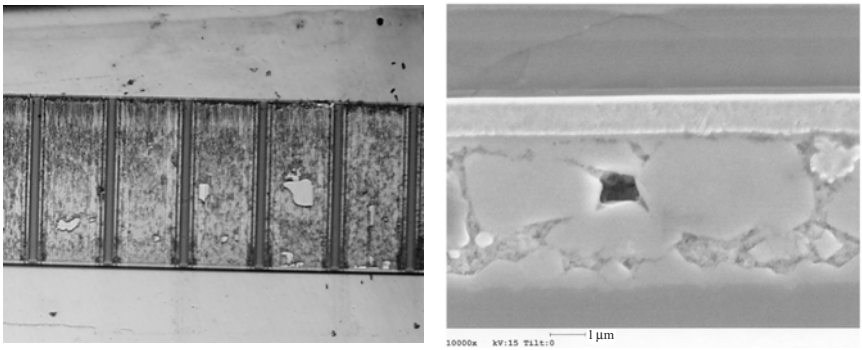

FIGURE 3.10. Left: Sample illustration of voids and nonwetting areas on the laser bar p-side after mounting. Right: Formation of intermetallics in a very thin solder junction due to an excess of Au

In a diode laser heat is mainly generated in the active zone – this is the light-creating and -guiding region in the waveguide of the laser emitters. The hottest point in a diode laser is located at the intersection of waveguide and front facet, the coldest point in a diode laser is located somewhere at the boundary of the heat sink – for example, at the water inlet in the case of a water cooled microchannel heat sink.

The temperature of the diode laser bar effects its electro-optic properties like efficiency and reliability. In order better to understand the key role of cooling, the impact of temperature on these properties is analyzed in the following.

3.3.1.1. The Influence of Temperature on Electro-Optic Efficiency

Semiconductor properties are temperature-dependent – and so are diode laser property parameters like threshold current I_{th} and slope efficiency η_s. Their thermal behavior can be described by exponential relations like

$$I_{th}(T + \Delta T) = I_{th}(T) \exp\left(\frac{\Delta T}{T_0}\right) \tag{3.2}$$

and

$$\eta_s(T + \Delta T) = \eta_s(T) \exp\left(-\frac{\Delta T}{T_1}\right), \tag{3.3}$$

where T_0 is the temperature constant of the threshold current and T_1 is the temperature constant of the slope efficiency. Raising the laser diode temperature increases its threshold current and reduces its slope efficiency. As a result, its optical output power

$$P_{opt}(T) = \eta_s(T)(I - I_{th}(T)) \tag{3.4}$$

will decrease and so will electro-optic efficiency

$$\eta_{eo} = \frac{P_{opt}}{P_{el}} \tag{3.5}$$

do, too. If one decides to rise electrical current – and thereby electrical input power – to maintain the initial optical output power, the electro-optic efficiency will keep on staying on lower level. Table 3.2 gives a calculation example for these laser parameters at temperatures T and $T + \Delta T$ using $I_{th} = 15\,\text{A}$, $\eta_s = 1.11\,\text{W/A}$, $T_0 = 120\,\text{K}$, $T_1 = 500\,\text{K}$ and $\Delta T = 10\,\text{K}$.

Table 3.2. Influence of temperature rise on laser parameters

Temperature	Operational current, $I(A)$	Optical output power, P_{opt} (W)	Electro-optic efficiency, η_{eo} (%)
T	60.0	50.0	46.8
$T + 10\,\text{K}$	60.0	47.6	44.6
$T + 10\,\text{K}$	62.2	50.0	44.9

To summarize, based on the above-mentioned values, temperature rises of $\Delta T < T_0$ cause an almost linear optical output power loss of 1 W every 4 K. Good cooling is thus required to keep this kind of power loss as low as possible.

3.3.1.2. The Influence of Temperature on Lifetime

High-power devices are – especially when put into operation – subjected to different degradation mechanisms. These degradation mechanisms are in general dependent on temperature T. In many cases, the temperature-dependent term of the related MTTF_i (mean-time-to-failure) of each degradation mechanism i can be described by Arrhenius' law:

$$\mathrm{MTTF}_i = A_i \exp\left(\frac{E_{A,i}}{k_B T}\right), \tag{3.6}$$

where $E_{A,i}$ is the activation energy of the i-th degradation mechanism, A_i is a degradation mechanism specific constant, and k_B is the Boltzmann constant. Activation energies are typically in the range of 0.2–1.0 eV, provided temperature does not promote any significant phase-changing effect (glass transition of a polymer, melting of a solder). A degradation mechanism can be easily identified among others when it is predominant, e.g., when A_i and the ratio of $E_{A,i}$ and T are small enough. It is obvious, that at higher temperatures degradation mechanisms with higher activation energies become predominant.

In general, a (visible) degradation process is a superposition of different (invisible) degradation mechanisms. The resulting (measured) lifetime is determined by

$$\langle \mathrm{MTTF} \rangle = \left(\sum_i \frac{1}{\mathrm{MTTF}_i}\right). \tag{3.7}$$

One can describe this resulting MTTF in the same form as Eq. (3.6) by using appropriate temperature-dependent factors $A(T)$ and $E_A(T)$:

$$\langle \mathrm{MTTF} \rangle = A(T) \exp\left(\frac{E_A(T)}{k_B T}\right). \tag{3.8}$$

The lifetime-reducing effect of a temperature rise ΔT can be quantified by the ratio of the MTTF's at temperature $T + \Delta T$ and T. Provided that the temperature rise is small enough for the factors $A(T)$ and $E_A(T)$ to be approximately constant, one obtains

$$\frac{\langle \mathrm{MTTF}(T + \Delta T) \rangle}{\langle \mathrm{MTTF}(T) \rangle} = \exp\left(-\frac{E_A}{k_B T} \frac{\Delta T}{(T + \Delta T)}\right). \tag{3.9}$$

As an example, at $T = 40°C$, a temperature rise of $\Delta T = 10\,K$ reduces lifetime by 50% when $E_A = 0.6\,eV$. Appropriate cooling of high-power diode lasers is thus a key issue to extend their lifetimes.

3.3.2. Conduction Cooling

Dirk Lorenzen

3.3.2.1. The Heat Equation

Denoting by $\lambda_{ij}(\mathbf{r})$ the components of the thermal conductivity tensor, the stationary temperature distribution $T(\mathbf{r})$ at each point $\mathbf{r} = (x, y, z)$ within a closed spatial region created by a spatial thermal power density $p_{th}(\mathbf{r})$ is determined by the stationary equation of heat conduction

$$\partial_i \, \lambda_{ij} \, \partial_j = -p_{th} \tag{3.10}$$

within the region and the governing boundary conditions at the surface of the region ($i, j = x, y, z$). Supposing macroscopic isotropic heat conduction, which is common in microscopic polycrystalline material, the equation of heat conduction simplifies to

$$\lambda \, \partial_i \, \delta_{ij} \, \partial_j \, T = -p_{th}, \tag{3.11}$$

where λ is the isotropic thermal conductivity.

Boundary conditions can be of Dirichlet type (constant boundary surface temperature), Neumann type (constant heat flux density $\mathbf{j}_{th}$ through boundary surface), and Robin type (constant heat transfer coefficient α at boundary surface). A constant boundary surface temperature is an ideal assumption of having no heat-transfer-limiting effects. It is thus a special case of the Robin's boundary condition in the limit of $\alpha \to \infty$. Since this does not appear in practice, Dirichlet's boundary condition is only of mathematical interest.

Neumann's boundary condition is useful in three cases: In the case of heat flux out of the region, it may represent the limited heat flux density acceptance of a Peltier module (TEC = thermo-electric cooler). In the case of heat flux into the region, it may replace the diode laser bar volume region by an appropriate heat flux density distribution on the heat sink's surface. Such a simplification is justified when the laser bar is mounted epi-side down onto the heat sink and when all heat created in the active zones of the laser bar passes through the heat sink. The third, special, case of zero heat flux density is similar to Robin's boundary condition in the limit of $\alpha \to 0$. It is applied to all boundaries where heat transfer is very low compared to relevant heat transfer areas.

Robin's boundary condition represents all heat transfer mechanisms like natural and forced convection of air and water. It may replace a thermal interface including attached cooling means or a liquid-cooled microchannel structure (cf. Chapter 3.3.4).

Figure 3.11 shows a heat sink with thermal boundary conditions that are common for thermal modeling of diode lasers.

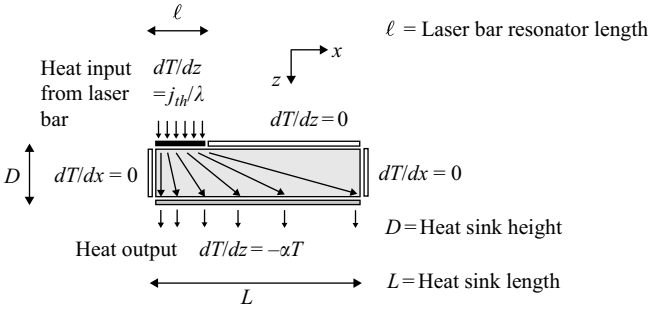

FIGURE 3.11. Heat dissipation and thermal boundary conditions in the heat sink of a diode laser. The arrows represent the heat flux paths

3.3.2.2. Thermal Optimization of Heat-Conducting Bodies

There are three main design rules that help reduce the thermal resistance of a heat sink body:

1. using a material of very high thermal conductivity,
2. arranging that material in a way that it surrounds the heat source as complete as possible,
3. spreading the heat over a big area.

The first point is obvious. The second and the third points serve to increase the number of heat flow paths and to reduce heat flux density. Heat spreading, especially, is necessary due to the finite heat transfer at the boundary (bottom side) of the heat sink. The higher its heat transfer coefficient, the less heat needs to be spread. In the fictive case of an infinite heat transfer coefficient, no heat spreading would be necessary, and a heat sink would not make a sense. It is thus the task of a heat-spreading body to provide an appropriate thermal matching between a given heat source (diode laser bar) and a given heat absorbing device (TEC, microchannel structure).

Heat spreading in lateral directions (coplanar with heat input area) requires some heat sink extension in transversal direction (perpendicular to heat input area). On the other hand, this transverse direction (thickness) must not exceed a certain limit, where heat spreading is accomplished and any additional material in transverse direction would result in nothing more than extending the heat flow path, corresponding to an increase of the thermal resistance.

Calculation of the thermal resistance of a heat sink shaped like a parallelepiped requires a numerical solution of the heat equation with the boundary conditions described above. A heat sink thickness optimization procedure can thus only be carried out stepwise numerically, too. In the lateral direction, heat sink length and width are always optimized when they are of infinite size. Hence an optimization procedure of a reasonable heat sink length and width, and thereby heat sink thickness, is required. In a first attempt, such a procedure will not take into account the emitter structure, defined by emitter width, emitter pitch and the ratio of both – the

so-called filling factor f, but only laser bar width b and laser resonator length ℓ. Limiting ourselves to an optimization in laser resonator direction (heat sink length) one can perform heat sink size optimization within the following four steps:

1. Determine the maximum heat sink thickness $d_{\max}$ for a heat sink of nearly infinite length (we use $L_{\max} = \ell + 5\,d_{\max}$) by minimizing the thermal resistance down to $R_{th,\min}$.
2. Reduce heat sink length to a value of an optimal length L_{opt} where the corresponding thermal resistance is 5% higher than that calculated in step 1.
3. Determine an optimal heat sink thickness d_{opt} using heat sink length L_{opt} by minimizing the thermal resistance down to $R_{th,\text{opt}}$.
4. To save on expensive heat spreader material (like CVD diamond), determine a minimum heat sink thickness $d_{\min}$, that results in a thermal resistance $R_{th,\max}$ whose value is 5% higher than that of $R_{th,\text{opt}}$.

The result of such an optimization procedure can be represented for every heat sink material (every thermal conductivity) by a graph displaying both, the optimal heat sink thickness from step 3 and the optimal heat sink length from step 2 versus heat transfer coefficient at the bottom side of the heat sink. Figure 3.12 is an example for the case of a copper heat sink, where the lower limit dash represents the minimum heat sink thickness $d_{\min}$ determined in step 4 and the upper limit dash represents the maximum heat sink thickness determined in step 1. As one can see, for heat transfer coefficients above 0.4 W/mm^2/K, the optimal heat sink length becomes equal to the laser resonator length $\ell = 0.94$ mm. In turn, the optimal heat sink thickness becomes zero, which cannot be visualized on the logarithmic scale.

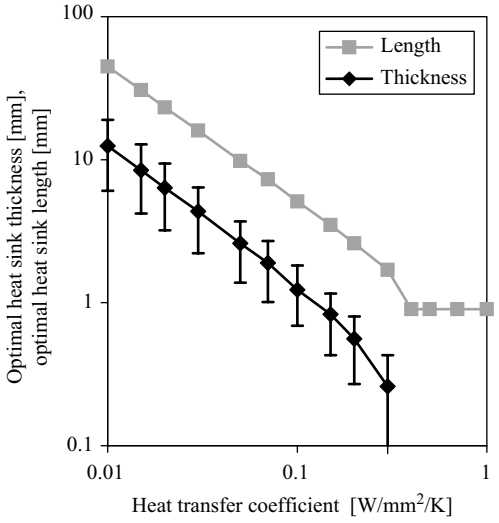

FIGURE 3.12. Optimized heat sink dimensions for a given heat transfer at heat sink bottom side. Laser bar resonator length is 0.9 mm

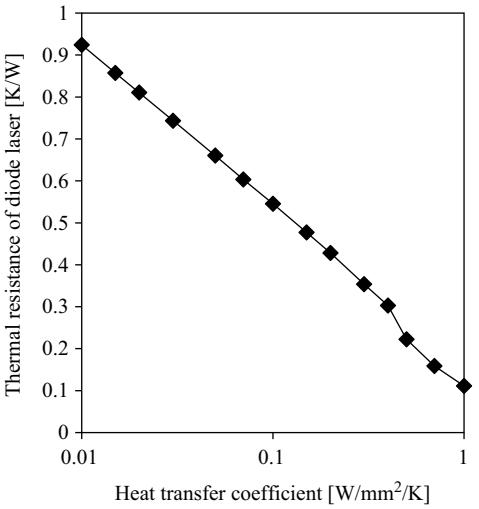

FIGURE 3.13. Optimized heat sink thermal resistance for a given heat transfer at heat sink bottom side. Laser bar width is 0.9 mm

Additionally, the thermal resistance curve in Fig. 3.13 for a laser bar of 10 mm width (100% filling factor) sustains slight kink at 0.4 W/mm^2/K.

Such a high value of the heat transfer coefficient can only be achieved by water-cooled microchannel structures made from copper, diamond, or thermally analogous materials with channel dimensions below 50 μm (width) and above 500 μm (height). As long as such structures are not producible and manageable in operation at a reasonable low effort, heat spreading in heat sinks is always a concern when designing an appropriate cooling arrangement for high-power diode laser bars.

Besides this, there are three reasons for maintaining a certain heat sink thickness, even when the cited optimization procedure would not require it:

1. Stability: Direct contact with the cooling medium should be avoided. The enclosure of a cooling arrangement requires a wall thickness in the range of 0.2–0.4 mm when stable operation conditions are required.
2. Emitter structure: The inter-emitter heat spread effect of a heat sink reduces the thermal resistance by a factor of $1/f$ compared to no heat spreading (heat sink thickness zero). Inter-emitter heat spreading is accomplished within a thickness of half of the emitter pitch.
3. No limit of cooling: Even when the heat sink thickness is bigger than the optimal value, enhancement of the heat transfer coefficient will still improve the thermal resistance.

In the case of a cooling system based on conduction cooling only, high-quality thermal interfaces between heat sink and cooling plate correspond to heat transfer coefficients in the range of 0.01–0.03 W/mm^2/K. In this case, heat sinks should have a thickness of about 6 mm and a length of at least 20 mm. Their thermal resistance can be further reduced by heat spreading in bar width direction. For this

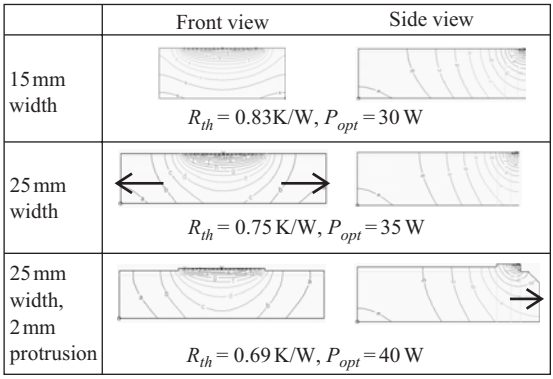

FIGURE 3.14. Development steps of a conduction-cooled heat sink towards a 40 W diode laser. The pictures show temperature distributions in heat sink front and side view, calculated by commercial 3D-FEM Software. The bottom side heat transfer coefficients were $\alpha = 0.0125\ \mathrm{W/mm^2/K}$ for the 15 mm wide heat sink and $\alpha = 0.01\ \mathrm{W/mm^2/K}$ for the 25 mm wide heat sinks. Laser bar structure: 19 emitters of 150 μm width in 500 μm pitch, resonator length 1 mm

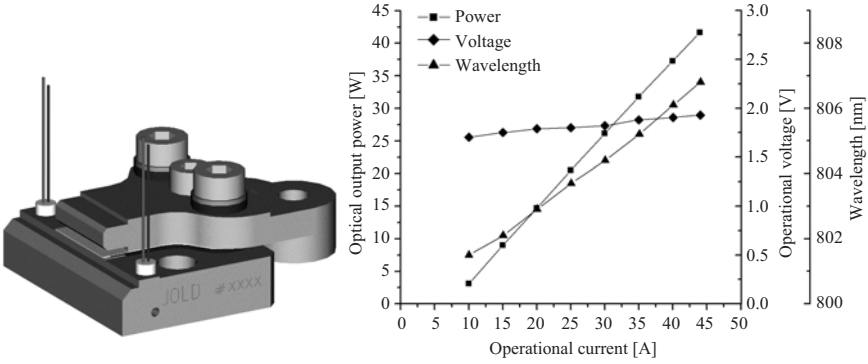

FIGURE 3.15. Left: A 40 W conduction-cooled diode laser with heat sink protrusion and integrated temperature sensors (courtesy of Jenoptik Laserdiode GmbH, patent pending). Right: Measured electro-optical characteristics of a 40 W conduction-cooled diode laser

reason, common conduction-cooled diode lasers are equipped with heat sinks of 15–25-mm width. Additionally, a heat sink protrusion in light emission direction may reduce the thermal resistance once again. It is obvious that such a protrusion must not impede free light propagation of the emitted diode laser light beams.

Figure 3.14 illustrates such a stepwise thermal resistance reduction by enlarging heat sink width and introducing a protrusion. The resulting optical output powers have been calculated assuming an electro-optical efficiency of 47% by allowing a temperature difference of 30 K between cooling plate and laser bar ($T = 55°\mathrm{C}$). In conclusion, the result of the simulation proves that a heat sink of a conduction-cooled 40-W diode laser should exhibit a protrusion for sufficient cooling. The picture of such a diode laser is represented in Fig. 3.15 (left).

The thermal resistance can be approximately determined experimentally by measuring the center wavelength λ_C of the laser emission spectra, the optical output power P_{opt}, and the operational voltage U as a function of the operational current I as displayed in Fig. 3.15 (right). Using $\kappa = 0.285\,\text{nm/K}$ as temperature drift coefficient of the wavelength, the slope of a linear regression on the values of λ_C/κ as function of $P_{th} = UI - P_{opt}$ would correspond to a thermal resistance of 0.63 K/W. This value is 0.06 K/W lower than the predicted 0.69 K/W, because the emission spectra are created by the mean value of the temperature distribution in all active zones and not by the maximum temperature at the laser facet.

3.3.3. Thermo-Electric Cooling

Thermo-electric cooling is based on the Peltier effect, by which a temperature difference $\Delta T_{\max}$ is created between the interfaces of different materials forming a Peltier element when an electrical current $I_{\max}$ is passing through them. If, additionally, external heat power P_{th} is present at the cold side of the Peltier element, this heat power will be transferred to the hot side of the Peltier element. This procedure is accompanied by a reduction of the temperature difference down to $\Delta T < \Delta T_{\max}$. Combining a number of n Peltier elements by connecting them electrically in series and thermally in parallel, one obtains a Peltier module or a thermo-electric cooler (TEC), that may transport n times more heat power than a single Peltier element at a constant temperature difference. The condition $\Delta T = 0$ at a Peltier operational current $I = I_{\max}$ defines the maximum heat power $P_{th,\max}$ that can be absorbed at the cold side of a Peltier module.

In contrast to natural heat conduction, the external heat flux direction through a Peltier module is parallel to the artificially created thermal gradient as long as $P_{th} < P_{th,\max}$. Under this condition of useful TEC operation, thermal resistance of a Peltier module is negative:

$$R_{th,Pe} = -\frac{\Delta T}{P_{th}}. \tag{3.12}$$

Therefore, by inserting a Peltier module in the heat flux path of a conduction-cooled system, the thermal resistance can be significantly reduced. The example of such an enhanced cooling system is shown in Fig. 3.16: Despite an ambient temperature of 30°C, the laser can still be operated at 55°C. Without TEC support, ambient temperature must have been below 10°C. A second advantage of a TEC is its tunability. Sensing the diode laser temperature in the heat sink, its value can be used as input signal for a controller that adjusts the Peltier current to set up a desired laser temperature. It is thus possible to control not only laser temperature but also the laser emission wavelength, which is important for pumping applications.

The achieved temperature difference between cold and hot side of the Peltier module can be determined from the parameter field of the TEC device, which

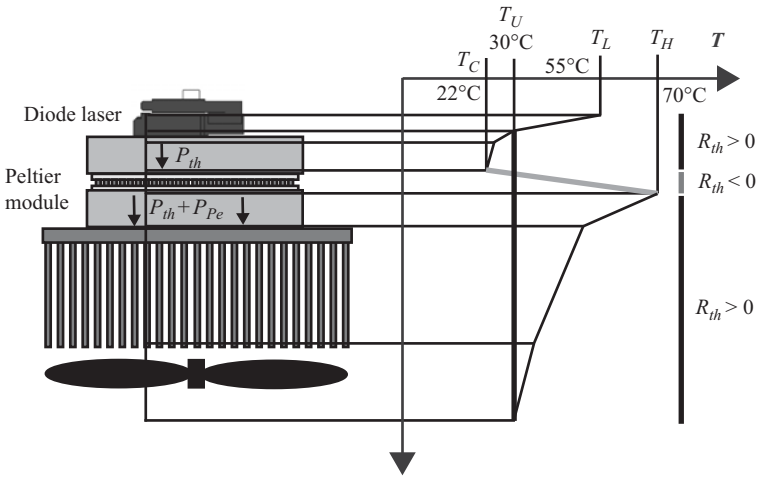

FIGURE 3.16. Cooling arrangement for a conduction-cooled diode laser with integrated TEC with schematic diagram of the temperature profile along a selected heat flux path. In the Peltier region a negative thermal resistance and thus an inversed temperature difference is created

takes the general form of

$$\Delta T = \frac{1 - f(I/I_{\max})}{g(I/I_{\max})} \Delta T_{\max} \frac{P_{th}}{P_{th,\max}}, \tag{3.13}$$

where f and g are functions of $I/I_{\max}$ that depend on the internal thermo-electric figures of merit. At $I = I_{\max}$, for example, $f = 0$ and $g = 1$. Whereas temperature difference is fixed for a given TEC cooling configuration, the hot-side temperature T_H – and thereby the cold-side temperature T_C – are not. These temperatures depend very sensitively on the hot-side thermal resistance of the system, because at the hot side of a Peltier module both the heat power P_{th} of the diode laser and the complete electrical power P_{Pe} of the TEC have to be removed.

As the maximum transportable heat power $P_{th,\max}$ scales with the number N of Peltier modules and the hot-side thermal resistance reduces as about $1/N$, high laser-heat powers can be dissipated by increasing the number of Peltier modules. Additionally, depending on the efficiency of hot-side cooling, a higher number of modules might be necessary to establish a desired cold side temperature. This relationship is exemplified in Fig. 3.17, assuming a heat source of $P_{th} = 70$ W, and Peltier modules capable of transporting $P_{th,\max} = 100$ W at $\Delta T = 0$ and providing $\Delta T_{\max} = 64$ K at $P_{th} = 0$. In the present case, the ambient (water, air) temperature has been set to 25°C. In the case of hot-side convective water cooling, a single Peltier module is sufficient to remove the heat power and to achieve a cold-side temperature in the range of 15 to 25°C even at Peltier currents $I < I_{\max}$. In the case of convective air cooling, at least two modules are necessary to shift temperature

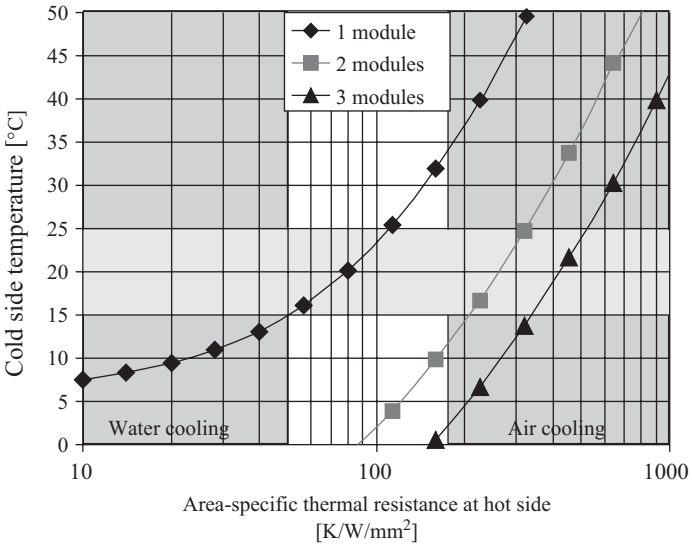

FIGURE 3.17. TEC cooling arrangements for a 70 W heat source are demonstrating the effect of hot side heat transfer on cold side temperature for different numbers of modules. Ambient temperature is 25°C, $P_{th,\max} = 100$ W per module, $\Delta T_{\max} = 64$ K

of the cold side down to 25°C. At an elevated ambient temperature of – let's say, 40°C – three modules are necessary to ensure a tolerable cold-side temperature.

3.3.4. Microchannel Heat Sinks

Jens Biesenbach

3.3.4.1. Operation Principle, Design and Fabrication

To achieve advanced cooling for diode laser bars operated at increased power levels or with increased lifetime compared to conduction-cooled heat sinks, convection-cooled heat sinks are widely used in all diode laser applications that allow the use of cooling fluids, mainly water. Industrial and medical laser systems that accomplish not only a few single-diode laser bars but need higher power and at the same time a compact design make use of convection-cooled heat sinks. These heat sinks are available as silicon- or copper-based versions. Silicon has the advantage of very precise microstructuring techniques known from microelectronic processing, allowing an optimized fine structure convection area. Copper has the two main advantages of very high thermal conductivity, being three times higher than for silicon, and to be electrically conductive with very low resistance allowing current levels up to 100 amps (cw). In the case of silicon heat sinks this would require very thick metallization layers with numerous disadvantages for the manufacturing and bar mounting processes.

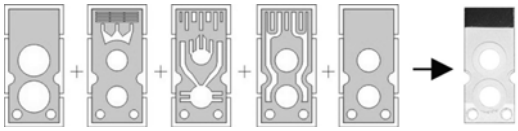

FIGURE 3.18. Schematic illustration of heat sink structure

For these reasons, copper coolers are today the dominant technology for convection-cooled heat sinks. More than 90% of heat sinks are designed to achieve a turbulent flow in a metal fin area with optimized convection. The heat sinks are mainly adapted to system design requirements in terms of their outer dimensions, electrical contacts, and water connections. A few concepts are available that make use of improved convection by impinging water to the cooling area. This can even be combined with a phase change, depending on the fluid media and the operating conditions.

The well-established standard convection-cooled heat sink is based on a design concept shown in Fig. 3.18. Thin copper sheets are 2D-structured by microetching or laser cutting. By stacking these structured sheets and joining them together, a 3D-channel structure is generated. To join the copper sheets soldering, diffusion bonding or eutectic (direct) copper bonding can be used. The bonding technologies provide a product that is highly heat resistant for further soldering and manufacturing processes; typically, a maximum temperature for further processes of 850°C is allowed. In case of a solder joint between the different heat sink layers the choice of solder material, especially its melting point, has to be well considered with respect to the further processing. A common solder to join the heat sink layers is eutectic AuSn, which is also used for mounting laser bars to submounts; in this case the mounting process has to be designed in a way to avoid re-melting of the heat sink bonds. However, there are ways to overcome this limitation, such as isothermal solidification of the AuSn solder, which forms an AuSn phase with a much higher melting point than eutectic AuSn.

After bonding the heat sinks in large multi-element frames, they are pressure tested, singled, and mechanically machined to the specified dimensions. If these heat sinks are used for direct mounting of laser bars without submounts, the mounting surface typically is ultra-precision diamond turned, which provides a mirror-like surface with excellent flatness and high surface purity. In the next process step, different metallization layers are applied as diffusion barriers and for solderability.

3.3.4.2. Design Rules

For microchannel heat sinks, the principle design rules of the conduction-cooled heat sinks also apply:

1. Optimized heat spreading achieved by –
   a) material with high thermal conductivity
   b) design to allow approximated 3D heat spreading (Fig. 3.19)

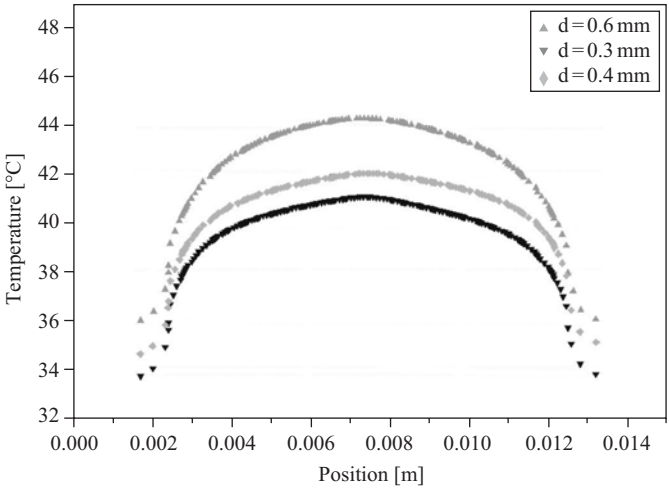

FIGURE 3.19. Dependence of R_{th} from thickness of copper heat sink

c) reducing the heat transfer distance to the sink, i.e., the convection area, as trade-off of the spreading area

When compared to conduction-cooled heat sinks, the fluid and convection characteristics also have to be considered, leading to the following design rules:

2. Fluid characteristics to allow high convection heat transport –
   a) fluid with high heat capacity
   b) fluid with low viscosity
   c) fluid with high thermal conductivity to optimize the thermal resistance for the boundary layer
3. Optimized fin design for maximum convection area and sufficient temperature gradient at the boundary layer to the fluid.
4. Channel design as a compromise between manufacturing limitations, operational limitations (risk of obstruction, balance of flow rate and pressure drop), and convection optimum by enforcing turbulent flow.
5. Compatibility of channel material with the cooling fluid to avoid corrosion.

The issues mentioned in 1a and 1b are addressed in Chapter 3.3.2. But for convection-cooled heat sinks, the different design aspects interfere and are influencing each other. FEM simulations are used for a combined analysis of the thermal conduction in solid-state designs and the thermal convection and flow characteristics of the cooling fluid. So-called engineering fluid dynamics (EFD) software is used to optimize the overall design and cooling performance (Fig. 3.20).

The optimal thickness of the spreading layer (see design rule 1c) between the laser bar and the micro channels is a function of the material's thermal conductivity and the convection characteristics of the underlying channel structure. At a certain thickness of the heat spreading area, a further increase of the thickness

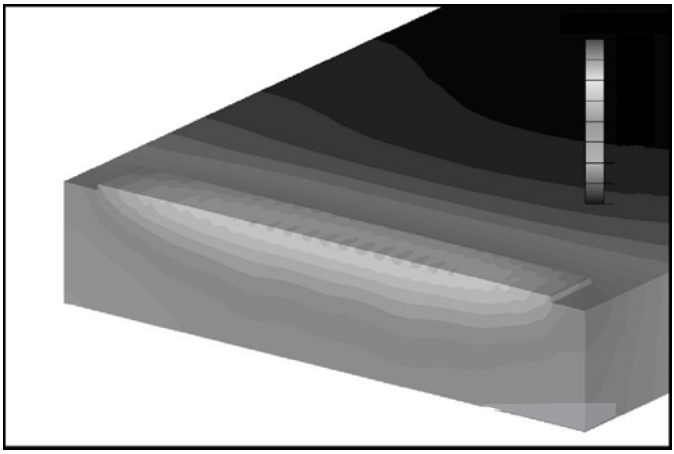

FIGURE 3.20. Schematic illustration of diode laser heat sink design

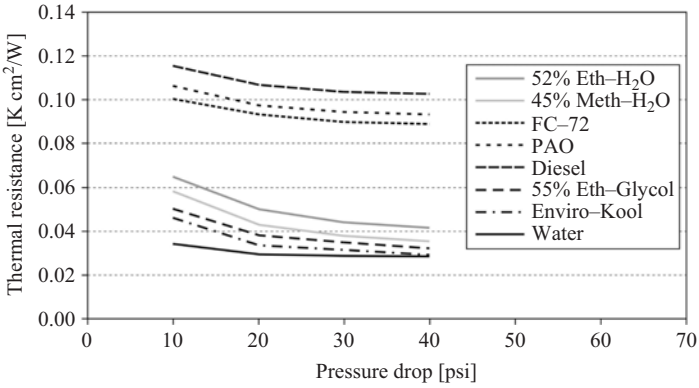

FIGURE 3.21. Dependence of the thermal resistance R_{th} on the pressure drop for different cooling fluids based on individually optimized designs

still increases the cooling area, but the larger area cannot be efficiently cooled by convection, because the temperature gradient at the boundary layer is reduced with increased distance to the heat source. As a result the thermal resistances increases. Below this optimum thickness the heat spreading is too low to achieve a sufficient size of the effectively convection-cooled area.

The influence of the fluid type on the thermal resistance is shown in Fig. 3.21. Water shows the optimum performance while other fluids, having advantages in terms of a lower freezing point or being less corrosive against copper, show a significant higher thermal resistance. However, depending on the required operation conditions, these drawbacks have to be overcome by compensating the lower cooling performance with reduction in output power level of the laser bar or adapting the cooler design to the fluid characteristics.

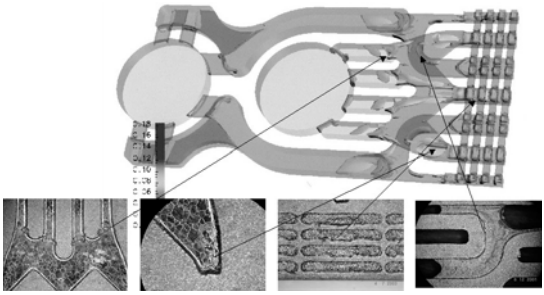

FIGURE 3.22. Flow analysis displaying areas of high velocity and vortex possibility, which correspond with corrosion affected areas in real devices

The design rules 3 and 4, addressing the fin and channel design, are also considered when optimizing of the cooler design for low thermal resistance. However, as reliability can also be limited by corrosion and erosion effects, the channel design is predominantly determined by the flow analysis, which concentrates on avoiding local peak flow areas and vortex generation in the cooling area. Figure 3.22 shows a flow analysis of a heat sink design, showing corrosion-affected areas known from field failures and their correspondence with peak flow rates exceeding the average flow rate by nearly one order of magnitude.

3.3.4.3. Performance: Thermal Resistance, Flow Rate, and Pressure drop

Microchannel heat sinks are usually operated with low-conductive and high-purity water, since water is the best suited fluid to achieve superior convection performance. The measurements shown in the following diagrams have been performed on the same heat sink design. The thermal resistance is a function of the flow rate (Fig. 3.23). This function tends to a limit with increasing flow rate. The intention of this measurement is not to achieve an operation point close to the best cooling performance, but rather to evaluate an operation point with sufficient cooling on minimized flow rates to avoid corrosion by high fluid velocities.

Besides the flow rate, the pressure drop is an important value to determine peripheral equipment such as the fluid pumps required to operate the diode laser assembly (Fig. 3.24). For high-power systems, e.g., a diode pumped solid-state laser with 800 diode laser bars, the specification of the fluid pumps is strongly affected by the performance of the single microchannel heat sink, and both total flow rate and pressure drop have to be kept within certain limits to avoid excessive costs for such peripheral devices.

The pressure drop is also an indicator of hydraulic losses in the heat sink, which is a design factor that enables erosion.

3.3.4.4. Corrosion Effects and Lifetime

Corrosion is a combination of several factors and conditions, all resulting in a dissolution or abrasion of the heat sink's base material, which is pure copper in

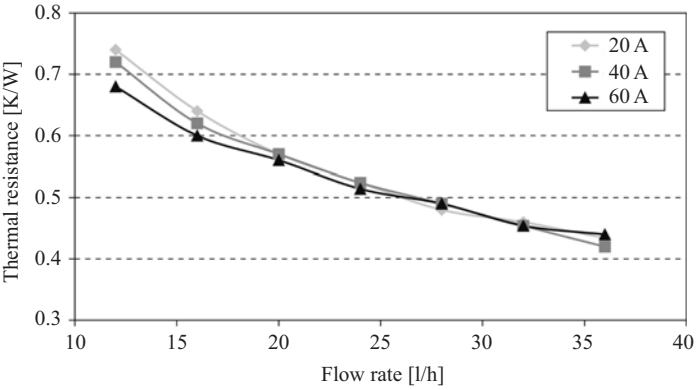

FIGURE 3.23. Thermal resistance R_{th} vs. flow rate measured at different power levels, defined by the laser bar operating current

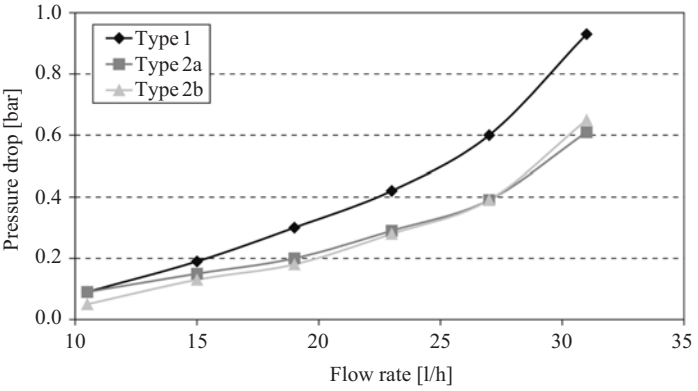

FIGURE 3.24. Pressure drop as a function of the flow rate for a non-optimized heat sink geometry (type 1) and two different heat sink variations optimized for reduced pressure drop (type 2a and type 2b)

most cases. These factors and conditions are

1. erosion
2. chemical reaction and dissolution
3. electrochemical processes
4. biological reactions

Typically, the corrosion of diode laser heat sinks involves not only one of these factors but a combination of several factors.

To avoid erosion, the heat sink design has to be optimized for homogeneous flow, avoiding peak flow and vortex areas. Also high flow rates should be eliminated and can be compensated by an efficient flow design. Chemical reactions of the

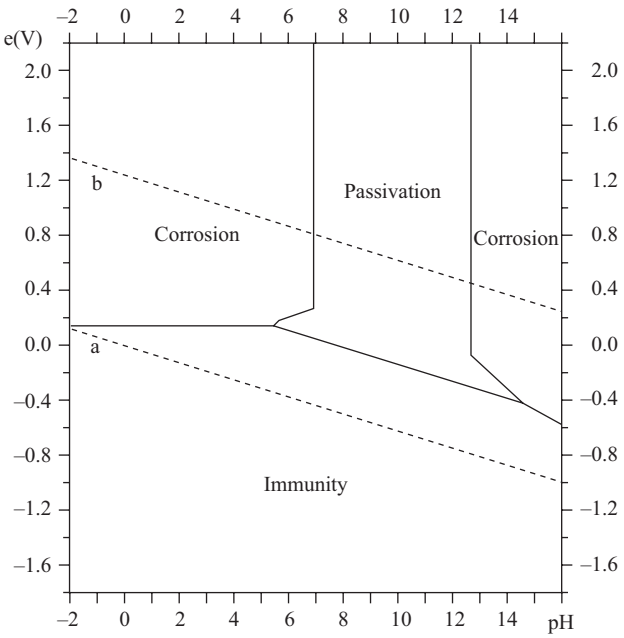

FIGURE 3.25. Passivation of copper in pH ranges (after [3.28])

copper base material with the cooling fluid can be controlled by coating the copper heat sinks with inert material, such as galvanic gold/nickel layers. The natural passivation of the copper surfaces can also be considered, however at a pH value of less than 7 self-passivation fails, leading to corrosion of copper (Fig. 3.25).

Especially when de-ionized (DI) water is used, the pH value can be influenced by a minimum amount of contaminants, since this water is not buffered. Therefore easily a pH value of less than 5 can be achieved, which will enforce the chemical corrosion. Therefore, very-high-purity DI water has to be chosen. By controlling the conductivity of the DI water, the pH value can also be controlled, because the conductivity in DI water is also an indirect indicator for the pH value; a conductivity lower than 2 μS/cm does not allow a pH value lower than 5.5 (Fig. 3.26).

Special corrosion-protective additives can be added to the cooling water to form a protection layer on the copper surface, changing the electrochemical potential of the copper surface and thus protecting it from chemical corrosion, even with water in the non-passivating lower pH zone. These layers resist also the shear forces by high flow velocities, because they continuously rebuild in affected areas.

Electrochemical reactions affect only those areas of the heat sink, that are exposed to high electrical fields. For example, in a stacked arrangement, at the inlet/outlet area of the heat sinks the distance to the neighboring heat sink is small and therefore the electrical field is high enough to initiate a galvanic process at these positions. In the inner channel structure, the external electrical field is shielded as in a Faraday's cage, and therefore electrochemical corrosion does not

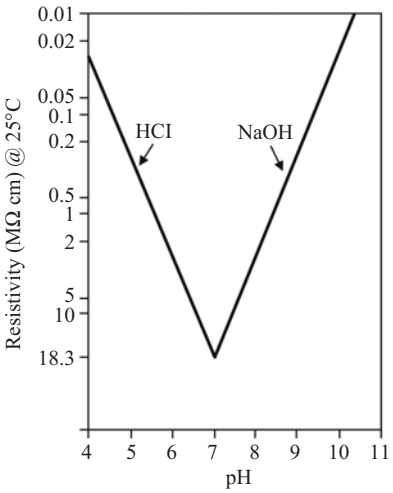

Figure 3.26. Passivation of copper; pH value vs. conductivity (after [3.29])

occur. Electrochemical reactions can – besides solution of copper – also lead to the deposition of reaction products, affecting the water flow, e.g., in the area of the sealing elements of a stacked array.

Biological contamination can hardly be avoided over years of operation of a closed water circuit under sometimes poorly controlled ambient conditions. However, UV-light can be used to extend the service intervals by keeping the water circuit uncontaminated and reducing the growth rate in case of contamination. Since some biological contaminants produce very acidic (pH 1) or very alkaline (pH 14) residues, which are both extremely aggressive to copper, a very clean installation procedure and decontamination procedure has to be applied. Not only the aggressive residues and the formation of ventilation cells (see Fig. 3.27) is an issue, but also the obstruction of the heat sink's microchannels by organic films residues coming off from the inner channel surfaces and forming a blockade. Blocked microchannels can cause a device failure by local overheating due to the locally reduced flow rate.

3.3.5. Diamond Heat Spreaders

Konstantin Boucke

As already mentioned in section 3.1, the thermal resistance of a diode laser package can be reduced by using a material with a higher thermal conductivity to form a heat spreader between laser bar and heat sink body. By its high thermal conductivity, the heat spreader distributes the heat flux from the laser bar over a larger surface, thus reducing the heat flux density and, for given heat transfer coefficients at the interfaces, leading to reduced thermal resistance.

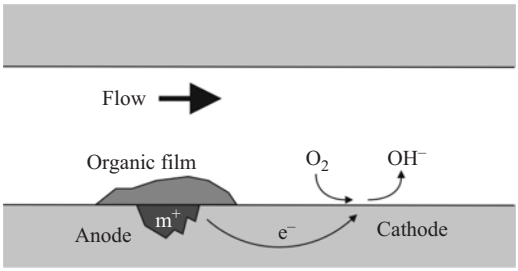

FIGURE 3.27. Organic film and corrosion caused by ventilation cells

With respect to its very high thermal conductivity, diamond is the optimum material for heat spreading applications: The thermal conductivity of CVD diamond is in the range between 1,200 and 1,800 $Wm^{-1}K^{-1}$. CVD diamond heat spreaders are widely used in the optical telecom field with single emitter laser diodes. For high-power applications and laser bars, there are mainly two reasons why diamond heat spreaders did not establish on the market:

1. Compared to single emitters as used in the telecom field, for laser bars comparably large diamond heat spreaders are required, making them very expensive. Costs are further increased by the required metallization for the transport of high currents and the additional mounting step required to fix the heat spreader on the heat sink.
2. Due to the small CTE of diamond (1.5–2.0 ppm/K), the CTE mismatch to GaAs-based laser bars (6.5–7.0 ppm/K) is comparably high, and together with the high rigidity of diamond it generates a strong tensile strain in the laser bar, reducing the lifetime.

CTE matching – also with diamond containing packages – is addressed separately in section 3.4. But even if CTE matching is not the main goal pursued by this packaging approach, it is still necessary to take the CTE mismatch into account, because the very rigid diamond layer could otherwise impose too much stress on the laser bar.

A simple way to deal with the expansion mismatch is to structure the diamond submount in a way that weakens the material, leading to a lower effective Young's modulus and reducing the stress acting on the laser bar. In Fig. 3.28 the structuring of the diamond heat spreader is illustrated: The heat spreader is cut by laser-cutting in a comb-like structure. The spacing of the cuts is adapted to the pitch of the laser bar to be mounted on the heat spreader. This is necessary to make sure that all emitters of the laser bar are placed in the center of one of the heat spreader's fingers, requiring also a sufficient positioning accuracy in lateral direction during the bar-mounting process.

The packaging of the laser bar with a diamond heat spreader requires a two-step soldering and mounting process: In a first step the diamond heat spreader is soldered to the heat sink using a solder with higher melting point. In a second step

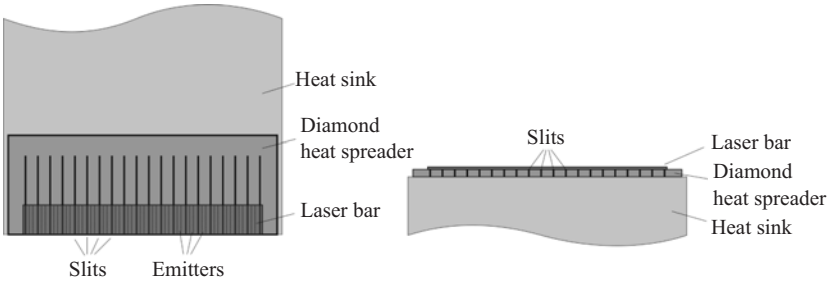

FIGURE 3.28. Schematic drawing of the laser bar package with a structured CVD diamond heat spreader

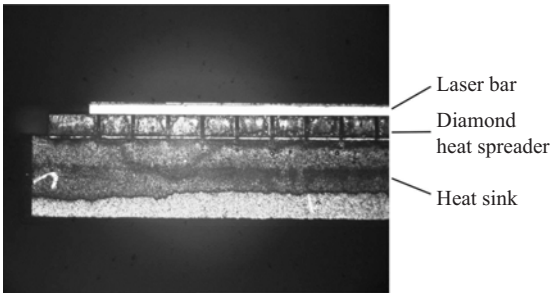

FIGURE 3.29. Front view of a laser bar mounted on a structured CVD diamond heat spreader and a copper micro-channel heat sink

the laser bar is mounted on the diamond heat spreader with indium soft solder as it is commonly used for mounting bars on substrates with deviating CTE. This order of soldering has been chosen to avoid the higher stressing of the laser bar that would occur when the laser bar is first soldered – with a high-temperature solder – to the diamond heat spreader. Figure 3.29 shows the front view on a laser bar mounted on a structured diamond heat spreader.

Laser bars of the same type have been mounted directly on microchannel heat sinks as well as with the structured diamond heat spreaders in order to compare their performance and characteristics. From this comparison, the following results could be extracted:

1. With the diamond heat spreader, the thermal resistance is reduced by approx. 25%;
2. the electro-optical performance is not affected;
3. due to the two-step mounting process, the laser bar's "smile" is enlarged from approx. 1 μm to approx. 4 μm;
4. the lifetime is significantly reduced to only ~1,000 hours, compared to ~10,000 hours using a standard package.

The reduced lifetime is probably caused by the still high residual stress imposed on the laser bar by mounting on diamond; as a consequence of the improved thermal resistance the operating temperature is reduced, but this positive effect is cancelled by the negative impact of additional stress. This shows that the diamond heat spreader concept cannot be directly applied to large semiconductor chips; instead more advanced packaging approaches are necessary.

3.4. Expansion-Matched Packages

Dirk Lorenzen

In Chapter 3.3, thermal aspects of packaging high-power diode laser bars have been investigated. Since a good thermal contact for laser bars requires an appropriate mechanical contact – generally formed by a solder joint – mechanical aspects of mounting are of equal rank.

The mechanical aspects of mounting comprise the properties of the mounting substrate, especially its coefficient of thermal expansion, and the stress state in the laser bar mounted thereon. The knowledge of these parameters requires special measurement techniques, which will be described in detail below and applied to a selected substrate sample including related laser bar packages.

3.4.1. Introduction

3.4.1.1. The Interest of Expansion Matching

Standard packaging of diode laser bars consists of soldering the laser bars p-side-down onto a heat sink. This process generally induces stress in the laser bar. The amount of the created stress depends on the solder and the heat sink material properties: regarding the solder, it concerns mostly its solidification temperature, its yield and ultimate tensile strength; regarding the heat sink material, it concerns mostly its Young's modulus and its coefficient of thermal expansion (CTE). Assuming a hard solder material with a yield strength comparable to that of the heat sink, an upper limit of packaging-induced stress can be given by

$$\sigma_{\max} = E\,\Delta\alpha\,\Delta T \tag{3.14}$$

where E is the Young's modulus of the heat sink, $\Delta\alpha = \alpha_1 - \alpha_2$ is the difference of the CTE α_1 of the laser bar and the CTE α_2 of the heat sink and $\Delta T = T_s - T_a$ is the temperature difference between solder solidification temperature T_s and ambient temperature T_a. The more the CTE of the heat sink differs from that of the laser bar (GaAs: 6.5 ppm/K), the higher is the induced stress. Assuming that stress in the laser bar must not exceed 35 MPa – which is half of its fracture strength [3.12] – one obtains an allowable CTE difference of 1 ppm/K as maximum.

Standard heat sink materials with high thermal conductivity like copper (400 W/m/K) or diamond (1,800 W/m/K) exhibit a strong thermo-mechanical mismatch to GaAs: the CTE of copper is about 17 ppm/K, that of diamond about

1.5 ppm/K [3.13]. In order to avoid high packaging stresses in the laser bar, a soft solder is normally employed to balance out the thermal stresses by plastic deformation. A soft solder package, however, experiences limits in high-power and pulsed operation because of its sensitivity to electro-migration and thermal fatigue.

Nevertheless, the influence of the remaining stress on the lifetime of the laser bar has been proven. Recently, defect creation in laser chips has been shown to originate from packaging-induced stress.

The wide interest in providing a highly reliable package justifies the research for heat sinks with a CTE close to that of the laser material. Such heat sinks will be named shortly "expansion-matched" or "CTE-matched," as their coefficient of thermal *expansion* is *matched* to that of the laser material. Once such an expansion-matched heat sink has been found, it will hardly remain necessary to use soft solder. The soft solder could then be replaced by reliable hard solder, extending the limits of diode laser operation.

3.4.1.2. Expansion-Matched Materials

There are four categories of materials suited for expansion-matching:

1. pure materials like chemical elements or compounds,
2. alloys which are physically homogeneous on a microscopic scale,
3. composite materials which are physically homogeneous on a macroscopic scale,
4. material arrangements of macroscopic parts made from some of the preceding material types.

Expansion-matched candidates of the first category of materials are chemical elements like iridium or tantalum and compounds like alumina (aluminum oxide) and beryllia (beryllium oxide). A common alloy with a CTE close to that of GaAs is Kovar (Fe54Ni29Co17). Composite materials are typically formed by two pure materials or alloys that are mutually insoluble: powder of the higher melting material (tungsten, invar, silicon carbide) is dispersed in a matrix of lower melting material (copper, silver, aluminum). In all three categories cited so far, none of the existing materials reaches the thermal conductivity of copper. The only exception is a recently published composite of diamond particles in a copper matrix [3.14]. But this material also suffers from a mechanical limitation inherent to all composite materials: the manufacturing process does not provide a surface flat enough to ensure low smile (less than 1 μm peak-to-valley bow) packaging of laser bars. Milling, grinding or polishing of composite materials has only limited effect on their surface quality due to the different hardness of the materials. Chip-out of hard material particles or hollows in areas of the soft matrix metal are not compatible with high-quality reliable laser bar packaging.

In conclusion, an appropriate expansion-matched material can only be realized by combining materials in category 1, 2, or 3 in a macroscopic arrangement (material category 4), where the mounting surface for the laser bar is provided by a material of category 1 or 2. If this material is an isolator like diamond, an

additional metallization must be applied to enable the supply of electrical current to the laser diode.

3.4.1.3. Expansion-Matched Arrangements

There are three types of material arrangements to be distinguished:

1. a first type consisting of an expansion-matched base material of category 1, 2, or 3, combined with a material of category 1 or 2 in a way that does not considerably change the thermo-mechanic properties of the base material, but enhances the thermal properties and the surface quality of the assembly;
2. a second type, consisting of non-expansion-matched materials stemming from category 1 or 2 with high thermal conductivity combined with each other to provide an expansion-matched assembly whose final thermal property is conditioned by the ratio of materials used.
3. a third type, combining the expansion-matching intention of the second type with the reduced mechanical influence of one combination partner in the first type. This type provides an arrangement with an elevated content of the material with less mechanical influence and higher thermal conductivity.

One example of each type is sketched in Fig. 3.30.

As an example for the first arrangement type, let's consider an arrangement of diamond substrate segments bonded to a bulk composite material heat sink made of tungsten-filled copper. The number and the size of the diamond segments is chosen with respect to the laser diode emitters. Heat spreading is improved by the diamond substrate parts to ensure a thermal resistance that is low enough for operation. Expansion-matching is accomplished by the rigid heat sink body of composite material.

The significance of the second type is explained by a symmetric triple layer arrangement of two diamond substrates and a copper layer in-between. Both materials are not expansion-matched; nevertheless, they have a CTE that is lower than that of GaAs (diamond: 1.5 ppm/K) and higher than that of GaAs (copper: 17.0 ppm/K). The combination of both materials in an appropriate layer thickness ratio should thus give an expansion-matched assembly. This ratio can be

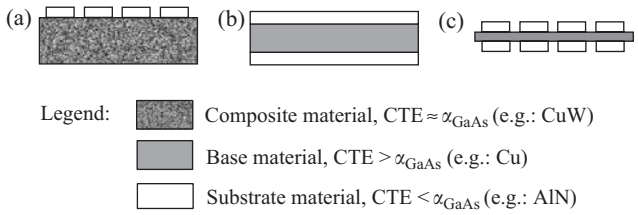

FIGURE 3.30. Examples of the three different types of expansion-matching arrangements: (a) (left) diced substrate on rigid composite body; (b) (middle) closed three-layer system; (c) (right) partially diced three-layer system

calculated from the general formula of the resulting average CTE of such a layer system [3.15]:

$$\langle\alpha\rangle = \frac{\alpha_1 E_1 d_1 (1-\nu_2) + \alpha_2 E_2 d_2 (1-\nu_1)}{E_1 d_1 (1-\nu_2) + E_2 d_2 (1-\nu_1)}, \tag{3.15}$$

where d_1 (d_2) is the sum of thicknesses of layers of a first (second) material, α_1 (α_2) is the CTE of the first (second) material, E_1 (E_2) is the Young's modulus of the first (second) material, ν_1 (ν_2) is the Poisson's ratio of the first (second) material. It should be noted that this equation holds only for layers of a thickness that is thin compared to their lateral dimensions. Following Eq. (3.15), a CTE-matched layer system would require a volume copper content three times the diamond content.

In order to give a rough estimate of the thermal quality of these substrates, the notion of effective thermal conductivity (ETC) is introduced as being the mean value of in-plane averaged lateral thermal conductivity and out-of-plane averaged vertical thermal conductivity:

$$\lambda_{eff} = \frac{1}{2}\left(\frac{\lambda_1 d_1 + \lambda_2 d_2}{d_1 + d_2} + \lambda_1 \lambda_2 \frac{d_1 + d_2}{\lambda_1 d_2 + \lambda_2 d_1}\right). \tag{3.16}$$

λ_1 and λ_2 are the thermal conductivities of the first and second materials, respectively. For a CTE-matched layer system, the resulting effective TC is about 600 W/m/K. The high content of copper prevents the high thermal conductivity of diamond from being predominant.

The way to an expansion-matched substrate with much higher effective thermal conductivity is through a combination of arrangement type a and type b: In type a, the dicing of diamond leads to a strongly reduced mechanical influence on the rigid CuW-body; in type b, the closed diamond layer needs a high amount of copper to fulfill the expansion-match condition. If we apply the dicing of diamond of type a on the layers in type b, its mechanical influence will be reduced and the ratio of copper reduces in favor of a higher diamond content, that is, a higher effective thermal conductivity. This arrangement belongs to the type c and will be analyzed in detail in section 3.4.5 by the measurement methods described in the following.

3.4.2. Measurement of Thermal Expansions

The CTE measurement of mounting substrates is great challenge for two reasons: First, the CTE must be measured in-plane, that is, in the plane of the surface of the substrate; second, this surface is small ($3 \times 10\,\mathrm{mm}^2$). If a CTE-map of the device should be produced, a resolution of $1\,\mathrm{mm}^2$ is desirable. Limiting the thermal load steps to $\Delta T = 10\,\mathrm{K}$, each ppm/K requires the detection of a 10-nm displacement.

Optical imaging techniques are preferred to measure such small displacements accurately. Among these one can distinguish between incoherent techniques like Moiré fringe analysis [3.16] and coherent techniques like holographic interferometry [3.17]. Whereas the first technique requires the preparation of the sample with

an adequate fringe pattern, the latter one only needs a rough surface to produce a speckle pattern under illumination with coherent light of wavelength λ. More than a decade ago, digital holography started to supersede analog holography in displacement measurements. Nowadays, using electronic speckle pattern interferometry (ESPI), even personal computers are fast enough to calculate correlations of speckle patterns in less than a second [3.17]. The ESPI measurement principle and evaluation have been described in detail in [3.18].

Every deformation experiment requires its own deformation generator. In the case of stress-induced expansion (tensile) tests for E-modulus or Poisson ratio determinations, this is the task of a pulling machine in which the sample has to be fixed appropriately. In our case of temperature-induced expansion tests for CTE measurements, a heat generator like an oven is needed. Compared to tensile tests, two novel difficulties have to be overcome: (a) the fixing of the samples and (b) disturbances by heated air. During heating, the sample must be fixed tight enough to prevent it from shifting, and it must stay free enough to ensure an unimpeded expansion. Vacuum fixing and weak leaf spring clamping have been successfully tested dependent on the type of substrate. Fixing of the samples is additionally important because the oven has been tilted vertical. In this arrangement the ESPI illumination and imaging system (ESPI sensor) is not located above the oven, where a measurement could be affected by refraction index variations of heated air, but beside the oven as shown in Fig. 3.31.

For every sample being measured, a reference plate of a known CTE is co-measured in the same run. By this procedure, a failed series is immediately identified. It is obvious, that this reference plate should exhibit a CTE close to the desired value of GaAs to have the best comparability. For this reason, a [001]-wafer chip of GaAs itself is the ideal reference.

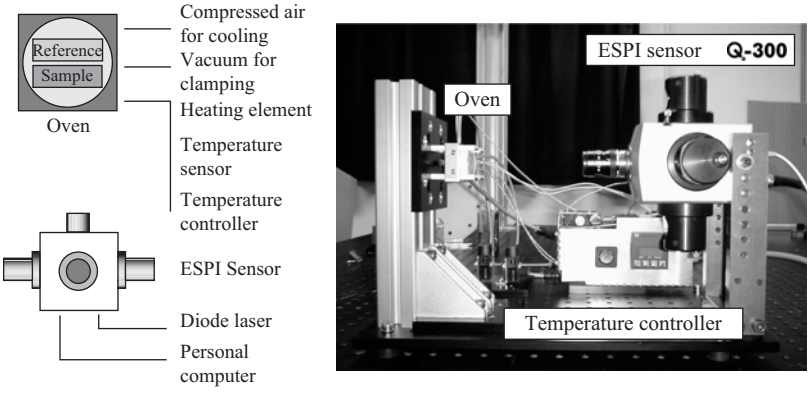

FIGURE 3.31. ESPI thermal expansion measurement setup principle (left) and setup realized in the laboratory (courtesy of Dantec Ettemeyer GmbH)

3.4.3. Photo-Elastic Stress Measurement

A stress field in a translucent body influences its dielectric and therefore light-refracting properties. Optically isotropic crystals especially become birefringent under mechanical load. Different indices of refraction are responsible for different velocities and directions of light propagation. Optically birefringent media are able to change the polarization state of a light wave [3.19]. If one manages to detect these variations of the polarization state of a light probe beam by means of a polariscope, one is able to gain information on stress level, type and direction in the deformed device [3.20,3.21].

In order to measure stresses in mounted laser diode bars it is recommended to employ an experimental setup, where the scanning field is the facet plane and the viewing direction is along the longitudinal (resonator) direction of the laser bar [3.15]. Spatial resolution can be enhanced by using a laser probe beam. This configuration of laser reflexion polarimetry (LRP) uses a 1,300-nm linearly polarized diode laser beam of intensity I_0 that hits the front facet of the laser bar at the place of its waist. A certain light portion passes through the laser bar until it hits its back facet, where it is partially reflected back into the laser bar toward the front facet. The reflected light in total consists of two parts: a first stress-insensitive part (directly reflected by the front facet) and a second stress-sensitive part (passed though the laser bar). The first part possesses a polarization equal to the initial one; the polarization of the second part is affected by stress direction, stress magnitude, and length of optical path in the laser bar.

The relative phase shift of the components of the polarization vector experienced under a single travel forward or backward through the laser bar is proportional to the mean lateral stress σ averaged along the resonator length.

The intensities of the two beams generated by a polarizing beam splitter used as analyzer are $I_{||}$ (intensity of light with original polarization) and $I_{\perp}$ (intensity of light with 90° detuned polarization). By defining a depolarization as

$$D = \frac{I_{\perp}}{I_{\perp} + I_{||}} = D_{\max} \sin^2 \Gamma, \tag{3.17}$$

one obtains depolarization values oscillating between zero and the depolarization maximum $D_{\max}$ with a stress fringe period of

$$\sigma_{\pi} = \frac{\lambda}{2\ell C_{\sigma}}, \tag{3.18}$$

where C_{σ} is the stress-optic constant, ℓ is the resonator length, and λ is the wavelength of the probe light. In the ideal case of a totally transparent laser front facet, one obtains $D_{\max} = 1$. Depending on the laser facet coatings, the maximum depolarization values may drop down to 0.001, which is close to the fringe detection limit.

To summarize, the number of depolarization fringes is a measure for the amplitude of lateral normal stress that is predominant in packaging-stressed laser bars.

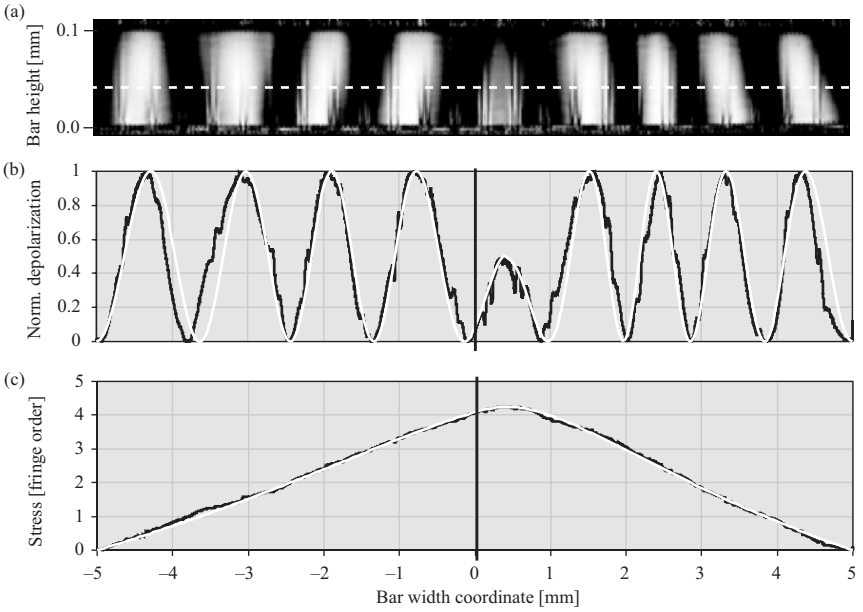

FIGURE 3.32. Evaluation procedure in a photo-elastic stress measurement from a depolarization fringe field (a), via a normalized depolarization line track (b), to a linear normal lateral stress distribution along the laser bar width (c)

A demodulation procedure unveils the stress distribution along the bar width. This process is visualized in Fig. 3.32. Starting with a fringe-modulated depolarization picture (a), one extracts a normalized line track (b). A predefined fit function supports the demodulation procedure executed in (c) to display the linear stress distribution.

The quantification of the stress level itself is mediated by the stress-optic constant C_σ which in turn depends on stress state and direction with respect to the crystal lattice and probe beam orientation as well as on the piezo-optic coefficients of the material which are in general highly dispersive. In contrast to semi-insulating GaAs, the piezo-optic coefficients of highly n-doped semi-conducting GaAs are unknown. As long as these values are not available, the LRP method can only provide qualitative results. These results, however, enable statements about more or less stressed laser bars.

Nevertheless, there is one crucial drawback inherently associated with the LRP measurement principle: The method does not allow us to distinguish between positive (tensile) and negative (compressive) stress. This statement holds for both absolute and relative stresses. The latter becomes relevant for all stress levels reaching half a fringe period. In this case, a diminution of the fringe intensity could mean a decrease of stress as well as an increase. This problem is due to the ambiguity of the sine-square function related to its arguments. In other words: if the

general stress behavior in the laser bar is unknown, a photo-elastic measurement cannot provide this information.

Thermo-mechanic modeling has shown that lateral normal stress increases continuously from the edges to the center of the laser bar. If mounting in practice does not differ substantially from the ideal assumptions, the LRP method is well suited to detect relative stress levels in laser bars with a high resolution.

3.4.4. Electro-Optic Stress Measurements

Stress in a semi-conducting crystal does not only influence its optical properties but also its electrical properties. Uniaxial or biaxial (e.g., non-hydrostatic) stresses and strains reduce crystal symmetry and release the degeneracy of the electronic band structure, especially that of the valence band (V) in a heavy hole (HH) and light hole (LH) part. Increasing the stress results in a further energetic shift splitting the HH and LH valence bands towards or away from the conduction band (C). The shift direction of each sub-band depends on the stress sign [3.22].

In a semiconductor superlattice like a quantum well (QW), the energy bands form discrete levels, that are already split in sub-bands by the quantum dimension effect. Under stress, these energy levels shift similar as in bulk material – the only difference lies in the stress sensitivity. In practice, the quantum well is already intentionally stressed by a epitaxial lattice mismatch against the waveguide for two reasons: On the one hand, stressed quantum wells enable a higher laser efficiency. On the other hand, the wavelength of light emitted by electron-hole recombination depends on the energy level difference E_g (in eV) between the involved conduction and valence band states as

$$\lambda = \frac{hC}{eE_g} \tag{3.19}$$

(h = Planck constant, c = velocity of light, e = elementary charge). Hence, an appropriate mechanical band-structure engineering delivers a desired laser wavelength – or more generally: spectral properties of electro-optic transitions are defined by the stress sensitive band-structure.

Packaging-induced stresses or strains in quantum wells of laser diode bars are typically one order of magnitude lower than epitaxial stresses (strains). The associated band gap shifts $\mathrm{d}E_g$ are some meV and some tens of meV, respectively. The shift induced by a packaging stress (strain) variation $\mathrm{d}\sigma$ ($\mathrm{d}\varepsilon$) is in general a slowly varying function of the stress (strain) amplitude and sign itself: $\mathrm{d}E_g/\mathrm{d}\sigma = f(\sigma)$ ($\mathrm{d}E_g/\mathrm{d}\varepsilon = f(\varepsilon)$). Furthermore, it depends on the initial state of epitaxially induced stress – an issue that is important for quantum wells, but not for waveguide and bulk GaAs substrate which are nearly unstressed before mounting. This is a second reason for which – besides different material compositions – stress-induced band gap shifts are different for wave-guide and quantum well.

As described above, stress amplitudes can be determined if one measures the wavelength of any type of electro-optic conversion process. These processes could be

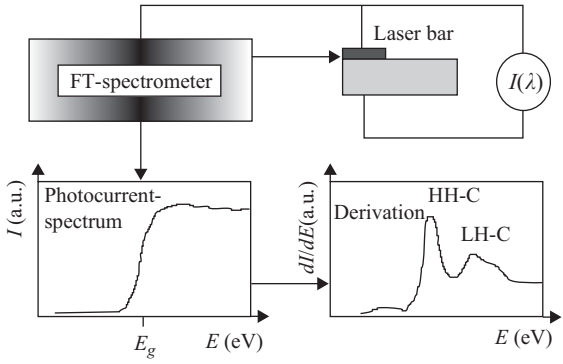

FIGURE 3.33. Measurement principle and evaluation example at photocurrent spectroscopy as tool for electro-optic stress determination

1. electrically induced spontaneous emission (electro-lumiscence spectroscopy, ELS);
2. electrically induced stimulated emission (laser pulse spectra, LPS);
3. optically induced spontaneous emission (photo-luminescence spectroscopy, PLS);
4. optically induced electrical current (photocurrent spectroscopy, PCS).

One of the most accurate and reproducible techniques today is photocurrent spectroscopy. Energy gap shift of less than 0.5 meV can be resolved.

The experimental procedure has been developed at the Max-Born-Institute in Berlin/Germany and is sketched in Fig. 3.33. It employs a Fourier-Transform Spectrometer [3.23] to illuminate the laser bar which are now working as unbiased photodiodes. The spectral sensitivity of the device is registered as a photocurrent spectrum $I = f(E)$. The electro-optic transitions take place at the steepest increase of the photocurrent. A derivation of $\mathrm{d}I/\mathrm{d}E$ is displaying the spectral positions of them as maxima. If unpolarized light is used, both transitions, HH-C (TE polarized) and LH-C (TM polarized) can be observed.

One advantage of incoherent electro-optic stress measurement techniques like photocurrent spectroscopy is a polarization-dependent distinction of the two main different transitions: from heavy-hole to conduction band (HH-C) which is TE-polarized, and from light-hole to conduction band (LH-C), which is TM-polarized. These transitions co-exist in the quantum well and in the waveguide (WG) of the laser bar. All of them show a different spectral behavior $\mathrm{d}E_g/\mathrm{d}\varepsilon$ under stress loaded in bar width direction [3.24].

A photocurrent spectroscopy scan of the laser bar from one end via its center to the other end shows a hill shaped distribution of the transition energies in the case of a compressively strained laser bar. For diode laser bars, mounted with an indium solder onto a copper heat sink, the strain difference center-edge amounts to about $\Delta\varepsilon \sim -4\text{–}5 \times 10^{-4}$ [3.13], which corresponds to a stress of 50–60 MPa [3.15].

In case of a tensile strained laser bar one would remark a valley-shaped distribution. Since the edges of the laser bars are free of normal stress, ideally, the energy transition values at the outer ends coincide for all laser bars that stem from the same epitomical run – whether they are differently mounted or not [3.25].

The band-gap energy shift can be measured with an error of ±0.5 me. Stress resolution is thus limited to ±5 MPa – about 10% – of the typical stress maximum in laser bars. In the presented photo-elastic stress measurement setup, the stress resolution amounts to ±10 kPa, which is factor 500 better.

Unlike the photo-elastic measurement method, the electro-optic method is able to detect stresses in quantum well and wave-guide. Moreover, due to light absorption, the depth of information is limited to some micrometers in the wave-guide and some tens of micrometers in the quantum well – which enables a certain longitudinal resolution. On the other hand, the electro-optic method does not allow us to separate different stress states and – and this is the main disadvantage with respect to the photo-elastic method – the laser bar has to be equipped with two electrical contacts on the epi-side and the substrate-side. The electro-optical method, however, is able to distinguish compressive and tensile stress and to determine the overall stress behavior.

In summary, both techniques have their pros and cons – together, they form a well-suited pair of tools for the qualification and quantification of stresses in laser bars.

3.4.5. Investigation of an Expansion-Matched Package

3.4.5.1. Substrate Design

As a CTE-matched substrate, the promising design derived in Chapter 3.4.1 has been chosen. It consists of a center copper layer, surrounded at both sides by a linear array of diamond substrate fins [3.26]. As it is easier to handle a diamond layer as one part rather than an array of free substrate parts, a serpentine structure has been chosen. Figure 3.34 shows the principle of a three-layer system as mounting substrate for a diode laser bar, consisting of two diamond serpentine layers and a thin copper middle foil. It is obvious that the number and lateral dimensions of the serpentine legs must fit to the number of emitters in the laser bar in order to avoid the emitters being placed on a groove, where heat cannot be well dissipated. Adapted to a laser bars type with 25 emitters of 400-μm pitch, the diamond layers have been designed with 25 serpentine legs.

Results of thermo-mechanical calculations carried out by the finite element method (FEM) are predicting a CTE-matched design for copper layers of 60–70 μm thickness when the thickness of each diamond layer is 300 μm. Hence, a series of substrates with copper thicknesses of 200, 150, 100, 50, and 25 μm has been produced.

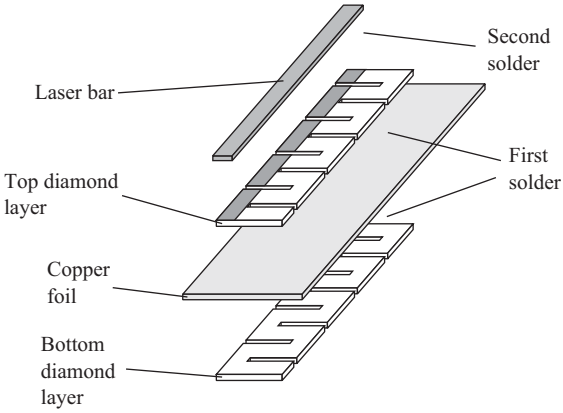

FIGURE 3.34. Design of a CTE-matched substrate with high diamond content

3.4.5.2. CTE Measurement

In order to determine the CTE of these substrates, thermally induced deformations in both lateral (10 mm width) and longitudinal (3 mm heat spreading length) directions have been measured using a Q-300 ESPI sensor of Dantec Ettemeyer GmbH. The sample is heated with a constant slow-heating rate of 0.125 K/s in order to avoid too big difference between the temperature measured at the thermoelement sensor and the sample itself. A fringe pattern is registered every 10–15 K of temperature rise between 30°C and 150°C. At the end of each measurement series, the corresponding displacements are added up, and deformation and CTE are calculated. Figure 3.35 shows a live picture of GaAs reference and diamond-copper-diamond sample in the oven and the CTE maps of both of them. One remarks high fluctuations of CTE in the surfaces originating from speckle noise limiting the map resolution. However, averaging the CTE over a larger area provides satisfying results with an error of approximately ± 1 ppm/K per $\text{mm}^{1/2}$ length of averaging.

As a result of the thermal expansion measurements, the CTE of the GaAs substrate has been determined to be 6.5 ± 0.2 ppm/K, which is quite close to the value of 6.2–6.3 ppm/K in [3.27]. Of the diamond-copper-diamond (DCD) substrates three to four pieces of each copper foil thickness have been measured.

Figure 3.36 summarizes the CTE-results of the samples comparing the measurement results with the CTE curve calculated numerically by FEM. They are in a remarkable agreement with each other. The dashed curve in Fig. 3.36 represents the averaged CTE as resulting from a closed layer system without grooves according to Eq. (3.14).

3.4.5.3. Stress Measurements

Having created CTE-matched substrates, it is still a matter of interest whether stress is really reduced in laser bars mounted onto them. A comparison with laser

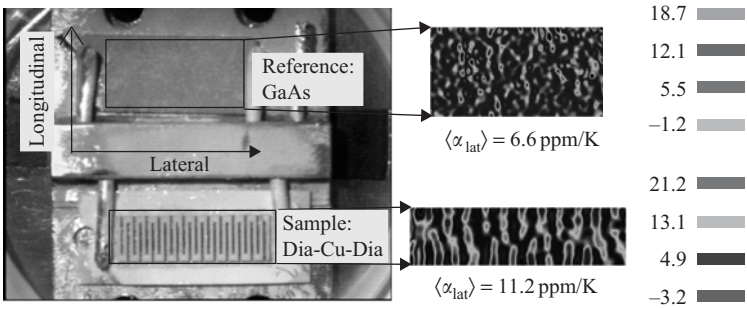

FIGURE 3.35. GaAs reference and diamond-copper sample in the CTE oven and CTE maps of them

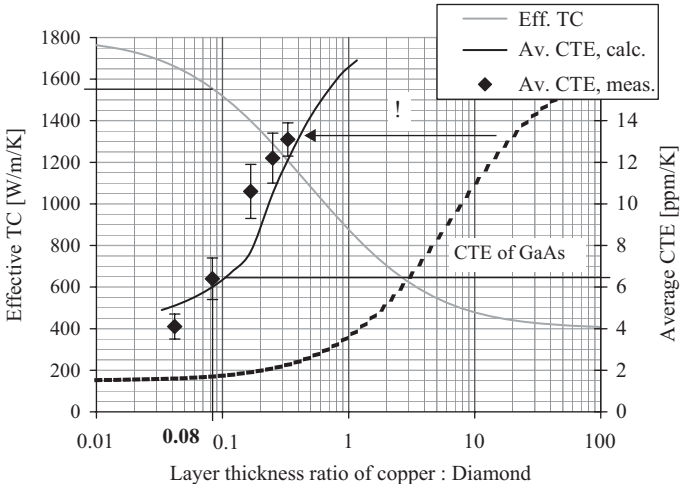

FIGURE 3.36. Measured and calculated CTE values of diamond-copper-diamond substrates with artificial ductility. Less then 10% of copper is needed for CTE-match, resulting in a high effective thermal conductivity (TC) of more than 1500 W/m/K

bars mounted with indium solder on bare copper heat sinks and on copper-tungsten Cu15W85 substrates (CTE = 7.5 ppm/K) should finally highlight the usefulness of the designed substrates. Laser bars, all originating from the same wafer and epitaxial run, have thus been soldered with indium onto these carriers and onto diamond-copper-diamond substrates (DCD) with 25-, 50-, and 100-μm copper foil thickness. The laser bars mounted on substrates have then been attached to a copper carrier by an electrically conductive adhesive to facilitate mechanical fixing and electrical contacting.

The mounted laser bars have been laterally scanned by laser reflection polarimetry and photocurrent spectroscopy in order to obtain a stress distribution from the left side to the right side of the bar. Figure 3.37 is showing the stress distribution of

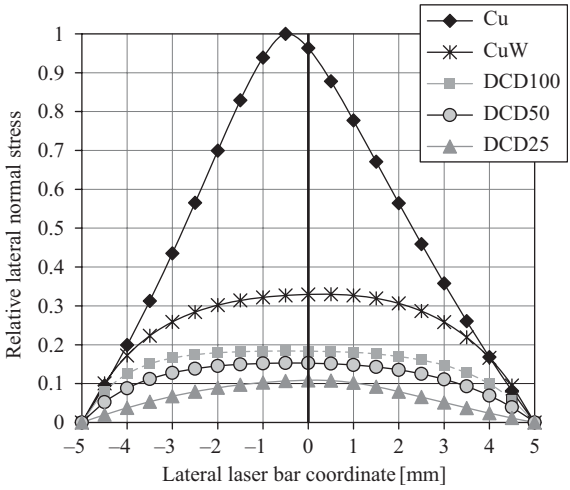

FIGURE 3.37. Stress distribution as obtained by laser reflection polarimetry in laser bars put in relation to the standard mounting on copper

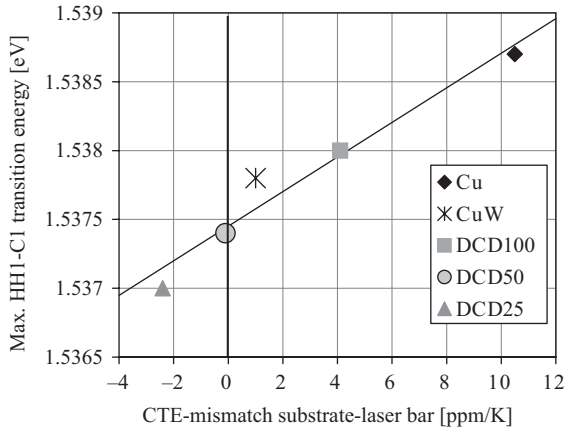

FIGURE 3.38. Maximum transition energy near center of differently mounted laser bars

the DCD in relation to standard mounting on copper and stress reduced mounting on CuW as obtained by the photo-elastic measurement method. In all cases the stress maximum is located near the center of the 10-mm laser bar. Note that one cannot distinguish between compressive and tensile stress. However, the stress amplitude is lowest for the DCD25 and DCD50 substrates.

The electro-optic stress measurement should enable a differentiation between tensile and compressive stress. A more instructive view can be obtained, if the maximum energy gap values of the (1hh→1e) transition from near the center of the laser bar are represented in dependency of the CTE of the mounting substrate as

it is shown in Fig. 3.38. The comparison with CuW substrates clearly emphasizes the nearly stress-free mounting on 50-μm DCD substrates, whereas the 2-μm DCD substrate is the only one inducing tensile stress in the laser bar.

3.4.5.4. Conclusion

CTE and stress measurements pointed out a CTE-matched substrate permitting nearly stress-free mounting. This substrate has been designed as a candidate of expansion-matched arrangements of type c in section 3.4.1. The thermal optimization of this type is however achieved at the price of losing the biaxial expansion-matching in both directions, lateral bar width direction and longitudinal resonator length direction, as it is provided by the arrangement of type b. The dicing in the lateral direction provides uniaxial expansion matching in lateral bar width direction. In resonator length direction, the CTE remains as in type b with the layer thicknesses of type c, that is considerably lower than 6.5 ppm/K due to the high amount of diamond. For short resonator lengths of less than 0.3 mm, this is not a problem, since stress is not so much accumulated by structures of which the length is of a size similar to that of its thickness. For resonators longer than 0.6 mm, stress becomes saturated at a high level that might be harmful to the laser diode. This issue becomes relevant when reliable hard solder should be used for mounting. In such a case, arrangements of types a and b that provide biaxial CTE-match must be considered.

3.5. Mounting of Micro-Optics

Thomas Brand

Micro-optical elements for shaping the radiation emitted by a laser bar are an indispensable part of all systems using direct diode laser power. Only with an individual processing of the emission of the multitude of emitters of a laser bar or stacked array is it possible to maintain the initial beam quality and focusability in a way to make it useful for material processing.

Due to the low thickness of the epitaxial waveguide layers of a laser diode in the vertical (fast) direction, the aperture angle of the nearly diffraction limited beam reaches a value of 60–70° at 95% power content. To collect and collimate the laser power with an adequate efficiency, high-numerical-aperture cylindrical lenses are essential. Without micro-optics, the beam diameter grows very quickly to an extent that makes it difficult to work with.

A comparison of different types of microlenses and their performance is given in Chapter 4.2. The most widely used lens type for all direct applications where the conservation of the beam parameter product is of importance is the plane-concave aspheric cylindrical lens. Typically, the effective focal length of such a lens is in the range of below 1 mm and the back focal length (distance between the laser bar and the plane surface of the lens) is a few hundred microns. Mounting these

lenses in front of laser bars may result, e.g., in a fast-axis collimated diode laser beam with a full width of 0.8 mm and a full divergence angle of 5 mrad in the fast direction, containing 95% of the diode laser power. The slow direction remains unaffected at this stage.

The accuracy of alignment, reliability of fixture, and long-term stability even under rough environmental conditions is of main concern for the further evaluation of the mounting procedure. As will be shown in Chapter 4, the precision of the axial position of a fast axis collimating lens has to be better than 1 μm, and the maximum tilt must not be larger than 0.1 mrad in order to reach optimum performance. Of course, the accuracy has to be guaranteed to retain for the complete lifetime of the diode laser bar which is typically more than several thousand hours. This demands for some features of the mount that have to be fulfilled.

The fixture of the micro-optics has to be flexible enough to withstand thermal cycling and to balance the different thermal expansion of the glass lens and the heat-sink material of the laser diode. On the other hand, it has to be stiff enough to ensure a stable connection between lens and carrier.

Best results are achieved with UV curable adhesives. But care has to be taken to ensure that out-gassing of the adhesive is low (quoted "100% solid") to prevent contamination of the laser diode front face. Since the adhesive bonding is sensitive to small changes in the process, all relevant parameters have to be controlled to prevent performance variations. That includes not only more common considerations like shelf life or curing time and aging, but also as an example the humidity during application which can affect the properties of the product. A clean, dust-free environment has to be provided for the mounting.

As a further important feature to be considered in the design of the mount, transmission of the laser diode wavelengths through the adhesive must be high enough to avoid heating of the micro-lens due to scattered light and fluorescence from the laser bar. Excessive heat can degrade adhesives even though a preferred type can withstand temperatures up to 125°C, which is far above the typical operation temperature of a diode laser.

Details of the positioning and mounting procedures are described in Chapter 4. Worth mentioning is the fact that alignment of micro-lenses has to be done always in an active mode, with some optical power emitted from the laser bar. The reason for this is the tolerance of the position of the laser bar soldered onto the heat sink. With an active approach, these tolerances can be compensated for by the micro-optics.

References

[3.1] Boucke K, Jandeleit J, Brandenburg W et al. (2001) Proceedings of the SPIE 4285, 165.

[3.2] Jandeleit J, Brandenburg W, Scholz Ch et al. (2000) Proceedings of the SPIE 3945, 270.

[3.3] Both W (1986) Metallurgische reaktion von gold in Weichloten. Ursache der Kontaktdegradation Optoelektronischer Bauelemente, Feingerätetechnik, Berlin, p. 35.

[3.4] Tomm J et al. (2004) Device deformation during low-frequency pulsed operation of high-power diode laser bars. Applied Physics Letters 84, 3525–3527.
[3.5] Solder Alloy Physical Properties Table (2005) Indium Corporation of America, New York, http://www.indium.com/products.
[3.6] Kriebel F (1992) Technologische Aspekte zum flächenhaften Fügen in der Hybrid- und Mikrosystemtechnik, VDI-Berichte Nr. 960.
[3.7] Beuers J (1992) Mechanical properties of soft solder materials for electronic applications. In: Verbindungstechnik in der Elektronik. DVS-Berichte No. 141, ISBN 3-87155-446-4.
[3.8] Beuers J (1991) Kriterien zur umfassenden Charakterisierung innovativer Weichlotwerkstoffe. Proceedings of ELMAT 91 Materials in Micro Electronics.
[3.9] Bader S (1990) Entstehung und Aufbau Isotherm Erstarrter Schichtverbindungen, DVS-Berichte No. 129.
[3.10] Strobeck I (1992) Ermüdungsuntersuchungen von Lotwerkstoffen im Mikrobereich. In: Verbindungstechnik in der Elektronik, DVS-Berichte No. 141, ISBN 3-87155-446-4 [3.13].
[3.11] Weizel W (1962) Physikalische Formelsammlung, Bibliographisches Institut, Mannheim, Band 2, Optik, Thermodynamik, Statistik, Relativitätstheorie; ID: B0000BU3J0.
[3.12] Hu JM, Pecht M (1991) Temperature dependence of the mechanical properties of GaAs wafers. Journal of Electronic Packaging 113, 331–336.
[3.13] Moelle C, Szücs F, Hecht HJ, Röhrs P, Johnston C, Chalker PR, Werner M (April 16–18, 1997) The thermal expansion coefficient of diamond. Proceedings of Micro Materials Conference, Berlin, 493–496.
[3.14] Yoshida K, Morigami H (2004) Thermal properties of diamond/copper composite material. Microelectronics Reliability 44(2), 303–308.
[3.15] Lorenzen D (2003) Methoden zur zuverlässigkeitsorientierten Optimierung der Aufbau- und Verbindungstechnik von Hochleistungs-Diodenlaserbarren. PhD Thesis. Technical University of Berlin, Verlag Dr. Köster, Berlin.
[3.16] Post D, Han B, Ifju PG (2000) Moiré methods for engineering and science – Moiré interferometry and shadow Moiré. In Rastogi PK (ed.): Photomechanics, Springer Topics in Applied Physics, volume 77 Springer-Verlag, Berlin, Heidelberg, pp. 151–196.
[3.17] Rastogi PK (2000) Principles of holographic interferometry and speckle metrology. In Rastogi PK (ed.): Photomechanics, Springer Topics in Applied Physics, volume 77 Springer-Verlag, Berlin, Heidelberg, pp. 103–150.
[3.18] Lorenzen D, Hennig P (2003) Highly thermally conductive substrates with adjustable CTE for diode laser bar packaging. Proceedings of the SPIE 4945, 174–185.
[3.19] Pérez JP (1991) Optique Géométrique, Ondulatoire et Polarisation, 3ème édition. Masson, Paris.
[3.20] Chen TY (2000) Digital photoelasticity. In Rastogi PK (ed.): Photomechanics, Springer Topics in Applied Physics, volume 77 Springer-Verlag, Berlin, Heidelberg, pp. 197–232.
[3.21] Dally JW, Riley WF (1991) Experimental Stress Analysis, 3rd Edition. McGraw-Hill, Inc., New York.
[3.22] Coldren LA, Corzine SW (1995) Diode Lasers and Photonic Integrated Circuits. John Wiley & Sons, New York.

[3.23] Tomm JW, Baerwolff A, Jaeger A, Elsaesser T, Bollmann J, Masselink WT, Gerhardt A, Donecker J (1998) Deep level spectroscopy of high-power laser diodes. Journal of Applied Physics 84(3), 1325–1332.
[3.24] Tomm JW, Gerhard A, Müller R, Biermann ML, Holland JP, Lorenzen D, Kaulfersch E (2003) Quantitative strain analysis in AlGaAs-based devices. Applied Physics Letters 82(23), 4193–4195.
[3.25] Tomm JW, Gerhardt A, Lorenzen D, Hennig P, Roehle H (2002) Diode laser testing by taking advantage of its photoelectric properties. Proceedings of the SPIE 4648, 9–21.
[3.26] Lorenzen D, Dorsch F (2003) Mounting substrate and heatsink for high-power diode laser bars. US patent no. US 6,535,533 B2.
[3.27] Adachi S (1996) Thermal expansion coefficient of GaAs. In Brozel MR, Stillman, GE (eds.): Properties of Gallium Arsenide, INSPEC. The Institution of Electrical Engineers, London, UK.
[3.28] Pourbaix M (1963) Atlas D'Équilibres Élecctrochimiques. Gauthier-Villars, Paris, p. 389.
[3.29] Angell K (1993) pH-Measurement. Technical Note 93-01. Culligan Water International, USA.

4
Incoherent Beam Superposition and Stacking

Peter Loosen, Alexander Knitsch

4.1. Introduction and Survey

Peter Loosen

4.1.1. Beam Quality of Incoherently Combined Beams

Beam quality is a measure of how tightly a beam can be focused. The higher the beam quality, the smaller the spot size and the higher the laser intensity. According to the ISO-standard [4.1] this property can be characterized by the beam-parameter product (Q or BPP), multiplying the waist radius (w_0) and the far-field divergence (θ_0) of the beam. In the best case, i.e., without any aberrations, this beam-parameter product remains constant, if the beam is transformed by passive optical components such as lenses or mirrors (Eq. 4.1).

The minimum value for the beam-parameter product is the so-called diffraction limit and is given for a beam with the wavelength λ by λ/π. The beam-parameter product, normalized to this minimum value, is called the "times diffraction limited factor" (M^2), as it directly indicates how far away the quality of a beam is from diffraction limit.

$$Q = \mathrm{BPP} = w_0 \cdot 1/2\theta_0 = const. \tag{4.1}$$

$$M^2 = \frac{\mathrm{BPP}}{\lambda/\pi} = \frac{w_0 \cdot \theta_0}{\lambda/\pi}.$$

For a given numerical aperture of the focusing system (NA_f) and a rotationally symmetric beam with a total power of P, the average laser intensity in the focal plane (I_f) is given by:

$$I_f = \frac{P \cdot NA_f^2}{\pi} \cdot \frac{1}{Q^2} \tag{4.2}$$

$$= \pi \cdot NA_f^2 \cdot B$$

$$B = \frac{P}{\pi^2 \cdot Q^2} \quad [W\,cm^{-2}\,sr^{-1}]$$

B denotes the brightness of the beam and is introduced into Eq. (4.2) as an abbreviation; the physical meaning will be discussed later in this chapter. Equation (4.2) is widely used in many applications of conventional lasers with a single coherent and circular symmetric beam.

In contrast to conventional lasers, diode laser systems with incoherent beam combination are built up from one- or two-dimensional arrays of individual beams as discussed in Chapter 3. For the calculation of the beam-parameter product of such beams it is necessary to determine the far-field divergence angle (θ_{tot}) as well as the radius of the beam in the waist (w_{tot}) for the total intensity distribution of the emitter array. In Fig. 4.1 a typical geometry is shown for the simplified one-dimensional case, where $2N + 1$ similar intensity distributions $I_0(x)$ are equally spaced with a distance of x_0, each distribution having a radius of w_0.

Both x_0 and w_0 are defined according to the ISO-standard [4.1] as first- or second-order moments of the intensity distribution, respectively ($I_0 =$ one-dimensional intensity distribution; $\sigma_x =$ second order moment of I_0; $P_0 = total$ power of I_0):

$$w_0 = 2\sigma_x \quad \sigma_x^2 = \frac{1}{P_0}\int x^2 \cdot I_0(x)\,dx \tag{4.3}$$

$$x_0 = \frac{1}{P_0}\int x \cdot I_0(x)\,dx$$

The intensity distribution (I_{tot}) and the power (P_{tot}) of the total beam are given by:

$$I_{tot} = \sum_{n=-N}^{N} I_0(x + n \cdot x_0) \tag{4.4}$$

$$P_{tot} = (2N+1)\int I_0(x)\,dx = (2N+1)P_0$$

From Fig. 4.1 it can easily be concluded that the far-field divergence angle of the total beam (θ_{tot}) equals that of an individual beam:

$$\theta_{tot} = \theta_0 \tag{4.5}$$

The beam radius of the total beam (w_{tot}) can be calculated according to the ISO-standard from the second-order moment (σ_x) of the total intensity distribution ($I_{tot}(x)$) as:

$$w_{tot}^2 = 4\sigma_x^2 = \frac{4}{P_{tot}}\int x^2 \cdot I_{tot}(x)\,dx \tag{4.6}$$

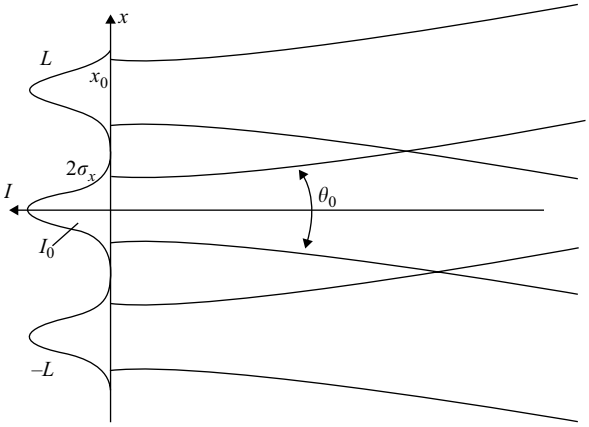

FIGURE 4.1. Example for a one-dimensional array of individual, similar emitters, propagating from the beam waist at the left to the right

Insertion of Eq. (4.4) into Eq. (4.6), coordinate transformation ($\tilde{x} = x + n \cdot x_0$) and minor rearrangement gives the following relation for the radius of a total beam, consisting of M individual beams ($M = 2N + 1$):

$$w_{tot}^2 = 4\sigma_x^2 + \frac{1}{3}(M^2 - 1) \cdot x_0^2 \tag{4.7}$$

$$w_{tot} \cong 1.14 \cdot M \cdot w_0 \cdot F \quad (\text{for } x_0 \gg \sigma_x, M > 2),$$

$$F = \frac{x_0}{2w_0} \text{ (filling factor)}$$

As a rule of thumb it can be stated that a beam consisting of M individual beams has a radius which is roughly M times larger than the radius of the individual beam, if the beams are densely packed (filling factor $F \approx 1$). The beam-parameter product of the total beam is then M times the beam-parameter-product of the individual beam:

$$Q_{tot} = w_{tot} \cdot \theta_{tot} \cong M \cdot w_0 \cdot \theta_0 = M \cdot Q_0 \tag{4.8}$$

Real beams are always two-dimensional. In many practical devices, arrays as shown in Fig. 4.2 are used. With Equation (4.8) the beam quality of the total beam can easily be calculated separately for each dimension. Equation (4.8) is very useful as well for the calculation of beam rearrangement processes such as shown in Fig. 4.3.

A line-shaped beam with different beam-parameter products in the two orthogonal directions ($Q_{x,0}$, $Q_{y,0}$), as it is common in many diode laser setups, can be

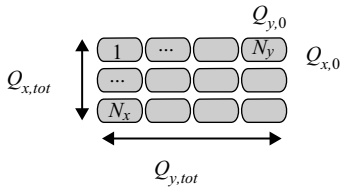

FIGURE 4.2. Two-dimensional array of emitters

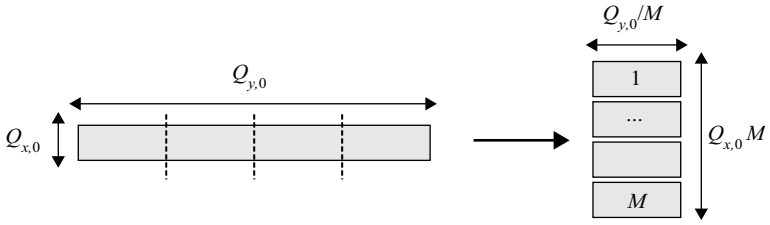

FIGURE 4.3. Rearrangement of the beam

transformed into a beam with quadratic cross-section by cutting the line-shaped beam into separate segments and subsequent optical rearrangement of the individual beam segments. In the literature and in commercial systems a couple of optical systems are described and used for carrying out this transformation [4.3–4.6]. The number of necessary beam segments (M) and the resulting beam-parameter products of the equivalent rectangular-symmetric beam Q_{xy} are given by:

$$Q_{xy} = Q_{x,0} \cdot M = Q_{y,0}/M \quad M^2 = Q_{y,0}/Q_{x,0} \tag{4.9}$$

$$Q_{xy} = Q_{x,0} \cdot \sqrt{Q_{y,0}/Q_{x,0}}$$

$$= \sqrt{Q_{x,0} \cdot Q_{y,0}}$$

The brightness of a beam B [W cm^{-2} sr^{-1}] is the laser power per emitter area (A) and solid angle (Ω) and for the case of the rectangular symmetry in Fig. 4.2 is given by ($\mathrm{A} = 2w_{0,x} \cdot 2\mathrm{w}_{0,y}$, $\Omega = 2\theta_x \cdot 2\theta_y$):

$$B_{tot} = \frac{P_{tot}}{16 \cdot Q_{x,tot} \cdot Q_{y,tot}} = \frac{M \cdot N \cdot P_0}{16 \cdot M \cdot Q_{x,0} \cdot N \cdot Q_{y,0}}$$

$$= \frac{P_0}{16 \cdot Q_{x,0} \cdot Q_{y,0}} = B_0 \tag{4.10}$$

This is the well-known brightness theorem [4.2], which states that in the best case, i.e., without any aberrations, the brightness of the total beam B_{tot} is the same as for the individual beam B_0.

4.1.2. Basics of Incoherent Beam Combination

Incoherent beam combination of individual diode lasers is widely used in high-power diode laser systems. It is a straightforward way to achieve relatively high output powers at high system efficiency, although the potential to achieve high beam quality is limited as explained in the following.

Schematic pictures of technical setups are given in Fig. 4.4. At low output power in the range upto approximately 100 W, where only a couple of diode lasers is needed, the techniques of direct coupling into a fiber bundle or the utilization of beam transformation systems are common. At higher output power up to several kilowatts another setup is used: the individual diode lasers are stacked on top of each other or arranged in parallel.

The basic physical principles used in all systems are shown in Fig. 4.5. The most common arrangement utilizes "spatial multiplexing", where the individual laser beams are simply set side-by-side in a one- or two-dimensional array, thus increasing output power as well as size of the beam. Two complementary techniques, which are increasing output power at constant beam size, are also shown: in polarization multiplexed systems two mutually perpendicularly polarized beams are coupled via a polarization coupler; in wavelength multiplexed systems several beams with different wavelengths are coupled with appropriate optical elements (e.g., edge-filters), so that the combined beams are collinear.

The global goal of all these techniques is generally to create a laser beam with high output power and a beam quality as high as possible. Beam quality is usually measured with the beam-parameter product (BPP, see section 4.1.1), denoted as

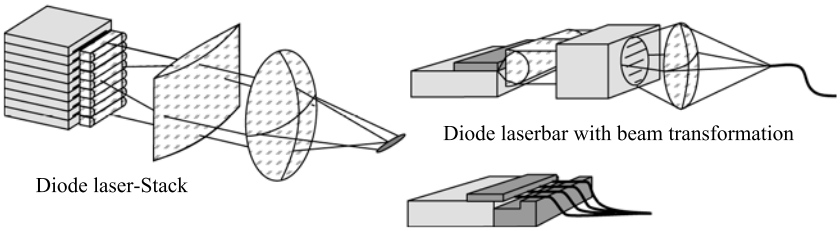

FIGURE 4.4. Schematics of different technical setups for incoherent beam combination: Stacking (left), fiber coupling of a transformed beam (upper right) and direct coupling into a fiber bundle (lower right)

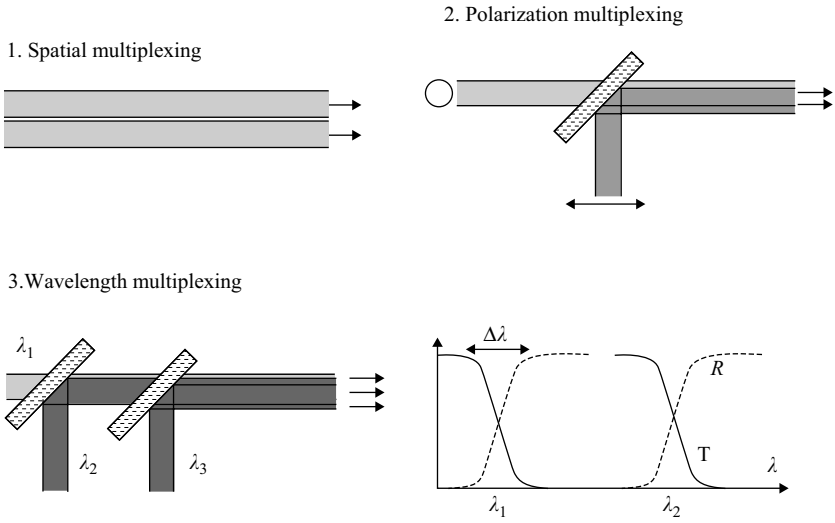

FIGURE 4.5. Basic principles of incoherent beam combination

Q: the higher the quality, the lower the Q. In physical terms the goal therefore can be described as to maximize the brightness B of the beam, which is the ratio of laser power and beam-parameter products in the two orthogonal directions x and y (see section 4.1.1).

The maximum achievable brightness B_{tot} of a diode laser system can be linked to the brightness B_0 of the elementary diode laser type, on which the system is built, by the following overall relation:

$$B_{tot} = \eta_{FAC} \cdot \eta_{PL} \cdot \eta_{StQ} \cdot \eta_{FF} \cdot \kappa_P \cdot \kappa_W \cdot B_0 \tag{4.11}$$

$(\eta \leq 1, \kappa \geq 1)$ with :

η_{FAC} : optical quality of the fast axis collimation,
measured as the relation of
beam parameter products (BPP)
$\eta_{FAC} = Q_{x,0}/Q_x$
Q_x : BPP behind the micro optical lens
$Q_{x,0}$: BPP before the micro optical lens

η_{PL} : power losses at the optical components
$\eta_{PL} = P_{tot}/M \cdot P_0$
M : number of combined beams

η_{StQ} : "Stacking quality"

$\eta_{StQ} = \theta_x / \theta_{x,tot}$

$\theta_{x,tot}$: fast axis divergence of the total beam

θ_x : fast axis divergence of an individual beam

η_{FF} : "Filling factor quality"

$\eta_{FF} = F_x \cdot F_y$

$F_{x,y}$: Filling factors in $x-$ and y $-$ direction

κ_P : Brightness increase by polarization coupling

$\kappa_P = 2$

κ_W : Brightness increase by wavelength coupling

$\kappa_W = j$ (j $-$ number of coupled wavelengths)

The first step to building high-brightness diode laser systems is obviously to develop high-brightness semiconductor-chips, which means chips with high output power and high beam quality. This is described in Chapter 2 of this book. If a diode laser system is build based on these chips, Eq. (4.11) tells us that without polarization and wavelength multiplexing ($\kappa = 1$) the brightness of the chips can be conserved ($B_{tot} = B_0$) in the best case, which means without any of the losses in power and beam quality, indicated in Eq. (4.11). In real cases however, losses in beam quality and therefore in brightness will arise due to imperfect lenses (η_{FAC}), power losses at optical components in the system (η_{PL}), aperture underfilling (η_{FF}, see Fig. 4.1) and stacking imperfections (η_{StQ}, see Fig. 4.6). All these processes and technical measures to minimize these losses are discussed in the sections 4.2 and 4.4.

With polarization and wavelength multiplexing the brightness of the systems can be increased – at the cost of the mixture of polarization states and a broad wavelength spectrum of the diode laser system. Both, however, can be accepted in most cases of industrial applications, as materials processing usually is not very sensitive against changes in polarization and wavelength – at least not in

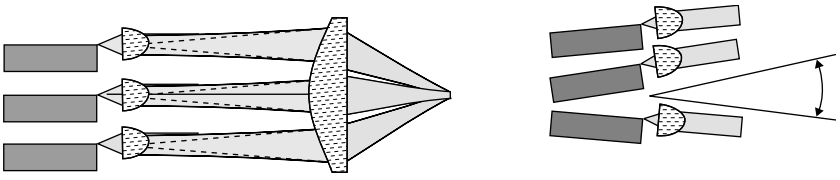

FIGURE 4.6. Reasons for beam degradation in diode laser stacks: Aperture underfilling (left) and angular tolerances of the individual diode lasers (right)

the range discussed here. Brightness increase by polarization and wavelength multiplexing is reflected in Eq. (4.11) in the two factors κ_p (for polarization) and κ_w (for wavelength). Principles, technical setups, and achieved results are discussed in section 4.3.

4.2. Beam Collimation

Veit Blümel, Sandra Huke, Bernd Köhler, Martin Traub

4.2.1. Fast Axis Collimation and Types of FAC-Lenses

A typical property of diode lasers is the highly divergent emission in the direction perpendicular to the pn-junction, the so-called fast axis. Numerical apertures of upto 0.8, i.e., full divergence angles of approximately 100°, are not unusual. Therefore, in most cases where diode lasers are directly used, a collimation of this fast axis is necessary. A mechanically simple solution for beam collimation is a cylindrical lens as shown in Fig. 4.7. An important requirement for this cylindrical lens is, that as much beam quality and laser power as possible must be conserved, i.e., the beam-parameter product in the fast axis behind the lens should be close to the diffraction limit as it is the case right at the emission facet of the diode laser.

In order to compare different lens types and to assess the lens performance in relation to the physical limit, ray-tracing calculations have been carried out as explained in Fig. 4.8 [4.7]. For the calculations, a diode laser with a diffraction-limited beam, i.e., with Gaussian intensity profile in y-direction, has been used as a source. The numerical aperture (NA = 0.77 in all examples discussed below) is the divergence angle where the intensity is reduced to $1/e^2$ of the center value. For the one-dimensional case approximately 95% of the total power falls within this numerical aperture. In addition to the fast axis divergence, a numerical aperture

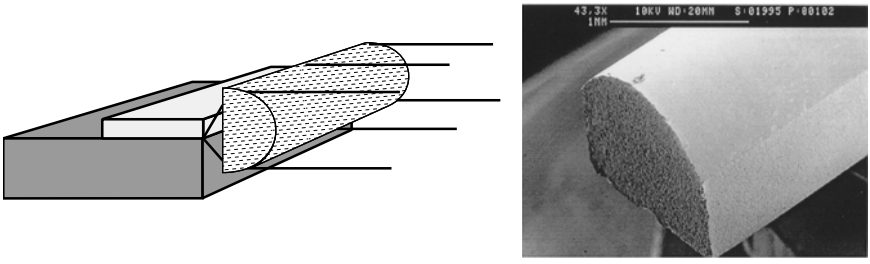

FIGURE 4.7. Principle of fast axis collimation with a cylindrical lens (left) and SEM-picture of a sample (right), which has been manufactured from high-refractive index glass with an ultra-precision grinding technique

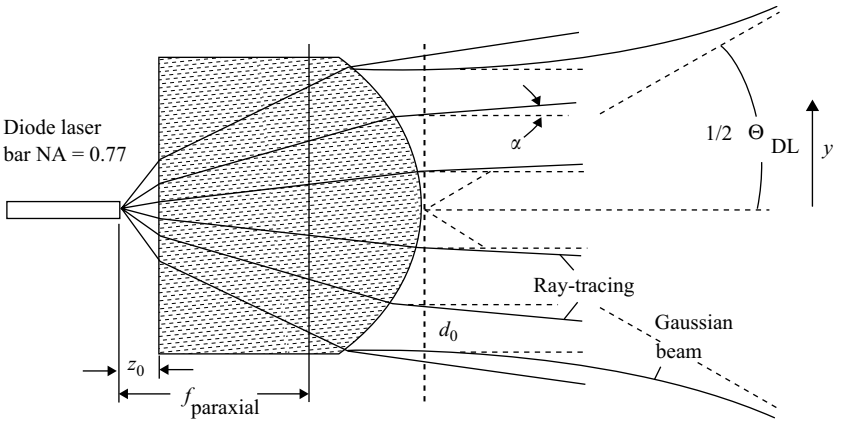

FIGURE 4.8. Ray-tracing calculation for the fast axis collimation of the diode laser emission by a cylindrical lens

in the *x*-direction (slow axis) of 0.084 (approximately 5°) has been taken into consideration in all the calculations given below. This is a typical divergence angle for many diode laser emitters.

From the source point a fan of equally spaced rays has been traced through the lens, each ray carrying the local laser intensity. Behind the lens the intensities of the rays are summed up and plotted against the angle α (Fig. 4.9). These curves are compared with the case of a diffraction-limited Gaussian beam with the same diameter d_0 as the fan of rays which leaves the lens (dotted line in Fig. 4.9). If the curves calculated by ray-tracing are in the range of this dotted line, the lens is assumed to be sufficient for a high quality collimation of the beam.

Figure 4.9 clearly shows that beams with high numerical aperture as discussed here cannot be collimated adequately with standard plano-spherical or bi-convex lenses: even if lens materials with high refractive indices are used, the numerical aperture of the collimated beam (defined as the angle with 95% power enclosure) is more than ten times bigger than for the ideal case of a diffraction-limited beam (θ_{DL}). This is the reason why easy-to-manufacture plastic lenses cannot be applied here, because plastics typically have low refractive indices. The lens with the highest performance in the diagram is a single lens made from high refractive index glass which has an aspherical surface, optimized for the emission characteristics of the diode laser bar. However, even with such an optimized lens the diffraction limit cannot be achieved under all conditions. The reason for this is the linkage of the fast axis and the slow-axis divergence [4.8] due to Snell's law.

Nowadays several manufacturing techniques are available to produce aspheric glass micro-lenses, as shown in Fig. 4.7, with the necessary accuracy in the submicrometer range: ultra-precision grinding [4.9] or ultrasonic shaping with a hard-metal mold [4.10].

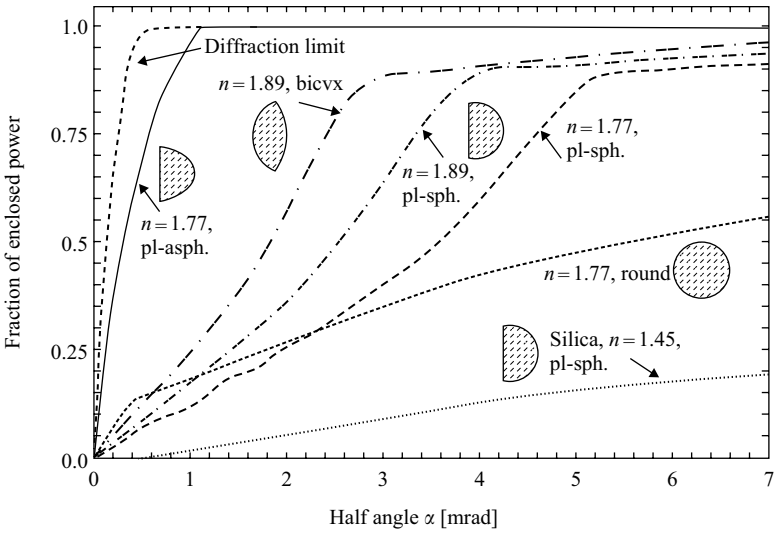

FIGURE 4.9. Calculated comparison of the quality of diode laser beams, after collimation by different types of cylindrical lenses (diode laser $NA_{fast} = 0.77$, $NA_{slow} = 0.084$)

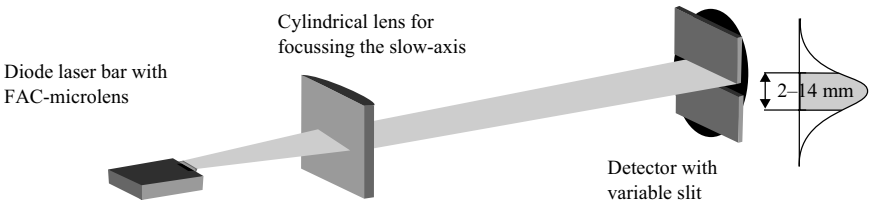

FIGURE 4.10. Setup for measuring the quality of a fast axis collimation lens (FAC)

To determine the collimation quality several methods of lens characterization are in use. The general method is the measurement of the power content in a desired area with different techniques according to ISO 11146. For example the collimation quality can be measured by the method of a moving slit (Fig. 4.10). The far-field power content is measured with a power detector in a distance of 1,000 mm. With respect to the divergence in slow axis a cylindrical lens for focusing the laser beam onto the detector is applied. In front of the detector there is a slit with a variable aperture in fast axis from 2 to 14 mm.

By simple geometry the opening slit is correlated to the divergence angle after the fast axis collimation (e.g., the power content inside the 5-mm slit is equal to the power content within a divergence of 5 mrad). Although the setup takes adjustment and tilting errors into account the measurement indicates the quality of different types of FAC-lenses, as shown in Fig. 4.11. The beam-parameter product (BPP) after the fast axis collimation can be defined via the enclosed power over the divergence angle. For example, with 95% power content and a beam height

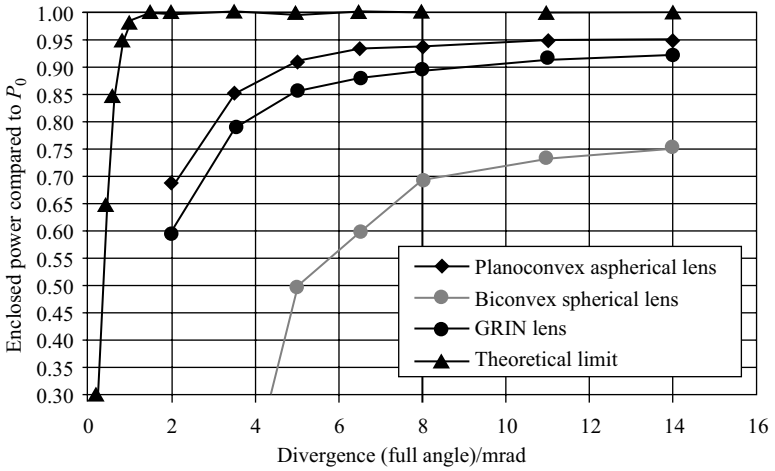

FIGURE 4.11. Measured performance of different types of FAC-lenses compared to the theoretical limit

of 0.8 mm after the FAC-lens, the remaining divergence angle is about 8 mrad. The corresponding beam-parameter product drops to 1.6 mm mrad compared to a theoretical limit of about 0.3 mm mrad (see Eq. (4.1)).

With commercially available fast-axis micro-lenses, a power throughput in excess of 95% (including AR-coating) and a beam quality behind the lens of approximately twice the diffraction limit can be achieved in the best cases [4.7].

4.2.2. Accuracy of Alignment of FAC-Lenses

Micro-optical elements behave highly sensitive to displacement out of their optimal position. The sensitivity of a micro-lens is reciprocal to its focal length so that the FAC-lens with a focal length of approximately 500–1,000 µm determines the positioning system accuracy. In the following an FAC with a focal length of 560 µm will be considered in its six degrees of freedom (Fig. 4.12).

The beam quality depends on several factors like *smile* (see Fig. 4.19), divergence angle of the individual emitters and accuracy of the lens mounting. Since *smile* and divergence angle have to be considered as given constants the latter aspect is most important to achieve an optimum beam quality.

In the sensitive alignment process axial defocusing and lateral beam twist directly lead to a significant loss of beam quality. Axial defocusing is caused by linear translation in z-direction and tilt of β_y. If the FAC-lens is aligned to the emitter facet the beam diverges uniformly by changing the axial position (Fig. 4.13).

In comparison, a tilt around the centre axis of the lens (β_y), i.e., an axial displacement of the edges of the FAC (Fig. 4.14), results in a divergence distribution rising from a minimum in the centre to a maximum at the edges. Dependent on the focal length of the FAC the precision of adjustment can be in the sub-micron

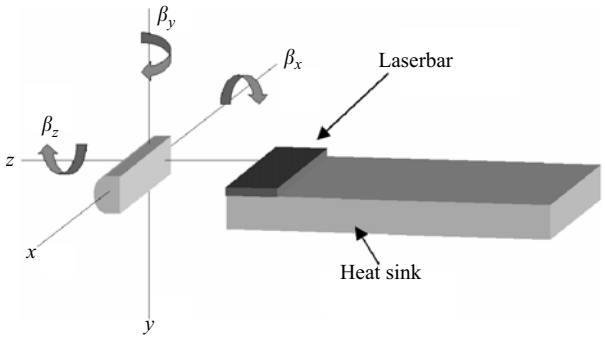

FIGURE 4.12. Degrees of freedom in adjusting an FAC micro-lens

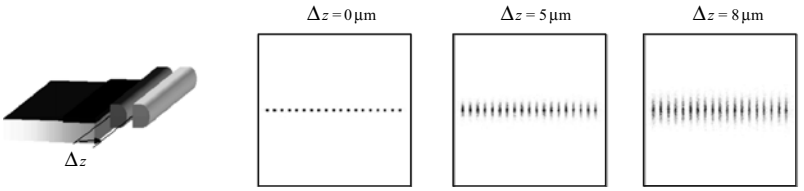

FIGURE 4.13. Qualitative image of an axially defocused beam generated by translation in z-direction

range. For example, an FAC with $f_{FAC} = 560\,\mu m$ requires an adjustment tolerance of approximately 0.5 μm. Corresponding to the maximum allowable displacement in z-direction the value for the maximum tolerable tilt about the vertical axis β_y is about 0.1 mrad (Fig. 4.15). To emphasize the impact of displacement on the beam quality Figs. 4.13 and 4.14 show the qualitative results of extreme axial defocusing. A typical value for the divergence angle after collimation $\theta_{c,y}$ is 4 mrad, leading to a substantial degradation at a factor of 2 of the theoretical value of $\theta_{c,y} \approx 2$ mrad for the collimated single diode laser bar with an FAC with $f_{FAC} = 560\,\mu m$.

Achieving a high beam quality also means that each collimated emitter has to propagate in the same direction. Especially for a diode laser stack this is of particular importance (see section 4.4.1.3). This can be realized by taking advantage of the fact that the deflection angle of an individual beam depends on the vertical position of the FAC (Fig. 4.16).

The precision of adjustment is given by the specified BPP. To avoid further degradation of the beam quality an optimum alignment of the FAC lens is very important. A realistic value for mounting precision in fast axis is $\Delta y = 0.2\,\mu m$ resulting in a deflection angle of $\delta = 0.4$ mrad (Fig. 4.17).

Another, somewhat less sensitive, alignment error is given by a tilt β_z around the z-axis which directly leads to a tilt of the beam line about the propagation direction. That is the same effect as described in Figs. 4.16 and. 4.17, but the individual emitters receive different deflection angles after collimation. The mounting

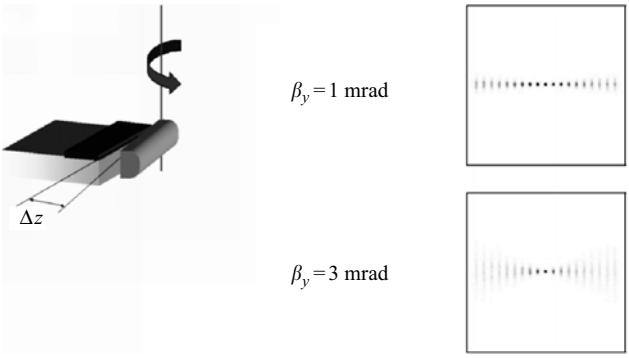

FIGURE 4.14. Qualitative image of an axial defocused beam generated by tilt β_y

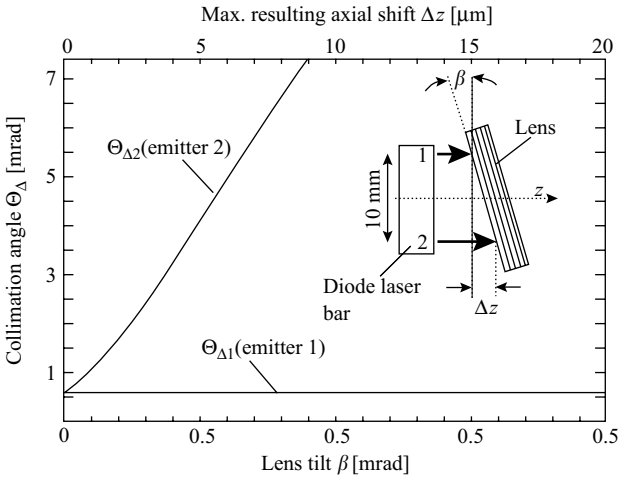

FIGURE 4.15. Quantitative description of the linear displacement of the FAC in z-direction and the resulting collimation angle θ [4.11]

accuracy for β_z is defined by Eq. (4.12).

$$\Delta\beta_z = \arctan \frac{\Delta y}{l_{FAC}/2} \tag{4.12}$$

Assuming a maximum tolerable deflection angle of $\delta = 0.4$ mrad, which leads to a linear displacement $\Delta y = 0.2\,\mu$m (see Fig. 4.17) and a length of the FAC-lens $l_{FAC} = 10$ mm, the mounting accuracy is given by $\Delta\,\beta_z < 0.04$ mrad.

In Fig. 4.18 the correlation between tilt of the lens $\Delta ß_z$ and the resulting tilt of the beam line is illustrated.

One important fact, which cannot be compensated for, is the deformation of the mounted diode laser bar, the so-called *smile* [4.11]. *Smile* means a deflection of

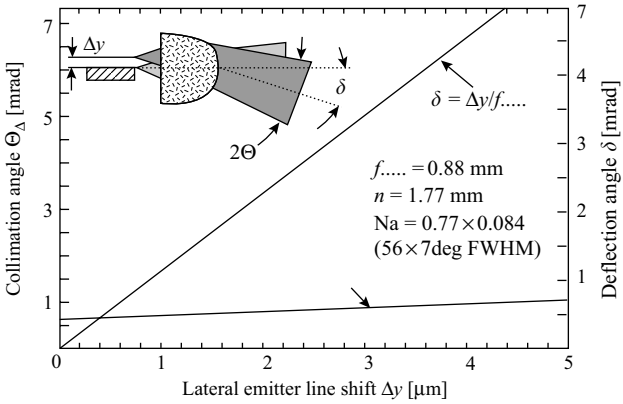

FIGURE 4.16. Quantitative description of the linear displacement of the FAC in *y*-direction and the resulting deflection angle δ

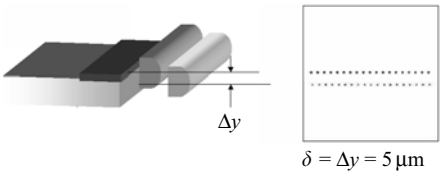

Δy [µm]	$\delta = \Delta y / f_{FAC}$ [mrad]
0.2	0.4
0.4	0.7
0.6	1.1
0.8	1.4
1.0	1.8
1.2	2.1
1.4	2.5
1.6	2.9
1.8	3.2
2.0	3.6

FIGURE 4.17. Increase of the deflection angle δ dependent on the linear displacement Δy in fast axis

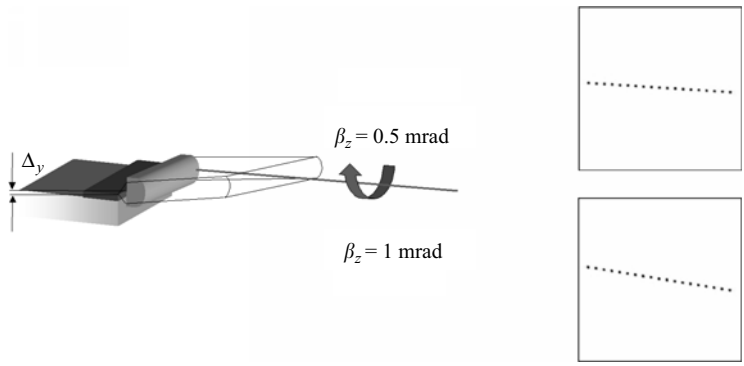

FIGURE 4.18. Qualitative imaging of tilt-induced displacement by β_z which causes a slope in the beam pattern

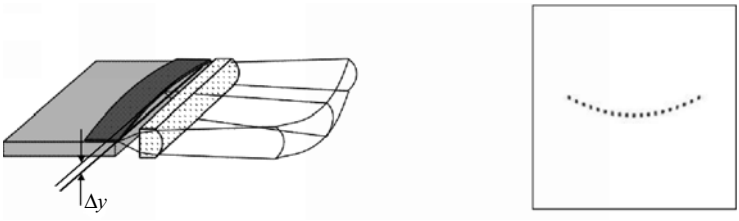

FIGURE 4.19. Qualitative imaging of the *smile*-effect Δy generated by a deformation of the laser bar in fast axis

the laser bar in fast axis and reduces the beam quality significantly (Fig. 4.19). A lot of mechanical tolerances in heat-sink and measurement equipment, soldering process as well as thermal and mechanical stresses generate the *smile*. In Fig. 4.19 the *smile*-induced deflection angle is shown, which decreases from the edge of the laser bar into the centre and causes a *smile* at the detector.

A deflection of $\Delta y = 1\,\mu\text{m}$ (peak to valley) already increases the total beam diameter $2w_y$ (see Eq. (4.13)) upto $2\,\mu\text{m}$ and reduces the beam quality with a factor of 2, assuming a beam radius of $w_{y,emitter} = 0.5\,\mu\text{m}$.

$$2w_y = 2w_{y,emitter} + \Delta y \tag{4.13}$$

So the *smile*-induced divergence angle after collimation of the total laser bar θ_{smile} describes a combination of divergence angle $\theta_{c,y}$ and the deflection angle after collimation δ of each single emitter (Eq. (4.14)).

$$\theta_{smile} = \theta_{c,y} + \delta \tag{4.14}$$

Since $\theta_{c,y}$ will be received to the greatest possible extent, the deflection angle runs linearly with this misalignment in respect of the origin position. According to the numbers in the table in Fig. 4.17 a *smile* of $\Delta y = \pm 1\,\mu\text{m}$ (both directions possible) leads to a deflection angle of $\delta = 1.8$ mrad. Assuming a divergence angle after collimation of $\theta_{c,y}/2 = 2$ mrad and a *smile* of $\Delta y = 1\,\mu\text{m}$, the total divergence angle of an individual laser bar is $\theta_{smile}/2 = 2.9$ mrad. *Smile*-induced losses in beam quality are given by η_{smile}.

$$\eta_{smile} = \frac{\theta_{c,y}}{\theta_{smile}} = \frac{\theta_{c,y}}{2w_y/f_{FAC}} \tag{4.15}$$

The summation of all tolerances like *smile*, several kinds of aberration and misalignment of micro-optics leads to a decreased beam quality of a single diode laser bar.

4.2.3. Slow Axis Collimation

As described in the previous sections, beam collimation of the diode laser bar in fast axis direction is necessary in most applications because of the high divergence

in fast axis. Due to the moderate divergence in the slow axis, beam collimation in this direction is not required for many cases. Furthermore, due to the emitter structure of a diode laser bar collimation of the slow axis is much less efficient compared to the collimation in fast axis. Whereas fast axis collimation can reduce the divergence of a diode laser bar from, e.g., 60° (full angle) down to a few milliradian (factor of about 200), beam collimation of the slow axis will only reduce the beam-divergence at a factor of about two.

However, beam collimation of the slow axis is one important approach to improve the BPP and therefore the brightness of a diode laser bar. Increasing the brightness of a diode laser bar by means of slow axis collimation is a consequence of filling factor enhancement. Aperture underfilling in the slow direction is a result of the typical diode laser bar structure, which is composed of several individual emitters with emitter size d_{em} separated by the pitch distance p (see Fig. 4.21). The filling factor F_{slow} in slow axis is defined by Eq. (4.16)

$$F_{slow} = \frac{d_{em}}{d_{Pitch}} \tag{4.16}$$

Filling factor enhancement in slow axis can be realized by using appropriate micro-optics for individual collimation of the emitters. The slow axis collimation lens (SAC) is a cylindrical lens array whereby the number of segments corresponds to the number of emitters of the diode laser bar. Each single emitter is collimated by one segment of the cylindrical lens array (see Figs. 4.20 and 4.21).

Individual collimation of each emitter leads to an increase of the individual beam diameter and in consequence to a reduction of the beam divergence. Therefore the BPP of the diode laser bar is improved, because the total beam diameter in the slow direction remains nearly constant. The theoretical limit for the beam diameter increase of one emitter is given by the pitch to emitter size ratio $1/F_{slow}$. Accordingly the maximum beam divergence reduction and thus the improvement of the BPP is given by the factor F_{slow}. However, it should be emphasized that the BPP of the individual emitter is unchanged.

It is important to notice that individual collimation has to take place before the adjacent beams begin to overlap. This limits the distance d of the micro-lens array to the diode laser bar. The focal length f_{SAC} of the individual lens segments of

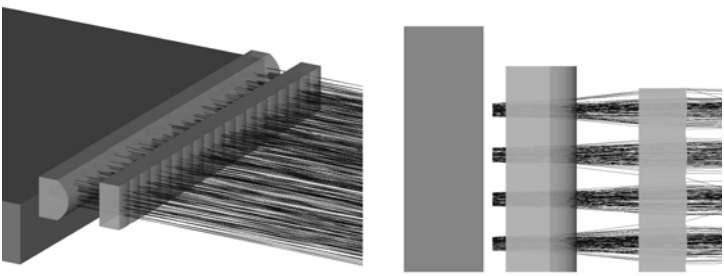

FIGURE 4.20. Principle layout of a slow axis collimation lens array (SAC)

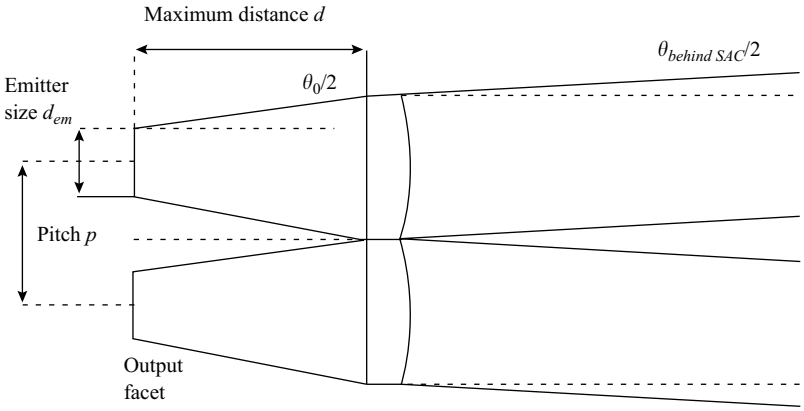

FIGURE 4.21. Principle of filling factor enhancement in the slow direction by means of a slow axis collimation array (SAC)

the SAC is also determined by this distance (Fig. 4.21). The maximum distance d and therefore the maximum focal length $f_{SAC} = d$ is a function of pitch, emitter size and slow axis divergence angle (see Eq. (4.17)).

However, if the set-up is described under the simplifying assumption of geometric optics, there is one significant drawback when using a standard SAC consisting of individual single cylindrical lenses. Due to the limitation in the distance of the SAC the ratio of focal length to emitter size is also limited, so that the focal length is only few times larger than the emitter size. It is well known that effective collimation of an extended light source requires a focal length that is significantly larger than the light source itself. The residual beam divergence after collimation of an extended source with a collimating lens of focal length f_{SAC} is given by Eq. (4.18). This equation is derived from simple geometrical optics considerations.

According to Eq. (4.18), a beam divergence reduction by means of a standard SAC is only possible for pitch-to-emitter size ratios larger than two. For a pitch-to-emitter size ratio of two the divergence after collimation is identical to the original divergence angle and therefore the BPP remains unchanged. Furthermore, for pitch-to-emitter size ratios below two the divergence of the beam is even increased compared to the original beam.

$$d = \frac{p - d_{em}}{2 \cdot \tan(\theta_0/2)} \tag{4.17}$$

$$\theta_{behind\ SAC}/2 \approx \left(\frac{d_{em}}{2 \cdot f_{SAC}}\right) = \arctan\left(\frac{\tan(\theta_0/2)}{p/d_{em} - 1}\right) \tag{4.18}$$

A further reduction of the beam divergence can be achieved by using a more sophisticated slow axis collimation array, whereby the individual lens segments consist of, e.g., two cylindrical lenses for slow axis collimation (telescope arrays).

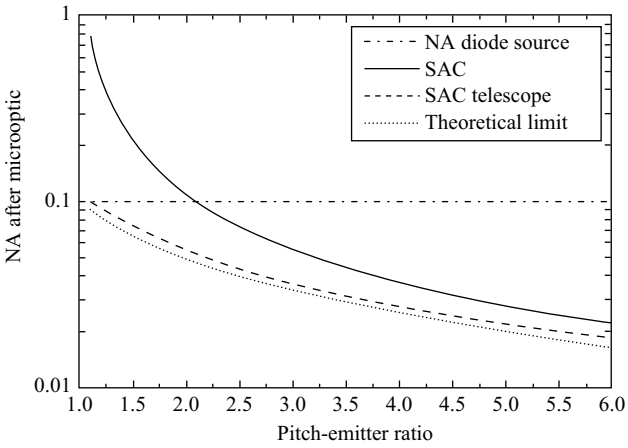

FIGURE 4.22. Comparison of beam divergence reduction by means of a standard slow axis collimation lens array (SAC) and a lens array consisting of individual telescopes (SAC telescope). The initial beam divergence of the diode source is NA = 0.1

The correlation between beam divergence reduction and pitch-to-emitter-size ratio is shown in Fig. 4.22 for a standard SAC and an SAC telescope, respectively. The initial beam divergence of the diode laser source in the slow direction is NA = 0.1 (corresponding to a beam divergence half angle $\theta_0/2$ of 5.7°).

The beam divergence reduction by means of a SAC telescope is close to the theoretical limit, which is given by the factor F_{slow} (see Eq. (4.16)) and is again derived from simple geometrical optics considerations. It should be noted that the transition zones between to adjacent lens segments also contribute to the deviation from the theoretical limit. Typical values for useful apertures are 90 to 95%.

Increasing the brightness by means of aperture filling is not only possible in slow axis, but also in fast axis where diode laser stacks with individual diode laser bars arranged on top of each other are considered (see section 4.3.3).

4.2.4. Homogenization of High-Power Diode Lasers

For numerous applications of high-power diode lasers like polymer welding, hardening of metals and illumination for surface inspection, a top hat intensity distribution for at least one direction is demanded. In general, this distribution is ideal for applications where a homogeneous intensity distribution is needed at the work piece that is stable over time. Since the fast axis offers a defined Gaussian distribution, usually the slow axis distribution is homogenized and thereby transformed to a top hat distribution.

The far-field intensity distribution of the slow axis of a high-power diode laser can be approximated by a super-Gaussian distribution that is implemented as a source type for ray-tracing programs like ZEMAX™.

$$I(\theta) = I_0 e^{-2\left(\frac{\theta}{\alpha}\right)^{2G}}, \tag{4.19}$$

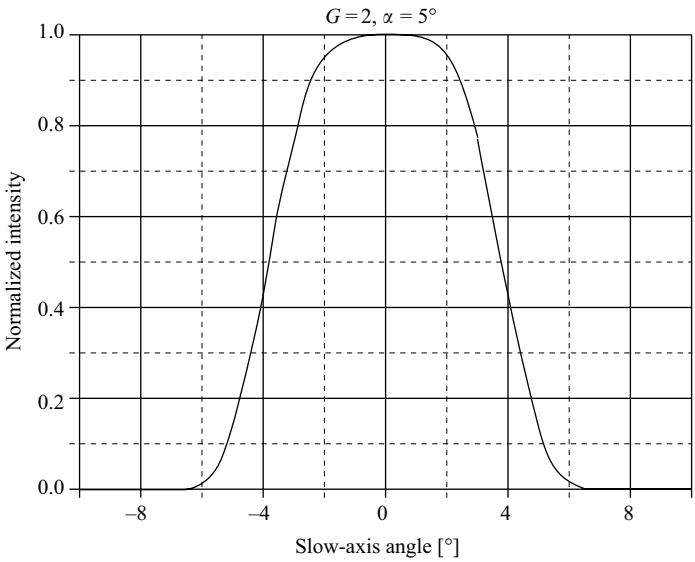

FIGURE 4.23. Super-Gaussian distribution for $\alpha = 5°$ and $G = 2$

where I_0 is the peak intensity at $\theta = 0$, α is the angle of divergence, and G is the super-Gaussian factor. For $G = 1$, the distribution becomes a true Gaussian one, and for higher values of G, it becomes more squared. For commercially available high-power diode lasers, the parameters G and α can be found by least-square-fitting of the measured far-field distribution to Eq. (4.19). The following calculations are performed for $\alpha = 5°$ and $G = 2$, which are reasonable values for the slow axis of commercially available high-power diode lasers without slow axis collimation. Figure 4.23 shows the calculated intensity distribution for these parameters.

To model the far-field distribution of the diode laser to be homogenized more precisely, the normalized measured far-field distribution can be used to weight the rays traced through the system.

For the homogenization of high-power diode lasers, a light pipe is frequently used. This light pipe is formed by a brick-shaped glass block with polished front and end faces and polished side walls. The radiation of the diode laser is usually focused by cylindrical lenses on the front face for one-dimensional homogenization and focused by spherical lenses for two-dimensional homogenization. While propagating through the light pipe, the radiation is reflected by the side walls by total internal reflection, thus no losses occur for these reflections. By each reflection, the far-field distribution of the diode laser is segmented and all segments are overlaid spatially at the end face. If the number of reflections and thereby the number of segments is large enough, a homogenized near field distribution is achieved at the end face of the light pipe. The far-field distribution is not influenced by the light pipe for parallel side walls. The basic concept of the light pipe is shown in Fig. 4.24. For a more detailed discussion on this concept, see [4.13]. This technology is implemented in the systems described in Chapters 6.3.4 and 6.3.6.

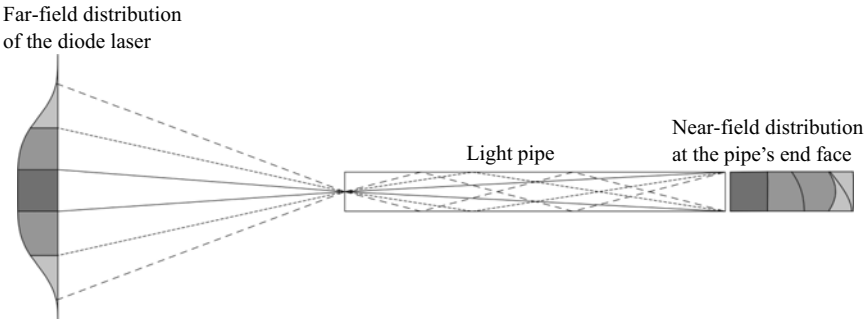

FIGURE 4.24. Homogenization of a diode laser using a light pipe

The end face is usually imaged on the workpiece. For one-dimensional homogenization where the slow axis is homogenized, an anamorphotic relay system is used that focuses the fast axis on the work piece. A telecentric relay system maximizes the depth of field which is demanded for most applications. It is also possible to use a tapered light pipe that increases the numerical aperture of the exiting laser beam by each reflection, thus increasing the angle of divergence of the exiting beam.

The homogenization is mainly influenced by the angle of divergence of the diode laser beam in combination with the aspect ratio of the light pipe and its index of refraction. The number of reflections is increased by a higher angle of divergence of the diode laser and by a higher aspect ratio of the light pipe. To avoid coupling losses and very accurate alignment of the light pipe, its front face should be slightly larger than the diode laser beam. The angle of divergence of the diode laser beam is limited by the numerical aperture of the following optical system as well as the critical angle of the chosen material. Since the index of refraction of the light pipe's material influences the angle of divergence inside the light pipe according to Snell's law, a material with a low index of refraction is preferred, and therefore fused silica is usually chosen. It also offers a very low absorption combined with a very low coefficient of thermal expansion, thus leading in a very high damage threshold of the light pipe.

As shown in Fig. 4.24, only a few reflections are necessary for a sufficient homogenization of sources with a smooth, symmetric and continuous far-field distribution. If the diode laser bar is simply focused on the front face of the light pipe, the angular distribution corresponds to the near field distribution of the diode laser bar and is thereby modulated by the non-emitting areas between the emitters and power changes from emitter to emitter. By the failure of some emitters, this modulation becomes worse and the top hat distribution at the end face cannot be maintained. The influence of a modulated far-field distribution is shown in Fig. 4.25. This effect is extremely disturbing if the fast axis of a diode laser stack is homogenized. For the fast axis, a relatively small number of emitters with a significantly low filling factor yields in a highly modulated far-field distribution, if the stack is simply focused on the front face of the light pipe.

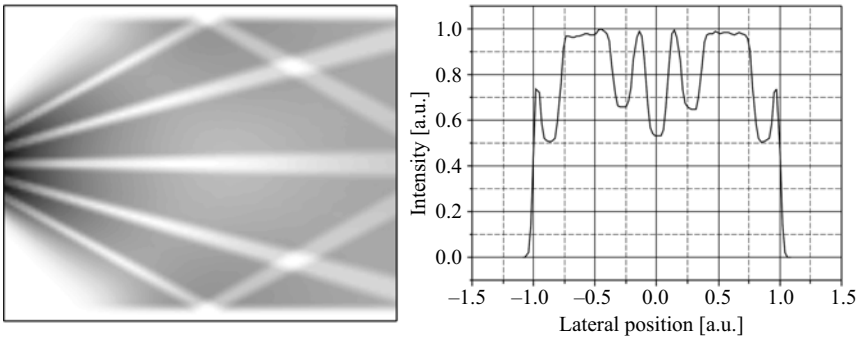

FIGURE 4.25. Intensity distribution inside the light pipe for a modulated far-field distribution calculated by non-sequential ray-tracing (left); cross section at the light pipe's end face (right)

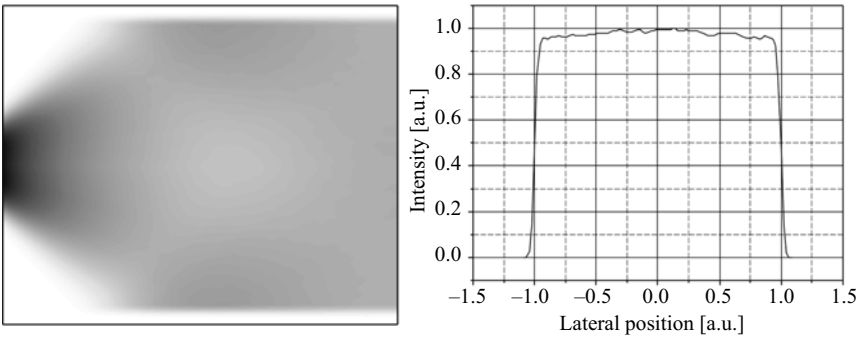

FIGURE 4.26. Intensity distribution inside the light pipe for a non-modulated far-field distribution calculated by non-sequential ray-tracing (left); cross section at the light pipe's end face (right)

Obviously neither an increased numerical aperture of the diode laser beam nor an increased length of the light pipe can smooth out the modulation of the far-field distribution. If the far-field distribution of the diode laser is smooth and not modulated, the intensity distribution at the end surface is a nearly perfect top hat (see Fig. 4.26).

To transform the far-field distribution of the diode laser on the front face of the light pipe, it is necessary to image the facet of the diode laser instead of focusing the diode laser on the front face. For the fast axis, it is usually sufficient to shape the beam by an afocal telescope that reduces the field size and increases the numerical aperture of the beam. Instead of imaging the diode laser's facet on the front face of the light pipe, a micro-lens array can be used to smooth the far-field distribution at the front face.

4.3. Techniques for Beam Combination

Bernd Köhler

The output power of commercially available individual diode laser bars is limited to 50–100 W. In order to increase the total output power of a diode laser system, multiple single diode lasers can be stacked on top of each other or arranged side by side in a 2D assembly. However, this form of spatial multiplexing also increases the total beam size. Consequently, the total beam quality of the system characterized by the beam-parameter product (Q or BPP) is reduced.

The aim of all beam combination methods is to increase the power of the system while maintaining the beam quality and thus increasing the brightness of the system. This is accomplished by coupling the radiation of individual elements into the same optical path. Incoherent coupling of several individual elements can be implemented via polarization multiplexing, wavelength multiplexing and spatial multiplexing. Schematical pictures of these multiplexing methods are shown in Fig. 4.5 (see section 4.1).

4.3.1. Polarization Multiplexing

Polarization multiplexing is achieved by combining two mutually perpendicular polarized beams into the same optical path via a polarization multiplexing element. If necessary the polarization state of one diode laser bar can be rotated with an appropriate half wave retardation plate. Due to the fact that there are only two independent polarization states, the maximum theoretical increase of brightness is limited to a factor of two when combining two individual beams with equal power.

Polarization multiplexing is generally realized with polarization beam-splitter cubes that consist of precision high tolerance right angle prisms cemented together with a dielectric coating on the hypotenuse of one of the prisms. However, for high-power applications the use of beam-splitter cubes is limited to the damage threshold of their cemented interface. Thin film polarizers and birefringent crystals are also widely used as polarization multiplexing devices, especially in high-power systems because of their high resistance against intensive laser power.

Generally, thin film polarizers are made of plane parallel plates with one uncoated side and a dielectric coating on the other side. The polarizer is orientated in such a way that the s-polarized beam is reflected and the p-polarized beam is transmitted. To minimize the losses for the transmitted beam (p-pol.) the angle of incidence for the transmitted beam should be close to the brewster angle θ_B (Fig. 4.27).

The multilayer dielectric coating has to meet several demands when used in combination with high-power laser radiation. Primary requirements are hard and mechanically resistant layers, environmentally stable coatings regarding temperature, moisture and intensive radiation exposure, high damage thresholds, steep slopes, and low transmission losses.

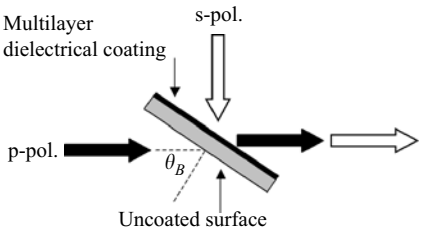

FIGURE 4.27. Schematic setup of combining two beams via polarization multiplexing by means of a thin film polarizer

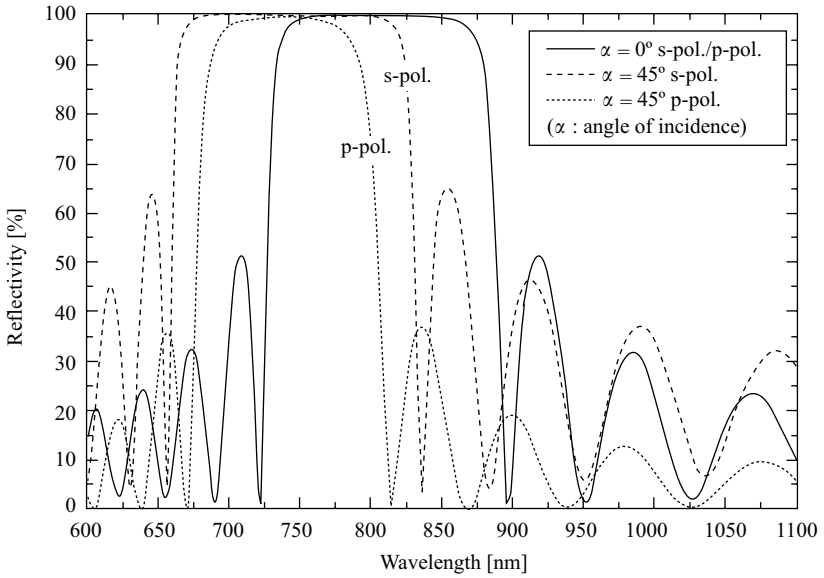

FIGURE 4.28. Polarization dependent reflection and transmission characteristics of a simple dielectrical multilayer system consisting of 14 pairs of quarter-wave films for two different angles of incidence (0° and 45°)

A single dielectrical layer simply consists of an optically transparent material with a refraction index n and an optical thickness which is a fraction of the wavelength (usually one-quarter or one-half wavelength) of the laser beam. Multilayer systems are composed of multiple single layers with alternating low and high refractive index. According to Fresnel's law at each single layer the incident beam is divided into a reflective and a transmissive part. The overall reflection and transmission characteristics of the surface are calculated by computing the multiple beam interferences of all layers.

The basic functionality of a polarization coupler based on a multilayer dielectrical device can be derived from Fig. 4.28. This diagram shows the reflection

and transmission characteristics of a very simple periodical multilayer system consisting of 14 pairs of quarter-wave films with alternating high refractive index n_H and low refractive index n_L. The theoretical reflectivity $R_{[HL]^N}$ of such a system is computed by Eq. (4.20) for normal incidence (n_1 = refractive index of ambient atmosphere; n_2 = refractive index of substrate; N = number of dielectric film pairs) [4.14].

$$R_{[HL]^N} = \left(\frac{n_1/n_2 - (n_H/n_L)^{2N}}{n_1/n_2 + (n_H/n_L)^{2N}} \right)^2 \tag{4.20}$$

Figure 4.28 also shows the effect of polarization and angle of incidence on the spectral reflectivity of the multilayer system. For normal incidence ($\alpha = 0°$) the polarization has no influence on the reflectivity. Increasing the angle of incidence leads to a split of the reflectivity characteristics for the s-polarized and the p-polarized beam, respectively. This split becomes evident for incident angles larger than approximately 20°. Furthermore, at oblique angles ($\alpha \neq 0°$) the reflectivity band is shifted toward shorter wavelengths. The reflectivity increases for s-polarized beams and decreases for p-polarized beams. In addition the reflectivity band for s-polarization is broadened, whereas the reflectivity band for p-polarization is narrowed.

Thin-film polarizers make use of the splitting of the reflectivity curves at oblique angles. However, the multilayer design of real polarization couplers has to be a lot more complex to provide suitable coupling efficiencies over an appropriate wavelength range. In addition the sensitivity of the thin film polarizers in terms of angular tolerances of the incident beam has to be considered particularly with regard to diode lasers with minor beam quality and significant divergences.

The manufacturing method of the thin film coating is of great importance for the properties of the polarization coupler especially when used with high-power devices. Thin film coatings fabricated with conventional reactive evaporation suffer from porous layers, which may lead to the incorporation of water into the layer. Heating of the element, e.g. because of inevitable absorption of a small part of the incident laser beam, will reduce the water concentration in the layer. Consequently – due to the dependency of the refraction index on the water concentration – the spectral transmission and reflection characteristics of the beam coupler will change with temperature and laser power. For instance, the edge of such a beam coupler will shift approximately 13 nm toward shorter wavelengths, when heated from 25°C to 100°C [4.15]. This corresponds to a temperature shift of approximately 0.2 nm/°C.

The porosity and the incorporation of water into the layer can be reduced with ion-assisted-deposition (IAD). Further improvement with regard to temperature stable dielectric devices is achieved with the ion beam sputtering (IBS) fabrication method [4.15]. The thermal drift of a short pass fabricated with the IBS method is reduced from 13 nm down to 0.3 nm, which corresponds to a thermal shift of less than 0.01 nm/°C. In addition to the nearly temperature- and power-independent

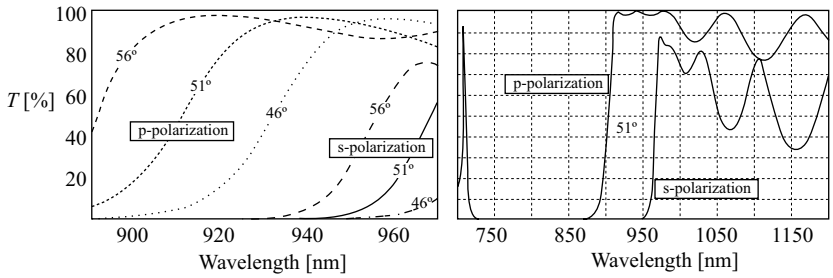

FIGURE 4.29. Comparison of spectral characteristics of a polarization beam splitter fabricated with conventional thermal evaporation (left diagram) and ion beam sputtering (right diagram)

behavior IBS-fabricated devices provide lower losses, an improved edge steepness of the spectral characteristics, and higher damage thresholds.

Figure 4.29 shows a comparison of the spectral characteristics of a polarization beam splitter fabricated with conventional thermal evaporation and ion beam sputtering (IBS), respectively. Additionally, in the left diagram the angular sensitivity of the reflection and transmission characteristics is shown for an angular range of $\pm 5°$, which corresponds to the typical divergence of a diode laser beam in slow axis. At the design wavelength of 940 nm, the losses for the conventionally fabricated wavelength coupler are in a range from 3% to 23% for the p-polarized wave and 2% to 5% for the s-polarized wave. In contrast the maximum losses for the IBS polarization coupler are only 3% for both the s-polarized and the p-polarized wave. Furthermore, the much steeper slope of the IBS-coated device is evident. As a consequence the spectral distance between 10% and 90% transmission is reduced from 30 nm down to 20 nm. However, even for the IBS-fabricated device the spectral range that provides low losses for the whole angular range from $\pm 5°$ is relatively small, which results in high demands on the tolerances of the diode laser wavelength.

Practical experience shows that normally the central wavelength of the reflected and the transmitted beam are not identical. One method to improve the overall efficiency of polarization multiplexing is the right choice of wavelengths for the reflected and the transmitted beam, respectively. Although the wavelengths for polarization multiplexing are equal it will be advantageous according to Fig. 4.29 if the module with a slightly shorter wavelength is reflected, whereas the module with the longer wavelength should be transmitted.

4.3.2. Wavelength Multiplexing

Wavelength multiplexing is achieved by combining beams with different wavelengths into the same optical path. In general, wavelength multiplexing can be realized with any kind of dispersive element, such as prisms, gratings, interferometers, etc., that provide a sufficient wavelength-dependent beam separation.

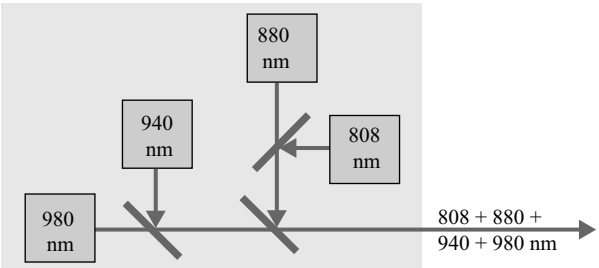

FIGURE 4.30. Typical setup of a wavelength-multiplexing concept to combine four diode laser modules with different wavelengths into the same optical path as used, e.g., in a high brightness kW-system described in Chapter 6.2.5

The brightness of a wavelength-multiplexed system is increased by a factor of N_λ, where N_λ is the number of coupled wavelengths.

According to polarization multiplexing, wavelength multiplexing for high-power lasers is realized with thin film dielectric mirrors. The basic functionality of a wavelength coupler can also be derived from Fig. 4.28. However, the design of the multilayer system has to be much more sophisticated to provide good coupling efficiencies and high extinction ratios, respectively. A typical setup for a wavelength-multiplexing concept is shown in Fig. 4.30. Four diode laser modules with different wavelengths are coupled into the same optical path by means of three dielectric wavelength-multiplexing devices.

The design of the dielectric mirrors is dependent on the arrangement of the individual modules. In principle the dielectric mirrors can be designed either as a bandpass or a band-stop filter [4.16]. With regard to efficiency bandpass filters are preferable because in practice the transmission losses of dielectrical interference filters are higher than the reflection losses. However, the design of a bandpass makes high demands on the fabrication process because of its high sensitivity to layer thickness tolerances.

In order to maximize the number of beams that can be multiplexed in a specific wavelength range, the wavelength distance between two adjacent beams should be as small as possible. However, some parameters limit the minimum feasible distance between the two beams, which should be coupled into the same optical path. First of all the linewidth of the laser beams has to be small compared to the distance of their center wavelengths. The minimum wavelength distance is further limited by the slope steepness of the reflection and transmission curves of the wavelength coupler.

Additionally, to provide sufficient coupling efficiencies for all operating conditions, the wavelength shift of the diode spectra as a function of current and temperature has to be taken into account. Wavelength multiplexing of beams with mixed polarization states (e.g., as a result of prior polarization multiplexing) also increases the minimum wavelength distance due to the splitting of the transmission curves for different polarization states.

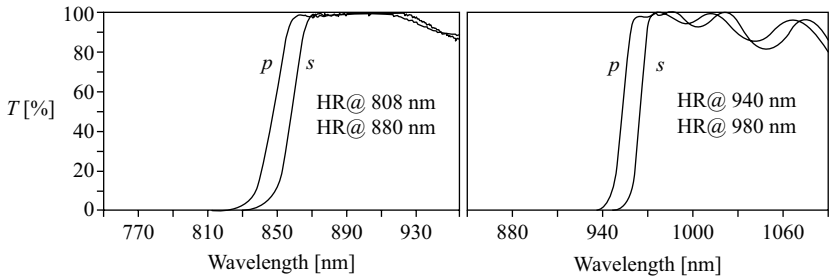

FIGURE 4.31. Reflection and transmission characteristics of typical wavelength couplers (here designed as longpass) in order to combine 808 nm and 880 nm (left diagram) as well as 940 nm and 980 nm (right diagram)

Figure 4.31 shows the reflection and transmission curves of two different wavelength couplers, which are designed as a longpass; i.e., the beam with the shorter wavelength is reflected and the beam with the longer wavelength is transmitted. Due to the improved slope steepness of IBS-fabricated devices the necessary wavelength distance could be significantly reduced compared to conventional thermal evaporated mirrors. The minimum wavelength distance of two unpolarized beams is about 40 nm in the infrared spectral region around 900 nm.

It is evident from Fig. 4.31 that the minimum spectral distance could be reduced further if both beams have the same polarization state. For instance, in a wavelength range from 780–980 nm the superposition of eight different wavelengths with equal polarization state is possible [4.17]. Considering that generally the slope of the transmission curve for the s-polarized wave is steeper, it is advantageous to combine s-polarized beams with regard to efficiency and minimum wavelength distance. Examples for technical implementations of different wavelength-multiplexing setups are described in detail in Chapters 6.2.1 and 6.2.5.

4.3.3. Spatial Coupling and Filling Factor Enhancement

Spatial multiplexing by arranging several individual diode lasers in 1D or 2D arrays increases the output power at the cost of the total beam quality of the system. As a consequence of the arrangement free areas between the individual diode lasers are inevitable. This aperture underfilling is quantified by the so-called filling factor F (see Eqs. (4.7) and (4.16)). According to Eq. (4.11) the total brightness of the laser system can be improved by means of filling factor enhancement. In the following several methods for increasing the filling factor in fast axis are presented where filling factor enhancement in slow axis is described in section 4.2.3.

Stacking diode lasers on top of each other in fast axis is a common practice for power scaling of diode laser systems. Efficient cooling requires mounting the diode laser bars on actively cooled microchannel heat sinks. As a consequence the vertical distance between two adjacent diode laser bars is determined

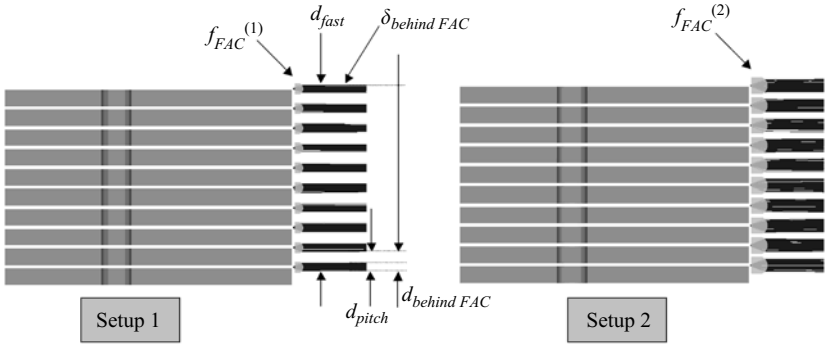

FIGURE 4.32. Enhancement of filling factor in fast axis by means of a FAC with enlarged focal length

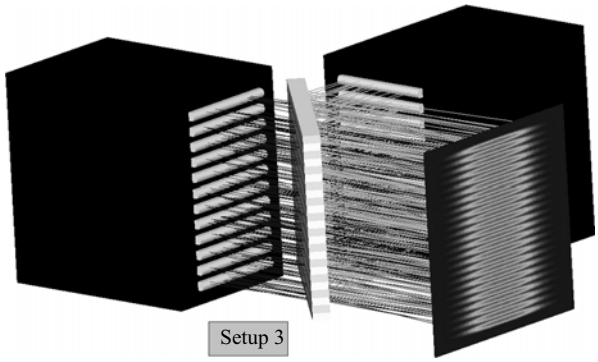

FIGURE 4.33. Enhancement of filling factor in the fast direction by means of combining two stacks with a dielectric mirror with an appropriate segmented coating

by the extension of the heat sinks, which leads to a minimum vertical distance (pitch) of about 1.7 mm.

The filling factor F_{fast} in fast axis is defined by Eq. (4.21). According to Eq. (4.21) the filling factor can be optimized by either increasing the number m of diode laser bars within a given aperture d_{fast} or by increasing the diameter $d_{behind\ FAC}$ of the collimated beam behind the FAC. These two different techniques of aperture filling are clarified in Figs. 4.32 and 4.33.

$$F_{fast} = \frac{m \cdot d_{behind\ FAC}}{d_{fast}} \tag{4.21}$$

The left part of Fig. 4.32 shows a stack of m individual diode laser bars each provided with a fast axis collimating lens leading to a collimated beam diameter of about $1/2\, d_{Pitch}$. The enhancement of the filling factor by increasing the beam diameter behind the FAC is shown in the right part of Fig. 4.32. The magnification

TABLE 4.1. Characteristic parameters for two different methods of filling factor enhancement (see Fig. 4.32 and Fig. 4.33)

	Setup 1	Setup 2	Setup 3
f_{FAC}	$f^{(1)}$	$f^{(2)} \approx 2f^{(1)}$	$f^{(3)} = f^{(1)}$
$d_{behind\ FAC}$	$1/2 d_{Pitch}$	$\approx d_{Pitch}$	$1/2 d_{Pitch}$
$\theta_{behind\ FAC}$	$\theta^{(1)}_{behind\ FAC}$	$\approx 1/2\theta^{(1)}_{behind\ FAC}$	$\theta^{(1)}_{behindFAC}$
d_{fast}	$(m - 1/2)\ d_{Pitch}$	m d_{Pitch}	m d_{Pitch}
Total power	$mP_{Diode\ laser\ bar}$	$mP_{Diode\ laser\ bar}$	2 $mP_{Diode\ laser\ bar}$
$BPP_{stack,fast}$	$BPP^{(1)}_{total}$	$\approx 1/\sqrt{2}\ BPP^{(1)}$	$\approx BPP^{(1)}$
$BPP_{stack,total}$	$BPP^{(1)}_{total}$	$\approx 1/\sqrt{2}\ BPP^{(1)}$	$\approx BPP^{(1)}_{total}$
Brightness	$B^{(1)}$	$\approx 2B^{(1)}$	$\approx 2B^{(1)}$

of the beam diameter is achieved by using a FAC with an increased focal length $f^{(2)}_{FAC} > f^{(1)}_{FAC}$. Furthermore the residual divergence of the collimated beam is reduced and finally the BPP of the diode laser stack is improved.

The second method of filling factor enhancement is shown in Fig. 4.33. Two stacks are combined in such a way that the free apertures of one stack are filled by the other stack. Consequently, the number m of diode laser bars within the given aperture is increased and according to Eq. (4.21). the filling factor is increased as well. Increasing the filling factor by combining two or more stacks is realized with a prism stack or dielectrical mirrors with an appropriate segmented coating. It is important to notice that efficient spatial coupling makes high demands on the stacking technique especially on the mechanical tolerances of the stack. This is also valid for the prism stacks and the segmented mirrors. In contrast to the first method the beam divergence behind the FAC remains constant, so that the BPP is not improved. However, the second method has the benefit that the total power is increased according to the number of diode laser bars.

In Table 4.1 characteristic parameters of both methods are summarized. Both techniques of aperture filling finally lead to the same improvement of brightness of the total beam. It should be noted that the definition of beam-parameter product and brightness for beams with rectangular symmetry has to be applied (see section 4.1.1 and [4.18]).

As a matter of fact, the beam quality of each single diode laser bar is not improved by means of filling factor enhancement and spatial coupling. The improvement in brightness of the diode laser stack is merely a consequence of filling factor enhancement.

An alternative method for increasing the filling factor in fast axis is the so-called optical stacking technique [4.11]. The individual diode laser bars are not stacked on top of each other but located side by side in an appropriate 2D-arrangement. Subsequently the beams are combined by means of 90° folding mirrors or prisms. The individual alignment of the beams ensures high beam quality. A further advantage is the possibility to use thick mechanically stable heat sinks with regard to minimization of *smile* and mechanical deformation of the bars.

4.4. Stacking Techniques

Sandra Huke, Markus Röhner

For the direct application of diode laser modules in materials processing a high brightness is necessary. Scaling the output power by stacking single diode laser bars in vertical direction leads to losses in beam quality and makes great demands on micro-optic mounting and stacking techniques. This section describes aspects like the necessity of high precision optical and mechanical components as well as the positioning accuracy and geometrical stacking precision.

4.4.1. Height and Quality

Arranging the diode laser bars to linear stacks is the most common approach to increase optical output power. However, since the output aperture of the resulting beam increases with the amount of stacked diode laser bars, the beam-parameter product (BPP) also scales with stacking height (see Eq. (4.8)).

There are two ways of setting up a fast axis collimated stack: either by mounting the FAC lenses to the individual diode laser bars before stacking or by mounting the FAC lenses after the bars have been stacked on top of each other. By stacking after having mounted the FAC, stacking faults, i.e., angular deviations of the individual beams, can cause a substantial degradation of the beam quality of the stack. By mounting the FAC micro-lenses after stacking, such stacking faults can be compensated for.

Another aspect which has to be considered is the fluid dynamical behavior in a stack (see section 4.4.1.1). In spite of increasing stacking height, the cooling efficiency has to be equal at each single microchannel cooler.

4.4.1.1. Fluid Dynamical Behavior in a Stack

Stacking denotes an arrangement of individual laser bars mounted on a heat sink with a constant pitch on top of each other. The maximum stacking height is limited by the beam quality as well as the cooling efficiency.

The heat sink has to meet several independent requirements. Most important, the heat generated during diode laser operation due to conversion losses within the pn-layer of the semiconductor has to be dissipated efficiently. At the same time, a maximum package density, resulting in a high filling factor, has to be achieved to ensure high brightness of the combined laser beam. These rather contradictory requirements can be overcome by means of microchannel cooling technology as described in Chapter 3.

The heat sinks can be stacked on the top of each other and generate an equal distribution of coolant at each heat sink. For clarification Fig. 4.34 shows an equivalent network, which describes the fluid dynamical proportion in a stack of five microchannel coolers. The resistance of the coolant inlet is smaller than the resistance of the single microchannel coolers, i.e., at first a water column is built up in the cooler inlet so that the coolant distributes nearly contemporaneous in each single microchannel cooler.

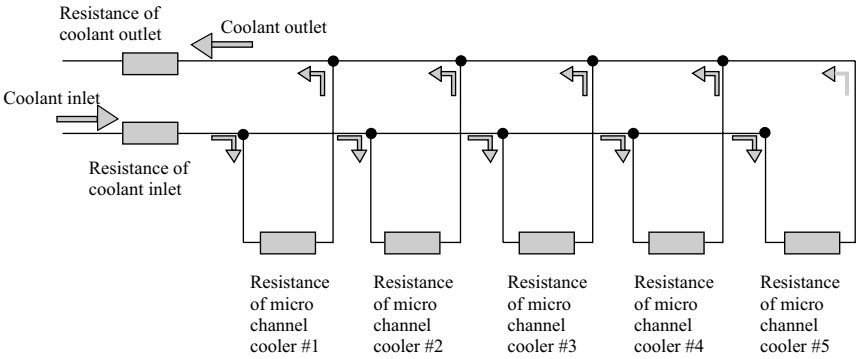

FIGURE 4.34. Equivalent network for the coolant distribution in a diode laser stack

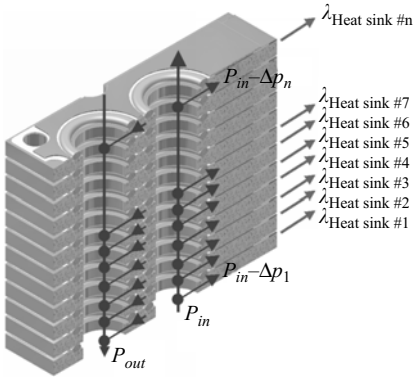

FIGURE 4.35. Cooling circuit in a diode laser stack

To define the maximum stacking height with respect to cooling efficiency, one effect is helpful. The emitting wavelength of a laser diode is dependent on the cooling temperature and efficiency of the active layer in the semiconductor. A typical value for the wavelength shift in the semiconductor material is 0.3 nm/K. Since the n individual heat sinks in a stack are connected in parallel to the coolant circuit, they notice a pressure drop Δp between water inlet and outlet with increasing stacking height (Fig. 4.35).

As pressure defines the flow rate within the microchannel coolers, this may result in a temperature shift in flow direction of the coolant. To define the maximum stacking height for a given cooling design, the wavelength of each single laser bar has to be measured before and after stacking.

Figure 4.36 shows the wavelength measurements of 29 laser bars with a specified wavelength of 940 nm measured at a constant cooler temperature of 22°C. The dark line indicates the wavelength values of the single laser bars before stacking and the bright line shows the values after stacking the bars on top of each other.

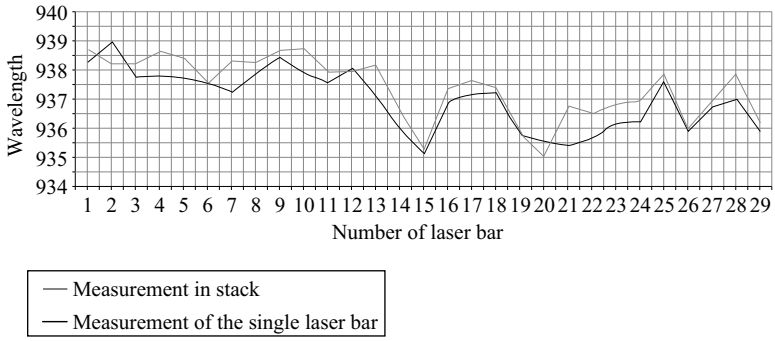

FIGURE 4.36. Wavelength shift of single diode laser bars before and after stacking at a constant temperature of cooling water

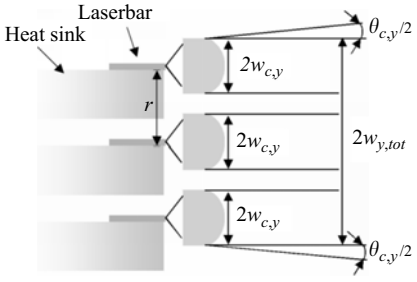

FIGURE 4.37. Scaling of the waist radii w_y of single collimated laser bars to the waist radius of a stack $w_{stack,y}$

If a significant pressure drop, i.e., wavelength shift, occurs, the two curves in the diagram should diverge. As shown in Fig. 4.36, no substantial difference can be observed. This result proves that a sufficiently uniform cooling pattern can be achieved at a stack height of up to 29 laser bars and more.

4.4.1.2. Beam Quality of a Stack

The previous sections have shown that from the mechanical point of view spatial coupling of individual laser beams by stacking is a simple way to increase output power. However, apparent losses in beam quality limit the amount of diode laser bars, which can be stacked in fast axis direction. Neglecting optical and mechanical misalignments, the total beam quality of a stack $Q_{y,tot}$ (see Eq. (4.8)) decreases linearly with the stack height (Fig. 4.37).

Depending on the requirements of application, beam quality and output power have to be adjusted by means of the filling factor. For many cases especially with regard to fiber coupling (see section 4.5) a symmetric beam of highest radiance is demanded.

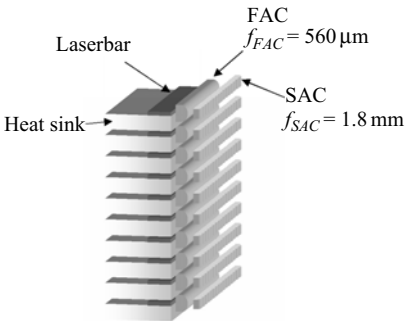

FIGURE 4.38. Stack of 10 equidistant assembled bars with FAC and SAC

TABLE 4.2. Effect of fast and slow axis collimation on the beam parameters of single-diode laser bars and a perfect stack of ten laser bars

Beam parameters			Fast-axis	Slow-axis
Divergence angle	[mrad]	$\theta_{x/y}/2$	610	79
Emitter/bar dimension	[mm]	$w_{x/y}$	0.0005	5
BPP	[mm mrad]	$Q_{x/y}$	0.305	395
Divergence angle after collimation	[mrad]	$\theta_{c,x/y}/2$	2	40
Beam diameter after collimation	[mm]	$w_{c,x/y}$	0.4	5
BPP after collimation	[mm mrad]	$Q_{c,x/y}$	0.8	200
Total beam radius of the stack	[mm]	$w_{c,x/y,tot}$	8.5	5
BPP of the stack	[mm mrad]	$Q_{c,x/y,tot}$	17	200

The example in Fig. 4.38 describes a stack of 10 individual laser bars with a filling factor in fast axis of $F_y = 0.5$.

The BPP in Table 4.2 shows that in theory a symmetrical beam could be achieved by stacking approximately 100 diode laser bars. In fact the maximum stacking height is limited to 20 to 50 bars because of the described alignment errors (see section 4.2.2) and stacking faults, described in the following section.

4.4.1.3. Stacking Accuracy

As mentioned before, an important aspect interfering with the BPP arises from mechanically related stacking faults affecting the fast axis as well as the slow axis. In a typical diode laser stack the beam of each individual emitter is collimated in both dimensions by FAC and SAC lenses. If the lenses are mounted to the diodes before stacking, mechanically induced alignment errors become apparent within the resulting beam (Fig. 4.39). Mechanical tolerances may sum up, depending on various factors.

The stacking accuracy is generally in the range of $\delta = 4$–5 mrad (half angle) in fast and slow axis and leads to a reduction of the stacking efficiency η_{StQ} compared to perfect stacking (see Table 4.2). The stacking efficiency η_{StQ} describes the ratio

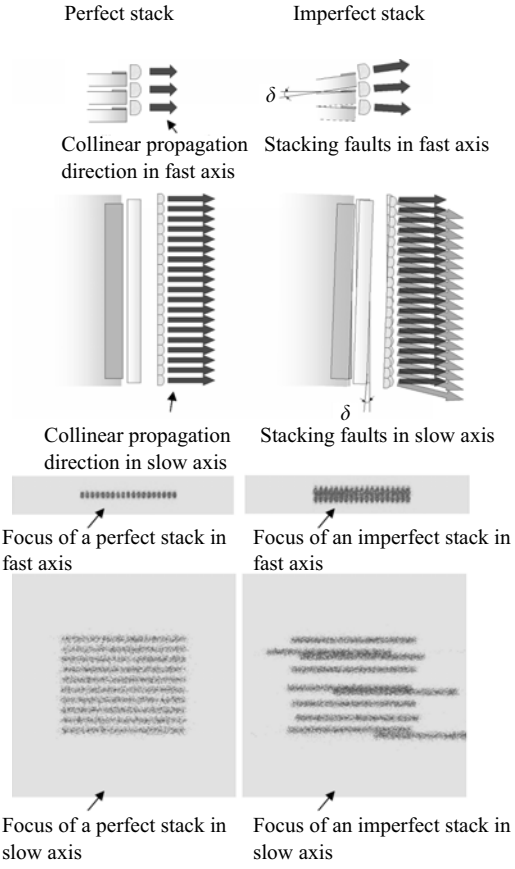

FIGURE 4.39. Comparison of a perfect stack (left) and an imperfect stack (right) collimated in fast and slow axis

between the divergence angle of a perfect stack and an imperfect stack (Eq. (4.22)).

$$\eta_{StQ} = \frac{\theta_{c,y}}{\theta_{y,tot}} \tag{4.22}$$

An efficient way to increase the stacking accuracy significantly is given by mounting the micro-optics after stacking the individual diode laser bars (Fig. 4.40). This way, angular displacements of the individual diode laser bars can be compensated by linear displacement of the micro-lenses. This effect is used to realize collinear propagation of the individual beams. Regarding the individual diode laser bars, this procedure leads to slight losses in beam quality mainly due to increased aberrations caused by the deliberately misaligned FAC. By translating the FAC in fast axis to generate the optimum deflection angle the beam cannot be collimated correctly, since the beam passes the FAC out of the center (see Fig. 4.16). After all

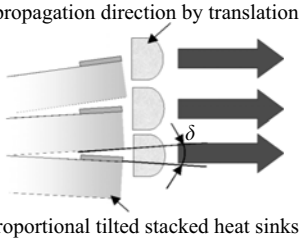

FIGURE 4.40. Compensated stacking faults by mounting the FAC lenses after having stacked the single diode laser bars

this means that the beam quality of a stack η_{StQ} can be improved at the expense of the beam quality $\eta_{FAC/SAC}$ of the individual diode laser bars.

4.4.2. Micro-Optic Mounting

To create a mounting station suitable for serial production it is necessary to check the required precision of adjustment and the achievable precision of mounting. These two boundary conditions eventually lead to the right mounting strategy and technology. Furthermore, the resolution of the imaging system has to match the desired precision of the adjustment.

For a reliable and reproducible mounting process, the resolution of the imaging system has to be adapted to the required positioning accuracy of the micro-optic components (see section 4.2.2). To account for the asymmetrical divergences in fast and slow axis and the resulting different focal lengths of the collimation optics, beam detection has to be done by means of two independent imaging systems (Fig. 4.41). Each imaging system consists of two main subunits, which determine the resolution: the beam-shaping unit consisting of lenses, beam splitter and screen, and the detector unit comprising CCD-camera, frame grabber, and monitor. Due to higher sensitivity in fast axis the magnification has to be higher than in slow axis. The magnification is given by

$$M = \frac{f_{lens}}{f_{FAC/SAC}} \tag{4.23}$$

Mounting micro-optics after stacking requires higher efforts compared to the mounting process to individual laser bars [4.12]. Various factors, including high-power, beam analyzing, monitoring, and overall handling of the components, have to be considered when designing the mounting station. To achieve the required precision of adjustment and repeatability, a semi-automated process is inevitable.

The most common way of mounting micro-optics to a laser bar is to use a carrier, serving as link between micro-optics and heat sink. The assembly has to meet several requirements, most notably the mechanical and thermal stability. The latter aspect is achieved by using components and glue, which are transparent for the incident laser radiation.

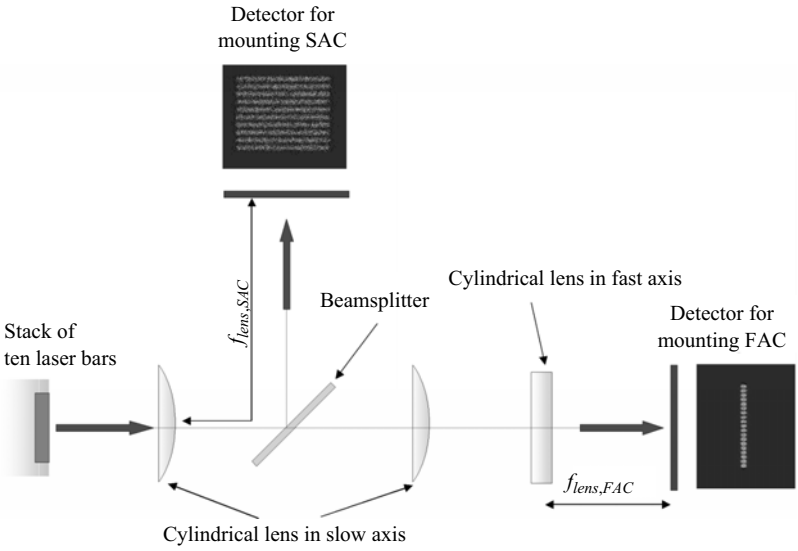

FIGURE 4.41. Imaging system for mounting FAC and SAC lenses at a mounting station

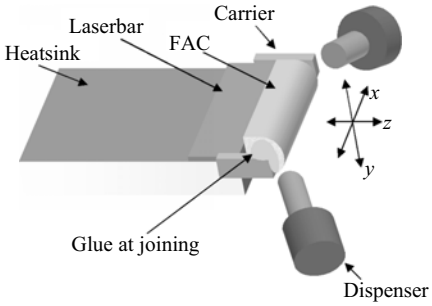

FIGURE 4.42. Dispensing glue on the joining elements. Due to volume shrinkage the wetting of different areas generates a misalignment in three axes and therefore has to be considered at mounting

For an effective mounting process a short processing time is essential. A good compromise is given by UV curable glue, which cures in seconds and features high temperature resistance and optical transparency for the typical laser wavelengths. A major disadvantage is the inherent volume shrinkage. This leads to a linear displacement of the joinable elements in three directions during the curing process illustrated in Fig. 4.42. In general the linear shrinkage of UV curable glue ranges between 2% and 5%. This effect can be minimized in designing an adapted joint geometry. Otherwise the shrinkage has to be accounted for by using a linear offset when mounting the micro-optic elements.

The adjustment of the micro-optics during laser operation requires suitable beam analyzing tools. The function of this analyzing system is to detect the intensity distribution of the collimated beam and to compute the centroids in fast and slow axis. To ensure sufficient accuracy of the alignment a high magnification of the combined beam of the stack and the individual laser bar is necessary.

The focus of the individually collimated beams of a stack is representative for the beam quality. This effect is utilized for the adjustment of micro-optics to the stack. Each individual laser beam has to be focused on a reference line by linear displacement Δy and Δx of the FAC and SAC, respectively. The adjustment procedure is illustrated in Figs. 4.43–4.45. If the adjustment of the micro-optics is done properly, the centroids of all individual diode laser bars form one common centroid at a given reference line (Fig. 4.45).

Another criterion for beam quality is the total beam dimension represented by the respective frames in Figs. 4.46 and 4.47. Depending on the calculation method the frame includes 86% ($1/e^2$) of the total output power. In summary, an optimum adjustment is achieved at minimum frame dimension and the beam centroid matching the reference line as shown in Figs. 4.46 and 4.47. Based on the analysis of these CCD pictures, the deflection and divergence angle after collimation for an individual diode laser bar as well as for a whole stack can be determined.

The object distance of the FAC lens is approximately 100 µm. To avoid a collision with the laser bar while aligning the micro-lens, the distance has to be monitored continuously. This can be ensured by means of CCD-cameras and macro-objectives in three directions (twice sidewise and one in front of the stack). Due to limited space, the geometrical dimension of the CCD-cameras employed has to be minimized. Other important processes which have to be monitored are the vacuum gripper for the optical components and the application of the UV curable glue.

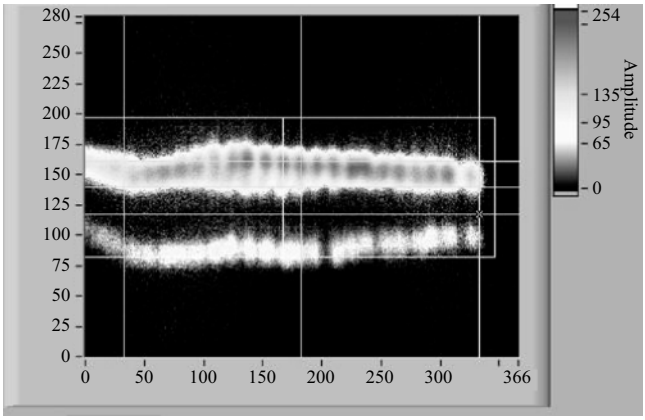

FIGURE 4.43. FAC mounting to a diode laser bar in a stack. The upper beam is the summation of already collimated beams in a stack and the lower one is the collimated beam of a not yet fixed FAC

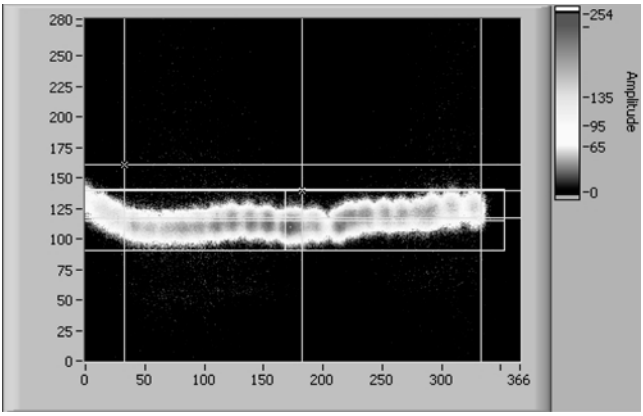

FIGURE 4.44. Offset before starting curing the glue. For optimal adjustment of the FAC to the single bar the already collimated beams of the stack are blinded out

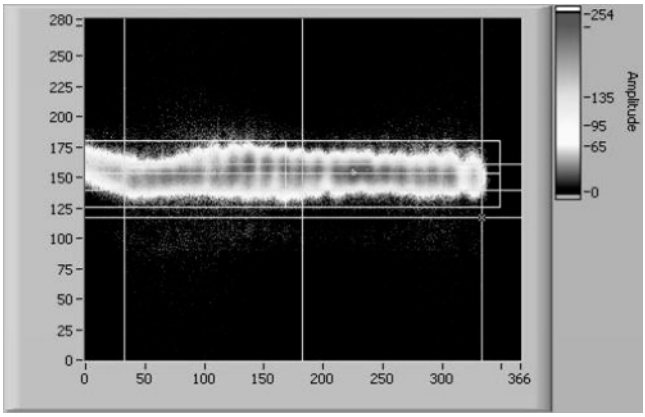

FIGURE 4.45. Focus of an already collimated stack in fast axis. The centroid is slightly above the reference line. The propagation angle of the whole stack is 1 mrad with respect to the mounting plate

4.4.3. Beam Propagation Characterization of Diode Laser Stacks

As described in the previous section many influences can decrease the optical properties and increase the focus size of a diode laser stack. The optical properties, especially the beam-parameter product, can be easily measured by focusing the whole stack on a line.

Figure 4.48 shows a typical arrangement for measuring the beam quality. A diode laser stack, e.g., consisting of six diode laser bars, is focused in fast axis direction with a cylindrical lens on a line. By measuring the beam radius w_f and for

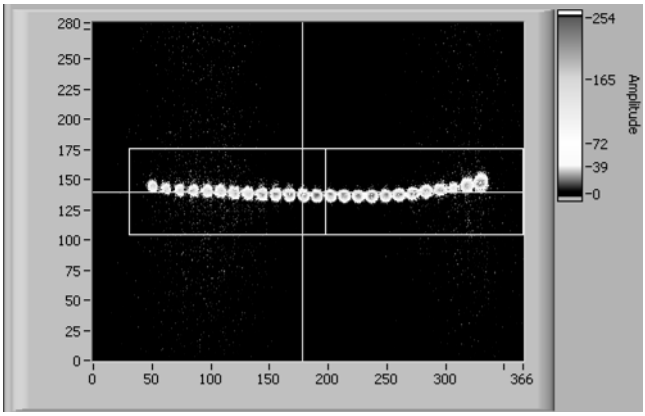

FIGURE 4.46. Image of an individual diode laser bar with a *smile* of 1 μm with the centroid on the reference line in fast axis. That means the deflection angle is negligible and the total divergence angle is about 1.8 mrad due to little *smile* plus additional 2 mrad in divergence after FAC

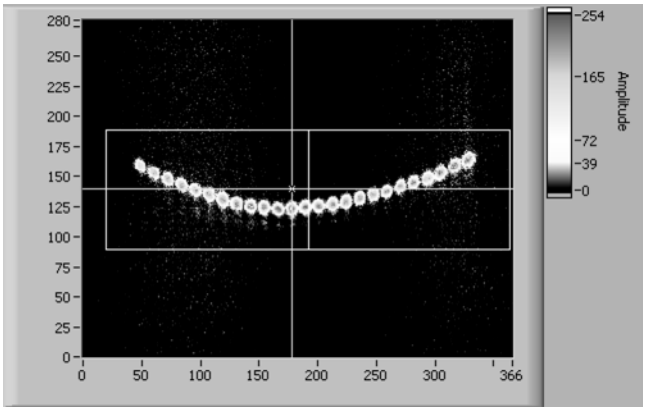

FIGURE 4.47. Image of a diode laser bar with a *smile* of 5 μm with the centroid on the reference line in fast axis. That means the deflection angle is negligible and the total divergence angle is about 9 mrad caused by heavy *smile* plus additional 2 mrad in divergence after FAC

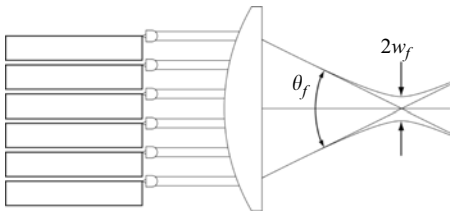

FIGURE 4.48. Arrangement to measure the beam-parameter product of a diode laser stack

a given divergence angle θ_f, the beam-parameter product *BBP* can be calculated analog Eq. (4.1).

To determine all these errors mentioned above, each diode laser bar of a stack must be characterized. The principle setup of such a characterization is shown in Fig. 4.49.

The characterization system is based on selecting the emission of a single diode laser bar from the stack using a slit, consisting of two prisms. The stack is placed in front of the prisms. The slit is adjustable with a translation stage.

With the special design of the prisms, the radiation of the other diode laser bars is reflected into the water-cooled beam traps. Furthermore they ensure that no radiation on the front side is reflected back to the stack. The slow axis of the bar is imaged with two cylindrical lenses on the detector (CMOS chip) while the beam propagates free in fast axis direction. The CMOS camera has been chosen due to its extraordinary high dynamic range with a logarithmic scale, allowing measurements in a large power range. The CMOS camera is built in a housing, to prevent the camera from stray light. The housing, including the CMOS camera and a lens, are mounted on a linear motion drive to take images at various propagation distances.

The setup can measure the parameters of the stack like *smile*, torsion, or propagation angle for each bar automatically (Fig. 4.50). At first the system determines the position of each diode laser bar in the stack. By moving the whole device along the stack, the prisms separate the radiation of each single diode laser bar. During this process the CMOS camera operates like a power detector and out of these data the system calculates the position of each bar. In the next step the radiation of each diode laser bar is measured. The system moves to the first bar, determined in the step before, and takes an image of the diode laser bar. Afterwards the system identifies the position and the size of the beam radius in fast axis. This procedure is performed for all diode laser bars.

The images are also used to calculate the stacking pitch, the lateral offset between different bars, torsion around propagation axis, *smile*, and the relative power of all single emitters. Hereafter the camera moves along the propagation axis to different positions and again takes images of the diode laser bars (Fig. 4.51). With these

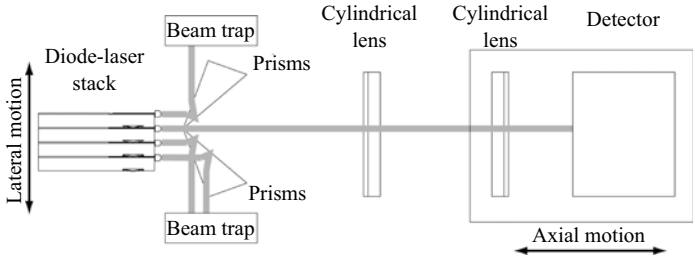

FIGURE 4.49. Principle setup of the characterization device. The beam of a diode laser bar is separated by two prisms. The detector is mounted on a linear stage in propagation axis to take images at various distances

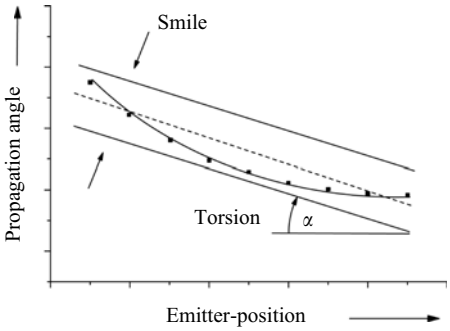

FIGURE 4.50. Principle results of a measurement including torsion around propagation axis, *smile*, and average beam propagation for a diode laser bar

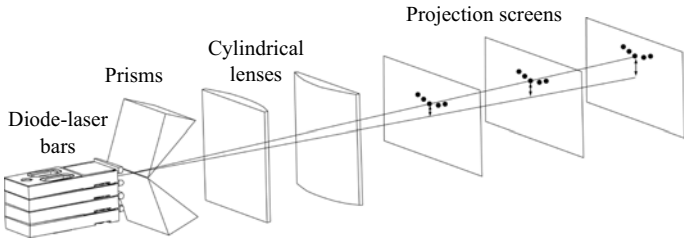

FIGURE 4.51. The separated bar is imaged with two cylindrical lenses onto a plane in different propagation distances

TABLE 4.3. Accuracy of different measured parameters like stacking pitch, torsion around propagation axis or average beam propagation

Stacking pitch	$\pm 50\,\mu m$
Smile	$\pm 0.25\,\mu m$
Torsion around propagation axis	± 0.1 mrad
Lateral offset	$\pm 25\,\mu m$
Relative output power	$\pm 3\%$
Average beam propagation	± 0.2 mrad

data, the system determines the propagation behavior of all bars and the beam propagation for each bar like average propagation angle in fast axis and angular deviation of the whole stack. The accuracy of the different parameters is given in Table 4.3.

The stacking pitch can be measured with an accuracy of $\pm 50\,\mu m$. Due to the influence of the micro-lens a higher accuracy is not possible. The accuracy of *smile* and torsion detection depends on the resolution of the camera system and imaging optics. Typically the accuracy is about $\pm 0.25\,\mu m$ and ± 0.1 mrad for torsion around the propagation axis.

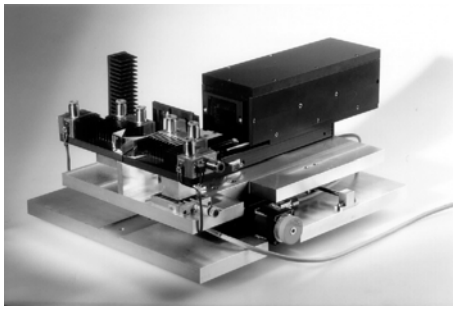

FIGURE 4.52. Characterization device for high-power diode laser stacks

The accuracy of the lateral offset only depends on the imaging optics. In order to achieve a higher accuracy than ± 30% for relative output power, the camera has to be calibrated. With an increase of the number of chosen measuring positions in propagation axis the accuracy of the average beam propagation can be reduced from ± 0.8 mrad to ± 0.1 mrad.

Figure 4.52 shows the overall setup for beam propagation analysis of diode laser stacks. The application area of this device is the quality control of diode laser stacks.

4.5. Beam Symmetrization and Fiber Coupling

Bernd Köhler

The basic goal of beam shaping is the adaptation of the asymmetric beam profile of a diode laser bar to the particular demands of the desired application. Typical demands on the spot geometry are line spots, circular spots (especially required for fiber coupling), or elliptical spot profiles. Furthermore, for many applications the homogeneity of the intensity distribution is of special interest. Another important issue is the shape of the intensity distribution which can, e.g., be Gaussian, super-Gaussian, or top hat. In this section the focus will be on symmetrization of the beam-parameter product (BPP) of a diode laser system.

4.5.1. Basic Principles of Beam Shaping

The output beam of a diode laser bar is characterized by a highly asymmetric profile with regard to beam dimension and divergence angle (Fig. 4.53). Typical values for the source width are 10 mm in slow axis and 1 μm in fast axis with divergence angles of typically 5–7° and 35° ($1/e^2$ half-angle), respectively. Consequently the resulting beam-parameter products in both axes are very different. Whereas the beam quality in fast axis is about 1 mm mrad and thus nearly diffraction limited, the beam quality in slow axis is in the region of 400–500 mm mrad, which is far beyond the diffraction limit (see section 4.2.1).

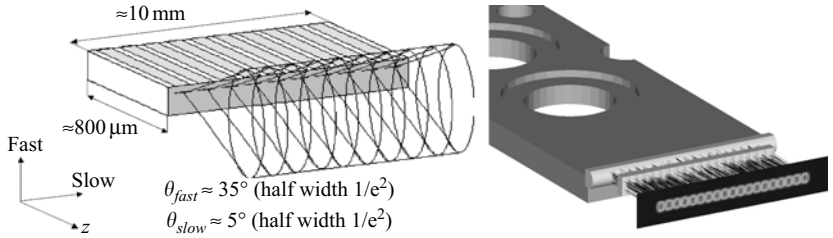

FIGURE 4.53. Typical output characteristics of a diode laser bar without micro-optics (left) and with micro-optical elements for beam collimation in fast and slow axis (right)

TABLE 4.4. Typical parameters of different types of diode laser bars*

Diode laser bar type	Bar width (mm)	Number of emitters	Emitter width in slow axis (µm)	Emitter width in fast axis (µm)	Pitch (µm)	Filling factor in slow axis
Broad area A	10	25	200	1	400	0.5
Broad area B	10	19	150	1	500	0.3
Tapered structure	10	25	10	1	400	0.025

* Note that the slow axis emitter width of the tapered structure is the size of the virtual source inside the cavity. The emitter size on the output facet of the tapered structure is 200 µm.

The first beam shaping element which follows the diode laser bar usually is a microcylindrical lens for collimation of the fast axis (FAC). The high divergence angle in this direction requires a lens with a high numerical aperture of at least 0.6. Typically the focal length of the FAC is below 1 mm in order to keep the beam diameter small after collimation (see section 4.2.1).

If the focus of application is on output power and not on beam quality subsequent micro-optical beam shaping elements are not necessary. Therefore a diode laser bar with FAC is the basic unit of a high-power diode laser system without main emphasis on beam quality.

The maximum achievable beam quality of a diode laser bar in slow axis is dependent on the ratio of emitter size and emitter pitch. Enhancement of the beam quality can be achieved by means of a cylindrical lens array (SAC-array) for individual collimation of the single emitters in slow axis. Improvement of beam quality by means of an SAC-array is a consequence of an enhancement of the filling factor. The maximum theoretical enhancement factor strongly depends on the emitter structure of the diode laser bar and is defined by the inverse ratio of emitter size and emitter pitch (see section 4.2.3). In Tables 4.4 and 4.5 a summary of typical parameters is given for different types of diode laser bars.

The data in Tables 4.4 and 4.5 show that the beam quality of the single bar without micro-optics is independent from the diode laser bar type. Fast axis collimation leads to a slight degradation of the BPP in fast axis. The extent of the degradation strongly depends on the quality of the FAC with regard to lens aberration,

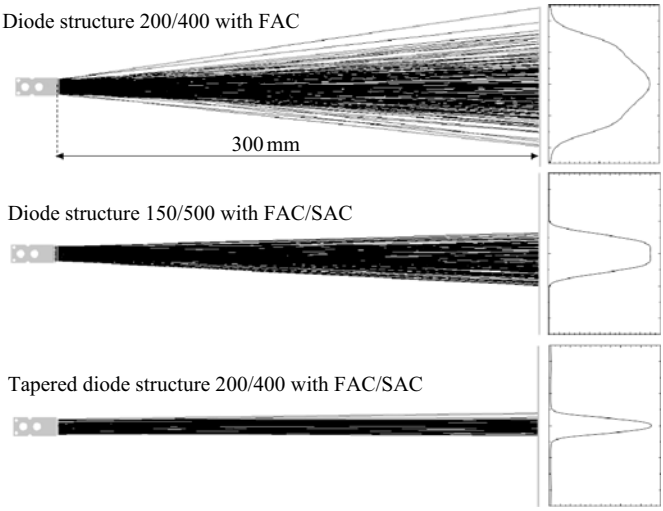

FIGURE 4.54. Simulation of the slow axis divergence for different types of diode laser bars after micro-optical elements for beam shaping (see Table 4.5)

misalignment, and *smile* (see section 4.2). The difference in beam quality in slow axis becomes apparent when an SAC-array is added to the diode laser bar for filling factor enhancement (see section 4.2.3). Practical experiences have shown that filling factors of about 0.9 are feasible, which is close to the theoretical limit of 1.

Figure 4.54 shows a simulation of the slow axis divergence for different types of diode laser bars. Corresponding to the values in Table 4.5, the divergence in the slow axis is significantly reduced when an SAC-array is inserted. Note that the emitter size of the tapered diode laser bar on the output facet equals the emitter size of broad-area structure A. However, the virtual emitter size of the tapered diode laser bar, which is responsible for the beam quality, is located inside the cavity and is significantly smaller (see Table 4.4).

Due to the asymmetric beam profile diode laser bars are principally predestinated for the generation of a line focus. For example a line focus is simply generated by collimating the fast axis with a micro-cylindrical lens (FAC) and imaging the output facet of the diode laser bar in the slow axis to the target. However, there is one significant drawback when using this simple setup. The inhomogeneous intensity distribution on the output facet, which is a consequence of the emitter structure, is transmitted to the target. This inhomogeneous intensity distribution is insufficient for many applications. Typical demands on the line focus are a homogeneous intensity distribution in slow axis (e.g., homogeneity $\pm$ 5% peak to valley) and steep edges of the top hat profile. In order to improve homogeneity, waveguides are used. The basic idea of such a waveguide is beam mixing by multiple reflections inside the waveguide and imaging the output aperture of the waveguide onto the target (see section 4.2.4).

An alternative method for homogenization is the insertion of an array of microlenses into the beam. The principle of such a lens array is to divide the beam into a

TABLE 4.5. Comparison of BPP for different types of diode laser bars with and without micro-optics

Diode laser bar type	Beam width slow axis (mm)	Beam width fast axis (mm)	Filling factor slow axis	Half-angle divergence slow axis (mrad)	Half-angle divergence fast axis (mrad)	BPP slow axis (mm mrad)	BPP fast axis (mm mrad)
Without micro-optics							
Broad area A	10	0.001	0.5	90	610	450	0.3
Broad area B	10	0.001	0.3	90	610	450	0.3
Tapered structure	10	0.001	0.025	90	610	450	0.3
With micro-optics in fast and slow axis (FAC and SAC)							
Broad area A	10	0.8	0.9 - 1	50	3	250	1.2
Broad area B	10	0.8	0.9 - 1	30	3	150	1.2
Tapered structure	10	0.8	0.9 - 1	3	3	15	1.2

number of segments corresponding to the number of micro-lenses within the array. Afterward the individual segments are superimposed in the focal plane by means of an appropriate field lens.

Normally the intensity distribution has a top hat profile in slow axis and a Gaussian profile in fast axis. However, a top hat profile in fast axis can also be obtained by means of a waveguide or a micro-lens array operating in fast axis.

The aspect ratio of the line is adjustable by using anamorphic macro-optical systems. Such devices have different magnification factors in slow and fast axis and are usually realized with cylindrical lenses or prisms (see Fig. 4.60). In principle any aspect ratio is possible by using the appropriate imaging optics. It is evident that even quadratic spots are feasible. However, it should be noted that the asymmetric beam-parameter product is unchanged when using such optics to generate a symmetric spot.

For example a quadratic spot size is generated at the cost of a high asymmetry in beam divergences. Therefore efficient coupling of a diode laser bar into an optical fiber by means of a simple imaging optic is not possible. Even if the spot size fits the fiber diameter, the corresponding highly asymmetric numerical aperture of the beam circumvents efficient fiber coupling. To match both, the core diameter and the numerical aperture of the fiber a symmetrization of the beam-parameter product of the diode laser bar is necessary. Symmetrization of diode laser systems will be explained in the following section.

4.5.2. Theory of Symmetrization

As described in the previous section, the beam profile of a single diode laser bar is highly asymmetric in slow and fast axis. However, for many applications a symmetric beam in terms of adapted beam-parameter products in both axes is required. In materials processing, a symmetric beam is important with regard to independency of the process direction. A symmetric spot size is also required for end pumped solid-state rod lasers. Furthermore, a symmetric BPP is necessary for efficient fiber coupling.

The basic idea of beam symmetrization by means of a beam rearrangement process was already described in section 4.1.1 (see Figs. 4.2 and 4.3). In this section beam symmetrization will be explained in more detail in particular in the context of fiber coupling efficiency.

The basic principle is illustrated in Fig. 4.55. The left part of Fig. 4.55 schematically shows the asymmetry of a diode laser system with respect to the beam-parameter product Q or BPP.

For a single diode laser bar the ratio $Q_{y,0}/Q_{x,0}$ is about 500:1. The beam quality of the whole system can be described by an overall BPP $Q_{tot,rms}$, which is defined by the RMS-value of $Q_{x,0}$ and $Q_{y,0}$. Another way to define the total BPP of such a system is the geometric mean $Q_{tot,geom}$ of $Q_{x,0}$ and $Q_{y,0}$ (Eq. (4.24)).

$$Q_{tot,rms} = \sqrt{Q_{x,0}^2 + Q_{y,0}^2}; \quad Q_{tot,geom} = \sqrt{Q_{x,0} \cdot Q_{y,0}} \tag{4.24}$$

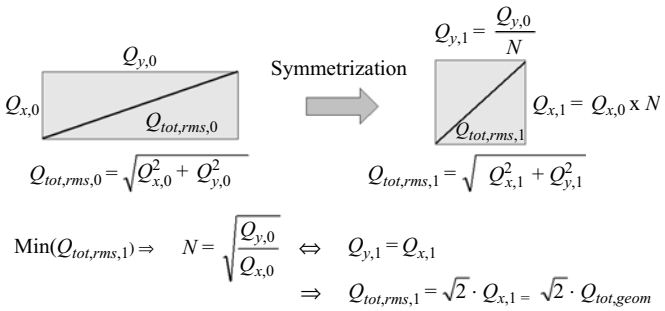

FIGURE 4.55. Basic principle of symmetrization of a diode laser system with respect to the BPP. The different BPPs are adapted by shifting beam quality from one direction to the other direction. The symmetrization is equivalent to a minimization of the RMS-value $Q_{tot,rms}$ of the total BPP

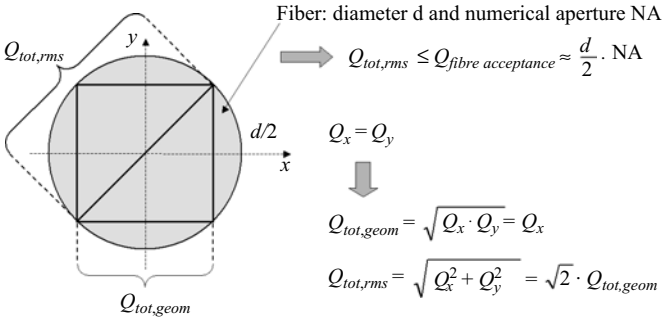

FIGURE 4.56. Comparison of different definitions for the BPP of a symmetrized beam with regard to fiber coupling efficiency

It should be pointed out that the RMS-value takes account of the asymmetry of the BPP, whereas the geometric mean contains no information on asymmetry. This is confirmed by the calculation of the BPP defined by the geometric mean of Q_x and Q_y with and without symmetrization, which yields the same result, i.e., $Q_{tot,geom,1} = Q_{tot,geom,0}$ (see Fig. 4.55).

In addition the RMS-value, $Q_{tot,rms}$ is more suitable for the estimation of fiber coupling efficiency, which is clarified in Fig. 4.56. Efficient fiber coupling requires a beam with an appropriate symmetrized beam quality. An upper limit for the necessary BPP can be defined by the diameter and the numerical aperture of the fiber. A simple geometrical consideration shows that the RMS-value $Q_{tot,rms}$ of the total BPP should not exceed the value $Q_{\text{fiber acceptance}}$, which is defined by the fiber parameters. For a symmetrized beam ($Q_x = Q_y$) the RMS-value of the BPP exceeds the geometric mean by a factor of $\sqrt{2}$.

Beam symmetrization is realized by shifting beam quality from the direction with good beam quality to the direction with minor beam quality, so that finally

the beam-parameter products in the two orthogonal directions are equal. The adjustment of the BPP corresponds to a minimization of the overall BPP $Q_{tot,rms}$. The total BPP described by the geometric mean $Q_{tot,geom}$ remains unchanged after the adjustment, because it is independent from division and subsequent spatial rearrangement. This is synonymous to the fact that the total brightness of a system is not influenced by division and rearrangement. An improvement of the total brightness of a system can only be achieved by means of filling factor enhancement, polarization multiplexing, or wavelength multiplexing (see section 4.1). Therefore, in a given system with different beam-parameter products, the geometric mean $Q_{tot,geom}$ is a measure for the minimum BPP that can be achieved by simple division and rearrangement. The optimum number N of divisions in order to minimize the total BPP $Q_{tot,rms}$ is given by the square root of the initial BPP ratio.

4.5.3. Symmetrization of Typical Diode Laser Systems

Generally two basic concepts of symmetrization can be distinguished. For low-power systems which are based on one or only a couple of diode laser bars, symmetrization is commonly realized by beam shaping with respect to the emitter structure of each individual diode laser bar. These systems usually cover a power range from 30 to 500 W.

In Table 4.6 a summary of parameters is given for the symmetrization of three different types of diode laser bars. The optimum number of divisions strongly depends on the beam quality in slow and fast axis (see Table 4.5). For typical broad-area diode laser bars the optimum number of divisions is in the range of the number of emitters. Taking into account the total width of 10 mm the geometrical dimensions of individual beam shaping or symmetrization elements are about 500 µm. Therefore, it becomes evident that symmetrization has to be realized with sophisticated micro-optical components. As can be seen from Table 4.6, filling factor enhancement in slow axis by means of a SAC reduces the optimum number of divisions. Table 4.6 also shows the difference between the RMS-value $Q_{tot,rms}$ and the geometric mean $Q_{tot,geom}$ by a factor of $\sqrt{2}$ for a symmetrized beam, i.e., for a beam with optimum number of divisions (see Fig. 4.56).

Recently a couple of beam division and rearrangement devices have been created (Fig. 4.57). Typical examples are the step-mirror beam-shaping technology, optical-path rotating devices based on cylindrical lens arrays, reflective or refractive beam-director and -redirector arrangements on the basis of micro-prisms, and emitter-based fiber-coupling elements leading to fiber bundles [4.5, 4.19–4.24].

An important advantage of an emitter-based division and rearrangement is the prevention of a spatial overlap of adjacent emitters and therefore a subsequent enhancement of the filling factor is still possible. Without filling factor enhancement in slow axis the total BPP is independent from the emitter structure of the diode laser bar (see Table 4.6). In order to use the full capacity of beam quality in slow axis it is mandatory to enhance the filling factor by individual treatment of each single emitter.

TABLE 4.6. Comparison of beam symmetrization for different types of diode laser bars (see Table 4.4) for the definition of the different diode laser type)

Diode laser bar type	Number of division	Filling factor	BPP slow axis (mm mrad)	BPP fast axis (mm mrad)	Total BPP $Q_{tot,rms}$ (mm mrad)	Total BPP $Q_{tot,geom}$ (mm mrad)
Bar without division						
Broad area A	1	0.5	450	1.2	450	23
Broad area B	1	0.3	450	1.2	450	23
Tapered structure	1	0.025	450	1.2	450	23
With optimized filling factor in slow axis and no division						
Broad area A	1	1	250	1.2	250	17
Broad area B	1	1	150	1.2	150	13
Tapered structure	1	1	15	1.2	15	4
With optimum division and no filling factor enhancement						
Broad area A	19	0.5	23	23	33	23
Broad area B	19	0.3	23	23	33	23
Tapered structure	19	0.025	23	23	33	23
With optimized filling factor in slow axis and optimum division						
Broad area A	14	1	17	17	24	17
Broad area B	11	1	13	13	19	13
Tapered structure	4	1	4	4	6	4

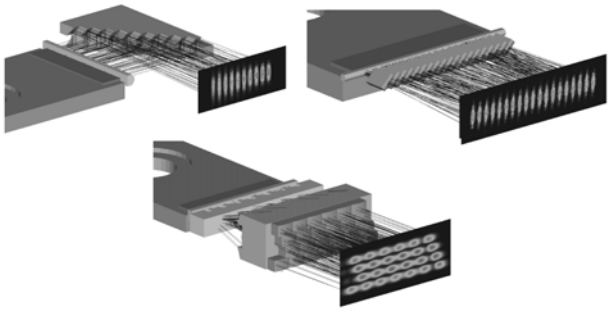

FIGURE 4.57. Three different approaches for the symmetrization of single-broad-area diode laser bars: step-mirror beam-shaping technology (top left) [4.6]; optical-path rotating device based on a cylindrical lens array (top right) [4.22]; refractive beam director and redirector on the basis of micro-prisms (bottom) [4.21]

The sophisticated micro-optics in combination with high mounting efforts result in relatively high costs per bar. Hence a beam division with regard to each single diode laser bar is only practicable for systems with a limited number of bars.

For diode laser systems with an output power of more than 500 W macro-optic rather than micro-optic elements are used for beam shaping and beam symmetrization.

Besides the factor of expense the main reason for the transition from micro-optic to macro-optic beam-shaping elements is founded in the typical setup of these high-power systems. High-power diode laser systems are usually based on the combination of diode laser stacks, where the individual diode laser bars are stacked on top of each other. Stacking of diode laser bars on top of each other results in a degradation of the BPP in fast axis. The BPP approximately scales with the height of the stack because the divergence is primarily not influenced by stacking. However, due to stacking faults the divergence can be increased for a stack with a large number of diodes as well (see section 4.4.1).

As a consequence of the increase of the BPP in fast axis the asymmetry between the fast and the slow axis is reduced. Thus stacking is one way to adapt the BPPs of a diode laser system. However, this is achieved at the costs of the total BPP which will be significantly larger than the optimum BPP of a single bar. It becomes evident that the optimum number of divisions for a symmetric BPP decreases, so that macro-optical elements can be inserted for beam shaping. In Table 4.7 a summary of parameters is given exemplarily for the symmetrization of a stack composed of four diode laser bars.

The data in Table 4.7 show that the BPP in slow axis is not affected by stacking, whereas the BPP in fast axis increases. So stacking leads to a reduced asymmetry of the total output beam. The optimum number of divisions for a symmetric BPP is significantly reduced from 19 to 7 for a single bar and a diode laser stack with four bars, respectively. The optimum number of divisions decreases further with increasing numbers of bars per stack so that macro-optical components are applicable for the symmetrization of a diode laser stack.

TABLE 4.7. Comparison of beam symmetrization parameters for a diode laser stack with four diode laser bars and FAC*

Stack with four diode laser bars	Number of division	Filling factor	BPP in slow axis (mm mrad)	BPP in fast axis (mm mrad)	Total BPP RMS (mm mrad)	Total BPP geom. Mean (mm mrad)
Without division						
Broad area A	1	0.5	450	9	450	65
Broad area B	1	0.3	450	9	450	65
Tapered structure	1	0.025	450	9	450	65
With optimum division						
Broad area A	7	0.5	64	65	91	65
Broad area B	7	0.3	64	65	91	65
Tapered structure	7	0.025	64	65	91	65
With optimized filling factor in slow axis and optimum division						
Broad area A	5	1	48	48	68	48
Broad area B	4	1	37	37	53	37
Tapered structure	1	1	12	12	17	12

* The stacking pitch in fast axis is about 1.8 mm. The calculations are based on a residual fast axis divergence of 3 mrad and a beam diameter of 0.8 mm in fast axis after FAC.

The implementation is usually done with plane parallel plates or appropriate prism arrays (see Fig. 4.59) [4.25, 4.26]. These macro-optical components do not consider the individual emitter structure of the diode laser bar. Due to the mixture of beams from different emitters after the division element, subsequent aperture filling is not possible any more. However, aperture filling by means of an SAC-array is still possible before the beams are divided. This leads to a reduced number of divisions and an improvement of the total BPP (see Table 4.7).

An alternative method for symmetrization of a diode laser stack can be realized with a set of rotated macroscopic cylindrical lenses [4.27]. However, the relatively simple setup of such an arrangement results in a worsening of the total BPP which will only be the arithmetic mean of the original BPPs.

Another important fact can be derived from Tables 4.5 and 4.7. Symmetrization of a stack with tapered diode laser bars and SAC is simply realized by choosing the appropriate number of diodes per stack with the additional benefit that the divergences of slow and fast axis are equal. Therefore no subsequent beam-shaping optics is necessary.

As a matter of fact symmetrization by an increasing number of diodes per stack is also possible for broad-area diode laser structures. However, there are some significant drawbacks when compared with a stack of tapered diode laser bars. For broad-area diode laser bars the symmetrization by an increase of diode laser bars per stack would require more than 150 diode laser bars without filling factor enhancement and still more than 50 bars if an SAC-array is added. Furthermore the total BPP will be significantly larger compared to a stack of tapered diode laser bars. In addition the divergence angles and beam widths are still not adapted after this kind of symmetrization.

It is evident that the optimum number of divisions strongly depends on the beam-parameter product in slow and fast axis. In Fig. 4.58 the correlation between number of division, fast axis divergence, and the resulting total BPP $Q_{tot,rms}$ after division is shown exemplarily for a diode laser stack with four diode lasers bars. The optimum number of divisions as a function of the residual fast axis divergence is indicated by the dashed line in Fig. 4.58. The better the fast axis quality the higher is the optimum number of divisions for a resulting symmetric BPP. The residual divergence of the diode laser stack in fast axis is mainly influenced by the focal length and quality of the FAC, *smile* of the diode laser bars, and stacking faults (see section 4.4.1).

Figure 4.59 shows the basic principle of symmetrization of a diode laser stack. In this example, the BPP of a diode laser stack with 12 diode laser bars is symmetrized [4.25]. The first step is the segmentation of the slow axis into three parts by a combination of three prisms. Subsequently each of the three parts is spatially rearranged by means of a plane parallel plate with an appropriate angle and thickness. Thereafter the BPP is symmetrized in fast and slow axis.

Even though the BPPs are equal after symmetrization it becomes apparent from Fig. 4.59 that this does not automatically apply to the beam size. After the BPP has been symmetrized the absolute beam size in fast axis is significantly larger than in slow axis. Because the beam divergence in slow and fast axis is not influenced by

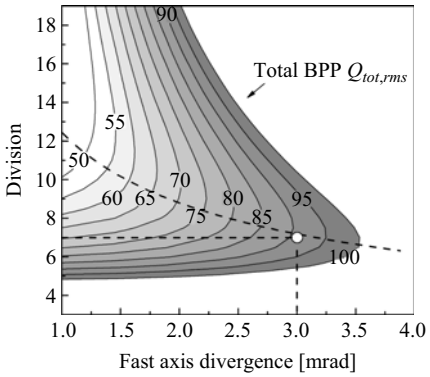

FIGURE 4.58. Correlation between division, fast axis divergence (half-angle $1/e^2$), and the resulting total BPP $Q_{tot,rms}$. The optimum number of divisions as a function of the beam quality in fast axis is indicated by the dashed line. The data are calculated for a diode laser stack with four diode laser bars without SAC and a stacking pitch of about 1.8 mm

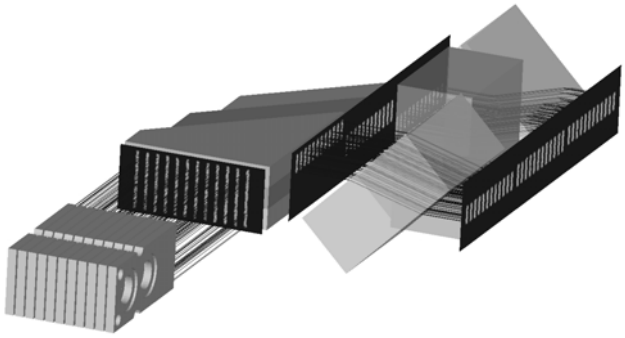

FIGURE 4.59. Principle of symmetrization of a diode laser stack with 12 diode laser bars [4.25]

the rearrangement the asymmetry in beam divergence corresponds to an asymmetry in beam width.

For a symmetric spot size in the focal plane or fiber coupling a cylindrical focusing optics with different focal lengths in fast and slow axis has to be applied. So the final step in symmetrization will be the adaption of the divergence angles and the beam widths for both axes. Due to the symmetry of the BPP, an adaption of the beam divergence will automatically lead to an adaption of beam width and vice versa.

The adaption is carried out with anamorphic optical systems. Figure 4.60 shows two possible implementations. In the left part of Fig. 4.60, the beam adaption is realized by means of two prisms, whereas on the right side a beam compression

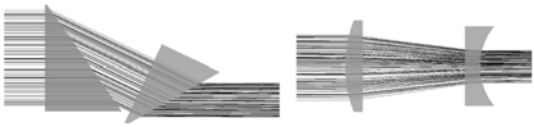

FIGURE 4.60. Adaption of beam divergence and beam aperture by means of anamorphic optical systems like prisms (left) and a cylindrical telescope (right)

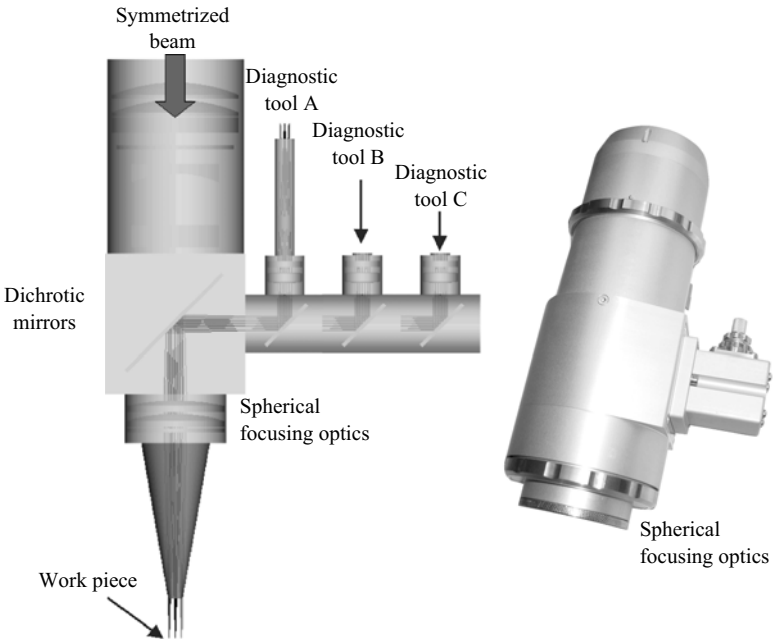

FIGURE 4.61. Principle setup for the insertion of on-axis beam diagnostic devices (left part). Example for a technical implementation of a focusing optics for a high-power diode laser with an on-axis beam diagnostic device (here, e.g. standard SMA connector for a pyrometer signal) [4.28]

with a cylindrical telescope is shown. After symmetrization of the BPP and adapting the beam sizes spherical objectives can be used for fiber coupling or the generation of symmetric spot sizes. The spot size and the working distance will scale with the focal length of the spherical objective.

A symmetrized beam with regard to BPP and beam aperture also offers the opportunity of a modular insertion of on-axis optical sensor devices for process diagnostic systems, e.g., pyrometer, CCD-cameras, or integral detectors. The diagnostic system can be inserted between the beam symmetrization unit and the spherical focusing optics (Fig. 4.61).

4.6. Beam Quality Limits and Comparison to Coherent Coupling

Peter Loosen

A general guideline and roadmap for the development of high-power diode laser systems can be elaborated, if for typical industrial and laboratory systems the achieved beam quality in terms of the beam-parameter product (Q or BPP) is plotted against the output power of diode laser systems and is compared which other lasers, which are common in industrial manufacturing (Fig. 4.62). In order to simplify the diagram, the beam-parameter product of non-rotational symmetric beams, which are common for some diode laser systems, have been converted into the BPP for a rotational-symmetric beam by means of the formalism discussed in sections 4.1 and 4.5.

The figure shows that basically the BPP of diode laser systems scales roughly with the square root of the output power ($Q \propto P^{1/2}$). This is a result of the brightness conservation relation, discussed in section 4.1. The variety of different means for increasing the brightness discussed in the foregoing sections leads to a considerable increase in brightness of the systems in the past years, which is expressed by the shift of the inclined diode laser line to the lower right part of the diagram.

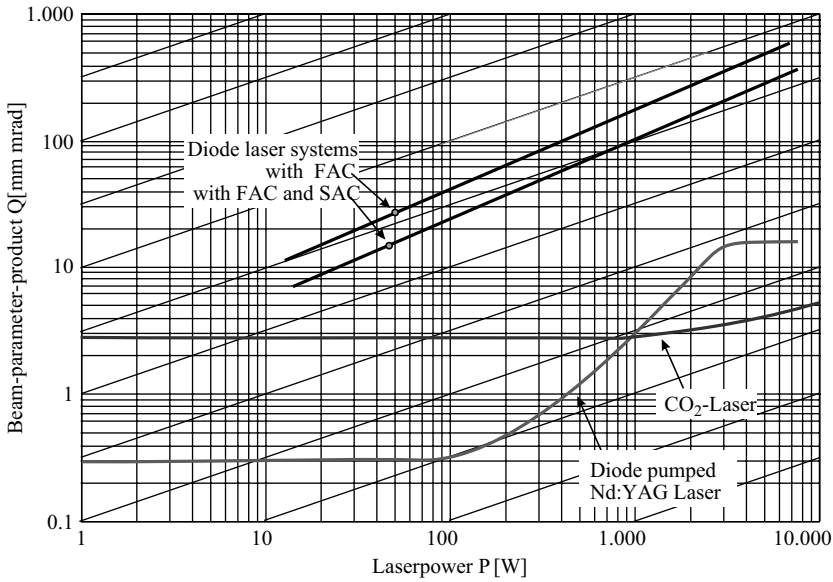

FIGURE 4.62. Rated power and beam-parameter product of CO_2, diode-pumped Nd:YAG, and diode laser systems (data as of end 2005)

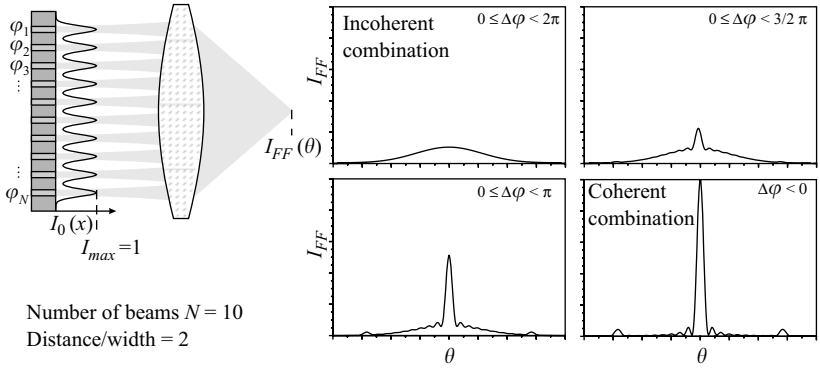

FIGURE 4.63. Comparison between incoherent and coherent beam combination: In a numerical simulation several coherent beams with similar intensity distribution are superimposed in the focal plane of a lens. The coherence between the beams is increased from the top left to the lower right by reducing the statistical phase differences among the beams

In contrast to diode lasers with incoherent beam combination, classical lasers such as CO_2 or Nd:YAG lasers show a beam quality which is basically independent from output power. This behavior holds up to certain powers, where the beam quality is degraded not by fundamental physical processes but by technical limitations, mainly caused by thermal degradation of the active medium. The comparison of these classical lasers with high-power diode lasers demonstrates, that the diode laser systems with the highest available qualities are presently (2006) in the proximity of lamp-pumped Nd:YAG lasers. With improvements of semiconductor chips as well as beam shaping and multiplexing, it can be expected that in the future, diode laser systems will be comparable to the classical lamp-pumped Nd:YAG lasers.

Even with these future achievements it does not seem to be possible to achieve significant further increases in beam quality with an incoherent beam combination.

This is a basic limitation of the principle of incoherent superposition of beams and could only be overcome if techniques were used that make it possible to phase-couple the individual diode laser emitters and thus create an array of coherently operating beams. The transition between these two states of operation ("incoherent" to "coherent") and the resultant increase in beam quality is illustrated in Fig. 4.63.

In the upper-left part the far-field intensity distribution of an emitter array is shown, where the emitters are incoherent, i.e., are emitting completely independent from each other. In the numerical simulation shown this has been modeled by introducing a statistically varying phase shift between the individual emitters. If the variance of this phase shift is narrowed to zero, which means physically that the beams are becoming more and more coherent, the intensity profile in the far-field is considerably narrowed by interference processes and thus the beam quality is increased correspondingly.

Techniques for coherent coupling of arrays of beams have been extensively studied over the past 20 years for many classical lasers, such as CO_2 and solid-state lasers, and in the past few years for different types of diode lasers as well. For diode lasers some recent approaches seem to be promising [4.29–4.31] but still have to be assessed for industrial use in terms of production costs, robustness, and stability.

List of Terms and Symbols

c	Optical gain, threshold gain
D	Electric current, threshold current
η	Optical intensity
F	Optical power
f	Intensity reflectivity of mirrors 1 and 2
FAC	Time
fast axis, g_{th}	Temperature
g	Ambient temperature
I	Heat-sink temperature
i, i_{th}	Velocity
k	Stripe width, ridge width, lateral width
λ	Vertical or transverse direction
M^2	Horizontal or lateral direction
$\dot{m}$	Propagation or axial direction
n	Efficiency
NA	Laser wavelength
NA_{beam}, NA_{fiber}	Vacuum wavenumber
N_F	Series resistance
n_{core}, $n_{cladding}$	Thermal resistance
ν, ν_0	Diameter
OPD	Focal length
P	Beam-quality parameter
R_1, R_2	Refractive index
R_S	Index of refraction of core/cladding
R_{th}	Full-beam divergence angle (measured at $1/e^2$)
SAC	Coolant mass-flow rate
slow axis	Speed of light
t	(Linear) fill factor
T	Numerical aperture
T_a	NA of beam/fiber as defined by manufacturers
T_{hs}	Fresnel number
θ	Fast axis collimation (lens)
v	Slow axis collimation (lens)
W	Transversal direction
x	Lateral direction

y Optical path difference
z Frequency, center frequency

List of Constants

$c = 1/\sqrt{\varepsilon_0 \mu_0} = 2.997925 \times 10^{10}\,\mathrm{cm/s}$	Speed of light in vacuum
$E_{ph}\lambda_0 = 1.239852\,\mathrm{mmeV}$	Photon energy × wavelength
$e_o = 8.854188 \times 10^{-14}\,\mathrm{C/(Vcm)}$	Reduced Planck constant
$-h = h/(2\pi) = 6.582173 \times 10^{-16}\,\mathrm{eVs}$	Boltzmann constant
$k_B = 8.617347 \times 10^{-5}\,\mathrm{eV/K}$	Thermal energy at 300 K
$k_B T = 25.85204\,\mathrm{meV}(T = 300\,\mathrm{K})$	Free-electron rest mass
$m_0 = 9.109534 \times 10^{-31}\,\mathrm{kg}$	Elementary charge
$q = 1.602189 \times 10^{-19}\mathrm{C}$	Dielectric constant
$\mu_0 = 4\pi \times 10^{-9}\,\mathrm{Vs^2/(Ccm)}$	Permeability in vacuum

References

[4.1] ISO/DIS-Standard 11 146, International Organization for Standardization.
[4.2] Born M, Wolf E (1980) Principles of Optics: Electromagnetic Theory of Propagation, Interference and Diffraction of Light. Cambridge University Press, Cambridge.
[4.3] Albers P, Heimbeck HJ, Langenbach E (1993) Focusing of diode lasers for high beam quality in high-power applications Lens and Optical Systems Design, Proceedings of the SPIE 1780, 533–538.
[4.4] Clarkson WA, Hanna DC (1996) Two-mirror beam-shaping technique for high-power diode bars. Optics Letters 21(6), 375–377.
[4.5] Endriz J (1992) Brightness conserving optical system for modifying beam symmetry. US Patent 5,168,401.
[4.6] Ehlers B, Du K, Baumann M, Treusch HG, Loosen P, Poprawe R (1997) Beam shaping and fibre coupling of high-power diode laser arrays. Proceedings of the SPIE 3097, 639–644.
[4.7] Sturm V, Treusch HG, Loosen P (1997) Cylindrical micro-lenses for collimating high-power diode lasers. Proceedings of SPIE 3097, 717–726.
[4.8] Loosen P, Treusch HG, Haas CR, Gardenier U (1995) High-power laser-diodes and their direct industrial applications. Proceedings of the SPIE 2382, 78–88.
[4.9] Biesenbach J, Loosen P, Treusch HG, Krause V, Kösters A, Zamel S, Hilgers W (1994) Fabrication of aspheric cylindrical micro-lenses with the diamond turning technology. Proceedings of the SPIE 2263, 152–163.
[4.10] Product information (1999) Limo Corp./Dortmund, Germany (http://www.limo.de).
[4.11] Loosen P (2001) High-power diode lasers for direct applications in high-power diode lasers. In Diehl R (ed.): Springer Series Topics in Applied Physics, volume 78.
[4.12] Huke S (2001) Mikrooptikmontage im Hochleistungsdiodenlaserstapel, Diplomarbeit, University of applied sciences, Münster.
[4.13] Smith WJ (1990) Modern Optical Engineering: The Design of Optical Systems, 2nd Edition. McGraw-Hill, New York, pp. 263–265.
[4.14] Litfin G (2001) Technische Optik in der Praxis. Springer-Verlag, Berlin, Hiedleburg.
[4.15] Ebert M, Ebert J (2000) Magnetron-Sputtern im Mikrowellenplasma im Vergleich zu konventionellen Aufdampfverfahren. Photonik 1, 34.

[4.16] Groß T (2002) Wellenlängenmultiplex-Verfahren für die Direktanwendung von Hochleistungs-Laserdioden. In Diehl R (ed.): Optische Technologien Band 5, Hochleistungsdiodenlaser für die Direktanwendung, (Projektverband NOVALAS), p. 51.
[4.17] Knitsch A, Luft A (2002) Diodenlasermodule höchster Brillanz für die Lasermaterialbearbeitung. In Diehl R (ed.): Optische Technologien Band 5, Hochleistungsdiodenlaser für die Direktanwendung, (Projektverband NOVALAS), p. 17.
[4.18] Bachmann F (2004) Chances and limitations of high power diode lasers in high-power diode laser technology and applications II. In Mark S. Zediker (ed.): Proceedings of the SPIE 5336, p. 95.
[4.19] Yamaguchi S, Daimon M, Chiba K, Kobayashi T, Saito Y (1996) Optical path rotating device used with linear array laser diode and laser apparatus applied therewith. US Patent 5,513,201.
[4.20] Head D, Baer T (1996) Apparatus for coupling a multiple emitter laser diode to a multimode optical fiber. International Patent WO 96/38749.
[4.21] Ullmann C, Krause V, Koesters A (1998) Optical arrangement for use in a laser diode system. US Patent 5,808,803.
[4.22] Lissotschenko V, Mikhailov A (1999) Anordnung und Vorrichtung zur optischen Strahltransformation. European Patent EP 1 006 382.
[4.23] Nightingale JL, Rekow M (2000) Laser diode integrating enclosure and detector. US Patent 6,061,374.
[4.24] Goering R, Schreiber P, Heinemann S, Roellig U, Nickel M (2002) Optical arrangement for balancing the beam of one or more high power diode lasers arranged one above another. US Patent 6,337,873.
[4.25] Biesenbach J, Pfeffer F, Noeske A (2000) Einrichtung zur Strahlformung eines Laserstrahls und Hochleistungs-Diodenlaser mit einer solchen Einrichtung. German Patent DE 198 46 532 C1.
[4.26] Krause V, Ullmann C (1997) Laseroptik sowie Diodenlaser. European Patent EP 0 863 588.
[4.27] Kugler N, Ashkenasi D (2002) Strahlformung und Symmetrisierung der Emission von mikrokanalgekühlten cw-stacked Arrays für die Direktanwendung mit dem, Beam-Twister. In Diehl R (ed.): Optische Technologien Band 5, Hochleistungsdiodenlaser für die Direktanwendung, (Projektverband NOVALAS), p.69.
[4.28] Product information (2004) Rofin-Sinar-Laser; Hamburg (http://www.rofin.com/); Dilas Diodenlaser GmbH, Mainz (http.//www.dilas.com).
[4.29] Raab V, Skoczowski D, Menzel R (2003) Tunable broad area diode lasers with improved brightness and brilliance. LASE. Proceedings of the SPIE 4973.
[4.30] Chi M, Thestrup B, Mortensen JL, Nielsen ME, Petersen PM (2003) Improvement of the beam quality of a diode laser with two active broad-area segments. Journal of Optics A: Pure and Applied Optics 5, 338–341.
[4.31] Brauch U (2001) Coherent beam combining in High-Power Diode Lasers. In Diehl R (ed.): Springer Series Topics in Applied Physics 78.

5
Laser Systems Beam Characteristics, Metrology, and Standards

Bert John Neubert, Wolf-Dieter Scharfe

5.1. Introduction

The favorable characteristics of laser light are its power, its "focusability," its temporal behavior, and its narrow wavelength bandwidth. The lifetime of the laser device is another key aspect. The aim of laser metrology is to obtain reliable information about the laser device and its output. Standard measurement procedures are needed for the comparison of different lasers. It is desirable to compress the information about a laser to a few figures of merit. Of course a figure of merit strongly depends on the specific application.

For material processing, the beam power P and the size of the focus spot are of paramount importance. The area of a power density distribution can be characterized by its widths, d_x and d_y:

$$\text{area} = \frac{\pi}{4} d_x d_y \tag{5.1}$$

The size of the beam widths in the focus, d_{x0} and d_{y0}, and depend on how strongly the beam is focused. In other words, they depends on the convergence angles, Θ_x and Θ_y, of the light. To a good approximation the beam-parameter product,

$$Q_x = \frac{1}{4} d_{x0} \Theta_x, \tag{5.2}$$

does not change when the beam propagates through an optical system. This makes the beam-parameter product a useful tool, as is illustrated by the following two examples. The convergence angle Θ_x that can be achieved is limited by the numerical aperture of the focusing optical system. If the beam-parameter product of the beam is known, the minimum beam width, d_{x0}, that can be achieved by a specific focusing system can be easily calculated using Eq. (5.2). In reverse the maximum beam width of a collimated beam is limited by the aperture of the output of the optical system. The minimum divergence angle, Θ_x, that can be achieved by such a system follows from (5.2). Thus the beam-parameter product is a measure of how well a beam can be focused or collimated.

A Gaussian beam has the least beam-parameter product of all beams of the same wavelength. It is common to normalize the beam-parameter product of a beam to

the beam-parameter product of a Gaussian beam of the same wavelength:

$$M_x^2 = \frac{Q_x}{Q_{x\,\mathrm{Gauss}}} = \frac{\pi}{4\lambda} d_{x0}\Theta_x, \tag{5.3}$$

The normalized beam-parameter product, called the beam propagation ratio, M^2, is a widely accepted figure of merit.

The beam-parameter products, in the x- and y-direction, and the beam power can be combined to the beam brightness:

$$B = \frac{16P}{\pi^2 d_{x0} d_{y0} \Theta_x \Theta_y} = \frac{P}{\pi^2 Q_x Q_y} = \frac{P}{\lambda^2 M_x^2 M_y^2}. \tag{5.4}$$

For beams where the minimum beam widths, d_{x0} and d_{y0}, are at the same z-position, the average power density in the focus is proportional to the brightness of the beam:

$$\frac{P}{\mathrm{area}} = \frac{P}{\frac{\pi}{4} d_{x0} d_{y0}} = B\frac{\pi}{4}\Theta_x\Theta_y. \tag{5.5}$$

This chapter reviews the characterization of a laser device by its beam power, propagation of the beam width (beam propagation ratio), the positional stability of the beam, the wavefront of the beam, and the lifetime of the device. The emphasis lies on the measurement procedures proposed by the ISO standards. As the ISO standards referred to encompass more than two hundred pages, details have to be omitted here. In addition to the ISO standard the aim of this chapter is to outline the theoretical background of laser beam characterization and to introduce the most common experimental techniques to determine the quality of a laser beam. Although a detailed knowledge of the theoretical background is not needed to perform a standard measurement, it helps to understand the influences of the optical elements on the laser beam performance and to estimate the validity of the measurement results.

It has to be mentioned that the laser wavelength influences the absorption of the laser beam by the workpiece, but the wavelength bandwidth is of minor importance. The polarization also influences the performance of a laser cutting steel [5.1,5.2]. The polarization and wavelength of the beams of single emitters are used to combine different laser beams using wavelength and polarization multiplexing (Chapter 4). Their measurement is not discussed here.

This chapter is structured as follows: In section 5.2 the theoretical background of the description of laser light is briefly reviewed. In section 5.3 the width of a power density distribution is defined. Section 5.4 discusses the propagation of the beam width. This leads to the definition of the beam propagation ratio, M^2, and a classification of beams. The measurement of the beam power is discussed in section 5.5. In section 5.6 different setups to measure the power density distribution of a beam are introduced. The evaluation of the measured profiles according to the new ISO standard using an iterative method for calculation of the beam width

as well as the determination of the beam propagation ratio, M^2, are discussed. The measurement of the beam positional stability and the wavefront of a laser beam are introduced in sections 5.7 and 5.8. In section 5.9 the characterization of a laser lifetime is discussed. In section 5.10 the laser safety is briefly discussed. In section 5.11 a table of ISO standards related to the characterization of laser beams is given in section 5.12 more practical limits for the characterization of diode laser are given.

5.2. Theoretical Background of Beam Propagation

Laser beams are commonly characterized by their power density distribution, their wavelength, and their state of coherence. As the underlying theory of time-integrated signals is not included in many elementary textbooks it is briefly introduced here. The mutual coherence and the Wigner distribution are the most common descriptions of time-averaged signals. They are related by the Fourier transform to each other.

Although there are a lot of equations in this section the emphasis lies on the physical idea of beam propagation and not on mathematical details.

5.2.1. Preliminaries

Light can be described as an electromagnetic vector field that obeys the Maxwell equations. As neither the electric nor the magnetic field of light can be measured this is not very helpful when it comes to the characterization of a laser beam by measurements. In addition, it is laborious to directly apply the Maxwell equations to an experimental situation. In order to obtain a description of light that can be applied to the experimental situation some simplifications are necessary. One of the most common approximation in optics is the restriction to monochromatic (one wavelength), linear polarized light travelling primarily along the z-axis in a homogenous dielectric medium. This way the beam of light can be described by a scalar amplitude $\varphi(x,y,z,t)$ [5.3–5.5]. The electric field $\vec{E}$ is related to the scalar amplitude the following way:

$$\vec{E}(x,y,z,t) = \vec{e} \cdot \varphi(x,y,z,t) \cdot e^{\mathrm{i}(\omega t - kz)}, \tag{5.6}$$

where $\omega = \frac{2\pi c}{\lambda}$ is the angular frequency defined by the speed of light, c, and the wavelength λ, $k = \frac{2\pi}{\lambda}$ is the wave number, and $\vec{e}$ is a unit vector indicating the direction of the polarization. The incorporation of a temporal integration corresponding to the integration time of the detector leads to the idea of coherence that is explained in the following section.

5.2.2. Mutual Coherence

If one deals with stable single-mode lasers, φ is independent of time and the beam can be sufficiently described by φ. In all other cases, φ fluctuates strongly

with time. This is especially the case for high-power semiconductor lasers. These fluctuations can neither be measured nor dealt with in numerical models. Therefore it is useful to incorporate a detector integration time time in the description of the laser beam. This leads to the idea of coherence that is introduced in this section.

If the electromagnetic field amplitude, or φ, is time independent, the beam is said to be fully coherent. This is the case for single-mode laser beams. For all other beams they fluctuate in time. For common material processing these fluctuations are of minor importance. It is the time average power density that governs the process.[1] As the fluctuations are beyond the range of most measurement systems it is hard to characterize them. Therefore, it is useful to take a detector integration time into account when describing the beam. This is done by the correlation of the paraxial electromagnetic field at two conjugate points x_1, y_1 and x_2, y_2 called the mutual coherence [5.6]:

$$\Gamma(x_1, y_1, x_2, y_2) = \frac{1}{T} \int_0^T \varphi^*(x_1, y_1, t + t_0)\varphi(x_2, y_2, t + t_0)dt, \qquad (5.7)$$

where φ is the paraxial complex amplitude of the electric field, and φ^* is the conjugate complex of φ. If the fluctuations in the field φ, are faster than the integration time, T, the mutual coherence, Γ, neither depends on the integration time, T, nor on the time the integration begins, t_0.

One has to note that the paraxial field amplitude, φ, refers to monochromatic light (light at one wavelength λ). The fluctuations in φ that are eliminated in (5.7) lead to a broadening of the wavelength spectrum. Thus Γ refers to light with wavelengths within a small range around λ (quasimonochromatic light).

If the beam is a superposition of two beams of different wavelength (see Chapter 4), it has to be treated by a mutual coherence for each wavelength. If the beam is a superposition of two beams of different orthogonal polarizations (see Chapter 4), it has to be treated by a mutual coherence for each state of polarization. If the optical components in the path of the combined beam are neither wavelength nor polarization selective all mutual coherence functions will propagate similarly. In this case the combined beam can be treated as an incoherent superposition of the single beams (the mutual coherence distributions simply add).

5.2.3. Wigner Distribution

The Wigner distribution is the Fourier transform of the mutual coherence. It is used in sections 5.3 and 5.4 to analyze the propagation of the beam width through linear optical systems. It can be also used to obtain the wavefront of a laser beam (section 5.8).

---

[1] Here "common material processing" refers to continuous wave (cw) and long pulse laser operation. This does not include short pulse (fs) laser processing.

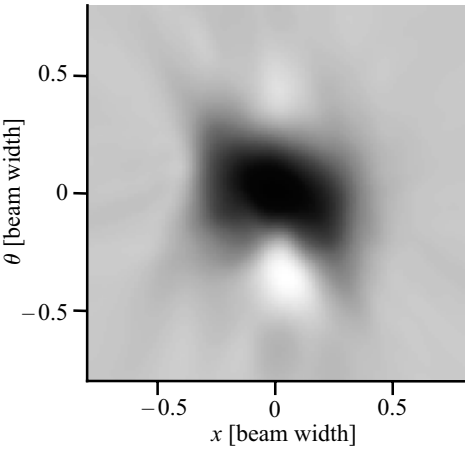

FIGURE 5.1. Wigner distribution in slow-axis direction of a tapered semiconductor laser measured at 2A. Scaling: black = 1; white = − 0.11

The Fourier transform of the mutual coherence with respect to the distance between the two mutual points is called the Wigner distribution [5.6][2]:

$$WD(x,y,\theta_x,\theta_y) = \frac{1}{\lambda^2}\iint \Gamma\left(x+\frac{1}{2}s_x, y+\frac{1}{2}s_y, x-\frac{1}{2}s_x, y-\frac{1}{2}s_y\right) e^{ik(\theta_x s_x+\theta_y s_y)}\,ds_x ds_y \tag{5.8}$$

It can be thought of as a geometrical phase space density describing the amount of beam power traveling from the point x, y into the direction given by the angles in the θ_x, θ_y in the x-z- and y-z-plane. In contrast to this simplified view, the Wigner distribution can take on negative values. This is the case if diffraction occurs. As an example, the Wigner distribution in slow axis direction of a tapered semiconductor laser is shown in Fig. 5.1.

5.2.4. Propagation of the Wigner Distribution Through Linear Optical Systems

The beam of a high-power semiconductor laser is partially coherent. The simplicity of the propagation of the Wigner distribution through linear optical systems makes the Wigner distribution a powerful tool for the analysis of the propagation of a partially coherent beam. It is the basis for the definition of the beam propagation ratios introduced in section 5.4.

---

[2] The Wigner distribution was introduced by E. Wigner to the fields of statistical mechanic as a quantum mechanical correction [5.7]. Nowadays it is used in many fields of physics. Optic-related introductions to the Wigner distribution can be found in [5.8] and [5.9].

The propagation through a distance of free space, a thin lens, or a spherical interface can be approximated as a first-order optical system that can be represented by an ABCD matrix:

$$\mathbf{S} = \begin{pmatrix} A_{xx} & A_{xy} & B_{xx} & B_{xy} \\ A_{yx} & A_{yy} & B_{yx} & B_{yy} \\ C_{xx} & C_{xy} & D_{xx} & D_{xy} \\ C_{yx} & C_{yy} & D_{yx} & D_{yy} \end{pmatrix}. \tag{5.9}$$

The propagation of the Wigner distribution through ideal ABCD optical elements is a coordinate transformation [5.10]:

$$WD_o(x, y, \theta_x, \theta_y) = \left(\frac{n_o}{n_i}\right)^2 WD_i\left(\mathbf{S}^{-1}\begin{bmatrix} x \\ y \\ \theta_x \\ \theta_y \end{bmatrix}\right), \tag{5.10}$$

where n_i and n_o are the refractive indices at the input and the output plane of the optical system and $\mathbf{S}^{-1}$ is the inverse of the optical system matrix $\mathbf{S}$.

5.3. Power Density Distribution

The power density on the workpiece is closely related to the performance of the laser device. It can be measured using a variety of devices (see section 5.6). A power density distribution can be characterized by its widths and orientation (see section 5.3.2). The propagation of the widths of the power density distribution (beam widths) is well understood (see section 5.4).

The power density is defined as the power P_a impinging on an infinitesimal small area divided by the size of the area a :

$$I = \lim(a \to 0)\frac{P_a}{a} \tag{5.11}$$

From this definition it is obvious that the power density depends on the orientation of the area in space.

The power density in a transverse plane of a paraxial beam can be calculated from the coherence, Eq. (5.7), or the Wigner distribution, Eq. (5.8):

$$I(x, y) = \Gamma(x, y, x, y) = \int WD(x, y, \theta_x, \theta_y)\, d\theta_x\, d\theta_y. \tag{5.12}$$

The beam power is the power in a transverse plane:

$$P(z) = \int I(x, y, z)\, dx\, dy. \tag{5.13}$$

5.3.1. Power Density Distribution in the Far Field

The power density distribution far away from the beam source can be described by a distribution of beam power per angle. It is called the far-field power density distribution.

The far-field power density distribution of a paraxial beam can be calculated from its Wigner distribution:

$$I_{ff}(\theta_x, \theta_y) = \int WD(x, y, \theta_x, \theta_y) dx\, dy. \tag{5.14}$$

5.3.2. Widths of a Power Density Distribution in a Transverse Plane

There are numerous possibilities to define the width and area of a two dimensional distribution. Because of its simple law of propagation (see section 5.4), the concept of second-order moments has become the most important one in the recent years.

The center of the power density distribution is given by the first order moments:

$$\langle x \rangle = \frac{1}{P} \int I(x, y) x dx\, dy, \text{ and } \langle y \rangle = \frac{1}{P} \int I(x, y) y dx\, dy. \tag{5.15}$$

The second-order moments of the power density distribution are defined as

$$\langle x^2 \rangle = \frac{1}{P} \int I(x, y) \big(x - \langle x \rangle\big)^2 dx\, dy \tag{5.16}$$

$$\langle y^2 \rangle = \frac{1}{P} \int I(x, y) \big(y - \langle y \rangle\big)^2 dx\, dy \tag{5.17}$$

$$\langle xy \rangle = \frac{1}{P} \int I(x, y) \big(x - \langle x \rangle\big)\big(y - \langle y \rangle\big) dx\, dy. \tag{5.18}$$

In Fig. 5.2 the power density distribution of a TEM 10 Hermite-Gaussian beam is shown. On the left the beam's principal axes are aligned with the coordinate system. In this case the beam widths are defined as –

$$d_x = 4\sqrt{\langle x^2 \rangle}, \text{ and } d_y = 4\sqrt{\langle y^2 \rangle}. \tag{5.19}$$

In the right part of Fig. 5.2, the principal axes enclose an azimuth angle γ with the coordinate system. In this case d_x and d_y are defined as the width of the beam along those principal axis that is closer to the x-coordinate axis and the y-coordinate axis respectively. The azimuth angle and the beam widths can be calculated directly from the second-order moments of the power density distribution

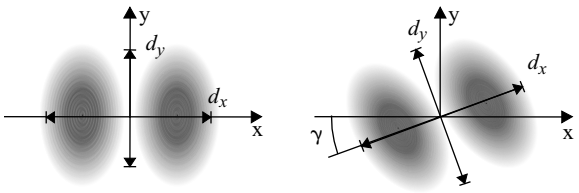

FIGURE 5.2. Power density distribution of a TEM 10 Hermite-Gaussian beam. Left: The principal axes are aligned with the coordinate system. Right: The principal axes enclose an azimuth angle γ with the coordinate axes

using the following equations.

For $\langle x^2\rangle \neq \langle y^2\rangle$:

$$\gamma = \frac{1}{2}\arctan\left(\frac{2\langle xy\rangle}{\langle x^2\rangle - \langle y^2\rangle}\right), \tag{5.20}$$

$$d_x = 2\sqrt{2}\left(\langle x^2\rangle + \langle y^2\rangle + \frac{\langle x^2\rangle - \langle y^2\rangle}{|\langle x^2\rangle - \langle y^2\rangle|}\sqrt{(\langle x^2\rangle - \langle y^2\rangle)^2 + 4\langle xy\rangle^2}\right)^{\frac{1}{2}}. \tag{5.21}$$

d_y is obtained by interchanging x and y. For $\langle x^2\rangle = \langle y^2\rangle$:

$$\gamma = \frac{\langle xy\rangle}{|\langle xy\rangle|}\frac{\pi}{4}, \tag{5.22}$$

$$d_x = 2\sqrt{2}(\langle x^2\rangle + \langle y^2\rangle + 2\langle xy\rangle)^{\frac{1}{2}} \text{ and} \tag{5.23}$$

$$d_y = 2\sqrt{2}(\langle x^2\rangle + \langle y^2\rangle + 2\langle xy\rangle)^{\frac{1}{2}}.$$

It has to be noted that γ is not defined by Eq. (5.22) if $\langle xy\rangle = 0$. In this case the power density distribution is round and γ may be chosen arbitrarily.[3]

5.4. Propagation of the Beam Widths

The propagation of the widths of the power density distribution (beam widths) through linear optical systems can be derived from the propagation of the Wigner distribution. However, the orientation of the principal axis of the beam and the beam widths behind an arbitrary linear optical system can be predicted from a set of measurements of the beam widths. A knowledge of the Wigner distribution is not required. This makes the beam widths a powerful tool for the characterization of

[3] It should be noted that round does not mean rotationally symmetric here. For example, a quadratic top hat distribution is round in the sense of the second-order moments.

laser beams. The propagation of the beam width is used to classify beams in section 5.4.2. Stigmatic and simple astigmatic beams that are commonly encountered in experimental situations are analyzed in some detail in section 5.4.3.

5.4.1. Theoretical Background

The propagation of the widths, d_x and d_y, of the power density distribution, I, is linked to the propagation of the second-order moments, $\langle x^2\rangle$, $\langle y^2\rangle$, and $\langle xy\rangle$ and via Eqs. (5.21) and (5.23). The second-order moments of a power density distribution are the second-order spatial moments of the Wigner distribution (see Eq. (5.12)). For example, inserting Eq. (5.12) into Eq. (5.16) results in:

$$\langle x^2\rangle = \frac{1}{P}\int WD(x,y,\theta_x,\theta_y)(x-\langle x\rangle)^2 dx\,dy\,d\theta_x\,d\theta_y, \tag{5.24}$$

where the beam power, P, Eq. (5.16) can be calculated using:

$$P = \int WD(x,y,\theta_x,\theta_y) dx\,dy\,d\theta_x\,d\theta_y, \tag{5.25}$$

and the first-order spatial moment, Eq. (5.15), can be obtained from the Wigner distribution using:

$$\langle x\rangle = \frac{1}{P}\int WD(x,y,\theta_x,\theta_y) x\,dx\,dy\,d\theta_x\,d\theta_y. \tag{5.26}$$

In order to analyze the propagation of the spatial second-order moments one has to look at all second-order moments of the Wigner distribution:

$$\left\langle x^i y^j \theta_x^m \theta_y^n\right\rangle = \frac{1}{P}\int WD(x,y,\theta_x,\theta_y)(x-\langle x\rangle)^i (y-\langle y\rangle)^j (\theta_x-\langle\theta_x\rangle)^m (\theta_y-\langle\theta_y\rangle)^n \, dx\,dy\,d\theta_x\,d\theta_y, \tag{5.27}$$

where $i,j,m,n \in [0,1,2]$ and $i+j+m+n=2$.

The propagation of the second-order moments of the Wigner distribution through a linear optical system follows from the propagation of the Wigner distribution, Eq. (5.10). It can be conveniently described using a matrix of second-order moments, called the beam matrix [5.10]:

$$\mathbf{P} = \begin{pmatrix} \langle x^2\rangle & \langle xy\rangle & \langle x\theta_x\rangle & \langle x\theta_y\rangle \\ \langle xy\rangle & \langle y^2\rangle & \langle y\theta_x\rangle & \langle y\theta_y\rangle \\ \langle x\theta_x\rangle & \langle y\theta_x\rangle & \langle\theta_x^2\rangle & \langle\theta_x\theta_y\rangle \\ \langle x\theta_y\rangle & \langle y\theta_y\rangle & \langle\theta_x\theta_y\rangle & \langle\theta_y^2\rangle \end{pmatrix} \tag{5.28}$$

The propagation of the beam matrix through a linear optical systems can be written as a multiplication of matrices:

$$\mathbf{P}_o = \mathbf{S}\cdot\mathbf{P}_i\cdot\mathbf{S}^T, \tag{5.29}$$

where **S** is the optical system matrix, Eq. (5.9), and the indices *i* and *o* refer to the input and output plane of the optical system, respectively.

There are two invariants of this transformation: The first is called effective beam propagation ratio,

$$M_{\text{eff}}^2 = 2k\sqrt[4]{\det(\mathbf{P})} \geq 1, \tag{5.30}$$

where det(**P**) is the determinant of the beam matrix **P**. It is a generalization of the concept of beam propagation ratios as will be seen in section 5.4.3. The second is called intrinsic astigmatism,

$$a = 4k^2\left[\langle x^2\rangle\langle\theta_x^2\rangle - \langle x\theta_x\rangle^2 + \langle y^2\rangle\langle\theta_y^2\rangle - \langle y\theta_y\rangle^2 + 2\left(\langle xy\rangle\langle\theta_x\theta_y\rangle - \langle x\theta_y\rangle\langle y\theta_x\rangle\right)\right] - M_{\text{eff}}^{2\ 2} \geq 0. \tag{5.31}$$

It indicates whether a beam can be transformed into a stigmatic one using a linear optical system (see section 5.4.2).

It has to be noted that the principal axis of the beam may rotate as the beam propagates through free space. This motivates the classification of beams introduced in the subsequent subsection.

5.4.2. Beam Classification

Beams are classified according to the propagation of their beam widths through stigmatic optical systems [5.11–5.13]. The classification is demonstrated in Fig. 5.3.

A beam with round power density profiles, $d_y \approx d_x$, in all transverse planes of a free space propagation is called **stigmatic** (top line of Fig. 5.3).[3] In addition, it is required that, if the beam passes through a cylindrical lens, the principal axis coincide with the axes of the cylindrical lens. A simple stigmatic beam is characterized by:

$$\langle xy\rangle = 0,\ \langle x\theta_y\rangle = 0,\ \langle y\theta_x\rangle = 0,\ \langle\theta_x\theta_y\rangle = 0, \tag{5.32}$$

and

$$\langle x^2\rangle = \langle y^2\rangle,\ \langle x\theta_x\rangle = \langle y\theta_y\rangle,\ \langle\theta_x^2\rangle = \langle\theta_y^2\rangle. \tag{5.33}$$

A beam whose *x*- and *y*-related beam widths are not equal, and whose orientation of the principal axes does not change when propagating through free space, is called **simple astigmatic** (center line of Fig. 5.3). In addition, it is required that, if the beam passes through a cylindrical lens of the same orientation as the beam, the azimuth angle remains invariant too. By rotation the coordinate axes can be aligned with the principal axes of the beam. Doing so, Eq. (5.32) is also valid for simple astigmatic beams. If the coordinate axis are not aligned with the beam principal axis only $\langle x\theta_y\rangle = \langle y\theta_x\rangle$ is true.

All other beams are called **general astigmatic**. In most cases such a beam changes its principal axis when propagating through free space (bottom line **of**

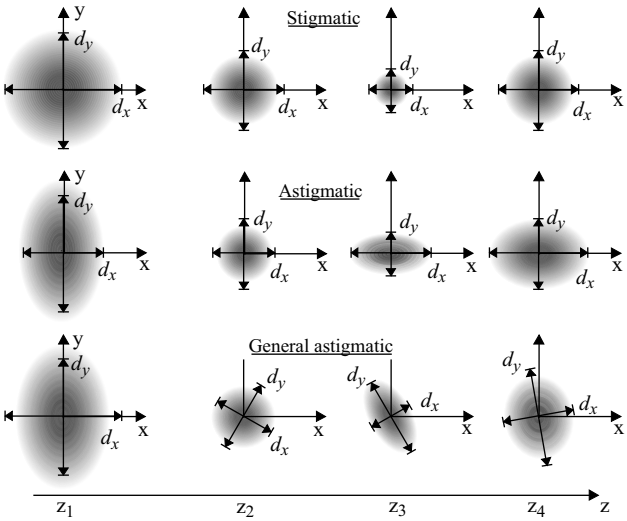

FIGURE 5.3. Power density profiles, $I(x, y)$, as the beam propagates along the beam axis (z-axis). The beam in the top line is stigmatic. Its beam widths reach their minimum value at $z = z_3$ (beam waist). The beam in the center line is simple astigmatic. Its x and y related beam widths reach their minimum values at $z = z_2$ and $z = z_3$, respectively. The beam in the bottom line is general astigmatic. Its principal axis rotates as the beam propagates.

Fig. 5.3). It is, however, possible that the principal axis does not change and, therefore, the beam appears to be simple stigmatic or simple astigmatic. In such a case the propagation behavior behind a cylindrical lens will reveal the general astigmatism.

Generally, the class of a beam can be modified using a linear optical system. There are, however, general astigmatic beams that cannot be transformed into stigmatic ones. This is the case if the astigmatism a (Eq. (5.31)), is greater than zero. In this case the beam is called **intrinsic general astigmatic**. It should be noted that Eq. (5.31) contains the difference between combinations of second-order moments. Therefore it is hard to determine a experimentally.

A stigmatic (rotationally symmetric and linear) optical system does not change the class of a beam. For further details see [5.14].

In most cases the aim is to create a stigmatic beam. The symmetry of a stigmatic beam enables to create a small spot size and thus a high-power density (see for example Fig. 5.3). Generally the output of a semiconductor laser is highly asymmetric. Using a cylindrical lens (FAC lens) to collimate the beam in direction perpendicular to the semiconductor layers a stigmatic or simple astigmatic beam can be obtained. If the FAC lens is not aligned with the semiconductor layers the resulting beam is general astigmatic (see Fig. 5.4). As this situation corresponds to suboptimal collimation it is commonly avoided by optimizing the fast axis collimation.

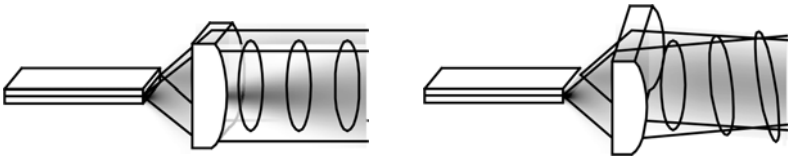

FIGURE 5.4. Collimation of a semiconductor laser. Left: The cylindrical fast axis collimation lens is aligned with the x and y-axis (defined by the semiconductor layers). The resulting collimated beam is simple astigmatic. Right: The cylindrical lens is rotated about the *z-axis*. The resulting beam is not collimated well. In addition, it is general astigmatic

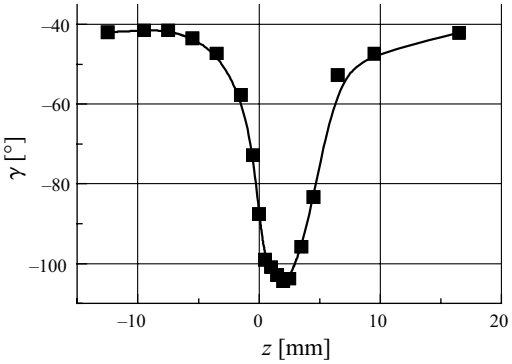

FIGURE 5.5. Orientation of the principal axis of the beam of a 1 KW diode laser system as it propagates. The rotation indicates that the beam is general astigmatic. At $z = 0$ the beam is in its waist. The Rayleigh range is 2.46 mm

The propagation of the orientation of the y-axis of the power density distribution measured at a 1-kW diode laser system is shown in Fig. 5.5 as an example of a general astigmatic beam. Further research has to be done to assess the effect of a general astigmatism on the laser performance. For the sake of simplicity the following sections only deal with stigmatic and simple astigmatic beams.

5.4.3. Propagation of the Beam Widths of Stigmatic and Simple Astigmatic Beams

Because of their symmetry the most desired beams are stigmatic ones. General astigmatic beams are commonly avoided. Therefore, this section only deals with stigmatic and simple astigmatic beams. For these types of beams the propagation of the beam width is ruled by simple laws.

In the following it will be assumed that the coordinate system is aligned with the principal axis of the beam. Doing so the beam widths are (Eq. (5.19)):

$$d_x = 4\sqrt{\langle x^2 \rangle}, \text{ and } d_y = 4\sqrt{\langle y^2 \rangle}. \tag{5.34}$$

The position where d_x reaches its minimum value, $d_{x0} = 4\sqrt{\langle x^2 \rangle_0}$, is called beam waist position z_{0x}. It can be obtained from the following equation:

$$z_{0x} = \frac{\langle x\theta_x \rangle}{\langle \theta_x^2 \rangle}. \tag{5.35}$$

The mixed moment $\langle x\theta_x \rangle$ is zero at z_{0x}.

The propagation of the beam width can be expressed as:

$$d_x(z) = d_{x0}\sqrt{1 + \Theta_x^2 \left(\frac{z - z_{0x}}{z_{Rx}}\right)^2}, \tag{5.36}$$

with the full-width far-field divergence (width of the far-field power density profile (Eq. (5.14)):

$$\Theta_x = 4\sqrt{\langle \theta_x^2 \rangle}, \tag{5.37}$$

where the second angular moment is given by Eq. (5.27). z_{Rx} is the Rayleigh range:

$$z_{Rx} = \sqrt{\frac{\langle x^2 \rangle_0}{\langle \theta_x^2 \rangle}}. \tag{5.38}$$

The beam width reaches $\sqrt{2}$ of its minimum value at a distance of one Rayleigh range away from the beam waist:

$$d_x(z_{0x} \pm z_{Rx}) = \sqrt{2} d_{x0}. \tag{5.39}$$

The beam-parameter product, the product of the minimum width and the far-field divergence,

$$Q_x = \frac{1}{4} d_{x0} \Theta_x, \tag{5.40}$$

is an invariant of the propagation through rotationally symmetric optical systems and linear cylindrical lenses whose cylinder axis are aligned with the principal axis of the beam. It is minimal for a coherent Gaussian beam (TEM_{00} mode). The beam-parameter product normalized to the one of a coherent Gaussian beam of the same wavelength is called the beam propagation ratio M^2 [5.15]:

$$M_x^2 = \frac{Q_x}{Q_{x\,\text{Gauss}}} = \frac{\pi}{4\lambda} d_{x0} \Theta_x = \frac{4\pi}{\lambda} \sqrt{\langle x^2 \rangle_0 \langle \theta_x^2 \rangle} = \frac{4\pi}{\lambda} \sqrt{\langle x^2 \rangle \langle \theta_x^2 \rangle - \langle x\theta_x \rangle^2}. \tag{5.41}$$

It follows that

$$M_x^2 \geq 1, \tag{5.42}$$

where the minimum value is reached by a coherent Gaussian beam (TEM_{00} mode).

Using M^2, the propagation of the beam width can be written as

$$d_x(z) = d_{x0}\sqrt{1 + \frac{(M_x^2)^2}{d_{x0}^4}\frac{16\lambda^2}{\pi^2}(z - z_{0x})^2}. \tag{5.43}$$

All y-related values and formulas are obtained by interchanging x and y in Eq. (5.43). It is commonly used to obtain the beam waist position, z_{0x}, the minimum width, d_{x0}, and the beam propagation ratio, M_x^2, by fitting Eq. (5.43) to a set of measured beam widths.

It can be concluded that the free-space propagation of the beam widths of a simple astigmatic beam is characterized by six parameters only: $d_{x0}, z_{0x}, d_{y0}, z_{0y}$ and M_x^2, M_y^2. Instead of the beam propagation ratios M_x^2, M_y^2, the far-field divergences Θ_x, Θ_y or the Rayleigh ranges z_{Rx}, z_{Ry} can be used. In addition the orientation of the principal axes of the beam has to be recorded. For a stigmatic beam the x- and y-related figures are the same and thus three parameters suffice. In contrast to a simple astigmatic beam, a general astigmatic beam has to be characterized by the ten independent elements of the beam matrix (5.28).

M^2 is increased by diffraction, aberration of the wavefront, and by loss of coherence [5.16]. In a transverse plane, M^2 can be calculated as the square root of the sum of the three influences:

$$M^2 = \sqrt{{M_{\text{diff}}^2}^2 + {M_{ab}^2}^2 + {M_{\text{cohe}}^2}^2}. \tag{5.44}$$

where $M_{\text{diff}}^2 \geq 1$ describes the influence of diffraction, $M_{ab}^2 \geq 0$ the influence of aberration, and $M_{\text{cohe}}^2 \geq 0$ the influence of the lack of coherence. As an example, M^2 and its components are depicted for mixtures of TEM_{00} and TEM_{10} Hermite-Gaussian modes in Fig. 5.6. The pure TEM_{00} mode is the well known Gaussian beam. Its M^2-value is 1. The M^2-value increases linearly with the power fraction of the TEM_{10} mode [5.15]. At an even mixture of both modes the power density distribution is relatively smooth and the main contribution is the coherence term, M_{cohe}^2. The power density of the pure TEM_{10} mode is strongly modulated. Its M^2-value is given solely by diffraction. The general rule is that higher order modes have higher M^2-values due to strong modulation in the power density distribution causing diffraction. If different transverse modes are mixed, the resulting power density distribution is smoother but the M^2-value increases due to incoherence. The components of the TEM Hermite-Gaussian modes do not change as the beam propagates. This is generally not the case. In Fig. 5.7 the propagation of the components of M^2 of a Gaussian beam with a spherical aberration is shown. M^2 is an invariant of this propagation. Its components, however, do change as the beam propagates. In the beam waist ($z = 0$), the power density distribution is Gaussian and the contribution of diffraction is minimal. The deviation of the M^2-value from one results solely from the spherical distortion of the wave front. As the beam propagates both the power density distribution and the wave front change their shape. Consequently, the contribution of diffraction and aberration to M^2 change too. The influence of a spherical aberration was treated in detail by Siegman [5.17].

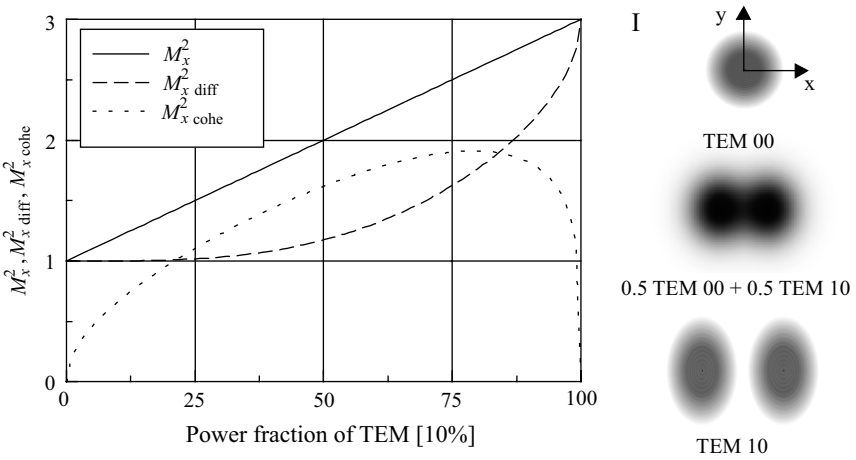

FIGURE 5.6. Left: Components of M^2 of a mixture of a TEM10 and a TEM00 Gauss-Hermite modes. Right: Power density distributions of a pure Gaussian beam, a mixture of TEM10 and TEM00 of even powers, and a pure TEM10 Gauss-Hermite mode

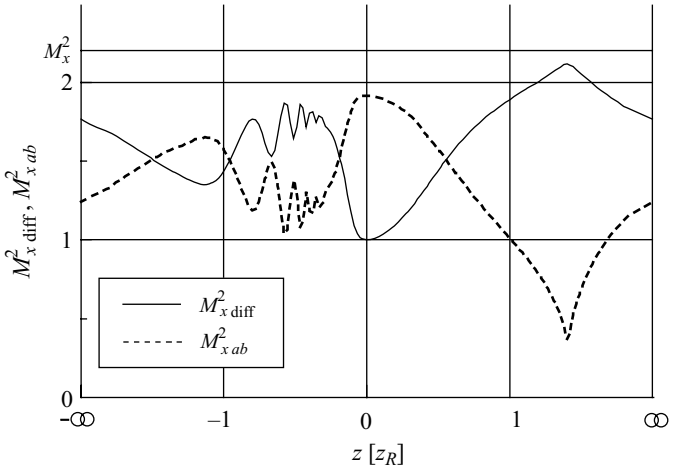

FIGURE 5.7. Components of M^2 of a Gaussian beam with a spherical aberration as the beam propagates through free space. In the beam waist ($z = 0$) the power density distribution is Gaussian and the wavefront is spherically distorted

The intrinsic astigmatism, Eq. (5.31), of a simple astigmatic beam is

$$a = \frac{1}{2}\left(M_x^2 - M_y^2\right)^2. \tag{5.45}$$

Thus a beam with different beam propagation ratios M_x^2 and M_y^2 can not be made stigmatic using linear optical systems. The output of a semiconductor laser bar is intrinsic general astigmatic, $M_x^2 \neq M_y^2$. Beam shaping techniques, designed to generate a stigmatic beam, are described section 4.3 of this book.

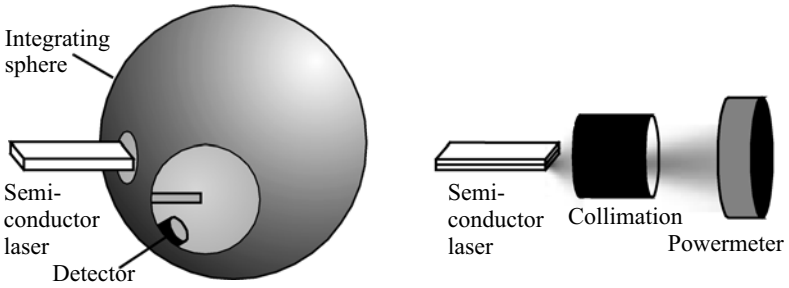

FIGURE 5.8. Measurement of the power of a semiconductor laser. Left: Ulbricht sphere. The radiation is reflected from the surface at the inside of the sphere until it hits the detector. A shield is inserted between the laser and the detector to prevent direct irradiance that might destroy the detector. Right: Measurement of the power of a collimated beam

5.5. Measurement of the Beam Power

Semiconductor laser emit their radiation into half space ($z>0$) in a wide range of angles. To collect all their power an integrating Ulbricht sphere has to be used (**see Fig. 5.8,** left).

Once the beam has been collimated a power detector with a flat detection surface can be used. A setup with such a "power meter" is depicted on the right of Fig. 5.8. In this way the power of a complete laser system is commonly determined. Due to losses introduced by the collimation optics the power of the semiconductor laser itself is not known.

5.6. Measurement of the Power Density Distribution and the Beam Propagation Ratio, M^2

In this section the most common devices to measure the power density distribution or related distributions are presented. The calculation of the beam widths from a measured power density distribution is explained. Different setups for the measurement of the beam propagation ratio, M^2, are discussed.

5.6.1. Camera Systems

CCD-cameras offer a way to quickly obtain the two-dimensional power density distribution of a beam. There exists a wide range of different camera types. Typical specifications are –

Time to obtain one profile (exposure time): 17 ms
Resolution (size of one pixel): 10 μm
Size of the profile: from 512×768 pixel ($4.6 \times 7\,\text{mm}^2$) up to $2,048 \times 3,072$ pixel ($18 \times 28\,\text{mm}^2$)
Dynamic range (digitalization): 8 Bit to 16 Bit (with cooling)
Input beam power: μW-range

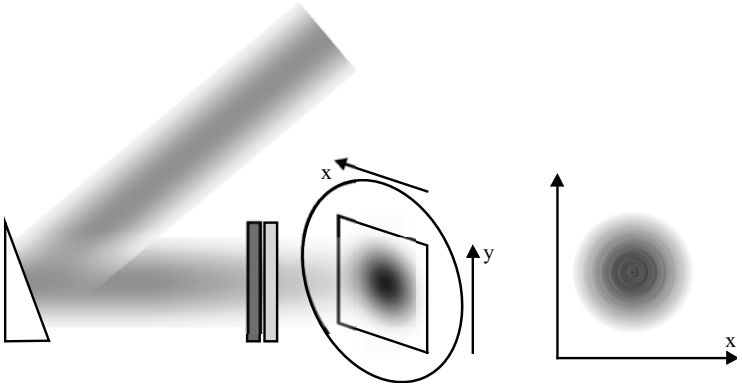

FIGURE 5.9. Setup for the measurement of the power density profile using a CCD-camera. The beam is attenuated using a wedged glass mirror and absorbing filters

The main drawback of a camera is its low saturation threshold. The beam has to be attenuated without changing its characteristics. This can be done by reflecting the beam using a wedged glass mirror (see Fig. 5.9). The power of the reflected beam is about 4% of the original beam power if the beam is almost perpendicular to the glass surface. If the beam hits the glass surface at an angle (greater 10°), the reflected power depends on the state of polarization of the beam. The fine tuning of the beam power can be done by absorbing filters. Care has to be taken that the absorbed power does not lead to a thermal deformation of the filter (thermal lensing). The sensitivity of the camera can be tuned by the electronic gain and the exposure time. One has to note that a wide range of beam widths and, therefore, power densities have to be measured for the determination of the beam propagation ratio (see below). Preferably the optical elements are not changed between two power density measurements at different z-positions. However, many camera systems do not have a sufficient electronic adjustment. In this case a different choice of absorbing filters has to be used for each measurement. As each filter changes the optical path length slightly this complicates the measurement and evaluation process.

If a strong beam attenuation is used, one has to take care that stray light from the original beam does not hit the camera. For example, the stray light of a 1 W laser system can easily exceed a few mW.

5.6.2. Mechanical Scanning Devices

The main advantage of a scanning device is that the area scanned by the device can be chosen for each scan. As the scan is done mechanically it takes some time to obtain the scan. Moving-slit and moving-knife-edge system measure the one-dimensional projected power density distribution and the integrated projected power density distribution, respectively. This way the scan time is reduced, but less information about the beam profile is recorded. The power behind the pinhole, slit,

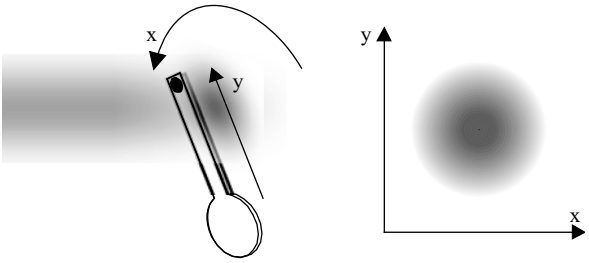

FIGURE 5.10. Moving-pinhole system to measure the power density profile of a kW laser system

or knife edged is detected by a single power detector. Depending on the materials used and on the type of power detector, mechanical scanning devices are used for all kinds of power ranges. In most cases the dynamic range can be adjusted electronically for each scan. Of course scanning devices can only be used for lasers whose output remains stable during the scan time.

Moving Pinhole

A moving pinhole system is depicted in Fig. 5.10. Because of the small exposure time of the pin, a moving pinhole system can resist high beam powers. The power density profile obtained is in cylindrical coordinates. Typical specifications are –

Time to obtain one profile: 2 s (for 256×256 data points)
Maximum resolution (pinhole diameter): 25 μm
Size of the profile: $8 \times 8\,\mathrm{mm}^2$
Dynamic range (digitalization): 10 Bit
Input beam power: kW-range
Moving pinhole systems are commonly used to characterize laser systems in the kW range without beam attenuation

Moving-Slit and Moving-Knife-Edge Systems

A moving slit system is depicted in Fig. 5.11. A metal plate with a thin slit is moved through the beam. The power transmitted by the slit is

$$P_{ms}(x_1) = \int_{x_1}^{x_2} \int_{y_1}^{y_2} I(x', y)\, dx'\, dy, \tag{5.46}$$

where x_1, y_1 and x_2, y_2 are the coordinates of the bottom left and the top right corner of the slit. If the slit height, $y_2 - y_1$, is greater than the beam width in y-direction, and the modulations of the projected power density profiles in x-direction are smaller than the slit width, the signal of the moving slit system is proportional to the projected power density distribution:

$$P_{ms}(x_1) \propto \text{slit width} \cdot \int_{-\infty}^{\infty} I(x, y)\, dy. \tag{5.47}$$

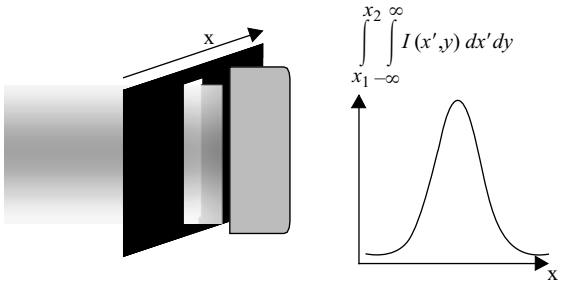

FIGURE 5.11. Moving-slit system to measure the projected power density distribution

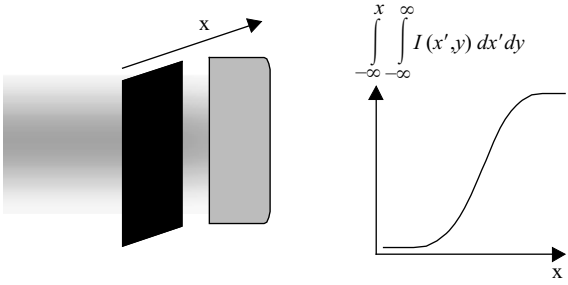

FIGURE 5.12. Moving-knife-edge system to measure the integrated projected power density distribution

As a thin slit with a high ratio of height to width is sensitive to thermal stress, the power a moving slit device can take is limited.

A moving-knife-edge system is depicted in Fig. 5.12. A plate with a well-defined edge is moved through the beam. The power that passes the edge is the integrated projected power density:

$$P_{\mathrm{mne}}(x) = \int_{-\infty}^{x}\int_{-\infty}^{\infty} I(x',y)\,dx'\,dy, \tag{5.48}$$

Moving-knife-edge systems can be built for a wide range of beam powers and power densities.

A moving-slit or moving-knife-edge scan is sufficient to calculate the beam width in the direction of the scan. If the power density profile is separable along the x- and y- axis, the two-dimensional profile can be characterized by a scan along the x-axis plus a scan along the y-axis.

In some devices the slit or knife edge is included in a rotating drum. In this way the scan time is reduced. If the scan range is small compared to the drum diameter, the scan is approximately done in a transverse plane. Typical specifications are:

Time to obtain one profile: 1 s (linear scan), 10 μs (rotating drum)
Maximum resolution: 25 μm (slit width) 1 μm (mechanical limit)
Slit height, knife edge height: 7 mm
Size of the profile: 2048 data points (up to 25 mm)
Dynamic range (digitalization): 10 Bit
Input beam power: mW- up to W-range
(moving slit), mW- up to kW-range (moving knife edge)

5.6.3. Measuring a Beam Caustic

In order to determine the beam propagation ratio, M^2, using Eq. (5.43), the width of the power density distribution at several z-positions of the beam caustic (z-section of the focused beam including the beam waists) has to be measured. If the beam waist is not accessible, the beam has to be focused. The focal length of the focusing lens influences the Rayleigh range and the maximum power density of the beam caustic. It has to be chosen to meet the requirements of the detector system. The z-position is altered by moving the detector system (see Fig. 5.13, top left). As most detector systems are comparatively heavy it is difficult to move them precisely. In addition, mechanical scanning devices are preferably fixed on a rigid mount. An alternative is to use two moving mirrors (see Fig. 5.13, right). Care has to be taken that the mirrors do not influence the beam properties by polarization dependence of the reflection. This method is restricted to a large focal length of the focusing lens. A different method is to move the focusing lens (see Fig. 5.13, bottom left).

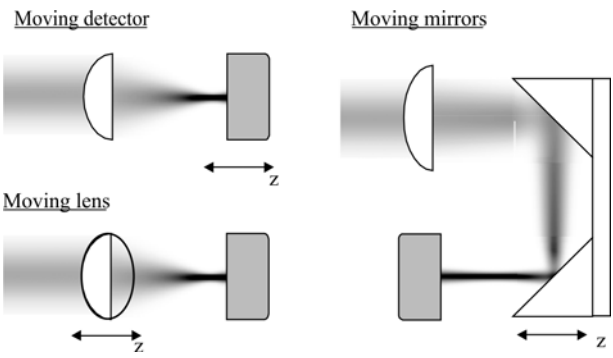

FIGURE 5.13. Measurement of the power density profiles at different *z-positions*. Different setups to realize the movement along the *z-axis*

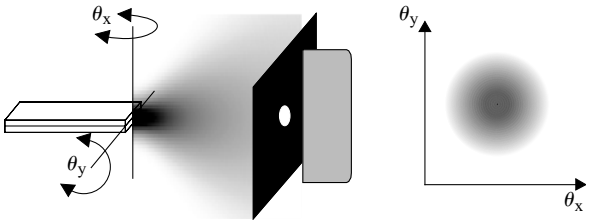

FIGURE 5.14. Measurement of the far-field power density profile

5.6.4. Power Density in the Far Field Measurement

The far-field power density profile of a semiconductor laser can be measured by rotating the semiconductor about a point in the laser facet (see Fig. 5.14). If the area of the pinhole in angular coordinates is smaller than the modulations of the far-field power density profile, the beam power that passes a pinhole a sufficiently large distance away from the device is proportional to the far-field power density profile:

$$P_{\text{pinhole}}(\theta_x, \theta_y) \propto \text{pinhole area} \cdot I(\theta_x, \theta_y). \tag{5.49}$$

Alternatively to the rotation of the semiconductor 0 the pinhole can be moved can be moved on the surface of a sphere centered at the facet of the semiconductor.

5.6.5. Evaluating the Widths of a Measured Power Density Distribution

The beam widths are calculated from the second-order moments of the power density distributions (Eqs. (5.21) and (5.23)). The second-order moments can be calculated from Eqs. (5.15–5.18). Due to the $(x - \langle x \rangle)^2$-term in the integral of Eq. (5.16) the parts of the profile away from the center of the beam, $\langle x \rangle$, have a comparatively high impact on the resulting second-order moment. Each measurement profile contains a noise component. The lower limit of the digitalization is chosen to result in an above zero value for all parts of the profile. This way it is assured that small signals are not ignored. The zero level of the power density is chosen to result in an average power density of zero for parts of the profile where the power density is zero. Therefore, the power density has to include negative values.

In order to limit the influence of noise of the detector system on the calculated beam width, the integration area has to be restricted [5.11–5.13]. In Fig. 5.15, the beam width calculated from a measured power density profile is shown for different sizes of the measurement area. Clearly the beam width grows with the size of the area. The reason is a wrong determination of the zero level of the power density profile (wrong "offset correction"), noise at the boundary of the measurement area that lead to an increased beam width. The beam widths calculated by iteration

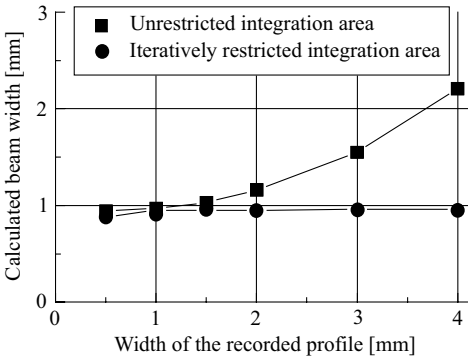

FIGURE 5.15. Beam width calculated from a measured power density profile for different sizes of the measurement area

using the procedure explained in this section is not affected by the size of the measured profile.

Using a restricted integration range, Eqs. (5.15) through (5.18) have to be slightly modified:

$$P_{3\mathrm{dia}} = \int_{x_1}^{x_2} \int_{y_1}^{y_2} I(x,y)\,dx\,dy, \tag{5.50}$$

$$\langle x\rangle_{3\mathrm{dia}} = \frac{1}{P_{3\mathrm{dia}}} \int_{x_1}^{x_2} \int_{y_1}^{y_2} I(x,y)x\,dx\,dy, \tag{5.51}$$

$$\langle y\rangle_{3\mathrm{dia}} = \frac{1}{P_{3\mathrm{dia}}} \int_{x_1}^{x_2} \int_{y_1}^{y_2} I(x,y)y\,dx\,dy, \tag{5.52}$$

$$\langle x^2\rangle_{3\mathrm{dia}} = \frac{1}{P_{3\mathrm{dia}}} \int_{x_1}^{x_2} \int_{y_1}^{y_2} I(x,y)(\langle x - \langle x\rangle_{3\mathrm{dia}})^2 dx\,dy, \tag{5.53}$$

$$\langle y^2\rangle_{3\mathrm{dia}} = \frac{1}{P_{3\mathrm{dia}}} \int_{x_1}^{y_1} \int_{x_2}^{y_2} I(x,y)(\langle y - \langle y\rangle_{3\mathrm{dia}})^2 dx\,dy, \tag{5.54}$$

and

$$\langle xy\rangle_{3\mathrm{dia}} = \frac{1}{P_{3\mathrm{dia}}} \int_{x_1}^{y_1} \int_{x_2}^{y_2} I(x,y)(x - \langle x\rangle_{3\mathrm{dia}})(y - \langle y\rangle_{3\mathrm{dia}})dx\,dy, \tag{5.55}$$

with

$$x_1 = \langle x\rangle_{3\mathrm{dia}} - 6\sqrt{\langle x^2\rangle_{3\mathrm{dia}}} \text{ and } y_1 = \langle y\rangle_{3\mathrm{dia}} - 6\sqrt{\langle y^2\rangle_{3\mathrm{dia}}}. \tag{5.56}$$

For the projected power density distribution obtained by a moving slit or a moving knife edge system Eqs. (5.50), (5.51), and (5.53) are used. In this case the y-integration has already been performed by the detector system. As the first and

second-order moments are initially not known, one has to begin with a guessed integration area. An iterative procedure follows. The general effect of this method is to underestimate the second-order moments and thus the beam widths. The size of this effect depends on the power density profile. It is interesting to note that this approach allows to study the propagation of the second-order moments of hard edge diffracted beams, which diverge if the integration area is not restricted [5.18].

5.6.6. Determination of the Beam Propagation Ratio, M^2

The beam propagation ratio, M^2, is obtained from a fit of the law of the propagation of the beam width, Eq. (5.43),

$$d_x(z) = d_{x0}\sqrt{1 + \frac{(M_x^2)^2}{d_{x0}^4}\frac{16\lambda^2}{\pi^2}(z - z_{0x})^2}, \tag{5.57}$$

to the measured beam widths. An example is shown in the left of Fig. 5.16. The fit should be done minimizing the sum of the squared relative difference of the theoretical to the measured beam widths. Otherwise the small beam widths in the beam waist have a lower impact on the resulting M^2 than the beam width away from the beam waist. This effect is visualized in Fig. 5.16. The fit is done both ways. In the right of Fig. 5.16 the relative deviations of the fits to the measured beam widths are shown. The fit by minimizing the absolute deviation leads to very high relative deviation in the beam waist.

In addition, a well balanced set of z-position should be taken. The ISO-standard proposes to measure power density profiles in at least 10 different z-positions. Approximately half of the measurements shall be distributed within one Rayleigh

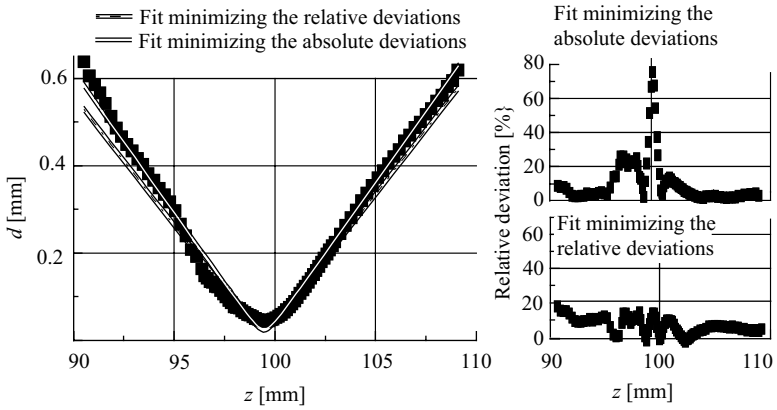

FIGURE 5.16. Determination of the beam propagation ratio, M^2. Left: Fit of the theoretical propagation of the beam width to the measured ones. The fit minimizing the absolute deviations results in $M^2 = 1.4$. The fit minimizing the relative deviations results in $M^2 = 1.9$. Right: Absolute value of the relative deviation of the fitted beam width to the measured one

length on either side of the beam waist, and approximately half of them shall be distributed beyond two Rayleigh lengths from the beam waist.

If the z-positions are equally spaced, this criterion is generally not met. In order to select the right z-positions the waist position and the Rayleigh length have to be estimated prior to the measurement. Commonly the beam widths that enter the evaluation process can be chosen after a preliminary data evaluation.

5.7. Beam Positional Stability

The center of a power density distribution may vary with time. A movement of the beam center in a plane perpendicular to the average beam direction may be caused by either a random parallel shift of the beam axis or a random variation of the direction (angular movement) of the beam axis or by both. Periodical recordings of the position of the beam center results in a two dimensional distribution of the center of the beam (see).

The beam positional stability, Δ_x and Δ_y, characterizes the movement of the center of the power density profile, $\langle x \rangle$, $\langle y \rangle$ (Eq. (5.15)) in a plane perpendicular to the propagation. Similar to the power density itself, the recording of the position of its center is a two-dimensional distribution (see the left of Fig. 5.17). The beam positional stability is defined as four times the standard deviation of the position of the center of the beam from the center position [5.19]. Δ_x and Δ_y are the widths of the distribution of beam positions. They can be calculated analogous to the equations of section 5.3.2. In a first step Δ_x, the center of gravity x_M of n temporal beam positions $\langle x \rangle_i$ has to be calculated:

$$\mathrm{X}_M = \frac{\sum_i \langle x \rangle_i}{n}, \tag{5.58}$$

The standard deviation is

$$\mathrm{S}_x = \left[\frac{\sum_i (\langle x \rangle_i - x_M)^2}{n-1} \right]^{1/2}, \tag{5.59}$$

and the beam positional stability in this axis is $\Delta_x = 4 * \mathrm{s_x}$. In each transverse plane 1,000 power density profiles should be recorded. The beam positional stability propagates along the beam axis in the same way the beam width does. In Fig. 5.17 the measured beam positional stability at different positions along the z-axis is shown. It has to be noticed that the position of the minimum beam positional stability may not coincide with the beam waist. The product of the beam positional stability and the beam angular stability does not vary when the beam propagates through stigmatic optical systems. The ISO standard proposes to measure the beam positional stability within three different time scales: short-term stability, the total time of the stability measurement is 1 second; medium-term stability, the total time of the stability measurement is 1 minute; long-term stability, the total time of the stability measurement is 1 hour.

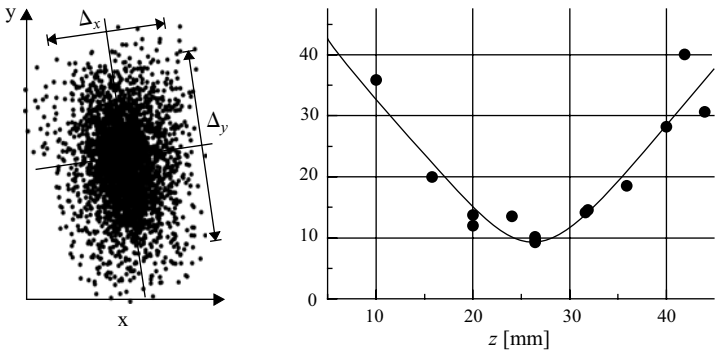

FIGURE 5.17. Beam positional stability Left: Centers of the power density distributions at different times. Right: Propagation of the beam positional stability measured at a kW semiconductor laser

5.8. Wavefront of a Laser Beam

The wavefront W of a beam is defined as the surface perpendicular to the time averaged local direction of the beam. The local direction of a beam is given by the time average Poynting vector distribution $\bar{\bar{S}}$:

$$W(x,y,z) \perp \bar{\bar{S}}(x,y,z). \tag{5.60}$$

It has to be noted that a continuous surface does not always exist. For paraxial beams the wavefront of a beam is defined by a minimizing the squared difference between the transverse coordinates of the time average Poynting vector and the gradient of a continuous surface, W, [5.20]:

$$\iint \frac{1}{I(x,y)} \left[\left(\bar{S}_x(x,y) - I(x,y) \frac{\partial}{\partial x} W(x,y) \right)^2 + \left(\bar{S}_y(x,y) - I(x,y) \frac{\partial}{\partial y} W(x,y) \right)^2 \right] dx\, dy \to \min . \tag{5.61}$$

The wavefront is defined as the resulting continuous surface W.

Shack–Hartmann and Hartmann sensors are standard systems to measure the wavefront in astronomy and the field of testing of optical components. They are also used to characterize laser beams. The principle scheme of operation of the wavefront sensors is shown in Fig. 5.18. The beam is intersected by an array of lenses (Shack–Hartmann sensor) or an array of pinholes (Hartmann sensor). At a distance f the resulting spot pattern is measured using a CCD-camera. For Shack–Hartmann sensors f is taken equal to the focal length of the array lenses. If the beam has a plane wave front parallel to the array, the spot of each lens (hole) has the x- and y-coordinates of the center of the lens (hole). If the wave front of

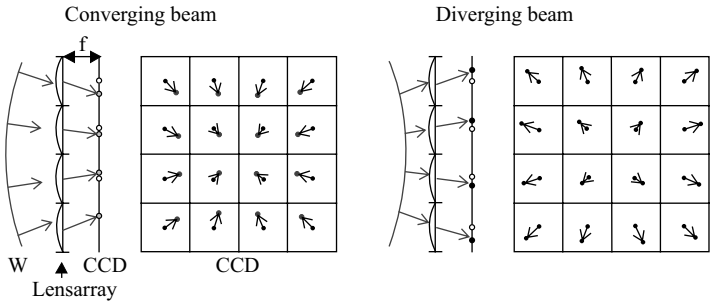

FIGURE 5.18. Two typical situations in Shack-Hartmann measurements. Left: The wavefront, W, is converging. The focus spots of the lenses on the CCD-camera move towards the center of the beam. Right: the wavefront is diverging. The spots move away from the center of the beam

the part of the beam that enters a lens or hole is tilted abut the y-axis, the spot on the camera is shifted by Δx. The shift is proportional to the x-component of the Poynting vector [5.20]:

$$S_x(x,y) = \frac{\Delta x}{f} I(x,y). \tag{5.62}$$

5.9. Lifetime

Semiconductor lasers are not designed for repair. The end of life (EOL) is reached, if a "catastrophic optical damage" occurs, the output power drops below a predetermined value, or some other specification is not met any longer. High-power diode laser devices often consist of several single laser diodes which are produced in rather large quantities. This allows statistical methods to estimate the lifetime of the device from the lifetime of the single components.

The International Standard ISO 17526:2003 defines a drop of the output power by 20% as EOL-criterion [5.21]. An alternative method is to keep the output power constant and to increase the current automatically. An increase in current by 20% is defined as the EOL. As the output power depends almost linearly on the laser current both methods give the same results.

During a product's life, the failure rate of the single semiconductor lasers may change. In general three periods can be discerned. The initial failure period is identified by a decreasing rate of failures. Substrate or processing faults dominate this period. Screening methods such as "burn-in" under elevated operating conditions are used to eliminate those diode lasers before shipment to the customer. The next period exhibits a constant failure rate which is governed by random failures only. Finally in the third period the failure rate is increasing due to wear-out. In the high-power regime diode lasers fail mainly due to degradation of the output power and destruction of the facet coating – typical wear failures.

Under normal operating conditions, high-power diode lasers have lifetimes in the region of some 10,000 hours. In manufacturing processes, quality assessment should not last this long. Therefore, it is common to extrapolate the lifetime from the degradation of the power versus time. Only if the power depends linearly on time an extrapolation can be used. The standard deviation of the linear fit, used for the extrapolation, from the measured data should not exceed 5%. Otherwise a linear dependence of the power on time can not be assumed. It is advisable to limit the extrapolation seven times this duration of the test measurement.

A method to accelerate the aging employs higher junction temperatures and higher currents during the test. The acceleration factor $A(T)$ follows from the life-stress relationship. In case of temperature accelerated tests the Arrhenius relationship is commonly used [5.22]:

$$A(T) = \exp\left[-\frac{\mathrm{E}}{\mathrm{k}}\left(\frac{1}{T} - \frac{1}{T_0}\right)\right], \tag{5.63}$$

where E denotes the activation energy, k the Boltzmann-constant, T the absolute temperature in K, and T_0 the temperature of the normal operation mode in K.

Care must be taken to avoid misinterpretation of the results due to different damage mechanism with respect to different stress (current or temperature) levels. A convenient way to evaluate the lifetime data x of a random sample is the Weibull analysis [5.22]. This method can be used if the failure probability $F(x)$ follows a Weibull distribution,

$$F(x) = 1 - \exp\left[-\left(\frac{x}{t}\right)^b\right]. \tag{5.64}$$

Here t denotes the characteristic lifetime and b the shape parameter respectively. In a so-called Weibull plot:

$$\ln\left[\ln\left(\frac{1}{1 - F(x)}\right)\right] \tag{5.65}$$

is plotted against the logarithm of time. The relation between the two quantities follows from

$$\ln\left[\ln\left(\frac{1}{1 - F(x)}\right)\right] = b\ln(x) - b\ln(\mathrm{t}). \tag{5.66}$$

Thus the shape parameter b is the slope of the straight lines in the Weibull plot. Different slopes at different loads (powers) indicate different mechanism of failure (see Fig. 5.19). An acceleration of the aging process and a subsequent evaluation by the Arrhenius relationship can only be used if the shape parameters of Weibull plots at the different loads are the same. Eq. (5.64).

Ideally a lifetime measurement discovers the influence of characteristic manufacturing or operating data on the laser performance. Most challenging is a pulse

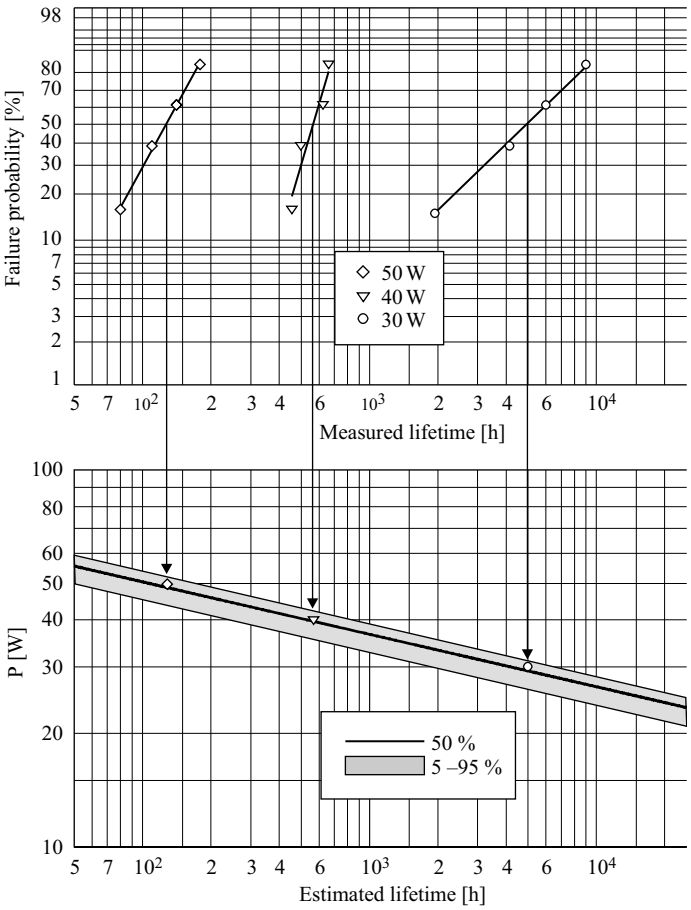

FIGURE 5.19. Top: Weibull plot for different output powers. At each power level four laser diodes were used. Each failure of a diode results in a point whose horizontal position indicates the time until failure. The failure rate follows from the regression of the data. Bottom: Woehler diagram for the estimation of the maximum operation power that can be used for an intended lifetime, if a certain probability of failure is accepted. The diagram is generated from the data obtained by the Weibull plots. For example the Weibull plot for 50 W indicates a failure rate of 50% for a lifetime of about 120 h

mode operation with the pulse frequency corresponding to the thermal time constant of the substrate. This causes mechanical stress depending on the applied current (power). This scheme of operation can be analyzed using the Woehler diagram plotting the power (load) versus the number of pulse cycles. In the case of a fixed frequency the number of pulse cycles is proportional to the time of the measurement. Figure 5.19 shows a Woehler diagram of single quantum well arrays obtained from the three Weibull graphs under different powers shown in the top. This allows us, for example, to calculate the maximal power for a lifetime of

10,000 h with a likelihood of 95% (here about 24 W). Of course, this model is only valid for pulsed mode operation. It also fails in the permanent strength domain where the slope of the Woehler graph becomes zero due to absence of failures at low stress levels.

5.10. Laser Safety

According to the International Standard IEC 60825-1 lasers are classified with respect to their hazard potential. Based on the wavelength and on the duration of the emission, threshold intensities, called MPE (maximum permissible exposure) are given for a risk-free illumination of the human's eye or skin. Since lasers used in material processing require high-power densities they automatically drop into the highest category: class 4 (in continuous-wave mode the power exceeds 0.5 W). By shielding the beam delivery and the processing area, the risk has to be reduced to a safe level, which means class 1 must be achieved for the complete system. Inside the machine, on the illuminated side of the laser guards the intensity may exceed the MPE whereas outside of the laser area the level has to be observed strictly. As the laser beam propagates, the intensity is reduced inversely with the square of the distance to the beam waist (compare Eq. 5.36). The distance to the beam waist at which the safe MPE level is reached is called NOHD (nominal ocular hazard distance). The NOHD defines the distance to the laser source where access should be restricted to experienced people only. In this laser control area the human risk has to be assessed with respect to the direct beam as well as to reflected and scattered radiation. The risk assessment should consider a single foreseeable source of failure, too.

In the visible and near infrared region, the skin can tolerate a great deal more exposure to laser energy than the eye. This is mainly due to the focusing effect of the cornea and the lens which increases the power density impinging on the retina up to 300,000 times. This, however, is only valid of visible radiation as well as the near ultraviolet and the near infrared region whereas far infrared radiation is completely absorbed in the outside layer of the cornea.

The minimum spot size a laser beam might generate on the retina depends on the propagation ratio M^2 and the width of the waist as well as the actual width at the pupil.

What is specific for diode lasers?

High-power diode lasers emit at wavelengths in the near infrared, predominantly between 800 and 1,000 nm. In this spectral range most of the radiation reaches the retina and may severely damage the eye by causing retinal burns, but it also affect the lens, causing cataracts. Especially with diode lasers adequate eye protection is a priority with all safety instructions when the MPE is exceeded. It is very important to adapt the goggles to the laser wavelength and the power density of the accessible beam.

Generally, the beam of a high-power diode laser is not diffraction limited and should be treated as an extended source. This is expressed by a relaxation factor

Table 5.1. Nominal ocular hazard distance NOHD

Parameter	Unit	Nd:YAG	Diode Laser
Power	kW	4	4
Wavelength	μm	1.06	0.808
M^2	-	36	700
Beam-parameter product	mm ∗ mrad	12	180
MPE	W/m^2	50	15
NOHD of free propagating beam	m	8400	1000
NOHD of focused beam	m	50	46

C_6 to the MPE that can vary between 1 (diffraction limited, $M^2 = 1$) and 100/1.5 = 66.7 for a large source ($M^2 \gg 1$).

Unfortunately, the IEC standard about laser safety is not based on the second-moment definition of the beam width as explained in the ISO standards. IEC defines the beam width at 1/e of the full maximum. The focusing of the eye is not calculated in terms of the M^2 and the waist position of the laser but by the angular subtense (the angle under which the beam is seen from human's eye).

It is interesting to compare a diode laser with a typical Nd:YAG laser for material processing at a power level of 4 kW with respect to the potential hazard caused by the free propagating beam, the focused beam, and the scattered beam. Table 5.1 gives an estimation which is based on the following simplified calculation:

$$\mathrm{NOHD} = \mathrm{W} \cdot \sqrt{\mathrm{P}/(\pi \cdot \mathrm{MPE})}, \tag{5.67}$$

where P denotes the power, $W = 2/\Theta$ for the collimated beam (Θ beam divergence), $W = 2{*}f / D$ for the focused beam (f, focal length; D, beam diameter on the lens), and W = 0.71 for the scattered beam.

The laser hazard distance is nearly 10 times larger for the Nd:YAG whereas there is no significant difference for the focused beams as this NOHD only depends on the numerical aperture of the focusing optics. Although even experts still believe that diffuse reflections of the diode laser are not dangerous the calculations show the opposite.

5.11. Table of International Standards related to Laser Metrology

The progress of the international standards is shown in Table 5.2, reflecting the status of 2004 (more recent data may be found under http://isotc.iso.org for documents developed by committee ISO/TC172/ SC9):

Table 5.2. International standards for lasers and laser-related equipment*

ISO standard		Status/month of publication
11145	Vocabulary and symbols	Nov. 2001, amendment in preparation
11146	beam propagation ratios	1999, to be replaced
11146	-1 Stigmatic and simple astigmatic beams	Sept. 2004
	-2 General astigmatic beams	Oct. 2004 FDIS
	-3 Beam classificatuion (background information)	Feb. 2004 Technical Report
11554	Energy and temporal characteristics	Apr. 2003, in revision
11670	Beam positional stability	Apr. 2003, Corrigendum May 2004
12005	Polarization	Apr. 2003
13694	Power density distribution	Apr. 2000
13695	Spectral characteristics	June 2004
15367	-1 Laser beam wavefront, terminology	Oct. 2003
	-2 Laser beam wavefront, Shack-Hartmann sensors	June 2004 FDIS
17526	Lifetime of lasers	June 2003

* DIS = draft international standard; FDIS = final draft international standard.

5.12. Practical Hints for Measurements

General remark: Please confirm that the measuring equipment (especially for the beam width) complies to the cited standards, because some do not despites assurances by the manufacturer.

Before measuring the beam widths and propagation ratios –

- The laser should be warmed up as specified by the manufacturer.
- Dust, smoke, and gases should not affect the beam path.
- The laboratory z-axis should be aligned with the beam axis.

First check the symmetry of the beam. If the ratio of the beam widths in the principal axes $d_{\sigma x}/d_{\sigma y}<0.87$, only three independent parameters are needed. For example, this is the case for beams leaving a symmetric fiber.

If the beam is not circular, it shall be tested for general astigmatism as described in ISO 11146-2. Beams whose principal axis rotate more than 10° during propagation are general astigmatic. But even non-rotating beams may be general astigmatic (hidden general astigmatism). In this case the symmetry has to be broken by inserting a cylindrical lens following the instructions of ISO 11146-2 (see section 5.4.2).

Truncation of the beam by detector size or limiting apertures should be avoided. The minimum size is approximately 1.6 times the local beam diameter d_σ in order to keep the power, respectively, energy clipping, below 1%.

Noise and background radiation should be corrected (see ISO/TR 11146-3).

High spatial resolution is necessary, especially for diffracted beams.

The detector and amplifier should have a high signal-to-noise ratio. The linearity should be checked and the damage threshold observed. Otherwise an attenuator should be employed. Any wavelength, polarization, and angular dependency and non-uniformity as well as thermal effects shall be corrected by calibration.

The reflection of a wedged glass substrate is a good sample of the beam carrying about 4% of its power. Neutral density filters should be used for pre-attenuated beams only as they tend to form thermal lenses.

Propagation measurements require power density profiles over at least six Rayleigh lengths, including the beam waist. If the waist is not accessible an artificial waist should be generated by focusing the beam through an aberration-free optical system. Then the distance from the focusing element to the artificial waist shall be determined. Together with the known focal length this allows the calculation of the original beam waist position and Rayleigh length.

The measured power density distributions shall be evaluated on the basis of the second-order moments. As explained in section 5.6.5, the integration limits shall be determined by iteration. Other definitions of the beam dimensions may cause strong deviations to the hyperbolic fit, especially in a range close to the beam waist.

Often alternative methods are used to measure the beam widths, such as "variable aperture," "moving-knife-edge," or "moving-slit." Ideally the second-order beam widths are calculated from the measurement data as explained in this chapter. Sometimes the beam width is calculated from clip levels (power transmittance levels), for example, twice the distance between the knife-edge positions where 16% and 84% of the beam power passes the knife edge. Although diameters d_i based on these methods strongly depend on the shape of the power density distribution, correlation factors c_i between these and the second moment diameter d_σ can be introduced.

$$d_\sigma = \frac{d_i}{M_i}\left[c_i\left(\sqrt{M_i^2} - 1\right) + 1\right] \tag{5.68}$$

According to ISO/TR 11146-3 these correlation factors c_i are 1.14 for the variable aperture, 0.81 for the moving knife-edge, and 0.95 for the moving slit method, respectively. The correlation factors are verified for $M^2 < 4$.

The square root of the beam propagation ratio is given by

$$\sqrt{M^2} = c_i\left(\sqrt{M_i^2} - 1\right) + 1 \tag{5.69}$$

where M_i^2 denotes the propagation ratio measured by the alternative method.

References

[5.1] Niziev VG, Nesterov AV (1999) Influence of beam polarization on laser cutting efficiency. Journal of Physics D 32, 1455.
[5.2] Olsen FO (1980) Cutting with polarized laser beams. DVS Berichte 63, 197.
[5.3] Siegman AE (1986) Lasers. University Science Books, Mill Valley, CA.
[5.4] Svelto O (1998) Principles of Lasers, 4th Edition. Plenum Press, New York.
[5.5] Mandel L, Wolf E (1995) Optical Coherence and Quantum Optics. Press Syndicate of the University of Cambridge.

[5.6] Bastiaans MJ (1978) The Wigner distribution function applied to optical signals. Optics Communication 25, 26.
[5.7] Wigner E (1932) On the quantum correction for thermodynamic equilibrium. The Physical Review 40, 749.
[5.8] Mecklenbräuker W, Hlawatsch F (eds). (1997) The Wigner Distribution, Elsevier Science B.V., Amsterdam, Netherlands.
[5.9] Schleich WP (2001) Quantum Optics in Phase Space. Wiley-VCH, Berlin.
[5.10] Bastiaans MJ (1979) Wigner distribution function and its application to first-order optics. Journal of the Optical Society of America 69, 1790.
[5.11] ISO 11146-1:2004 (2004) Lasers and laser-related equipment – Test methods for laser beam widths, divergence angles and beam propagation ratios – Part 1: Stigmatic and simple astigmatic beams. International Organization for Standardization.
[5.12] ISO/FDIS 11146-2:2004 (2004) Lasers and laser-related equipment – Test methods for laser beam widths, divergence angles and beam propagation ratios – Part 2: General astigmatic beams. International Organization for Standardization.
[5.13] ISO/TR 11146-3:2004 (2004) Lasers and laser-related equipment – Test methods for laser beam widths, divergence angles and beam propagation ratios – Part 3: Intrinsic and geometrical laser beam classification, propagation and details of test methods. International Organization for Standardization.
[5.14] Nemes G (2002) Intrinsic and geometrical beam classification, and the beam identification after measurement. Proceedings of the SPIE 4932, 624.
[5.15] Siegman AE (1990) New Developments in laser resonators. Proceedings of the SPIE 1224, 2.
[5.16] Neubert BJ, Eppich B (2005) Influences on the Beam Propagation Ratio μ^2. Optics Communications 250, 247.
[5.17] Siegman AE (1993) Analysis of laser beam quality degradation caused by quartic phase aberrations. Applied Optics 32, 5893.
[5.18] Amarande S, Giesen A, Hügel H (2000) Propagation analysis of self-convergent beam width and characterization of hard-edge diffracted beams. Applied Optics 39, 3914.
[5.19] ISO 11670:2003 (and Technical Corrigendum 1:2004) (2003) Lasers and laser-related equipment – Test methods for laser beam parameters – Beam positional stability. International Organization for Standardization.
[5.20] ISO 15367-1:2003 (2003) Lasers and laser-related equipment – Test methods for determination of the shape of a laser beam wavefront – Part 1: Terminology and fundamental aspects. International Organization for Standardization.
[5.21] ISO 17526:2003 (2003) Optics and optical instruments – Lasers and laser-related equipment – Lifetime of lasers. International Organization for Standardization.
[5.22] Gertsbakh I (2000) Reliability Theory. Springer.

6
Diode Laser Systems

Friedrich Bachmann

This section describes different diode laser systems for several special applications in the materials processing area. All these systems are based on diode laser bars, which are combined in a special way to provide the best laser beam and optimal controllability for a distinct application. The applications with these systems are described in Chapter 7.

6.1. Introduction

As described in the previous sections, high-power diode lasers mainly consist of a high number of individual emitters. Several techniques for forming and combining the laser radiation from such individual emitters are available today and have been described and discussed in detail. However, the (incoherent) combination of these individual laser beams and the beam quality of the individual emitters are limiting factors if high brilliance is desired; thus, a very prominent goal of scientists is the improvement of beam quality and power of high-power diode lasers. The results of such investigations are described in section 6.2.

On the other hand, the "modular" character of a diode laser, i.e., the fact, that a high-power diode laser is consisting of so many individual laser sources, offers a unique opportunity, namely to combine such individual sources (a bar or even a stack) in a very special way, which is adapted to the application. As an example, bars or stacks might be combined to a long line or a polygon, to form an annular beam as schematically depicted in Fig. 6.1. Such systems are described in section 6.3.

6.2. Multi-Purpose Diode Laser Systems

The application of lasers in materials processing is in most cases, e.g., for cutting and deep penetration welding, related to the high energy density, which can be generated from a laser source. As is well known, high-power diode lasers are superior to the conventional gas and solid-state lasers, among other reasons, because of their high electrical to optical efficiency and their small size; but because of the

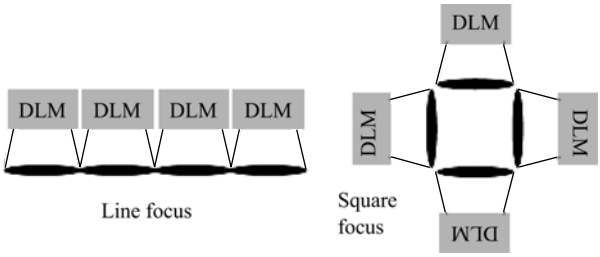

FIGURE 6.1. Scheme of a line focus (left) or square focus (right) generated from individual diode laser modules (DLM)

TABLE 6.1. Overview of the high-brilliance systems

Laser system	Code	Section
Optical cutting plotter with 100 W	Cutting plotter	6.2.1
Kilowatt system with broad area emitters	kW-stack	6.2.2.1
Kilowatt system with p- and λ-coupling	kW-pol & λ-stack	6.2.2.2
Kilowatt system with slow-axis collimation	kW-slow-col	6.2.2.3
Fiber coupled kilowatt system	kW fiber coupled	6.2.3
High-brightness system with 100 W	100 W high-brightness	6.2.4
High-brightness kilowatt system	kW high-brightness	6.2.5

facts described in Chapter 4, the beam quality and thus, the power density which can be reached at the workpiece are limited. Several methods to improve that situation have been investigated or are described in the literature (see Chapter 4). The systems described in this section are all driven by the efforts to reach highest brilliance possible using the semiconductor material available. Table 6.1 gives an overview over the high-brilliance systems as described in section 6.2.

6.2.1. Optical Cutting Plotter with 100 W Output Power

Alexander Knitsch and Reinhard Ifflaender

As described in Chapter 4.6, the beam quality of high-power diode lasers is limited. Thus, the application for materials processing is restricted to certain applications which do not require extremely high focusability. Nevertheless, improvement of brilliance is a main target in the high-power diode laser development. Progress in the epitaxy of the semiconductor diodes, in mounting, and in heat sink techniques has led to systems which now allow to consider laser diodes for direct applications. In the following, a laser system with a moderate power of 100 W and an optimized beam quality is described, which uses commercially available state-of-the-art broad-area emitter diode laser bars.

6.2.1.1. Layout and Design of the System

To optimize output power and beam quality simultaneously, the radiation from six linearly polarized diode laser bars of three different wavelengths were superimposed by wavelength and polarization coupling (see Chapter 4.1.2), as shown in Fig. 6.2. Thus, with a power of 30 W per bar and no optical losses up to 180 W optical power could be expected.

Radiation from each single emitter of the bars is collimated in the fast axis with cylindrical micro-lenses of high numerical aperture (see Chapter 4.2.1). A micro-cylindrical array then collimates the slow-axis of each emitter (see Chapter 4.2.5); this results in a series of nearly parallel beams close to each other, i.e., with a filling factor close to one. Each laser diode bar has a selected wavelength and is nearly linearly polarized.

The parallel beam arrays of the laser bars with the wavelengths 808, 910, and 980 nm are first spectrally superimposed by dielectric edge filters. After a double pass through a λ/4 retardation plate, the polarization of one of the spectrally mixed beam arrays is rotated by 90°. Both, now differently polarized beams are then combined by means of a polarization beam splitter. The beam quality of the resulting beam array is roughly the same as the beam quality of one single bar; the power, however, is sixfold the power of a single bar if losses are neglected.

As is well known, the slow-axis of each single emitter shows a much lower beam quality than the fast-axis. This will be compensated with a special step mirror

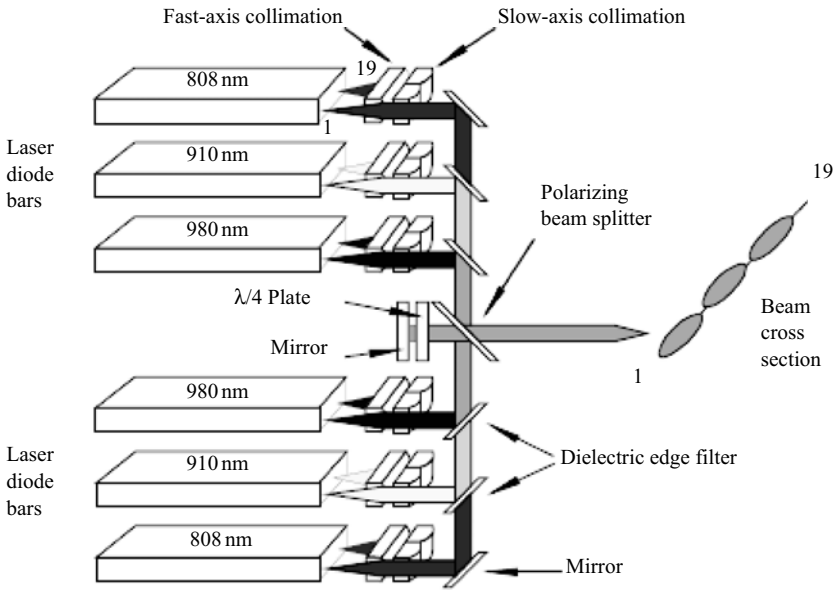

Figure 6.2. Optical design to superimpose and arrange laser radiation from bars with different wavelengths and polarization

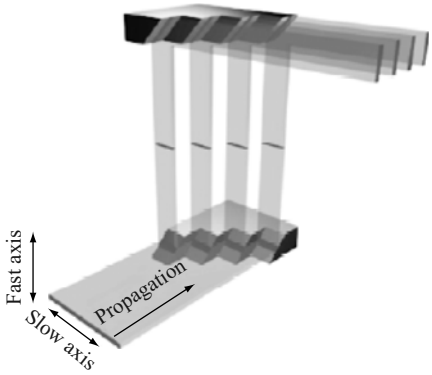

FIGURE 6.3. Rearrangement of the rays to achieve nearly equal beam quality in both axes by the mean of a step mirror arrangement [6.1]

(see Chapter 4.5.3). To match the beam quality in both axes the linear array of the 19 single beams is rearranged by two step mirrors [6.1]. Fig. 6.3 shows the setup with two step mirrors. Each of the 19 beams from each bar has a beam quality of about 0.5 mm $*$ mrad in the fast axis and a beam-parameter-product is about 0.5 mm $*$ mrad (fast axis) and 19 $\times$ 12 mm $*$ mrad (slow axis), respectively. Stacking all rays in the fast axis perfectly together would increase the beam-parameter-product to 19 $\times$ 0.5 mm $*$ mrad = 9.5 mm $*$ mrad and reduce the beam-parameter-product in slow direction to that of a single emitter, i.e., 12 mm $*$ mrad. So the resulting combined beam has a beam quality of 12 mm $*$ mrad in one axis and 9.5 mm $*$ mrad in the other. This is sufficiently below the 15 mm $*$ mrad, the target beam quality for this unit. Unfortunately, as will be shown later, due to the imperfections in lenses, mirrors, and adjustment, it is nevertheless not possible to achieve this low value in the beam-parameter-product with a broad area laser setup.

Even if the beam quality (i.e., the beam-parameter-product) is now almost symmetric in both axes, the beam still differs in size and divergence in the two axes. With two single cylindrical negative lenses and a spherical collimating lens, which form a telescope, the beam is expanded and optical differences in both axes are compensated for, as far as possible. In the expanded and now parallel beam a dichroitic mirror for observation can be inserted. Precise optics, corrected for all wavelengths, then focus the beam onto the workpiece. Figure 6.4 shows a sketch of the entire optical arrangement.

6.2.1.2. Optical Simulation

The optical beam was simulated in two steps throughout the whole optical system with a non-sequential ray-tracing program. Starting with the emission characteristic of one single emitter, the rays from all emitters to a plane just behind the step mirrors were traced. The results give some ideas about possible efficiency and focus diameter.

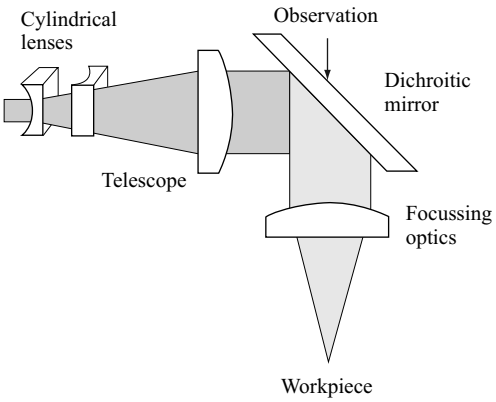

FIGURE 6.4. Optical setup to focus the diode beam at the workpiece

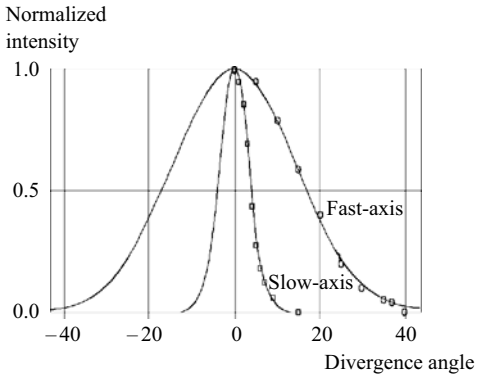

FIGURE 6.5. Measured (marks) and simulated (lines) intensity distribution of the two axes

The normalized intensity distribution of a single emitter in the far field can be well described by the equation

$$J_x = \exp\left(-\frac{\theta_x}{7^\circ}\right)^2 \qquad \text{for the slow-axis and}$$
$$J_x = \exp\left(-\frac{\theta_y}{29^\circ}\right)^2 \qquad \text{for the fast-axis.} \tag{6.1}$$

In Fig. 6.5 the measured and fitted angular intensity distribution of a single emitter for both axes is shown. Figure 6.6 shows the normalized calculated divergence at the reference plane and the measured divergence of the combined beam at a diode current of 50 A. The calculated divergence in the fast axis is much smaller than the measured since no lens and alignment errors are taken into account in the model.

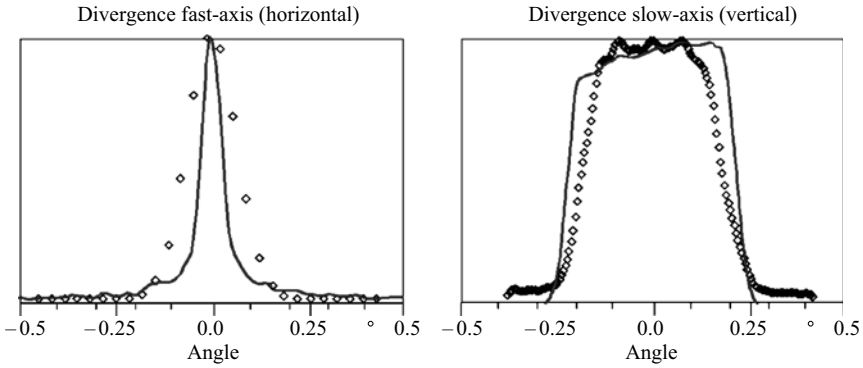

FIGURE 6.6. Measured (marks) and calculated (lines) angular intensity distribution in the two axes behind the step mirrors

TABLE 6.2. Calculated spot size, divergence, and beam quality in the focal plane at the workpiece surface

Axis	Size	Divergence	Angle	Beam quality
Fast	0.09 mm	227 mrad	13°	10 mm ∗ mrad
Slow	0.2 mm	262 mrad	15°	27 mm ∗ mrad

In a second step the rays starting from the first reference plane were traced through the optics to the workpiece surface. The smallest spot size was achieved with a telescope lens of 200 mm and the focusing lens with 100 mm focal length. Table 6.2 gives the calculated values for spot size, divergence and beam-parameter product. The beam quality is limited by the slow-axis with a value of 27 mm ∗ mrad.

6.2.1.3. Optical and Mechanical Realization

The optical setup of the laser module is shown in Fig. 6.7. Commercial broad-area diode laser bars are assembled with the water-cooled heat sink. Each set of three diode bars of three different wavelengths are stacked together with a common cooling. Precise soldering of the bars onto the micro-channel cooler is extremely important [6.2]. The so called *smile,* deviations of the emitters from a straight line, must be minimized whatsoever and very exact mounting must be performed, as only a difference of one micron in height will result in half of the beam quality. As described in detail in Chapters 4.2 and 4.4 very strict conditions have to be observed for the selection, quality and mounting of the fast- and slow-axis collimation micro-optics as well as for the stacking. The step mirrors are made from copper and coated with a highly reflective coating; nevertheless, water cooling was found to be necessary for thermal stability of the system.

The laser module containing water and power connections is combined with the optical system as shown in Fig. 6.8. A binocular with a cross hair allows the

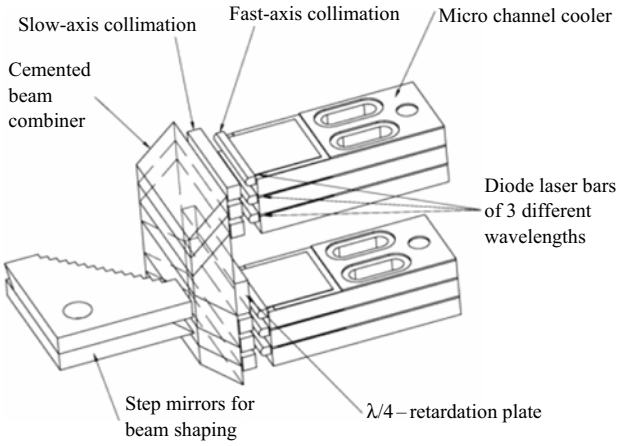

FIGURE 6.7. Setup of the laser module

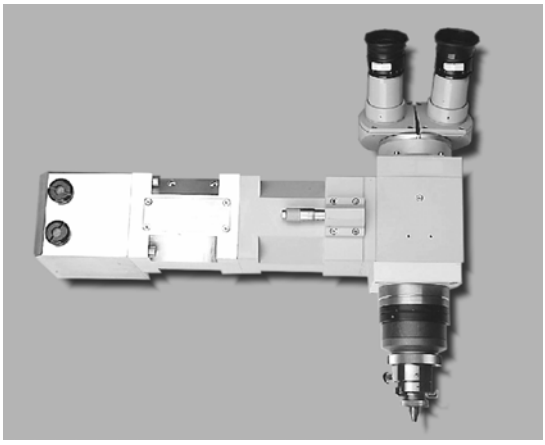

FIGURE 6.8. Diode laser module with beam expander, microscope, and processing optics

alignment of the workpiece and the observation of the application process. The optics can be equipped with a gas jet nozzle.

6.2.1.4. Characterization of the System

The dependence of laser power at the workpiece from diode laser injection current shows a threshold at about 7 A and a linear increase of output power to 140 W at 50 A. Laser power, electrical characteristics, spot size, and beam quality are summarized in Table 6.3.

As stated in Chapter 4 each individual component for beam forming or beam combination generates losses in power. A detailed investigation, shown

Table 6.3. Performance parameters of the diode laser device (All values were measured at the workpiece plane and at a diode current of 50 A)

Laser power	Spot size	Beam quality	Opt.-el. efficiency
140 W	0.2 × 0.25 mm	20 × 22 mm ∗ mrad	23 %

Table 6.4. Optical efficiency of the optical components at the different wavelengths

	808nm	910nm	980nm
Fast-axis collimation lens	0.95	0.95	0.95
Slow-axis collimation lens	0.86	0.86	0.86
Average of chroitic coatings	0.70	0.80	0.90
Reflecting polarization coating	0.99	0.99	0.99
Transmitting pol. coating (incl. λ/4 plate)	0.96	0.93	0.93
Polarization degree of the laser bars	0.75	0.85	0.90
Step mirrors	0.86	0.86	0.86
Total efficiency	0.36	0.46	0.54

in Table 6.4, gives the efficiency for all optical components. It can be clearly seen that the total efficiency is significantly determined by the polarization degree of the laser bars and by the dichroitic filters.

Cutting application tests have been successfully performed: Mild steel up to 1 mm thickness was cut with a power of 125 W with the assistance of oxygen. Details can be found in Chapter 7.2.2.

6.2.2. Free-Space Propagation Systems in the kW-Range

Thomas Brand

In this section three diode laser systems representing the use of diode laser bars at different development stages are described. All systems are based on broad area diode laser bars, but with improved brightness of the individual emitters. Such bars consist of individual emitters with a width of the emitting area in the range of 150–200 μm and a pitch between the emitters of 400 and 500 μm. Furthermore, the systems differ on increasingly sophisticated beam forming and beam combination techniques.

6.2.2.1. Diode-Laser Systems with Broad-Area Emitters

The first approach to build up a high-power diode laser system for direct application is to use a stacked array of diode laser bars without any sophisticated

beam-shaping optics. Of course, as with every effort to employ diode lasers as a source, the highly divergent fast-axis radiation has to be collimated. Therefore, the beam of each individual bar in the stack is collimated in fast direction with an aspheric cylindrical lens with a high numerical aperture (see Chapter 4.2). The collimation of the nearly diffraction limited emission of the fast direction with an optimized fast-axis collimation (FAC) lens can reduce the divergence (half) angle to a value of approximately 2–3 mrad with a full beam height ($1/e^2$) of below 0.8 mm.

In a stack, the fast-axis beam-parameter-product, as well as the output power, scales with the number of bars applied, i.e., the total height of the "source." The laser bars mounted on micro-channel-cooled heat sinks can be stacked on top of each other. According to the thickness of the heat sinks the center to center pitch of the bars is 1.8 mm. This technique makes it possible to build up stacks of up to several ten bars (see Chapter 4.4).

Since the collimated beams emitted from the laser bars fill less than 50% of the total aperture of the stack in the fast direction, methods to combine two stacks by filling the gaps are accomplished ("spatial coupling"; see Chapter 4.3.3 for details). Matched stacks of micro-prisms or segmented reflective mirrors are typical means for coupling one stack into the other without changing the beam-parameter-product $w_0 \times \theta_0$. One large cylindrical lens is collimating the whole stacked arrays in slow-axis direction.

The laser system was realized with bars providing a maximum power of 40 to 50 W, with a fast-axis divergence (half angle) of 35° to 40° and a slow-axis divergence (half angle) of 5° to 7°. The bars have an emitter width of 200 μm and a pitch or 400 μm. Two stacks of 20 laser bars each are superimposed with spatial coupling, to form a single rectangular beam with a dimension of approximately $10 \times 36\,\text{mm}^2$. After that, the divergent slow direction is collimated with an $f = 150$ mm cylindrical lens (positioned in the focal distance from the stack). Because of the slow-axis divergence of up to 90 to 100 mrad, the beam diameter is increased by a factor of three to four at the position of the collimating slow-axis lens. This leads to a more symmetrical profile of 30 to 40 $\times$ $36\,\text{mm}^2$. The collimated beam is then focused to the working plane with a conventional spherical lens system. However, since the divergence in fast and the slow axis direction are so much different, the focus dimensions have an aspect ratio of 1:8 to 1:20, depending on the beam quality of the stack and the design of the optics.

Figure 6.9 summarizes the optical design of this laser system: The two superimposed stacked arrays on the left hand side are collimated in slow direction with the large cylindrical lens in the center of the drawing. Focusing is achieved with the spherical lenses. The small square gives the position of the focal plane. The beam shape in the focal plane is a line focus of approximately 4 mm $\times$ 0.5 mm, as shown in the insert in Fig. 6.9. The optical output power plotted versus the diode current (P-I-characteristics) shows the typical behavior with a threshold at about 13 A and then a linear increase to about 1,600 W at 55 A.

Clearly visible is one of the key advantages of high-power diode lasers from the head of such a laser as shown in Fig. 6.10: This head, which provides

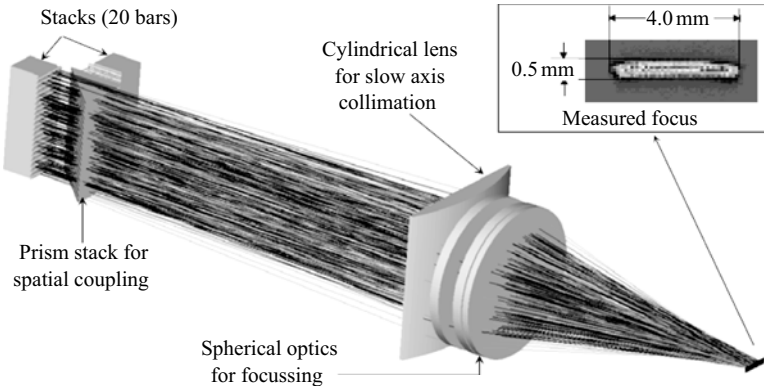

FIGURE 6.9. Ray-tracing visualization of the kilowatt diode laser system with broad-area emitters; the insert shows a cross section of the beam in the focal plane

FIGURE 6.10. Commercial version of the 1.5 kW diode lasers system with broad-area emitters

more than 1.5 kW laser power has a size of just 350 × 120 × 120 mm and a weight of 8 kg.

6.2.2.2. System with Polarization Coupling, Wavelength Coupling, and Beam Rearrangement

For many applications, especially if fiber coupling is desired, it is obvious that the beam properties of the laser system described above are unsuitable. The beam quality is apparently inadequate to fit into a fiber. Most requirements of surface treatment can be met with the aspect ratio of the beam given by the laser described in section 6.2.2.1. But this is no longer valid for welding and other applications where a higher brightness or a more symmetrical beam profile is necessary. All efforts to

couple the diode laser power into a fiber must fail if the beam-parameter-product of the laser is insufficient. This means, not only the beam dimensions have to fit the fiber core diameter, but also the divergence angle must fit into the numerical aperture of the fiber. In order to realize that, the beam emitted by a stacked array must be rearranged and shaped.

A typical beam-parameter-product of a standard stacked array or a superposition of stacked arrays is about 400–500 mm $*$ mrad in the slow direction, whereas fast direction depends on the height of the stacks. The largest fiber available at the moment is a 1.5-mm core diameter silicone clad fiber with a numerical aperture of 0.37. This corresponds to a beam-parameter-product of about 277 mm $*$ mrad for a circularly symmetric laser beam to be accepted by the fiber.

If we suppose a square (rectangular) shape of the beam, the beam-parameter-product in either direction should be lower than approximately 180–190 mm $*$ mrad to fit into the fiber. Applying these data to the slow axis, it seems to be appropriate to use a beam shaping scheme that reduces the beam-parameter-product (e.g., the aperture $w_{0,\mathrm{slow}}$ of the stack) to one third, for example by "cutting" the aperture into to three equal parts. After this, the three parts are stacked on top of each other to form a beam that is three times as high as before in fast direction and has a width of one third of the width of a bar in the slow direction. Thus, the beam-parameter-product in slow-axis direction is reduced to one third, whereas the one in fast-axis direction is increased by a factor of three.

Using the limiting factor of the core diameter and the numerical aperture of the fiber, the height of the stack and the number of bars that can maximally be used in one stack can be determined. While the slow direction is reduced from 450 mm $*$ mrad to 150 mm $*$ mrad, as described above, the fast direction was allowed to increase its height and thus, the beam-parameter product, by the factor of three to a value that should not exceed 180 mm $*$ mrad. Since the divergence angles in either direction have not been affected at all so far, one can conclude that the original beam-parameter product of the stacked array must not be higher than 60 mm $*$ mrad in the fast direction. Assuming a (half)-divergence angle of 5 mrad of the collimated fast direction, the full height of a stack must be below approximately 24 mm, corresponding to 10–12 laser bars on top of each other if a height of 1.8 mm is assumed for the heat sink. To increase power further while maintaining the beam quality polarization coupling (see Chapter 4.3.1.) and wavelength coupling (808 and 940 nm, see Chapter 4.3.2) are also employed for this system. A sketch of the entire beam forming, combination and arrangement system is schematically depicted in Fig. 6.11.

The crucial point is, that even though the beam dimensions after the rearrangement are different in slow and fast direction, the beam-parameter-product, i.e., the beam quality or focusability is nearly symmetric in both axes, which is of course favorable for the coupling into an optical fiber.

Still the characteristics of the diode bars are maintained in this optical design: as shown in Fig. 6.12 the beam profile has a top-hat distribution in the slow direction (y-direction) and a near Gaussian distribution in fast direction (x-direction). The intensity distribution has a more or less rectangular shape of 1.3 $\times$ 0.8 mm. With

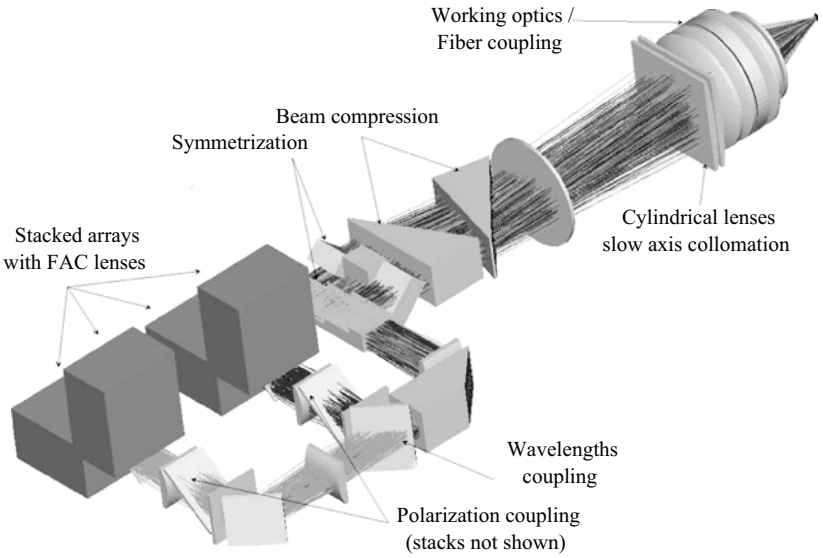

FIGURE 6.11. Beam shaping arrangement [6.3]; symmetry is achieved by "cutting" the slow-axis emission into three parts and rearranging on top of each other in the symmetrization section

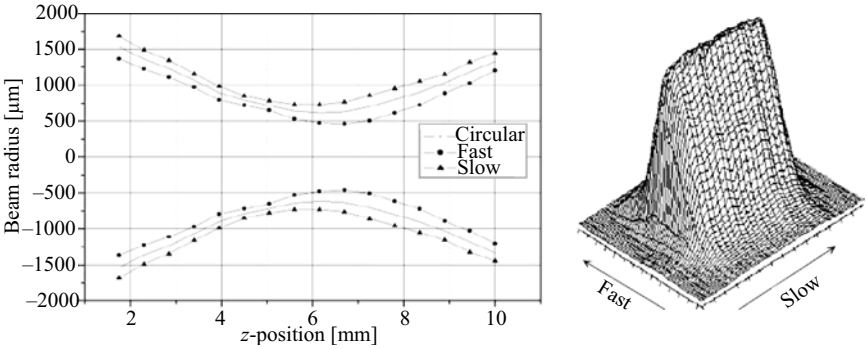

FIGURE 6.12. Measurement of the beam of the laser system passing through the focal plane of the $f = 66$ mm optics

a focal length of the coupling optics of 66 mm the beam matches into the 1.5 mm core diameter and 0.37 NA optical fiber. A photograph of the laser head, which has a size of 540 mm × 225 × 175 mm and a weight of 18 kg is presented in Fig. 6.13.

6.2.2.3. Laser system with Additional Slow-Axis Collimation

To couple 2 kW laser power into a high power 1.2 mm core-diameter silica/silica fiber with a numerical aperture of 0.22, further reduction of the beam-parameter

FIGURE 6.13. Laser system with polarization and wavelength coupling as well as with beam rearrangement; fiber coupling is possible but not shown here

product is necessary. Compared to the laser system described in section 6.2.2.2, this is a further improvement of the beam quality by a factor of two.

Taking the beam-parameter-product of the full laser bar width in the slow direction and the height of a stacked array as a whole in the fast direction, the best result one can achieve after beam shaping, is a value that corresponds to the square root of the product of the slow- and the fast-direction beam quality. This value does not consider the fill factor of the laser bars because the entire front face of the stack is regarded as the source of the radiation. To reduce the beam-parameter-product of a stack further, one has to take measures to reduce for example the initial value of the beam divergence but without increasing the width of the source. This can be done by collimating the slow-axis direction of each broad area emitter on the laser bar individually with the help of a micro-optical slow-axis array (see Chapter 4.2.5).

As the beam-parameter-product is constant, the divergence angle of the radiation of a single emitter after collimation θ_f with a cylindrical lens depends on the size of the source and the focal length of the lens. However, as can be easily shown, with an emitter structure used in the two systems above (200-μm emitter size with a pitch of 400 μm) it is not possible to reduce the slow-axis divergence with a collimation of the single emitters significantly. The reason for this is, that the divergence angles of neighboring emitters limit the maximum distance (i.e., the focal length of the collimating cylindrical lens) where the slow-axis array can be placed without overlapping of adjacent rays (see Chapter 4.2.4, Fig. 4.21). Therefore, for significant improvement, one has to switch to narrower emitters or larger pitch or both; for example bars with a 150 μm emitter structure and a pitch of 500 μm are used in this system. Of course the power which can be extracted from such a bar is reduced due to the smaller fraction of emitting areas on the facet (150 μm/500 μm (30% emitting area) compares to 200 μm/400 μm (50% emitting area)) as long as same technology is used. Thus, in this case the target for the bars is to reach about same optical data (about 30° half-angle divergence in fast direction and about 10° half-angle divergence in slow direction), but about 40% higher power (of course at the same lifetime) to compensate for the geometrical losses. Using such bars an optimized slow-axis collimation lens array is able to reduce the slow-axis divergence and hence the beam-parameter-product by at least a factor of two and increasing the fill factor of the slow direction at the same time, i.e., maintaining the beam width.

The development of the system described in section 6.2.2.2 has shown that the beam-parameter-product in the fast direction is rather critical to alignment accuracy. Thus, in order to improve the beam-parameter-product also in the fast direction, the alignment tolerances of the stacks were reduced by high precision positioning of the micro-lenses, leading to a half-angle divergence of about 3 mrad (compared to 5 mrad in the system before). Both measures enable us to reach a resulting beam quality twice as good as before. With several minor optical changes in the beam propagation configuration and a newly designed working optic (that fits the numerical aperture of 0.22), the laser was modified to allow for coupling the diode laser power of 8 stacked arrays into the 1.2-mm 0.22-NA fiber.

The beam-parameter-product of the laser system was measured before the fiber coupling to be 115 mm $*$ mrad at an output power of 3.1 kW from this laser. Size and form of the laser head is almost same as in Fig. 6.13.

6.2.3. Fiber-Coupled System in the kW Power Range

Klaus Stolberg and Veit Blümel

Another approach, which allows more flexibility for the beam-forming and beam-combining technology as mechanical restrictions are not as severe as in the systems described in section 6.2.2 is the purely fiber-coupled kilowatt system described in the below.

6.2.3.1. Layout and Design of the System

As the basic element 25 individual laser bars are stacked vertically to reach the kilowatt power region. Since it is absolutely necessary to isolate emitted beams from the bars for defined beam transformation, fast-axis collimation lenses (see Chpater 4.2.1) are assembled. To enhance the brightness and thus, the total power at constant beam quality further, wavelength multiplexing, combining 808- and 940-nm lasers as well as polarization multiplexing are employed. Both semiconductor materials are horizontally polarized with respect to the PN-junction (TE-polarized), so one stack of each wavelength was assembled mechanically with 90° turn to get a perpendicular orientation (Fig. 6.14). Multiplexing of polarization directions was performed with dielectric polarization multiplexers; “PMX” and wavelength multiplexing was realized with the dielectric wavelength multiplexer “WMX.” In the result a non-symmetrical divergence angle of 17.5 mrad (fast) $\times$ 200 mrad (slow) and a cross section of 44 mm (fast) $\times$ 10 mm (slow) have been achieved (see Fig. 6.15, left).

To make the resulting bundle of individual beams symmetric the so-called “director-redirector principle” [6.4] can be used (Fig. 6.16). Here the bundle of each laser bar is sliced into N “beamlets” by a special glass prism. This “director” prism tilts 1/N of the bundle horizontally into different propagation angles relative to the main propagation axis and vertically toward the center of this axis. At the

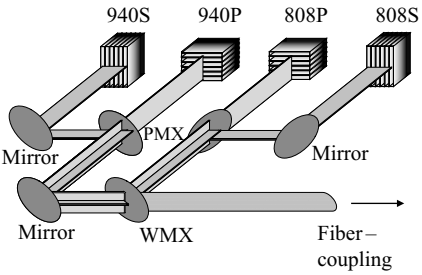

FIGURE 6.14. Optical setup: 808- and 940-nm units are combined by polarization and wavelength multiplexing

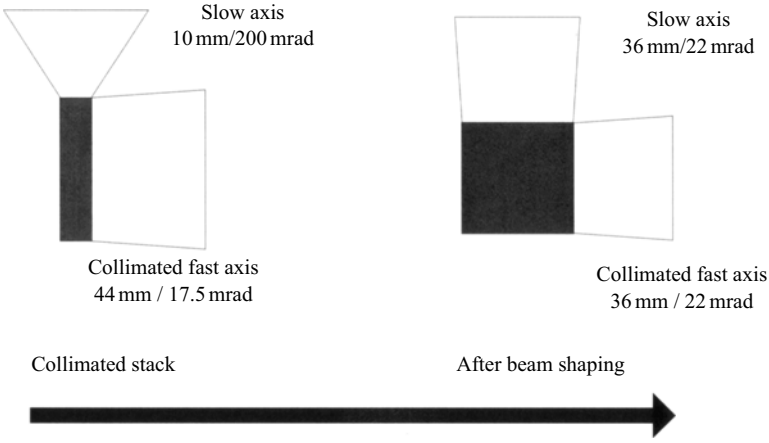

FIGURE 6.15. Beam symmetrization: asymmetric cross section (filled rectangle) and divergence angle (trapezoid, opening angle symbolizes beam divergence) are transformed

propagation point where beamlets are crossing in different heights a second special prism is allocated. This "redirector" prism is redirecting different propagation directions of the N beamlets into the direction of the main propagation axis. For the laser described here N is chosen as 3. Thus, in the result of this procedure one gets a total bundle of beamlets with unmodified total divergence angles but with a reduced beam width in the slow-axis (factor 1/3). The beam-parameter-product is nearly symmetric but has different divergence angles. Divergence angles can be modified easily by using a telescope of crossed cylindrical lenses, so that finally a totally symmetric beam is produced (Fig. 6.15, right). By these data theoretically a beam-parameter-product of about 200 mm $*$ mrad can be reached.

It is easy to calculate that for a quartz fiber with 1.5-mm-core-diameter and NA $= 0.33$, a beam-parameter product of 252 mm $*$ mrad results. This type of fiber is commercially available and was used with a length of up to 10 m without remarkable transmission losses in this system.

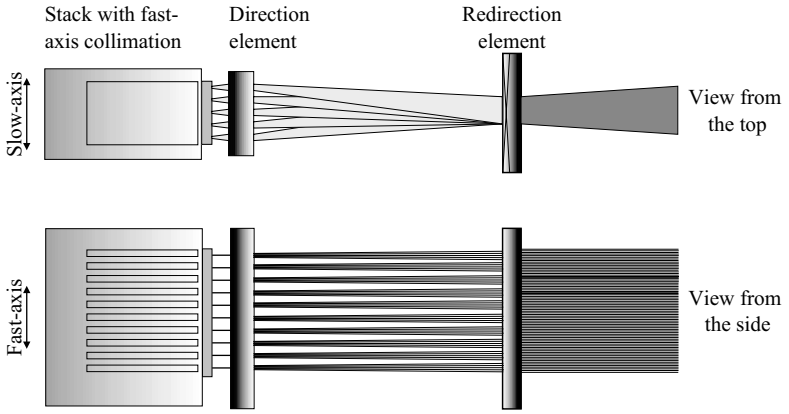

FIGURE 6.16. Beam shaping with director-redirector principle: collimated emission from laser bars is sliced into beamlets; the beamlets are directed into different heights and directions, at the cross point the beamlets are redirected into common propagation direction

TABLE 6.5. Summary of power losses on the optical beam path in the system

Position	Relative losses	Power level
Stack without micro-optics		100%
Fast-axis collimation	−5%	95%
Symmetrization of beam-parameter product	−10 %	86%
Symmetrization of divergence angle	−5%	81%
Polarization multiplexing	−10%	73%
Wavelength multiplexing	−5%	69%
Fiber coupling	−15 %	59%

6.2.3.2. Description and Characterization of the System

If 40 W are extracted from a single bar, about 4 kW optical power are generated in the system by the stacks. However, losses on the optical components are unavoidable. The highest loss is generated at the entrance facet of the fiber, so that an efficient water cooling for the fiber plug is mandatory. In Table 6.5 an overview of typical optical power losses in the entire pathway between laser emitter and fiber output is given. The power at the fiber output was measured to be about 2.2 kW at a maximum current of 55 A, whereas the threshold is typically at 13 A.

A focal spot size of 1 mm diameter at a 34 mm working distance could be demonstrated with the processing optics, also 2 mm at 83 mm and 3 mm at 140 mm, respectively. The laser head with covers removed is shown in Fig. 6.17; the four stacks as well as the multiplexing optics and the fiber coupling can be recognized.

Because of the large core diameter and numerical aperture of the fiber a high dispersion of modes is guided by the fiber. As a result an intensity homogenization effect occurs, which gives a very smooth top-hat shaped circular intensity

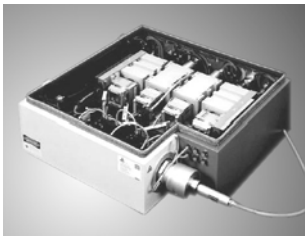

FIGURE 6.17. Laser head of fiber coupled kW system: 4 stack units with 808/940 nm can be seen in the upper right as well as beam combination and forming in the bottom

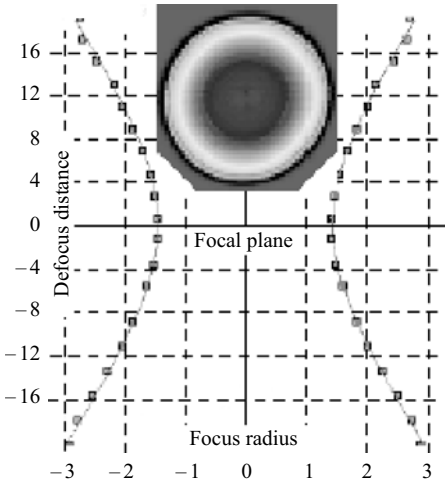

FIGURE 6.18. Caustic measurement and intensity distribution of the fiber-coupled kW system, focused at spot size 1.4 mm at 82 mm working distance; result of caustic measurement is BPP = 202.9 mm ∗ mrad

distribution (insert in Fig. 6.18) in the focal plane. The beam-parameter-product calculated from the caustics as shown in Fig. 6.18 fits quite well with the data above.

A structural overview of the system is given in Fig. 6.19. All electrical and cooling components had been assembled in two 19-inch standard racks with total dimension of 1,200 × 700 × 10000 mm^3 (including laser head, Fig. 6.20).

Power supplies for laser diodes have to be selected using strong attention on preventing overshooting of diode current and transients of negative voltage. In this setup each stack was driven by a separate power supply with parallel control of one control unit. Protection against ESD is given by inserted shortcut relays inside the laser head, which shorten the stacks whenever the power supply is switched off. This way the laser head can be handled independently of power supplies. For dust and moisture protection the laser head containing all optical elements up to the fiber entrance was designed with a rubber sealing. Hermetical housing of laser

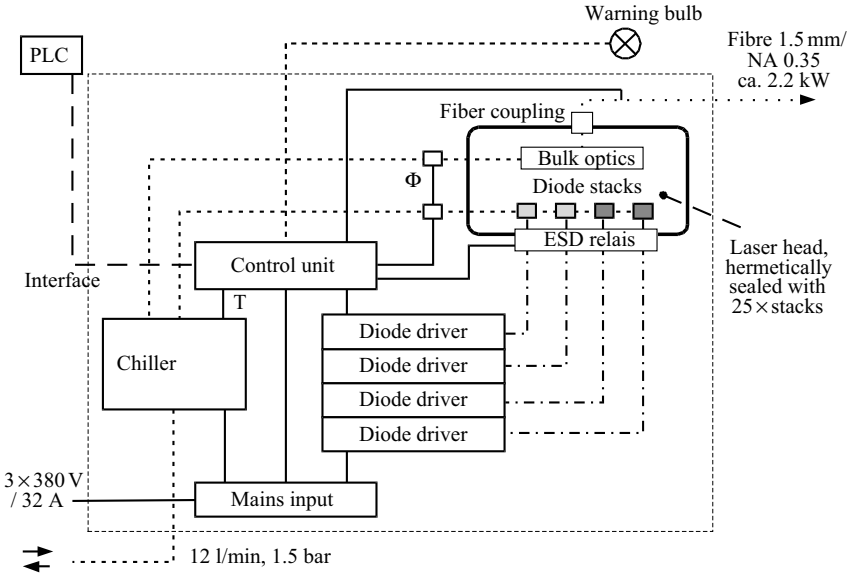

FIGURE 6.19. System overview of fiber-coupled kW system: a hermetically sealed laser head with laser units and bulk optics is supplied with power and cooling; control unit supervises critical parameters and translates to a bidirectional external interface operation commands and status information

FIGURE 6.20. Fiber-coupled kW system assembled in 19-inch racks: left side, cooling device; right side, power driver and system control, on top: laser head

units was assembled to enhance the protection class, allowing handling of housed laser units outside the clean room.

The light path was set up symmetrically for 808 and 940 nm with some water-cooled beam stops at critical points. Achromatic fiber-coupling optics were used

with water cooled entrance aperture. The optics were adjustable in x-, y-, and z-direction relative to beam axis. Fiber was assembled in a commercial high-power laser plug with an outer diameter of 28 mm, which was assembled into the coupling optics unit. To prevent damage by overheating, the fiber was protected by a thermo-switch inserted inside the plugs at entrance and output aperture.

6.2.4. High-Brightness 100-W System with Tapered Laser Bars

Alexander Knitsch

For further development in beam quality of high-power diode laser systems, a new type of diode laser bars has been realized recently. Compared to commercially available broad-area diode laser bars the lateral design of tapered diode laser bars consists of a ridge waveguide and a tapered section, where the tapered structure determines high output power and the high brightness is provided by the ridge waveguide structure (see Chapter 2.5). Unfortunately the different lateral structure leads to astigmatism effects which are also thermally affected in continuous wave operation. Hence in terms of diode laser systems with fast- and slow-axis collimation micro-optics the full characterization of tapered diode laser bars is mandatory. Whereas the wavelengths and divergencies of tapered diode laser bars are relatively easy to measure, the beam profile is actually not, as its lateral source point is apparently located inside the tapered structure. With telecentric optics, the caustics of the individual emitters of the bars are detected by the use of a fiber sensor with a resolution of 10 μm in the fast- and slow-axis directions. Subsequently, with beam analysis software the astigmatism can be calculated.

6.2.4.1. Layout and Design of the Characterization

The caustics of the tapered laser bars have been measured with a fiber sensor, where the fast- and slow-axis is scanned in propagation direction with a 4 μm monomode fiber (Fig. 6.21). First of all each selected emitter has to be separated from the other emitters of the bar. This is achieved by a copper diaphragm with a corresponding pitch where the other emitters are reflected to a beam dump. The separated beam is now imaged with telecentric optics of high numerical aperture, so that the full caustic can be detected.

The individually measured data are transferred via the fiber and a photodiode to the computer. Caustic characteristics in fast and slow axis are illustrated (Fig. 6.22) after analysis by beam-analyzer software [6.5]. From this caustic characteristics the location of the foci in fast-and slow-axis can be calculated with a resolution of 10 μm. The error tolerance is also displayed and does not exceed 3% of the measured values. Naturally astigmatism, beam quality, divergence angles and Rayleigh lengths can be determined from the caustic characteristics as well. The entire measurement procedure is programmed with LABVIEW© software; the full

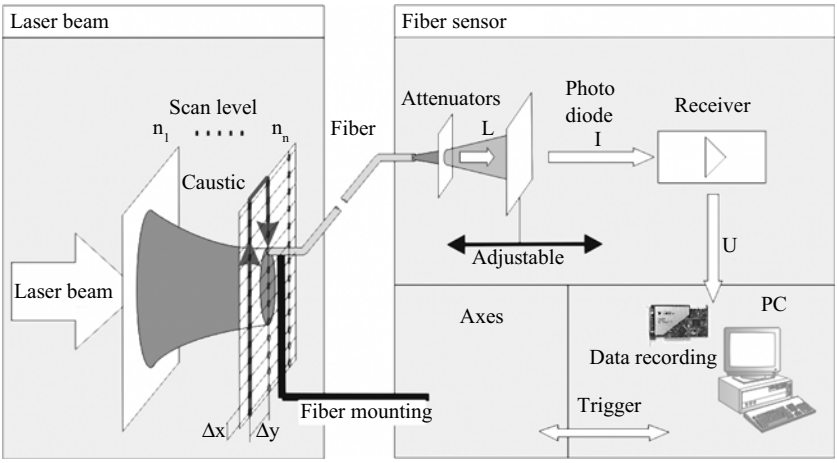

FIGURE 6.21. Principle of the caustic measurement with a fiber sensor

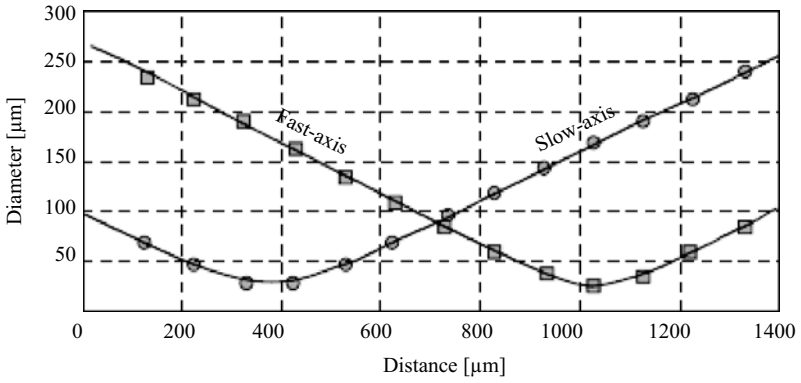

FIGURE 6.22. Fit of the caustics of tapered laser emitter in fast-and slow-axis

characteristics of one individual emitter can be obtained over the entire applied current range within one working step.

6.2.4.2. Optical Simulation

The selected beam is scanned along the propagation in the fast- and slow-axis directions with the fiber sensor. The resolution in both axes perpendicular to the optical axis (in and parallel to the pn-transition plane) is 5 µm, whereas the increment in propagation direction is 100 µm with a total traverse path of 1,300 µm. That results in a total of 13 plane scans for each current level. As a control of the measurements a simulation of an emitter of a tapered laser bar with an estimated astigmatism of 600 µm has been performed. Comparison with real measurement and analysis shows good conformity with the simulation (Fig. 6.23).

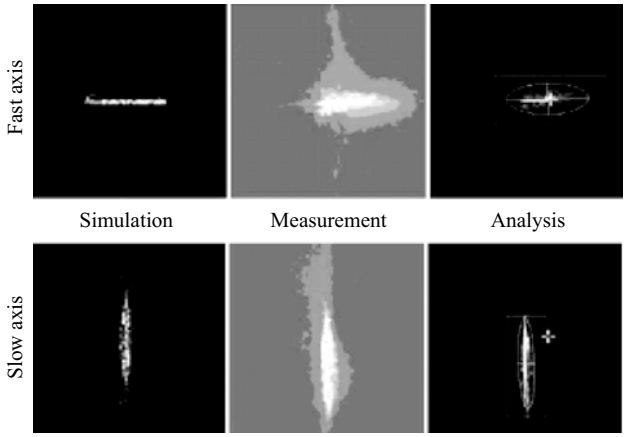

FIGURE 6.23. Simulation, measurement, and analysis (from left to right) of a single emitter of a tapered diode laser bar within the fast-axis focus (top) and the slow-axis focus (bottom)

6.2.4.3. Characterization of the Tapered Diode Laser Bars

From the caustic analysis the location of the two foci can be calculated; the difference determines the astigmatism. As wavelength coupling is supposed to be applied in the system, the astigmatism for one diode laser bar of each wavelength (808, 940, and 1040 nm) has been measured over the current range from 30–70 A. To get the information of the homogeneity over the entire laser bar, several emitters from each bar have been chosen for the measurement. A characteristic example of the shape of fast and slow axis foci of an emitter is shown in Fig. 6.24 (top), whereas the dependence of the astigmatism over the applied current range and for several emitters of 808 nm bars is shown in Fig. 6.24 (bottom). It can be clearly seen, that the astigmatism of the 808 nm bars amounts to approximately 650 μm. Depending on the injection current, the astigmatism rises with about 1 μm/A, it is quite homogeneous over the bar and even over several bars. In the high current range from 60 to 70 A, a saturation effect for most of the emitters is visible. Results for the 940 and 1,040 nm tapered laser bars are essentially the same as those for the 808 nm bars.

By and large the measured astigmatism characteristics follow the theoretical predictions and first tests on single-emitter structures [6.6] fit very well into the terms of carrier-induced and thermal dependence. The increase of astigmatism over the applied current of about 1 μm/A also shows good conformity with theory as well as the saturation effect at higher currents. No fluctuations of astigmatism over the bar, which would be a disqualification in terms of slow-axis collimation arrays have been detected.

The tapered diode laser bars emphasize their good beam quality in slow-axis direction; the beam-parameter-product as well as the beam propagation factor M^2 are depicted in Fig. 6.25 for bars at 808 and 1,040 nm wavelength. For the emitters

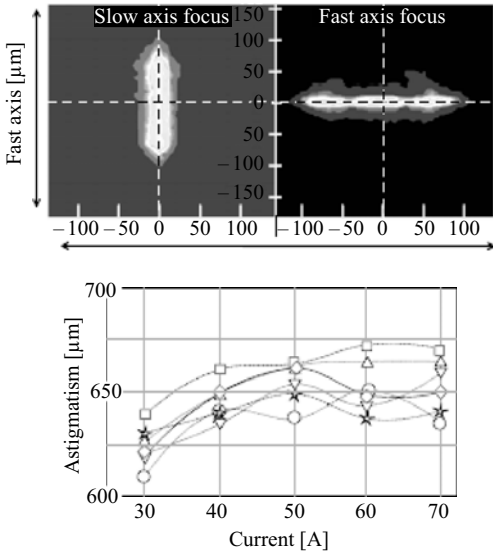

FIGURE 6.24. Top: Slow- and fast-axis foci of an arbitrary emitter. Bottom: Astigmatism characteristics over current for 6 (tapered) emitters of an 808-nm bar

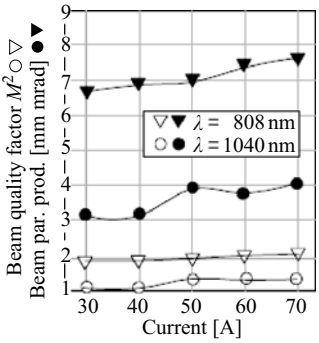

FIGURE 6.25. Beam quality of a tapered diode laser bar in slow axis vs. current for selected emitters

of the 808 nm bars the lateral beam-parameter-product amounts to 2 to 3 mm $*$ mrad at an operational current of 70 A. These results correspond to M^2 values of 6 to 8, whereas the homogeneity over the bars correlates with the astigmatism characteristics; however slight differences over the various laser bars have been found. From the 1,040 nm bars we obtain a beam-parameter-product of less than 1.3 mm $*$ mrad, corresponding to M^2 values of about 4. Like the astigmatism characteristics the homogeneity not only over one bar but also different bars is very good. Compared to broad-area diode laser bars with a typical structure of 150/500 (broadness/pitch in µm) and a typical beam-parameter-product of about

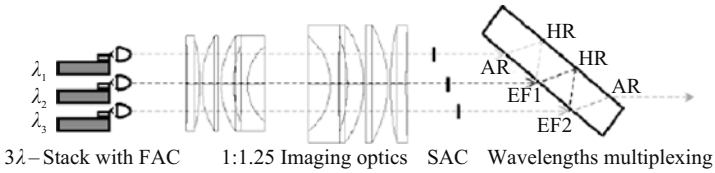

FIGURE 6.26. Schematic of a high-brightness system with imaging optics, following slow-axis collimation and wavelength multiplexing with a multi-filter [6.7]

7 mm ∗ mrad in slow-axis the tapered bars gain up to a factor 4 in the lateral beam-parameter product. Hence for the whole tapered bar (i.e., in the average of slow-and fast-axis) an improvement in beam quality up to a factor of 2 is possible.

6.2.4.4. Realization of a High Brightness System

The astigmatism characteristics of the tapered diode laser bars described above require an adjustment according to operating current. Due to the emission characteristics of the tapered diode laser bars with its additional high divergence in slow-axis direction a possible setup for a high brightness system is presently only possible with special imaging optics (Fig. 6.26). Whereas the fast-axis collimation has to be adjusted straight after the laser bar, the slow axis must be imaged to adjustable collimation arrays because after the fast-axis collimation the radiation of the single emitters is not separated anymore.

On one hand the 1:1.25 imaging optics adjust the pitch of the diode laser bar (400 μm) onto commercially available micro-optic arrays with a pitch of 500 μm; on the other hand, the single emitters are separated again after the imaging optics. The different wavelengths as well as manufacturing tolerances of the used tapered diode laser bars lead to slightly various astigmatism values so that the slow-axis foci of the laser bars may vary after the imaging optics. This can be accommodated by the individual adjustment of the slow-axis arrays for each laser bar.

To obtain a high brightness system after all collimation optics, the radiation of the tapered diode laser bars can be superimposed by the use of a plan-parallel plate, which is spanned coated with edge-filters, the so-called multi-filter [6.7], shown in Fig. 6.26. With a complete setup of three tapered diode laser bars of different wavelengths, a high brightness system with an output power of about 100 W and a beam-parameter product of less than 15 mm ∗ mrad is intended.

6.2.5. High Brightness kW-System with Tapered Diode Laser Bars

Bernd Köhler

In this section a diode laser system based on tapered diode laser bars is described, providing a combination of power and beam quality which is comparable to that of high-power lamp-pumped solid-state rod lasers. Until now diode laser systems

with an output power in the kW range were based on broad-area diode lasers (see Chapter 2.4). However, the output of these kilowatt laser systems is characterized by a strongly asymmetric beam profile, which is a consequence of the asymmetric beam-parameter-product of broad-area diode laser emitters. Apparently the output of such a laser system cannot be coupled efficiently into a fiber without symmetrization of the beam-parameter-product by complicated and expensive beam shaping systems (see Chapter 4.5). On the other hand, the market requires fiber coupling for a variety of applications.

The main benefit of tapered diode lasers (see Chapter 4.5) is the combination of high output power and high beam quality. Tapered diode laser bars provide about an order-of-magnitude higher brightness than conventional broad-area semiconductor lasers. This allows the design of high-power laser systems with an almost symmetric beam profile without the necessity of using complicated beam shaping systems.

6.2.5.1. Layout and Design of the System

Like conventional high-power laser systems based on broad-area diode bars (see sections 6.2.2 and 6.2.3), the basic unit for a high-power diode laser system composed of diode lasers is a stack, where the individual tapered diode laser bars are arranged on top of each other. Each single diode bar is provided with appropriate micro-optics for collimating both the fast and the slow axis, respectively. The basic properties of tapered diode lasers are discussed in detail in Chpater 2.5 of this book. Beam shaping and symmetrization of tapered diode lasers is described in detail in Chapter 4.5. Power scaling is realized with different coupling principles, including spatial multiplexing, polarization multiplexing, and finally wavelength multiplexing. For a detailed description of these coupling principles see Chapter 4.3. A scheme of such a laser setup is shown in Fig. 6.27.

According to Fig. 6.27 the system is based on the combination of a total of 16 individual stacks. For each wavelength first of all two stacks are coupled into the same optical path via spatial multiplexing. Subsequently the two stack pairs are coupled via polarization multiplexing. Since all individual bars have the same polarization it is necessary to rotate the polarization vector of two stacks with an appropriate half-wave plate. Finally, the wavelength modules each with four stacks are coupled via wavelength multiplexing with suitable edge filters. As described in Chapter 4.5 of this book, symmetrization of the laser beam is simply realized by selecting the appropriate stack height. Consequently, in contrast to a high-power laser system based on broad-area diode bars after power scaling no subsequent beam symmetrization as used in the systems described in section 6.2.2 is necessary. Finally the beam is coupled into an optical fiber by means of a suitable focusing optics.

It should be noted that polarization and wavelength coupling of tapered diode lasers put high demands on the thin film coupling devices, because the spectral

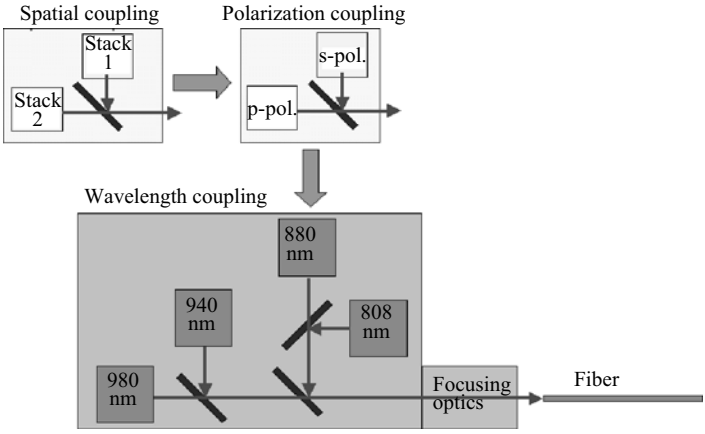

FIGURE 6.27. Schematic representation of the setup of the high-power, high-brightness diode laser system

width of tapered diode lasers is significantly larger (typically > 5 nm) than the spectral width of conventional broad-area diode lasers. As mentioned in Chapter 4.3, the spectral width has an important impact on the coupling efficiency.

In addition to the broad spectrum, there are some more drawbacks that have to be considered when building a high-power laser system out of tapered diode lasers. These drawbacks are mainly a result of the characteristic design of tapered diode lasers which leads to a difference in source position for the slow and the fast direction, respectively (see also section 6.2.4). Whereas the source position of the fast-axis is on the output facet of the diode bar, the virtual source position of the slow-axis is located inside the diode bar at the end of the waveguide. As described in Chapter 4.5 this astigmatism defines the characteristics of the micro-optics, particularly with regard to the position and the focal length of the slow-axis collimation lens. The drawbacks for the design of a high-power system built up of many individual tapered diode lasers appear because the source position of the slow-axis is not fixed but varies as a function of current and temperature (see section 6.2.4). Furthermore, the source position can vary for different emitters on an individual tapered diode laser bar. As a result, beam collimation of the individual emitters is not optimal, and therefore the overall beam quality is reduced. Finally this leads to an increased spot size on the workpiece or a reduced coupling efficiency into an optical fiber.

Figure 6.28 shows a simulation of the influence of characteristic parameters with regard to the coupling efficiency of an optical stack of tapered diode laser bars into an optical fiber. Each single diagram in this figure shows the influence of the variation of one parameter, whereas the remaining parameters are maintained constant. The basic parameters of the simulation are a slow-axis divergence of 7° (half-angle), an emitter size in slow-axis direction of 20 μm, an astigmatism of 600 μm, and a fast-axis divergence of 30° (half-angle).

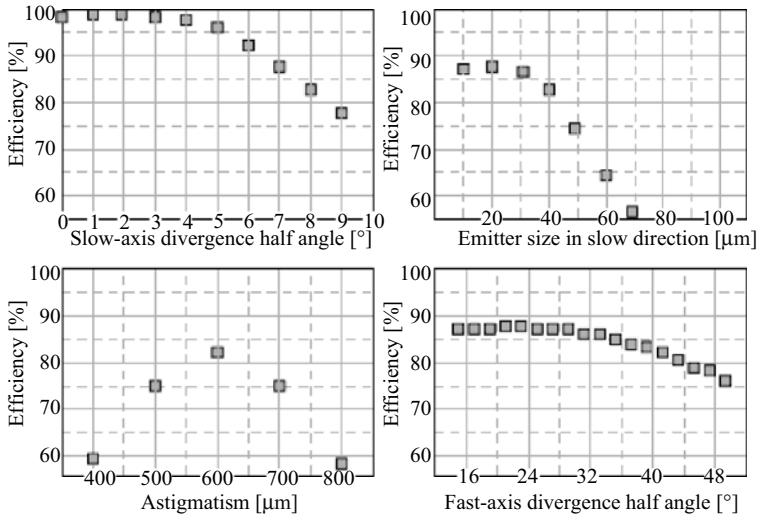

FIGURE 6.28. Simulation of coupling efficiency of a tapered diode laser stack into an optical fiber (see text)

6.2.5.2. Optical and Mechanical Realization

As described in the previous section, the beam quality and therefore the coupling efficiency strongly depends on the characteristics of the individual tapered diode laser bar. Until now high-power tapered diode laser bars with well-defined and reproducible properties were not available. In order to realize an efficient system consisting of many single diode bars, a detailed characterization of the individual diode bars is inevitable. Therefore, each individual diode laser bar was analyzed with regard to power, center wavelength, spectral width, astigmatism, polarization state, and virtual emitter size. These investigations revealed remarkable differences of the characteristic parameters of tapered diode lasers for different wavelengths. For instance, the average output power per bar at a current of 78 A was 41 W at a wavelength of 808 nm, 21 W at 880 nm, 50 W at 940 nm, and 53 W at 980 nm. The average spectral bandwidth was 8 nm at 808 nm, 13 nm at 880 nm, 7 nm at 940 nm, and 10 nm at 980 nm. Furthermore, significant differences were observed even for diode laser bars with the same design wavelength. Further data on the characterization of individual tapered diode laser bars are found elsewhere in this book (Chapter 2.5, section 6.2.4).

In order to maintain the beam quality of individual laser bars, the micro- optics for collimating the slow-and the fast-axis were mounted after stacking the single diode bars on top of each other (see Chapter 4.4). Afterwards each individual stack was characterized with regard to power, beam quality, and fiber-coupling efficiency. These experiments showed a decrease in coupling efficiency as a function of increasing current. In the low-current regime slightly above threshold

Table 6.6. Typical coupling efficiencies of tapered diode laser stacks at different wavelengths*

Coupling efficiency at	808 nm	880 nm	940 nm	980 nm
	600 μm fiber, 0.22 NA			
Low power (current)	80% (20 A)	73% (40 A)	77% (10 A)	77% (10 A)
High power (70 A)	57%	62%	36%	54%
	800 μm fiber, 0.22 NA			
Low power (current)	82% (20 A)	83% (40 A)	80% (10 A)	81% (10 A)
High power (70 A)	67%	75%	46%	61%

*The efficiencies are given for low current slightly above threshold and a typical operating current of 70 A, respectively. The fiber core diameters were 600 μm (top) and 800 μm (bottom), respectively (numerical aperture 0.22)

current the coupling efficiency was approximately 80% for all wavelengths. However, increasing the current led to a wavelength-dependent decrease in coupling efficiency. The results are summarized in Table 6.6.

The decrease of coupling efficiency with increasing current was further investigated by measuring the beam quality of the stacks with an appropriate beam diagnostic device (see Chapter 5).

Figure 6.29 shows the beam profile of an 808 nm stack for two different currents of 20 A (left) and 70 A (right). The measurements show a dramatic decrease of beam quality with increasing current, which is according to the decrease of coupling efficiency. The beam-parameter-product rises from 35 mm ∗ mrad at 20 A up to 95 mm ∗ mrad at a current of 70 A. This behavior is primarily ascribed to the worsening of beam quality in the slow direction with increasing current. The beam diameter of the slow direction is enlarged from 1.4 mm up to 3.6 mm, whereas the beam diameter in the fast direction is nearly constant in the current range of 20–70 A. The worsening of the beam quality especially in the slow direction is a consequence of the variation of position, size and divergence angle of the virtual source of the slow axis.

The decrease of beam quality with increasing current has to be considered when designing the mechanical setup of the laser system. Adjustable slow-axis imaging optics as described in section 6.2.4.4 for the 100 W system seems not to be

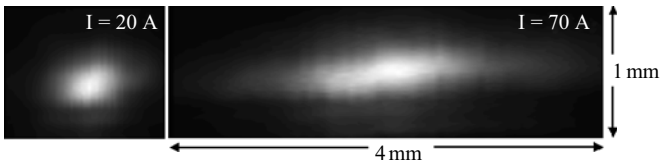

Figure 6.29. Beam quality measurements of a 808-nm tapered diode laser stack for two different currents of 20 A (left) and 70 A (right)

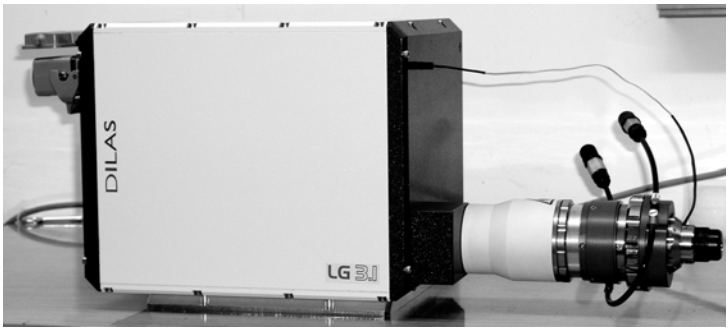

FIGURE 6.30. Mechanical setup of the high-power, high-brightness tapered diode laser system with fiber coupling unit

feasible for the kW-range system with higher stacks and four wavelengths. As a consequence, with increasing current some part of the beam will be cut off by components inside the device, which will finally lead to a loss in output power and to a heating of the components. On the other hand, this truncation is desirable for fiber coupling because it reduces the exposure of the fiber. Therefore apertures inside the device have to be designed carefully to minimize heating of the fiber.

The mechanical setup of the laser unit is shown in Fig. 6.30. The geometrical dimensions of the head are 350 $\times$ 270 $\times$ 280 mm (length $\times$ width $\times$ height), and its total weight is 29 kg, including the fiber coupling unit; that is apparent on the right side in the figure. Taking into account the fiber-coupling unit the length is increased to 660 mm.

6.2.5.3. Characterization of the System

The system was characterized in detail with regard to beam quality, total output power, and fiber-coupling efficiency. Figure 6.31 shows the output power as a function of diode current. The maximum output power was 3,230 W at a current of 75 A. It should be noted that the current for the 940-nm module was limited to 60 A, because of the decrease in beam quality with increasing current (see Fig. 6.29), which was in particular observed for the 940-nm module. This limitation leads to the small deviation of the power versus current characteristics from linear above 60 A.

A measurement of the beam quality of the laser head without fiber is shown in Fig. 6.32 for an operating current of 40 A. Focusing the beam with an objective with a focal length of 98 mm leads to a beam diameter of 0.65 mm in the fast direction and 0.95 mm in the slow direction, respectively. Taking into account the total optical output power of 1285 W at a current of 40 A, the resulting intensity in the focal plane is 265 kW/cm^2. The beam quality is characterized by a beam-parameter-product of 49 mm $*$ mrad for the fast direction and 83 mm $*$ mrad for the slow direction, respectively. Increasing the current to 70 A will raise the power

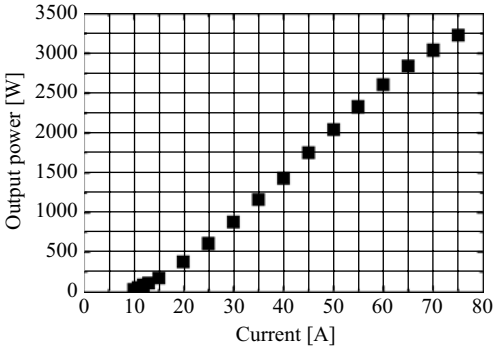

FIGURE 6.31. Optical output power of the system in Fig. 6.30 as a function of the operating current

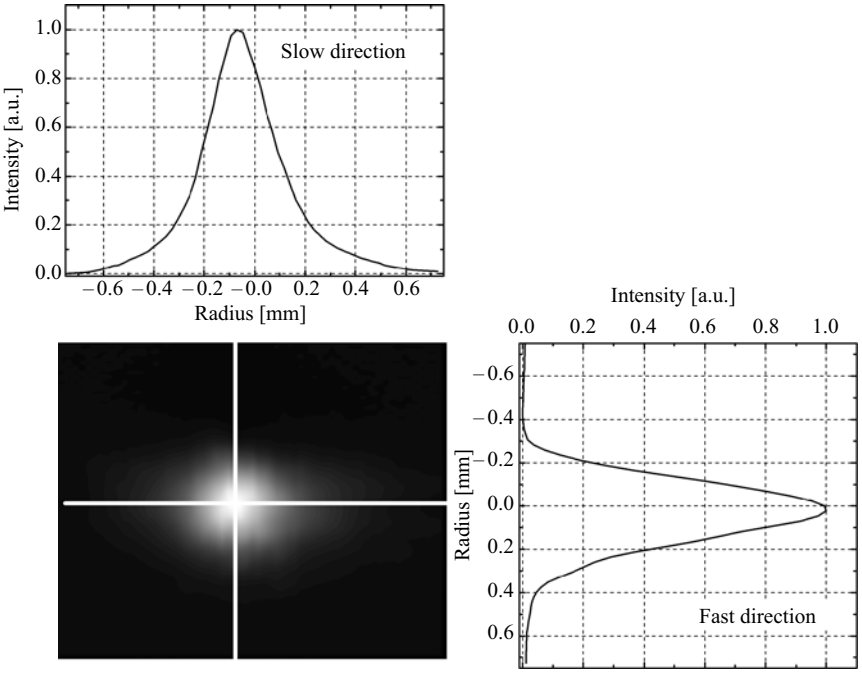

FIGURE 6.32. Characterization of beam quality of the laser head in Fig. 6.30 without fiber for an operating current of 40 A. The focal length of the objective is 98 mm

by a factor of 2.5, but the intensity will not increase by the same factor due to the broadening of the spot size with increasing current.

The results for fiber coupling are shown in Fig. 6.33 for two optical fibers with core diameters of 800 μm (left diagram) and 600 μm (right diagram), respectively.

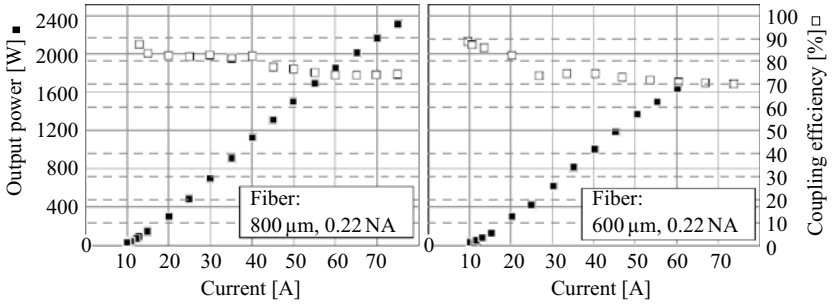

FIGURE 6.33. Output power and coupling efficiency for an 800 µm fiber (left) and a 600 µm fiber (right), both with a numerical aperture of 0.22

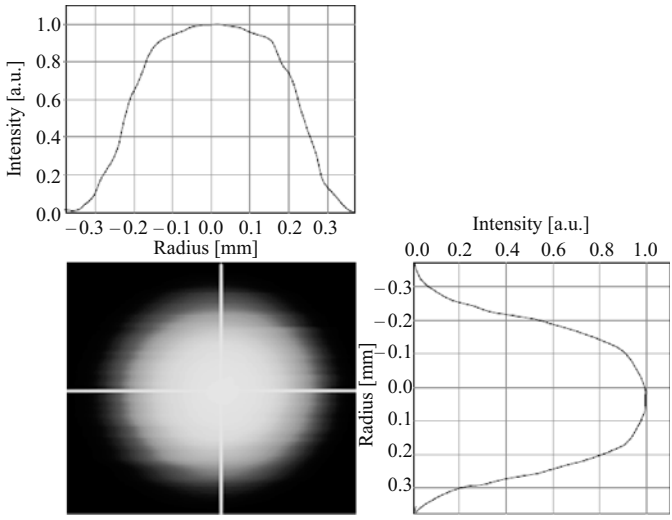

FIGURE 6.34. Characterization of beam quality of the fiber coupled version for an operating current of 75 A. The fiber has a core diameter of 800 µm and a numerical aperture of 0.22. The focal length of the objective is 62 mm

The numerical aperture of both fibers is 0.22. Maximum output power was 2,380 W at 75 A for the 800-µm fiber and 1,650 W at 60 A for the 600 µm fiber. The corresponding coupling efficiencies are 72% and 68%, respectively. It should be noted that for the 600 µm fiber, the current of the 940 nm module was limited to 50 A because the decrease in beam quality with increasing current above approximately 50–60 A will primarily result in a heating of the fiber.

Figure 6.34 shows a measurement of beam quality behind the 800 µm fiber and at a current of 70 A. Focusing with an objective with a focal length of 62 mm leads to a beam diameter of 0.52 mm in the focal plane. Taking into account the

total power of 2,380 W after the fiber, the resulting intensity at the focal plane is 1.1 MW/cm^2. This intensity makes the system competitive to lamp-pumped solid-state lasers and allows it to be used for deep penetration welding and other applications, which require high power densities, as proven by experiments which are described elsewhere in this book (see Chapter 7.1.2).

In the future the design and fabrication of tapered diode laser bars has to be improved in order to build reliable systems with reproducible properties. It should be noted that the system described did not use the full theoretical capacity of tapered diode laser bars with regard to beam quality. This was due to the drawbacks mentioned in the sections above. The main problem was the decrease in beam quality with increasing current. Systems based on tapered diode lasers have the capability to reach a beam-parameter-product in the range of 10 to 30 mm $*$ mrad with an output power in the multi-kilowatt range. However, further developments in the design and fabrication of tapered diode laser bars and the design of the laser systems are necessary to reach that goal.

6.3. Modular Diode Laser Systems

In a high-power diode laser device high power is generated by – in most cases – incoherent superposition of individual laser emitters, which provide just a few watts output power. What looks like a disadvantage in the first glance, offers the chance for a modular setup, i.e., the possibility to arrange these emitters or bars, respectively, in a way which is adapted to a certain application. As an example, linear or ring-shaped focus geometry can be realized, as schematically depicted in Fig. 6.1. Furthermore, the individual devices can be controlled separately in power and in time, so that special spatial and temporal profiles can be generated. This can be even realized for each individual emitter, which provides the highest spatial resolution. The following chapter describes such systems, which are summarized in Table 6.7 in detail.

Table 6.7. Overview over the modular diode laser systems

Laser system	Code	Section
Soldering laser integrated into a gripping tool	Soldering laser	6.3.1
Individually addressable intensity line	Addressable line	6.3.2
Modules for contour adapted plastics welding	Polymer line welder	6.3.3.1
Homogenized line modules	Line module	6.3.3.2
Diode laser for line cutter	Line laser	6.3.4
Annular diode laser beam tool	Ring focus laser	6.3.5
Process-controlling modular hardening system	Hardening system	6.3.6
Segmented ring-shaped milling support laser	Milling laser	6.3.7

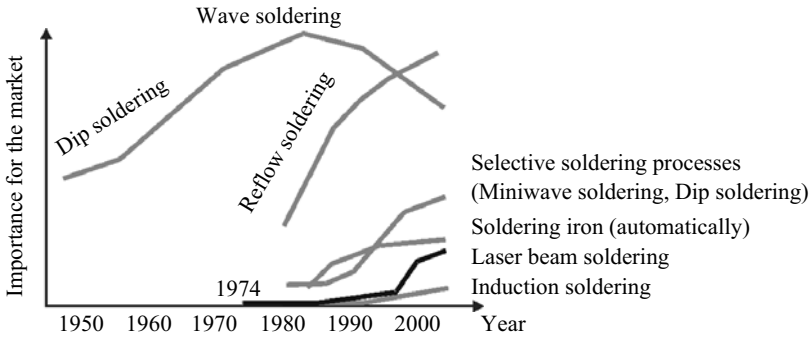

FIGURE 6.35. Previous and future development of different soldering processes [6.8]

6.3.1. Soldering Laser, Integrated into a Gripping Tool – "Pick and Join"

Lüdger Bosse

Due to the increasing integration and miniaturization of microelectronic circuits laser radiation is a suitable tool for joining in micro-fabrication. Compared to conventional techniques it has the advantages of a controlled and locally limited heat input as well as reduced thermal and mechanical stresses. Today laser beam soldering is a non-standard manufacturing process for electronic packaging and interconnection technology because of both the high investment costs and the belief that it is a complex and sophisticated joining technique [6.8]. Most of the industrial applications of laser beam soldering are constricted to selective soldering tasks. These applications are characterized by specific demands for heat sensitivity, geometry, or flexibility, for example. In comparison to mass soldering techniques, like reflow soldering with infrared radiation or wave soldering, the actual market share of laser beam soldering is poor (Fig. 6.35). However, in the field of selective soldering tasks, laser beam soldering is very much in demand; and due to the development of high-power diode laser systems as reliable and suitable beam sources for industrial fabrication, laser beam soldering has become more and more attractive.

With the aim to enlarge the field of application, an advanced mounting and assembly technology called "Pick & Join" has been developed. This new interconnection technology combines the two individual processes of mounting and assembly into one single process step. As a result, this technology shows positive characteristics of a Pick & Place system, for example, the high accuracy in positioning, on one hand, and the well-known advantages of a laser joining process, on the other. Due to this powerful combination, a few challenging problems in joining applications, for example, the state-of-the-art three-dimensional soldering tasks (3D-MID [moulded interconnect device]) could be solved.

As part of these technical advances, a flexible working head for mounting and assembly of different electronic devices has been developed (Fig. 6.36). This working head was specified for soldering different, rectangular packages of multi-leaded

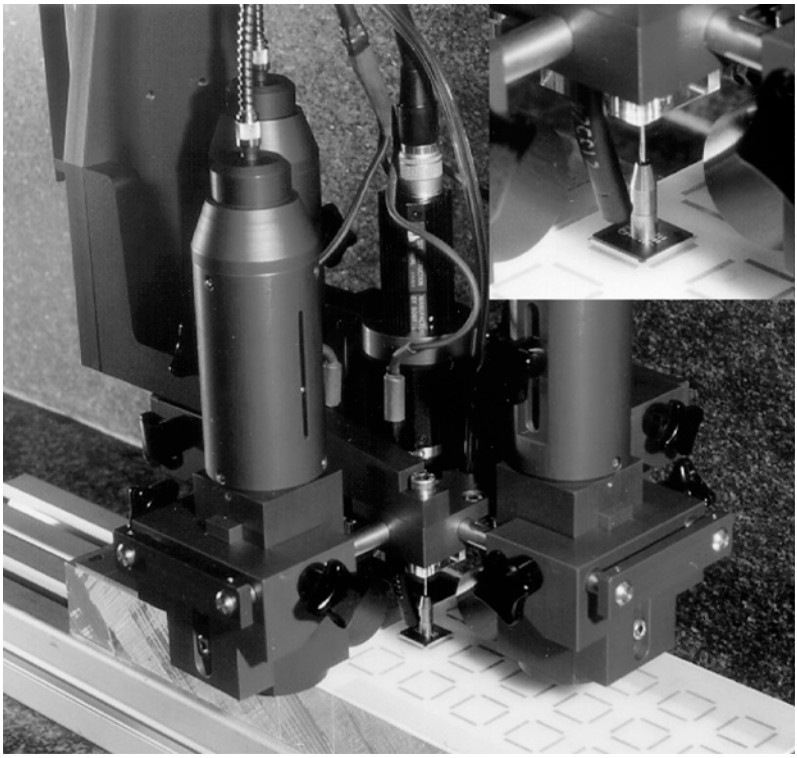

FIGURE 6.36. Working head for mounting and assembly of different electronic devices using radiation of diode laser systems as heat source; the insert shows the gripping tool

surface-mounted devices (SMD). As a consequence thereof, the focal geometry of the optical system consists of four independent, adjustable lines, arranged in a rectangle.

6.3.1.1. Layout and Design of the Working Head

Basically the working head consists of three different functional groups:

- a device-specific gripper,
- a flexible beam-delivery/beam-shaping system for the laser radiation, and
- a process-monitoring system.

In the field of electronic assembly, different concepts of gripping are established, for example, grippers using mechanical actuators, vacuum, or adhesives. Each of these concepts shows specific advantages for respective application [6.10]. For example the "MicroGrip" [6.11], a gripping-tool using frozen air humidity or a dispensed fluid as gripping medium, reduces mechanical stresses for the picked device. However, regarding the examined mounting and assembly technology, the dimensions of the gripper are inapplicable and the freezing process is counterproductive to the soldering process.

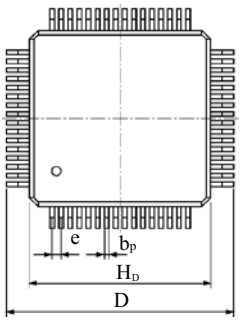

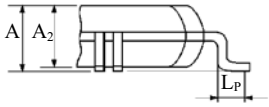

	A	A_2	b_p	D	e	H_D	L_P
min	1.2	0.95	0.17	9	0.5	7	0.45
max	1.6	1.5	0.45	22	0.8	20	0.75
Dimensions [mm]							

FIGURE 6.37. Dimensions of different quad flat packs (QFP)

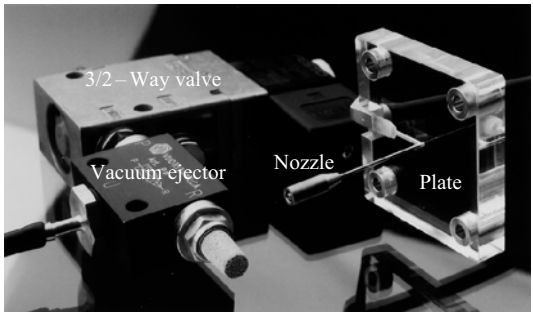

FIGURE 6.38. Main parts of the designed vacuum gripper: 3/2-way valve, plate, vacuum ejector, nozzle

Referring to the defined specifications, the gripping-tool has to pick up different electronic devices and hold them in position during the soldering process simultaneously. In Fig. 6.37 possible dimensions of different quad flat packs (QFP) are shown, for example. As a result, a certain range of weights and dimensions have to be considered for the design. Due to this fact a flexible, non-shape-adapted vacuum gripper was designed and constructed for the specified soldering tasks. In Fig. 6.38 the main components of the gripping tool, a 3/2-way valve, the plate, a vacuum ejector, and the nozzle are depicted.

Based on different soldering tasks, the focal geometry of the laser has to be tunable in the range of the specified devices. The optical path and the focal geometry are realized by a lens system with one single redirection. Using commercial, ray-tracing software,[1] the layout and the alignment of the optical components were calculated. The necessary redirection of the beam path is primarily caused by the arrangement of the soldering tasks. Furthermore, the requirement of a compact realization of the working head was considered.

[1] ZEMAX®, Optima Research Ltd.
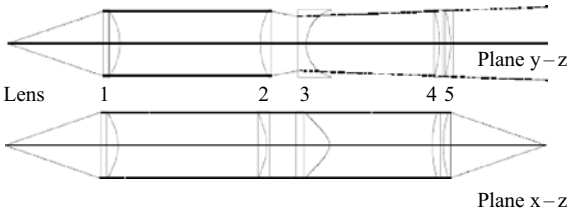
FIGURE 6.39. Arrangement of the optical components based on numerical simulation

The resulting setup of the optical components is presented in Fig. 6.39. In each of the four heads a fiber-coupled (600 μm core diameter) diode laser device with an output power of 50 W is used as an energy source for the soldering. Lens 1 is a spherical lens collimating the laser radiation emitted from the fiber core. Lenses 2 and 3 are cylindrical lenses, which determine the length of the focal geometry (plane y-z). In detail, the length of the focal geometry could be adjusted by changing the distance between these two lenses (principle of zoom lens). The following cylindrical lenses 4 and 5 are focusing the radiation in the x-z-plane. Replacing the combination of lens 4 and lens 5, the width of the focal geometry can be changed. A mirror is positioned between the lenses 3 and 4 into the radiation path for the positioning of the line focus. The optical system has a tunable length of the focus in the range of 9 mm up to 25 mm and a discrete width of the focus of 0.5 and 1 mm, respectively.

According to the state-of-the-art, a process visualization, based on a CCD-camera and a frame-grabber card, was integrated as a process-monitoring system into the working head. Normally this kind of vision system can be used for fully automatic identification of the devices as well as for monitoring of the positioning process. Furthermore, a downstream quality check of the solder joints can be realized by the same hardware equipment. All these requirements, the optical specifications of the camera system and of the zoom lens, for example, the image resolution, the spectral sensitivity range, the working distance or the frame rate, have to be checked individually for each application. Apart from examining the hardware in detail, the arrangement of the vision system within the working head has to be considered. The optimal position of the vision system is above the gripped devices. At this position the optical distortions and possible shadowing effects are minimized. Due to the fact that standard illumination is not applicable, because of the insufficient brightness and homogeneity, four white-light-emitting diodes are integrated into the working head as well (Fig. 6.40).

6.3.1.2. Characterization and Functionality Check of the System

After assembly of the working head, all functional groups were tested and characterized according to the defined requirements. Depending on the geometry of the nozzle, a wide range of surface-mounted devices with a plane surface can be

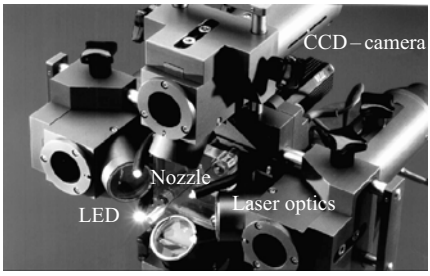

FIGURE 6.40. Bottom view of the working head

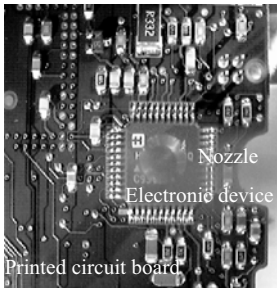

FIGURE 6.41. Picture frame recorded of the process monitoring system

picked. Due to the dimensions of the active vacuum area, the weight of the devices is not critical. The tolerable weight is a maximum of 6.3 g with a safety of 100%.

The accuracy of the assembly process is predominantly ascertained by the technical characteristics of the positioning system. Undesirable deviations, caused by the supply of the devices or by the gripping process, can be readjusted in combination with the integrated vision system. In Fig. 6.41, a recorded frame of the assembly process is depicted. This single frame demonstrates qualitatively required characteristics of the integrated vision system. For example, the optical resolution is sufficient for identifying the device on one hand and for precise mounting and assembling of the devices on the other. Due to the tunable extra-illumination, the brightness in the joining area can be optimized.

For the soldering process, exact positioning and flexible adjustment of the laser beam are the main criteria. Therefore, the characteristics of the beam shaping were tested thoroughly. In addition to the qualification of the beam shaping the mechanical arrangement of the four foci was checked optically in consideration of working area and of orthogonality. Figure 6.42 (left) demonstrates that the positioning and the shape of the focal geometry correspond obviously with the dimensions of defined devices. Moreover, the rectangular alignment of the optics achieves the specified requirements. In Fig. 6.42 (right) the working area and the flexibility of the arrangement, based on the characteristics of the mechanical solution, is displayed by photomoniting of two single frames. Numerically the working area is limited to rectangular devices in the range of $6 \times 6\,\mathrm{mm}^2$ up to $24 \times 24\,\mathrm{mm}^2$.

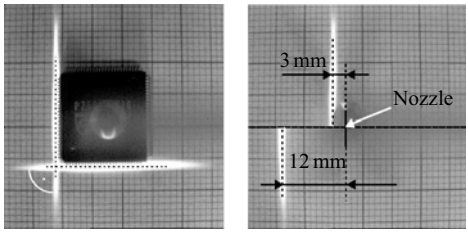

FIGURE 6.42. Left: Arrangement of two single focal geometries for demonstrating the orthogonality of the arrangement. Right: Range of the interaction area, rectangular devices in the range of $6 \times 6\ mm^2$ up to $24 \times 24\ mm^2$

After testing all functional groups of the working head individually, the whole process flow of the developed mounting and assembly process was examined. For this purpose an assortment of four SMDs with different weights and dimensions was chosen. The devices were a TSOP28/32T19.7-T1,[2] a PLCC20M,[3] a QFP80T30-5.0,[4] and a LQFP100T19.7-2.0.[5] A printed circuit board consisting of glass fiber reinforced epoxy resin (FR4) with corresponding pad geometry was designed as substrate. The solder paste used, S-Sn60Pb/F-SW32/85-2, was dispensed by a screen process. The melting temperature of the lead composed solder alloy is 183°C. In Fig. 6.43 a printed circuit board with interconnected electronic devices is depicted, for example.

By means of these results the realized working head can be used for mounting and assembly of different, rectangular packages of multi-leaded SMDs. Furthermore, the advantages of the mounting and assembly technology "Pick & Join," the high accuracy in positioning, on one hand, and the well-known advantages of a laser joining process, on the other, could be demonstrated in principle. Using a high-power diode laser as a beam source, laser beam soldering is an attractive and economical technology for selective soldering tasks in an industrial setting.

6.3.2. Individually Addressable Intensity Line

Markus Röhner

In order to open new fields of applications for high-power diode lasers in micro-system technology and printing industry, for example, soldering electronic

---

[2] TSOP28/32T19.7-T1 Thin Small Outline Package, contacts 32, dimensions $8 \times 20\ mm^2$ (thickness 1mm), pitch 19.7 mil (0.5 mm).

[3] PLCC44M Plastic Leaded Chip Carrier, contacts 20, dimensions 0.35" sq. (thickness 4 mm), pitch 50 mil (1.27 mm).

[4] QFP80T30-5.0 Quad Flat Pack, contacts 80, dimensions $14 \times 20\ mm^2$ (thickness 2.7 mm), pitch 50 mil (1.27 mm).

[5] LQFP100T19.7-2.0 Low Profile Quad Flat Pack, contacts 100, dimensions $14 \times 14\ mm^2$ (thickness 1.4 mm), pitch 19.7mil (0.5 mm).

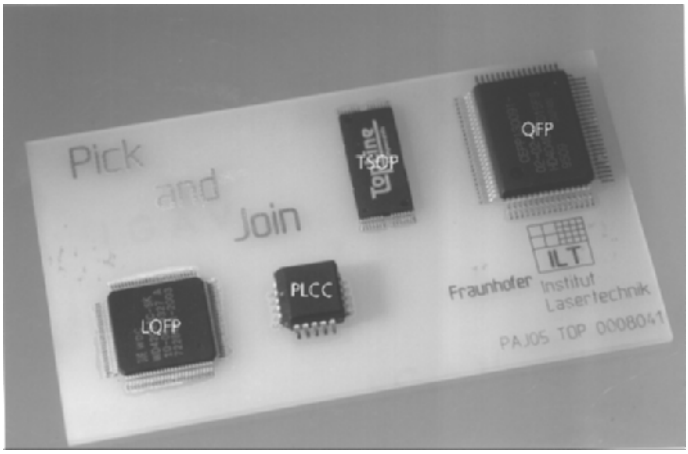

FIGURE 6.43. Printed circuit board with different electronic devices LQFP100T19.7-2.0 (Pitch 0.83mm), PLCC20M (Pitch1.27mm), TSOP28/32T19.7-T1 (Pitch 0.5mm), QFP80T30-5.0 (Pitch 0.8mm)

components or rapid prototyping, the intensity profile has to be adjusted to the workpiece's respective geometry. In addition to the temporal variation, a spatial adjustment is often indispensable. While the temporal modulation is achieved via the laser energy supply, altering the intensity profile of a conventional diode laser system is only possible by choosing a different optical imaging system. A diode laser bar consists of many emitters, which are separated electrically. By using special assembly technique the output power of each emitter can be controlled independently. Thus the intensity profile can be modulated temporally and spatially.

The system built and described here should combine the following aspects: An intensity line of 150 µm width and of 10 mm length with a spacing of 150 µm between the emitters, which can be controlled individually. The intensity line should be modularly expandable by steps of 10 mm each.

6.3.2.1. Layout and Design of the System

High-power diode laser bars consist of 19 up to 48 emitters arranged in a linear row. These emitters are typically multi-stripe or broad-area emitters (see Chapter 2.4). A schematic drawing of a diode laser bar with 19 broad-area emitters is shown in Fig. 6.44. Typically the width w of a bar is 10 mm. The cavity-length l is 1–2 mm and the thickness t about 100 µm. A pitch p between 100 µm and 500 µm (depending on emitter width) and emitter width e between 100 µm and 200 µm are characteristic for such a high-power diode laser bar. The quotient of emitter width and pitch is the fill factor f, which is typically between 30% and 50%.

Due to the monolithic structure, all emitters in a diode laser bar have a common cathode. In contrast, the anode of each emitter is electrically separated from its

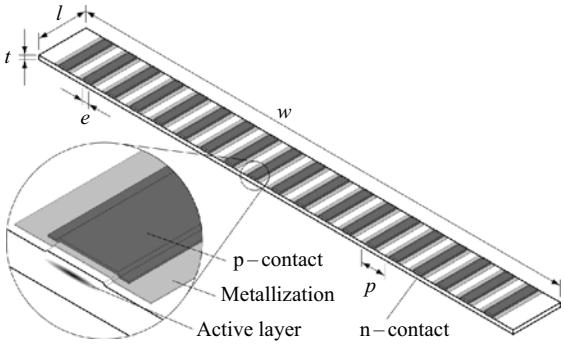

FIGURE 6.44. Schematic drawing of high-power diode laser bar with 19 broad-area emitters [6.12]

neighbors, hence the metallization of the anode is segmented. For more efficient cooling junction-side down assembly, in which all emitters in a diode laser bar are connected electrically parallel, is normally applied [6.13] (see also Chapter 3.2). Applying this assembly technique makes an independent output power control of each emitter impossible. In contrast, p-side-up assembly will maintain the electrical separation, however, at the expense of less efficient cooling. By wedge bonding each emitter can be easily connected to its own power supply, the output power of each emitter can be controlled independently. This principle of individually addressable diode laser bars is well known in telecommunication industry; the main difference is the output power of each emitter (10–50 mW for telecommunication diode laser, but 500–1,000 mW for high-power diode laser [6.14]).

The main challenge to address the single emitters in a high-power diode laser bar is thermal and electrical management in order to avoid cross talking [6.15]. The output power of a diode laser depends on current and junction temperature as a result of heat sink temperature, heat conduction and transfer as well as waste power [6.16]. Especially, p-side-up assembly increases the thermal stress of the emitters. In addition, the low thermal conductivity of GaAs increases the thermal influence of neighboring emitters. Electromagnetic fields inside and outside the diode laser bar, for example, caused by field strength within the area of bond wires, induct voltages into neighboring electrical circuits. Therefore the output power of neighboring emitters can be affected. The influence on the optical output characteristics (e.g., optical power or wavelength) depends on different electro-optical properties as characteristic temperatures, slope efficiency, or wavelength shift, which can be different for each diode laser bar. Ohmic cross-talk occurs when two or more electrical circuits have a common impedance. As a result of this, the voltage drop over this impedance increases. Fortunately, the voltage drop can be neglected, because the power supply is current controlled. Therefore, no ohmic cross-talk occurs. Capacitve and inductive cross-talk are caused by electromagnetic fields outside the laser bar. The influence depends

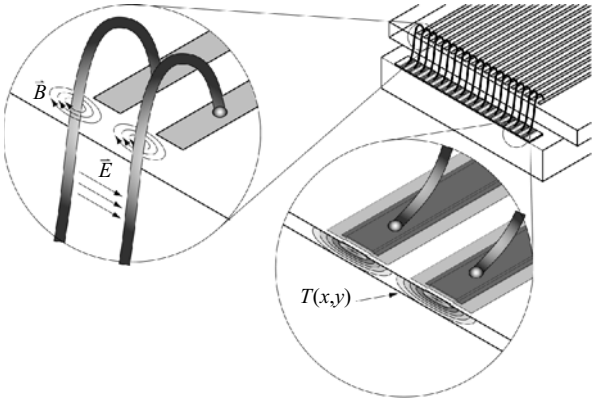

FIGURE 6.45. Due to current and voltage rise, electromagnetic fields induce currents into neighboring electric circuits. According to the temperature distribution, caused by the waste power of an emitter, the temperature of an emitter depends on the output of neighboring emitters [6.12]

on the capacitive and inductive coupling as well as on voltage and current rise (see Fig. 6.45).

The current rise time dI/dt is about $1 \cdot 10^6$ A/s for typical diode laser power supplies. The voltage rise time depends on the U-I characteristics of diode lasers. A good approximation for voltage rise time dU/dt is 10^7 V/s. The simulation and the experiment prove,, that both thermal and electric cross-talking are of no significant importance for the application [6.12].

Apart from the fact that typical diode laser bars cannot be spatially modulated, a low fill factor of diode laser bars is a disadvantage for numerous direct applications, because many applications require a completely filled intensity profile. Due to the geometry of the diode laser bar the fill factor is usually less than 50% . With certain different methods (for example, slow-axis-collimators) the fill factor can be increased up to 100% [6.12]. There are three different methods of increasing the fill factor.

- The first method is by using slow-axis collimators (see Chapter 4.2.5) With this method a fill factor of almost 100% can be reached. But this method is not suitable for many different diode laser bars, because the design of slow-axis collimators depends on the radiation of the diode laser bar, which differs.
- The second method is to turn the diode laser bar around the propagation axis, so that the space between emitters is reduced. This method is very simple to realize. The fill factor is free adjustable.
- The third method is to nest different bars together (see Fig. 6.46). Two bars with a fill factor of 50% are combined by polarization, wavelength, or spatial multiplexing (Chapter 4.3).

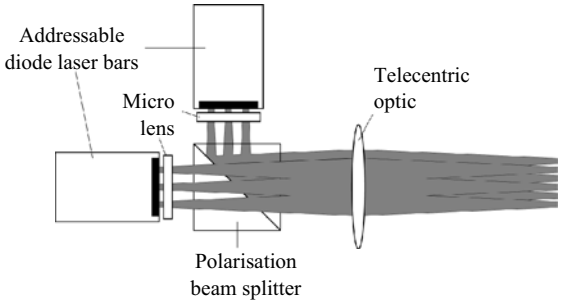

FIGURE 6.46. Two diode laser bars, combined with a polarization beam splitter, are nested together and imaged with a telecentric optic [6.12]

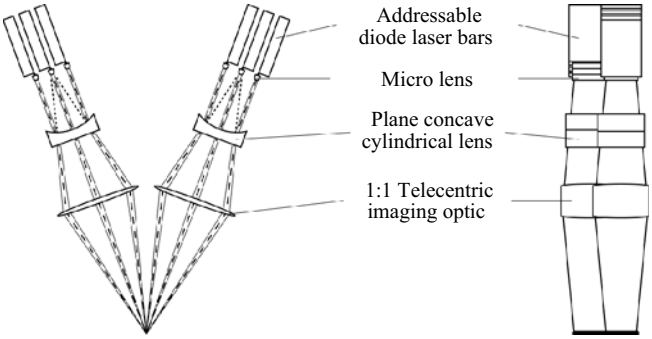

FIGURE 6.47. Opto-mechanical setup for one system with two modules to get an individually addressable intensity line with a length of 20 mm [6.12]

Choosing the appropriate method depends on the optical system and the diode laser bars. If the diode laser bars have a fill factor of 50%, the tilt method is easy to realize. For a lower fill factor the slow-axis method or nesting should be used. But especially for redundant systems the nesting method is not so simple to realize.

6.3.2.2. Optical and Mechanical Realization

To realize the system with an individually addressable intensity line, three bars are used with an emitter width of 150 μm and a pitch of 500 μm. To increase the fill factor of the bars from 30% up to 100%, three bars are nested together with spatial multiplexing in order to get a closed line with a length of 10 mm, as described above. The three bars are stacked vertically in one module. The bars are imaged with a telecentric 1:1 optic onto the workpiece. A concave cylindrical lens focuses the three bars onto a line and compensates the astigmatism. The system is built modularly, so that the line is extendable to 20, 30, or 40 mm. Figure 6.47 shows the schematic setup of the system, the three vertically stacked diode laser bars and

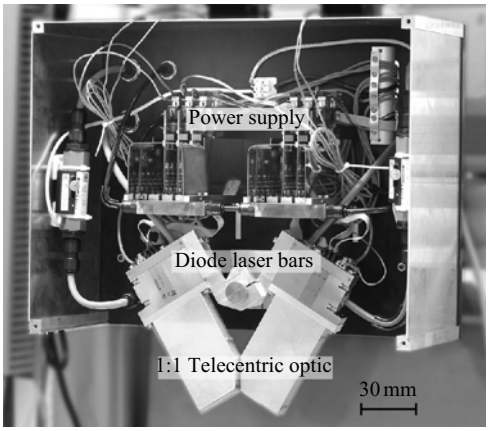

FIGURE 6.48. Picture of the individually addressable intensity line [6.12]

the 1:1 telecentric optic, which images the bars onto the workpiece. The width of one module is 14 mm, due to the dimension of the heat sinks. To get a closed line with two modules (the width of focus is only 10 mm), the modules must be arranged under an angle.

Each emitter is connected to its own power supply through bond wires, so that the emitters can be controlled individually. The power supply delivers a current of 1 A at a maximum frequency of 1 kHz and is connected to a personal computer by a CAN-bus interface.

6.3.2.3. Characterization of the System

Figure 6.48 shows the two modules with three bars each and the 1:1 telecentric optic. Above the two modules, which are arranged under an angle, there are the power supplies for the diode laser bars. The system has a width of 600 mm and a height of 500 mm.

With this setup an output power of 0.8 W and a focus size of $150 \times 150\ \mu m^2$ for each emitter is reached. Due to the $2 \times 3 \times 19 = 114$ emitters, which are arranged in a linear row the complete focus size is about 20×1 mm (see Fig. 6.49). The smile of the diode laser bars is between 0.4 and 0.8 μm, and therefore too big for this optical setup. Because of the similar smile of the diode laser bars, the smile is not a problem in fact, even though a smaller smile would be better and would make a smaller focus possible. In Fig. 6.49 blackouts of some emitters are readily identifiable. As an average about 1.67 emitters of each diode laser bar suffer a blackout. To compensate for emitter blackouts the system must be build redundant, so that each spot is composed of two emitters of different diode laser bars.

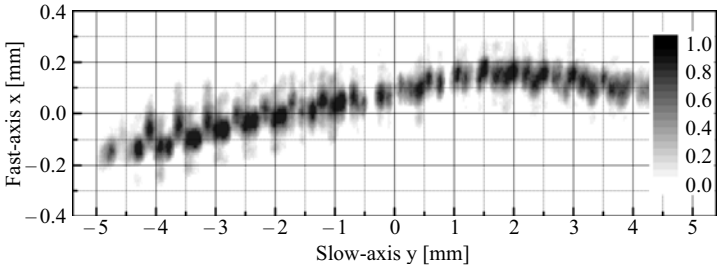

FIGURE 6.49. Focus of one module with three diode laser bars, consisting of 19 emitters ($3 \times 19 = 57$ emitters) [6.12]

6.3.2.4. Outlook

The system described above can be used for soldering electronic components on electronic circuit boards, simultaneous welding of polymers, or different materials processing applications in micro-system technology. It can also be used in special parts of biomedical sciences, for example reading out bio-chips for protein analysis. Nevertheless, the main field of application is the printing and display industry.

To demonstrate the features and possibilities of individually addressed diode laser bars, a further system was built for printing onto a polymer foil, based on the results of the realization of this system [6.17]. This system consists of two diode laser bars with 48 broad-area emitters each, which are combined by polarization multiplexing. The two diode laser bars operate in parallel. Thus, the emitters are superposed exactly, and the system is twice redundant. The power supply provides a maximum current of 1.2 A for each emitter with a maximum repetition frequency above 30 kHz. A 1:1 telecentric optic images the diode laser bars onto a polymer foil. A concave cylindrical lens compensates for the astigmatism. To increase the fill factor the two diode laser bars can be turned around propagation axis. To print out characters or patterns, the polymer foil needs to be moved perpendicular to the intensity line (labeling direction). This relative movement of polymer foil is realized by using a motorized translation stage. Power supply and motorized translation stage are controlled by a personal computer. Figure 6.50 shows the demonstration device.

This setup allows a fast generation of complex patterns with individually addressed diode laser bars (see Fig. 6.51) The dot size is about 100 μm in diameter. Due to the turning of diode laser bars around the propagation axis, the total height of the letters and therewith the focus line is about 6 mm. The writings are slightly curved, because the used diode laser bars are not absolutely straight-line. But if necessary this curve can be compensated for by the control logic. By using this system, a sufficient quality level of the labeling is achieved. Higher resolution and finer patterns seem to be practicable using suitable optics and an adjusted laser source [6.16].

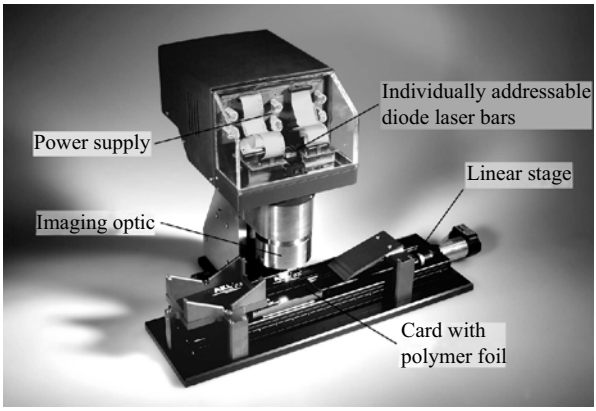

Figure 6.50. Demonstration device for printing polymer foils. Two individually addressable diode laser bars are combined with polarization multiplexing and imaged with a 1:1 telecentric optic onto polymer foil. A motorized translation stage moves the card with the polymer foil across the focus line [6.12]

Figure 6.51. A result of labeling experiments. The font size is about 6 mm and length about 30 mm. The labeling takes less than 2 seconds [6.12]

6.3.3. Line Modules for Contour-Adapted Plastics Welding

Veit Blümel, Alexander Knitsch, Ulrich A. Russek, Klaus-Peter Stolberg

One of the applications which has been boosted by the high-power diode lasers is laser polymer welding. However, so far almost exclusively vector welding has been applied, where a focused diode laser is scanned over the seam geometry. In this section, systems for an alternative technique, the so-called contour-adapted simultaneous welding are described, which allow us to form a line of laser light from individual modules with a line-shaped emission.

6.3.3.1. Basic System for Contour-Adapted Welding

As the emitting line of a single diode laser bar with its output power of some 10 W is sufficient for the polymer welding process, compact and flexible modules

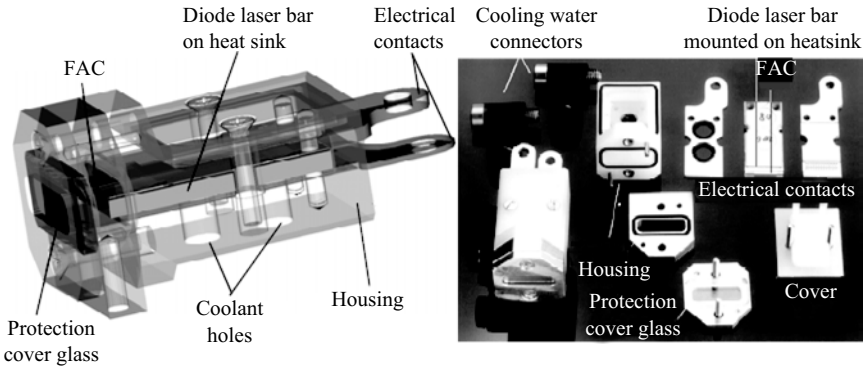

Figure 6.52. a (left): Layout of a compact diode laser module; b (right): Components of the single diode laser module

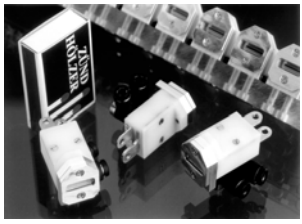

Figure 6.53. Setup and possible linear arrangement of the compact diode laser modules

consisting of a single diode laser bar can be arranged to permit simultaneous laser welding. Within this application, the entire weld seam is irradiated as a whole and welded with one single laser pulse. By means of appropriate beam forming and guiding a homogeneous intensity distribution fitting to the entire weld seam geometry has to be generated, which represents the challenge of the simultaneous process.

Layout and Design of the System

An easy task is irradiating a rectangular weld seam by lining up several diode laser modules to generate a simultaneous weld. The first step consists of developing and constructing diode laser modules with an intensity distribution that allows us to place several modules in a line and with a size placing them side by side. In Fig. 6.52a (left) a sketch of the diode laser modules is depicted, while Fig. 6.52b (right) shows the components of one diode laser module. Finally, Fig. 6.53 shows the modules as well as a linear assembly of several modules.

Optical and Mechanical Realization

The diode laser bars are mounted on a heat sink and the radiation is collimated in fast-axis direction (see Chapter 4.2.2). After the micro-lens adjustment the bars are set into POM (polyoxymethylene) plastic housings with made of brass, with contact-flags,

O-rings, and a protection glass cover. The housing isolates the components from the outside and presses them together. This creates the necessary pressure to ensure electrical contact and sealing. Alignment pins ensure that the components are correctly positioned and reduce the tension in the contact-flags.

The outer dimensions are $20 \times 20 \times 50\,\text{mm}^3$ (width × height × length) and the weight of each single module is only 40 g. The compact dimensions and conical edges of the modules allow them to be arranged at right angles to each other.

Characterization of the System

The developed diode laser modules have been implemented in a laser welding system to realize simultaneous laser beam welding of thermoplastics. The six diode laser modules have been mounted in a component part carrier, while each module can be placed individually concerning x-y-z coordinates as well as turned around an angle. Therefore, each diode laser module can be positioned separately to irradiate a certain part of the weld seam. Figure 6.54a (left) shows a schematic depiction of the laser welding system while in Fig. 6.54b (right) the components realizing the system can be seen. The main components of the system are:

- 6 diode laser modules (808 nm, max. 30 W)
- 6 electrical devices (max. 6 V, 40 A)
- 6 water flow control units (interlock system)
- 1 chiller
- 1 personal computer with control software program (32 bit, 400 MHz, 128 MB RAM) and I/O devices
- digital and analog PC cards for communication and control units of the system

Since the individual diode laser modules show different current–power characteristics, connecting them electrically in a row does not seem to be practical. Furthermore, allowing individual pulse shaping in time, an individual electrical control is very attractive. Therefore, the electrical power is supplied by six

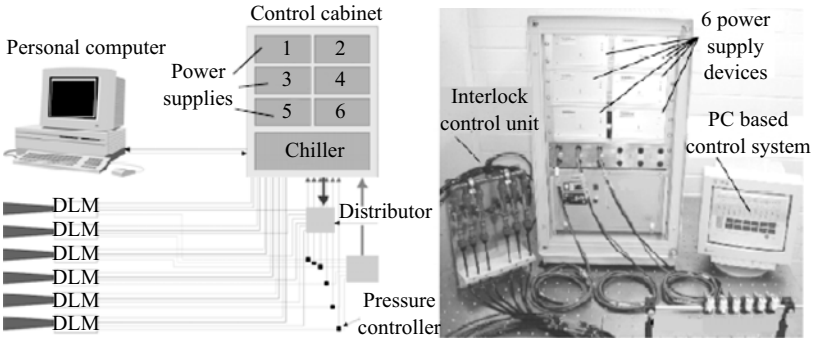

FIGURE 6.54. a (left): Schematic depiction of the laser system for simultaneous laser beam welding of thermoplastics; b (right): Main components of the laser system for simultaneous laser beam welding of thermoplastics

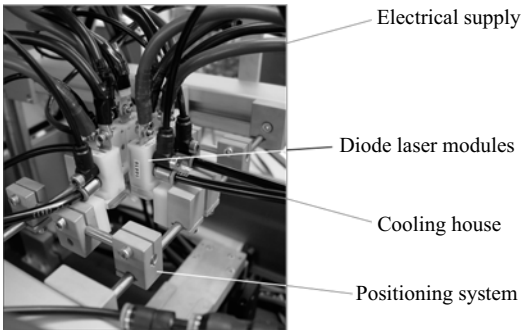

FIGURE 6.55. Assembling of six diode laser modules (first generation) for simultaneous polymer welding

devices supplying maximal 6 V and 40 A. The cooling of the diode laser system is performed with one chiller as well as with an individual water flow control unit for each diode laser module. So each diode laser module consists of its own electrical and cooling water connections including individual interlocks. A special software program allows the individual pulse shaping of each diode laser module while giving the opportunity to adapt current over time to the needs of application or weld seam position.

The first employed system for the simultaneous polymer welding process contains six diode laser modules (Fig. 6.55). The six identical modules are arranged in a way they irradiate the entire rectangular weld seam contour of a sample box ($20 \times 40\,\text{mm}^2$) allowing simultaneous welding with one single diode laser pulse. The modules supply a maximum output power of about 30 W at 40 A at a wavelength of 808 nm. The beam shape is a line, $1 \times 10\,\text{mm}^2$, at a working distance of about 100 mm. Even if only six modules have been used, the setup allows the individual control of 12 diode laser modules at a time. If the application of the contour (depending on the desired geometry) requires even more diode laser modules, the system can be easily extended.

Experiments have proven the applicability for simultaneous polymer welding. The results are illustrated in detail in Chapter 7.1.5 of this book. However, first systematic experiments, like those shown in Fig. 6.56, employing the high-power diode laser modules depicted in Fig. 6.52 and Fig. 6.53, have shown shortcomings also. Since these diode laser modules do not have any homogenizing optical elements, lining up their intensity distributions did not generate a homogenous intensity distribution along the entire weld seam. Instead, the individual emitters show a fluctuation in their individual power, which generates a rather inhomogeneous profile if they are overlapping in the far field. Furthermore, the edges of the beam profile are not sufficiently steep so that inhomogeneities in the overlap region of the modules are unavoidable. This corresponds to alternating weld quality along the weld seam, which is of course unacceptable.

Therefore, the setup of the second generation of high-power diode laser modules contains a homogenizing optical element guaranteeing, on the one hand,

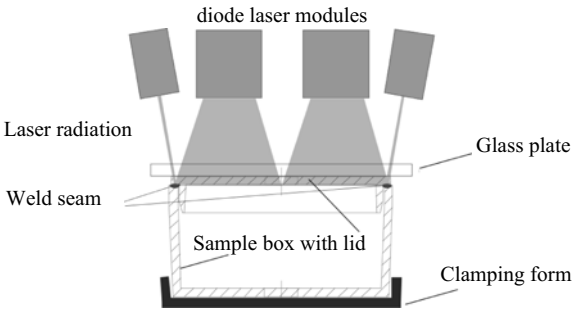

FIGURE 6.56. Assembling of six diode laser modules for simultaneous welding of polymeric samples boxes

a homogenous intensity distribution of each diode laser module as well as, on the other hand the opportunity to line the modules up while obtaining an overall homogenous intensity distribution along the entire weld seam.

6.3.3.2. Homogenized Line for Contour-Adapted Welding

First experiments above have shown, that for contour-adapted simultaneous welding of plastics with lasers, the homogeneity of the line modules should be better than $\pm 5\%$. For stacking the modules side by side the edge of the beam should be rather steep. The maximum width of the housing must allow a side-by-side positioning without a gap in the line contour. The required working distance is about 100 mm.

Layout and Design of the System

The target for this system is to generate a sharp-edged homogeneous line of $1 \times 20\,\text{mm}^2$. To achieve the sharp edge, an optical image of the laser source has to be generated. Otherwise the required steepness could not be obtained. To get the 20-mm width of the line, a 2:1 transformation of the diode laser bar (which has a width of 10 mm) is needed. With the fast-axis divergence of about 60° and a fast-axis collimating lens with a focal length of 0.9 mm, the beam waist at the exit plane of the lens has a height of about 1 mm, which is appropriate for the application.

If the diode laser bar is transformed directly, the power distribution of the beam at the target would be similar to the power distribution of the source. Since the source contains several single emitters, the modulation can reach values up to 100% . For this reason a homogenizer which mixes the emitting light in the direction of the slow-axis, while sustaining the line in the direction of the fast-axis, is needed. For achieving the best results the optical path within the homogenizer should be rather long. After a number of preliminary tests the minimum length of 200 mm was defined. In order to let the housing not become too large the optical path must be folded, which is clearly visible from the optical design as shown in Fig. 6.57.

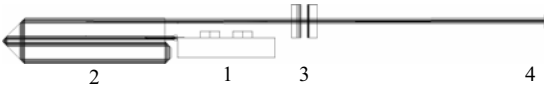

FIGURE 6.57. Optical design of the diode laser module to generate a beam with the dimensions $1 \times 20\,\text{mm}^2$ (1 = diode laser bar mounted on heat sink collimated with FAC-lens; 2 = homogenizer; 3 = objective for the 2:1 transformation (contains 2 cylindrical lenses); 4 = machining plane

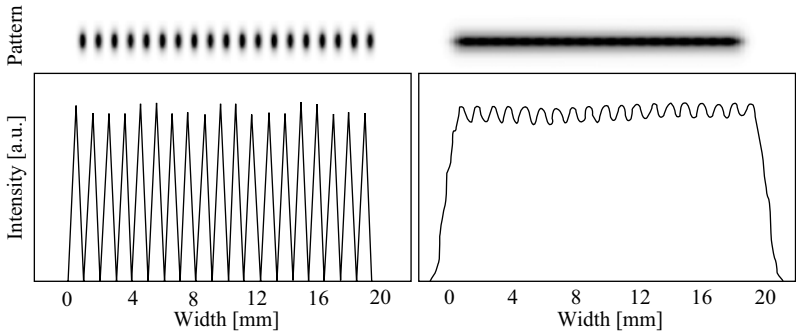

FIGURE 6.58. Computation of the expected results: at the left side without the homogenizer the structure of the emitters is well to be seen, at the right side the rays are mixed, so that it comes nearly to a continuous line

The results of the simulations for the optical design shown above are represented in Fig. 6.58. Although the results of the simulation represent an almost perfect homogenization, the real results will differ from that. The reason is the difference of the single emitters with regard to their power and their ray-emitting characteristics as already pointed out above.

Optical and Mechanical Realization

The optical power of an element is delivered from one diode laser bar mounted on a standard passively cooled heat sink. The heat sink itself is cooled by water with industrial quality. The diode laser bar is collimated with a fast-axis collimation lens. The output power of the module is up to 15 W. The main part of the homogenizer is a cuboid of $43 \times 14 \times 10\,\text{mm}^3$. To realize the deflections there are two small prisms wringed to the cuboid. A picture of the cuboid is shown in Fig. 6.59, where also the wringed surfaces are marked.

The diode laser and the homogenizer (parts 1 and 2 in Fig. 6.60) are mounted on a base plate in which the water and the power lines for the laser are integrated. The image forming objective with the two cylindrical lenses (part 3 in Fig. 6.60) is attached separately for simple exchange, as other optics might be used for other line widths or working distances. The diode laser housing is dust proof with the dimensions: $140 \times 20 \times 45\,\text{mm}^3$ (Fig. 6.61a). The weight is about 300 g. Due to the outer dimensions the units can be combined side by side to generate a longer line, consisting of sections of 20 mm (Fig. 6.61b).

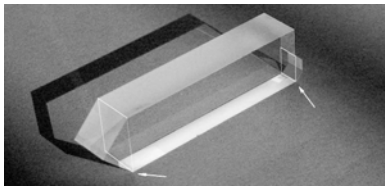

FIGURE 6.59. Homogenizer consisting of several prisms, the prisms are wringed to the main body at both ends of it

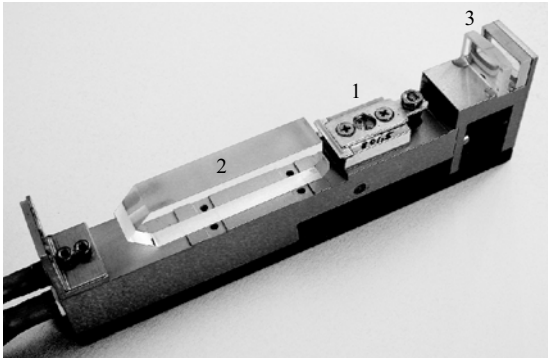

FIGURE 6.60. Setup of the diode laser unit (explanation see Fig. 6.57); the changeable objective consisting of 2 cylindrical lenses (No. 3) is clearly shown

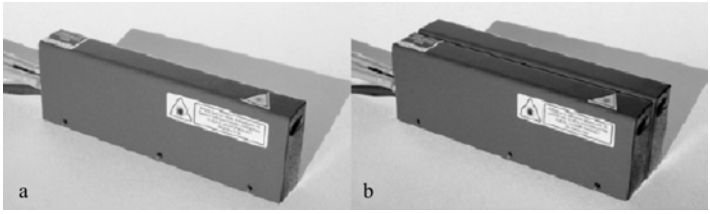

FIGURE 6.61. Diode laser unit with housing (a); the width of the housing is exact 20 mm to arrange the modules side by side (b) to get a continuous line

Characterization of the System

Altogethersix modules are combined in the system. These modules were arranged in a rectangle shape with the dimension 20 × 40 mm (Fig. 6.62). The intensity distributions of two selected modules are shown in Fig. 6.63. As can be seen in the pictures the homogenization is not fully successful as the modules are still showing different beam shapes. It has been found that the symmetry of the intensity

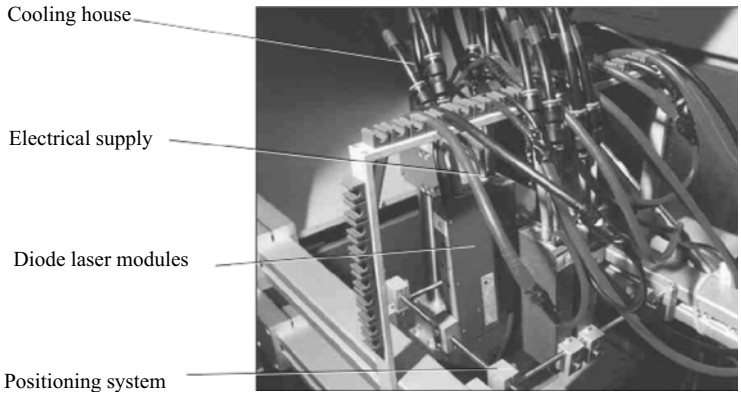

FIGURE 6.62. Assembly of six diode laser modules with homogenizers for simultaneous polymer welding

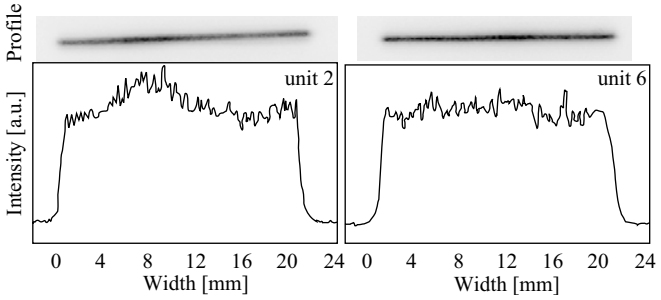

FIGURE 6.63. Intensity distributions of two homogenized units measured in the working plane

distribution is rather sensitive to the alignment of the homogenizer. However, even if both modules are optimally aligned, unit 2 shows much more modulation than desired, while unit 6 comes close to the target distribution. The reasons are-as described above – the different emitting characteristics of the different diode laser bars. These results show that the optical length within the homogenizer of about 200 mm is still too short for a complete statistical mixing of the rays of a common diode laser bar. For a better statistical mixing the optical path should be elongated and/or the angles of the rays within the homogenizer have to be increased for getting more reflections at the parallel side surfaces. These conditions have to be balanced with the request of the width of the line.While the optical path to the machining plane is extending, the width of the line increases.

With that arrangement a cover could be welded to its plastic housing. In spite of the lack of homogeneity of some modules, the welding experiments were quite satisfying (see Chapter 7.1.5). They show also that the requirements of such a machine can be adapted to the desired process results.

6.3.4. Diode Laser Line Cutter

Dieter Plum, Martin Traub

Cutting of metals is usually performed with a nearly circular spot of high intensity that is moved over the workpiece following the cutting contour. For separating thin metal sheets with a width of 40 mm simultaneously without moving parts, a diode laser system providing a beam with a high aspect ratio, greater than 100, has been developed. A homogenous power distribution over the width of the line is essential for this application to avoid local hot spots and uncut areas, and thus lead to smooth cutting edges. To maximize the power intensity of the line, a top-hat distribution is required over the width of the line, while perpendicular to this direction, a Gaussian power distribution is ideal for this application.

6.3.4.1. Optical Setup

Conventional high-power diode laser bars (wide area emitters, see Chapter 2.4) offer a diffraction limited Gaussian intensity profile for the fast-axis, while the slow-axis intensity profile has neither the required top-hat shape nor a Gaussian distribution and depends on the diode laser structure. Therefore a waveguide has to be implemented as a homogenization tool for the slow-axis of the diode laser line cutter. The principle of this device is shown in Fig. 6.64. At the entrance position ($z = 0$), a divergent Gaussian beam enters the brick-shaped waveguide that is made of fused silica. As the side surfaces are polished, rays hitting these surfaces are reflected by total internal reflection. The beam is homogenized by multiple reflection [6.18].

For the realized diode laser system, the slow-axis of four diode laser stacks with six bars each is focused by cylindrical lenses onto the entrance surface of the waveguide. To optimize the angular distribution of the slow axis, a micro-lens array is placed in front of the waveguide. The focused diode laser stack suffers from the modulated far field distribution due to the pitch of the stack. This modulation is reduced by the micro-lens array, and the far-field distribution is smoothened. Thereby, the length of the waveguide can be reduced to 100 mm for a sufficient homogenization effect. The slow axis is homogenized by the waveguide, and a top-hat distribution for the slow axis is achieved at the exit surface of the waveguide, while the fast axis is not influenced by this device. Due to the high aspect ratio of the focus, which is needed for this application, cylindrical lenses are used to shape the fast-axis and slow-axis behind the waveguide separately. While its exit surface is imaged in the direction of the slow-axis by six cylindrical lenses on the workpiece, the fast-axis is focused by two cylindrical lenses. The optical setup for the slow-axis and for the fast-axis is shown in Fig. 6.65.

6.3.4.2. Description of the System

As already mentioned above, for this application, four stacks are arranged in the slow-axis direction. Each diode laser stack consists of six diode laser bars with fast-axis collimation. Thus 24 diode laser bars are used offering in total an output power

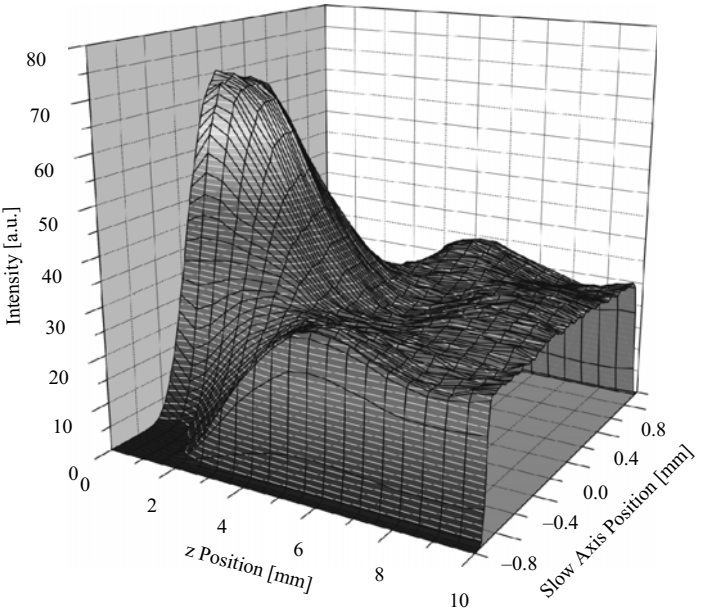

FIGURE 6.64. Homogenization of a Gaussian intensity profile by total internal reflection inside a waveguide. The beam enters the waveguide at the position $z = 0$ mm, while the exit surface is located at the position $z = 10$ mm. The Gaussian distribution is converted to a top-hat distribution

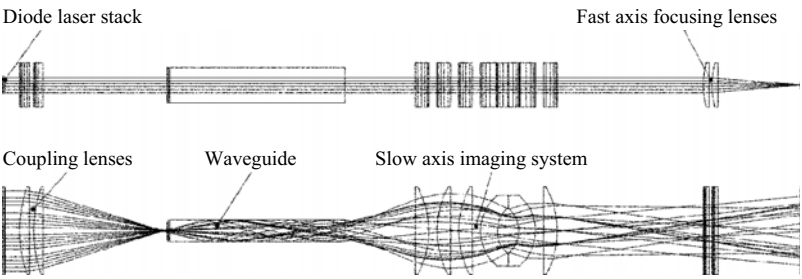

FIGURE 6.65. Optical setup of the fast axis (top) and slow axis (bottom) consisting of coupling lenses, waveguide, imaging system for the slow axis and focusing lenses for the fast axis

of about 1 kW. All optical components are arranged linearly on a common base plate which is covered by a housing made of aluminum. The waveguide is mounted on a water-cooled copper frame to remove the heat dissipated by this component efficiently. A nozzle is placed between the workpiece and the last focusing lens to supply process gas and to avoid contamination of the optical components. The overall width of the optical setup amounts to 500 mm. Figure 6.66 shows the realized system without the cover.

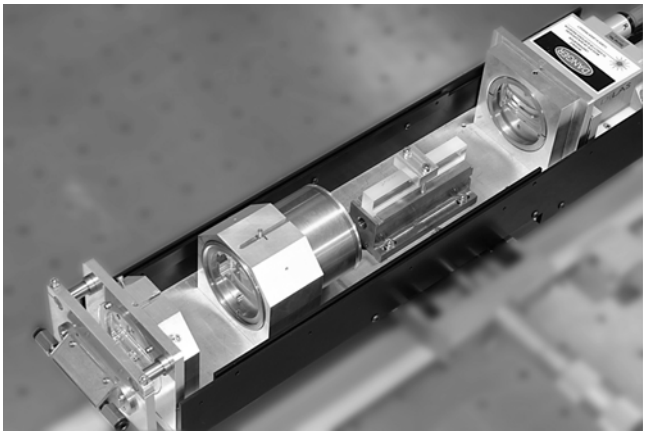

FIGURE 6.66. Setup of the diode laser line cutter without housing, consisting of the fast-axis focusing lenses, the slow-axis relay system, waveguide, and diode laser stack (from left to right)

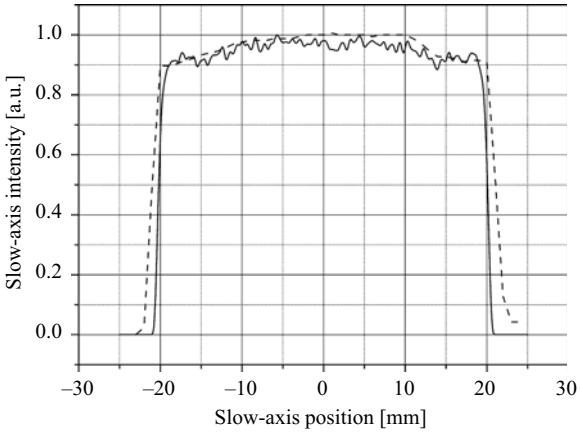

FIGURE 6.67. Measured results (dashed) and results of the ray tracing (solid) for the slow-axis of the diode laser line cutter

6.3.4.3. Results

Conventional tools for beam diagnostics are difficult to use for a line with a width of 40 mm. Therefore, the power distribution of the slow-axis and the fast-axis has been measured separately. For the fast-axis, a small section of the line has been analyzed using a CCD camera. A slit with a width of 1 mm has been moved by steps of 1 mm along the slow axis and the power behind the slit has been recorded to measure the slow axis intensity profile. To calculate the power distribution achieved by the setup, three-dimensional non-sequential ray tracing has been performed. The results of the ray tracing and the measurement of the slow-axis distribution are shown in Fig. 6.67.

The optics generate a line with a width of 40 mm and a length of 0.2 mm. The result is an almost perfect top-hat profile for the slow axis with a homogeneity of more than 90% and an edge steepness less than 5% . In the fast axis the Gaussian profile is maintained. The optical efficiency (output power of the optics divided by the power measured after the fast-axis collimators of the diode laser benches) amounts to 78% .

Cutting experiments have proven the feasibility of the system, and simultaneous welding of thin metal sheets has also been performed (see [6.19] and Chapter 7.2.3).

6.3.5. Annular Diode Laser Beam Tool

Alexander Knitsch

As mentioned above high-power diode laser systems feature the modularity to form different beam shapes adapted to a respective application. For burn-off stabilized flame cutting or laser hybrid cutting an annular focus geometry surrounding a gas nozzle or another laser beam is ideal. Thus, an annular diode laser beam tool with an output power of 2 kW has been developed.

6.3.5.1. Layout and Design of the System

To realize the annular diode laser beam of high output power, ten identical diode laser modules are coaxially arranged around a cylindrical carrier as shown in figure Fig. 6.68. Each of the ten diode laser modules consists of a commercially available diode laser stack with six broad-area diode laser bars (see Chapter 2.4). After the collimation in fast- and slow-axis directions, the radiation of the stack is focused with beam shaping optics (cylindrical telescope and focusing lens) to a line with the dimensions of $3 \times 0.6\,\mathrm{mm}^2$. By the use of adjustable bending

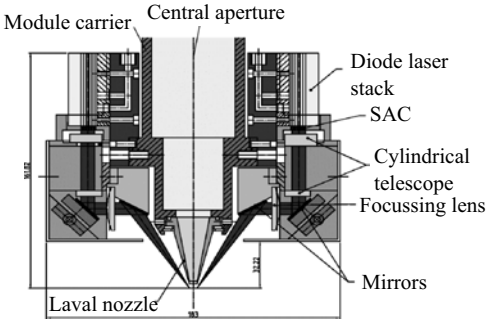

FIGURE 6.68. Schematic arrangement of the diode laser modules around a cylindrical carrier with a central aperture

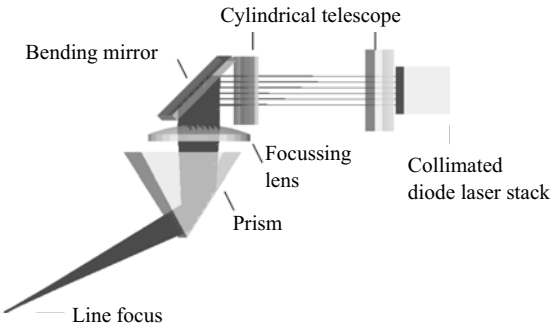

FIGURE 6.69. Ray tracing of the single diode laser modules

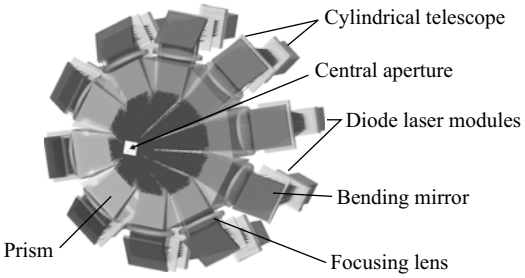

FIGURE 6.70. Ray tracing of the annular diode laser beam tool

mirrors, the linear foci of each single module can be aligned to form an annular beam spot.

6.3.5.2. Optical Simulation

Prior to the optical and mechanical realization an optical simulation of the single diode laser modules (Fig. 6.69) as well as of the whole laser beam tool is made (Fig. 6.70). The optical rays were traced with a non-sequential ray-tracing program. Starting with the emission characteristic of one emitter the rays from all emitters and bars to the focal plane were traced. The results give some ideas about possible efficiency, the focal ring diameter, and ring width.

Fig. 6.71 (left) shows the annular intensity distribution of the whole laser beam tool where the diode laser modules are adjusted in a way to form a decagon with little overlap. Out of the simulation the ring diameter amounts to 5 mm with a ring width of 0.6 mm.

6.3.5.3. Optical and Mechanical Realization

The optical and mechanical setup was realized immediately following the optical simulation. After the adjustment of the collimation micro-optics of each

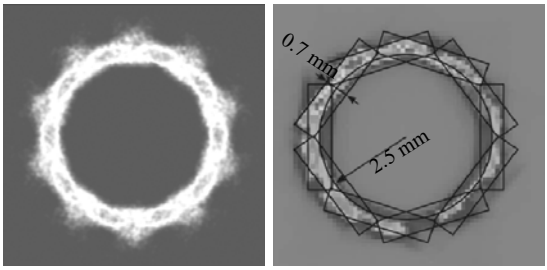

FIGURE 6.71. Annular intensity distribution of the diode laser beam tool: calculated (left) and measured (right)

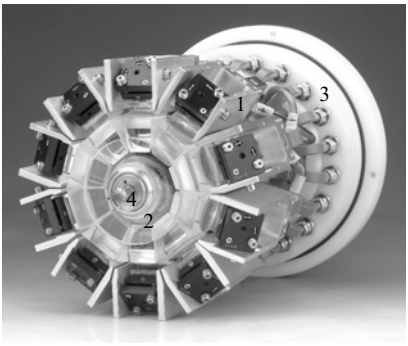

FIGURE 6.72. Annular diode laser beam tool with ten single modules (1), protective glass (2), water connection and power supply (3), and cross-jet nozzle (4)

laser stack, the single modules were completed by mounting the telescope and focusing optics as well as the adjustable bending mirror to the stack carriers. Afterwards the ten modules were mounted on the module carrier, as shown in Fig. 6.72. The water and power supply of the single modules run to the upper housing cover where on the reverse side the annular diode laser beam is emitted.

To protect the device's laser optics against staining by fume deposition and splatters, a cross-jet nozzle that generates a circumferential, radial outward directed compressed air jet is integrated as well as a protective glass. The annular diode laser beam tool features a central pass aperture that can be used to coaxially feed cutting and shielding gases as well as welding or brazing filler material toward the interaction zone. Furthermore, it is possible to create a laser–laser hybrid beam tool by passing a second, focused laser beam generated by a gas or solid-state laser through the central aperture. Thus a hybrid beam with a center of high-power density surrounded by the diode laser ring can be realized and used for welding and cutting applications. In the latter case the central laser beam has to be passed through the cutting nozzle.

Table 6.8. Performance parameter of the annular diode laser beam tool*

Laser output power	Ring diameter	Ring width	Working distance
2,000 W	5 mm	0.7 mm	50 mm

*If not stated otherwise all values were measured at the workpiece plane and at 50 A diode current.

6.3.5.4. Characterization of the System

With an output power of 200 W for each module, the maximum power of the annular diode laser beam tool amounts to 2 kW at the workpiece. The measured focal intensity distribution is shown in Fig. 6.71 (right), where the line foci of the ten modules form the simulated decagon with little overlap. Out of the measurement the ring diameter amounts to 5 mm with a ring width of 0.7 mm. The results suit very well with the optical simulation. Data are summarized in Table 6.8.

First experiments have proven the applicability for flame-cutting applications, where the central pass aperture of the annular diode laser beam tool is used to feed cutting gases coaxially by a Laval-nozzle or a CO_2 laser beam toward the interaction zone (see Chapter 7.2.4). Single-shot welding technology without relative movement of the workpiece and laser beam has also been demonstrated with the annular diode laser beam tool (see Chapter 7.1.2.3).

6.3.6. Process-controlling Modular Diode Laser System for Transformation Hardening

Alexander Drenker, Dieter Plum, Jan Sommer, Martin Traub

Transformation hardening is one of the most attractive processes for high-power diode lasers, since their moderate beam quality and their low power density is sufficient for many applications [6.20]. Basically, laser hardening generates less distortion than conventional methods, but nevertheless warpage is still a problem that often occurs in the case of high precision parts.

The purpose of the process-controlling modular diode laser system (PMDS) is to overcome the problems with warpage. Mainly this will be achieved by simultaneous treatment of all loaded areas of a workpiece with the help of the modular diode lasers. As an example Fig. 6.73 shows the simultaneous hardening of the four ball-bearing tracks of a linear guidance rail. More details about applications of this system can be found in Chapter 7.3.2

The Process-controlling Modular Diode Laser System (PMDS) consists of:

- five diode laser modules with integrated pyrometers,
- five modular process-control units,
- the real time process software for communication and process-control and
- the graphical user interface.

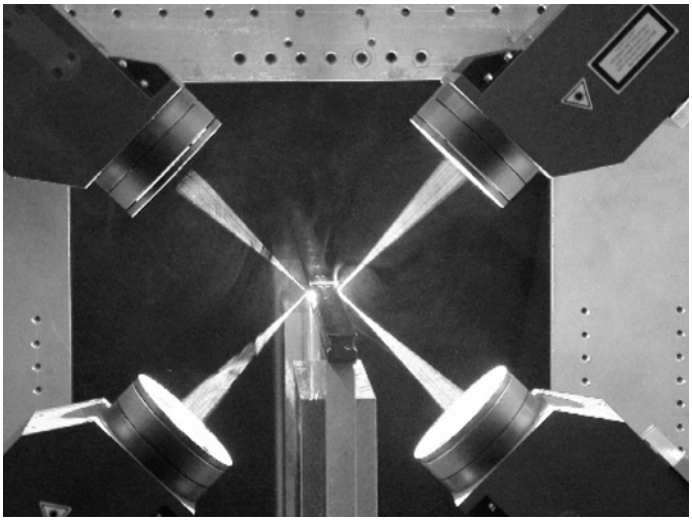

FIGURE 6.73. Application example; simultaneous hardening of four ball bearing guiding tracks with four diode laser modules

6.3.6.1. Diode Laser Module with Slow-Axis Homogenization and an Integrated Pyrometer

For applications like hardening, a top-hat intensity distribution for one direction and a Gaussian beam profile for the other direction, are demanded. Diode lasers offer a diffraction-limited Gaussian beam profile for the fast axis, but the power distribution of the slow axis depends on the type of diode laser used and is neither Gaussian nor top-hat. Assuming a constant output power of each emitter, an aperture placed a few millimeters behind the emitters where the single emitters are overlapped, results in sharp edges with a flat plateau for the slow-axis of the diode laser stack (see Fig. 6.74a, left, for the distribution created with an aperture placed 10 mm behind the diode laser bar). However, power changes of single emitters over time yield in a change of the distribution as shown in Fig. 6.74 b. In this case, 50% of the diode laser bars emitters have failed, so the width of the line has changed significantly and the steepness of one edge is reduced. It is very evident that such a profile would considerably change the beam parameters and a hardening process defined with the profile in Fig. 6.74a would fail. In addition, the aperture absorbs about 10% of the diode laser bar's optical output power. Thus a homogenization tool is used for this module to shape the slow-axis to a top-hat distribution. If the homogenization tool is well designed, i.e., all parameters as length, aspect ratio, and numerical aperture are chosen carefully and well adapted to the diode laser's intensity distribution, a top-hat profile can be realized that is independent of the power emitted by each emitter. Thereby, a fail-save diode laser system can be realized for these applications.

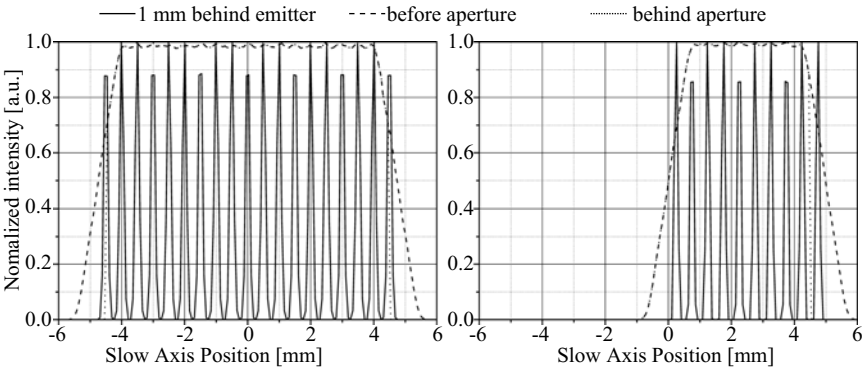

FIGURE 6.74. (a) Left: Intensity distribution for a 10 mm diode laser bar 1 mm behind the emitter (solid line), 10 mm behind the emitter (dashed line) and behind an aperture placed 10 mm behind the emitter with a free aperture of 10 mm (dotted line); (b) Right: Intensity distribution after nine emitters have failed

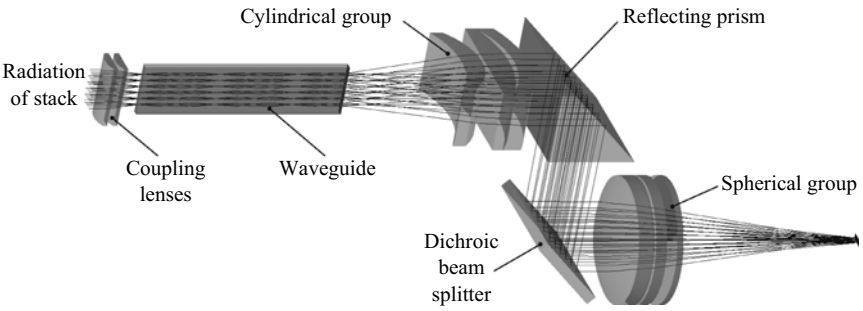

FIGURE 6.75. Optical setup of the diode laser module for hardening applications

For the diode laser module used for hardening, the slow-axis of a diode laser stack consisting of 12 diode laser bars is focused onto the entrance surface of a brick shaped silica waveguide by cylindrical lenses. The slow-axis is homogenized by multiple internal reflections inside the silica solid, while the fast axis propagates unchanged through the waveguide. At the exit surface of the waveguide, the near field of the slow-axis has a sharp top-hat distribution, while the fast axis still consists of 12 Gaussian beams. A group of three cylindrical lenses is used to collimate the beam exiting the waveguide for the slow-axis. Two spherical lenses focus the slow and fast-axis on the workpiece. Thereby, the cylindrical and spherical lenses act like a relay system for the slow-axis that images the exit surface of the waveguide onto the workpiece. A prism and a dichroic mirror between the cylindrical and spherical lenses are used to realize a parallel offset of the beam. The dichroic mirror separates the temperature radiation, which is generated at the surface of the workpiece from the laser beam path for the purpose of process control. The optical setup is shown in Fig. 6.75.

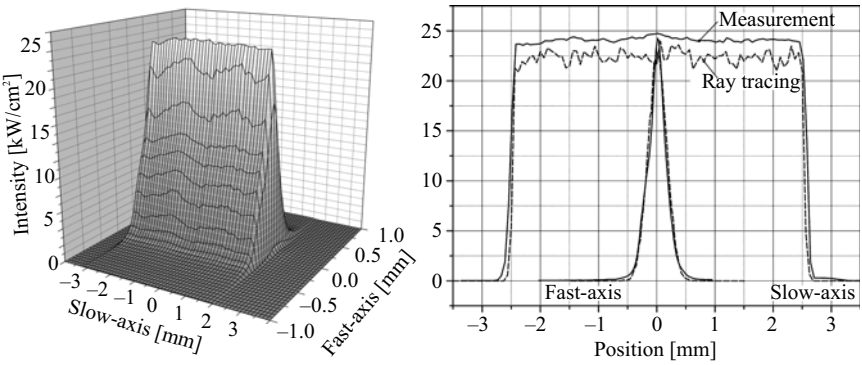

FIGURE 6.76. a (left): Intensity profile of the diode laser module at the workpiece. b (right): Comparison of the calculated and measured intensity profile of the diode laser module

The power distribution at the workpiece of the described optical system has a top-hat shape for the slow-axis and a Gaussian distribution for the fast-axis (Fig. 6.76a). For all five diode laser modules, only minor differences in the power distribution can be observed. A three-dimensional non-sequential ray tracing has been performed to estimate the intensity profile of the real system. The ray tracing shows good agreement with the measured intensity profile both for the slow- and fast-axis distribution, as depicted in Fig. 6.76b (right).

A solid aluminum frame is used for the diode laser system allowing an easy alignment of all optical components in a rugged, hermetically sealed housing. The realized system with an open cover is shown in Fig. 6.77.

The modules meet the following specifications:

- output power 450 W
- working distance 90 mm
- wavelength 808 nm
- spot size 1×5 mm(Gaussian $\times$ top hat)
- homogeneity $>90\%$

As mentioned above each diode laser module is equipped with a single color pyrometer. The pyrometer detects the near infrared temperature radiation (1,100–1,700 nm) emitted from the process zone in the focal plane of the diode laser module. A dichroic mirror inside the diode laser module splits off the temperature radiation from the laser beam path. An adjustable lens system focuses the temperature radiation into an optical fiber which is connected to an opto-electronic amplifier. All pyrometers are individually calibrated with the help of a black body radiation source. The pyrometers measure the radiation temperature roughly in the range from 500°C to 1500°C. The radiation temperature is the temperature of a black body that emits the same amount of radiation in the near infrared band as the measured object. However, the emission ratio of technical surfaces is always lower than the emission ratio of a black body reference source. Therefore the radiation temperature which is measured at a technical surface by the pyrometer is

FIGURE 6.77. Realized diode laser module

generally lower than the thermodynamic process temperature. To simplify matters in the following sections the process temperature will be used as synonym for the radiation temperature.

6.3.6.2. Process-Control Unit

Each process-control unit consists of three main functional blocks, a high-power current supply, a process temperature controller, and a supervising communication interface (Fig. 6.78). The latter links the graphical user interface to the process-control units via CAN-bus. The high-power current supply provides the electrical energy for the diode laser modules. Each temperature controller receives the temperature signals from the associated integrated pyrometer. Firstly, each controller determines the process temperature. Secondly, if the closed-loop control mode is enabled, each temperature controller adjusts the emitted laser power to achieve exactly the preset temperature individually in the associated process zone.

6.3.6.3. Real-Time Process Software

The functions of the PMDS are mainly carried out by the real-time process software, which is implemented in the microcontroller of the process-control units. The main functions are

- determination of the process temperature
- feedback control of process temperature

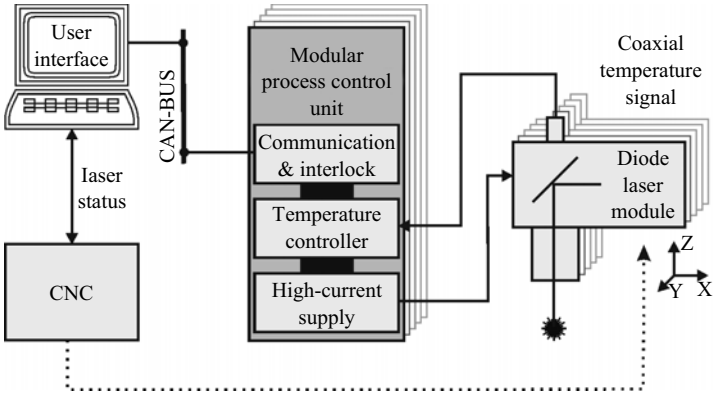

FIGURE 6.78. Block diagram of the process-controlling modular diode laser system

- recording and uploading of signals during processing
- CAN-bus communication
- safety interlocks

All analog input and output signals are sampled and digitized with a rate of 20 Hz and a resolution of 12 bit. The actual setting of the process temperature is determined from the temperature signal with the help of two parameters which are individually defined for each pyrometer during its calibration.

There are two modes of operation:

- the closed-loop process temperature control mode, and
- the open-loop power control mode.

In the closed-loop mode a digital proportional-integral (PI) controller is active. In open-loop control mode the PI controller is disabled. In this case the diode laser power is directly controlled by the desired setting. In both modes of operation the input for the desired setting process may be defined as a constant or as a path-dependent variable or externally by an analog signal from the CNC of the system, were the PMDS is applied to.

During processing of a workpiece, all signals are recorded until the memory of the microcontrollers is expired, which is the case roughly 150 s after a process has been started. If required for later off-line analysis, the recorded data can be uploaded via the CAN-bus onto a mass storage media in the graphical user interface. The data are written into a text file which can be processed with the common office software (e.g., EXCEL©).

For the CAN-bus communication a serial protocol is implemented, which enables the setup of each process-control unit, its secure and robust operation, as well as an effective and fast data transfer during upload of recorded process signals. A watchdog supervises the communication between graphical user interface and the process-control units. When the CAN-bus communication is interrupted for more than 1 sec the process-control unit generates a safety interlock.

6.3.6.4. Graphical User Interface

The graphical user interface (GUI) enables the operator to access the functions of the PMDS. The operator is guided through different windows and there is no programming knowledge required. The main software functions of the GUI are

- Initializing
- Processing
- Archiving

During the initializing phase the operator configures the PMDS by selecting the diode laser modules and entering the process velocity. If required, the controller mode as well as the controller parameters can be individually defined for each selected diode laser module. Otherwise it is possible to copy the actual configuration to the consecutive diode laser modules. Finally the configuration is checked and transmitted via the CAN-bus into the process-control units.

After initialization the PMDS is ready for the processing phase. After receiving the start signal from the CNC, the programmed process runs until it either is stopped by the CNC or the programmed process time expires. During processing every 200 ms a sample of all process signals is transmitted to the GUI to display an overview of the dynamic system behavior in a bar chart.

Finally the recorded process signals can be archivated. Therefore the GUI supports the upload of the recorded process data via the CAN-bus.

6.3.7. Ring-Shaped Laser Beam for Laser-Assisted Machining

Klaus Stolberg, Veit Blümel

Diode lasers have successfully been used as a local heat source in turning machines [6.22]. Here, the laser acts as an energy source for softening the material in front of the turning tool. Hard and brittle materials can be turned that way and the lifetime of the turning tool can be considerably elongated. To apply the same method to a milling machine is more complex as the machining direction is changing during the process and thus, the laser must be constructed in such a that way that it is always moving ahead of the milling tool in the milling direction. This section describes a diode laser system providing this feature.

6.3.7.1. Layout and Design of the System

As mentioned earlier, the working direction for milling processes changes depending on the workpiece geometry – resulting in the requirement of 360° access of laser beam around the milling tool. Thus, a machine concept has been developed which integrates a laser source with segments of a focus ring. A multiple-source laser system was designed, consisting of three identical laser devices with individual fiber coupling and processing optics. The processing optics were integrated into the milling machine, surrounding the front of the milling tool and generating a 90° heating zone formed by line-shaped foci of ca. $10 \times 2\,\text{mm}^2$ as depicted in Fig. 6.79. The assembly of the three heads can be turned around the milling tool.

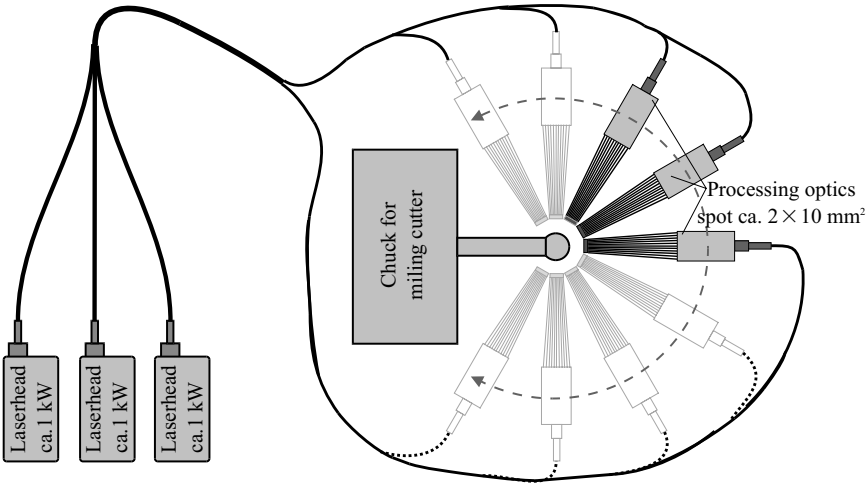

FIGURE 6.79. Concept of laser integration into a milling machine: three laser units are fiber coupled to three working optics creating a 90° focus consisting of three line spots. The 90° zone can be rotated around the milling tool for heating up the workpiece in the milling direction

6.3.7.2. Optical and Mechanical Realization

Compared to the fiber-coupled kilowatt system described in section 6.2.3, the laser which is necessary for the milling system demands optimized beam quality, because geometrical reasons and dynamics of moving optics limit the size and the weight of the optical components. Another argument for the necessity for improved beam quality is the demand for a maximum working distance, because the milling process generates particles like sparkles and swarfes from the workpiece with the risk for optics destruction.

The expected processing speed demands a total power in the range of 700–1,000 W. Thus, the optics were specified for a maximal diameter of 1 inch and a free working distance of more than 80 mm. The last optical surface should be shielded against dust or particles by a cover glass.

Many details of this laser are similar to the fiber-coupled kilowatt system which is described in section 6.2.3. The main differences between the two systems are:

- The beam quality demands require collimation in both the fast-and slow-axis (see Chapter 4.2) and thus bars with a fill factor of only 30% must be used instead of the 50% fill factor bars.
- To achieve the specified power, it was necessary to include an additional wavelength (880 nm) for the wavelength coupling, which enhances the brightness without loss of beam quality.
- The components of the working optics must be integrated into the milling tool, i.e., one goal of optics design is the functional integration, but not necessarily the minimum geometrical length.

In the optical pathway we started with a beam-parameter-product of about 200 mm ∗ mrad × 46 mm ∗ mrad (slow-axis × fast-axis) of fast- and slow-axis collimated stacks with six bars each. Symmetrization of the beam-parameter product was carried out by the director-/redirector-rearrangement technique with a ratio of 1:4, followed by an additional adaptation of beam divergence with a cylindrical lens. The method is described in section 6.2.3. After beam shaping we got a beam-parameter-product of 50 × 55 mm ∗ mrad, which is good enough for fiber coupling into 1 mm Ø/NA 0.11 fibers. After combining polarization directions for each individual wavelength using polarization multiplexers (PMX), wavelength multiplexers (WMX) were employed for the combination of the three wavelengths (Fig. 6.80) to get a maximal brightness. This multiplexed emission is then focused into a commercially available quartz fiber with a diameter of 1 mm and a numerical aperture of 0.11.

Within the mechanical limitations of the milling tool holder it was necessary to transmit the laser power from the output facet of quartz fiber to the workpiece. In a ray trace simulation a two-stage optics with a collimating and a focusing lens group has been designed (see Fig. 6.81).

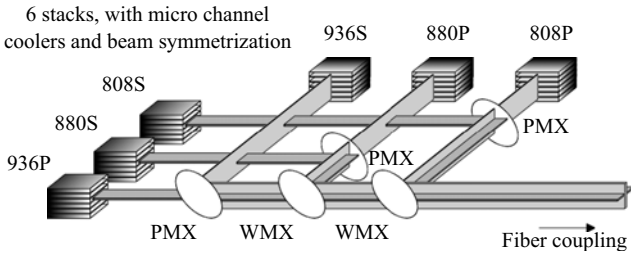

FIGURE 6.80. Optical arrangement of the milling support laser: 808, 880, and 940 nm stacks, with six laser diodes each, multiplexed by polarization and wavelength

FIGURE 6.81. Optical scheme of the processing optics with folding mirror: The diverging beam from the fiber output is collimated by the first lens group; the second lens group generates beam shape of 10 × 2 mm^2 in focus. The distance of both lens groups can be adapted to the geometrical limitations of the milling tool; the propagation direction is changed by a 52° full-metal folding mirror

This way the distance between both lens groups can be aligned to the needs of the mechanical construction without great influence on focus shape and size. The focused beam was folded by a 53° folding mirror to redirect the laser onto the workpiece in front of the milling tool with a free working distance of ca. 82 mm.

6.3.7.3. Characterization of the System

As shown in section 6.2.3, there is a set of loss factors inside the optical pathway beginning from collimation of the emitter output up to the fiber coupling optics. For the setup described here a total throughput of 52% was measured. Assuming a typical electro-optical efficiency of the laser bars of about 50%, a total plug-wall efficiency (without considering the losses in power drivers) of 26% can be calculated. A total power of ca. 900 W was measured at the end of the fiber at a current of 47A. The P-I characteristics of each module show a nearly linear behavior with a threshold at about 8 A.

The characterization of the beam has been performed by measuring the temperature distribution, which is generated if the beam hits the surface of a ceramic workpiece by a CCD camera (Fig. 6.82, top right): The top-hat profile of the laser beam as calculated in the simulation and shown in Fig. 6.82 (top left) resulted in smooth temperature distributions of the same size ($2 \times 10\,\mathrm{mm}^2$); cross sections of this temperature distributions in both directions are depicted in Fig. 6.82, right).

All electrical and cooling components had been assembled in two 19-inch standard racks with total dimension of $1,120 \times 800 \times 1,600\,\mathrm{mm}^3$ (including laser head, see Fig. 6.83).

The same methods and components as described in 6.2.3 have been used to establish a high level of reliability (Fig. 6.84):

- Shortcut relays inside laser head for ESD protection (not shown)
- Dust and moisture protection of laser housing
- Control of DI water flow and resistance
- Control of optics cooling water flow

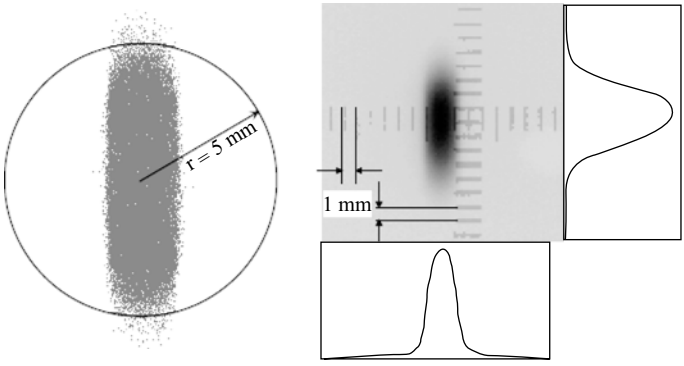

FIGURE 6.82. Beam characterization: Left side: ZEMAX® simulation of the optical intensity distribution; the circle shows a radius of 5 mm. Right side: CCD camera picture of the temperature profile on an irradiated ceramic plate and respective intensity measurements.

FIGURE 6.83. Milling support laser assembled in 19-inch racks: left side, cooling device, right side, power driver and system control, on top: laser head

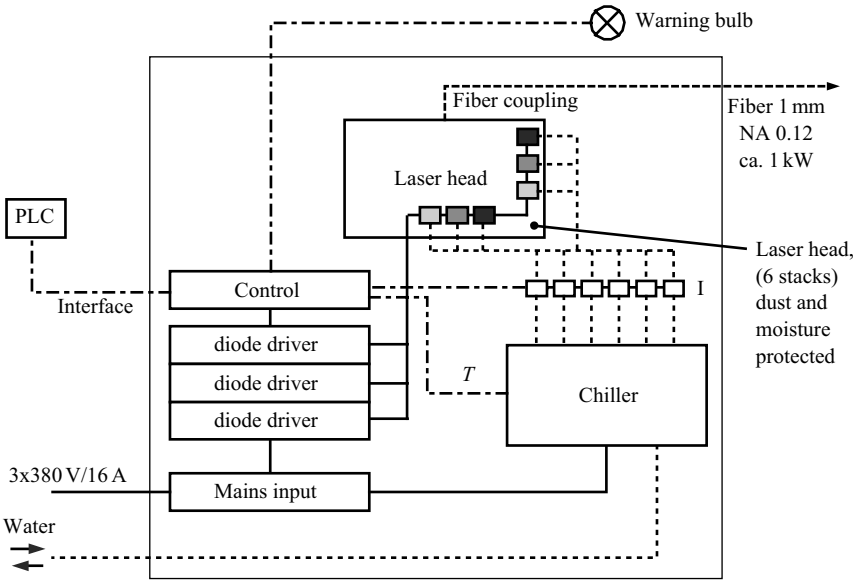

FIGURE 6.84. System overview of fiber-coupled kW system: hermetically sealed laser head with laser units and bulk optics is supplied with power and cooling; control unit supervises critical parameters and translates to an bidirectional external interface operation commands and status information

- Temperature control of cooling water
- External interlocks for laser safety
- Fiber-coupling with water-cooled entrance aperture
- Assembling of fiber into the focusing optics unit using a clamping technique
- Water-cooling of fiber plug by heat conduction via clamping connection
- Water-cooling of processing optics
- AR coating of optical surfaces in processing optics

The three laser units have been equipped with internal logics which supervise all internal failure signals and guide the laser head in case of emergency to a safe state. Besides that there is a complete signal interface, which is used for synchronizing laser modules with demands of milling process. Complete operation can also be controlled in local mode manually.

References

[6.1] Du KM et al. (1996) Anordnung zur Führung und Formen von Strahlen Eines Geradlinigen Laserdiodenarrays. Patent DE 44 38 368 C2.
[6.2] Brauch U, Loosen P, Opower H (2003) High-Power Diode Lasers for Direct Application in High-Power Diode Lasers. Springer, Berlin. pp. 303.
[6.3] Biesenbach J, Pfeffer F, Noeske A (1998) Einrichtung zur Strahlformung eines Laserstrahls und Hochleistungs-Diodenlasers mit einer solchen EInrichtung. Patent DE 19846532C1.
[6.4] Göring R, Posner T, Schreiber P (2000) Patent DE 10015245A1.
[6.5] Eppich B (1998) Die Charakterisierung von Strahlungsfeldern mit der Wigner-Verteilung und deren Messung, TU Berlin.
[6.6] Schmitt A (2001) InGaAs/AlGaAs Leistungslaser hoher elektro-optischer Effizienz und hoher Brillanz. Shaker, Aachen.
[6.7] Knitsch A et al. (2002) Diode laser modules of highest brilliance for materials processing. Photonics West 2002, San Jose, USA, Jan 19–25, 2002, SPIE, volume 4651.
[6.8] Bosse L, Schildecker A, Gillner A, Poprawe R (2002) Microsystem Technologies **7**, 215–219.
[6.9] Wolf E (2001) Productronic 10, 38–45.
[6.10] Poprawe R, Bosse L (2001) Statuskolloquium Sonderforschungsbereich SFB 440 Montage hybrider Mikrosysteme, 23–31.
[6.11] Droz S, El-Khoury M, Depeursinge Y, Gros B, Theurillat P, Michel JB, Monti M (2001) "MicroGrip", Mecatronics'01, 5th Franco-Japanese Congress and 3rd European-Asian Congress, Besaçon (FR).
[6.12] Röhner M (2004) Einzeladressierbare Diodenlaserbarren für lithographische Anwendungen, Dissertation, Rheinisch-Westfälische Technische Hochschule Aachen, Mai 2004, Shaker Verlag Aachen, Germany, ISBN 3-8322-2724-5.
[6.13] Solarz RW, Emanuel MA, Skidmore JA, Freitas BL, Krupke WF (1998) Trends in packaging of high power semiconductor laser bars. Laser Physics 8(3), 737–749.
[6.14] Carlin DB (1994) Individually addressed arrays of diode lasers. In Botez D, Scifres DR (Eds.): Diode Laser Arrays, Number 14 in Cambrigde Studies in Modern Optics. Chapter 3. Cambridge University Press, Cambridge. ISBN 0-521-41975-1.

[6.15] Mehuys DD, Welch F, Nam DW, Scifries DR (1990) High Power (>100 mW), low crosstalk (<0, 4%), individually addressed laser diodes. Electronics Letters 26(23), 1955–1957.
[6.16] Chow WW (1994) Semiconductor-Laser Physics , 1st Edition. Springer-Verlag, Berlin, Heidelberg. ISBN 0-387-57614-2.
[6.17] Boenig N, Roehner M, Boucke K, Poprawe R (2003) Demonstration device for individually addressed high-power diode laser bars. Proceedings of WLT-LIM, AT-Fachverlag 2, 93–96.
[6.18] Traub M et al. (2003) Homogenized high power diode laser systems for material processing and illumination. Proceedings of 2nd international WLT-Conference on Laser in Manufacturing, Munich, June 2003.
[6.19] Knitsch A et al. (2003) Adapted diode laser modules for material processing. Proceedings of 2nd international WLT-Conference on Laser in Manufacturing, Munich, June 2003.
[6.20] Bachmann F (2003) Application adapted diode laser systems: A result of the German national research project “MDS”. Proceedings of the 2003 Photonics West, San Jose, January 2003.
[6.21] Traub M et al. (2003) Homogenized high power diode laser systems for material processing and illumination. Proceedings of 2nd international WLT-Conference on Laser in Manufacturing, Munich, June 2003.
[6.22] N.N. (1998) Laser heating permits machine tool to turn brittle ceramics. Optics and Lasers Europe June 1998, 48.

7
Applications

D. Petring, R. Polzin, M. Becker

7.1. Joining Technologies

7.1.1. Introduction

D. Petring

Welding, brazing, and soldering are thermal processes used to join material. Laser technology has been applied for these processes for many years. The main principle of all laser-supported joining technologies is the absorption of laser radiation near to the contact area of the joining partners and – if used – also at the filler material, the transformation of the radiation energy into heat and the transition of part of the irradiated material into the molten (metals) or plasticized (polymers) state. This phase transformation allows the creation of a solid joint by resolidification of the molten or plasticized volume and bridging the gap between the joining partners. This happens spatially behind the interaction zone being moved along the joint track or simply temporally after the laser is switched off.

Of all the laser joining processes, the lowest power and power density is needed for polymer welding. Typically the power is in the range of some 10 W up to about 200 W, with a characteristic power density in the range of 10^3 W/cm^2. This is the reason why this application benefitted from diode laser technology when output power and focusability of diode lasers were still quite limited. Nevertheless, the progress in diode laser technology regarding power and beam quality increased polymer welding capabilities significantly. Scanner welding or simultaneous welding with special arrays of very compact laser diodes arranged along the welding contour would not be possible without the advancements of diode laser sources. The transmission welding technology, irradiating through an optically transmissive component onto an absorbing edge or surface at the interface to the lower joining partner, has revolutionized the technique of polymer assembling in many industrial applications.

Soldering and brazing are processes in which low-melting-temperature metals or alloys are used as filler material for joining metals with higher- melting temperature without melting the latter. The power density demands are somewhat higher than for polymer welding, i.e., about 10^3–10^4 W/cm^2, with powers in the range of some

10 W for spot soldering electrical contacts up to some kW for brazing seams, e.g. on automotive body-in-white components.

Finally, for laser welding of metals with high-power diode lasers, the recent developments in diode laser technology have been indispensable. Very attractive, regular heat conduction weld seams on visual edges of stainless steel bodies for kitchen sinks or automotive components are performed with power densities in the range of some 10^4 W/cm^2. Also, deep-penetration welding of steel sheets has been investigated and demonstrated for the first time during the MDS-project with power densities in the range of some 10^5 W/cm^2. The powers used for welding are in the range of 1 to 4 kW.

Meanwhile, high-power diode lasers have passed the threshold of acceptance for industrial joining applications in the order described above. The well-known advantages of semiconductor technologies regarding efficiency, compactness and modularity are promoting their dissemination continuously. Beside supplementing and partially replacing other laser types in standard system configurations, with modern high-power diode lasers new concepts like direct application of focused diode laser tools without a beam guiding system between laser source and working optics, and simultaneous or single-shot technologies with product-adapted beam patterns provide new opportunities for manufacturing industry. The following sections describe the various joining technologies presently achievable with high-power diode lasers and their applications.

7.1.2. Metal Welding

M. Beck, C. Benter, M. Brandner, C. Heimerdinger, M. Hölscher, M. Litmeyer, F. Lupp, A. Olowinsky, D. Petring, R. Quast, K. Spennemann, M. Steinicke

7.1.2.1. Process Principles and Equipment

Heat Conduction Welding

During heat conduction welding the absorbed laser beam energy heats the material above its melting point, but only to the point that a perceptible vapor pressure does not build up. The geometrical shape of the resulting melt pool and thus the depth of the weld are determined only by the heat conduction into the workpiece. Fundamental factors that influence heat conduction are the thermo-physical properties of the material as well as the geometrical shape and the temperature of the workpiece. Figure 7.1 schematically depicts the heat conduction welding process.

The heat conduction welding process proceeds in a particularly calm and stable manner. As a rule, the quality of the welds is generally immaculate, and welds in austenitic stainless steel especially can have an excellent visual appearance. The process can be applied to various joint geometries (e.g., butt joint or fillet weld at overlap joint). Normally, weld filler material is not applied.

In comparison to conventional welding processes, better results can be achieved with heat conduction welding by laser due to a lower energy input into the workpiece, limiting the melt volume and the distortion of the workpiece, and due

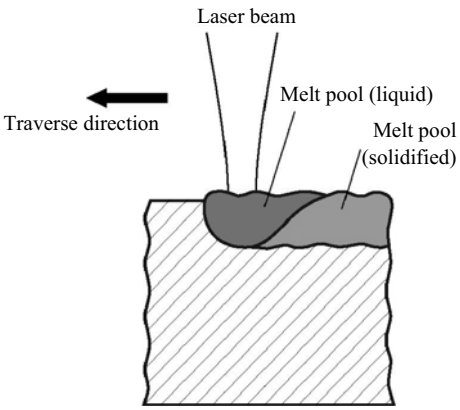

FIGURE 7.1. Scheme of heat-conduction welding process

to the lack of contact and practically wear-free process, leading to excellent reproducibility.

The maximum welding depth achievable by pure heat conduction welding is generally smaller than the laser seam width on the workpiece surface. This becomes clear by taking into account the dome-shaped melt-isotherms created by three-dimensional heat conduction propagating from a surface heat source into the workpiece. This source is formed by a laser spot covering a few up to 15 mm^2. Typical minimum power densities needed for welding steel are in the range of a few 10^4 W/cm^2.

Welding of aluminum and its alloys is complicated by their low beam absorptivity and high thermal conductivity. Therefore, compared to steel, higher powers and power densities are required. Both are strongly dependent on the type of contained alloying elements, e.g., manganese, silicon, or copper, and their concentrations. The absorptivity is particularly influenced by the surface conditions. As aluminum has an oxide layer on its surface the properties of this layer have a crucial influence on the degree of absorption and thereby on the welding capabilities of diode lasers regarding this material.

Increasing power as well as the area of the laser spot on the workpiece enables deeper welds. The first generation of high-power diode lasers in the 1–2 kW range, which became available in the second half of the 1990s, allowed for the above-mentioned power densities and resulted in maximum welding depths of 1–2 mm in steel sheets at low welding speeds below 1 m/min.

Transition Regime Between Heat Conduction and Deep-penetration Welding

Increasing power and power density, the regime of pure heat conduction welding is abandoned. By thorough visual inspection of the process behavior as well as experimental and theoretical analysis of the seam properties depending on beam power density (Fig. 7.2) during welding of 2-mm-thick mild steel at a feeding rate of 1.8 m/min, three process regimes are identified [7.1]. They vary continuously

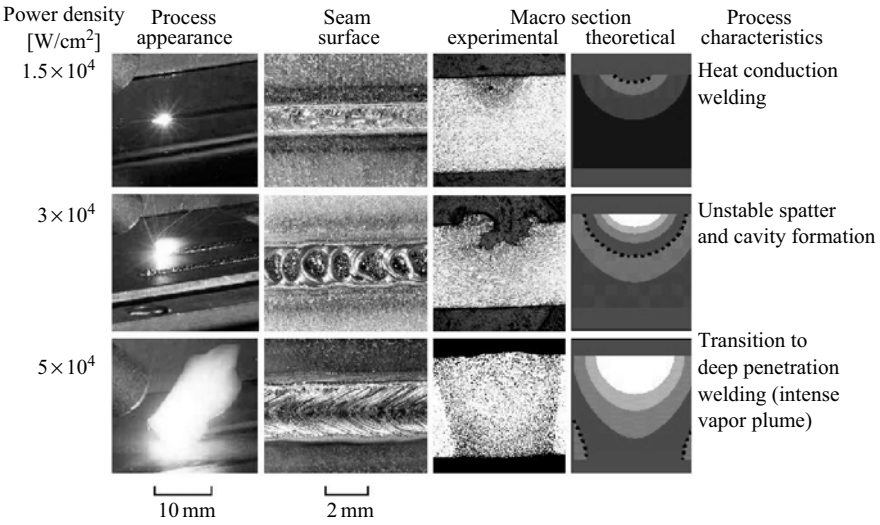

FIGURE 7.2. Process regimes for diode laser welding of mild steel, illustrating the transition from heat-conduction welding to deep-penetration welding [7.1]

from one to another within the power density range from 1×10^4 W/cm^2 to 5×10^4 W/cm^2. The applied high-power diode laser offers a maximum output power of 2.5 kW and an oblong focal spot measuring 1.7 mm × 3.8 mm.

At low power densities the process is characterized by a weak gleaming, a very regular, only minimally scaled seam surface with rounded solidification lines and a spherical fusion line in the cross-sectional view – corresponding to a pure heat conduction welding process. The aspect ratio (depth of weld to width of weld) is clearly below 1.

With increasing power density process disturbances occur in form of spatters accompanied by an increased shining due to starting evaporation. The seam surface is very irregular with stochastically formed craters. Also theoretically evaporation is expected at the surface of the molten pool, indicated by the white areas in the theoretical plots of Fig. 7.2.

Further increasing the power density leads to a significantly pronounced vapor plume and a relatively stable welding process without spatters, which changes to deep-penetration welding mode at power densities of about 5×10^4 W/cm^2 for the example of welding stainless steel [7.1].

Deep-Penetration Welding

In deep-penetration welding the absorbed laser beam energy heats the material beyond its evaporation temperature. Due to the ablation pressure of the emerging vapor, a vapor capillary is formed within the melt pool (Fig. 7.3). This effect allows for welds with large aspect ratios of, e.g., 1 to 10. The process itself proceeds by movement of the vapor capillary along the weld track. The material is melted at

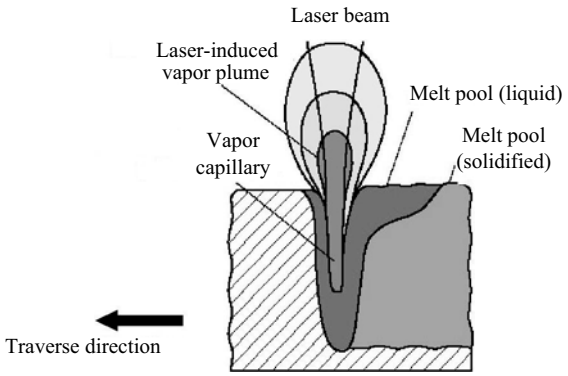

FIGURE 7.3. Scheme of deep-penetration welding process

the capillary's front, passes around the capillary on both sides, and meets a melt pool behind the capillary. The melt resolidifies at a certain distance, resulting in a continuous weld seam.

In an efficiently running deep-penetration welding process, multi-reflection within an adequately shaped capillary provides for an increased degree of absorption. The vaporized material inside the capillary is emitted perpendicularly from the laser-irradiated walls (mainly the capillary front in welding direction) and a part of it hits the rear wall where the vapor condenses. Another part of the vapor exits through the capillary's vent, where the laser beam enters the workpiece. In the case of full penetration welds an additional part of the vapor exits the workpiece at the vent on its bottom surface. In that case, the vapor capillary is forming a so-called "keyhole."

The pressure in the capillary is in equilibrium with the capillary forces due to surface tension of the melt, thus allowing the capillary to stay open and stable. The diameter of the capillary is in the range of the laser beam diameter.

For many welding applications, the "slim" seams with aspect ratios between 1 and 10 typical for deep-penetration welding performed with conventional lasers are desired due to reduced heat input per depth and resultant diminished distortion and increased process efficiency.

The first evidence of deep-penetration welding with a high-power diode laser was published in 1999 [7.2–7.4]. To ascertain the evidence of a deep-penetration welding process, four criteria have been defined to be fulfilled simultaneously (Fig. 7.4):

- intense vapor plume above the interaction zone,
- aspect ratio of seam depth to width higher than 1,
- horizontal dendrite formation perpendicular to weld center line in the seam cross section,
- seam geometry significantly deviating from simulated heat conduction welding result.

The example in Fig. 7.4 was created in 3-mm stainless steel [7.1].

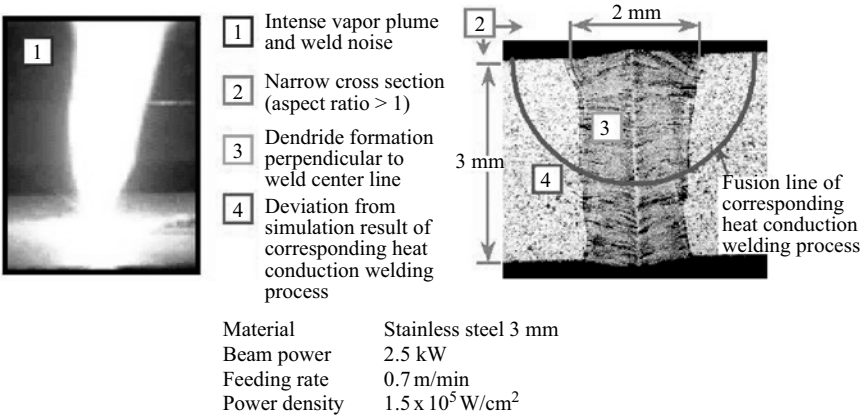

FIGURE 7.4. First evidence of deep-penetration welding with high-power diode laser [7.1]

Single-shot welding

Single-shot welding, also called "simultaneous welding" (especially in polymer welding), describes a joining technology without relative movement between the workpiece(s) and the laser beam. In conventional welding methods the welding path is normally traced by the laser beam with a given traverse speed. In single-shot welding, the complete path is irradiated simultaneously. Thus, the laser spot geometry has to correlate with the desired welding path on the workpiece.

The simplest geometry is a circular or oblong spot created by a conventionally focused laser beam used for spot welding applications. The principal setup of high-power diode laser devices theoretically allows for all kinds of shaped laser spots because of their modular design. The individual focus geometries (normally line-shaped) of many single high-power diode laser modules combined in one high-power diode laser device can be optically combined to form the desired shape. For practical applications, parts that can be joined cost-effectively are rather small (dimensions up to several centimeters) since the number of high-power diode laser modules and thereby the costs needed to create the weld seam with sufficient power density increases proportionally with the seam length to be welded simultaneously.

During the single-shot welding process, the workpiece is exposed to the laser light pattern for an adequate irradiation time which depends on parameters like power and power density as well as material parameters. Movement or reorientation of the laser beam during the process is not necessary, thus the handling system can be simpler and cycle rates are usually higher compared to processes that use sequential motion techniques. Since the workpiece is irradiated on the complete weld path simultaneously and for a shorter period of time, distortion due to a transient build-up of an unsymmetrical stress distribution can be significantly reduced.

Welding Equipment

Many of the macro-welding results presented in this book are produced with the laser sources described in Table 6.1 as the "kW-pol-stack" (section 6.2.2.2), the "kW-slow-col" (section 6.2.2.3), and the "kW-high-brightness" (section 6.2.5) (in the order of increasing beam quality). Besides the laser source itself, additional equipment is required in order to perform welding tasks. In the following sections some of the most important components and special considerations related to high-power diode lasers are explained.

"Cascaded" Cross-Jet

Especially during applications with partial evaporation, the laser optics of high-power diode laser devices must be protected against fume deposition and spatters. Normally, this is done by the use of a conventional cross-jet nozzle which creates a pressurized air stream that flows from several individual, small outlets that are arranged in-line. The resulting planar jet generates a cross-flow transversely to the laser axis, sometimes also called air-knife. In many cases, the cross-jet is not integrated in the setup but an attached part mounted between the bottom edge of the optics and the welding area.

The "cascaded" cross-jet nozzle is purpose-built for the requisitions of high-power diode laser beams and applications. Due to the limited beam quality of diode lasers the raw beam aperture has to be relatively large and the focal length of the focusing optics and thereby the working distance must be relatively short, in order to achieve the required power densities by a small F-number. Therefore, the main objectives for the design of the cascaded cross-jet are –

- flat, compact design
- mountable directly to the diode laser optics (integrated setup)
- large aperture
- broad pressurized air stream covering the complete aperture
- minimized disturbance of the welding zone
- variable pressurized air stream

A notable feature is the so-called "cascading" of the cross-jet nozzle. Differing from the above-mentioned conventional nozzles, the pressurized airflow is generated by two parallel, narrow slits with different gap widths. Thus, two different air jets and a "cascaded" mass flow are created. The basic concept is to choose a narrower gap for the lower slit than for the upper one. The lower, somewhat weaker flow supports the protective function of the upper stronger cross-jet flow and acts as a friction interface layer between the upper cross-jet flow and the resting atmosphere above the workpiece. The disturbance of the atmosphere or the shielding gas flow above the welding zone by suction or friction effects is thereby supposed to be minimized without affecting the protective properties of the cross-jet nozzle. The part of the pressurized airflow that is reflected at the integrated coverslide creates an additional local pressure gradient directed at the workpiece, supporting the protective properties against fume and spatters.

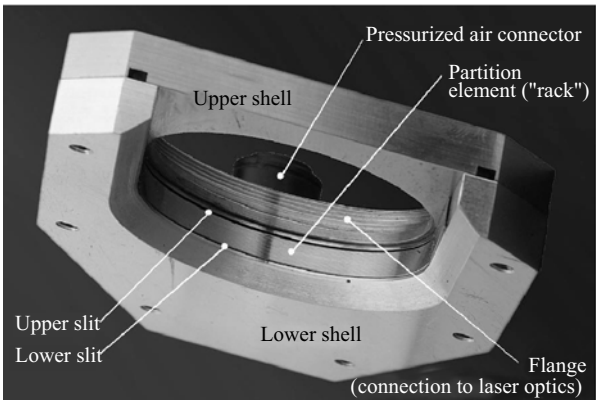

FIGURE 7.5. "Cascaded" cross-jet nozzle

Moreover, the cascaded cross-jet provides the opportunity to alter the dimensions of the outlet slits. A partition element ("rack") forms the slits together with the inner surfaces of the upper and lower shells (Fig. 7.5). By installing various racks, the dimensions of the outlet slits and thus the pressurized airflow can be varied.

Typical dimensions for the slits are 0.1 × 50 mm and 0.2 × 50 mm. The length of the slits matches the diameter of the coverslide. If a rack with one unmachined side is installed, a conventional, single pressurized air barrier is created. In this case, two different distances between air barrier and coverslide can be realized.

The nozzle body is attached to a flange that is screwed on to the laser optics. A detachable off-axis mount provides another way to install the cross-jet nozzle if it cannot or should not be attached to the laser optics. Moreover, this part and additional sidewise tapped holes provide mounting options for additional components such as shielding gas nozzles and filler wire feeding units. Thus, the cross-jet nozzle can be upgraded to a flexible processing head for high-power diode lasers.

The cross-jet nozzle proved itself during its application while welding various materials (stainless steel, mild steel, zinc-coated steel, aluminum) at working distances of only several centimeters. At a static pressure inside the pressure chamber of about 4 bar (0.4 MPa) about 800 L/min (0.8 m^3/min) of air flow through the total outlet area of 15 mm^2.

The cascaded pressurized airflow surpasses the flow of conventional nozzles in diverting spatter particles and protecting the laser optics. This could in particularly be observed while welding zinc-coated steel sheets. As a matter of course, also the cascaded cross-jet reaches its limits when the quantity of spatter formation gets too high and the working distance is very small, i.e. in the range of 50 mm and lower. During welding processes that create such intense spatter formation, accumulated debris on the coverslide can be observed even while the cascaded cross-jet nozzle is applied.

Coaxial Shielding Gas Nozzle

Another special item of equipment for welding applications with high-power diode laser is the coaxial shielding gas nozzle that can be attached to the laser optics and features an integrated coverslide holder (Fig. 7.6). It is an alternative to the conventional lateral or off-axis nozzles which generally consist of a simple copper tube. The coaxial arrangement permits welding results independent from the welding direction and without the necessity of turning a lateral nozzle according to the welding direction with an additional axis.

The desired shielding gas is fed radially into an annular flow channel below the coverslide. Several outlets distribute the shielding gas evenly into the gas chamber and the gas exits the nozzle coaxially to the laser beam which passes through the nozzle. The diameter of the outlet can be adapted to the application by installing different outlet bits with outlet diameters that range from 2 to 20 mm. The coaxial nozzle can be matched to different focal lengths of the laser optics by installing distance tubes with different lengths. The distance between the outlet

Figure 7.6. Coaxial shielding gas nozzle mounted to Rofin DL025

and the surface of the workpiece can be fine adjusted by a screw thread on the implemented distance tube.

The application of the coaxial shielding gas nozzle assures that the shielding gas flow hits the workpiece under the same angle as the laser beam and improves the handling of the setup due to the nozzle's integrated design and rotational symmetry.

Welding Head with Clamping Wheels

The laser welding head with clamping wheels (Fig. 7.7) is a very simple and flexible clamping concept. Nevertheless, a large enough working distance and F-number is required in order to avoid interference with the laser beam and beam optics. This has been a critical limitation with former high-power diode lasers having very low beam quality. But now, with the latest developments in diode laser technology, the available beam qualities are sufficient also for this type of equipment.

Its principle is based on a pressure-wheel system. The top wheel (pressure wheel) is used to position the laser optics relative to the component. A bottom wheel (backup wheel) makes it possible to clamp multiple panels. The wheel system is float-mounted, i.e., it adapts itself to the contours of the component.

Clamping is only carried out where the welding process is actually underway. For particularly large components, such as the door aperture of a car body, this is a suitable clamping method in order to avoid excessive clamping forces.

If the wheel head has a modular structure, various tasks can be carried out using the same basic system. Depending on the component situation, the following configurations are distinguished (Fig. 7.8).

1. Double-wheel system with small wheels
   a. for flange joints
   b. particularly suitable for small reorientation radii

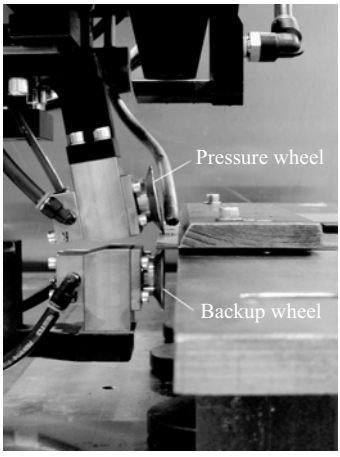

Figure 7.7. Welding head with clamping wheels

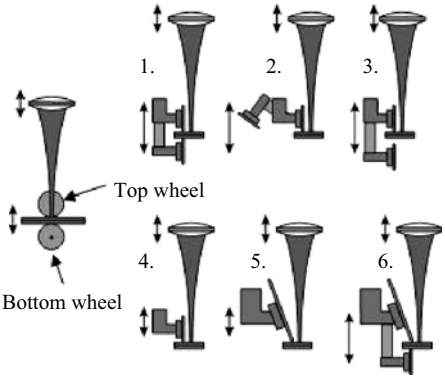

FIGURE 7.8. Principle of welding head with clamping wheels

2. Double-wheel system with backup wheel folded back
   a. for flange joints
   b. in addition, tasks with accessibility on only one side can be executed
3. Double-wheel system with backup wheel opened
   a. for flange joints
   b. in addition, tasks with accessibility on only one side and limited working area can be executed
4. Single-wheel system with small pressure wheel
   a. suitable for accessibility on only one side
   b. particularly suitable for small reorientation radii
5. Single-wheel system with large pressure wheel
   a. suitable for accessibility on only one side
   b. can also be used for profiled components (e.g., the roof channel of a car body)
6. Double-wheel system with large pressure wheel and small backup wheel
   a. for flange joints
   b. can also be used for profiled components, e.g., the roof channel of a car body)

A very narrow flange can be used to make window and door apertures in a vehicle larger, for example. A narrow flange can only be implemented, however, if the distance between the laser focus and the pressure wheel is minimized. This leads to a significant increase in the temperature load on the pressure and backup wheels. Moreover, the fouling of the wheels from weld spatter, etc., is increased.

Therefore, the wheel system must be designed with the following characteristic profile:

- Good high-temperature strength
- Virtually no adhesive effect with regard to weld spatter
- High resistance to wear
- High stiffness
- Easy to exchange
- High load capacity ($\geq$1,000 N)

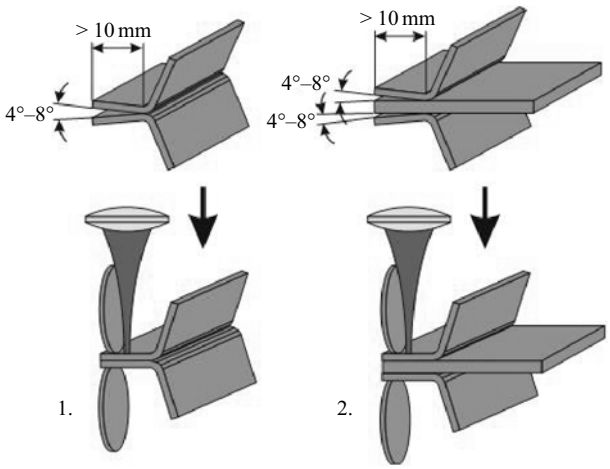

FIGURE 7.9. Suitable flange geometry for zinc-coated sheets

- Stiff, temperature-resistant mounting system
- Minimal marking of panels

If zinc-coated steel sheets are to be welded suitable component geometry can be used to allow outgassing of the zinc (Fig. 7.9).

The wheel head presses the mating panels into a defined position using either force control or position control. In the case of three-panel welds, it is advantageous if the middle panel is the one with the highest structural stiffness. The spring effect of the other mating panels then results in a certain "balancing" of the gap situation.

Sensors for Seam Finding

A large number of sensor systems for edge detection are available on the market. If the contours in the clamped state are constant from component to component, then simply determining the position of the edge in space is perfectly sufficient. This is done by determining the position and orientation of the component's edge by measuring it at a number of different points. So-called position sensors are used here. The coordinate system of the handling system is then adjusted using an offset, and the joining process can begin. If, however, both the position and the contour vary, then edge-tracking sensors are used. As a rule, edge-tracking sensors work in parallel with the joining process and continuously correct the position of the handling system. Offline systems are also available, however. These measure the complete contour before the joining process, and use the results to generate the motion program for the handling system.

Position Sensors

Depending on the material characteristics of the components (e.g., electrically conductive or non-conductive; direct, diffuse, or non-reflective), either contact or non-contact sensors are used.

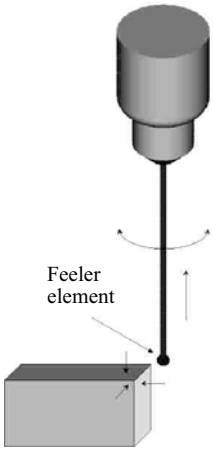

FIGURE 7.10. 3D feeder

Contact sensors: The **3D feeler** (Fig. 7.10) operates with an optical switch within the sensor. If the feeler element is deflected, the feeler generates a switch signal; the feeler can be deflected in any direction, either laterally or in the working direction.

A three-point bearing ensures that the starting position of the feeler element remains constant. If a crash occurs, a predetermined breaking point in the feeler element creates a defined fracture, and the feeler sends a fault message to the handling system. The feeler element can then be exchanged without the need for calibration.

Advantages

- Suitable for electrically non-conductive components
- Does not depend on the surface characteristics of the component (e.g., reflective, matt, oiled)

Disadvantages

- The measurement process involves contact, i.e., under certain circumstances paint finishes may become scratched.
- Plastic, easily deformed materials (e.g., rubber) cannot be measured reliably.
- The handling system must be able to react quickly (stop) in order to prevent the feeler element from being damaged during the measurement process.

The **touch sensor** (Fig. 7.11) generates the switch signal by means of an electrical contact between the tip of the feeler and the component. It is simple, for example, to use an existing wire feeder as a feeler. To guarantee reliable measurement in this case, the free wire length must remain constant. The wire cutting units which have long been used in connection with automated arc welding are particularly suitable here.

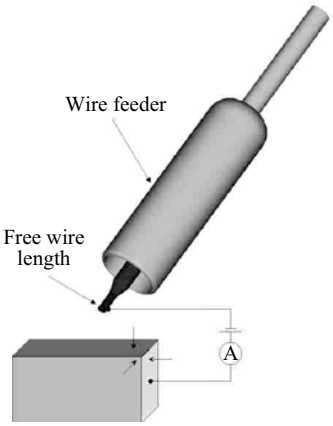

FIGURE 7.11. Touch sensor

Advantages

- Simple measurement setup
- Does not depend on the surface characteristics of the component (e.g., matt or reflective)
- No additional accessories (e.g., a measuring tip) are required if a wire feeder is used

Disadvantages

- Can only be used on electrically conductive materials.
- If a wire feeder is used, a wire-cutting unit may also be necessary.
- As is the case with the 3D feeler, here too the handling system must be able to react quickly.
- The measurement process involves contact, i.e., the measured surface may become scratched.

Non-contact sensors: Non-contact sensors generally operate according to the principle of laser triangulation (Fig. 7.12). By means of a laser diode, a spot of light is projected onto a surface. The diffuse reflection of the light is imaged by an optical system (receiver lens) on a CCD chip. The relationship between the position of the reflected light on the CCD chip and the distance of the sensor from the workpiece is known from triangulation. If the distance between the sensor and the target is changing, the image of the light spot moves to a different location on the CCD.

To ensure that the focus is sharp for every position of the workpiece, the lens plane (receiver lens) and the image plane (CCD chip) are inclined in such a way that they intersect at the emission point of the light source (laser diode). When a lens is used to form an image of a sloping object, the object plane, the image plane and median plane along the lens will all meet together at a common point. This so-called "Scheimpflug condition" leads however to a nonlinear relationship

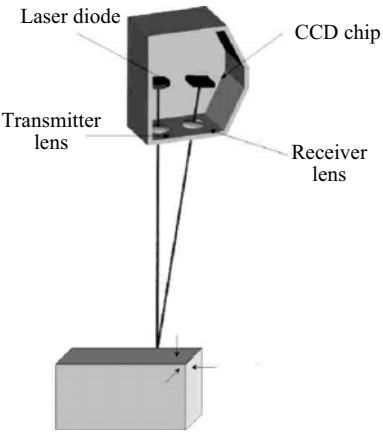

FIGURE 7.12. 1D profile sensor

between the distance of the sensor from the measured surface and the position of the spot of light on the CCD.

The functional capability of a triangulation sensor and thus its possible applications depend significantly on the optical characteristics of the object being illuminated. Light-colored materials which scatter light diffusely offer optimal measurement conditions, while dark and absorbing or directly reflecting objects can only be measured with limitations.

Advantages

- Non-contact measurement process.
- Robust measurement principle.
- Rapid reaction by the handling system is not required.
- Large measurement area (>200 mm) and measurement distance (>750 mm) are possible.
- Plastic, easily deformed materials (e.g., rubber) can also be measured.

Disadvantages

- Highly reflective surfaces or surfaces with a fine texture (e.g., from rolling) can lead to false measurement signals
- Higher capital investment costs compared to touch sensors or 3D feelers

Edge-Tracking Sensors

2D-light-section sensor: The 2D-light-section sensor (Fig. 7.13) is a modified type of triangulation equipment. Instead of a spot of light, a line of light is used. The profile of this line directly reflects the contour of the object. Evaluation of the profile produces a two-dimensional section through the object. The shape of the line could not be measured using only a one-dimensional sensor. Two-dimensional CCD sensors like those in video cameras are used here almost exclusively.

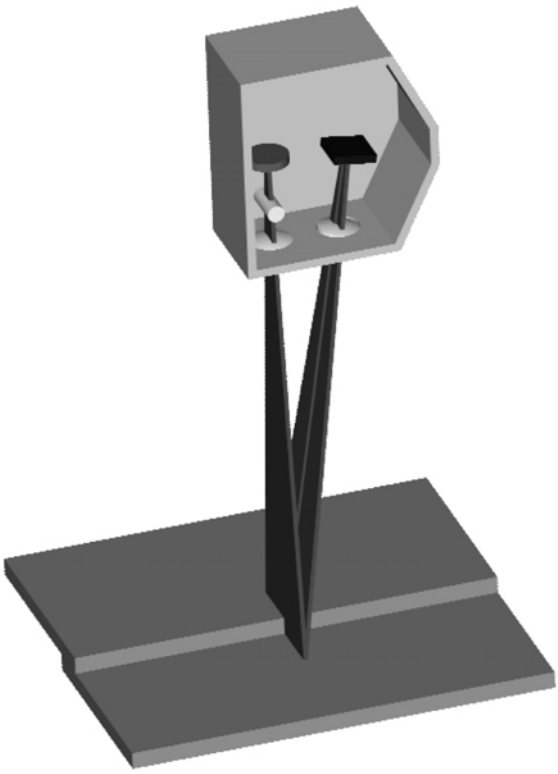

FIGURE 7.13. 2D profile sensor

Two-dimensional laser sensors using the triangulation method (light-section principle) provide a non-contact, high-resolution height profile of the weld groove or another workpiece. This height profile can be used to find the start of the weld, for joint tracking, or for other geometry-oriented processing steps. A subsequent check of the seam after welding is also possible. Unlike all of the other sensor principles, this one can also be used for very narrow types of joints.

It must be ensured that the light source projects a sharp, thin line onto the object. The best way to implement this is through the use of laser diodes, since they have very good focusing qualities. Conventional CCD sensors are used as detectors. The precision of the measuring system is determined by selecting the resolution of the sensor.

Advantages

- Non-contact measurement process.
- Robust measurement principle.

- Both the distance of the sensor from the component and the contour of the joint are measured.

Disadvantages

- Highly reflective surfaces or surfaces with a fine texture (e.g., from rolling) can lead to false measurement signals.

3D-light-section sensor: Unlike 2D-light-section sensors, with the 3D-light-section sensor (Fig. 7.14), a figure, e.g., a circle or group of lines, is projected onto the workpiece surface. In this manner not only the joint geometry, but also the position and orientation of the sensor relative to the component can be unambiguously acquired.

This information enables the handling system to move along a joint geometry autonomously. This autonomous guidance along the joint is monitored continuously. If the handling system moves out of a defined working range, the motion sequence is automatically stopped.

As a rule, the figure is generated through the employment of a lens system, or alternatively a scanner system.

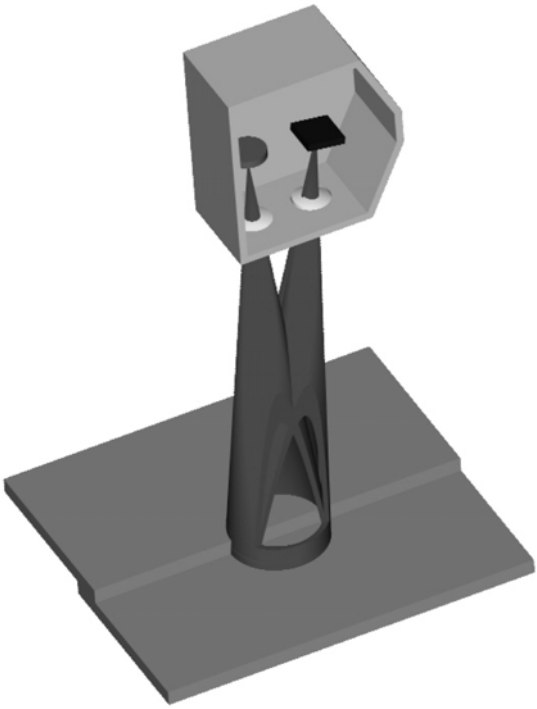

Figure 7.14. 3D profile sensor

Advantages

- Non-contact measurement process.
- Not only the joint form, but also unambiguous information about the position and orientation of the sensor relative to the component can be obtained.
- The handling system can be guided along the component joint autonomously.

Disadvantages

- Highly reflective surfaces or surfaces with a fine texture (e.g., from rolling) can lead to false measurement signals.
- Costly sensor system.
- Complicated commissioning.

Tactile Seam Tracking

One very simple principle for edge tracking is tactile seam tracking (Fig. 7.15). Here a measuring tip, or, if a wire feeder is already present, the free end of the wire, is continuously guided along the edge of the component. The mechanical coupling between the measuring tip or wire feeder and the laser optics ensures that the laser focus is positioned precisely relative to the component joint or filler material, both laterally and in the direction of the beam.

Figure 7.15. Tactile seam tracking sensor

Advantages

- Simple and robust principle
- Does not depend on the material characteristics (e.g., electrically conductive/non-conductive, matte or highly reflective)
- Simple commissioning

Disadvantages

- Contact measurement process
- Needs appropriate groove or edge dimensions for sensor guidance

7.1.2.2. Parameter Dependencies and Process Investigations

Bead-on-Plate Welding with High-Power Diode Lasers of Different Stages of Development

Welding test series on 2-mm-thick mild steel, stainless steel, and aluminum were conducted with high-power diode lasers of different stages of development. The objective was to assess the welding capability of the high-power diode laser devices which is mainly influenced by laser power, power density, welding speed, and type of the material. The high-power diode lasers used were a commercial Rofin DL025 (year of construction 1998), the "kW-pol-stack" (Rofin DL030S)(see Chapter 6.2.2.2) and fiber-coupled "kW high brightness" (see Chapter 6.2.5). The primary properties of these high-power diode lasers are summarized in Table 7.1.

All welds were bead-on-plate to rule out influences of the joint properties such as gap geometry or misalignment, and performed at the maximum output power of each high-power diode laser to reach the fastest possible welding speeds. Inert shielding gases were used to stabilize the process.

Additionally, simulations according to each test series were performed and compared with the experimental results. The calculations were carried out by "LaserWeld3D" software [7.5]. It is based on the Rosenthal solution of the heat conduction equation considering additionally the finite thickness of the workpiece. The material's absorption is set according to values obtained spectrometrically. For all calculations presented here the degree of absorption of steel materials has been

Table 7.1. High-power diode lasers of different development stages

HPDL-device	Maximum output power [kW]	Focal length [mm]	Focal spot dimensions [mm]	Power density [$\times 10^5$ W/cm^2]	Wavelength (nm)
ROFIN DL025	2.5	50	1.7 × 3.8	0.5	808
ROFIN DL030S	3.0	66	0.8 × 1.3	1.5	808, 940
"kW-high-brightness"	2.8	98	0.65 × 0.76	6.4	808, 880, 940, 980
"kW-high-brightness fiber-coupled"	2.1	62	0.55	7.6	808, 880, 940, 980

assumed to be 45% in good agreement with spectrometric results. The absorption of aluminum was set to values between 20% and 27.5%, depending on the alloy and the surface conditions. The absorption of aluminum is highly dependent on the surface conditions of the workpiece. The algorithm used by the process model is solely capable to calculate pure heat conduction, and does not take into account phase transitions and deep-penetration effects.

The following experimental and theoretical relations of welding depth vs. welding speed are shown in double-logarithmic graphs. Curves that appear linear are hyperbolic in reality.

Figures 7.16 and 7.17 show the results obtained with commercial lasers Rofin DL025 and Rofin DL030S. The values of welding speeds where the curves leave their horizontal course (corresponding with the thickness of the sheets) indicate the boundary feeding rates "BFR," i.e., the highest welding speed capable of creating welds that completely penetrate the sheet.

Due to its higher output power and considerably higher power density, the ROFIN DL030S high-power diode laser is capable of increasing the BFRs of mild steel and stainless steel by about 50% compared with the DL025 values. Also the welding depths in aluminum are increased, particularly in the higher speed range above 1 m/min.

The simulated and real welding depths match quite well for the DL025 results (Fig. 7.16). Even at the higher power densities of the DL030S in Fig. 7.17, theoretical and practical values correspond quite well, showing the same trend and range of depth. Nevertheless, the scattering of the experimental values is demonstrating destabilizing effects by vaporization.

The graphs in Figs. 7.18 and 7.19 show further massive increases of the BFRs, when the latest state-of-the-art device DF030 is applied. When the high-power diode laser is applied directly (i.e., in the same way as the other high-power diode

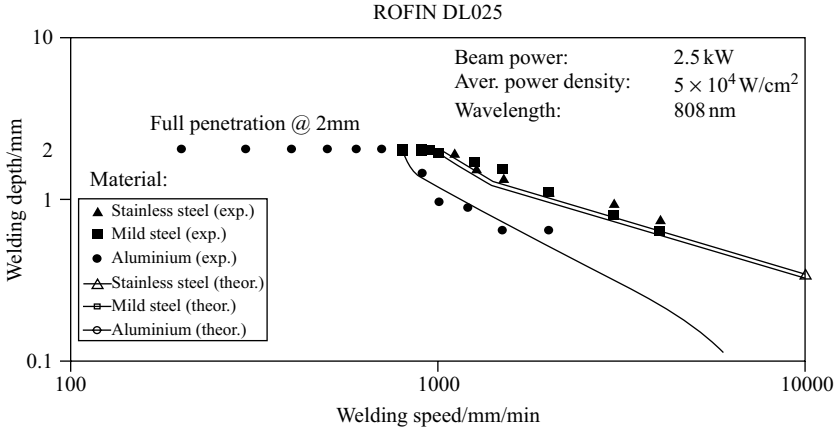

FIGURE 7.16. Practical and theoretical welding depth of 2.5-kW high-power diode laser (y.o.c. 1998)

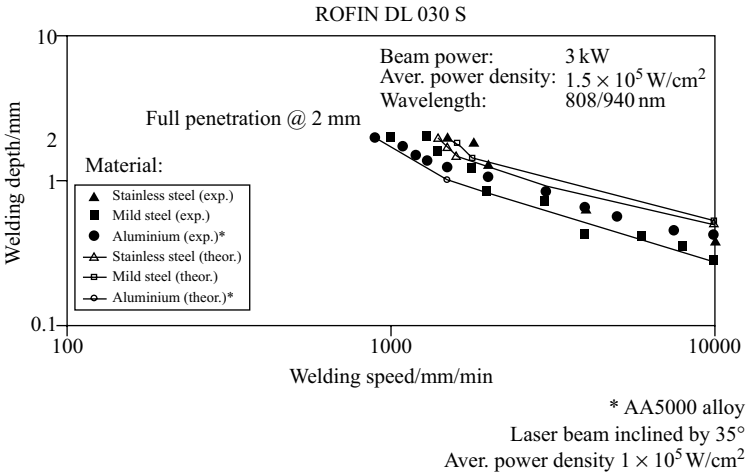

FIGURE 7.17. Practical and theoretical welding depth of 3.0-kW high-power diode laser "kW-pol-stack" (y.o.c. 2000)

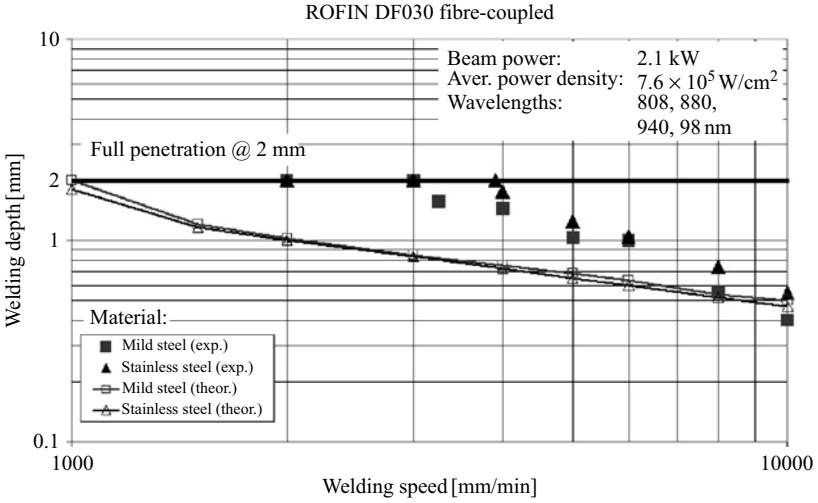

FIGURE 7.18. Practical and theoretical welding depth of fiber-coupled "kW-high-brightness" diode laser (y.o.c. 2003)

laser devices), the BFRs more than double the values reached with the DL030S due to the significantly higher power density. When the DF030 is utilized in the fiber-coupled mode (fiber diameter 800 μm), power density rises once again, although the accompanied loss of laser power inside the fiber makes for altogether slightly lower BFRs.

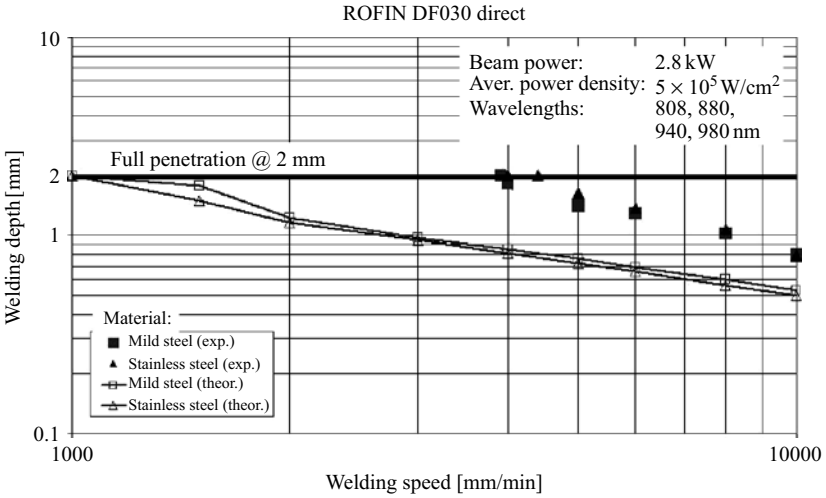

FIGURE 7.19. Practical and theoretical welding depth of directly applied "kW-high-brightness" diode laser (y.o.c. 2003)

It is obvious that the curves of the simulated results differ widely from the experimental welding depths which are clearly higher. This disambiguates that the welding process with DF030 runs in the deep-penetration regime that cannot be calculated by the simple heat conduction model used, like it is exemplified in Fig. 7.4, criterion number 4.

Recapitulating, Fig. 7.20 shows the BFRs achieved in 2-mm-thick stainless steel with the three different high-power diode lasers. The results with the DF030 in particular show the present welding capabilities of directly applied high-power diode lasers. Although the dimensions of the focal spot increase slightly and the beam's edges are not as clearly defined in comparison to the fiber-coupled mode the fastest welding speeds were reached in direct mode.

Influence of Beam Power and Focal Length

Determination of different influence variables is of interest for evaluating the potential of high-power diode laser systems for laser welding applications. Again, bead-on-plate welds reveal the parameter dependencies most clearly. The process parameters changed, are laser power (P_L), the focal length (f), and thus the focal spot size and the orientation of the focus (in fast-axis or slow-axis direction). The welding depth and the aspect ratio (t/b) of the seam versus the feed rate (v) are used to characterize the weld seam. The results shown below were obtained with a Rofin DL040S system (same construction as the "kW-pol-stack," Chapter 6.2.2.2) and the "kW high brightness system" (Chapter 6.2.5) based on bars with tapered laser emitters.

Figure 7.21 shows the welding depth as a function of the welding speed and dependent on the focal length and laser power used. The curves show a typical,

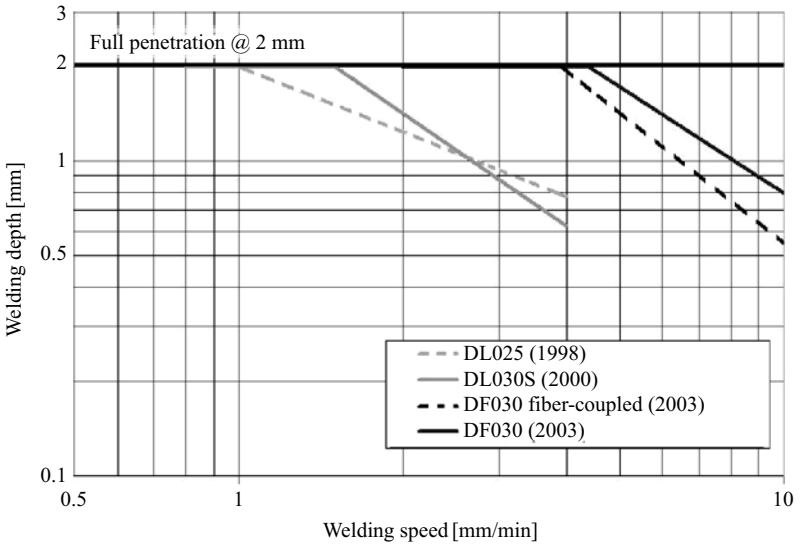

FIGURE 7.20. Comparison of welding depths in stainless steel of three high-power diode lasers of different stages of development

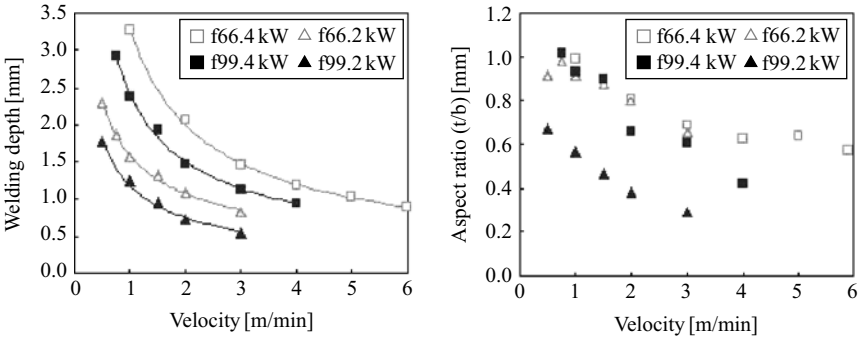

FIGURE 7.21. Welding depth and aspect ratio as a function of velocity, laser power and focal length – bead on plate welding of 16MnCr5 (Rofin DL040S; welding in fast-axis direction)

hyperbolic form. If shorter focal lengths are used, there is an increase in welding depth due to the smaller focal spot and the higher power density connected with it. In addition, doubling the laser power leads to about a doubling of the welding depth. If the aspect ratios of the weld seams are considered, it can be determined that the results with long focal length ($f = 99$ mm) and a power of 2 kW, describe a case of pure heat conduction welding. The other curves lie in the transition range between heat conduction and deep-penetration welding with aspect ratios up to a value of 1 at low speeds. This becomes clear from the cross sections in Fig. 7.22. Relatively steep weld flanks can be observed here and the beginning

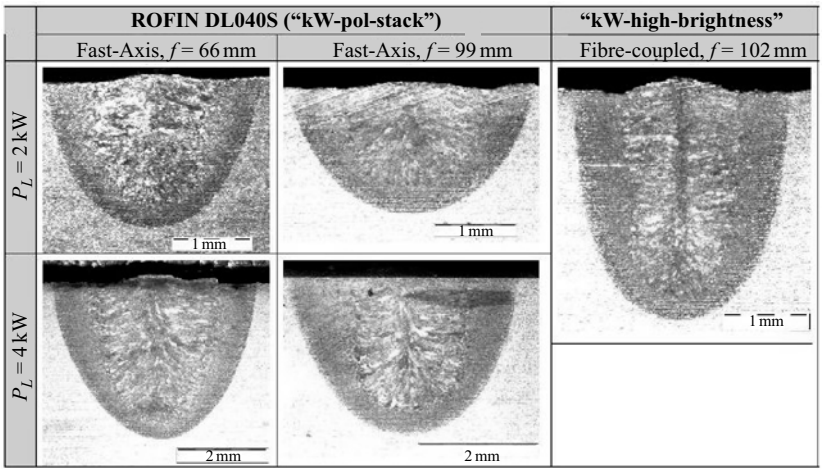

FIGURE 7.22. Cross sections of bead-on-plate welds – comparison of different laser sources, focal spots and laser power (16MnCr5, $t = 10$ mm; $v = 1$ m/min)

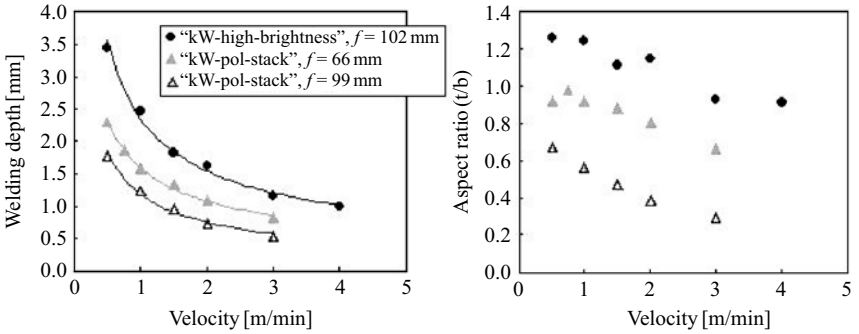

FIGURE 7.23. Welding depth and aspect ratio in dependence of laser source and focal spot – bead on plate welding of 16MnCr5 ($P_L = 2$ kW; welding in fast-axis direction)

of horizontally oriented dendrites. Since no abrupt change in the welding depth can be observed, it can be assumed that no transition to "pure" deep penetration welding occurs in the parameter range considered.

A further increase in the welding depth at the same power can only be achieved by using diode laser systems with higher beam quality. These beam sources (described in detail in Chapter 6) were developed in the scope of the German national diode laser related research project that is basis for this book (MDS, [7.6]), and tested with regard to their potential for welding. Figure 7.23 shows a comparison of the welding curves of two devices, the "kW-pol-stack" (Chapter 6.2.2.2) and the "kW high brightness" (Chapter 6.2.5), already demonstrated similarly in the previous section. The increase in welding depth due to the significantly smaller focal spot

and the higher power density can clearly be seen. It is worthwhile mentioning that the "kW high brightness" system was used here with the longest focal length and as a fiber-coupled system. These features can be of crucial importance for industrial applications. By increasing the power density, the transition to deep penetrating welding was achieved. The weld seams have steep edges (Fig. 7.22) and show aspect ratios >1 (Fig. 7.23).

Influence of Spot Orientation

Another important influence variable in welding with diode lasers is the alignment of the asymmetrical laser spot in feed direction. Without additional measures, the beam cross section of a diode laser is asymmetrical in principle due to the setup using bars. Figure 7.24 shows the effects of asymmetrical focal spots for different laser sources. In the beam sources tested, the fast-axis of the focus is equivalent to the short extension of the beam cross section. No matter what beam source, an advantage is seen in greater welding depth with alignment of the slow-axis parallel to the feed direction (long-axis in feed). On the other hand, the seam width tends to be larger during welding in fast-axis direction. The degree of difference in weld depths ultimately depends on the degree of asymmetry respectively the beam shape factor (ratio of long to short axis) and thus on the design of the laser. In comparison to the Rofin DL040S (same construction as "kW-pol-stack"; focus $0.9 * 1.3\,\text{mm}^2$, resp., $1.4 * 2.1\,\text{mm}^2 \Rightarrow$ factor 1.5), the Laserline System (focus $0.7 * 1.8\,\text{mm}^2$; factor 2.6) is clearly more asymmetrical with a distinct line focus. Because of this, larger differences in welding depth occur.

Influence of Focal Position

Figure 7.25 shows the welding depth versus focal position using the laser sources "kW-pol-stack" (Chapter 6.2.2.2), "kW-slow-col" (Chapter 6.2.2.3), and "kW high

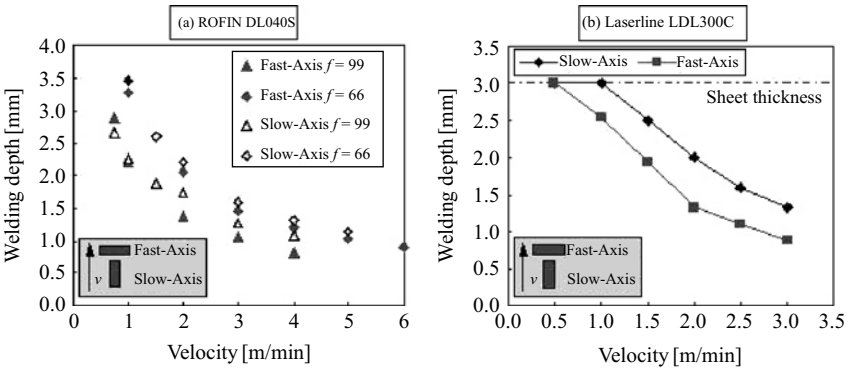

FIGURE 7.24. Welding depth in dependence of spot orientation – bead on plate welding of (a) 16MnCr5 (Rofin DL040S; $P_L = 4\,\text{kW}$) and (b) stainless steel (Laserline LDL3000C; $P_L = 3\,\text{kW}$

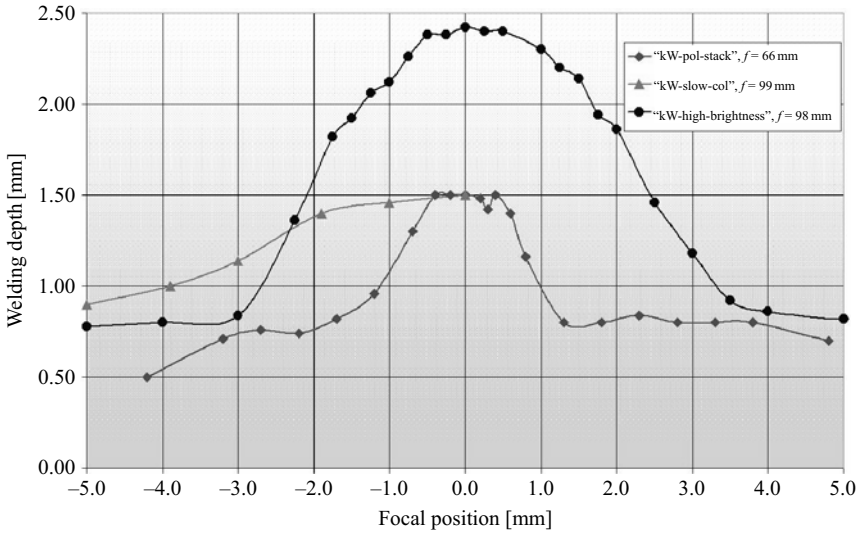

FIGURE 7.25. Welding depth vs. focal position

brightness" (Chapter 6.2.5) at a beam power of $P_L = 2500$ W. It has to be emphasized, that due to the stacking and beam combining principles of high-power diode laser systems, the beam intensity distribution is significantly varying with increasing distance from the focal plane. A variation of focal position is not only leading to a simple change of the spot size on the workpiece, like with conventional laser modes. It is rather causing a redistribution of beam parts in addition to some astigmatic effects and normal defocusing. Nevertheless, it is worthwhile to investigate the effect of changing distance of focus on the welding result with diode lasers.

The results are obtained by bead-on-plate welding into thick material with a welding speed of 2 m/min. The material used is S235 JR. The graph shows that the welding depth is highly increasing in the focal area. The increase of the welding depth may be promoted by the initiation of a deep-penetration welding process in the focus instead of heat conduction welding process outside the focal region. An additional indication for a deep-penetration welding process is a distinct vapor plume in the focal area. Outside of the deep-penetration welding area only a little vapor plume can be observed.

Influence of Gas and Nozzle Parameters

Shielding gases are often used with laser welding processes to stabilize the process, to increase the welding depth and to protect the weld seam against oxidation. Beside the type of applied shielding gas, e.g., argon, helium, or customized mixtures of gases with proportions of active gases, the nozzle parameters play an essential role. Shielding gas effects can be customized by adjusting the nozzle's orientation (trailing or leading) and the gas flow's impingement point ("foot point") (ahead of, central to or after the laser spot) as well as the nozzle angle. These parameters

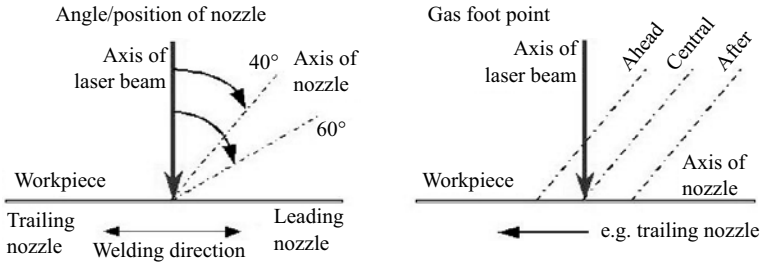

FIGURE 7.26. Nozzle parameters

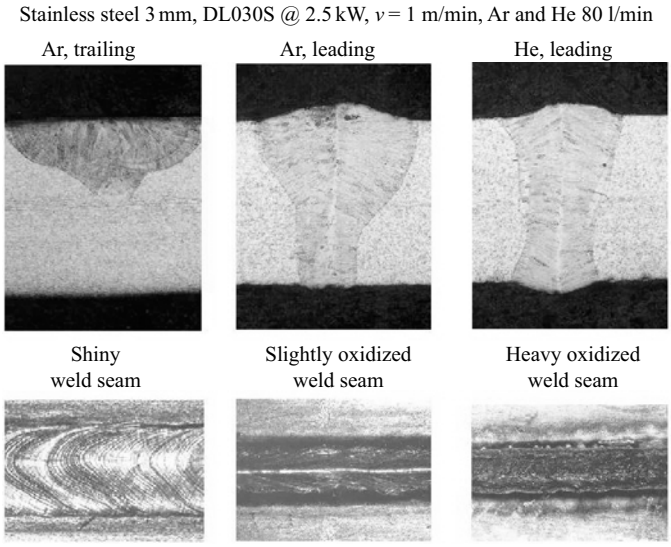

FIGURE 7.27. General impact of nozzle alignment and shielding gas on geometry and seam of weld

can be set according to the desired welding result. The various nozzle parameters are explained in Fig. 7.26.

As can be seen in Fig. 7.27, the welding process on stainless steel is predominantly dependent on the type of shielding gas and the flow conditions. The extent of the vapor plume, interference with the laser beam, and the degree of the weld seam oxidation can be influenced by the design and alignment of the gas nozzle and the type and flow rate of the shielding gas. The inner diameter of the lateral gas nozzle is 8 mm. The welding results are assessed by two criteria. One criterion is the glossiness and regularity of the weld seam, which proves the protective effect of the gas flow. Another criterion is the geometry of the weld's cross section, which is assessed in order to evaluate the process efficiency. The latter is mainly

determined by the type of process, i.e., heat conduction or deep-penetration welding. Slim welds (welding depth > width, aspect ratio > 1) are appraised favorably. They are achieved by reducing the interference of the laser beam and the vapor plume.

Stainless steel shows the glossiest and smoothest weld seam when a trailing nozzle and a gas foot point after the laser spot is applied. It is obvious that this configuration is best able to avoid oxidation and thus create shiny weld seams.

The volume of the molten material and particularly the weld depth increase when the nozzle's orientation is changed to leading. Simultaneously, oxidation of the seam surface is promoted. This occurs especially if the lighter helium is used as process gas. Also with this configuration the gas foot point should be set after the laser spot in order to suppress the vapor plume efficiently by the transversal gas jet components.

Another example of gas effects is demonstrated by welding with the fiber-coupled Rofin DF030 at a maximum power on the workpiece of about 2 kW. The welds were performed on 6-mm-thick stainless steel with a welding speed of 0.15 m/min and a shielding gas (Ar) flow rate of 60 l/min. The influence of the gas foot point's alignment becomes evident with a leading gas nozzle setup. The results are shown in Fig. 7.28. When the gas foot point runs 2 mm after the laser spot, the weld does not penetrate the sheet and its cross section is defined by a cup-shaped geometry. The wide, shiny, and smoothly scaled weld seam again gives evidence of the good protective effect of the gas flow. When the gas foot point is moved away another 2 mm from the laser spot, deep-penetration welding is initiated in this setup. A decidedly narrower, fully penetrating weld with parallel flanks and a dead, oxidized weld seam is the result, visible in Fig. 7.28.

The examples clearly show that by adjusting the shielding gas flow the welding result in stainless steel can be purposefully affected and thus effectively controlled when high-power diode lasers are to be applied.

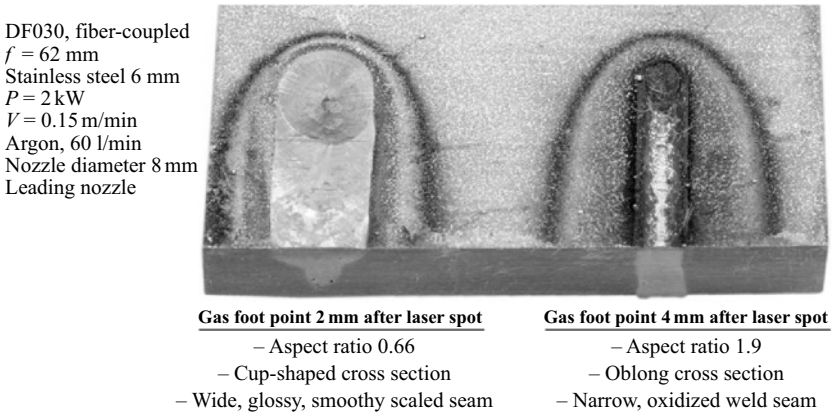

FIGURE 7.28. Stainless steel welds with different gas foot point alignments

The influences are far less distinctive when mild steel is welded. The welding depths in aluminum achieved with CO_2 or in plain air are 25% to 50% higher than the depths achieved with inert gases due to the active oxygen component ("surface-active element") of CO_2 and air. It initiates the so-called Marangoni effect, causing the direction of melt flow to reverse towards the center of the seam and thus resulting in deeper welds as well as oxidized seams.

Weld Structure

During thermal joining, because of the effects of heating, melting, resolidification and cooling, there are changes in microstructure. Partially, hardening in the weld seam occurs and influences strength properties. The extent of micro structural changes during diode laser welding is of interest in this context. In the following, hardness profiles and microstructure examination are used for illustration of typical metallurgical results.

Different materials were welded in butt joint configuration. As an example, Figure 7.29 shows the results of hardness measurements for a high-strength dual phase steel (DP600). Feed rates lying in the range of the full penetration limit are considered. Higher hardness values correlate with higher feed rates due to the higher cooling rates. The maximum hardness is located in the heat-affected zone. For the parameters shown, the maximum increase of hardness is 150 HV and thus lies only slightly above the values observed for conventional arc welding techniques. As a supplement, Fig. 7.29 shows the identified types of microstructure produced after welding, in comparison to the microstructure of the untreated material. The base material mainly consists of ferrite with small, embedded martensite islands. As a result of the high cooling rates, a fine-grained microstructure develops in the heat-affected zone. There is martensite formation and thus hardening. The resolidified welding microstructure itself shows somewhat coarser grain with less martensite formation. The hardness decreases slightly but the measured values are still higher than those of the base material.

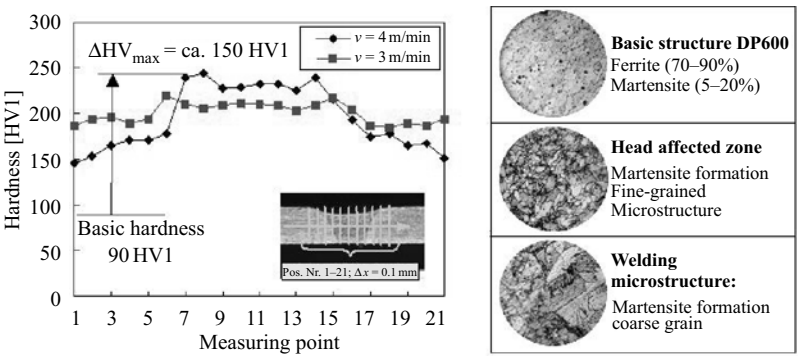

FIGURE 7.29. Welding of high-strength steel (DP600) – hardness profile and weld structure (System "kW-pol-stack" (Chapter 6.2.2.2); square butt joint; $P_L = 3$ kW; $f = 66$ mm)

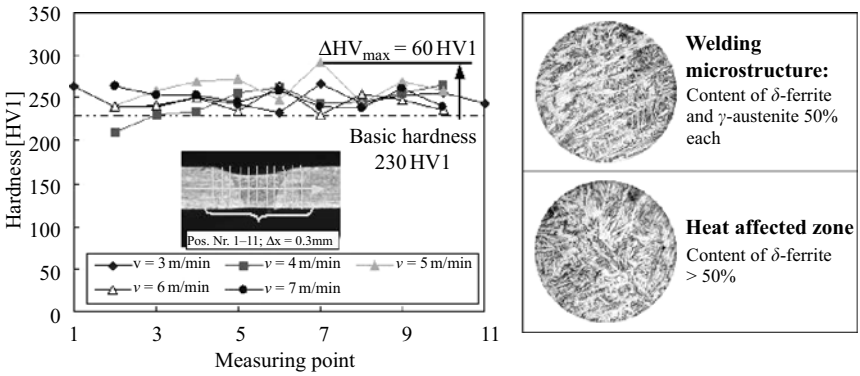

FIGURE 7.30. Welding of stainless steel (H400) – hardness profile and weld structure (System "kW-pol-stack," Chapter 6.2.2.2); square butt joint; $P_L = 3\,\text{kW}$; $f = 66\,\text{mm}$

Figure 7.30 shows the results of hardness measurements for a high-alloyed austenitic stainless steel 1.4376 (H400). The material combines high corrosion resistance with high strength and excellent formability. In contrast to the dual-phase steel, almost no hardening can be found, independent from the feed rate. On the average, a hardening of 20 HV is recorded with a base material hardness of 230 HV. In addition, no notable change in the welding microstructure can be observed (see Fig. 7.30, right). In order to find the reason for the low hardening it is necessary to look at the alloy composition. Due to the high nickel and manganese constituents, the material has a high percentage of austenite in the melt microstructure. In combination with the low carbon content, a notable martensite formation is prevented.

Single-shot Welding with an Annular Beam

To assess the welding capability of the annular beam device ("ring focus laser," see Chapter 6.3.5), variations of irradiation time have been performed on stainless steel and mild steel sheets of thicknesses between 0.3 and 1 mm. All spot welds were bead-on-plate and carried out in single shot technique (i.e., no relative movement). As shielding gas, argon was fed through the central pass aperture at 80 L/min. The annular focus spot provides a maximum power of 2 kW and its power density amounts to an average of 1.8×10^4 W/cm^2, a suitable value for heat conduction welding. Stainless steel and mild steel sheets of 1 mm thickness are fully penetrated at 400 and 450 ms, respectively. Stainless steel sheets of 0.5 and 0.3 mm thickness are penetrated at 100 ms and 60 ms, respectively. If the use of shielding gas is abandoned, 1 mm stainless steel can already be penetrated after 350 ms. The top sides of the spot welds still show the annular shape after irradiation times of 500 ms. Contrarily, the lower side of the bead-on-plate welds show that the sheet is firstly penetrated at the ring's center, from where the melt pool spreads outward in radial direction if the laser pulse is kept on. In the lower part of the sheet the

three-dimensional heat conduction leads to heat accumulation and a corresponding temperature maximum at the ring's center.

7.1.2.3. Application Results

Welding of Steel Joints

Square Butt Joints. For further evaluation of the performance capability of high-power diode lasers in welding, it is necessary to study characteristic butt geometries and seam shapes. Determination of weld curves (welding depth versus speed) forms the basis. In case of the square butt weld, the maximum welding speed that can be achieved with full penetration is of main interest. For this reason, the shortest possible focal lengths are used. For laser systems in direct use, the long axis of the focal spot (slow-axis) is orientated in the feed direction. Weld curves for different materials and sheet metal thicknesses are shown in Fig. 7.31. Depending on laser power and beam source, high full penetration speeds are achieved in the range between 1.25 and 4 m/min for 1.75-mm-thick mild steel sheets (DP600). In the case of stainless steel (thickness 1.25 mm), values between 2 and 6 m/min are achieved. In the examples shown, the increase in laser power as well as in beam quality (fiber-coupled high brightness system, Chapter 6.2.5) leads to a definite increase in the speed for full penetration. In spite of the longer focal length, almost the values of the device, which used only polarization and wavelength coupling ("kW-pol-stack," Chapter 6.2.2.2) at a laser power of $P_L = 3$ kW were achieved with the high-brightness system (Chapter 6.3.5) at $P_L = 2$ kW laser power. With these parameter combinations, an intensive vapor plume can be observed, which indicates a deep-penetration welding effect. This is supported by consideration of the corresponding cross sections (Fig. 7.32). These frequently have steep weld flanks and show an aspect ratio > 1. The weld undercut on the samples of high-strength steel can be attributed to the edge preparation by shear cut.

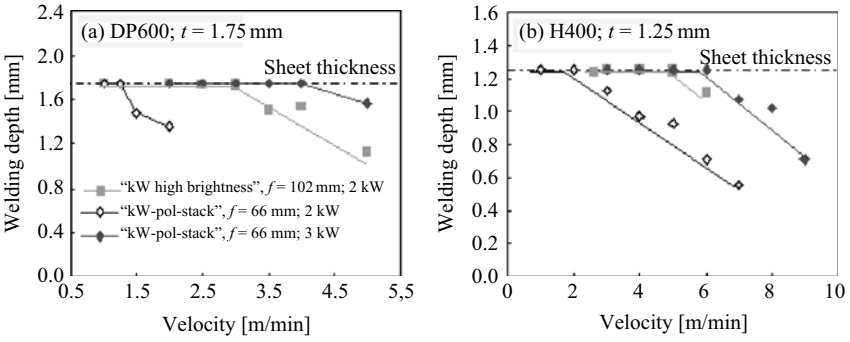

FIGURE 7.31. Maximum velocity for full penetration in dependence of laser power and laser source – square butt welding of (a) high-strength steel and (b) stainless (welding in slow-axis direction)

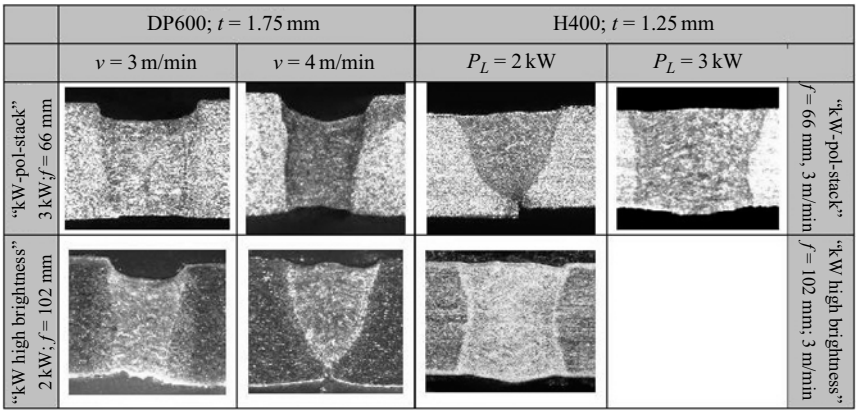

FIGURE 7.32. Cross sections of square butt welds for different materials, velocities, laser powers, and laser sources

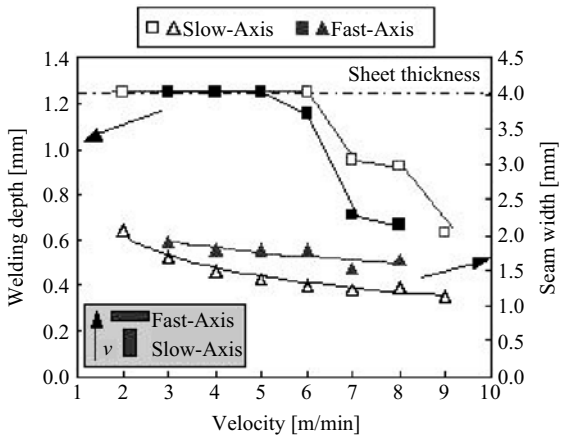

FIGURE 7.33. Influence of laser-spot orientation on square butt welding of stainless steel (System "kW-pol-stack" (Chapter 6.2.2.2); $f = 66$ mm; $P_L = 3$ kW; H400; $t = 1.25$ mm)

Figure 7.33 shows the effects of laser spot orientation on the welding process during welding of butt welds. As expected, during welding in the direction of the slow-axis, slightly higher full penetration speeds were achieved. During welding in the fast-axis direction, a wider melt pool, and thus a wider upper seam bead, is created (Figs. 7.33 and 7.34), which proves to be advantageous with regard to gap bridging capability.

For an implementation in series production, knowing the process tolerances is of great importance. The influence of focal position variations plays an important role, since in industrial application deviations in the working distance due to inaccuracy of devices and/or components, as well as of handling systems, have to be dealt with.

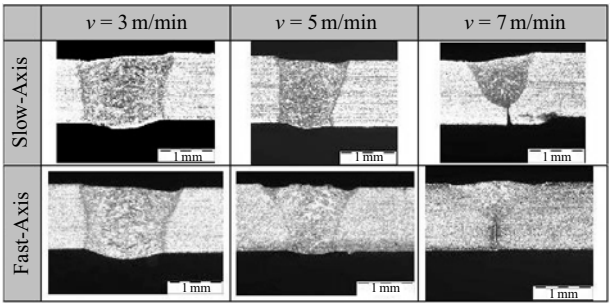

FIGURE 7.34. Influence of spot orientation on weld seam – square butt welding of stainless steel (System "kW-pol-stack" (Chapter 6.2.2.2); $f = 66\,\text{mm}$; $P_L = 3\,\text{kW}$; H400; $t = 1.25\,\text{mm}$)

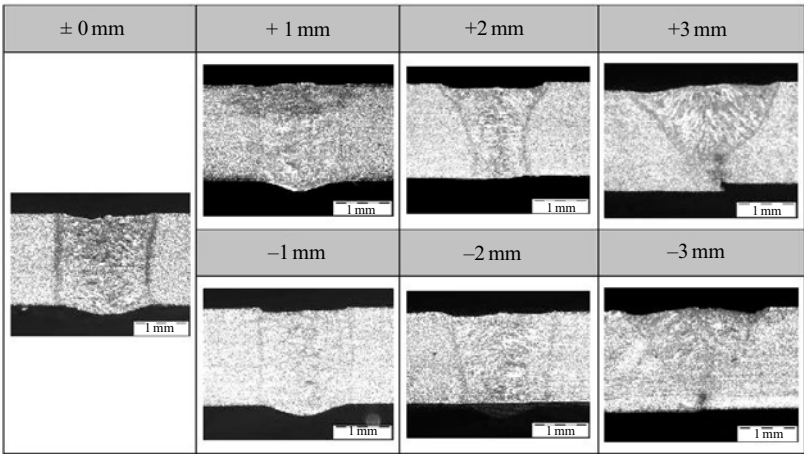

FIGURE 7.35. Comparison of square butt welds – variation of focal position (System "kW-pol-stack" (Chapter 6.2.2.2); $f = 66\,\text{mm}$; $P_L = 3\,\text{kW}$; $v = 2\,\text{m/min}$; Slow-Axis; H400; $t = 1.75\,\text{mm}$)

Because of the comparatively low beam quality and the associated short working distance and Rayleigh length, this could become critical with diode lasers. As an example, Fig. 7.35 shows weld results using a short focal length ($f = 66\,\text{mm}$) for stainless steel. In spite of the short focal length and the associated large beam divergence, no critical deviation from full-penetration welding is observed for a focal position variation in the range of ±Rayleigh length ($z_R = 2\,\text{mm}$). This is achieved by selecting a safe welding speed. Out of focus, the root width is reduced, but nevertheless, within the described tolerance range, full penetration can be guaranteed. However, at higher speeds, the tolerance range tends to narrow and has to be checked for use in the individual case.

Fillet Weld at Lap Joint. The fillet weld at lap joint is frequently used in the automotive industry. The joining geometry is of great interest for the use of diode lasers, since deep-penetration welding is not absolutely necessary to fulfill the requirements. In addition, the characteristics of the diode laser (asymmetrical beam profile) can have a positive effect on the welding result regarding the smoothness of the seam surface.

There are various influence variables. Particularly, the connection length of the seam at the joint interface determines the strength of the joint. If full penetration is not necessary, an evaluation of the fillet weld at lap joint according to the usual geometrical data used for seam specification does not give a suitable characteristic with regard to strength. Therefore, the definition of the connection length is introduced. The load case in real parts depends on the force directions and magnitudes. Thus, the definition of the bearing cross section is related to the worst case, i.e., to the direction with the smallest bearing length, the connection length a. In Fig. 7.36 the geometrical proportions and the different variables are sketched.

Figure 7.37 shows results using the connection length in dependence of various process parameters and Fig. 7.38 shows related macro-sections. As expected, the connection length decreases with increasing feed rate due to the shorter interaction times. With short focal length ($f = 66$ mm), clear differences can be observed in the connection length with respect to spot orientation and/or angle of incidence of the beam. As already seen with the butt weld, with slow-axis alignment of the spot, deeper and narrower seams are obtained. A major part of the seam is located in the lower plate and does not contribute to an increase in the connection length. According to this, the advantage of the long interaction zone cannot be used effectively. With fast-axis in parallel with the feeding direction, a wider melt pool is generated. Because of this, the edge of the upper sheet is easier to be met and melted, resulting in a uniform transition between upper and lower plate without notch. The weld seam is wide in the upper area and narrows in the area of the joining plane, since a majority of the energy is needed for melting the upper plate. This results in a smaller connection length in comparison to the slow axis alignment. If the beam angle of incidence is increased to 70°, a clearly higher welding depth can be achieved. The weld seam is narrow and the connection length increases

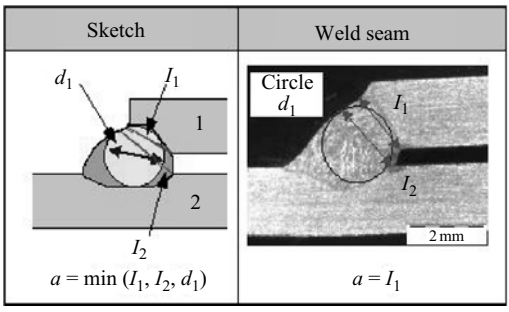

Figure 7.36. Fillet weld at lap joint – definition of connection length *a*

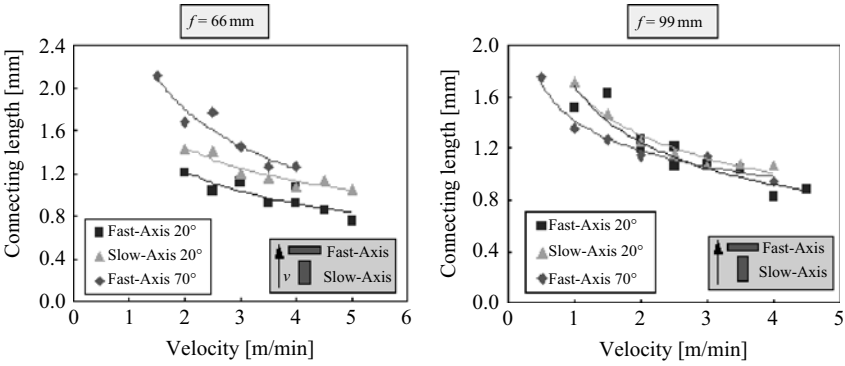

FIGURE 7.37. Influence of spot orientation, angle of incidence and velocity on connection length – fillet weld at lap joint (stainless steel; System "kW-pol-stack" (Chapter 6.2.2.2); $P_L = 3\,\text{kW}$)

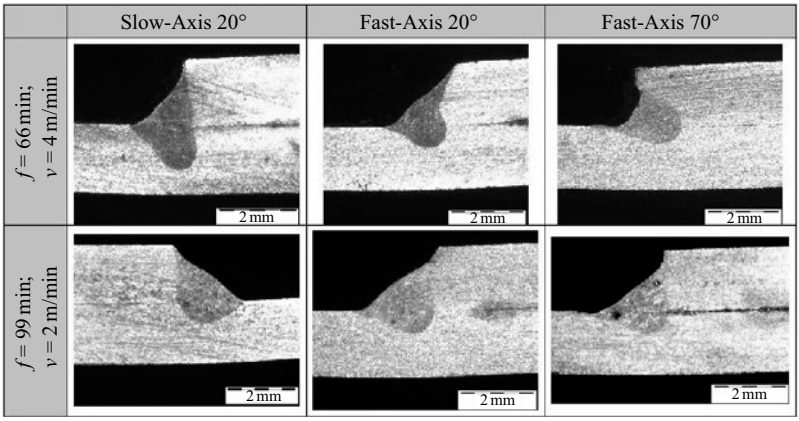

FIGURE 7.38. Influence of spot orientation, angle of incidence, and velocity on weld seam geometry – fillet weld at lap joint (stainless steel; System "kW-pol-stack" (Chapter 6.2.2.2); $P_L = 3\,\text{kW}$)

because of the flat beam angle of incidence in the direction of the joining gap. On the other hand, in some cases undercuts can be found that have a negative effect on dynamic strength and should be avoided.

In contrast to this, with the long focal length ($f = 99\,\text{mm}$) in the speed range between 2 and 4 m/min, almost the same values are achieved with all three settings. This is very advantageous with regard to possible applications, since no readjustment of the spot orientation or no precise compliance with the incidence angle seem to be necessary. One reason for this behavior can definitely be found in the available intensity, which is not adequate for a deep-penetration welding effect with the long focal length. With a pure heat conduction process, the limits

between the individual parameters blur. This means the seam shapes in the area of the joining plane are almost identical (Fig. 7.38). The angle of incidence also plays a subordinate role in this case. In contrast to the short focal length, the seam cross section in the lower plate is smaller and thus the positioning accuracy has to be considered more critically. However, the connecting length is almost constant for the beam orientations in Fig. 7.38.

The curves shown apply to the zero gap case and have to be verified using other realistic joint conditions. Frequently in series production, gaps occur due to manufacturing tolerances which have to be bridged by the joining process. For cost reasons, additional material should be avoided as much as possible. Tests with gap variations show to what extent gaps can be bridged without additional material during welding with the "kW-pol-stack" (Chapter 6.2.2.2). The possible gap bridging capability mainly depends on the melt volume. At constant laser power, the feed rate, focal length, and beam orientation can be identified as the most important influence parameters. In addition, positioning of the beam with respect to the gap plays a decisive role. The long focal length ($f = 99$ mm) has proven to be advantageous as a result of the large melt pool. In this case, the spot orientation is secondary. The results in Fig. 7.39 show that with suitable selection of parameters, gaps up to 0.5 mm can be safely bridged. If there are larger gaps (> 0.3 mm), a readjustment of the laser spot position in the direction of the upper plate is necessary to ensure uniform connection between upper and lower plate.

Circular Spot Welds and Tube-Sheet Joints with Annular Diode Laser Beam. The basics of the "ring focus laser" (Chapter 6.3.5) and the principle of the single shot technology applied here are described earlier in this chapter. Without relative movement, the workpieces are irradiated by an annular laser spot during a pulse of variable length. Applied laser powers are between 1.5 kW and 2 kW.

A possible application of the annular diode laser beam is spot welding on two overlapping sheets. Loadable joints are created in overlapped 0.8-mm-thick mild steel and 1-mm stainless steel sheets with irradiation times of 1 to 1.5 s. The spot welds penetrate the total thicknesses of 1.6 mm (mild steel) and 2 mm (stainless steel) in 1.5 s.

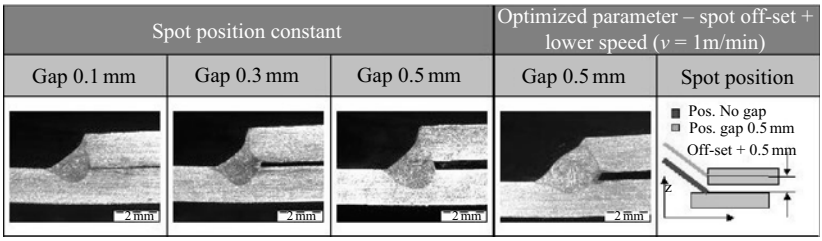

FIGURE 7.39. Welding of fillet welds – Gap-bridging ability using high-power diode lasers (System "kW-pol-stack" (Chapter 6.2.2.2); $f = 99$ mm; $P_L = 3$ kW; $v = 2$ m/min; Slow-Axis; angle of incidence $= 20°$; H400; $t = 1.75$ mm)

To give examples for tube joints, stainless steel tubes with outer diameters of 4, 5, and 6 mm and a wall thickness of 1 mm each are welded to 1-mm-thick stainless steel sheets with holes according to the tubes' diameters in various joint configurations. Radial annular welds are created when the fillet between the tube and sheet is irradiated on the component's side (i.e., the side with the tube sticking out). The same kind of weld can be produced on both sides of the tube in a symmetrical joint where the tube is stuck through the hole into the sheet. Axial annular welds are created on the backside of the sheet (i.e., tube facing away from the laser beam) when the face surface of the tube is leveled with the sheet's surface. Butt joints of two tubes are also possible. Adjustment of the annular laser spot's diameter is realized by defocusing. Figure 7.40 shows examples of the various tube joints.

All examples shown in the figure are produced at an irradiation time of 0.5 s, though auspicious results have been achieved at shorter times as well. Shielding gas was not applied. The integrated, radial cross-jet nozzle protects laser optics from fume or spatters.

The potential of single-shot welding with an annular beam becomes obvious especially for mass production of thin-walled tubular structures.

Welding of Aluminum Joints

In heat conduction welding of aluminum alloys larger spot sizes can cause deeper fusion penetration if the feed rate is sufficiently low. This clearly demonstrates that

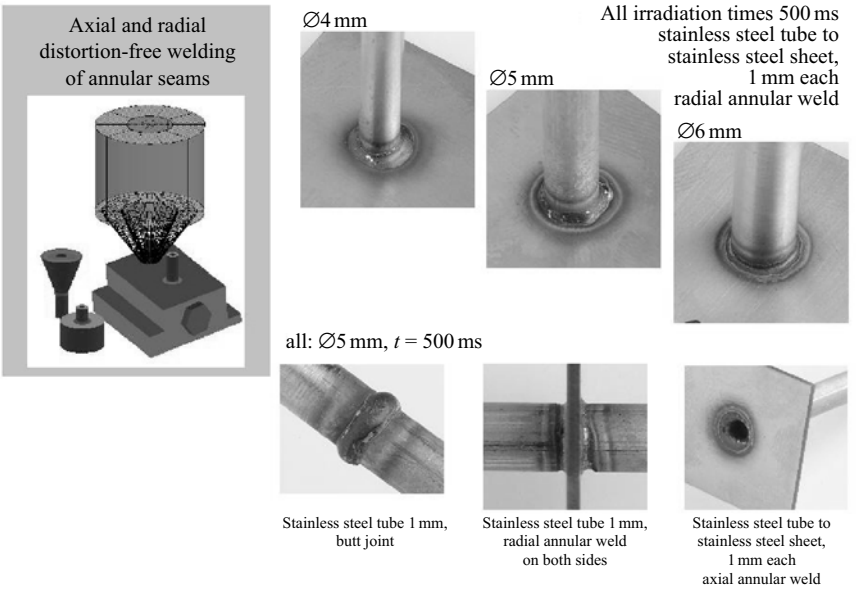

FIGURE 7.40. Stainless tubes welded to stainless sheets in single shot technology

higher power density is by no means always an unequivocal advantage in respect of the welding depth.

In order to create various beam sizes, the simplest method is to vary the working distance, i.e., to defocus the diode laser beam. With decreasing feed rates the optimal defocusing in respect of the achievable welding depth shifts to higher values. With increasing defocusing the width of the weld increases also according to the growing beam spot. Regarding the defocused diode laser beams it has to be noted that the spatial distribution of the beam out of focus changes considerably. Local distributions depend on the diode laser system setup. This implies an additional non-quantified influence beside the pure value of the focal position or the spot size.

When the laser beam of the Rofin DL030S ($f = 66$ mm, working distance 41 mm) is defocused by 15 mm (i.e., working distance 56 mm), a 6-mm-thick AlMg-alloy sheet is fully penetrated at 0.15 m/min. Contrarily, the welding depth is only 3 mm when the focused beam is applied. At 0.25 m/min, the welding depths are 4 mm with and 2 mm without the defocusing length of 15 mm. At welding speeds between 0.5 m/min and 1 m/min, the optimal defocusing length is around 10 mm, and the gain in welding depth is not that significant.

To perpetuate this idea, various 4-mm thick aluminum alloys of the 2000 and 6000 series were joined with the Rofin DL025 at an output power of 2 kW. For these defaults, the optimal defocusing length for achieving the largest welding depths was found to be 5 mm. Helium was used to shield the weld seam, and all welds were performed without melt pool support and root protection.

Some alloys such as AA2524 could only be butt-joined when the beam is defocused several millimeters. Fully penetrated butt joints were produced at welding speeds between 0.15 m/min and 0.35 m/min, depending on the type of alloy. When sheets of different alloy series such as AA6056 and AA2524 are joined, it is clearly visible in the cross section that the mixing of the melts is not homogeneous or complete. Figure 7.41 shows three examples of aluminum alloy butt joints with identical welding parameters.

Process Tolerances Regarding Gap and Offset

To assess process tolerances regarding gap bridging and offset clearing at butt joints, welding test series were performed with Rofin DL025 on 2-mm-thick

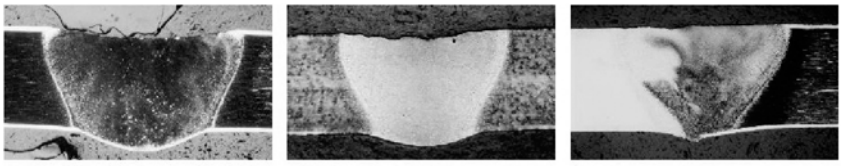

FIGURE 7.41. Butt joints on aluminum alloys with HPDL, welding speed 0.2 m/min, defocusing length +5 mm, shielding gas He 70 L/min

stainless steel and aluminum. Laser power at the workpiece was 2.3 kW. Contrary to the possible assumption that tolerances are higher when the welds are conducted with the laser spot's fast axis in welding direction (i.e., frontal width of the spot is 3.8 mm), the results in stainless steel as well as in aluminum showed better bridging and clearing capabilities when the spot's slow axis was in welding direction (frontal width 1.7 mm). This is due to the fact, that the spot dimensions are large in both directions with this old generation diode laser system. Therefore, the smaller beam axis is still big enough for bridging capabilities but prevents to waste energy by too wide melt tracks. Therefore, the results presented here deal with welds produced with that laser spot configuration only.

Process tolerances for stainless steel are appraised at 1 m/min. When the gap width is increased in discrete steps of 0.1 mm, continuous and fully penetrating welds are created up to a gap width of 0.4 mm. When the edges of the sheets form a gap with a varying width, it is essential whether the gap is widening or narrowing along the weld path. A gap width starting at 0 mm and widening to 0.5 mm can be perfectly welded all the way, the weld does not disrupt at 0.4 mm as could be presumed. If the weld is started at the gaping end, a continuous and fully penetrating weld is not generated until the gap width narrows to 0.35 mm. The beads and roots of the welds become more depressed at large gap width.

An offset of edges up to 1.5 mm can be cleared with fully penetrating welds. Up to this value, the extent of the offset has no influence on the geometrical shape of the welds' cross sections, which show a smooth transition between the upper and lower surfaces of the sheets. Figure 7.42 gives two examples of butt joints in stainless steel featuring gaps and offsets.

Analogous test series were performed on 2-mm-thick aluminum with a welding speed of 1 m/min (Fig. 7.43). At discrete gap widths, continuous and fully penetrating welds could be produced up to a gap of 0.3 mm. At a gap that narrows from 0.5 mm to 0 mm, a continuous and fully penetrating weld sets in at nearly the same width of 0.32 mm. A widening gap can be welded completely. Misaligned edges can be cleared up to an offset of 1.5 mm but with asymmetrically formed cross sections.

Many of the cross sections of joints that are welded with a gap show lack of fusion in the central regions. These welding defects are most probably caused by the oxide layer covering the sheet edges. The oxides melt at temperatures about

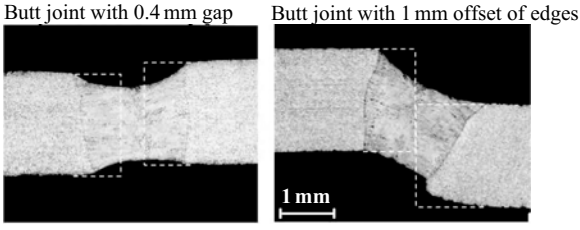

Figure 7.42. Process tolerances for butt joints in stainless steel, 2 mm

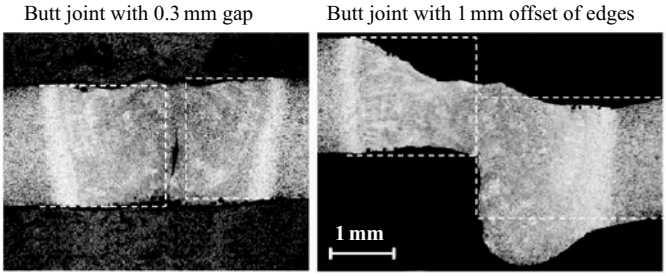

FIGURE 7.43. Process tolerances for butt joints in aluminum, 2 mm

three times higher than the melting point of aluminum. These temperatures are not reached reliably. The defects are formed when the heat conduction welding process melts the aluminum in the joint area but is only able to crack open and liquefy the oxide layers that cover the upper surface of the sheets. Thus the melts of both sheets can mix in the upper region and form a proper weld structure, whereas molten aluminum is enclosed in the flexible but solid oxide layers in the lower region of the melt pools and cannot mix sufficiently. This effect is larger if the edges are not in contact and a part of the laser light is transmitted unutilized through the gap.

It becomes clear that before heat conduction welding of aluminum with diode lasers a proper removal of the oxide layer on the sheet edges has to be carried out in order to avoid lack of fusion.

The awkward geometrical shapes of the welds with offset edges fall back on a similar problem. The cross sections are free of pores and the oxide layers are liquefied in the contact zone of the sheets, so the melts are able to mix. But gravity drags the melt of the upper sheet into the lower sheet's melt, thus too much melt is accumulated and adheres to the lower sheet. The excess material bulges the flexible but solid oxide layer and forms the inflated weld root beneath the lower sheet. Since too little material is now available at the upper edge, a constriction forms there. Nevertheless, in this case, the oxide layer forms some kind of melt pool support at the root of the weld, thereby reducing drop-through.

Automotive Applications

Multi-Layer Overlap Joints. A major goal within the MDS project was to improve the diode laser sources significantly with regard to beam quality and laser power. Figure 7.44 shows one of the first diode lasers employed (1996). Due to the low intensity of this laser and its short working distance, at that time it was not possible to carry out deep-penetration welding, which is a precondition for reliable production of lap joints.

Although lasers with a higher output power became available a short time later, their intensity was rather at the limits to initiate a deep-penetration welding process.

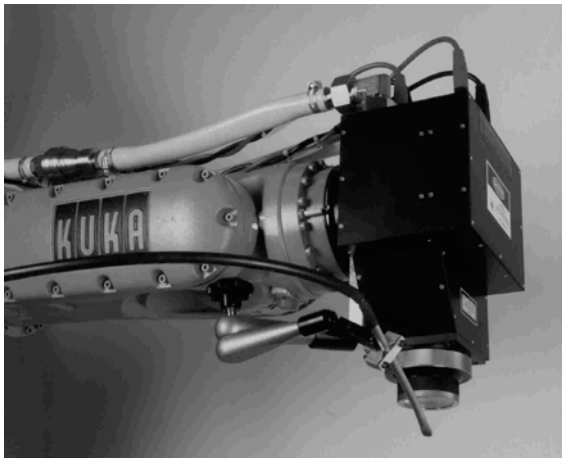

FIGURE 7.44. One of the first high-power diode lasers employed for materials processing (1996; laser power 1.5 kW; focal length $f = 50$ mm, working distance 35 mm)

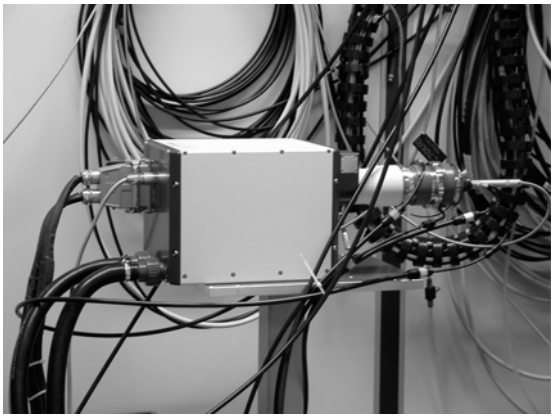

FIGURE 7.45. "kW high brightness" laser (2003; fiber coupling 800 μm, 0.22 NA, 2.3 kW, focal length $f = 100$ mm; working distance 78 mm)

Nevertheless, at least in stainless steel, the first deep-penetration welds could already be demonstrated [7.3, 7.4].

The photo in Fig. 7.45 shows the "kW high brightness laser" (Chapter 6.2.5). This laser is indicative of the state of development at the end of the research project [7.6] in the year 2003.

For the welding results shown here, the laser is coupled into a 0.8-mm fiber. Despite this fiber coupling, 2.3 kW of laser power are still available at the workpiece. Moreover, a larger working distance of 78 mm (35 mm in 1996) improves the accessibility of the joint area and the durability of the optics in practical operation.

It became possible to weld lap joints with a total material thickness of 3.2 mm at a welding speed of 1.2 m/min. As mentioned before, lap joints can only be created by means of deep-penetration welding.

The deep-penetration welding process with the diode laser (Fig. 7.46) shows no significant differences from welding with the Nd:YAG laser. There is no highly ionized plasma plume, such as those which occur when welding with a CO_2 laser, but rather a hot vapor plume (see also section 7.1.2.1). A number of welding results are presented below (Figs. 7.47–7.49). All weld cross sections show the typical characteristics of deep-penetration welding with laser radiation. The formation of the weld seam does not depend on the number of sheet layers as long as no gap is present between the layers.

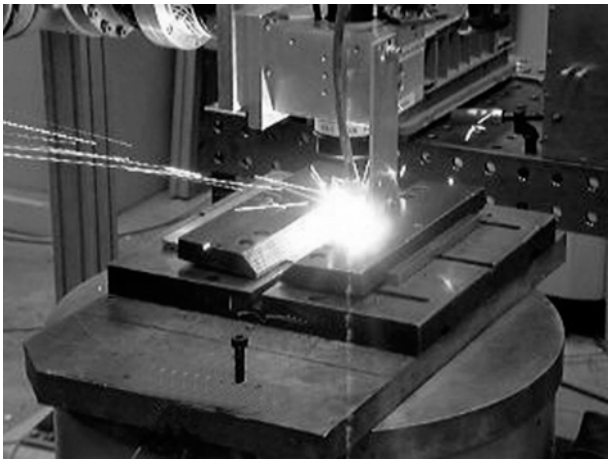

FIGURE 7.46. Welding process

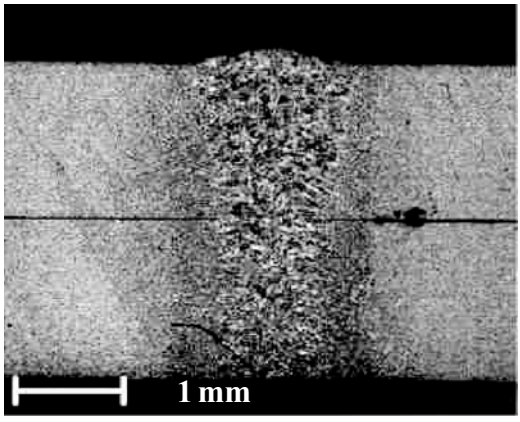

FIGURE 7.47. Welding sample (ZStE360), non-coated, $v = 1.2$ m/min, $P_L = 2.3$ kW

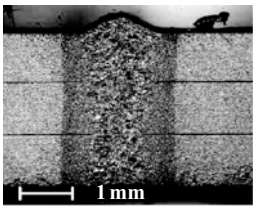

FIGURE 7.48. Welding sample (ZStE220), non-coated, $v = 1.2$ m/min, $P_L = 2.3$ kW

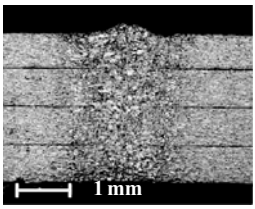

FIGURE 7.49. Welding sample (ZStE360), non-coated, $v = 1.2$ m/min, $P_L = 2.3$ kW

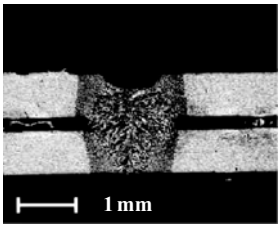

FIGURE 7.50. Welding sample (ZStE220), Zn-coated, $v = 3$ m/min, $P_L = 2.3$ kW

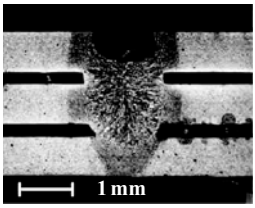

FIGURE 7.51. Welding sample (ZStE220), Zn-coated, $v = 1.5$ m/min, $P_L = 2.3$ kW

If the materials are zinc-coated, spatters occur, if no provision is made for out-gassing of the zinc vapor. In Figs. 7.50 and 7.51 the sheets are zinc coated and welded with an out-gassing gap of approximately 0.2 mm. The out-gassing gap represents an empty space which must be filled with material in the joint area. If no filler material is used, the upper weld surface obtains an undercut. The volume of this undercut corresponds to the gap volume at the joint interface.

The welding examples demonstrate that meanwhile state-of-the-art diode lasers are quite suitable as a tool for welding steel sheets. Since the working distance is still relatively small, however, the use of uncoated materials is to be considered preferably.

Test Application: Roof Bow. Ultimately, reliable statements on the capabilities of high-power diode laser systems for welding can only be made by testing the process on actual parts. Two different DaimlerChrysler car body roof components – the roof bow and the roof header – have been welded with the Rofin DL030S at a focal length of 100 mm and a maximum laser power at the workpiece of 2.8 kW. The extended focal length is applied in order to improve protection of the laser optics from spatters that might result in welding the partly galvanized body components. Spot dimensions are 1.5×2.3 mm^2 and power density with the long focal length is 0.75×10^5 W/cm^2. The laser optics are protected by the cascaded cross-jet and an additional tube-shaped nozzle with a flattened outlet that provided a forceful compressed air jet very close to the interaction zone. The latter diverts spatters shortly after they left the melt pool. The compressed air jets of both nozzles flow transversal to the beam axis in welding direction. Best results are attained with the laser spot's slow axis parallel to the main welding direction. Shielding gases are not applied as frequently demanded by the automotive industry.

Taut clamping of the welding assembly is provided by a custom-made clamping device; i.e., a wanted or unwanted formation of a gap between the joint partners is excluded. All parts consist of 1.2-mm-thick mild steel H340 (material no. 1.0548).

The roof bow consists of two uncoated parts that are already joined by six spot welds evenly distributed along the components' total length of one meter. The task is to join the parts on both sides with two continuous, fully penetrating fillet welds that run along the full length of the roof bow. Access to the welding area is limited by upturned edges of the lower part, thus the laser beam can only be inclined by 10° to improve accessibility of the fillet. The three-dimensional welding path was defined by 17 teach-in points. The welding head is manipulated by a 6-axis KUKA robot.

The maximum allowed feed rate is 1.05 m/min, in order to achieve fully penetrating welds. Spatter formation is minor due to the absence of zinc coatings. Figure 7.52 shows the roof bow and details of the weld.

The type of welding sequence is a crucial point for the resulting accuracy of the component.

First example: After the first weld track is completely performed from one end of the panel to the other, the component is welded at the opposite side. The robot's path deviates up to 1.5 to 2 mm from the actual fillet on the second side. About the first and last 120 mm of the panel are distorted inward/to the left whereas the middle section is bulged outward/to the right when looking in welding direction.

Second example: In order to reduce distortion due to unsymmetrical and transient heat input, one roof bow's side is joined with two welds that have their

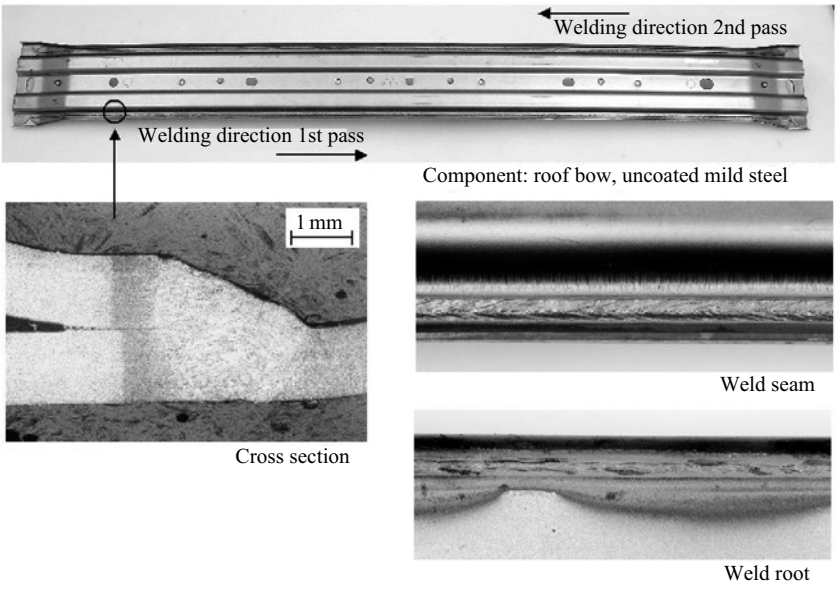

FIGURE 7.52. Roof bow welded at 1.05 m/min

common starting point in the middle of the weld path and are then continued to one end point of the weld path each.

Third example: One side of the roof bow is welded intermittently, starting in the middle and completing the weld in 150-mm-long sections alternately on the left and right to the starting point.

The second and third approaches show an improvement, i.e., less distortion on the opposite, still not welded side. But the robot's path partially is still too deviant so that some points of the path have to be corrected also in these cases.

Further improvement can be achieved by more complex welding sequences. However, the second approach is resulting already in an acceptable accuracy of the completed component regarding the integration in the car body. The remaining unacceptable efforts for re-teaching are avoided by the utilization of a seam-tracking sensor (see section 7.1.2.1). Thus, an automated manufacturing process can be realized.

Test Application: Roof Header. The roof header consists of two individual shells that are centered and clamped tightly to each other and have to be joined by a single, slightly curved fillet weld, about one meter long. The lower part is electrolytically galvanized, the upper part is hot-dip galvanized. Access to the fillet is not constricted so that an inclination angle of 45° can be applied. Since both joint partners are entirely zinc-coated and the joint itself is gapless, the risk of serious spatter formation is very high and precaution measures like the additional compressed air nozzle and the large focal length are appropriate.

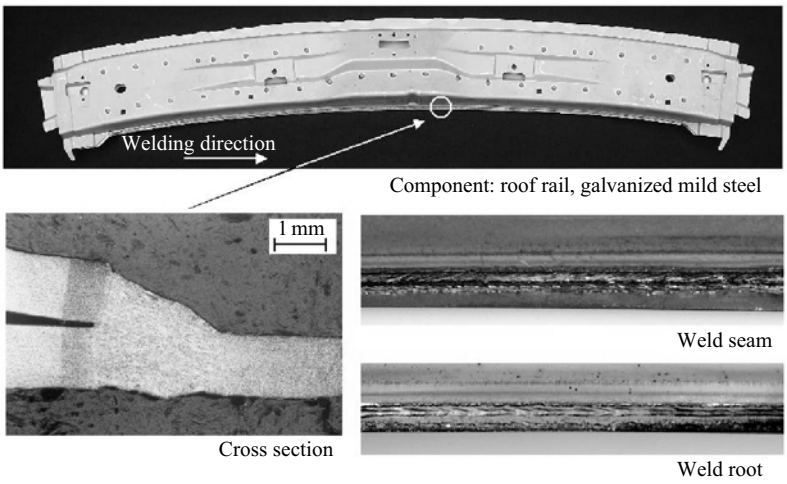

FIGURE 7.53. Roof header welded at 1.55 m/min

The fillet and the edge of the lower part are only about 5 mm apart which causes the temperature in the relatively thin lower sheet to rise quickly above the material's melting point due to heat accumulation. This results in holes and melt droplets along the weld when the welding speed is too slow or the beam is positioned too much on the lower part. With a properly adjusted beam path and an optimized welding speed of 1.55 m/min, excellent welds are achieved. Figure 7.53 shows a welded roof header and details of a typical weld.

Test Application: Axle Carrier. Basic feasibility is the first consideration of a test, i.e., weldability of the component under consideration of accessibility and similar boundary conditions. A component from the running gear is used as a demonstrator component. The axle component is designed in sheet metal shell construction and consists of two individual parts (upper/lower shell) that are welded together using a fillet weld on lap joint with six single seams (Fig. 7.54). Because of the use of tailored blanks, different sheet metal thickness combinations occur along the joining line. The component is currently manufactured in series production [7.7] with a Nd:YAG laser.

With real components, accessibility plays a decisive role for use of the diode laser. Because of the laser head that is significantly larger in comparison to the processing head for Nd:YAG lasers, in connection with the short working distances of high-power diode lasers an increased danger of collision due to interfering contours must be dealt with in spatial processing. For this reason, first accessibility tests for the used diode laser system are carried out using an offline programming system (TopLas3D®). In addition, the path is generated and the robot program created with this system. The collision analysis (Fig. 7.55) shows no restriction in the welding of outer longitudinal seams. For welding the inner arc seams, the

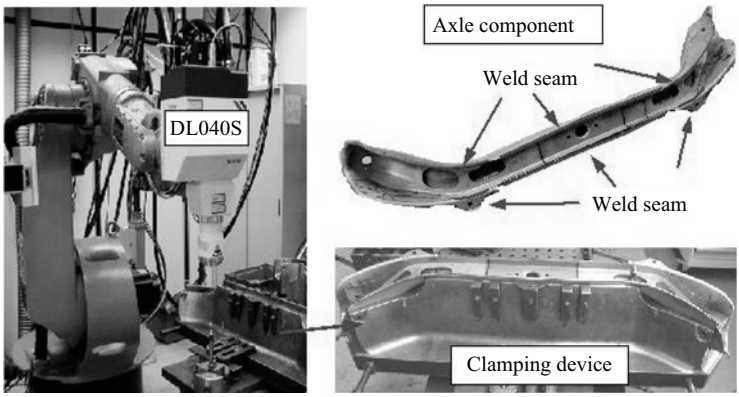

FIGURE 7.54. Welding of axle parts – cross member consisting of top and bottom shell and experimental setup with a Rofin DL040S system mounted on a robot

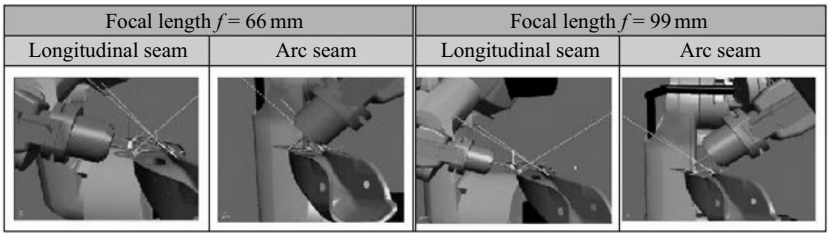

FIGURE 7.55. Accessibility check by using the offline programming system TopLas3D®

incidence angle has to be adjusted in both cases. In this process, the use of the short focal length is considered critical.

As a consequence of the results of the collision analysis, the focal length f = 100 mm is used in view of the advantages in accessibility. This focal length proves to be very tolerant to variations in the lateral angle and the beam orientation in feeding direction and demonstrates good gap bridging capability. Components were welded with good results and acceptable feed rates (Fig. 7.56). The seam shape mainly corresponds to the specifications and shows a soft transition between upper and lower plate. The gap dimensions that occur in the reshaped sheet metal shells can be bridged. As a supplement Fig. 7.56 shows snap-shots during the welding process. By the use of the fiber-coupled "kW high brightness system" (Chapter 6.2.5), due to its improved beam quality, very high speeds are possible with simultaneously excellent seam geometries.

Test Application: Tailored Blanks. An important contribution to automotive lightweight construction is the use of tailored blanks. Tailored blanks are individually designed sheets that can be made of different types of steel with different coatings

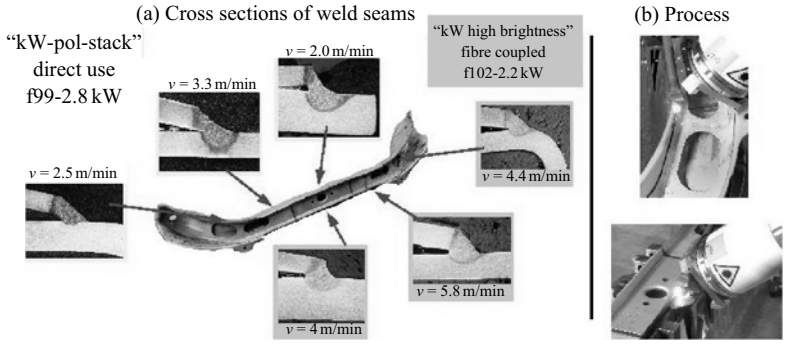

FIGURE 7.56. Welding of cross member – (a) comparison of laser sources and maximum velocity, (b) snapshots of welding process

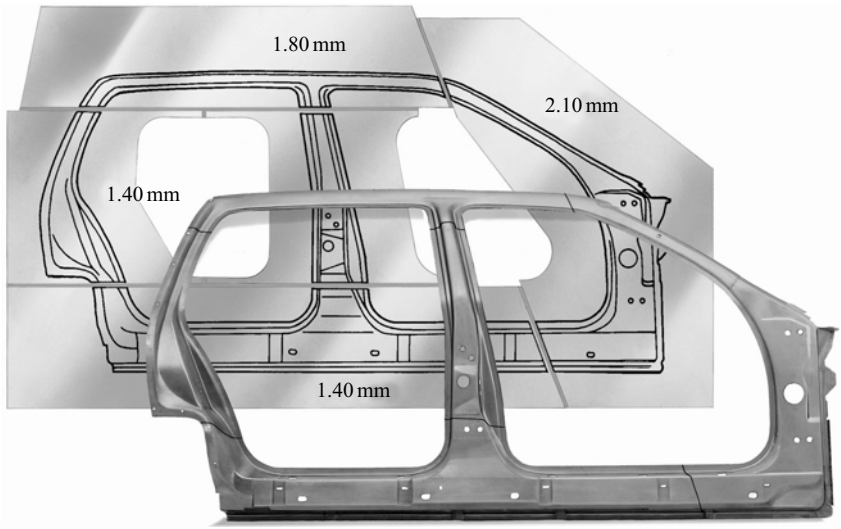

FIGURE 7.57. Automotive side panel with Tailored Blank for lightweight construction (source: ThyssenKrupp)

and thicknesses (see Fig. 7.57). This makes it possible to use optimized sheet characteristics for each specific area of a component.

Presently, tailored blanks are mainly manufactured by using laser beam welding. For this work CO_2- and Nd:YAG-lasers are common sources. CO_2-lasers are mainly used for joining of linear weld seams. Linear tailored blanks can be welded in continuous production lines which provide very high efficiency. To optimize automobile light-weight construction, today automobile manufacturers are calling for tailored blanks with nonlinear weld seams. For this work mainly fiber-coupled

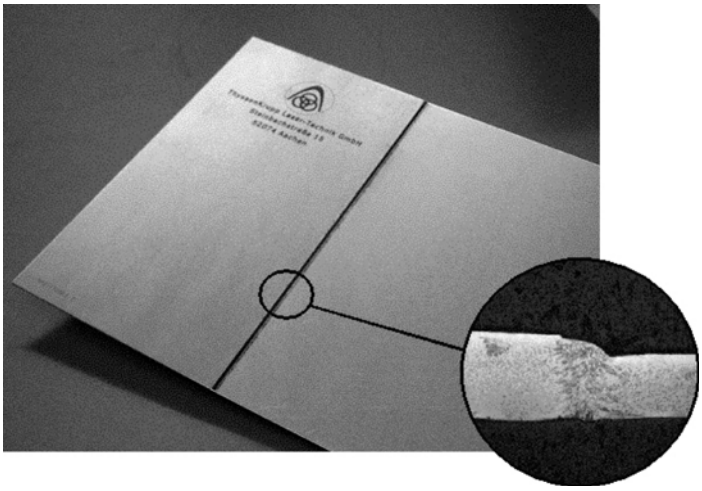

FIGURE 7.58. Diode-laser-welded Tailored Blank

Nd:YAG-lasers are used. They provide a very high flexibility and can be used in different kinds of handling systems, even robotics, without complicated mirror systems for beam guidance.

The joining of tailored blanks with direct and fiber-coupled high-power diode lasers has been investigated. With the laser "kW high brightness laser" (Chapter 6.2.5) in direct operation mode, linear tailored blanks with a thickness variation of $t_{1,2} = 0.9/1.2$ mm are welded at a speed of $v_S = 7.0$ m/min and laser power of $P_L = 2500$ W. The material used was the hot-dip galvanized steel grade DX 54 D+Z, which is common in automobile production. In fiber-coupled processing a welding speed of $v_S = 4{,}0$ m/min at a laser power of $P_L = 2000$ W could be reached.

In Fig. 7.58a diode laser welded tailored blank is shown together with its cross section. The bead and the root both have a very smooth surface. A tensile strength of $R_m = 330$ N/mm^2, which is equal to the tensile strength of the base material, is reached. The rupture is outside of the heat-affected zone (HAZ) in the thinner sheet. Cupping tests show good results, too.

Aeronautical Applications

A potential application for aeronautical components is the heat conduction welding of aluminum fittings to tubes (Fig. 7.59). The main advantages, compared to TIG welding, are greater speed, resulting in fewer distortions, and the fact that it is a highly automated process. Additionally, welding in heat conduction mode is a very tolerant process, which results in very smooth seams with very high quality, which is necessary for aeronautical applications particularly.

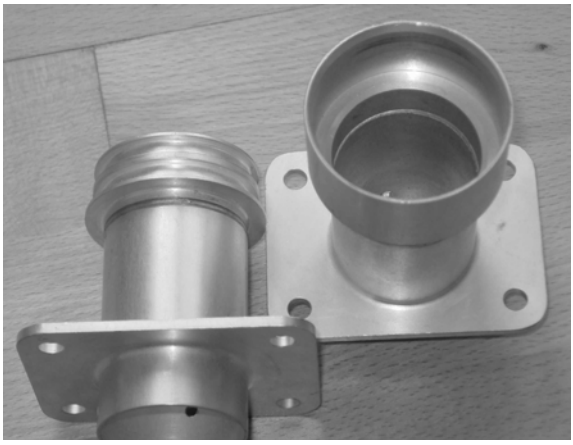

FIGURE 7.59. Welding of fittings for media tubes

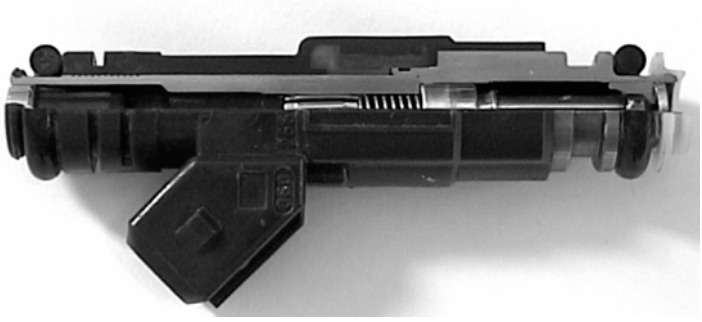

FIGURE 7.60. Gasoline injection valve

Precision Welding of Small Components

Heat conduction welding by laser is an excellent process for assembling and sealing precision parts like valves and sensors. One example is the injection valve in Fig. 7.60. This component is a typical product of mass production. In several plants worldwide more than 200,000 injection valves of this type are manufactured every day. Especially in applications like this, the economic advantages of diode lasers can make a significant difference in costs.

The component consists of three parts: the holding-on magnet, the tube, and the ball (see Fig. 7.61). The component is responsible for the sealing and opening of the valve. The valve is sealed when the ball is pressed into the valve seat by a spring. To open the valve a magnetic force is induced into the holding-on magnet and the ball is pulled away from the valve seat.

In current serial production the welds between holding-on magnet and tube as well as tube-ball are carried out with a fiber-coupled Nd:YAG laser. Within a

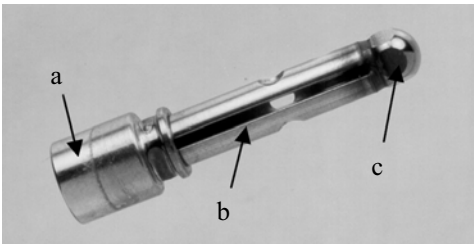

FIGURE 7.61. Component of injection valve consisting of (a) holding-on magnet, (b) tube, (c) ball

	Nd:YAG weld in serial production	Diode laser weld
Ball-tube weld	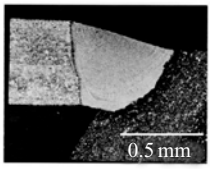	
Holding-on magnet-tube weld	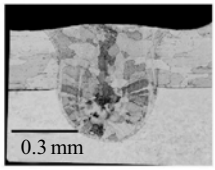	

FIGURE 7.62. Holding-on magnet-tube weld and tube-ball weld carried out with Nd:YAG laser and diode laser

feasibility study, a fiber-coupled diode laser with a fiber core diameter of 400 μm and a maximum output power of 500 W is used in order to evaluate its capabilities. The focal diameter on the workpiece is approximately 450 μm for both lasers. Due to better beam quality, the distance between optics and workpiece is well above 120 mm for the Nd:YAG laser, while for the diode laser, with a beam quality not quite as good, it is a little less. As the specified welding depth of several tenths of a millimeter only requires moderate laser power of less than 400 W, the danger of contaminating the optics is low also when the diode laser is used.

The welds shown in Fig. 7.62 are carried out with identical parameters regarding laser power and feed rate for both lasers. As the ball consists of high carbon steel the positioning of the weld seam between ball and tube is extremely critical. It has to be guaranteed that the content of carbon in the mixture of both steel types in the melt pool is low enough to achieve a weld seam without cracks. This is realized with both laser types. Also for the overlap weld between holding-on magnet and tube identical parameters for both lasers are applied and resulted in very similar welds, too.

Summing up, it can be said that the results of the laser used in serial production and the results of the diode laser are comparable and almost identical. The fact that the beam quality of the diode laser does not allow the same working distance as the Nd:YAG laser in this case does not make a big difference for the actual application. So in the future the decision about what laser type to be selected for applications like the one shown will not only be based on the question which type can technically meet the requirements of the weld. In a situation where both laser types fulfill the specification the factors costs and service become most important. This includes the cost of ownership for a laser system, the lifetime, e.g., of the diodes and the service quality.

Micro-Welding

To connect thin sheets with dimensions $<100\,\mu m$ with fillet welds at a lap joint, a diode laser system with the following specifications is used:

Power P_L	20 W
Wavelength λ	808/940 nm
Optical fiber diameter d	320 µm
Power density I	$2.5 * 10^4$ W/cm^2

The positioning of the laser spot with respect to the edge of the top sheet is crucial to the welding result. A bigger part of the spot – about two-thirds – should irradiate the top sheet, while the remaining part is melting the bottom sheet. A result for a sheet thickness of 25 µm is shown in Fig. 7.63.

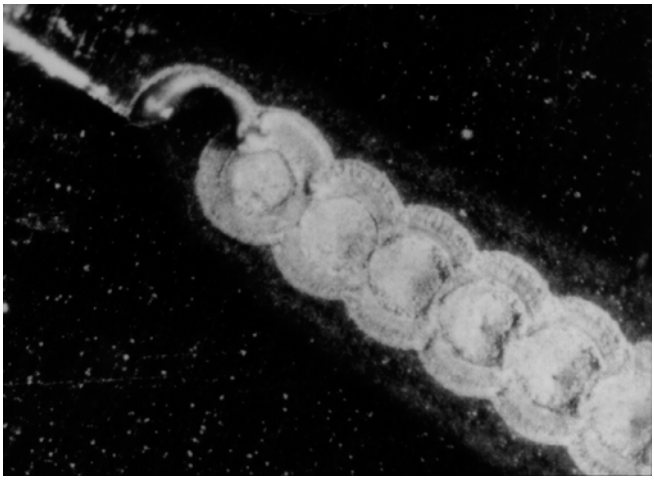

FIGURE 7.63. Pulsed weld seam. Sheet thickness 25 µm; seam width 300 µm; focus 320 µm; pulse length 14 ms; laser beam power 16 W

For thicker materials more power is needed. The specifications of the used systems are shown in the following table:

	Fisba	Laserline LDL300
Power	100 W	300 W
Wavelength	810 nm	800–940 nm
Working distance	55 mm	25 mm (to cover glass)
Focus dimensions	$0.7 \times 0.4\,\text{mm}^2$	$0.7 \times 2.3\,\text{mm}^2$

The line focus of the 300 W system can be used to weld thin sheets in one shot (see Fig. 7.64).

To weld a thin wire to a sheet metal the difference in volume and heat capacity in the two joining components wire and sheet has to be overcome. The joint configuration has been modified to enable a heat concentration in the melting zone. Figure 7.65 shows the combination of a thin wire welded between two small levers of copper.

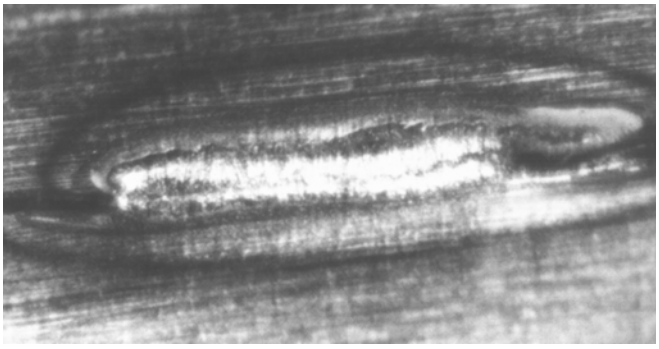

FIGURE 7.64. Single pulse with Laserline LDL 300. Sheet thickness 50 μm; laser beam power 250 W; pulse length 6 ms; spot size $0.7 \times 2.3\,\text{mm}^2$

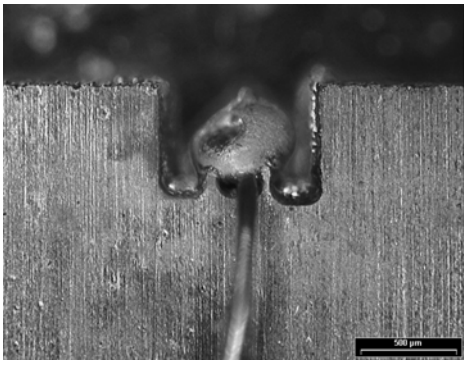

FIGURE 7.65. Single pulse diode laser welding of thin wire to sheet. Fisba FLS100; laser beam power 100 W; spot size $0.7 \times 0.4\,\text{mm}^2$; pulse length 575 ms

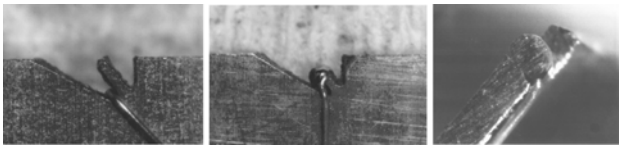

FIGURE 7.66. Left: Geometry adaptation of the wire/sheet joint. Middle: Molten lever with wire. Right: Cross section of wire / sheet joint

To simplify the assembly the wire can be clamped into a V-shaped cut out in the sheet (see Fig. 7.66). The remaining material is molten by means of the laser. Due to heat conduction also the wire reaches melting temperature and forms a common melt pool.

For micro-welding of components with dimensions near the 1-mm range the intensity of $2 * 10^4$ W/cm^2 with a power range of 100–300 W is sufficient to melt the components if specific geometrical adaptations of the parts lead to an appropriate heat concentration in the joint area. In addition, the process has to be adjusted by applying suitable pulse duration of the laser beam, in order to reach the melting phase.

7.1.2.4. Modeling of the Welding Process

Semi-Analytical Simulation of Heat Conduction Welding

A software package that simulates the heat conduction welding process has been developed [7.5]. The "LaserWeld3D" software is based on a semi-analytical modification of the Rosenthal solution of the heat conduction equation. The surface heat source is moved across the workpiece and generates a stationary temperature distribution that can be calculated. The finite thickness of the workpiece (sheet thickness) and the limited heat flow at the bottom surface of the sheet is considered by virtual heat sources below the workpiece. Enthalpies due to phase transitions are not taken into account.

The thermo-physical material properties are approximated by temperature-averaged (i.e., constant) values. Within the semi-analytical approach phase transitions are only allowed for by the identification of the transition temperature. Relevant properties of several commonly used materials are preset within the program. For other materials, the values for melting point, vaporization temperature, as well as thermal diffusivity and heat conductivity can be set freely by the user. In addition, the material's absorption highly influences the simulation result, thus the degree of absorption has to be set to a realistic value, e.g., obtained by spectrometric measurements.

Various types of power density distributions such as Gauss mode (circular), diode-Gauss-mode (rectangular), and annular modes are implemented in the software and can be geometrically adapted to the experimentally found beam distribution of the real laser system by corresponding input parameters. Specifications of laser power at the workpiece and welding speed complete the parameter set list.

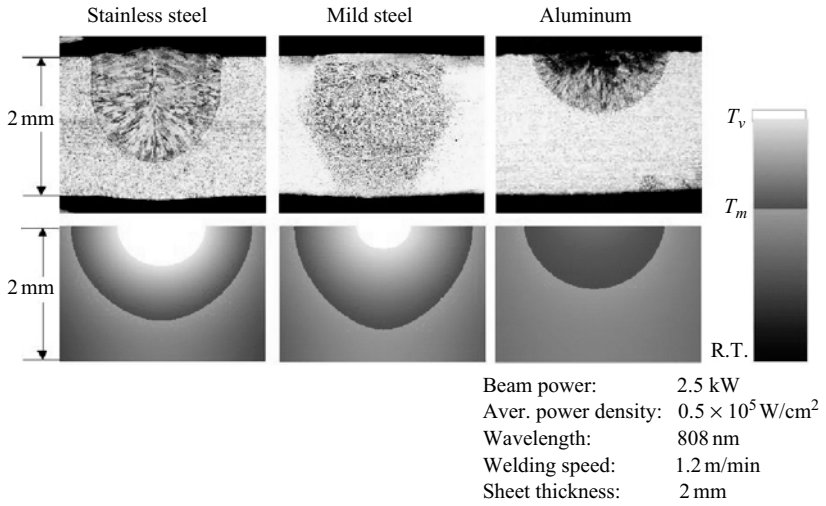

FIGURE 7.67. Comparison of cross sections, experimentally achieved and calculated by LaserWeld3D [7.5]

The resulting 3-dimensional temperature distribution is calculated and visualized in various representations within a few seconds on a standard personal computer.

Figure 7.67 shows theoretical and experimental cross sections in 2-mm-thick mild steel, stainless steel, and aluminum. The welds are performed with a Rofin DL025 at 1.2 m/min.

Taking into account the simplicity of the model approach, the simulated and real weld seam geometries match quite well. The theoretically predicted local attainment of the vaporization temperature in both steel materials, which is indicated by the white areas in the top parts of the simulated seams, is confirmed experimentally by the formation of a vapor plume. The spherical fusion line of the aluminum weld is typical for a pure heat conduction welding mode.

LaserWeld3D is easily operated and due to its fast computation abilities extensive parameter variations can be calculated with acceptable efforts, as demonstrated with the results presented in Figs. 7.16–7.19 of section 7.1.2.2. The software also provides the opportunity to calculate the transient (i.e., time-dependent) Rosenthal solution for unmoved surface heat sources. This feature can be applied to simulate single shot welds.

Numerical Simulation of Deep-Penetration Welding

In the model for simulating heat conduction welding, a surface heat source is implemented and heat transfer to the workpiece is described by heat conduction. For a more accurate computation of welding depth when welding with a high-power diode laser a process model is required that takes the interactions between

the laser beam, solid material, and liquid material into account. The DC-LASIM process model [7.8] calculates the weld pool geometry according to the material, laser and process parameters. The model simulates the formation of the vapor capillary taking multiple reflection, plasma absorption, weld pool currents, and heat conduction into account.

In order to simulate deep-penetration laser welding on body parts, the DC-LASIM program was developed further. The reading of experimentally determined beam intensities was made possible for this purpose. In addition, an analytical approximation of the measured power density distribution was conducted in order to simulate the welding process for high-power diode lasers with non-circular beam shapes. The simulation software contained already analytical process models for CO_2 and Nd:YAG lasers. The feasible seam geometries were expanded to include the radius-end/face-end hem flange. Furthermore, there was verification of the process model based on the example of laser welding on blanks. In addition, automated optimization of laser power as a function of the feed rate was performed with the aid of the DC-LASIM program module "OPTI."

Due to the automated transfer of results from DC-LASIM to the finite element program MARC, the requirements for simulation-based optimization of process strategy were met in order to reduce distortion during laser welding.

In order to calculate the distortion during laser welding on a component with a high-power diode laser a finite element simulation model was created. In the first step simulation was conducted under simplified assumptions. Then the model was approximated to reality and micro-structural transformation was taken into account. In parallel with the computation of distortion the interface between process simulation (DC-LASIM) and finite element simulation (MARC) was developed further. That ensured automatic data transfer and an updating of process parameters throughout the entire simulation of the component.

DC-LASIM currently can calculate the following seam geometries

- I-seam
- Fillet weld
- Face-end and radius-end hem flange

and the following joint geometries

- Butt joint, square
- Lap joint
- T-joint

For simulation, required input settings consider the laser (e.g., type, power output, focal length, focus dimensions), technological parameters (e.g., feed rate, angle of incidence, beam offset), inert gas parameters (e.g., gas type, volumetric flow), details of the workpiece material, sheet thickness, and the seam/joint geometry to be welded.

A comparison of a calculated and the corresponding experimental seam geometry of one of the first published deep-penetration welds performed with a diode

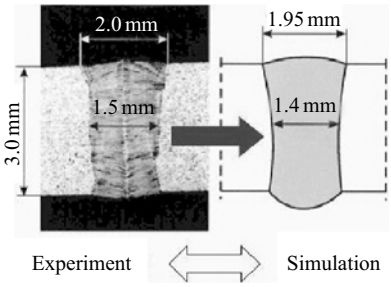

FIGURE 7.68. Comparison between simulated and experimental butt weld; (technological parameters: power $P_L = 2.5\,\text{kW}$; beam dimensions $d_{0,x,86,5\%} = 1.05\,\text{mm}$; $d_{0,y,86,5\%} = 1.2\,\text{mm}$; welding speed $v_W = 0.7\,\text{m/min}$; material: stainless steel)

laser [7.4] is shown in Fig. 7.68. It is a butt joint in 3-mm stainless steel. Theory and practical result correspond very well.

The heat input calculated with DC-LASIM can be transferred to the FEM system MARC/MENTAT in order to calculate the distortion of components. The appropriate interfaces and transformation algorithms are developed for this purpose.

The procedure has the following advantages compared with the procedures implemented hitherto:

- The temperature distribution in the component is determined by specifying spatial heat sources (equivalent heat sources) and not specified by boundary conditions.
- As a result, it is possible to determine the temperature distribution, caused by the spatially distributed heat sources, and thus take the energy distribution due to weld pool motion into account in the thermo-mechanical simulation.
- In addition, this means the heat input and temperature distribution of previous weld tracks can also be taken into account.

In the first step of component modeling, highly simplifying assumptions are made (straight, flush seam, and use of a single heat source). Calculation is performed with the previously calculated temperature distribution from DC-LASIM. The deviation between the results of simulation and the welding experiment is approx. 15%. The reasons for this are the material properties as a function of temperature, spatial, and temporal resolution of the moved, discrete heat source; the geometrically idealized rigid clamping, and the assumptions and approximations made in DC-LASIM (Fig. 7.69).

Technical advancements in computer technology throughout the project permitted a reduction in computation time by a factor of 10. Consequently, it is now possible to display a more realistic simulation model and thus optimize the welding process.

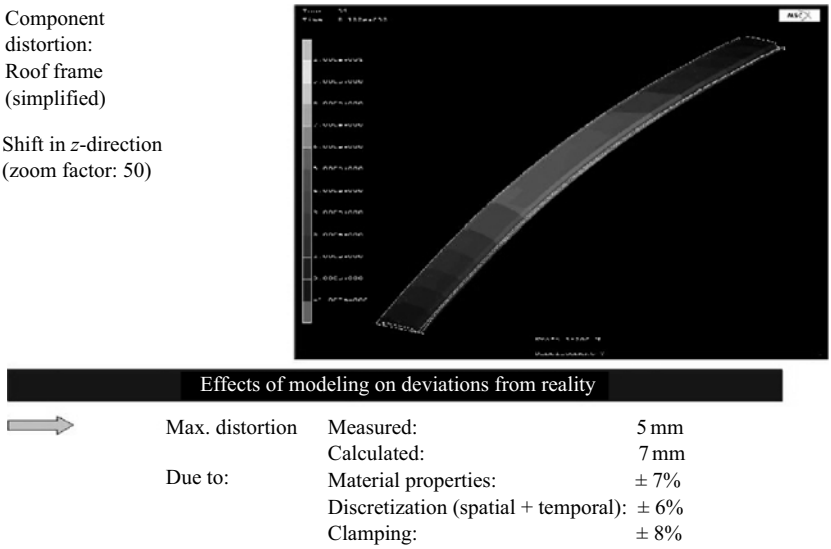

FIGURE 7.69. Simulation results – Output: distortion

7.1.3. Brazing

T. Hiermer, M. Hölscher

7.1.3.1. Process Principles and Equipment

Laser Brazing Process

Brazing is a thermal procedure for joining two metal sheets by using a plumb. For brazing the work temperature is more than 450°C, in contrast to soldering. The melting temperature of the plumb is less than the melting temperature of the sheet material. The sheets can only be joined if the liquid plumb is able to wet the surface of the metal parts. The wettability is characterized by the wetting angle α and can be classified as shown in Fig. 7.70.

Using the laser for brazing has one special benefit: No flux is necessary. The laser beam simultaneously activates the surface and melts the plumb.

Figure 7.71 shows a schematic of the laser brazing process on a hem flange. $CuSi_3$, an often-used brazing filler, has a solidus temperature of 910°C and a liquidus temperature of 1025°C. By adapted defocusing (see Fig. 7.71) and selection of an appropriate beam power and feed rate, the brazing filler is melted ($T > 1025$°C) and the base material remains below its melting point. Even a zinc coating (melting point 420°C, vaporization point 906°C) remains almost completely intact right next to the seam.

Zinc is 100% soluble in copper-based brazing filler ($CuSi_3$), meaning that melted zinc is not a problem. If, however, small pieces of zinc coating should come loose and be carried to the center of the seam by the motion of the brazing pool

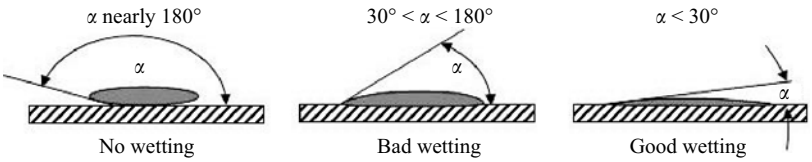

FIGURE 7.70. Wetting angle for no ($\alpha = 180°$), bad or good wetting ($\alpha < 30°$)

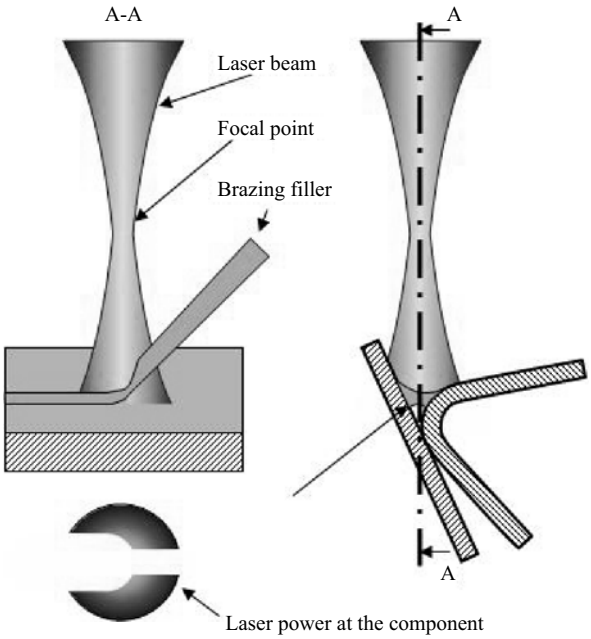

FIGURE 7.71. Principle of laser brazing

($T > 1025°C$), the result is spontaneous vaporization of the zinc particles. This can cause small pores on the surface or slightly below the surface of the brazed seam and therefore has to be avoided.

A characteristic feature of the laser brazing process on a hem flange is formation of a bridge (Fig. 7.71). Due to the short interaction time between the laser beam and the component, the component reaches the wetting temperature ($T_W \approx 1000°C$) only where the laser beam actually strikes it. Because of the occlusion of the laser by the filler material (Fig. 7.71), the sheet material below the center of the seam is not reaching the wetting temperature all the way to the contact point of the components. This results in the characteristic bridge formation. If the distance to be bridged is larger than the width of molten filler volume which can be carried by the surface tension of the brazing filler (see Fig. 7.73) defects in the brazed seam will result.

In order to obtain optimal brazing results, the relationship between melting of the filler and heating of the component to wetting temperature must be adjusted. This can be done by means of the parameters laser power, laser spot diameter on the component and processing speed.

Influence of the Component Radius

Figure 7.72 shows the influence of an increasing component radius. It can clearly be seen that as the radius increases, the incidence angle of the laser beam on the radius surface becomes steeper, resulting in lower laser intensity. This causes a significantly lower surface temperature on this component. If the wetting temperature of the brazing filler is not maintained, defects or insufficient seam bonding will result.

Influence of a Joint Gap

A joint gap increases the distance to be bridged between the two parts being joined (Fig. 7.73). If the distance is too large, the surface tension of the brazing filler can no longer support the filler volume to complete the bridge. This causes defects

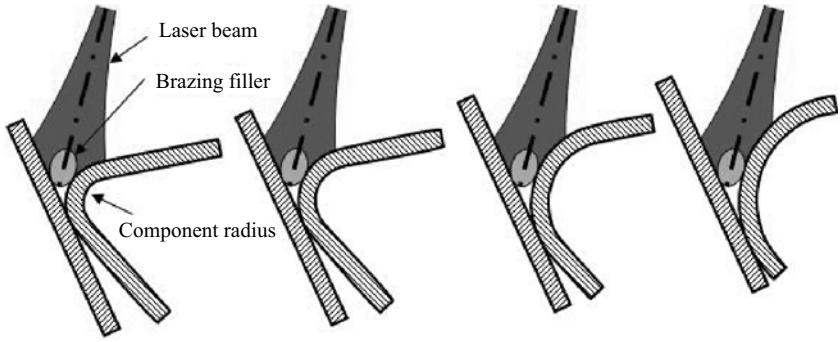

Figure 7.72. Influence of the component radius

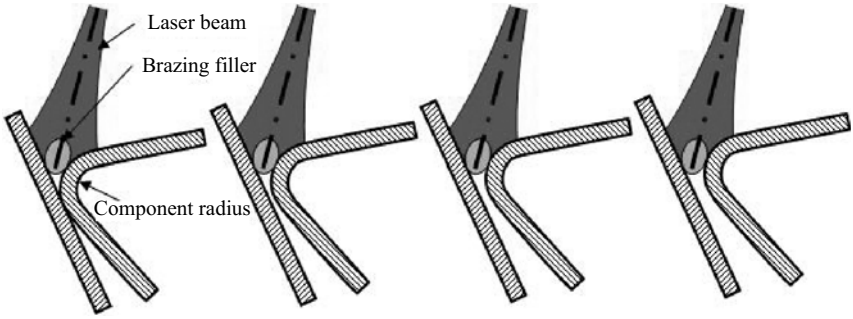

Figure 7.73. Influence of a gap

in the brazed seam. Moreover, the brazed seam sinks deeper into the component radius. The wider gap is also associated with an increase in the incidence angle of the laser beam (see also Influence of the Component Radius) and transmission losses through the open gap, as a result of which the surface temperature of the component radius is decreased. Again, if the surface temperature drops below the wetting temperature, bonding defects will occur in the brazed seam.

Influence of the Laser-Beam Angle

The inclination angle of the processing optics determines the size of the incidence angle of the laser beam on the component (Fig. 7.74) and by that the symmetry of illumination of the joint area. Ideally, the laser axis will coincide with the symmetry axis of the joint. Otherwise the heat input will be different on the joint partners. This results in differences in the seam bond.

Equipment

For brazing, typically lasers with a beam power in the range of 3 kW are used. In automotive applications the diode lasers are mounted on six-axis robots to allow for three-dimensional processing of component assemblies. The brazing head is equipped with a wire feeder to provide the filler metal and with an inert gas nozzle to protect the seam from oxidation.

The sheets to be joined are placed into rigid clamping fixtures. Constant seam geometry is guaranteed by the adjustment at stops. Chuck jaws actuated by pneumatics press the workpieces together, to ensure a symmetrical pressing over the complete seam length. Before putting the sheet metals into the clamping device they have to be released from dirt or oils to provide a clean technical zero-gap and a homogeneous surface.

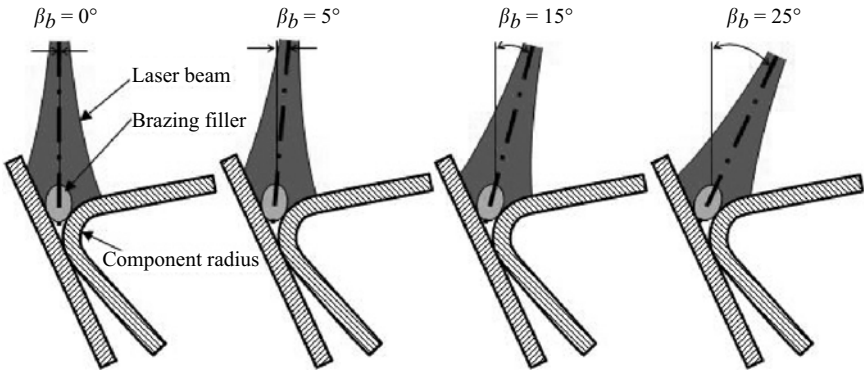

FIGURE 7.74. Influence of the laser beam angle

7.1.3.2. Parameter Dependencies and Process Investigations

Material of Sheet Metals and Brazing Alloys

For the execution of test series DC04 steel with different surface conditions – uncoated as well as coated with electrolytic galvanization (75 g/m^2) and first-generation organic coating – Bonazinc® 3000 was used. For the characterization of materials and coatings, see Table 7.2. The sheet thickness is 0.8 mm.

All coated sheet metals were coated only on one side. The coating was in both cases on the top. Two different brazing alloys were tested (Table 7.3).

The highest possible power of the diode laser was 3.0 kW at the workpiece and this was actually used for all brazing tests. The selected joint configuration was the fillet weld at an overlapping joint, which is used frequently in car-body construction. The joining partners were clamped with technical zero-gap.

Different combinations of process velocity and wire feed rate were tested according to the Table 7.4. The best brazing results are achieved with equal wire feed rate and brazing velocity. This is ensuring a very stable brazing process with minimum flow dynamics in the braze pool. Excellent joint properties could be achieved with velocities of 2.0 and 2.5 m/min.

Metallographic Investigations

The metallographic investigations evaluate the seam cross-section geometry, the occurrence of melting of the sheets, the wetting properties of the sheets, and the connection length at the lower sheet. An example is shown in Fig. 7.75.

Exemplary results for brazing of different sheet-filler combinations are shown in Fig. 7.76 for $CuSi_3$ and CuAl5Ni2. The surface of the brazing seam for the different

Table 7.2. Characterization of sheet metal coatings

Type of coating	Material	Zn (μm)	Pretreatment	Organ.coating (μm)
Without coating	Dc04-a	-	Without	-
Galvanized	Dc04+ze-a	10.0	Without	-
Bonazinc 3000	Dc04+oc-a	5.0	Without	2.5–4.5

Table 7.3. Materials, brazing alloy, and coatings

Material combinations			
		Brazing alloy	
Sheet material	Coating	$CuSi_3$	$CuAl_5Ni_2$
Dc04-a	Without coating	X	X
Dc04-a	Galvanized	X	X
Dc04-a	Bonazinc®	X	X

Table 7.4. Combination of brazing velocity and wire feed rate

Test matrix brazing velocity and wire feed rate				
	Wire feed rate v_d			
Brazing velocity v	1.5 m/min	2.0 m/min	2.5 m/min	3.0 m/min
1.5 m/min	X	X		
2.0 m/min	X	X	X	
2.5 m/min		X	X	X
3.0 m/min			X	X

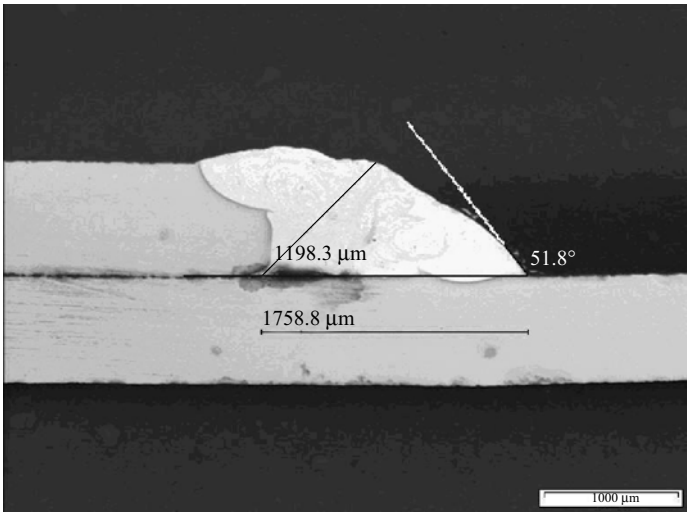

Figure 7.75. Example of a cross section (uncoated material with CuAl5Ni2 brazing alloy)

coatings and brazing alloys (left side) and the corresponding cross sections (right side) are shown.

7.1.3.3. Application Results

Based on parameter studies, the feasibility of brazing with a diode laser was demonstrated on a real automotive component: Front roof frames of the Mercedes Benz E-Class were brazed. The component and its location in the construction of the vehicle are represented in Fig. 7.77.

The brazing system setup including robot, diode laser, inert gas nozzle, and wire feeder, is shown in Fig. 7.78.

The seam is designed as fillet weld at the overlapping joint. Figure 7.79 shows a cross section of the brazed seam as well as the seam surface. During brazing with a copper based alloy and a laser power of 3 kW a velocity of 2 m/min is

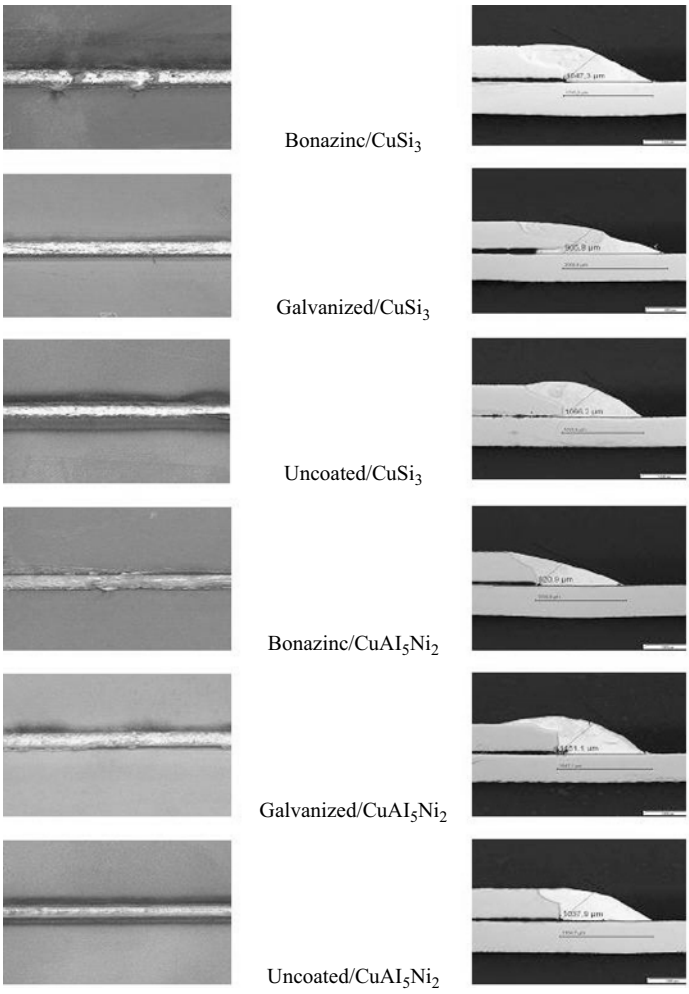

Figure 7.76. Brazing of different materials with two different brazing fillers: surfaces and cross sections

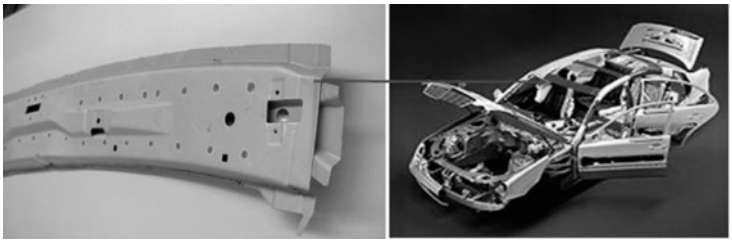

Figure 7.77. Roof header and body in white with roof header

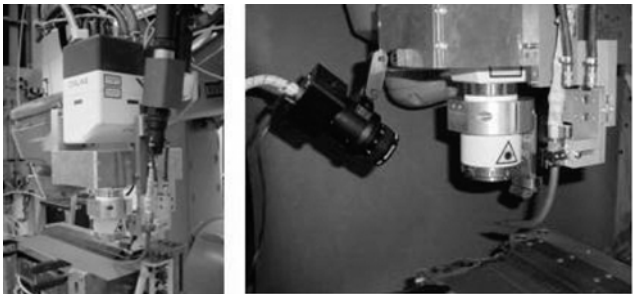

FIGURE 7.78. Experimental setup for laser brazing with diode laser

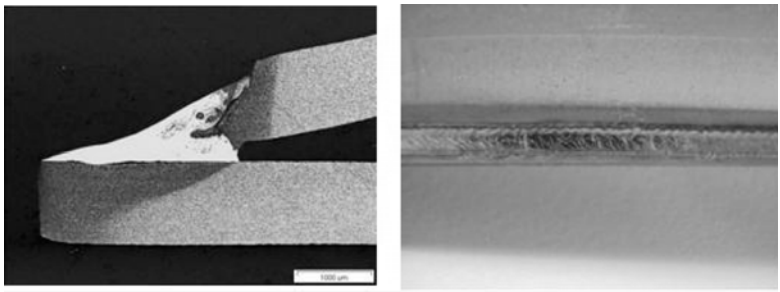

FIGURE 7.79. Results for brazing of roof header – cross section and top view

reached. The brazing with diode lasers profits from continuous, very regular seams with excellent sealing capability and corrosion resistance. The seams allow for component assemblies with high strength and rigidity.

7.1.4. Soldering

L. Bosse, F. Lupp

7.1.4.1. Process Principles and Equipment

Today laser beam soldering is a nonstandard manufacturing process for electronic packaging and interconnection technology in comparison to established mass production technologies such as condensation or wave soldering. However, due to the actual trend toward complex and cost-intensive products, laser beam soldering gains more and more attention for certain applications in this field. Due to the localized, non-contact, and controlled heat input, laser beam soldering is a well-suited technology for joining of fine-pitch as well as heat and electrostatic-sensitive components [7.9].

Since 1974, CO_2 and solid-state lasers (Nd:YAG) have been successfully applied in industrial production in the field of soft soldering or brazing [7.10]. Recently, the development of high-power diode lasers (HPDL) offered a new type of laser beam

source with the chance to reduce or eliminate disadvantages of the other mainstream laser sources. In comparison to CO_2- or Nd:YAG-laser sources, HPDL feature a higher electrical efficiency and a higher absorption (metal parts). Due to their compact size, diode lasers are well suited to be integrated into production cells or to be mounted on a multi-axes motion-system. Both the excellent optical and electrical characteristics and the combination of easy handling and maintenance-free operation at long lifetimes make diode lasers perfectly qualified for economical use in the field of mounting and assembly [7.11].

Temperature Control of the Soldering Process

The temperature, which can be easily detected with a pyrometer, is the most reliable process parameter for controlling the soldering process. By using a laser beam combined with a pyrometer and applying a working and measuring spot geometry adjusted to the interaction zone between beam and material, the optimum system approach for controlling the soldering process is achieved. The temperature distribution can be detected and temporally resolved, which gives information about the local heat input. Thus it can be used for on-line, closed-loop, laser power control of a soldering process. In [7.12–7.17] different applications of Nd:YAG and diodelasers combined with fast pyrometers for laser soldering are described for niche applications. The authors describe soldering with higher-melting lead-free solders, applications in environments at elevated temperatures, soldering on low-temperature substrates, or in the vicinity of temperature-sensitive parts. For control purposes, the temperature is acquired with fast pyrometers (response time $\leq$1 ms) in a defined position relative to the laser beam. During closed-loop process control, the control signal (temperature) is compared with upper and lower boundaries of reference signals. In some cases it is possible to predict the course of the soldering process and failures due to the characteristic of the temperature signal or the laser power, respectively.

Temperature measurement during soldering with a line-shaped laser beam is more difficult. In the following section, different methods, as shown in Table 7.5, will be discussed. In [7.18] temperature-controlled laser beam soldering is described. For joining QFPs and ICs the temperature is detected just at one leg as representative for the total row of legs (Fig. 7.80). It is assumed that this will be tolerable for a laser beam intensity distribution optimized to the part. However, it is obvious that failures like imperfect contacts or overheating will not be observed at other legs.

With a line-shaped measurement area of the pyrometer comparable to the line-shaped laser beam, different legs of a part can be detected at the same time during soldering (Fig. 7.81). It has been found that, on one hand, the signal-to-noise ratio is in the range of 30% even for an error-free soldering process. On the other hand, the difference of the signals for a good and a failed soldering process is sometimes just in the range of 10%. With increasing length of the measuring line, this problem, mainly arising from the lack of spatial resolution and the mixing of the signals of the different soldering spots, is even more critical. With this method, failures cannot be detected distinctly.

Table 7.5. Comparison of different temperature measurement methods for soldering with line-shaped laser beam

Temperature detection with –	Advantages	Disadvantages
Pyrometer measuring point: spot	Simple signal with standard pyrometer	Detection spot-wise, evaluation limited to measuring spot
Pyrometer measuring point: line	The complete soldering line is detected	Local failures with low signal cannot be discovered because there is no spatial resolution within the line
Pyrometer measuring point: scanner	Detection of all significant points of soldering line	Limited time resolution
IR-camera and image processing	Detection of complete temperature profile and in some cases of complete part	Costly and expensive, image processing limits time resolution

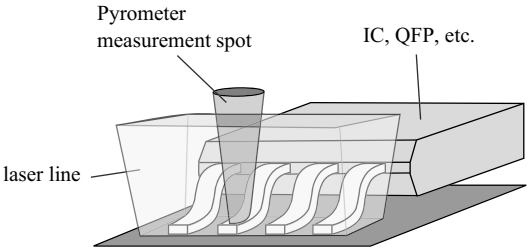

Figure 7.80. Line shaped laser beam combined with standard pyrometer and measurement spot

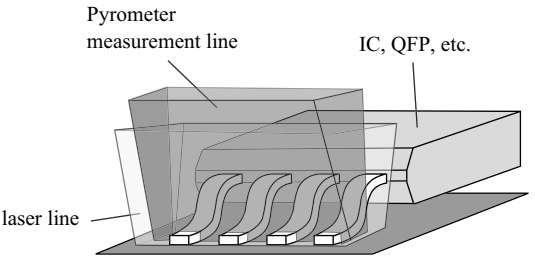

Figure 7.81. Line-shaped laser beam combined with pyrometer measurement line

The combination of scanner and pyrometer enables us to read the signal at all relevant positions in the laser soldering line (Fig. 7.82). The time resolution of the measurement is limited by the dynamic properties of the pyrometers. According to a rough estimation based on the dynamic behavior of a pyrometer the temperature

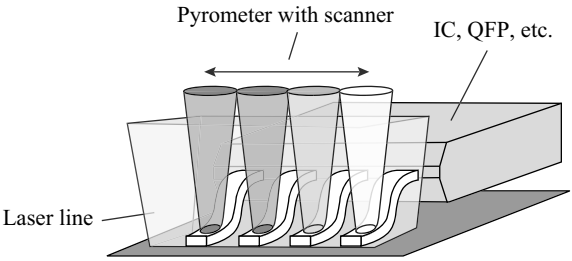

FIGURE 7.82. Line-shaped laser beam combined with pyrometer and scanner

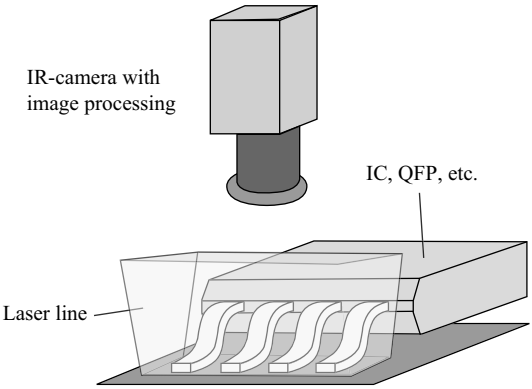

FIGURE 7.83. Line-shaped laser beam combined with IR-camera and image-processing system

at about 30 legs of an IC can be measured during the soldering process. With reduced pitch this number will decrease because of the changed dynamics of the scanner as it starts and stops. The result is that this method is appropriate only for a small or medium number of legs at an IC or QFP.

Applying an IR-camera (Fig. 7.83) combined with image processing is the most costly and extensive solution. For a soldering time of 3 s and a required resolution of $\pm 5\%$, the required dynamic of the image processing results in 25 ms. This means an image frequency of about 40 Hz. Current image-processing systems feature up to 120 Hz for a reduced number of pixels via a two-dimensional array or up to 128 Hz for cameras with a single row of pixels. For low-melting lead-free PbSn solders the standard temperature measurement intervals from $-20°C$ to $300°C$ with a resolution of 0.09 K are sufficient. Beside the fast detection of the leg temperature during the soldering process this system offers the opportunity to monitor the part temperature for overheating during soldering. In addition integrated position control is possible.

Components of a Laser Soldering System

The major components of a typical laser soldering system are a fiber-coupled, continuous-wave (cw) diode laser system and a processing head with an integrated pyrometric and power sensor (Fig. 7.84). The diode laser system used, e.g., for the automotive microelectronic application described in section 7.1.4.3 has a maximum optical output power of 500 W, which can be modulated by controlling the pump current. The diode laser radiation emitted from the optical fiber is collimated by a lens (lens 1) and reflected by a deflecting mirror (mirror 1). A part of the laser radiation is transmitted by the deflecting mirror (mirror 1) and collected by a power detector integrated for online monitoring. The power detection is done by a silicon photodiode electronically intensified by a trans-impedance amplifier circuit. The collimated laser beam passes through a galvanometer scanner and is focused by an *f*-Theta lens on the lead/solder pad area to generate the joint. The circular focus geometry of the laser beam is aligned to the center of the semicircle at the end of the terminal lead (Fig. 7.85). The working distance between the optics and the laser beam interaction area is about 80 mm. Using an image projection ratio of 1:2, the minimum focal diameter is 1.2 mm, which is the double the fiber core diameter of 0.6 mm.

7.1.4.2. Parameter Dependencies and Process Investigations

The laser soldering procedure is characterized by a typical temporal course of the process temperature, which can be reproducibly observed in the recorded pyrometric signal. The example below represents the soldering process of an automotive microelectronic device described in more detail in the next section.

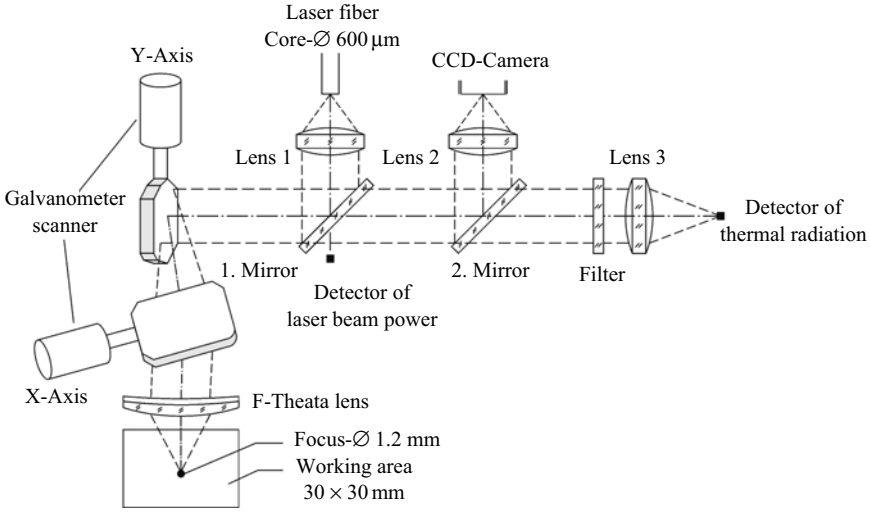

FIGURE 7.84. Structure of the processing head

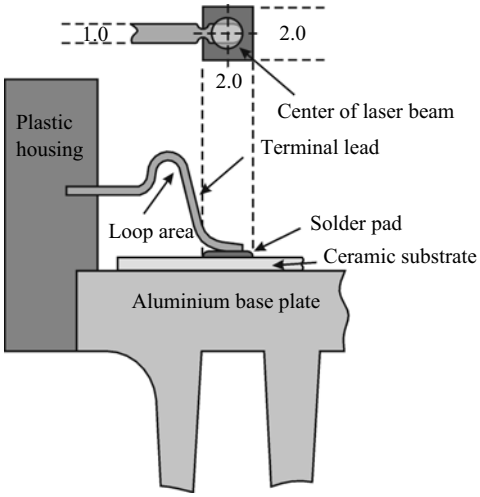

FIGURE 7.85. Solder joint configuration (dimensions in mm)

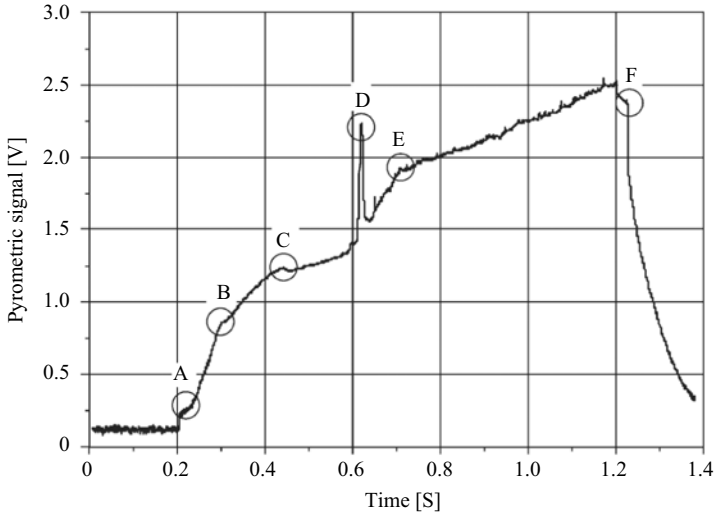

FIGURE 7.86. Pyrometric signal detected during soldering; irradiation time: 1,000 ms

In the temperature profile presented in Fig. 7.86, the laser is switched on at time $t = 0.2$ s. At point [A] the reduction of the ascending slope indicates the beginning activation of the applied adipic acid. The second changing in the pyrometric signal at point [B] is related to the onset of localized melting of the solder pad and out-gassing of volatile components. Due to the continued energy input by the laser beam the terminal lead reaches the wetting temperature (point [C]). At the beginning of the next phase there is a sudden improvement in heat dissipation

due to the wetting of the terminal lead, which often results in a short temperature decrease after point [C]. At point [D] a gas bubble consisting of volatile components emerges out of the molten solder. The variation of the signal curve following point [E] is induced by self-optimizing the surface tension and by superheating of the molten solder pool. After the laser beam is switched off at $t = 1.2$ s, very high cooling rates are observed. This high rate is caused by the optimized heat transfer into the aluminum base plate. At point [F] the solder solidifies. The change of the descending slope in the signal curve at the crystallization point [F] is known from the thermal analysis of solidification reactions in literature [7.19, 7.20].

7.1.4.3. Application Results

In the following section, two different soldering applications are discussed. The first soldering task emphasizes the optical and thermal advantages of laser-based assembly processes, and the second one demonstrates the process advantages of laser beam soldering by means of an automotive device.

Mounting and Assembly of Electronic Devices

In general flip-chips are joined either by soldering or by gluing, depending on the metallurgy of the bumps. Remeltable bumps composed of a PbSn-alloy or copper bumps with a PbSn-layer are soldered. Non-remeltable bumps made of a Ni-Au-alloy or copper bumps with a Ni-Au-layer are glued. Adapting the temperature compatibility of chip and substrate (e.g., Si-chip and printed circuit board FR4) most of the ICs and SMDs can be assembled in a mixed configuration and soldered in a reflow process. For solders with peak temperatures above 230°C ICs will be soldered in a separate process and SMDs have to be joined in a subsequent soldering process [7.21, 7.22].

Especially for complex and expensive multi-chip packages or high-density interconnect circuit boards (HDI)0 the unsoldering of defective single chips is recommended in case of a failure of a single chip on a completed circuit board. Therefore special underfillers have been developed which allow unsoldering with hot gas (1 min, 210–220°C). A disadvantage is poor temperature control and the thermal load of surrounding parts. One option is unsoldering with the laser beam, because of its precise power control and locally limited heat input [7.23].

Basically there are two concepts for transmissive soldering with the laser (Fig. 7.87): soldering with the laser beam by transmitting through the chip directly to the metal layers of the chip-circuits, or transmitting the laser beam through the printed circuit board to the chip or joints, respectively. The transmissive soldering through the circuit board is limited to the application of flexprints. The Kapton-foil as base material is transparent for wavelengths above 1,000 nm. Other circuit boards, especially multi-layer circuit boards, are not suited. For transmissive soldering uncoated Si-chips are required. Silicon as base material of integrated circuits or flip chips shows the characteristic to be transparent for wavelengths above 1,100 nm. This can be used for soldering flip-chip BGAs (ball grid arrays) with minimal thermal load, e.g., applying a laser with a wavelength of 1,300 nm.

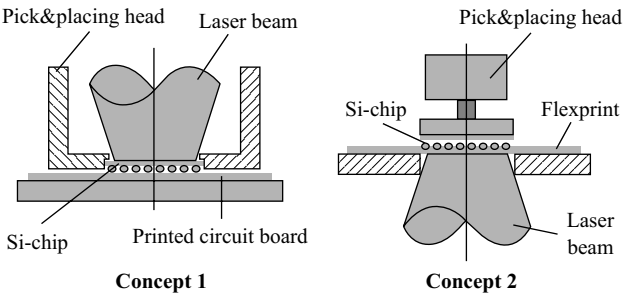

FIGURE 7.87. Concepts for laser soldering of flip-chips BGAs

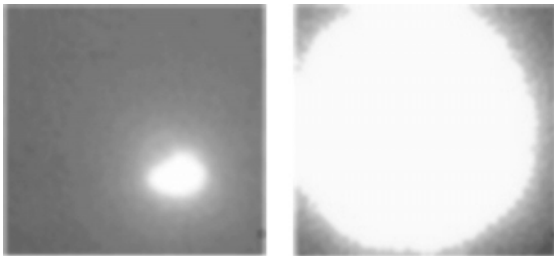

FIGURE 7.88. Temperature distribution in silicon chip (chip area = displayed area) after 5 ms pulse duration for 1,064 nm (left) and 1,300 nm (right) (IR-camera with image-processing system)

Therefore the laser beam is transmitting through the silicon and heating directly the metal layers of the IC circuits in order to deliver the heat to the bumps or joints, respectively.

For a standard laser wavelength of 1,064 nm, the laser beam will be absorbed on the surface of a silicon chip. Because of the lower thermal conductivity of silicon, the heat transfer to the bumps or the joints, respectively, is poor (Fig. 7.88, left). Applying a wavelength of 1,300 nm, the heat transfer is very fast because the laser beam transmits through the silicon body down to the metallic layers of the chip circuit. This results in an extensive and fast heating of the bumps because of the higher thermal conductivity and the low heat capacity of the metal layers (Fig. 7.88, right). Therefore the thermal load for 1,300 nm is smaller than for 1,064 nm and a lower laser energy has to be applied for melting the bumps.

Using a laser with a wavelength of 1,300 nm, there is no overheating of the metal layers and no modification of the doping profiles of the chips found during the soldering process (Fig. 7.89). For soldering flip-chip BGAs with an adapted beam diameter, 1 to 2 s of soldering time are required with 12 W laser power.

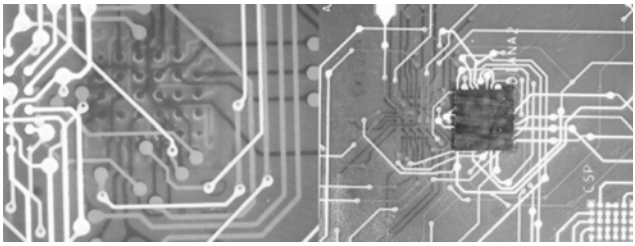

FIGURE 7.89. Soldered flip-chip: View on flexprint and BGA of chip below (left), view on uncoated front side of chip (right)

Electronic Modules for Automotive Devices

Electronic modules for the automotive environment are subject to very special requirements in terms of performance, functionality, and miniaturization, on the one hand, and reliability and durability on the other. The area under the hood, especially, calls for solutions with high-end properties in consideration of thermal conditions. As a consequence, the demands on the material choice, the packaging, and the interconnection technology are very sophisticated.

Thick-film or hybrid circuits have a high level of integration and an excellent performance profile in harsh environments [7.24]. This special kind of circuit consists of screen-printed layers of conductive, dielectric, or resistive materials on alumina (Al_2O_3) or less frequently on beryllia (BeO) substrate. These layers are applied in form of an ink or paste, are subsequently dried, and sintered at high temperatures, where they form a strong bond with the substrate. Thus a double-sided substrate with multi-layer and integrated resistors is obtained to which housed components can be soldered and naked dice can be bonded. For conductor tracks gold, silver, silver-palladium, and silver-platinum pastes are used, depending on the interconnection technology and resistance. The thicknesses of conductive layers are in the region of 10 μm for a fired track.

The interconnection from the substrate to the next package level, which is usually a plastic housing, is achieved by either a thick wire or ribbon bonding or soldered leads. Up to now the established types of soldering technologies are micro flame soldering and reflow soldering. The former allows the leads to be integrated into the housing but is a sequential process [7.25]. The latter is a parallel process, but the leads cannot be part of the housing. Since high temperature solder is used for automotive applications with maximum ambient temperature of 140°C, the plastic typically will not withstand the required reflow temperatures [7.24].

The specimen used in this example is an automotive microelectronic module (alternator regulator realized in thick-film technology) with solder pads printed on an alumina substrate. The housing has seven terminal leads to be soldered to the substrate. The dimensions and the compositions of the terminal lead and the solder pad are shown in Fig. 7.90 and Table 7.6. The entire alumina substrate is glued by a heat-conducting adhesive to an aluminum base plate.

Figure 7.90. Automotive microelectronic module in a plastic housing

Table 7.6. Specimen Data

Part name	Thick film alternator regulator
Materials	
Terminal lead	SAE CA 260 brass, 1/2 hard, nominal composition is 70% Cu–30% Zn, 1.0 mm wide × 0.3 mm thick, tin-plated. The end is semicircular in shape with a 0.5-mm radius
Solder pad	Sn10Pb88Ag2, 2.0 mm × 2.0 mm × 0.2 mm thick, melting point: 268°C (solidus)/290°C (liquidus)
Alumina substrate	94% nominal Al_2O_3, 0.5 mm thick
Aluminum base plate	Aa 3003-h14
Plastic housing	Polybutylene terephthalate with 30% glass fiber (PBT-gf30)

Table 7.7. Process conditions

Beam spot diameter	1.2 mm@$1/e^2$ (focal position)
Basic Conditions	No extra preheating No shielding gas against oxidation
Flux	Adipic acid (1.5%)
Terminal lead/solder pad contact	0.75-mm vertical deflection of the lead (corresponding contacting force ranged from approximately 50 to 150 g, depending on the length of terminal lead)

The terminal leads are formed and prepared for soldering by precise bending and tin-plating, as shown in Fig. 7.85. The terminal leads are positioned applying a low pressure on the corresponding solder pads. A small amount of flux (low concentrated adipic acid) is applied to the lead/solder pads before soldering. In contrast to the state-of-the-art micro-flame soldering process and the quoted laser beam soldering process of hybrid circuits no extra preheating of the specimen is necessary [7.25, 7.26]. Important process conditions are summarized in Table 7.7. The laser soldering system used is described in section 7.1.4.1.

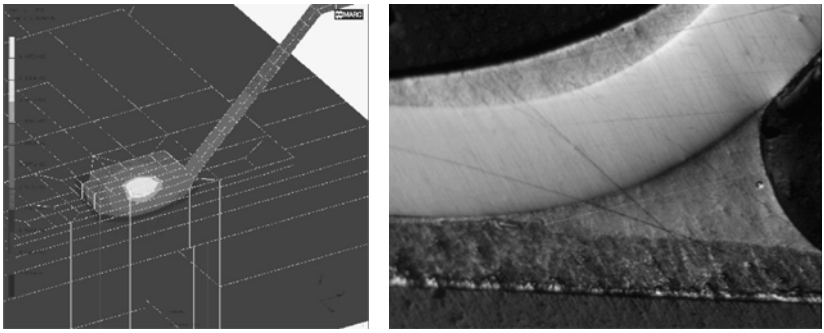

FIGURE 7.91. Left: Snapshot of the thermal behavior of an irradiated contact (computed). Right: Cross-sectional view of a soldered joint; optical power: 80 W, irradiation time: 1,000 ms.

The thermal behavior of the specimens is significant for the laser beam soldering process. Due to the harsh environments under the hood, the materials and the geometry are adapted and optimized. On one hand, the thermal characteristics of the specimens guarantee field-tested functionality, and on the other hand, they determine the conditions of the soldering process.

In order to get an idea of the thermal behavior during the soldering process, the temperature distribution caused by laser irradiation is simulated (commercial software[1]). Using the specified data as input for the simulation, a snapshot of thermal behavior of an irradiated contact is computed (Fig. 7.91, left-hand side). The right-hand side of Fig. 7.91 shows a cross-sectional view of a laser-beam-soldered joint.

Besides the substrate, the results of the simulation imply that the terminal leads consisting of 0.3-mm-thick tin-plated copper behave like heat sinks. Even though a temperature of slightly more than 600°C was applied, the solder pad on the ceramic substrate exceeds the melting point of the solder alloy only in a very localized area (Fig. 7.91, left-hand side). Due to this special fusibility of the solder pad, quantitatively determined by the selected process parameters and the given system properties, it is a very complex procedure to generate an adequate solder joint. The maximum duration of the irradiation is predetermined by the work cycle of the production line, whereas the lower limit of laser beam power is given by the needs of melting an adequate area of the solder depot. The upper limitation of the supplied power is exceeded if signs of overheating or cracks in the ceramic substrate occur. According to these demands a suitable process window has been found in context of a parameter study.

---

[1] Marc Mentat MSC Software Corporation
Marc Nonlinear Finite Element Solver with Parallel Processing
Mentat Graphical User Interface to the Marc Nonlinear Finite Element Solver

Apart from the interconnection requirements, a high production rate has to be ensured for the laser beam soldering process to remain attractive for mass production. For this reason, the total process period, especially the irradiation time, has to be as short as possible. But to achieve an adquate solder joint with reduced irradiation time, the laser power has to be increased. To avoid the hazard of superheating, the laser power has to be limited and controlled. Therefore, the thermal radiation from the interaction zone was detected and analyzed in more detail (see section 7.1.4.2).

In order to quantify the achieved quality of the solder joints, simple tensile/shear tests are accomplished. In Fig. 7.92 the arrangement for the tensile/shear tests (left) and exemplarily a force/elongation diagram of a laser-soldered specimen (right-hand side) is represented. A defined traction is applied by a curved wire. Furthermore, the failure points are indicated. The breaking strain is exceeded either at the terminal lead, at the area of reduced diameter, or within the reflowed solder pad. Since the strains cannot clearly be dedicated to be tensile or shearing stresses, the measured data are only meaningful in direct comparison. Therefore the obtained results are to be understood only as necessary and not as sufficient evaluation criteria.

Table 7.8 summarizes the obtained results of maximum tensile shear stress (R_m) related to specific terminal leads. The table represents in detail the average values (X_m), the standard deviation (S), and the coefficient of variance (ν). Due to the fact that the given reference values are usually reached or even exceeded with at least one process parameter set, the potential of laser beam soldering can be shown.

The presented results show that laser beam soldering is an attractive alternative in comparison to conventional soldering technologies for the presented kind of challenging soldering tasks. Apart from the well-known advantages of laser beam soldering, i.e., controlled and localized heat input as well as reduced thermal and

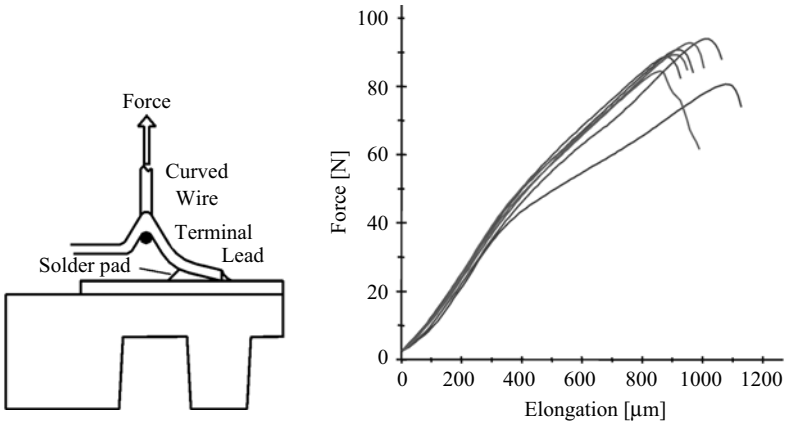

Figure 7.92. Left: Arrangement for the tensile/shear tests in principle. Right: Example of a force/elongation diagram of a laser beam soldered specimen; irradiation time: 300 ms

TABLE 7.8. Average value of maximum tensile shear stress (R_m) of micro-flame or laser-beam-soldered specimen*

R_m[N]	Micro flame soldered specimen (references)	Laser-beam-soldered specimen*			
		Irradiation time 1000 ms manual fluxing	Irradiation time 400 ms manual fluxing	Irradiation time 300 ms manual fluxing	Irradiation time 300..1000 ms automatic fluxing
Terminal 1					
X_m	87.5(6)	88.7(8)	78.5(8)	84.4(8)	88.1(6)
S	5.1	3.6	7.9	8.3	4.0
v	5.9	4.1	10.0	9.8	4.5
Terminal 2					
X_m	87.4(6)	84.0(8)	78.4(8)	81.8(8)	86.8(6)
S	1.8	4.9	6.1	8.9	3.4
v	2.0	5.8	7.8	10.9	3.9
Terminal 3					
X_m	85.5(6)	77.2(8)	76.8(8)	80.4(8)	85.0(6)
S	3.6	10.0	7.7	9.1	4.6
v	4.3	12.9	10.1	11.4	5.4
Terminal 4					
X_m	81.9(5)	79.1(8)	81.6(8)	80.5(8)	79.2(6)
S	3.7	1.35	0.7	1.8	2.6
v	4.5	1.71	0.9	2.2	3.3
Terminal 5					
X_m	91.2(6)	89.3(8)	88.3(8)	84.7(8)	92.8(6)
S	1.7	4.8	7.7	6.8	0.8
v	1.8	5.4	8.7	8.1	0.9
Terminal 6					
X_m	92.4(5)	93.5(8)	93.3(7)	93.3(7)	91.8(2)
S	1.4	1.4	1.1	0.9	0.1
v	1.5	1.5	1.1	1.0	0.1
Terminal 7					
X_m	79.5(5)	89.0(8)	93.9(8)	92.4(8)	80.0(6)
S	1.7	4.4	1.1	1.4	4.1
v	2.1	4.9	1.1	1.5	5.1

*$X_m =$ average value of R_m; $S =$ standard deviation, $v =$ variance. The number in parentheses refers to the considered terminals; the remaining ones are used for metallographic assessment.

mechanical stress, the achieved data and results prove quantitatively the potential of this technology.

7.1.5. Laser Beam Welding of Thermoplastics

B. Friedrich, F. Lupp, U. A. Russek

7.1.5.1. Process Principles and Equipment

Basics of Laser Beam Welding of Thermoplastics

Laser beam technologies incorporate innovative solutions to overcome limitations of conventional joining technologies. Laser beam welding of thermoplastics offers several technical advantages. The joining energy is fed contactless into the joining area, avoiding mechanical stress and thermal load to the joining partners. The

energy is supplied spatially (seam width on the order of 100 μm) and temporally (interaction time on the order of milliseconds) very well defined. Different process strategies lead to flexibility, product-adapted irradiation, short process times, and high-quality weld seams as well as to high integration abilities and automation potentials. During the joining process, no vibration, no thermal stress, and no particle release takes place. Therefore, destruction of mechanically and electronically highly sensitive components, such as microelectronics, is avoided. The workplace pollution is negligible compared to other joining technologies, such as gluing (fume) or ultrasonic welding (noise, pieces of fluff). Not only can microcomponents be welded in a reproducible way but also macro-components, while hermetic sealing along with a good optical appearance are obtained.

Laser beam welding of thermoplastics as an alternative and innovative joining technology was considered in the early years of laser technology. However, conventional polymer welding technologies solved the joining challenges of those days and cost considerations prevented the breakthrough of laser beam welding [7.27–7. 30].

Today, several joining demands cannot be met by conventional technologies, but only with laser radiation. Additionally, availability, efficiency, and affordability of laser beam systems improved significantly. Therefore, laser welding of thermoplastics has experienced an increasing industrial interest and acceptance.

Laser beam welding of thermoplastics may be examined from different points of view:

- joint geometry: butt joint or overlap joint.
- nature of irradiation: contour, quasi-simultaneous, simultaneous and mask welding.
- applied laser source: high-power diode laser, CO_2 laser, Nd:YAG laser, holmium-YAG laser.
- joining partner stability: form stable or flexible (like thin layers applied in packaging industries and life science).
- size of the joining partners: micro- or macro-parts.
- dimensions of the weld seam: micro- (seam width <200 μm) or macro-welding.
- type of thermoplastic joining partners combination. We may distinguish between welding similar (such as PA / PA, PC / PC, PP / PP) or dissimilar thermoplastics (such as ABS / PC, ABS / PMMA). In the following only welding of similar thermoplastics is considered.

Generally, all thermoplastics are laser weldable, if the optical, thermal, and geometrical properties are suited to the process demands. Therefore, amorphous, partially crystalline, glass-fiber-reinforced thermoplastics are weldable. Color substances and additives may be able to arrange product-specific aspects and process technical requirements.

Laser beam welding of thermoplastics uses the transformation of electromagnetic energy (laser radiation) into heat energy to plastify (melt) the thermoplastic joining partners spatially and temporally defined within the joining area. There are in principle two different joint geometries to distinguish: overlap joint

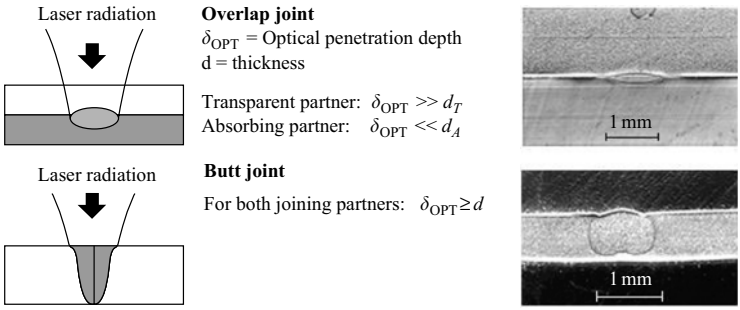

FIGURE 7.93. Differences of the two joint geometries (overlap and butt joint) concerning joining partner position, optical penetration depth δ_{OPT} (sketch, left) as well as optical appearance of the weld seam (depicted by means of microtome cuts, right)

and butt joint (Fig. 7.93), but the overlap joint has prevailed against butt joint geometry.

By applying overlap welding, two joining partners with different optical properties for the laser wavelength used are joined, as depicted in Fig. 7.93. The first irradiated – the (laser) transparent – joining partner, has to have the following optical properties: low degree of reflection, absorption, and scattering centers and as a result high degree of transmission. Thus, the laser beam is guided to the second – the (laser) absorbing – joining partner with minimal energy loss and scattering influence. The absorbing joining partner has to show a low degree of reflection and transmission and as a result high degree of absorption. Scattering is here of secondary importance because of the small optical penetration depth δ_{OPT}.

First, both joining partners are put in a clamping device in close contact. The laser beam accessibility of the entire weld seam has to be guaranteed. The joining energy (laser radiation) is brought into the joining area through the transparent joining partner, which experiences, if at all, negligible warm up. The joining area corresponds to the interface or the contact area, respectively, between the joining partners. There, the electro-magnetic energy of the laser radiation is transformed into heat by the absorbing joining partner. The energy transformation occurs due to absorption within the polymer matrix but, with laser wavelengths in the order of 800–1,100 nm, mainly due to additives such as carbon black, color pigments, and infrared absorbers. The locally and temporally defined energy input causes a plastification of the absorbing partner without putting significant mechanical, chemical, or thermal stress into the seam environment. Due to the absorption within the absorbing partner, local temperature and volume increase takes place, which causes an expansion of the plastified material and a close contact between absorbing and transparent joining partner. Now, by means of heat conduction, the transparent partner warms up and plastifies, too. To guarantee heat conduction between the joining partners, a close contact is imperative. Only small gaps may be bridged. The weld-seam-adapted clamping device presses the joining partners via a static pressure evenly against each other while minimizing the gap between

the joining partners. It is the only mechanical load on the partners. The clamping device fulfills two further tasks. On the one hand, it keeps both joining partners fixed in their final position during the joining process, while guaranteeing reproducible positioning and small production tolerances. On the other hand, the clamping supplies a pressure against the thermal expansion within the joining area. Volume expansion and clamping pressure result in an inherent joining pressure, which is also an appropriate temperature necessary for obtaining a material conclusive joining. High-quality weld seams are obtained by means of sufficient generation of plastified material as well as enough interaction time to establish diffusion processes. The fulfillment of these conditions is reached by means of appropriate selection and adjustment of the variable influencing quantities, such as optical and thermal properties, laser power, intensity distribution, feed rate, or interaction time and part tolerances (avoiding gaps). Process-adapted design minimizes process times and increases weld quality. The state of common plastification of joining partners in close contact allows thermal change of place as well as diffusion processes [7.31], leading to molecule chain penetration of the joining partners within the interaction area. After the solidification, a high-quality, material-conclusive joint is formed.

The plastified volume and therefore the needed joining energy for butt joint geometry are larger than for the overlap geometry. For overlap joints only a layer of about 30–300-μm thickness is plastified within the interface area of the joining partners, while the layer thickness depends on the type of thermoplastic, optical penetration depth, and applied process parameters. When applying butt joint welding, both joining partners have to be plastified along their entire butt joint area. Furthermore, even small changes of the optical penetration depth δ_{OPT} may cause large deviations of the process variables or the process results, respectively. δ_{OPT} may be changed easily by small deviations of the amount of additives applied to the basic polymer. Due to this the absorption behavior and the temperature distribution, but especially the plastified volume within the material thickness, may change. An uneven plastification layer may cause inherent stress. Additionally, exact positioning of the joining partners and the laser beam is more critical for butt joints. Therefore, the overlap joint has prevailed over the butt joint.

The contactless and locally constricted energy input characterizing many laser beam processes avoids thermal load or damage to the joining partners as well as their environment. Therefore, joining of sensitive components, for example, those that contain electrical sensors or microelectronic or photonic parts, is possible without impairing their functionality.

There are four main irradiation methods to distinguish:

- contour welding,
- mask welding,
- quasi simultaneous welding, and
- simultaneous welding,

which are explained in brief below.

Contour Welding. Contour welding is the most widespread irradiation method. The weld seam geometry is covered sequentially with a single laser beam focused into the joining area, which is locally heated, generating a small, plastified volume (Fig. 7.94). The sequential motion may be performed by the laser beam, the clamped joining partners or a combination of both, while applying handling systems or robots. Appropriate handling systems allow welding of 3D seam geometries. Gaps between the joining partners have to be avoided. Therefore, the design of the weld seam area and the manufacturing tolerances of the joining partners are of crucial relevance.

Characteristic features of contour welding:

- design freedom (flexibility in weld contour design)
- on-line process monitoring via pyrometry
- on-line closed loop process control via pyrometry and power feedback loop
- low optical expenditure
- lower laser power required
- dynamic motion system required
- cycle times corresponding to weld seam length/feed rate
- low gap-bridging capability

Applied laser beam sources

- high-power diode lasers either with or without fiber coupling and with different shapes of the applied intensity distribution
- Nd:YAG lasers either with or without fiber coupling offering higher beam quality than diode lasers

Variable parameters (after defining materials and their properties)

- laser power
- feed rate
- wavelength
- intensity distribution

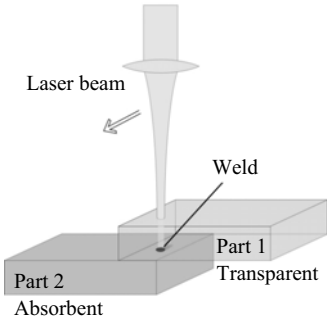

FIGURE 7.94. Schematic depiction of contour welding

- working distance
- clamping pressure

Typical process data employing high-power diode lasers

• spot size	$\geq 200\,\mu m$
• laser power	$< 200\,W$
• feed rates	$< 25\,m/min$
• interaction time	$> 1\,ms$

Mask Welding. In microtechnology, biology, and life science – especially in generating narrow seams ($\approx 100\ \mu m$) and complex seam designs – employment of masks is preferred. A mask between the laser beam source and joining partners guarantees irradiation only of areas to be welded (Fig. 7.95). High-power diode lasers with a collimated, homogeneous, line-shaped intensity distribution are preferred for this irradiation method. The possible resolution depends on the thickness of the transparent joining partner, the optical and thermal properties of both joining partners, and the intensity distribution as well as the arrangement laser source, clamping device, and mask.

Characteristic features of mask welding

- extra expenditure for mask design and manufacture as well as positioning system
- design freedom (flexibility in weld contour design)
- on-line process monitoring and control via pyrometry is limited
- low optical expenditure (but a homogeneous, line-shaped intensity distribution is required)
- high laser power required
- dynamic motion system required (often only one axis)
- cycle times corresponding to beam track length/feed rate
- low gap-bridging capability

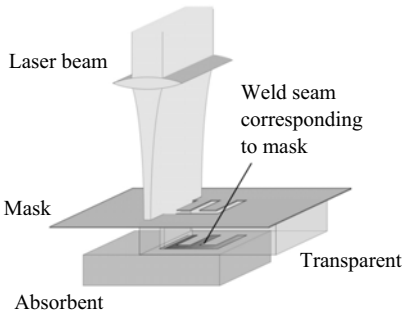

Figure 7.95. Schematic depiction of mask welding

Applied laser beam sources

- high-power diode lasers with or without fiber coupling and different shapes of the intensity distribution

Variable parameters (after defining materials and their properties)

- laser power, feed rate, wavelength, intensity distribution, working distance, clamping pressure

Typical process data applying high-power diode lasers

- spot size: line-shaped intensity distribution
  in fast axis: Gaussian, width $>500\,\mu m$
  in slow axis: top hat, length $<40\,mm$
- laser power $>200\,W$
- feed rates $<10\,m/min$
- interaction time $>2.5\,ms$

Quasi-Simultaneous Welding (Scanning Method)

Guiding the laser beam by means of fast galvanometric scanning mirrors over an arbitrary two-dimensional weld seam contour within a limited scanning field is called quasi-simultaneous welding (Fig. 7.96). An F-Theta-optic ensures the focal spot of the laser beam lying at each point of the scanning field plane within this plane. By choosing the correct interplay of scanning speed and laser power, the entire weld seam is transformed into a plastified state. Since the laser beam runs several times over the entire seam contour, intermediate losses of heat by thermal conduction may occur. Because of plastifying the entire weld seam, part tolerances may be compensated for.

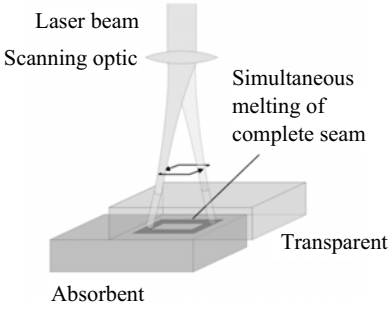

Figure 7.96. Schematic depiction of quasi-simultaneous welding

Characteristic features of quasi-simultaneous welding

- extra expenditure for scanning system
- design freedom while assuming the entire weld seam contour is within the scanning field
- limited on-line process monitoring or control via pyrometry and power feedback loop
- high laser power required
- no dynamic motion system required, if entire seam within scanning field ($<300 \times 300\,mm^2$)
- cycle times corresponding to (weld seam length $\times$ scanning repetitions)/scanning speed
- marked gap-bridging capability

Applied laser beam sources

- Nd:YAG lasers offer higher beam quality than diode lasers
- high-power diode laser are cheaper than Nd:YAG lasers

Variable parameters (after defining materials and their properties)

- laser power
- feed rate
- wavelength
- intensity distribution
- working distance (scanning field)
- clamping pressure
- working with or without melting or adding way, preservation time

Typical process data

- spot size — depending on laser source
  diode lasers $>500\,\mu m$,
  Nd:YAG-lasers $>20\,\mu m$
- laser power — $>200\,W$
- feed rates — $<10\,m/s$
- interaction time — depending on spot size and scanning speed:

  diode $>50\,\mu s$
  Nd:YAG $>2\,\mu s$

Simultaneous Welding. The compact and modular setup of high-power diode lasers permits simultaneous laser welding. The entire weld seam is irradiated as a whole and welded with one single laser pulse (Fig. 7.97, see also Chapter 6.3.3). Apart from short process times, which are of interest for big-lot production, simultaneous welding allows a more moderate irradiation (interaction). Additionally, it promises wider process windows, marked bridging capability, as well as enhanced weld strength compared to contour welding. By means of appropriate beam forming and guiding, a homogeneous intensity distribution fitting to the entire weld

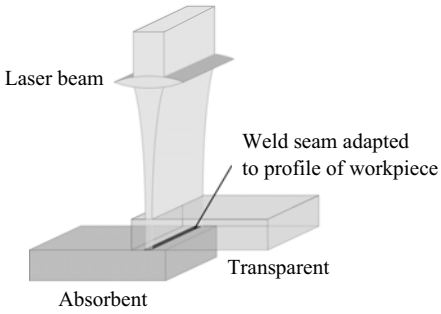

FIGURE 7.97. Schematic depiction of simultaneous welding

seam geometry has to be generated, which represents the challenge of the simultaneous process [7.33]. Assessing efficiency of simultaneous welding, aspects, such as size of the weld seam, required laser power, and cycle time, have to be considered. Because of plastifying the entire weld seam, part tolerances may be compensated.

Characteristic features of simultaneous welding

- extra expenditure for beam forming or guiding system
- limited design freedom
- on-line process monitoring and control via IR-camera
- high entire laser power required
- no dynamic motion system required, short cycle times independent of weld seam length
- marked gap-bridging capability

Applied laser beam sources

- high-power diode laser modules either with or without optical beam shaping and guiding system generating a homogeneous intensity distribution over the entire weld seam

Variable parameters (after defining materials and their properties)

- laser power
- irradiation time (interaction time)
- temporal shape of the irradiation pulse (pulse sequence)
- wavelength
- intensity distribution
- working distance
- clamping pressure
- working with or without melting or adding way, preservation time

Typical process data applying high-power diode lasers

- weld seam width $> 500\,\mu m$
- laser intensity $> 100\,W/cm^2$
- irradiation time > 50 ms upto 1 s

With contour welding, feed rates up to 25 m/min can be reached [7.32], whereas for simultaneous welding process times in the order of 0.5 s are realized already [7.33].

Laser Beam Sources

Different laser beam sources mainly operated in continuous wave mode are available for laser beam welding of thermoplastics. Laser beam welding of thermoplastics has been known since the early years of laser technology. However, the first systematic investigations date from the early nineties [7.27–7.30]. In the beginning CO_2 and Nd:YAG lasers have been in operation. Since CO_2 laser radiation ($\lambda = 10.6\,\mu m$) has a very small optical penetration depth in all thermoplastics, it has mainly been used for welding thin thermoplastic films and foils of packaging industry, either in overlap or butt joining geometry. Using CO_2 laser radiation for welding form-stable polymers would cause inefficient heating times as well as extended heat-affected areas and material degradation. Nd:YAG-laser radiation ($\lambda = 1,064\,\mu m$) penetrates uncolored thermoplastics of several millimeters thickness, while producing only small absorption, which allows the overlap joining process. Therefore, Nd:YAG-lasers have been used for welding form-stable thermoplastics. In the early years, laser welding of thermoplastics was not efficient compared to conventional technologies and was only been employed in special cases. However, laser beam welding of thermoplastics experienced a renaissance with the appearance and availability of high-power diode lasers, which are compact (small), reliable, efficient, easy to handle, as well as simple to integrate into industrial application [7.32]. High-power diode lasers offer wavelengths in the range from 750 to 1,800 nm – 800, 940, and 980 nm are the typically employed wavelengths [7.32]. In this wavelength range uncolored thermoplastics show a marked transparency, which is only limited by the thickness of the transparent joining partner, the additives added during the manufacturing process of the thermoplastic, and the scattering due to the crystallinity of the thermoplastic [7.31]. Absorption may be adjusted via color pigments such as carbon black. Another laser source occasionally employed is the so-called holmium-YAG laser, which emits laser radiation of 2-μm wavelength. Normally, at this wavelength the optical penetration depth for uncolored thermoplastics is larger than for CO_2 laser radiation but smaller than for radiation in the range of 800–1,100 nm. Therefore, it allows laser beam welding of two transparent joining partners to a certain extent [7.34]. One reason preventing industrial use is the cost of this laser beam source.

Presently most applications use high-power diode lasers. Their favorable cost [7.32] as well as the low laser-power and beam quality required for joining thermoplastics are among the principal reasons for their popularity, these laser sources are more and more industrially accepted and employed. Additionally, like

Nd:YAG-laser radiation, high-power diode laser radiation can be guided via glass fiber cables, facilitating implementation into existing production systems, such as employment of robots.

Process Equipment

Besides the joining partners, laser beam source, and electrical and cooling devices, additional equipment is necessary:

- a handling or robot system guiding the laser beam (contour or mask welding), scanner system (quasi-simultaneous welding), laser module positioning units, as well as a beam-forming and -guiding system (simultaneous welding).
- a clamping device, guaranteeing correct fixing and positioning of the joining partners. There are different devices available, which may be adapted to the actual geometry and needs of the joining partners [7.35]
- a load-and-unload system ensuring easy handling, while raising automation and throughput.
- on-line process monitoring. There are different on-line process monitoring systems available using signals from the process, such as melting or adding way, clamping pressure, or heat radiation.
- Laser safety conditions have to be fulfilled.

Strategies for Process Monitoring and Quality Control

There are several possibilities for process monitoring and quality control during or after laser welding of plastics, e.g.,

- measurement of the working temperature by pyrometry – the most common of the options,
- detection of the reflection of the laser beam,
- monitoring of the adding way during welding,
- measurement of the pressure during welding (only for simultaneous or quasi-simultaneous welding and thereon optimized clamping devices), and
- optical inspection of welded parts (only for clear transparent parts).

Pyrometer Measurement of Working Temperature during Contour Welding. The temperature range in which welding of thermoplastics is pyrouefes reasurement of wishing Temperature during possible lies between melting and decomposition temperature. This range may be small (only a few 10°C). A process-related signal presenting itself for process monitoring and control is the heat radiation emitted out of the irradiated area. The heat radiation can be detected by means of pyrometry [7.32,7.35]. If the joining partners are well adapted to the process, which means bridgeable gaps, constant optical properties, as well as no acceleration (or deceleration) phases during welding, the detected heat radiation signal stays almost constant. However, changes of the optical properties, the gap size or the feed rate along the weld seam contour lead to deviations of the process temperature and thereby of weld seam quality. This in turn results in a decreasing or increasing heat radiation signal. Therefore, the heat radiation signal can be used as input for a closed feedback loop. The laser power is controlled to keep

the temperature in the joining area within the appropriate temperature range. However, certain requirements have to be met for successful on-line process monitoring and control via pyrometry, such as

- The heat radiation has to be optically accessible by the detector.
- The imaged area should have an appropriate dimension in relation to the process zone, as the detector integrates over the temperature radiation of that image field.
- The detector should not be limited by a nonlinear spectral sensitivity.
- The obtained signal is not disturbed by other sources.
- Using process parameters being adapted to achieve a good weld a corresponding reference signal has to be defined.

In summary, on-line process monitoring and control via pyrometry for contour welding is a helpful tool to guarantee high-quality weld seams if employment requirements are fulfilled as well as adapted to process technical demands.

Pyrometer Measurement of Gap Bridging during (Quasi-)Simulations Welding. For contour welding it is quite common to use the signal strength of a pyrometer for on-line process monitoring. For simultaneous welding, control via pyrometry is limited because variations due to small defects disappear in the noise of the signal. On the other hand, a simultaneous process with one laser pulse offers the possibility of analyzing not only the strength but also the time dependence of the pyrometer signal. The temporal behavior of the signal allows the detection of gap bridging and the dimension of the gap which was bridged. An example of typical pyrometer signals is shown in Fig. 7.98.

At the beginning (depicted by ① in Fig. 7.98) material in the bottom part is heated up by the laser beam, melts, and begins to expand. As long as the melt does not touch the upper part, the resulting pyrometer signal is independent of the size

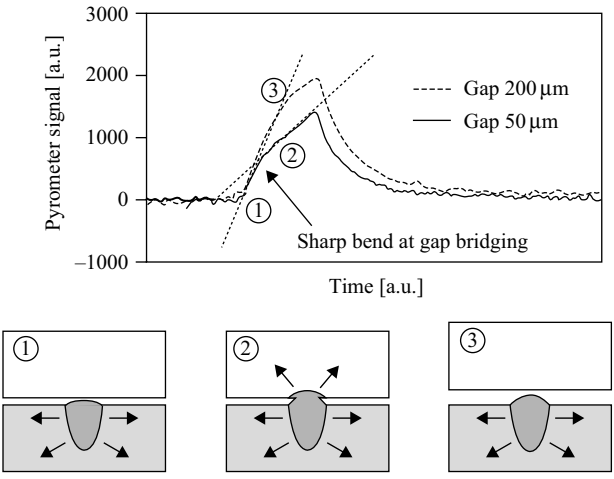

FIGURE 7.98. Detection of gap bridging by time-resolved pyrometry

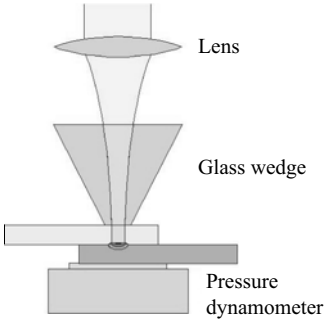

FIGURE 7.99. Setup for measurement of the pressure during welding

of the gap and is a function of laser power and heat conduction in the bottom part. For a small gap of, e.g., 50 μm, bridging occurs after a short time ②. At the point where the expanded melt touches the upper part, heat can also be conducted into that part. Therefore the slope of temperature increase will be smaller than before. A sharp bend can be seen in the curve at this point. The larger the gap, the later the bend occurs. If the gap is too large (here 200 μm), no bridging occurs ③ and one cannot find any sharp bend at all.

Pressure Measurement during (Quasi-)Simulations Welding. An indication of weld quality can be derived from the time-dependent pressure behavior during welding. As the pressure is built up only locally at the melting zone, two preconditions for the measurement have to be considered. The welding should be done (quasi-) simultaneously, and the clamping device should press down the workpiece mainly at the weld seam.

A useable setup for such measurements is shown in Fig. 7.99: the clamping device consists of a glass wedge. This results in a very small contact area and therefore a well-localized clamping force.

Image Processing with IR-Camera during Simultaneous Welding. The entire weld seam has to be monitored if simultaneous welding is applied. Different approaches which deliver a spatially resolved, process-related signal and allow on-line process monitoring (or control) for simultaneous welding have been discussed, such as piezo techniques, which monitor the change of the clamping pressure during the welding process; thermal or optical detector rows along the weld seam; or an IR-camera system, which monitors the heat radiation emitted by the weld seam. Corrections could be achieved by adjusting either the irradiation time or the entire laser power or the laser power of part of the entire weld seam contour.

If an IR-camera (Thermosensorik GmbH) is applied, a spatially resolved, process-related signal is obtained. A sample box made of polycarbonate is irradiated simultaneously with six diode laser modules (see Chapter 6.3.3). The irradiation period is about 0.6 s; the entire laser power is 80 W. Figure 7.100 shows the IR-camera image taken in the moment when the lasers are turned off.

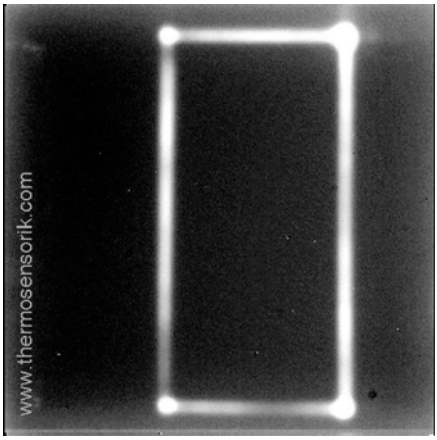

FIGURE 7.100. IR-camera picture of the simultaneously irradiated, rectangular weld seam $20 \times 40\,\text{mm}^2$ of a PC sample box. The picture is taken just when all six high-power diode laser modules are turned off

It indicates the heat radiation emitted from the irradiated rectangular seam geometry. Although, at the corners a higher heat radiation emission is detected, the entire weld seam is tight and withstands a burst pressure of about 10 bars. Nevertheless, high temperature at the corners as well as the not perfect homogeneity of the intensity distribution corresponding to the emitted heat radiation along the straight segments may cause reduced weld quality. Areas of sticking, good weld, and decomposition may alternate. Therefore, the adaptation of the intensity distribution to the weld seam geometry would offer an improved process performance. In any case the IR-camera supports individual adjustment of the laser modules to the seam contour, gives a measure of the temperature in the welding area during the process, and also indicates process failures, such as melt burr because of a gap or overheating. Process-adapted software of the IR-camera system permits quick image processing and therefore sophisticated on-line process control and post-process inspection [7.36].

7.1.5.2. Parameter Dependencies and Process Investigations

Process Technical Considerations

For obtaining high-quality welds during laser beam welding of thermoplastics, different design technical aspects have to be considered and certain requirements have to be fulfilled, such as

- constructional, laser-adapted design of the joining partners
  - guaranteeing appropriate clamping of the joining partners during the irradiation process
  - minimizing positioning tolerances of the joining partners

- avoiding or minimizing gaps between the joining partners
- ensuring accessibility, i.e., avoiding beam obstructing parts between laser source and joining area

• polymer-specific design of the joining partners
- guaranteeing welding suitability of the joining partners (polymer compatibility)
- considering influence of processing conditions on crucial demands of the laser process
- matching the physical properties (optical, thermal, mechanical) to the process
- considering type, concentration, distribution and size of additives
- avoiding impurities and moisture (especially for Polyamide) within the thermoplastics

• method-dependent factors
- irradiation method and joint geometry
- laser beam source (i.e., wavelength, power) and laser welding system
- joining parameters as well as their clamping strategy and parts load and unload

If laser beam welding is to be applied to an existing or new product, the laser-beam-adapted design has to be considered as early as possible during development.

Optical and Thermal Properties. Laser beam welding has to rely on other physical properties of the joining partners than conventional welding technologies. The optical and thermal properties are the most important properties to consider for laser beam welding. The optical properties of the employed materials have to allow the overlap process regarding the used laser beam wavelength. Dyes, crystallinity, additives, and other ingredients added to the basic thermoplastic influence the optical properties. On the other hand, they allow adaptation of the optical properties to the process technical needs. For welding of different thermoplastics their polymer compatibility has to be considered.

An important measure is the optical penetration depth δ_{opt}. It is defined as the length within a material in direction z of the beam propagation where the original radiation flux Φ_0 is reduced to 1/e. According to Lambert's law

$$\Phi(z) = \Phi_0 \cdot \exp(-\delta_{opt} \cdot z). \tag{7.1}$$

The decrease of the original radiation flux Φ_0 is caused by scattering and absorption. Since both physical phenomena appear at the same time it is difficult to separate them. From the physical point of view, absorption is the damping of electromagnetic waves while propagating through a spatially extended media. Here, absorption takes place because of the interaction of electro-magnetic laser radiation and matter (thermoplastic). Due to dielectric and magnetic losses of the media absorbed energy is transformed into heat energy. In contrast to absorption, scattering causes a change of the original intensity distribution due to an

interaction of laser radiation and matter. The latter means a change of the original beam propagation behavior of the laser radiation. While scattering is negligible within amorphous thermoplastics, it is of relevance within partially crystalline thermoplastics. Crystalline super structures (spherulites) are causing the scattering (a sort of multiple reflection). The original optical path becomes changed, summing up to a higher length. This again causes an increased absorption. Therefore, the absorption increases either with growing degree of crystallinity or at the same degree of crystallinity but smaller (and therefore more) spherulites. Together both effects (absorption and scattering) cause a broadening of the original intensity distribution and a decrease of the original intensity. Due to scattering, broadened intensity distribution may cause broader weld seams. Loss of laser power due to scattering and absorption within the transparent joining partner causes loss of laser energy for plastification within the joining area. Furthermore, the more laser energy is absorbed per length (volume) within the transparent joining partner, the larger the risk of burning the transparent thermoplastic. Accordingly, the process window becomes smaller. Obviously, knowledge concerning the optical properties is a crucial point of laser beam welding of thermoplastics. The optical penetration depth depends on the actually utilized thermoplastic (chemical compound, chemical ingredients), the morphology of the thermoplastic (e.g., degree of crystallinity) and the processing of the thermoplastic, the laser wavelength used; and furthermore, it depends on the nature, quantity (concentration), size, and distribution of the added substances, such as color additives, flame retardants, filling and reinforcement materials, and others.

Considering thermal properties of thermoplastics, such as melting and decomposition behavior, mechanical strength versus temperature, phase transition, heat conductivity, thermal expansion coefficient, or viscosity, welding of thermoplastics is quite different from welding metals. The temperature within the joining area has to be kept over melting and below decomposition temperature. This temperature range may be rather small [7.37, 7.38].

Mechanical strength versus temperature for thermoplastics is different for amorphous and partially crystalline thermoplastics. In particular, there are no distinct phase transitions for amorphous thermoplastics like there are for metals.

Considering the short interaction times of laser radiation with the thermoplastic and the low heat conductivity of polymers – on the order of 0.1–1 $W/(m \cdot K)$ – the intensity distribution is imaged into an energy density profile corresponding to a temperature profile within a layer of the dimension of the optical penetration depth.

The large thermal expansion coefficients of thermoplastics do not only support the mixing and diffusion of the thermoplastics to be welded, but may also cause inherent stress because of shrinkage, even after long periods of time after solidification. Viscosity of plastified (molten) thermoplastics is much larger than for molten metals; therefore, molten thermoplastics do not flow and mix sufficiently within the available interaction time without any external force, such as inherent pressure.

In summary, fulfilling optical and thermal process requirements is mandatory for obtaining high-quality welds.

Characteristic Curve and Process Parameter "Energy Input Per Unit Length". If process behavior is described and the process window location and extension are determined, a "characteristic curve" is commonly used, which displays the seam strength versus energy input per unit length (Fig. 7.101). Energy input per unit length is defined as laser power per feed rate. However, energy input per unit length is not a comprehensive process parameter, since it does not take all influencing aspects into consideration, such as beam shape, intensity distribution and process time scales. Therefore, process comparability is limited. An improved process characterization considers the interaction of

- material — physical and chemical properties
- process performance — interaction time(s), feed rate
- laser — power, intensity or intensity distribution
- product — joining partner, seam design

Figure 7.101 also shows microtome cuts of PP samples; the cuts have been performed for different energy inputs per unit length (numbers 1 to 4). Even if energy input per unit length is not the only characterizing process parameter, Fig. 7.101 shows a clear dependence of the welding result on these specific energy levels.

Gap Bridging Capability. Gaps between the joining partners influence the joining process and its result: a close contact and therefore thermal conduction between the joining partners is not possible; and thus, overheating of the absorbing joining

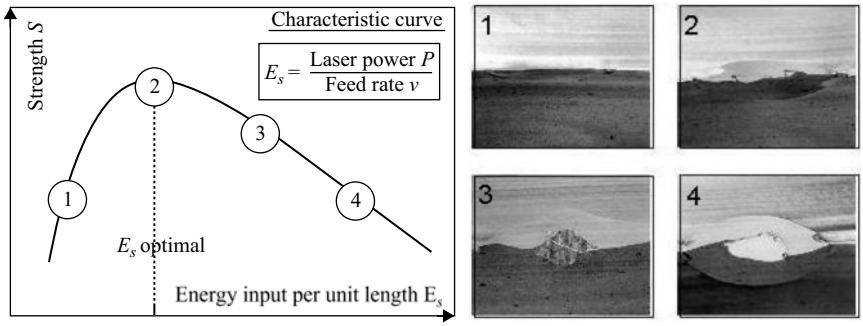

Figure 7.101. Left: Characteristic curve – strength vs. energy input per unit length E_S – depicting position and extension of the process window (1, adhesion – no weld, 2, optimal weld adjustment; 3, optimal adjustment left – bad weld; 4, decomposition – bad weld). Right: Corresponding microtome cuts of welded PP samples

partner may occur. Gaps are especially problematic if contour welding is applied. So it is absolutely necessary to avoid gaps. For example, gaps are due to

- manufacturing process (injection pins, shrinkage)
- parts tolerances
- clumsy clamping

There are strategies that improve gap-bridging capability to a certain extent. Firstly, clever weld seam design may minimize worsening weld quality because of gaps. Secondly, appropriate injection-molding conditions and tools may optimize joining partner tolerances. Thirdly, proper adjustment of the optical properties improves process performance and gap-bridging capability. For example, performing systematic examinations on gap-bridging capability, PP samples of different carbon black concentrations have been investigated. In summary, the lower the carbon black concentration (cbc),

- the larger the optical penetration depth, i.e., $\delta_{\mathrm{OPT}} \propto 1/\mathrm{cbc}$
- the larger the (possible) molten volume, i.e., $\delta_{\mathrm{OPT}} \propto$ molten volume
- the more moderate the temperature rise, i.e., $\delta_{\mathrm{OPT}} \propto 1/\nabla T(x, y, z)$
- the larger the gap-bridging capability, i.e., molten volume $\propto$ bridging capability

But this is only valid to a certain extent and at the expense of energy input per unit length necessary for melting.

Depending on the carbon black concentration and the applied welding strategy, different residual gap sizes could be bridged, if optical and laser beam properties were optimized: 75 μm for a circular spot (contour welding) and 150 μm for a line-shaped spot (contour welding) could be reached.

Determination of the Optical Properties of Parts To Be Welded. As mentioned before, one part has to be transparent and the other should absorb the radiation for overlap welding. Therefore, the optical properties of the joining parts are most important for investigations of the weldability. Most problems during laser welding of plastics occur due to dramatic reduction of the light transmission of the top part. As a rule of thumb, the higher the transmission, the easier the welding – or more specifically, the thickness of the part, the absorption coefficient, scattering effects within the material, and the beam power are parameters which define the available power at the interface between the transparent and the absorbing part. The beam power can only be raised up to a certain level, as decomposition of the material must be avoided in any case. Scattering and absorption properties of the top material depend on various parameters: the structural composition, the crystallinity of the polymer, fillers, glass fibers, additives as processing aids, fire-retarding agents, or heat stabilizers. Even if indications for the product are same, materials from different suppliers can have other ingredients, which can influence the optical properties and therefore the weldability. For validation of a manufacturing process, the optical properties of the material have to be taken into account. The measurement of reflection and transmission is not sufficient for that. The scattering of the laser beam is for some materials also a very important

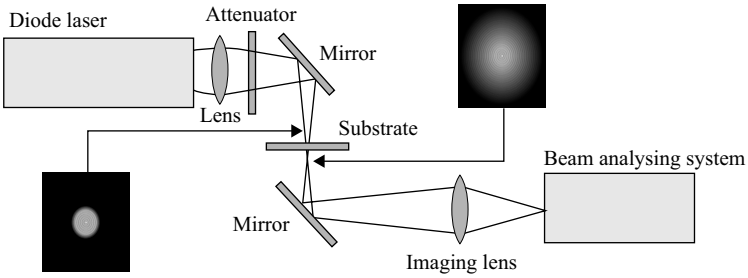

FIGURE 7.102. Setup for measurement of scattering

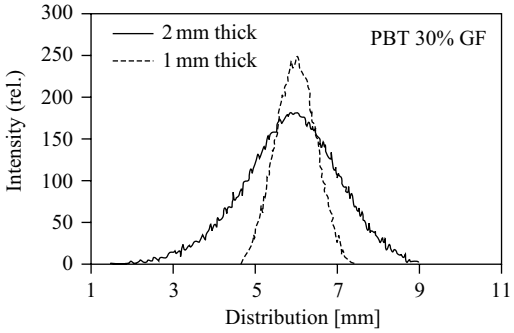

FIGURE 7.103. Scattering of the laser beam in PBT samples with 1- and 2-mm thickness

characteristic feature. Scattering of the radiation by the sample can be measured with the setup shown in Fig. 7.102.

In this setup an attenuated diode laser beam is focused onto the test sample and penetrates through it. A CCD camera takes a picture of the intensity distribution of the beam after it exits the test sample. The signal is transferred to a computer, where it is graphically evaluated.

Samples of different thicknesses and material concentrations of glass fibers show different intensity distributions. For amorphous polymers without any admixtures the laser power density distribution after transmission through the sample is nearly the same as before. Only some power losses occur due to refraction at the polymer/air as well as the air/polymer surfaces. For partially crystalline polymers or polymers with a large amount of glass fibers, the situation changes. Actually, the higher the grade of crystallisation or the higher the glass fiber concentration, the more evident is the broadening of the original intensity distribution due to the beam propagation through the sample.

As an example, the beam diameter after transmission of the sample will extend from 1.0 to 1.4 mm, respectively, to 3.1 mm for a 1- and 2-mm-thick sample of PBT, as shown in Fig. 7.103.

Additionally, it was noticed in some cases that the measured scattering depends on the position on the part and on the process parameters during molding. There

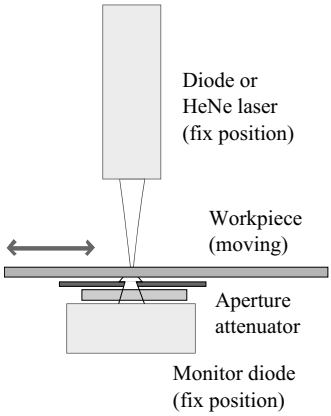

FIGURE 7.104. Setup for simple checking of optical properties of translucent parts

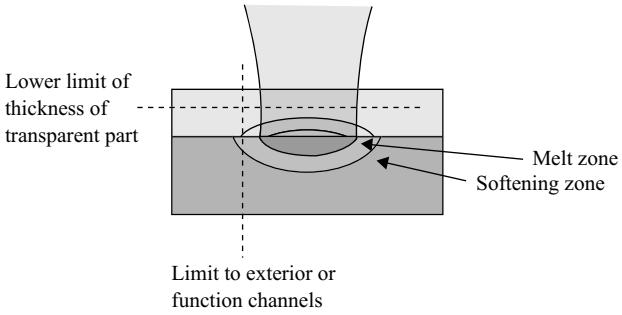

FIGURE 7.105. Negative effects due to softening of the material during welding

are two reasons for that. The orientation of the glass fibers depends on the flow direction of the melt, and the crystallisation grade varies with the temperature time profile during molding.

A simple setup shown in Fig. 7.104 can be used to test the reproducibility of the optical properties for different workpieces very quickly. This is done by measuring the amount of transmitted laser light along a defined track on the workpiece to be tested.

Influence of Geometry. Several rules must be observed regarding joining geometry. One of the most important concerns the softening zone in the material, which is created during welding. To create a weld, the laser beam has to heat up some material above the melting temperature. Due to thermal conduction at the same time a more or less large surrounding zone is warmed up to the Vicat softening temperature (defined in ISO306), as shown in Fig. 7.105. The difference between the softening and melting temperature and therefore the size of the zone strongly

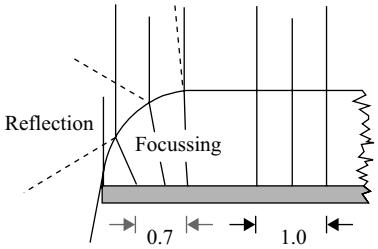

FIGURE 7.106. Negative effects at rounded surfaces

depends on the material used, e.g., for PBT Ultradur B 4406 the Vicat softening temperature is 170°C and the melting temperature is 223°C.

Smaller softening zones are also created in the transparent part. During heating normally every material expands, and consequently pressure is built up if the enlarged material is completely enclosed like it is for overlap welding with small gaps between the parts. If the softening zones adjoin the exterior of the workpiece or internal function channels, the pressure is high enough to press the softened material to the side. As consequence molten material can then flow out of the workpiece, creating a melt burr or flow into the function channels. Softening zones in the transparent part near the surface can result in dents at the surface due to shrinking processes during cooling down of the melt. Therefore, small distances between weld seam and exterior or function channels have to be critically observed.

A second example shows possible negative effects due to the geometrical shape of the workpiece itself. Rounded instead of flat surfaces have following disadvantages:

- A rounded surface acts as a lens, as illustrated in the example in Fig. 7.106. In the example the focus diameter decreases from 1 mm to 0.7 mm for a 1.3-mm-thick part. This means double power density.
- Reflection properties at a surface depend on the incident angle. For angles relative to the surface normal above 50° the reflectance increases highly up to 100% for an angle of 90°.
- The effective path length of the laser beam changes in relation to the position of the laser beam. For strong scattering materials like PBT this is problematic.

The accuracy of the laser beam position relative to the workpiece is never perfect in reality. Due to above-described effects, small variations of the position can result in large variations of the laser power density at the absorbing part and therefore in weld quality and reproducibility.

Joining of Plastic to Metal. Some plastic materials can be joined with metal. However, it is not a weld process; the plastic material acts as a hot-melt adhesive.

This has several consequences:

- The plastic material should be preferably transparent.
- The metal has to be heated up by the laser beam. Due to limited laser power and high heat conduction of metals the metal parts should not be too large. Thin sheets with 200-μm thickness or small pins give the best results.
- Not all plastic materials are usable for the joining. Practical types are plastic materials which are related to commercial hot-melt adhesives like PA.
- Preparation of the surface is very important, as it is with gluing processes. Therefore roughening and cleaning the surface improves the tensile transverse resistance and the long time reliability.

In Fig. 7.107 different surface preparation methods were tested for the joining of metal to PA66. Every metal part was cleaned by ultrasonics, but additionally some were cleaned by an excimer laser beam. Herewith remaining layers of dirt were almost completely removed. Tensile transverse resistance measurements were done immediately after the welding and 4 weeks later. In every case a decrease of the strength was measured; dramatic worsening is seen for the parts, which were only cleaned by ultrasonic.

Contour Welding

Laser System, Materials, and Samples. For welding flat samples (2 × 30 × 60 mm^3), a fiber-coupled high-power diode laser (Rofin DF x06) supplying up to 60 W is applied; the system generates an intensity distribution of Gaussian shape (spot diameter 800 μm, wavelength 940 nm). For welding rectangular sample boxes (20 × 20 × 40 mm^3), a fiber-coupled high-power diode laser supplying 50 W is applied (Gaussian shape, spot diameter 800 μm, and wavelength 803 nm). Investigation of flat test samples is focused on obtaining information concerning gap-bridging capability, while the weld is a 17-mm straight line. Investigation of the sample boxes is used for density and burst pressure tests, while the weld seam

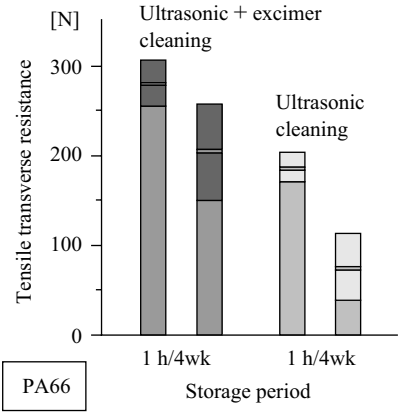

FIGURE 7.107. Long time reliability of joined parts with different preparation of the surface

is rectangular 20 × 40 mm^2. Three materials are investigated: PA, PC, and PP, without any additives. The joint geometry is always overlapping. The absorbing joining partners are colored black by adding carbon black. The handling system provides a maximum feed rate of 4 m/min.

Investigations and Results. Contour welding experiments are performed in overlap joint geometry at a constant clamping pressure; laser power, feed rate, and the gap size are varied. The quality examination of welded samples may be performed by means of destructive or non-destructive methods. Non-destructive examinations are, e.g., visual, ultrasonic, X-ray, tightness, thermographic methods, laser scanning microscopy, and computer tomography; destructive examinations are, i.e., tensile strength tests, burst pressure tests, microtome cuts, grinding and polishing of cross-sectional cuts for microscopy.

The flat samples of PA, PC, and PP are blackened with different carbon black concentrations, resulting in different optical penetration depths. In a first approach, different optical and thermal properties resulted in distinguished gap-bridging capabilities, illustrated in Table 7.9. A gap is regarded as bridgeable if the strength of the obtained weld is at least 80% of the strength for no gap.

The carbon black concentration of the contour welded sample boxes is kept constant at 0.3 weight percent. The welded boxes are tested for tightness and burst pressure. Table 7.10 gives a summary. Figure 7.108 shows the obtained burst pressure versus energy input per unit length for PA of three laser powers. Figure 7.109 illustrates microtome cuts of the weld seam for PA sample boxes welded with 3.6 W (see corresponding curve in Fig. 7.108).

Table 7.9. Summarizing overview of carbon black concentration, optical penetration depth and bridged gap for the investigated flat samples, while applying contour welding

Material	Carbon black concentration in weight percent	Optical penetration depth in µm ($\lambda = 808$ nm)	Optical penetration depth in µm ($\lambda = 940$ nm)	Bridged gap in µm
PA	0.2	52	61	50
PC	0.2	60	71	100
PP	0.7	43	46	50

Table 7.10. Summarizing overview of carbon black concentration, optical penetration depth, and maximum burst pressure for the investigated sample boxes, while applying contour welding

Material	Carbon black concentration in weight percent	Optical penetration depth ($\lambda = 808$ nm) in µm	Maximum burst pressure of tight boxes in bar
PA	0.3	47	10
PC	0.3	55	7
PP	0.3	71	8

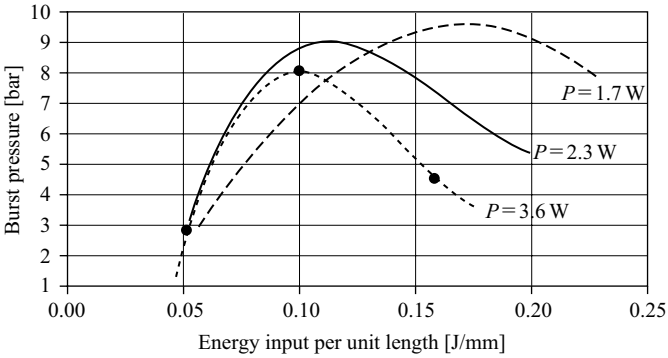

FIGURE 7.108. Burst pressure p versus energy input per unit length E_S for contour welded sample boxes of PA for three different laser powers

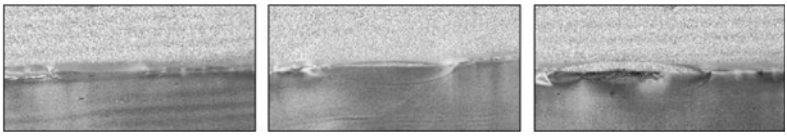

FIGURE 7.109. Microtome cuts of contour welded PA samples ($P = 3.6$ W). From left to right, increasing energy input per unit length E_S corresponding to constant laser power P but decreasing feed rate v. Left: Sticking; middle; good weld, right, decomposition (in the center of the heat affected zone). The entire length of depicted microtome cut areas is equivalent to about 1 mm

Simultaneous Welding

Laser System, Materials, and Samples. There are different strategies to accomplish simultaneous welding, such as (i) direct irradiation (without any beam shaping after the high-power diode laser module), (ii) applying classical optics, (iii) employing mask technology, and (iv) application of fiber bundles. At the moment, direct irradiation is the most common method, since sophisticated-laser-beam guiding and laser-beam-forming systems are not yet sufficiently developed. Applying direct radiation, the challenge consists in positioning the single high-power diode laser modules to the weld contour, which consists of straight lines. Additionally, the untreated intensity distribution of the single diode laser modules has to allow us to line up the single intensity distributions (see Chapter 6.3.3) to avoid inhomogeneities in the entire intensity distribution. Employing simultaneous welding also offers the possibility of not generating a closed weld seam contour but several single joints at a time (simultaneous tacking).

Performing simultaneous welding experiments with flat test samples one and with sample boxes six high-power diode laser modules are used. All six modules are identical, supplying radiation at a wavelength of 808 nm with a maximum output power of 15 W, while generating an intensity distribution at about a 100-mm working distance, which has the shape of a straight line ($20 \times 1\,\text{mm}^2$). The

six modules are arranged in such a way they irradiate the entire rectangular weld seam contour of the sample box (20×40 mm^2). The applied laser system allows individual steering and interlock control of the laser modules (see Chapter 6.3.3). Investigated materials and test samples are like those used for contour welding.

Investigations and Results. Simultaneous welding experiments were performed in overlap geometry at a constant clamping pressure; total laser power, irradiation time, and gap between flat specimens could be varied. Corresponding to experimental results of contour welding, the largest gap investigated was 150 μm. Since it is bridged for all three thermoplastics it may be that even larger gaps are bridgeable with simultaneous welding. Systematic investigations show that simultaneous welding offers larger process windows, an increased gap-bridging capability, as well as slightly higher weld strength than contour welding (illustrated in Fig. 7.110, right). The results of simultaneous welding of the sample boxes support this statement. Table 7.11 gives a summary (like Table 7.10). Figure 7.110 shows the obtained burst pressure vs. the energy per unit length for PA, at three different values for the laser power. Figure 7.111 illustrates microtome cuts of the weld seam for PA sample boxes welded with 62 W (see corresponding curve in Fig. 7.110).

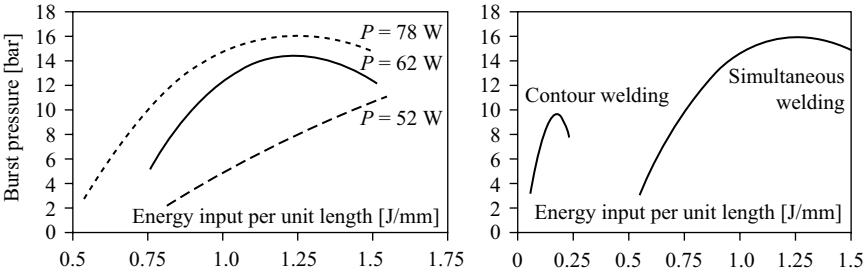

FIGURE 7.110. Left: Burst pressure p vs. energy input per unit length E_S for simultaneously welded sample boxes of PA. Right: Burst pressure p vs. energy input per unit length E_S for contour and simultaneously welded PA sample boxes

TABLE 7.11. Summarizing overview of carbon black concentration, optical penetration depth, and burst pressure for the investigated sample boxes, while applying simultaneous welding

Material	Carbon black concentration in weight percent	Optical penetration depth ($\lambda = 808$ nm) in μm	Maximum burst pressure of tight boxes in bar
PA	0.3	47	16
PC	0.3	55	10
PP	0.3	71	10

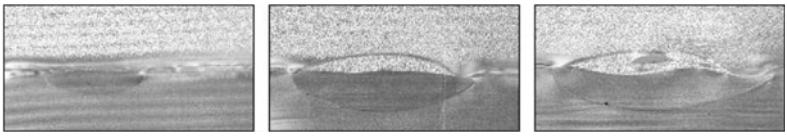

FIGURE 7.111. Microtome cuts of simultaneously welded PA samples. From left to the right: Increasing energy input per unit length E_s corresponding to constant laser power P and irradiated length l but increasing irradiation period t. Left: Sticking; middle, good weld; right, hole forming. The length of the depicted microtome cut areas is equivalent to about 1 mm

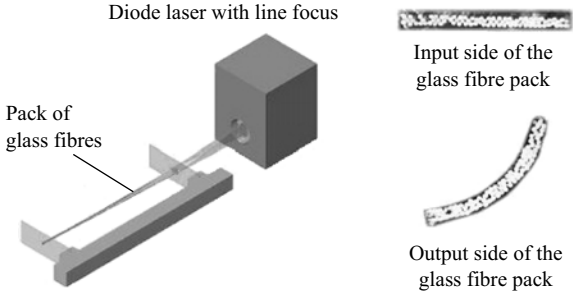

FIGURE 7.112. Glass fibers for rearrangement of the beam shape

The input of heat increases the volume of molten polymer. For the overlap joint geometry, this extension is related to the ability to bridge a gap between the joining partners.

Beam Shaping by a Pack of Fibers Arranged in the Desired Form. For simultaneous welding several laser sources have to be arranged in series so that the entire contour is heated up at the same time. In practice contours rarely are only straight lines. Therefore beam shaping is an important requirement. A promising method for this is the rearrangement of the beam shape by a pack of fibers arranged as a line at the input side and in the desired form at the output side, as shown in Fig. 7.112.

To get a high packing density, small glass fiber diameters have to be favored. On the other hand, large diameters are more practical for packaging and handling. In the tests described here glass fibers with a diameter of 220 μm were used as a compromise for small weld seams. Some problems occur due to single broken fibers, but resulting welds show even edges and no internal voids.

7.1.5.3. Applications and Outlook

Several companies recognize the advantages as well as the industrial demand for and interest in laser beam welding of polymers and offer laser systems or entire welding plants. Within Germany about 75 production plants have been put into operation in the last 5 years. Existing and potential laser welding applications can

be found in industries such as

- automotive industry (rear light, liquid container, connectors, electronic keys, dashboard, bumper),
- electronics industry (electronic housings, sensors, switches),
- medical industry (dialysis components, injection needles),
- building trades (polymeric windows, large dowels, pump housings), and
- household goods (funny glasses, polymeric dishes, shavers).

Laser beam welding offers specific process technical advantages compared to conventional joining technologies. However, laser beam welding will not and cannot replace existing technologies. It has to be seen as a complementary technology with process-inherent advantages and disadvantages. To exploit the numerous advantages, certain requirements have to be met, such as laser-adapted design, matching the optical properties, guaranteeing clamping and positioning during the irradiation process, and ensuring accessibility of the joining area by the laser beam. The imperative challenges for research and development are, at present, producing thinner weld seams for micro-applications, eventually by using mask technology or different laser beam sources; extension of colors of the joining partners which are still laser beam weldable; strategies for improving gap-bridging capability of large plastics parts, and improvement of the pre-, on-line, and post-process monitoring. Contour welding is the most widespread irradiation method. It presents high-quality weld seams and offers flexibility (freedom of design) as well as on-line process monitoring and control via pyrometry. Simultaneous welding requires an additional challenge to complete the process: clever beam forming and guiding is necessary to achieve a homogeneous and mixed intensity distribution over the entire weld seam contour. However, simultaneous welding offers shorter process times, extended process windows, and a marked gap-bridging capability. On-line and post-process monitoring as well as on-line process control may be achieved by IR-thermography. Current product development, as in the microelectronics and photonics industry, is challenged by tasks which often cannot be accomplished with traditional tools and therefore require for new, reliable joining technologies. Keywords are increasing packaging density and decreasing physical volume, both corresponding to a sensitive joining environment, efficiency, and big lot productions. Laser beam technology offers innovative solutions to overcome the limitations of conventional technologies. The process technical progress of the last years as well as current industrial applications and demands are justifying the assumption of increasing employment of laser beam welding of thermoplastics in the near future.

7.2. Cutting and Laser-Assisted Machining Technologies

7.2.1. Introduction

D. Petring

Since the 1970s, laser radiation has been used for cutting in industrial manufacturing, mainly because of the excellent focusability of laser beams. The

small working-spot size of typically some tenths of a millimeter allows for narrow kerfs and is thereby a precondition for higher accuracy and higher cutting speeds compared to what is possible with conventional thermal cutting techniques like flame or plasma cutting. Presently, more than 30,000 industrial CO_2 lasers with up to 6-kW beam power and with beam qualities of up to $K = 0.9$ are installed worldwide for flat sheet metal cutting. Many of them are applied in job shops. They profit from the high productivity of the laser machines, the excellent accuracy of the cut parts, and last but not least the flexibility of the manufacturing system regarding material, thickness, cut geometry, and lot size, which can be produced cost efficiently. Especially this high degree of flexibility is a continuously growing market demand and cannot be fulfilled by punch machines regardless of how many tools are employed. Each year more than 3000 new laser-cutting systems are installed worldwide. Three-dimensional cutting of, e.g., body and chassis components with Nd:YAG lasers, fiber-coupled to robots, shift the cutting process nearer to the end of the process chain, thus allowing for flexible production of a high number of variants and options, another factor increasing market demand.

However, the good focusability required for cutting is not yet available with high-power diode laser systems in the range of multi-kilowatt beam power. But it is only a question of time until laser scientists and engineers will solve this problem by improved design concepts for the diodes and the superposition of their radiation. The optical cutting plotter presented in Chapter 6.2.1 and the cutting investigations with this beam tool presented in the following section (7.2.2) describe a first step in this direction.

On the other hand the modular principle of diode laser systems offers special opportunities by delivering customized beam patterns beside the standard circular spot (see Chapter 6.3). In section 7.2.3 investigations on single-shot cutting with a line-shaped light pattern are described. The idea of this approach is in fact a light punch, working without contact with the cutting zone and melting or vaporizing the material along the cut path within one single beam shot. With this method, relative movement between laser beam and workpiece is not required during cutting. Repeated cutting-to-length of thin coil material into segments is one of the possible applications. A special process for thick plate mild steel cutting, described in section 7.2.4, can be carried out with an annular diode laser beam. It is used for preheating the material around an oxygen jet, which then can burn the kerf volume by an exothermal reaction. This demonstrates that good focusability is not always the key for laser-supported manufacturing. This is also true for laser-assisted machining, as described in section 7.2.5. Here the laser radiation is used to heat the workpiece ahead of the contact zone of a mechanical cutting tool in order to reduce the material strength and thereby improving the machining characteristics. The machining of very hard materials can profit especially from this approach.

It may become more obvious in the following sections that even a manufacturing process like cutting, normally assumed to be far away from the utilization of diode laser technology, is in fact a serious candidate for future applications of this new laser type.

7.2.2. Precision Cutting with the Optical Cutting Plotter

D. Petring, R. Polzin, B. Seme

7.2.2.1. Process Principles and Equipment

Laser Cutting Variants and Process Characteristics

Laser cutting is a thermal process where a focused laser beam, mostly together with a coaxial assist gas jet, is used to form a cutting kerf by local removal of material and relative motion between laser beam and work-piece. The type of cutting process is defined by the dominant phase transition caused due to the absorption of the laser beam energy [7.39, 7.40]. The process is called inert gas cutting or fusion cutting when the specimen is melted by the laser beam and an inert or at least non-reactive assist gas jet is used to drive out the melt. An example is stainless steel cutting with nitrogen, which results in shining cut edges free of oxides. During oxygen cutting the assist gas is oxygen which does not only eject the melt but in addition causes an exothermic chemical reaction with the material. The oxidation speeds up the process but produces oxidized cut edges. Pure oxygen is the preferential assist gas if mild steel is to be cut. A third technique of laser cutting is vaporization cutting, sometimes also called sublimation cutting. Here the material in the cutting kerf is removed by a transition into the gaseous state instead of ejection of melt. In this case an assist gas jet for material removal is not essential. Nevertheless, an inert gas jet is often used to protect the optics, to expel the vapor out of the kerf for avoiding re-condensation at the kerf walls and to prevent an oxidation of the specimen. For some materials (e.g., wood) the transformation to vapor state is achieved by chemical degradation. In other materials (e.g., graphite) a solid-vapor transition takes place due to sublimation. Compared to fusion cutting and oxygen cutting, vaporization cutting of metals requires higher intensities because not only the latent heat of fusion but also the latent heat of vaporization has to be provided. Vaporization cutting is easily achieved during processing of materials like wood, paper, and some ceramics and plastics that do not possess a liquid phase.

The main advantages of laser cutting in comparison to conventional cutting methods are a narrow kerf width that allows for complex contours, nearly perpendicular and parallel cut sides, and a very small heat load of the material. Of course these advantages only appear when the laser beam is focused to a small spot with a diameter of about 0.05–0.5 mm and when the Rayleigh length is in a range ensuring appropriate beam intensities along the whole cutting depth. Thus laser cutting makes high demands on the beam quality and precision cutting with diode lasers is a particularly challenging enterprise. For example, a Rayleigh length of at least 0.5 mm (suitable for a sheet thickness of up to about 1 or 2 mm) and a focal diameter of 0.2 mm require a beam parameter product of 20 mm mrad or less.

Power Balance for the Laser Cutting Process

Laser cutting not only makes high demands on beam quality, it also calls for a certain amount of beam power. A stable, steady-state cutting process requires

a proper balance of the incoming and outgoing power contributions in the interaction zone. The laser beam power absorbed and, in the case of oxidation cutting, additionally the exothermal reaction power, on one hand, have to correspond with the power necessary for heating and transforming the material along the cutting track on the other hand. The latter is obviously increasing with kerf width b_m, material thickness s, and cutting speed v_c – all three parameters representing the dimensions of the volume to be heated, transformed, and removed by the process.

The overall power balance for laser cutting [7.40] can be written as

$$P_C = A\,P_L + P_r = P_{T_p} + P_m + P_v + P_l \tag{7.2}$$

with the total amount of power P_C required for cutting, absorptivity A, the laser beam power P_L, the reaction power P_r, the power P_{T_p} for heating the kerf volume up to the process temperature T_p, the power P_m for melting the kerf volume, the power P_v for evaporating (part) of the kerf volume, and the power P_l for compensating heat conduction losses into the material beside the kerf. The different terms on the right-hand side of Eq. (7.3) are calculated by the following formulas [7.41]:

$$P_{T_p} = b_m\,s\,v_c\,\rho\,c[(1-\delta_v)(T_p - T_0) + \delta_v(T_s - T_0)] \tag{7.3}$$

$$P_m = b_m\,s\,v_c\,\rho\,\varepsilon_m \tag{7.4}$$

$$P_v = \delta_v\,b_m\,s\,v_c\,\rho\,\varepsilon_v \tag{7.5}$$

$$P_l = b_m\,s\,v_c\,\rho\,c(T_m - T_0)\left[\frac{\sqrt{2\pi}\,/\mathrm{Pe}}{\mathrm{e}^{\mathrm{Pe}^2}/4\mathrm{K}_0(\mathrm{Pe}^2/4)} - 1\right] \tag{7.6}$$

In Eq. (7.6) K_0 means the modified Bessel function of the second kind and zero order.

Within Eq. (7.3) to Eq. (7.6) ρ is the mass density, c is the heat capacity, δ_v is the proportion of vaporized kerf volume, T_s is the surface temperature of the cutting front, T_0 is the room temperature, ε_m and ε_v are latent heat of fusion and evaporation, T_m is the melting temperature, Pe is the Peclet number (defined by $\mathrm{Pe} = b_m\,v_c/(2\,\kappa)$), and κ is the average thermal diffusivity in the solid state.

Some of the above parameters are quite well known, e.g., from material data handbooks, others have to be calculated from additional equations within a self-consistent approach [7.41] or approximated by plausible or measured values.

In pure laser fusion cutting δ_v is equal to 0; in pure laser vaporization cutting δ_v is equal to 1. In both cases $P_r = 0$. The kerf width b_m can be approximated by the diameter of the laser beam at the surface plane of the workpiece or measured from kerf cross sections. The process temperature T_p is nearly identical with the melting temperature T_m for metals with high heat conductivity like copper and

aluminum, and approximately the average value of melting and evaporation temperature for other materials like steel and titanium. In the case of vaporization cutting, T_p is identical with T_s and amounts to the vaporization or degradation temperature T_v.

For metals the net absorptivity during fusion cutting is typically in the range between 0.15 and 0.4. The process profits from the elevated Fresnel absorption at inclination angles near the Brewster angle, which is between 80 and 90 degrees depending on laser wavelength and type of metal. In contrast, during oxidation cutting higher degrees of absorption can be assumed, if the angle of incidence is below 80 degrees, which is only true for correspondingly flat cutting fronts or divergent beams. For infrared laser radiation, the absorption behavior of oxides is similar to that of many plastics and other non-metals. It has to be mentioned that a total absorption of the whole laser radiation is very untypical during cutting. The laser beam is propagating along a quite steep cutting front and generally part of it is reflected or transmitted through the open kerf.

The reaction power P_r can be estimated from the power made available by the number of atomic reaction partners, namely, due to the oxygen flow on to the burning cutting front and due to the workpiece material flow into the interaction zone [7.40]. The minimum value of these two powers is a quite good approximation of the maximum available reaction power, because the reaction is obviously limited by the flow rate of the rarest type of reaction partner.

The laser power to be absorbed can now be calculated from the total power demand for the cut reduced by the maximum reaction power and from the obligatory power indispensable for heating the cutting front to ignition temperature. At low speeds the exothermal reaction can lead to an excess reaction power, which is avoided by reducing the gas pressure and pulsing the laser beam.

The Equipment

To demonstrate that beam quality and output power of presently available diode lasers are sufficient for precision cutting of material with a thickness of up to about 1 mm, an optical cutting plotter device has been built up (Chapter 6.2.1). The system reaches a high brilliance by multiplexing the beams of six broad-area diode laser bars incoherently. Expansion optics in combination with an achromatic lens are used to focus the superimposed beams into a spot of $0.2 \times 0.25\,\text{mm}^2$. The maximum optical power at the workpiece amounts to 120 W at a beam parameter product (BPP) of about 20 mm mrad. To generate an assist gas jet that is running coaxially to the laser beam, a standard cutting head with an adjustable conical nozzle was adapted to the diode laser device. In so doing a complete laser cutting tool with a weight of less than 10 kg and a size of only about 10 dm^3 is obtained, including the laser source without power supply. To perform cutting applications, the system can be installed, e.g., into a three-axis handling system as shown in Fig. 7.113 [7.42].

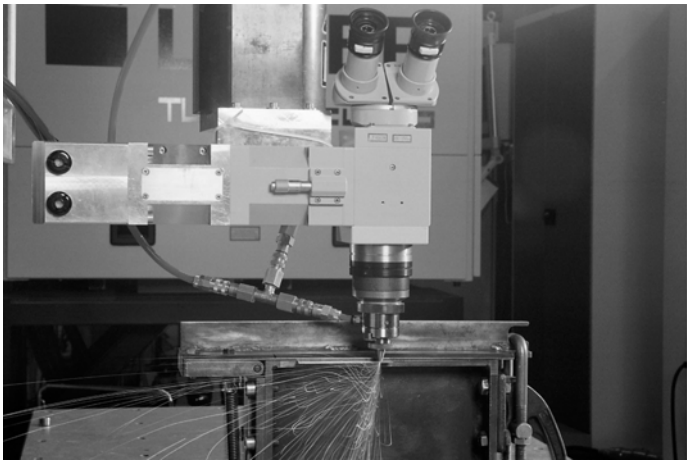

FIGURE 7.113. Cutting of 0.5-mm-thick stainless steel with the diode laser cutting plotter (laser power: 100 W, speed: 1 m/min)

7.2.2.2. Parameter Dependencies and Process Investigations

Relevant Parameters for Laser Beam Cutting

Laser cutting is related to a large number of parameters that must be optimized in order to obtain a good quality and a high cutting speed [7.40]. Below a list of the typically relevant parameters for laser beam cutting is given:

- parameters of the focusing optics: focal length, focal position, type of optics
- assist gas jet and nozzle parameters: type of gas, gas pressure, nozzle design, nozzle stand-off distance (distance nozzle to workpiece)
- cutting speed
- laser beam parameters: power at the workpiece, intensity distribution, beam quality or beam parameter product respectively, wavelength, mode of operation (pulsed or cw), raw beam diameter at the focusing optics, polarization
- workpiece parameters: thickness, material properties (e.g., thermo-physical and optical)

In this section a closer description of these parameters and their influence on the cutting process shall be given. The effects that are associated with the variation of some of these parameters are illustrated by presenting results achieved with the diode laser device.

Focusing of the Laser Beam

The dimensioning of the focusing optics for laser cutting aims at a small focal diameter and at a Rayleigh length typically in the range of about half to double sheet thickness s. This criterion for the Rayleigh length is not always essential but it allows a simple estimation of a suitable F number range. The F number is defined

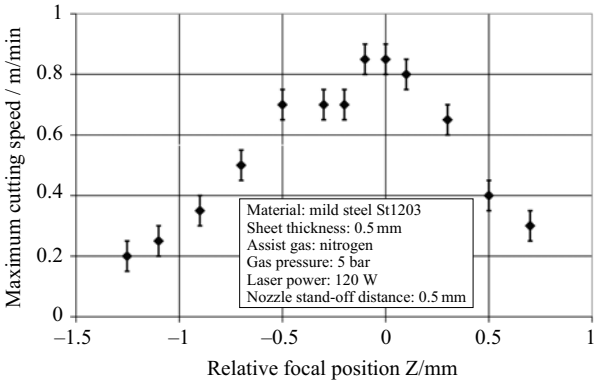

FIGURE 7.114. Variation of the maximum cutting speed with focal position for mild steel

by the ratio of focal length to raw beam diameter at the focusing optics. The focus diameter d_F is proportional to the F number with $d_F = 4 * \mathrm{BPP} * F$. The Rayleigh length z_R is proportional to the square of F with $z_R = 4 * \mathrm{BPP} * F^2$. Neglecting lens aberrations, which are dependent on the lens geometry and the lens material, the calculation of the suitable F number for the cutting plotter device and a sheet thickness of 1 mm results in $2.5 \leq F \leq 5$. Actually the cutting plotter has a BPP of about 20 mm mrad, uses an F number of 3, and achieves a Rayleigh length of about 0.7 mm.

The position of the focus in the material to be cut is an important adjustable parameter of the optical system. Figure 7.114 exemplifies the variation of the maximum cutting speed with the focal position for the inert gas cutting of 0.5-mm-thick mild steel. The diagram demonstrates that the cutting speed passes through a maximum when the focal position is varied. For all subsequent laser cuts that are described in this section the focal position has been adjusted in order to maximize the cutting speed.

Assist Gas Jet and Nozzle Parameters

The cutting nozzle is part of the cutting head and creates the assist gas jet. To ensure rotationally symmetrical conditions, the nozzle and thus the gas jet are adjusted concentrically to the laser beam. Because the laser beam has to pass through the nozzle, its aperture must be large enough to ensure undisturbed beam propagation. The cutting plotter is operated with a standard orifice diameter of 1.5 mm.

A critical parameter of the cutting process is the nozzle stand-off distance. On the one hand for an optimized melt ejection the nozzle has to be located as close as possible to the workpiece; on the other hand the nozzle stand-off must be large enough to avoid collisions. As a compromise, cutting is performed with a nozzle stand-off distance of 0.5 mm.

The assist gas pressure has to be high enough to ensure melt ejection and to avoid burr formation at the bottom edges. Figure 7.115 demonstrates that during inert

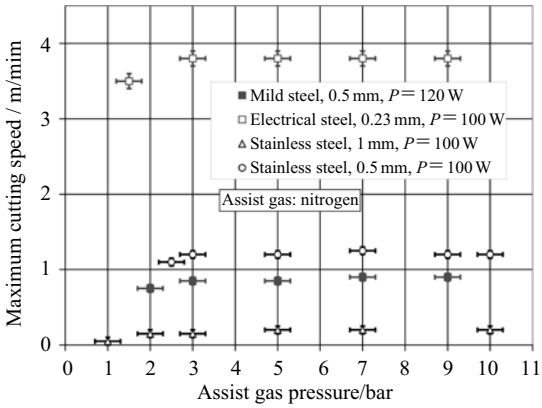

FIGURE 7.115. Variation of the maximum cutting speed with gas pressure for inert gas cutting

gas cutting of 0.23–1-mm-thick steel sheets a pressure of about 5 bar is sufficient to maximize cutting speed. A further increase of the pressure does not increase the obtainable cutting speed, but it allows for a better cutting quality in cutting of stainless steel with nitrogen. When oxygen is used as assist gas for cutting of mild steel, in order to avoid over-reactions resulting in burn-outs on the cut surface, lower pressures have to be used. On the other hand, higher pressures (e.g., above 5 bar) increase the maximum achievable cutting speed. This could be an option for simple separation tasks without high-quality demands.

Cutting Speed and Laser Beam Parameters

As discussed above, the cutting speed has to be adapted according to the available laser beam power. In practice a cutting operation with good performance is obtained at about 80–90% of the maximum cutting speed. In order to achieve an optimum cutting quality, the speed may have to be reduced even more.

Figure 7.116 shows maximum cutting speeds versus laser power for nitrogen assisted cutting of stainless steel sheets with thicknesses between 0.1 and 1 mm. The diagram demonstrates how the maximum cutting speed is increasing monotonously with the laser power at the workpiece and with decreasing sheet thickness. Beside the experimental points also theoretical curves are included. They have been calculated with the computer simulation program CALCut [7.43]. It is based on a self-consistent cutting model taking into account beam propagation and absorption within the kerf, heat conduction into the material, melting, and vaporization of the kerf volume as well as melt ejection out of the kerf by the cutting gas jet and vapor gradient induced melt flow. The special beam properties of the used diode laser are represented within the computer simulation by an equivalent circular spot with identical spot area and Rayleigh length and a Gaussian beam profile. The equations given at the beginning of this chapter are a simplified approximation of the three-dimensional, spatially resolved model used within CALCut. The theoretical curves in Fig. 7.116 correspond quite well with the

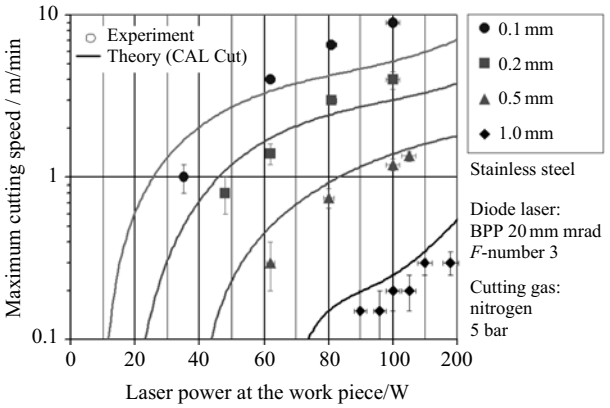

FIGURE 7.116. Comparison of calculated and measured maximum cutting speeds for nitrogen-assisted cutting of different stainless steel sheet thicknesses at varying laser powers

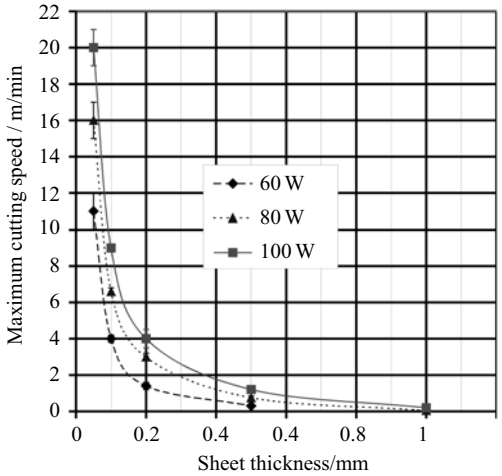

FIGURE 7.117. Variation of the maximum cutting speed with sheet thickness and laser power for nitrogen assisted cutting of stainless steel

practical results achieved with the diode laser, thereby demonstrating the suitable conditions offered by this new laser type for the investigated process regime. Both, the theoretical curves and the practical points in Fig. 7.116 reveal that a minimum power, increasing with sheet thickness, is required even for very low processing speeds, if a proper cutting process shall develop. Heat conduction losses into the surrounding material beside the kerf are responsible for this threshold to be overcome.

Figure 7.117 shows the maximum cutting speeds versus sheet thickness for stainless steel. The course of the curves has the typical hyperbolic appearance,

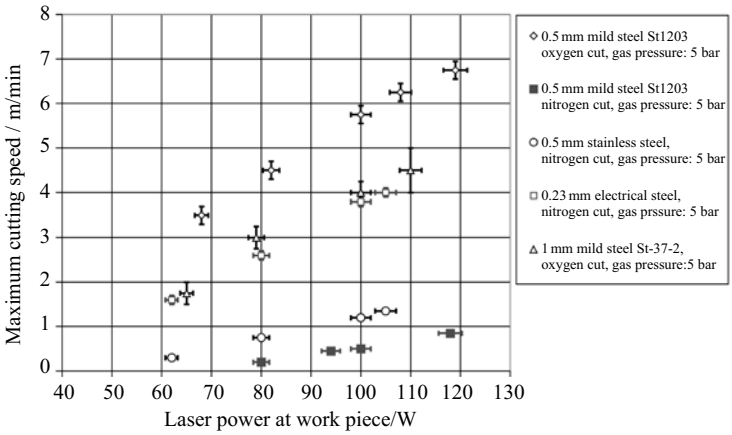

FIGURE 7.118. Variation of the maximum cutting speed with laser power for metal sheets

well known from the so-called "cutting curves" of thermal processes, depicting cutting speed versus material thickness.

Variations of the maximum cutting speed with the laser power for mild steel (0.5- and 1-mm thickness), electrical steel (0.23 mm), and stainless steel (0.5 mm) are compared in Fig. 7.118. The mild steel sheets were also cut with oxygen, whereas stainless steel and electrical steel were processed with the assist gas nitrogen only. The maximum cutting speed is increasing linearly with the laser power at the workpiece. For 0.5-mm-thick mild steel sheets at a power of 100 W, the use of the process gas oxygen allows for seven times higher cutting speeds in mild steel than the process gas nitrogen. Comparing nitrogen cutting of stainless steel and mild steel shows that stainless steel can be cut faster due to its lower thermal conductivity. Moreover, it has been demonstrated also that organic materials such as leather, paper, pasteboard, and cotton fabric can be cut with the diode laser device. Figure 7.119 shows the corresponding diagram of speed versus power.

Diode lasers emit linearly polarized radiation with a rectangular-shaped intensity distribution. Because the cutting plotter applies the technique of polarization coupling, its beam contains two linear polarization states that are oriented orthogonal to each other. The diode laser device was operated in the cw (continuous wave) mode only. Even though these conditions are not ideal for the cutting of contours the feasibility of contour cuts could be demonstrated (see below).

7.2.2.3. Application Results

Achieved Cutting Speeds and Cutting Qualities

Figure 7.120 summarizes the achieved maximum cutting speeds in metals and non-metals using 100 W laser power at the workpiece. For example, oxygen cuts in 0.5–1-mm-thick hot zinc dipped and uncoated mild steel sheets allow for

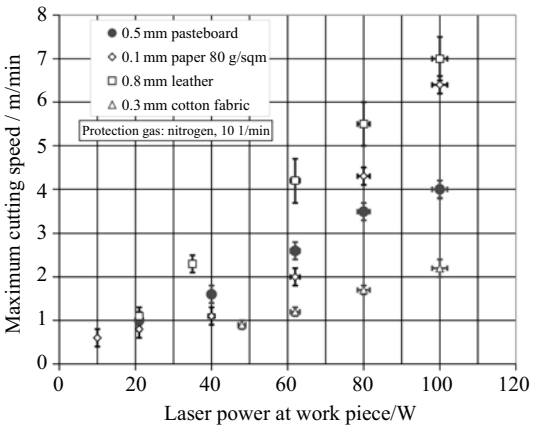

FIGURE 7.119. Variation of the maximum cutting speed with laser power for nonmetals

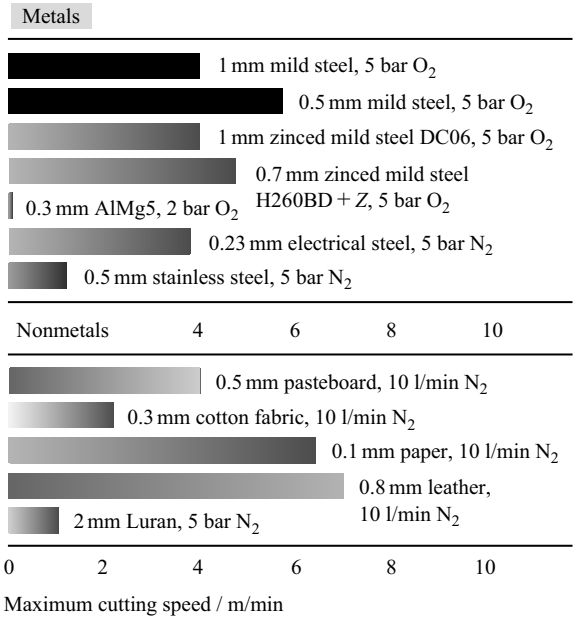

FIGURE 7.120. Maximum cutting speed for different metals and nonmetals at 100 W laser power

maximum cutting speeds of 4 to 6 m/min. Using nitrogen as cutting gas, 0.23-mm-thick electrical steel specimens can be cut with about 4 m/min. Cuts in aluminum (0.3-mm-thick AlMg5) are feasible but only at a very low speed and quality level. In addition it was also demonstrated that plastics such as Luran (trade name BASF) can be cut with the diode laser device.

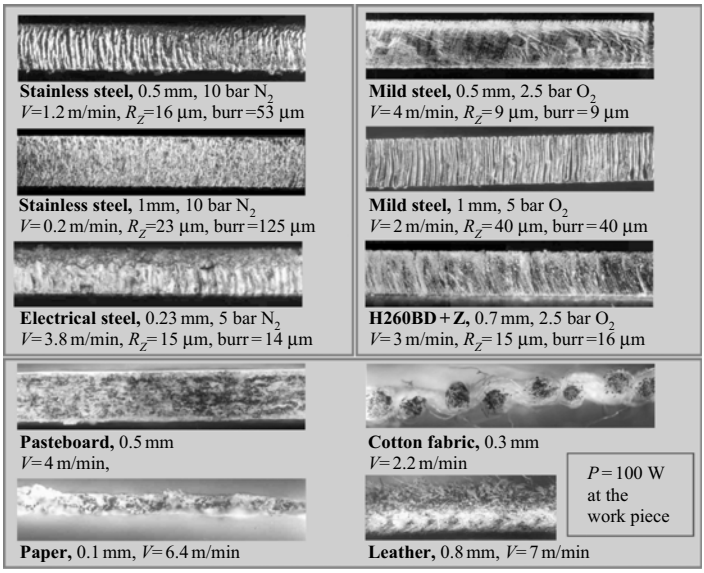

FIGURE 7.121. Cut edges for nitrogen cuts, oxygen cuts, and sublimation cuts

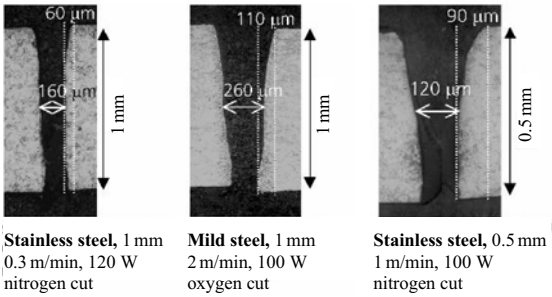

FIGURE 7.122. Cut kerfs for stainless steel and mild steel

Figure 7.121 shows the cut edges of fusion cuts in stainless steel and electrical steel and of oxygen cuts in mild steel and hot-zinc-dipped mild steel (H260BD + Z, Thyssen Krupp Steel). Moreover, sublimation cuts in organic non-metals are shown. In the sheet-thickness range of up to 0.7 mm cut-edge roughness of about 10–20 µm and a burr formation below 50 µm are achieved. For a sheet thickness of 1 mm the roughness rises to approximately 20–40 µm and the burr reaches values of up to about 125 µm. Depending on the type of material and the specimen thickness, the cut kerf width amounts to 120–260 µm (Fig. 7.122).

In Fig. 7.123 examples for contour cuts in 0.5-mm-thick pasteboard and 0.5-mm-thick stainless steel are presented.

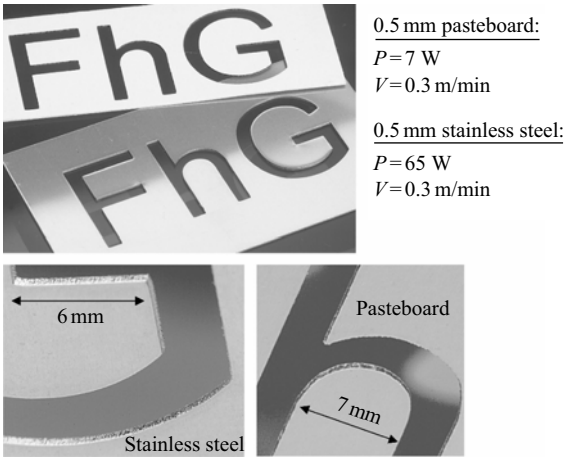

FIGURE 7.123. Examples for contour cuts

Economic Efficiency of Laser Cutting with HPDL in Comparison to State of the Art CO_2 and Nd:YAG Lasers

For laser cutting applications in the power range of about 100 W today usually pulsed Nd:YAG and cw CO_2 lasers are used. To check the economic competitiveness of the diode laser cutting plotter a calculation of profitability for laser cutting with an average power of about 100 W using a CO_2 laser, a Nd:YAG laser, and the diode laser device was carried out. The basis of the computation was a depreciation period of 5 years, a two-shift operation, and an availability of the laser device of 95%. Using these input requirements the calculation yielded the normalized fixed and running costs per hour shown in Fig. 7.124. The fixed costs include the expenses for the laser, the chiller, the handling system, the beam-guiding system, the beam-forming optics, the cutting head, and the rent of the floor space. Maintenance charges, electricity, assist gas expenses, and the costs for an operator make up the running costs.

Figure 7.124 demonstrates that the CO_2 laser is still the most economical choice. In addition, it offers an excellent beam quality. Due to their wavelength, CO_2 lasers in the power range of about 100 W are particularly convenient for the cutting of nonmetals like glass, wood, or plastics. However, cutting of thin metal sheets is also feasible. The Nd:YAG laser is the most expensive of the three considered systems. It allows the cutting of metal sheets with maximum precision. The Nd:YAG laser is also favored during processing of highly reflective and heat-conducting metals. Compared to CO_2 and Nd:YAG lasers, the diode laser device offers the lowest beam quality. Its fixed and running costs range between that of the CO_2 and the Nd:YAG laser system. But the total costs of the three systems only differ less than 10%, due to significant contributions of equipment besides the laser source to the complete systems and costs. Considering that the presented calculation of

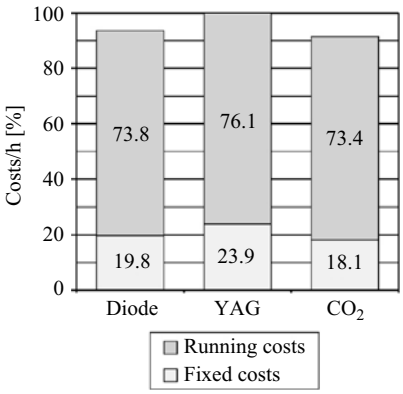

FIGURE 7.124. Comparison of the fixed and running costs for fusion cutting with the diode laser cutting plotter, a Nd:YAG laser and a CO_2 laser

profitability treats only one typical example and does not represent the actual conditions at a specific workshop, one can only state that the costs for cutting with the high-power diode laser system are similar to those using Nd:YAG or CO_2 laser systems. Consequently, the machining tasks and not the costs determine which of the three lasers is applied. Today the diode laser is favorable for applications that explicitly profit from a compact, light-weight cutting system and require only a medium cut quality. Moreover, in contrast to the CO_2 laser system, the diode laser device allows for a fiber coupling. It is foreseeable that with declining acquisition costs and increasing beam quality, high-power diode laser systems are on the way to become interesting for a variety of cutting applications.

7.2.3. Single-Shot Cutting-to-Length

D. Petring, B. Seme

7.2.3.1. Process Principles and Equipment

The single-shot cutting-to-length process and oxygen cutting with the annular beam device described in the next section use process-adapted beam shapes. To generate these beam geometries, the modularity of the diode lasers is utilized. Single-shot cutting-to-length works with a diode laser line beam generated by a linear arrangement of diode stacks and a subsequent beam homogenization and focusing. That way, an approximately 35-mm-long laser focus with a beam waist width of 0.2 mm and a Rayleigh length of about 0.5 mm is obtained. The maximum power at the workpiece amounts to 660 W. During single-shot cutting-to-length, the line beam is applied to irradiate narrow band material simultaneously along its entire width using one single laser pulse. At the same time the band section is pulled apart to generate the cut. Thus single-shot cutting-to-length of metals is a combination of a melting or vaporization process and a tearing-up process. Phase

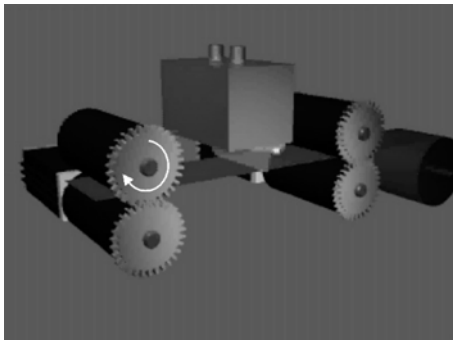

FIGURE 7.125. Principle of single-shot cutting-to-length

transition by vaporization is dominant for the processing of non-metals such as pasteboard. Due to the simultaneous processing of the complete cutting track of the specimen, the cutting time, which is by definition equal to the pulse duration necessary for cutting, does not depend on the width of the processed band as long as the required beam power per cutting length is available. In fact the single-shot cutting-to-length process could be described as some kind of laser punching operation.

To develop and demonstrate the single-shot cutting-to-length process, a demonstrator device has been set up. The principle of the device is illustrated in Fig. 7.125. It consists of the diode laser and two pairs of rollers that are driven by computer-controlled electric motors. During laser processing the right pair of rollers (Fig. 7.125) is fixed, and the other one generates the desired band tension. After the separation process, the cut part is ejected by the left pair of rollers and the right pair feeds the remaining band forward in order to prepare the next cut. Figure 7.126 shows the real demonstrator setup. To protect the optics and to reduce oxidation of the specimen nitrogen-shielding gas is supplied to the interaction zone via a slit-shaped nozzle where the laser beam is passing through.

7.2.3.2. Parameter Dependencies and Process Investigations

The tearing-up operation of the single-shot cutting-to-length process is determined by parameters that are not relevant in conventional laser cutting, namely, the band tension and the specimen's tensile strength. These parameters influence the cutting time. Figure 7.127 shows the cutting times versus the applied band tension for optimized focal positions. The sample material is 0.23-mm-thick electrical steel (tensile strength: 350 N/mm^2), 0.2-mm-thick stainless steel (tensile strength: 650 N/mm^2) and 0.1-mm-thick stainless steel. A laser power of 660 W at the workpiece and a bandwidth of 30 mm are used. At minimum band tensions the cutting times are determined by the fusing times of the specimens. Due to the higher thermal conductivity and the slightly larger thickness of the electrical steel band, its fusing time is longer than that of the 0.2-mm-thick stainless steel

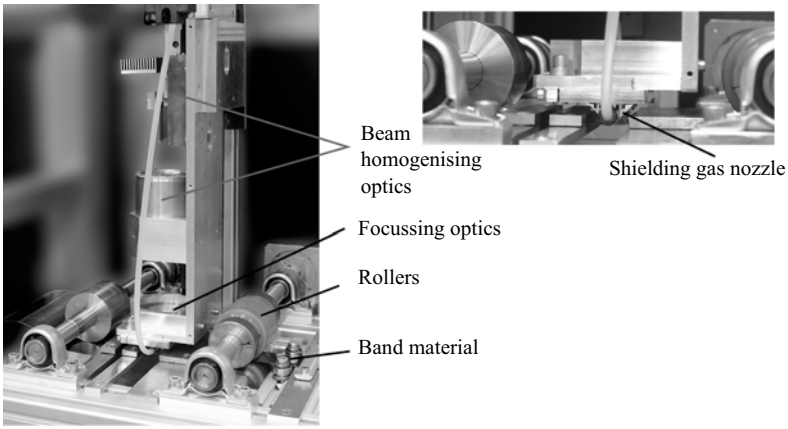

FIGURE 7.126. Demonstrator setup for single-shot cutting-to-length

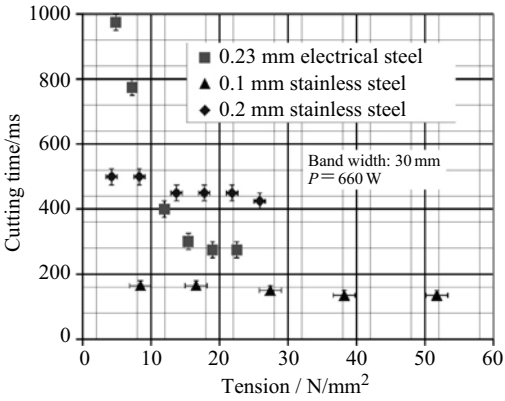

FIGURE 7.127. Variation of cutting time with band tension for different materials

samples. Hence, the cutting time curve for electrical steel starts at a longer time than the curve for stainless steel. With increasing band tension the electrical steel curve declines faster than the curves for stainless steel. This is due to the lower tensile strength of the electrical steel in comparison to stainless steel. The course of the curves reveals that with increasing band tension in addition to the melting of the track, the tearing process increasingly participates in the separation process. Thus at tensions above approximately 12 N/mm^2 0.23-mm-thick electrical steel can be cut faster than 0.2-mm-thick stainless steel. Of course, the 0.2-mm-thick stainless steel material requires longer cutting times than 0.1-mm-thick stainless steel specimens.

To calculate the specimens' fusing times the heating process was simulated with the LaserWeld3D software [7.44]. This simulation is based on the Rosenthal

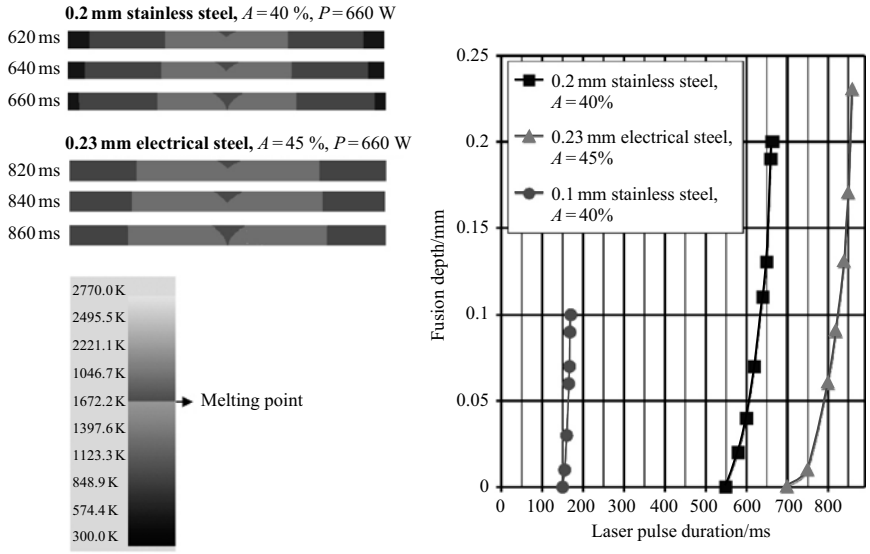

FIGURE 7.128. Simulation of the melting process for stainless steel and electrical steel with LaserWeld3D

solution of the heat conduction equation with consideration of finite workpiece thicknesses. The calculated propagation of the melt front is pictured with the corresponding processing time in Fig. 7.128. In the computations a laser line width of 0.2 mm and a laser power of 660 W are used. The assumed absorptivities A of 40% and 45% were measured spectrometrically at polished samples ($T \approx 300$ K). According to Fig. 7.128 the simulation results in fusing times of 170 ms and 660 ms for 0.1- and 0.2-mm-thick stainless steel, respectively. For 0.23-mm-thick electrical steel the calculation yields a fusing time of 860 ms. The calculated fusing times and the measured cutting times at minimum band tension (165, 500, and 975 ms, Fig. 7.127) are qualitatively in good agreement. Figure 7.128 also shows that melt is formed only after approximately 80% of the cutting time. Obviously a dominant time period is required for heating the track up to the melting temperature. In the remaining 20% of the processing time the melt front propagates from the irradiated top of the sheet to the bottom.

7.2.3.3. Application Results

Figure 7.129 shows cuts in 0.23-mm-thick electrical steel, 0.2- and 0.1-mm-thick stainless steel, and 0.5-mm-thick pasteboard using different band tensions σ. The figure illustrates that for electrical steel and stainless steel best cutting qualities are obtained in the range of high band tensions and thus short cutting times t. For decreasing band tensions and increasing cutting times the melting volume increases and melt adherences at the cut edges arise. However, if the pasteboard samples tear up due to the applied band tension, cutting quality is reduced drastically

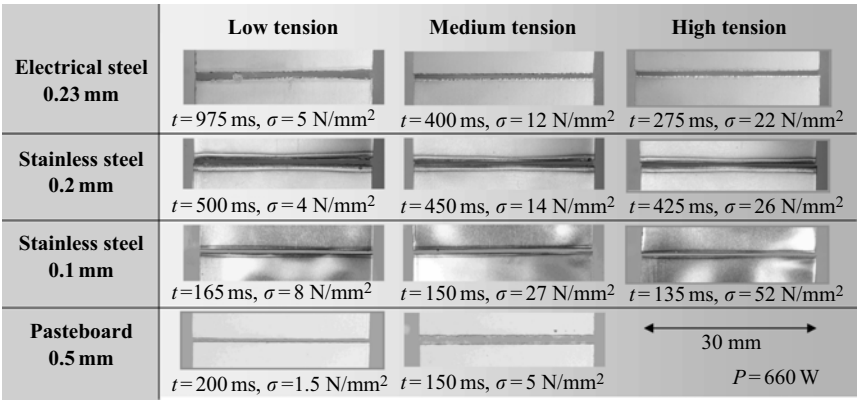

FIGURE 7.129. Cuts in electrical steel, stainless steel and pasteboard using different band tensions

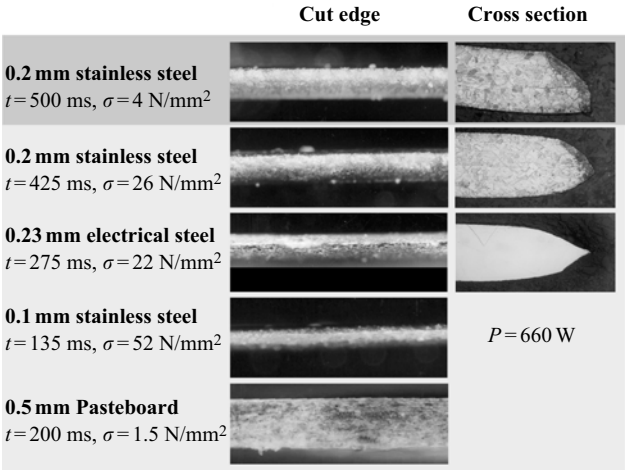

FIGURE 7.130. Cut edges and cross sections for steel and pasteboard specimens

due to fraying (see sample with $\sigma = 5$ N/mm^2 in Fig. 7.129). Therefore, best cutting results in pasteboard are obtained for minimum band tensions. It can be seen that optimal qualities are achieved at cutting times ranging from 135 ms to 425 ms, depending on the type of material and the sample's thickness. Thus for the used laser power, bandwidth, and materials, a typical cycle rate of the single-shot cutting-to-length device is some parts per second.

Figure 7.130 shows cut edges and cross sections for optimized parameters are shown. Apart from the first example at the top of the figure, the cut edges are free of burr and the shapes of the cross sections indicate that the samples tear up before they melt through when appropriate band tensions are applied. At the

top of Fig. 7.130 a stainless steel sample that melted through completely at low band tension is pictured for comparison. The associated cross section bears a great resemblance to the triangular calculated cross section for $t = 660$ ms shown in Fig. 7.128.

The single-shot cutting-to-length technique competes with mechanical shear cutting and punching processes. Mechanical processes are typically cost-effective for cutting of standard geometries and large lot sizes, whereas laser cutting reaches profitability typically for processing of varying, complex contours and low lot sizes. The punching with a contour-adapted laser beam is a completely new approach that combines laser cutting and punching. Laser punching avoids some of the disadvantages of mechanical punching, namely, the tool-wear and the high noise level. But it still possesses the disadvantage of missing flexibility concerning the producible contours. In addition the equipment costs for laser punching are high compared to pure mechanical machines. From this point of view optical cutting-to-length becomes attractive only if in the future the costs for modular diode laser systems are declining to about the cost level of a mechanical punch. On the other hand, new technologies for the creation of variable beam patterns with modular diode lasers involving scanner technologies, flexible beam guiding equipment or two-dimensional beam arrays may expand the future potential of the single-shot approach significantly by simultaneously allowing for short cycle times and high flexibility.

7.2.4. Oxygen Cutting with Annular Beam

D. Petring, B. Seme

7.2.4.1. Process Principles and Equipment

Oxygen Cutting Variants

To separate mild steel plates in industrial applications, the laser beam oxygen cutting process has been established for many years. Some basics of this technique have already been discussed in section 7.2.2.1. Due to the use of the assist gas oxygen an additional energy of about 4,800 kJ per kg burned iron is made available for cutting. Laser beam oxygen cutting is typically applied for machining plate thicknesses of up to about 20 mm. Processing thicker plates results in only marginally higher cutting speeds and partly worse qualities compared to the cheaper autogenous flame cutting techniques. By a combination of the laser beam oxygen cutting process and the autogenous cutting process, good cutting qualities and higher processing speeds than in the case of autogenous cutting can be achieved even for plate thicknesses above 20 mm. This combined or hybrid process is called burnoff-stabilized laser beam oxygen cutting [7.45, 7.46]. In this paragraph autogenous and burnoff-stabilized laser beam oxygen cutting of 10-, 20-, and 30-mm-thick plates with an annular diode laser beam device is described.

Autogenous Cutting

A cutting process is called autogenous if the power P_C necessary for cutting (see section 7.2.2.1) is supplied exclusively by the energy of the iron combustion reaction. To heat up the workpiece to the ignition temperature ($\approx$1350 K) that is needed for starting and sustaining the reaction, an external heat source like a flame or a laser beam is required. The heat source has to surround the oxygen jet generated by the cutting nozzle so that the top side of the cutting front is kept on ignition temperature constantly even if 2D contours are cut. Thus an annular diode laser beam is ideally suited to take over the preheating task during autogenous cutting.

The condition $P_C = P_r$ for an autogenous cutting process allows the calculation of the necessary burning proportion of the kerf volume. For the cutting of 10-mm mild steel with a speed of 1 m/min and a kerf width of 2 mm a power $P_C = 3$ kW is required, corresponding to a burning proportion of about 25%. In principle, the necessary burning proportion for cutting does not depend on the thickness of the workpiece. Hence there is no upper limit for the plate thickness suitable for autogenous cutting. But the maximal achievable burning proportion and thus the maximal achievable cutting speed during autogenous cutting is limited by the rate of diffusion of the reaction partners iron and oxygen through the iron oxide melt und the gas boundary layer on the cutting front. For mild steel plate thicknesses of 10 mm and more, autogenous cutting speeds are in the range of 1 m/min or lower. An increase in the cutting speed can be obtained by guiding a laser beam and thus additional energy into the cutting kerf. This is done in case of the burnoff-stabilized laser beam oxygen cutting (see corresponding section below).

Laser Beam Oxygen Cutting

Laser beam oxygen cutting differs from the autogenous cutting process essentially by the relative arrangement of the heat source and the oxygen jet. During autogenous cutting the top side of the cutting kerf is heated extensively by a heat source that surrounds the gas jet, whereas the oxygen-assisted laser cutting process uses a focused laser beam that passes coaxially through the cutting nozzle. At the workpiece's surface the diameter of the laser beam is much smaller than the diameter of the oxygen jet. This configuration allows the ignition of the iron combustion reaction inside the oxygen jet but outside of the laser beam because the material around the laser beam heats up to the ignition temperature by thermal conduction. Thus, for low cutting speeds ($<$1 m/min) the burning front tends to run out of the area illuminated by the laser beam. However, this pre-burning is unstable because the combustion expires without contact to the laser beam due to loss mechanisms like heat conduction and the formation of passivating scales. The reaction starts again, if the laser beam catches up the cutting front by virtue of the feed. As a result of these periodic interruptions of the cutting process rough drag lines appear at the cut edges, and the liberated average reaction power is reduced [7.47]. This power leakage limits the maximal processable plate thickness for laser beam oxygen cutting.

Burnoff-Stabilized Laser Beam Oxygen Cutting

In addition to a focused laser beam that passes through the cutting nozzle, the burnoff-stabilized laser beam oxygen cutting process applies a second heat source, as for example, an annular diode laser beam that surrounds the cutting nozzle and heats up the top side of the cutting kerf. In so doing the described loss mechanisms (see above) are compensated and the iron combustion is stabilized. Thus burnoff-stabilized laser beam oxygen cutting enables the processing of plate thicknesses above 20 mm with a cut edge roughness below 50 μm. The maximal achievable cutting speeds are determined by the power supplied to the interaction zone via the central laser beam that passes through the nozzle. Exactly as with the autogenous cutting process, the maximal processable plate thickness is theoretically unlimited. [7.45, 7.46].

The Equipment

The annular diode laser beam device contains ten adjustable laser modules that are coaxially arranged around a hollow cylindrical carrier so that a central passage aperture is formed. For oxygen cutting applications, the beam spots of the modules are adjusted in such a way that an annular preheating laser focus with a median diameter of 5 mm, a width of about 1 mm, and a maximal total power of about 2 kW is formed at the workpiece's surface. Oxygen is feed toward the center of the annular beam via the passage aperture and a Laval nozzle that is located at the aperture's end. For burnoff-stabilized laser beam oxygen cutting applications, the device features a central focusing ZnSe meniscus lens with a focal length of 15 inches. That way an additional CO_2 laser beam can be directed through the passage aperture and the cutting nozzle. To protect the setup against sputter and staining by fume deposition a housing with an annular beam outlet window is used. Furthermore a cross-jet nozzle that generates a circumferential, radially outward directed air jet is integrated (Fig. 7.131).

7.2.4.2. Parameter Dependencies and Process Investigations

The Laval Nozzle and Gas Jet Parameters

For autogenous and burnoff-stabilized laser beam oxygen cutting, convergent-divergent Laval nozzles are common [7.45, 7.46]. In contrast to simple conical nozzles Laval nozzles deliver a well-expanded free gas jet over a long range. The optimal gas pressures as well as the features of the generated gas jet depend on the nozzle's internal contour. Schlieren measurements revealed that the commercial Laval nozzles FK4 60-100 (Hinsdorfer Düsen GmbH) and Vadura 1215A 60-100 (Messer Griesheim) allow the generation of about 30 mm long free gas jets. Hence they are qualified for cutting plates with thicknesses of up to 30 mm. The mentioned nozzles possess a smallest aperture of 1.0 and 1.6 mm as well as an opening diameter of 1.9 and 2.6 mm, respectively. The opening diameter of the nozzle determines the diameter of the generated oxygen jet and therewith the cutting kerf width.

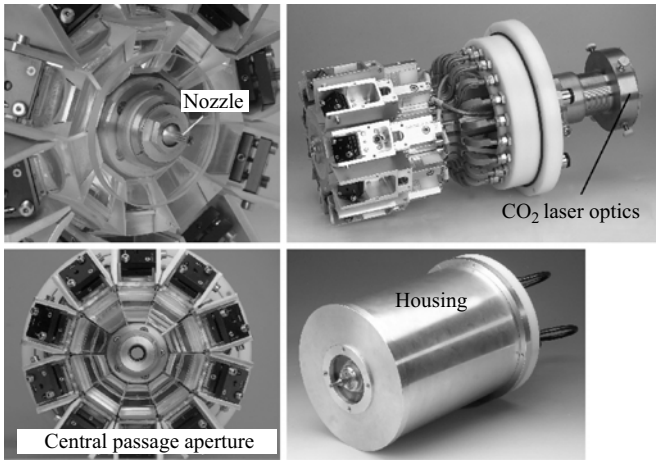

FIGURE 7.131. The annular diode laser beam device

Regarding the gas jet parameters also the purity of the oxygen is of importance. Impurities in the oxygen jet result in a reduction of the maximum cutting speed and a degradation of the cutting quality. Thus the used oxygen should be as pure as possible and the nozzle stand-off distance must be minimized in order to avoid a pollution of the oxygen jet by sucking in from ambient air. In practice an oxygen purity of 99.95% (3.5) has been proved as suitable. During cutting with the annular diode laser beam device a nozzle stand-off distance of 1.5 mm was used. For smaller distances the nozzle body hinders the free propagation of the diode laser beam and the danger of nozzle damage due to the close-by cutting process increases.

Laser Beam Parameters and the Focusing Optics

Figure 7.132 shows the variation of the maximum cutting speed with the power of the annular diode laser beam for autogenous cutting of 10-mm-thick mild steel using the nozzle FK4 60-100 and an optimized oxygen pressure of 15 bar. The annular beam heats the top side of the cutting front to ignition temperature but launches no laser power into the cutting kerf. Thus the diode laser makes no contribution to the power P_C necessary for cutting and hence the laser power can be reduced from 1,800 W to 700 W without a corresponding decrease of the maximum cutting speed. Only if the laser power is reduced so far that the ignition temperature at the sample's surface is no longer reached does cutting become infeasible. A diode laser power of 700 W is sufficient for cutting. Higher powers are not necessary to reach and sustain the ignition temperature and hence they would only disturb the cutting process by excessive melting of the top cut edges. Moreover, Fig. 7.132 demonstrates that the maximum cutting speed during autogenous cutting is limited by the speed of the iron combustion reaction and not by the available diode laser power. Figure 7.133 shows the autogenous cutting

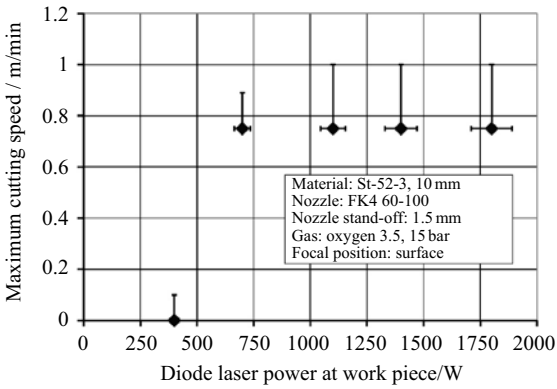

FIGURE 7.132. Variation of the maximal cutting speed with laser power for autogenous cutting

FIGURE 7.133. Autogenous cutting of 10-mm mild steel St52-3 with 700-W diode laser power and $v = 0.45$ m/min

of 10 mm mild steel with a diode laser power of only 700 W and a speed of 0.45 m/min.

For burnoff-stabilized laser beam oxygen cutting the central laser optics of the annular diode laser beam device was dimensioned in such a way that the focused beam is small enough to pass safely through the Laval nozzle when the focus is located within the nozzle's smallest aperture. Moreover, the Rayleigh length has to be large enough to ensure an acceptable propagation of the beam through the kerf. Focusing the available CO_2 laser of the beam quality $M^2 = 3.8$ using an F number of 15 delivers a suitable caustic for cutting with the Vadura 1215A 60-100 nozzle. The focal diameter amounts to 0.8 mm and the Rayleigh length is 12 mm.

Application Results

Figure 7.134 shows the achieved maximum cutting speeds during autogenous and burnoff-stabilized laser beam oxygen cutting of mild steel versus the plate thickness. Thereby optimized oxygen pressures and a diode laser power of 700 W at the workpiece were used. In the considered plate thickness range of 10–30 mm autogenous cutting with the nozzle FK4 60-100 enables processing speeds of 0.34 to 0.75 m/min. The corresponding cut kerf widths amount to 3 mm, measured at half of the plate thickness. Autogenous cutting of 30-mm-thick mild steel with the larger nozzle Vadura 1215A 60-100 allows for a 25% higher cutting speed compared to the nozzle FK4 60-100. But this rise of the cutting speed is associated with a bigger cut kerf width of 4.5 mm and with rougher cut edges (Fig. 7.136). The specimens pictured in Fig. 7.135 demonstrate that the homogeneity of the annular diode laser beam's intensity distribution is sufficient not only for symmetric straight cuts but also for autogenous contour cuts.

Burnoff-stabilized laser beam oxygen cutting of 10-, 20-, and 30-mm-thick plates using the nozzle Vadura 1215A 60-100 and a CO_2 laser power of 3.7 kW at the workpiece enables cutting speeds of 0.55 to 1.6 m/min. Figure 7.136 shows the achieved cut edge and cut kerf for the burnoff-stabilized cutting of 30-mm mild steel. Compared to autogenous cutting (top of Fig. 7.136) the cut kerf width measured at half of the plate thickness is about 1-mm narrower and the maximum cutting speed is about 30% higher. A CO_2 laser power of 4.7 kW at the workpiece allows for an even 50% higher cutting speed in 30-mm-mild steel compared to autogenous cutting (Fig. 7.134). To demonstrate the effect of the burnoff-stabilization on cut quality Fig. 7.136 also displays a cut edge generated with the CO_2 laser only. Apart from the missing annular diode laser beam, the used cutting parameters are identical to those applied for the burnoff-stabilized cut presented in the middle of Fig. 7.136. A comparison of the cuts exhibits a considerable smoothing of the

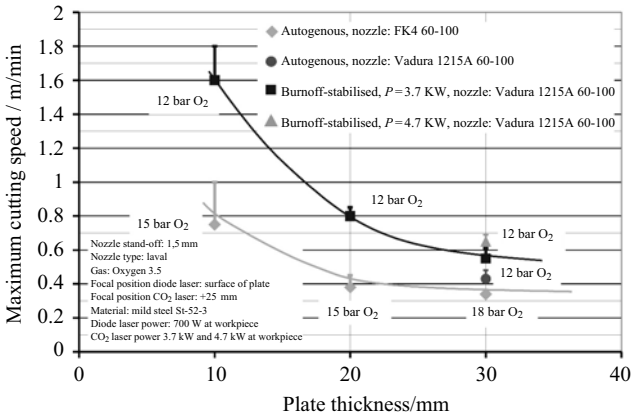

FIGURE 7.134. Variation of the maximum cutting speed with plate thickness for autogenous and burnoff-stabilized laser beam oxygen cutting of mild steel

FIGURE 7.135. Autogenous contour cuts in 10 mm mild steel ($v = 0.45$ m/min, nozzle: FK4 60-100)

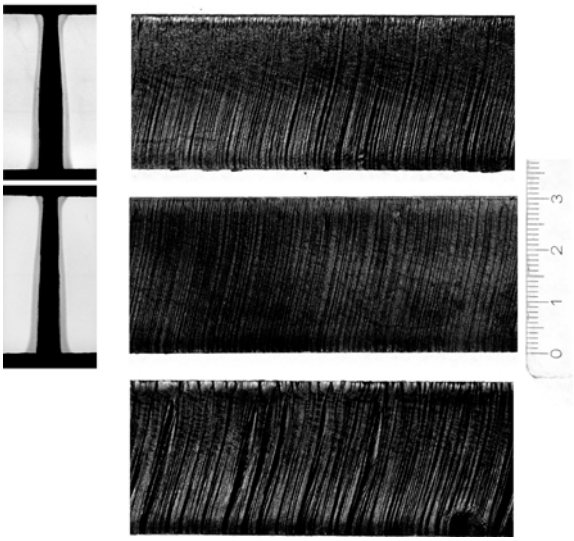

FIGURE 7.136. Cut kerfs and cut edges for autogenous cutting, burnoff-stabilized cutting and laser beam oxygen cutting with the CO_2 laser only

cut edge due to the burnoff-stabilization by the additional use of the annular diode laser beam.

Of course, the annular diode laser is a much more expensive heat source than a simple flame torch. But in comparison to a flame, the diode laser allows for higher intensities, smaller preheating spots and precisely controllable preheating powers. Consequently, the annular diode laser enables a faster start of the cuts, because ignition temperature can be reached very quickly. Moreover, it allows for smaller heat-affected zones and only minimum melting of the cutting edges compared to conventional flame cutting. Especially in combination with a central high-power laser beam, the cutting performance clearly surpasses flame cutting as well as laser oxygen cutting.

7.2.5. Laser-Assisted Machining

S. Bausch, A. Demmer, K. Groll, R. Herold, A. Mette

For manufacturing companies increasing globalization is resulting in a constant pressure to improve their products and manufacturing techniques. Technical progress leads to innovative products, whose individual components have to fulfill extremely accurate constructional demands. Wear resistance, temperature strength, weight reduction, and chemical endurance are substantial requirements requested in performance specifications for components in different industrial branches. A demand for efficient components is coming from aircraft and automotive industries as well as from the steel processing, mechanical bearings, medicine technology, and chemical industries. The rising demands on technical products regarding functionality, quality, and individuality can be fulfilled solely by the use of innovative, high-performance materials. Developments in materials technology are resulting in the emergence of materials whose outstanding characteristics often hamper manufacturing and hence a successful introduction into the market. The production of complex-shaped parts from advanced materials by conventional machining is characterized by extremely high tool wear, which impairs the attainable production quality, time, and costs. Previous approaches to increase economic efficiency focused on the development of more efficient cutting materials, enabling higher material removal rates and tool life, but at the same time creating higher tooling expenses. Alternative manufacturing concepts, in which the properties of the material for the subsequent machining are modified by a thermal treatment, require additional production steps and thereby increase setup and transportation times. Therefore the conventional manufacturing of components from advanced materials is, as a rule, characterized by increased production times and costs.

Thus innovative materials, in combination with efficient manufacturing technologies, are solely responsible for opening up new perspectives for the stable increase of competitive ability to the production industry. Technical options which emerge from classical approaches to process optimization are, however, frequently inadequate. The production of complex-shaped components from difficult to machine materials, for example, high-temperature-resistant steel, titanium,

nickel- and cobalt-based alloys, fiber- and particle-reinforced metals, and composites as well as advanced ceramics, requires the development of corresponding machining technologies that take into account the specific properties of the material and which are, at the same time, economically efficient. An approach to overcome the existing technical limitations and to increase the performance of conventional manufacturing technologies is hot machining. The thermal influence on the material's mechanical characteristics by using simultaneous heating during the machining process improves the material's machinability. Previous investigations took place with several different energy sources, such as flame, friction, resistance, and plasma heating. One common drawback of these heating sources was the insufficient power density at the workpiece. New perspectives arise as a result of the use of laser technology (laser-assisted machining). The demands on the heat source are suitably fulfilled by the laser because of its high power density, the locally constricted energy input, its flexible handling, and the reproducibility of its energy output. Particularly, modular, high-power diode lasers enable the design of application-adapted beam profiles and place at the user's disposal almost freely definable focal spot geometries and intensity distributions for the respective application.

7.2.5.1. Process Principles and Equipment

In laser-assisted machining operations, a laser beam is used to apply external energy in order to heat the material continuously. The energy absorbed by the material surface results in rapid heating of the material in the subsurface area. The objective is to achieve heating which is as strictly localized as possible and which affects only the machining zone directly ahead of the tool contact. The loss of material strength as a result of heating improves the machining characteristics considerably, thus increasing the efficiency of the process in terms of removal rates and tool service life (Fig. 7.137). When advanced ceramic materials are machined, heating of the material causes the glass phase in the material structure to plasticize. The amorphous glass phase demonstrates visco-elastic behavior at increased temperatures. Therefore, the deformation resistance is reduced, causing localized loss of material strength in the shearing zone and enabling ceramic to be machined using a geometrically defined cutting edge.

The decisive prerequisite for laser-assisted machining is the reduction of material strength at elevated temperatures, thereby improving the material's machining characteristics. The use of laser-assisted processes to machine advanced materials is economically viable only under these conditions. The selective and controlled introduction of heat is the principal condition for the reliable application of laser-assisted milling and turning. The objective is always to produce the required temperature profile in the material, which is the result of the relative motion between the material surface and the focal spot of the laser. Beyond the parameters relating to the application of heat, the cutting parameters, cutting speed, feed, and depth also exert considerable influence on the quality of the process – not only on chip formation itself but also indirectly on the temperature distribution in

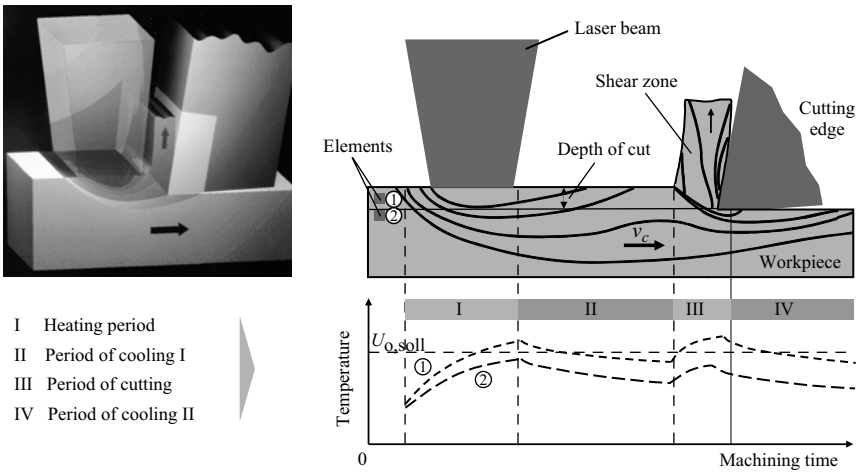

FIGURE 7.137. Laser-assisted machining: Principle and distribution of temperature in the cutting zone

the machining zone. In order to achieve quality and cost-oriented process design, it is essential to coordinate all process variables, taking into account all possible interactions. In addition to understanding the process technology, the availability of suitable machine tools, enabling an optimized positioning of the focal spot in relation to the tool contact zone, is vital for the successful use of laser-assisted technologies.

Machine Tool Prototype for Laser-Assisted Milling

The machine tool prototype for laser-assisted milling is based on a three-axis-portal milling machine with a vertically arranged spindle. The machine consists of three Cartesian linear axes. The workpiece is positioned with the *x*-axis, and the spindle is positioned with the portal consisting of the *y*- and *z*-axes. Furthermore, the machine tool is equipped with a tilt-turntable. The table has a perpetually turning c-axis and an $\pm 180°$ tilting a-axis. By this means it is ensured that the normal vector of the workpiece surface can always be positioned parallel to the rotational axis of the spindle. All five axes are closed loop controlled by the control system and are able to interpolate with each other. Thereby simultaneous five-axis machining and also the machining of free form surfaces are possible.

As already mentioned, it is essential for the realization of laser-assisted machining that the material volume to be chipped is sufficiently warmed up in the chip section, in order to ensure that an improvement of the machining properties is seen by the reduction of process forces and a possible higher stock removal rate. The warming up of the chip section is effected by three fiber-coupled diode lasers, each with an output of 1 kW and a focal spot of $9 \times 2\,\text{mm}^2$. With specially designed optics, which are detailed later on, the three focal spots are arranged in a circle

segment around the milling cutter. The focal spot position and size are laid out in such a way that the chip section from even the largest cutting width of 30 mm can be sufficiently warmed up.

During the machining of free-form surfaces, a constant change of the contact conditions of the milling tool takes place, so that a flexible positioning of the laser focal spots must be ensured. Furthermore, it is necessary to use smaller milling tools with a diameter down to 8 mm and additionally a variation of the tool length in order to achieve a flexible rough-down process of the workpieces. Due to these geometrical changes and the constant variation of the contact conditions, it is necessary that the position and form of the focal spot can be flexibly adapted to the different milling tools.

Using two additional linear axes, the position of the laser focal spots can be adjusted in the radial direction to the spindle according to the milling tool diameter and along the milling tool axis according to the length of the milling tool (Fig. 7.138). These two axes are implemented as positioning axes and can be open-loop-controlled by the tool machine. After a change of the tool diameter and tool length, the focal spots are adjusted accurately to meet the processing requirements. An additional rotation axis ensures that the laser focal spots are positioned around the tool during the simultaneous five-axes milling process according to the contact conditions [7.48]. Therefore the axes must interpolate with the rest of the tool machine axes.

In order to minimize the mass to be moved, the laser beam is directed by optical fibers with a numerical aperture of 0.22 and a diameter of 1,000 μm into the workspace. In order to prevent contamination or damage of the optics through chips or a braking tool it is mandatory for the integration of the lasers into the tool machine that the distance between the optics and the contact zone be maximized.

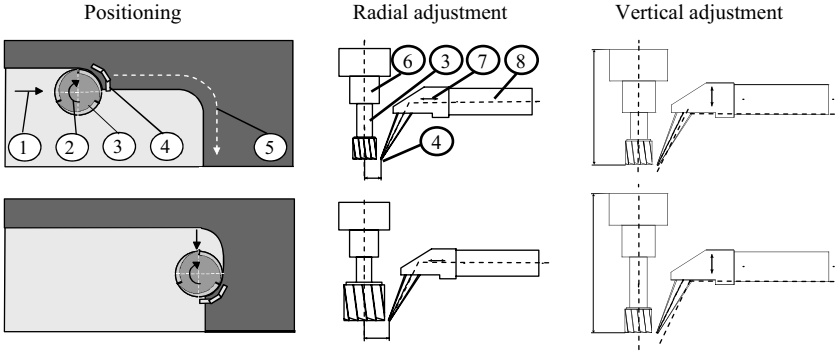

FIGURE 7.138. Resulting axes arrangements for the positioning of the laser focal spots depending on feed direction, tool diameter and tool length

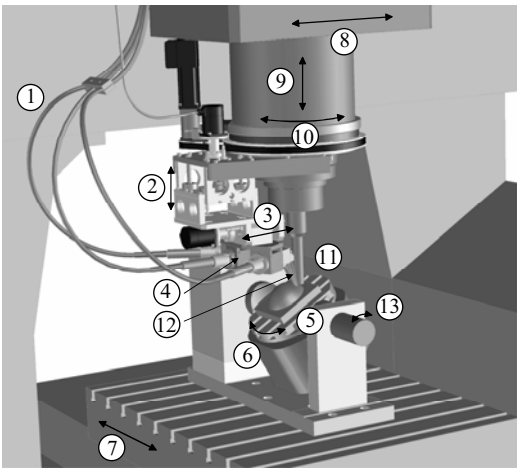

1. Fibre optic
2. Vertical focal spot adjustment
3. Radial focal spot adjustment
4. Collimation/focusing unit
5. Work piece
6. *C*-axis
7. *X*-axis
8. *Y*-axis
9. *Z* -axis
10. *W*-axis
11. Milling tool
12. Laser beam (3 × á 1 kW)
13. *A*-axis

FIGURE 7.139. Machine tool design for laser-assisted milling

Furthermore the angle between the tool axis and the laser beam has to be minimized in order to achieve better absorption characteristics and to avoid reflections back into the workspace. Due to the required large operating distance, a small angle of incidence, and the fact that the employed optical fibers need a radius of curvature of larger than 250 mm, the optical fibers are installed horizontally on the laser adapter. A tilt mirror reflects the laser beam onto the workpiece (Fig. 7.139).

The strongly divergent, circular output laser beam from the optical fiber is formed into a parallel beam with the help of a collimation unit and transformed afterwards by a cylindrically formed lens into an ellipse. The dissipated energy through decoupling, the beam forming, and the redirection of the beam, which become apparent in the form of warmth and decreasing power, are carried off by cooled housing components. In order to turn the laser beam to the workpiece, a planar deflecting mirror made of copper was manufactured with the help of ultra-precision turning technologies. The optical components are also equipped with a cooling structure, so that an even heat dissipation and no uneven material expansion can take place. The tilt mirror has no negative influence on the beam intensity and beam quality (Fig. 7.140).

The development of compact and powerful diode lasers in the multi-kilowatt range has enabled laser processes to be readily integrated into production line machine tools. Two examples for laser-assisted milling are illustrated in Fig. 7.141. Process temperature and behavior can be monitored actively by using a pyrometer.

The laser-assisted machining of Stellite materials was carried out using a direct application diode laser system (Laserline GmbH) and a fiber-coupled indirect application (Jenoptik AG). These systems were integrated in a three-axis milling machine whose capabilities were extended to five-axis machining by the integration of a rotary-swivel table.

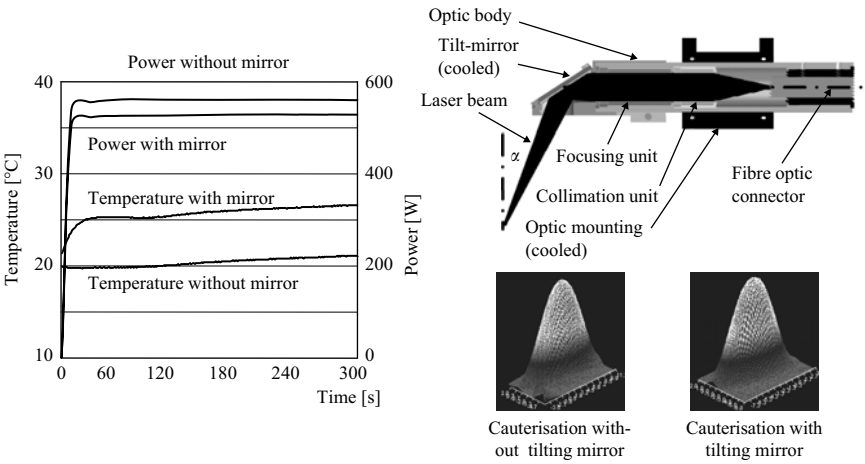

FIGURE 7.140. Influence of tilt mirror on beam quality and available laser power

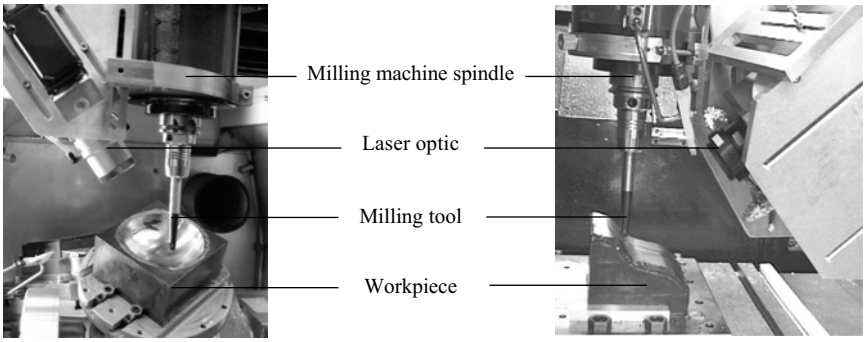

FIGURE 7.141. Experimental setup for laser-assisted milling: indirect application – fiber-coupled (left) and direct application (right)

Machine Tool Prototype for Laser-Assisted Turning

The special feature of the Hessapp® lathe is the hanging spindle whose position necessitates laser integration underneath the spindle in the lower working area. The diode laser can be integrated into the lathe both directly and indirectly using an optical fiber coupling into special lenses. Conversion work of the standard lathe working area is required for both alternatives in that at least two additional linear and one rotary axis (B-axis) are needed which permit movement of the laser in the *x*- and *y*-directions. Another swivel axis (A-axis) is required for optimum adjustment of the laser focal spot. The axes are controlled in the Hessapp® lathe by the Siemens control 840 D. Interpolation of the additional axes with the lathe axes is achieved with additional programming procedures.

The dust produced during metal cutting and the whirling chips are kept away from the laser lens, which is provided with an additional protective glass window and by an air knife. Nevertheless, regular manual cleaning is required.

As the standard window made of safety glass integrated into the cabin door does not fulfill safety standards, a laser protective window must be installed. Laser protective windows are offered by various manufacturers but are limited in terms of size for the protection level required for diode laser irradiation. A small standard window 100 × 200 mm severely restricts visibility of the working area so that a larger window has to be assembled from several standard windows and joined together in frames.

Direct Integration. Two diode lasers from different manufacturers were integrated into the lathe for comparison purposes. In spite of the small size of both laser systems they severely restricted the swiveling range in the available working area of 1,050 × 1,000 × 1,000 mm. In the case of direct integration, the choice of the laser lens regarding focal length and the resultant focal spot size is determined by the working area. Further restrictions result from the size of the component to be machined and the turret swiveling range which may be needed for the machining process. The "laser head immovability" also has a negative effect on the machining of components of different shapes and varying diameters in one clamping as well as different internal and external machining operations. In the case of clamping errors, a workpiece falling results, in the worst-case scenario, not only in the destruction of the lens but of the entire laser head.

One advantage of direct integration is that the use of an optical fiber which is sensitive regarding bending and torsion can be dispensed with. Additional costs for fibers, a collimation module, and a deflection cube are not incurred.

Fiber-Coupled System. With the fiber-coupled system the laser head is mounted on the laser cooling unit and installed outside the lathe. The optical fiber is connected to the laser head by a fiber coupling. The optical fiber is guided through cable ducts to the lathe and is inserted through the lathe roof into the working area. It ends in a collimator and in turn in a 90° deflection cube. A round focal spot of about 4.3 mm in diameter is produced with a lens ($f = 190$ mm). During the machining process it must be ensured that the fiber is not exposed to a high risk of breakage by torsion or bending. The minimum allowable bending radius is 250 mm.

The advantages of a fiber-coupled system are the small dimensions of the integrated lens and holder enabling a less restricted working area and a greater traversing path of the laser unit for machining different shapes and diameters. With fiber-coupled systems, clamping errors merely result in the destruction of the lens and possibly the optical fiber. Such damage is limited compared with direct integration. It can be rectified in a short time with spare parts in stock and does not lead to a prolonged production downtime.

7.2.5.2. Parameter Dependencies and Process Investigations

Laser-Assisted Milling of Hot- and Cold-Forming Tool Steels

The process and thereby also the resulting outcome are affected by a number of different factors during laser-assisted machining. Apart from the process parameters relevant during conventional milling, the influencing factors for defined heating also have to be taken into account. Besides the laser parameters, considerations include the thermal and optical characteristics of the material to be machined. Regarding high-quality and cost-effective machining, all process parameters have to be adapted regarding all reciprocal effects. Hence, the fundamental condition for stable machining is the formation of an appropriate temperature field in the cutting zone.

Given a suitable choice of the process parameters, laser-assisted machining enables the reduction of cutting forces due to the softening of the material's strength and the associated reduced deformation resistance during chip formation Fig. 7.142. In the case of hot and cold forming tool steels with a hardness of about 58-62 HRC, which are typically used in the die and mould making industry for the production of forging and deep-drawing dies, comparable results with an average reduction of process forces around 40–60% were achieved. Up to a limiting cutting depth, the decrease of process forces was almost linearly connected to the laser power.

Comprehensive use of the laser energy introduced into the workpiece requires thereby an optimal positioning of the laser focal spot in front of the milling tool. Adapted to the process conditions, the focal spot size is to be selected, heating the workpiece in the entire zone of tool contact. The distance between laser focal spot and tool contact (advance of laser focal spot) decisively affects the temperature

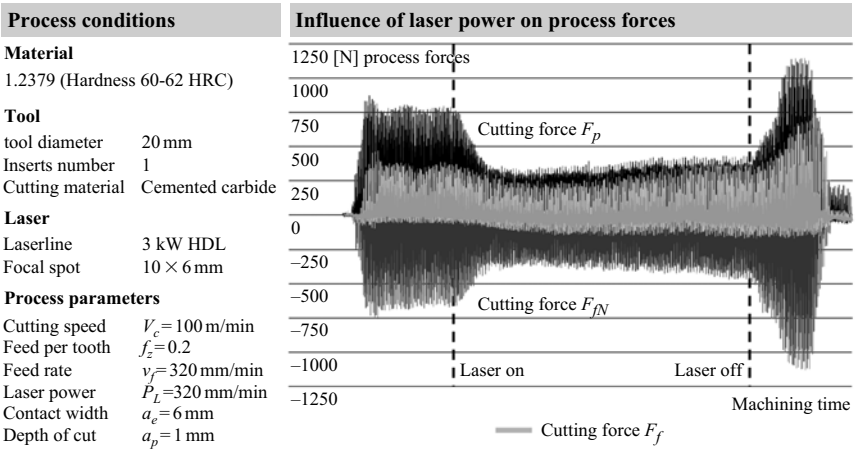

FIGURE 7.142. Influence of laser energy on process forces during milling of cold forming tool steel 1.2379

distribution in the chip section. A large distance between focal spot and tool contact leads to a renewed cooling of the machining zone by convection and thermal conduction into the workpiece within the time interval between heating up by the laser beam and the machining itself. In the case of a small advance of the laser focal spot, the time interval for heating the chip section by thermal conduction up to the depth of cut is insufficient. Additionally an impairment of the tool service life can take place under these conditions via excessively high temperatures at the workpiece surface as well as reflected laser radiation on the milling tool. In the case of laser-assisted milling of steel, an appropriate advance of laser focal spot with regards to minimum process forces and suitable tool service life results in a distance of 6–8 mm (Fig. 7.143). Under these conditions the tool service life of inserts made of cemented carbide can be doubled by the laser-assistance in comparison to conventional milling. The determined advance of the laser focal spot, however, has no general validity but changes according to the tool contact conditions and the accessibility for the laser beam. This requires a constant readjustment to the respective milling task.

Apart from the focal spot position, the process forces and tool service life arising within the laser-assisted milling of steel are determined by the reciprocal interaction between the laser beam parameters and the milling parameters. These affect, on the one hand, the heating of the machining zone and thus the material strength in the chip section. On the other hand, different chip sections (feed and depth of cut) as well as different cutting speeds arise as a result of the selected milling parameters. For the necessary temperature field in the machining zone, the energy input per unit length is crucial. Apart from the laser power the energy input per unit length is determined by the feed during laser-assisted milling. Despite constant energy input per unit length (realized by means of a temperature control), an increase of feed leads to a reduction of the heating and thermal conduction into the

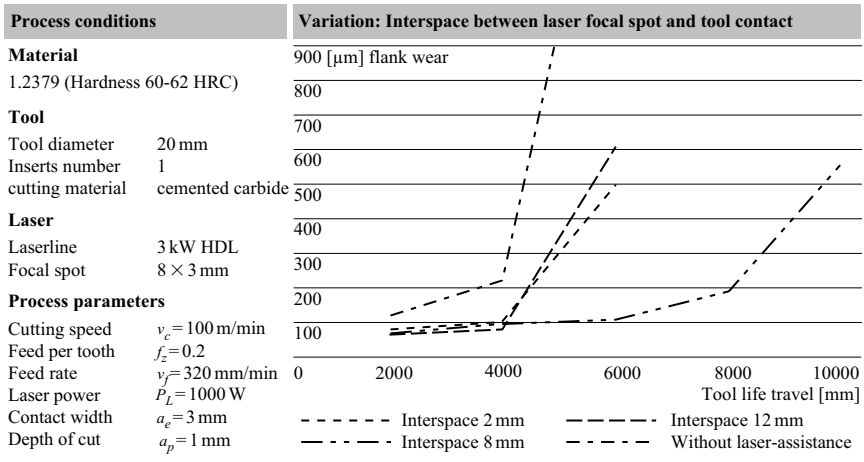

FIGURE 7.143. Influence of focal spot position in relation to tool contact on tool service life

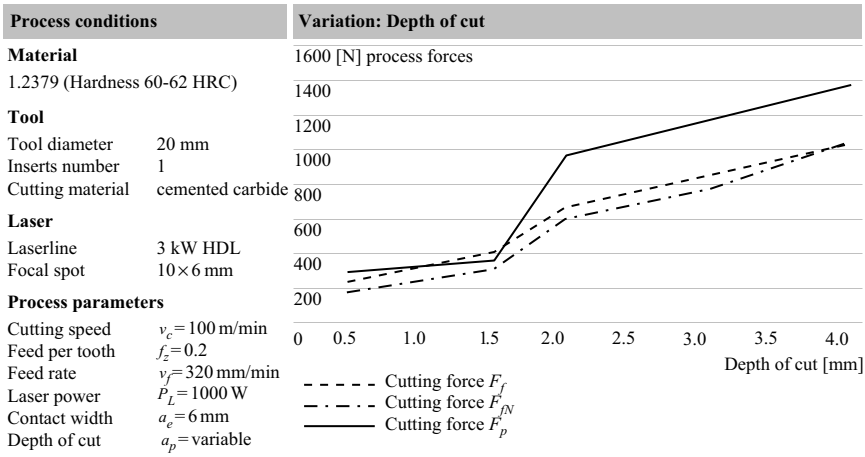

FIGURE 7.144. Influence of temperature distribution in the chip section on process forces at different cutting depths

workpiece depth. The resulting insufficient temperature in the chip section up to the depth of cut perpendicularly to the feed direction leads to an increase in process forces and tool wear due to the increasing deformation resistance. In comparison to growing feed per tooth, higher feed by growing cutting speeds reduces the increase in process forces because of additional frictional heat. The temperature field in the machining zone resulting from the process parameters limits therefore the depth of cut maximally attainable under economic aspects. On otherwise identical process conditions a linear dependence between the depth of cut and the process forces has been detected (Fig. 7.144). Beyond a limited cutting depth of 2 mm during laser-assisted milling of steel, however, a distinctly higher level of process forces is recognized due to an insufficient heating of the workpiece into 2 mm depth and more, which results additionally in intensified tool wear.

Thus, a higher feed simultaneously reduces the attainable depth of cut. With respect to economical machining, the maximum increase of material removal rates by laser-assisted milling of materials which are difficult to machine are limited among other things by the mechanical and thermal characteristics of the respective materials. Therefore to realize an optimized process and thus in the long run maximum process efficiency, the mentioned variables, focal spot positioning and laser and milling parameters, cannot be singularly regarded but have to be adapted with consideration to the respective machining task.

Laser-Assisted Milling of Stellite

Laser-assisted machining must consider combined laser and machining process parameters, for example, the laser power and cutting speed. Therefore, it is critical that the method by which the combined process works be understood. Figure 7.145 illustrates the correlation between tool wear and assisted laser power, depending

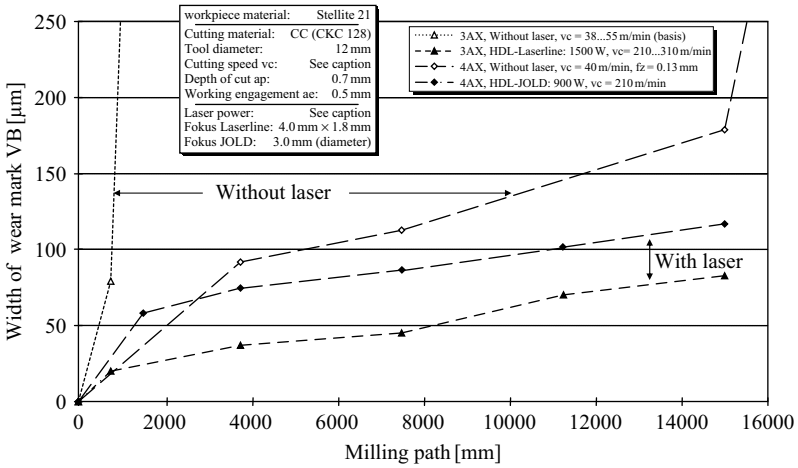

FIGURE 7.145. Tool wear variation with different combinations of laser and cutting parameters

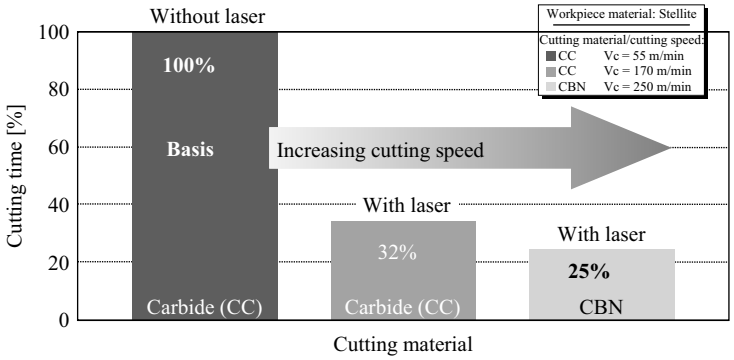

FIGURE 7.146. Parameter dependencies, cutting time, and cutting material

on the milling path. It is clear to see that increased laser power reduces the degree of tool wear for a given length of cut.

Furthermore, it can be seen in Fig. 7.145 that the direct application laser strategy yields superior wear results compared to the indirect application strategy. Besides the different power levels, this is due to the fact that the direct application rectangular focus geometry (4 × 1.8 mm) can be positioned closer to the milling tool than the 3-mm-diameter spot focus generated by indirect laser application.

Figure 7.146 illustrates the effect of varying tool materials. Harder cutting materials enable faster cutting in combination with laser assistance. Extensive testing revealed that CBN cutting material is the best option for fast Stellite machining. Finally, the cutting time can be reduced up to 75%.

In experiments conducted to date, cobalt-based alloys (e.g., Stellite) have in particular demonstrated excellent potential for benefiting from the advantages (e.g., improvement of workpiece quality) of laser-assisted machining.

Laser-Assisted Turning

To achieve an increase in productivity, it is necessary to increase the cutting parameters, i.e., the cutting speed, the feed, and the cutting depth, which, however, has a negative impact on the wear propagation behavior of the tool. This negative influence is promoted by the higher cutting temperature which results from the use of a laser. On the other hand, the material strength of the component is reduced by the laser irradiation, which ultimately leads to a reduction in the cutting forces. Hardened materials such as 42CrMo4 (1.7225, hardened to 62HRC), X210Cr13 as well as fiber-reinforced ceramics exhibit improved machining properties by laser-assisted machining with PCBN-cutting materials.

The flowing chips produced during laser-assisted turning prevent the laser beam from reaching the workpiece. These chips can be broken mechanically or deflected in order to avoid a negative impact on the machining process.

7.2.5.3. Application Results

Laser-Assisted Milling of Hot- and Cold-Forming Tool Steels

The decisive criterion of evaluating possible applications of a new technology in industrial production is the attainable quality of the produced parts. During the laser-assisted machining of metallic materials, an impairment of the functional characteristics of the machined components due to the thermal energy applied has to be avoided. Ideal process conditions, enabling a heating restricted to the workpiece area to be machined, are hardly to be realized because of the necessary high temperature gradient at the bottom side of the chip. Structural influences remaining after the machining are, however, reducible to a large extent by appropriate machining strategies under variation of the cutting depth (Fig. 7.147). Starting from the surface into the component, a hardness gradient with reduced hardness up to a distance of approximately 1 mm of the surface is recognized after laser-assisted milling of steel with a cutting depth of 1 mm. After laser-assisted milling with a 2-mm cutting depth, however, a hardness profile comparable to a conventional milling without laser-assistance is attainable. Therefore heating takes place only up to a depth of less than 2 mm with optimized parameters. These results agree with the respective process forces described before. Thereby, with acceptance of increased process forces and tool wear, the selection of an appropriate depth of cut enables on the one hand a laser-assisted machining without resulting changes of the material's structure in the rim zone. On the other hand the thermally affected rim zone can be removed by partitioning the machining in a laser-assisted roughing for the manufacturing of a near-net-shape component and by a subsequent conventional finishing of an overmeasure. The attainable part qualities with laser-assistance correspond thus in the long run to those of conventional milling.

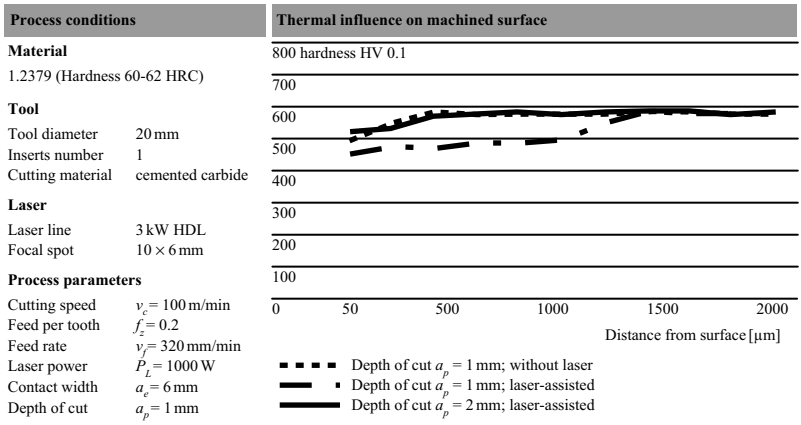

FIGURE 7.147. Thermal influence on the subsurface area after laser-assisted milling with different depths of cut

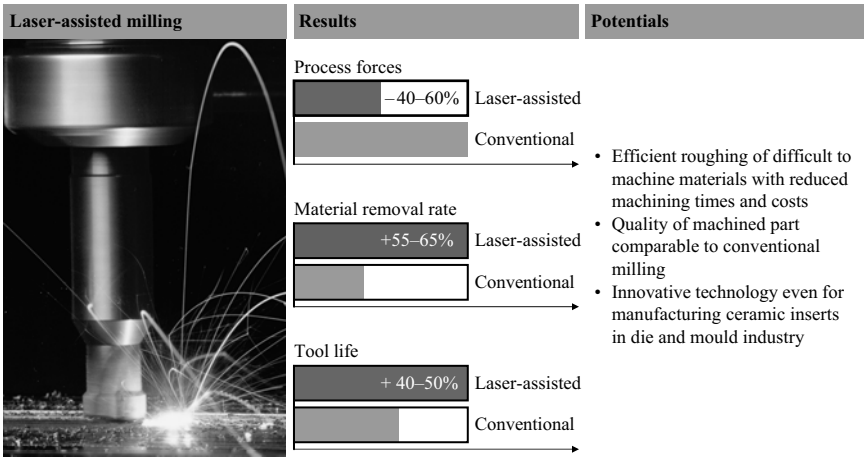

FIGURE 7.148. Potentials of laser-assisted milling for roughing of difficult to machine materials

The objective of a laser-assisted milling of steel is therefore an efficient roughing, whose potential is determined substantially by the attainable material removal rates within the limitations described before regarding feed and depth of cut. Modular diode lasers adapted to the respective machining task enable a further increase of material removal rates around 55–65% by extension of the heated workpiece area (increased width of cut). Thus the simultaneous reduction of the process forces and consequently the tool wear permits an efficient milling of materials which are difficult to machine with reduced machining times (Fig. 7.148) [7.49].

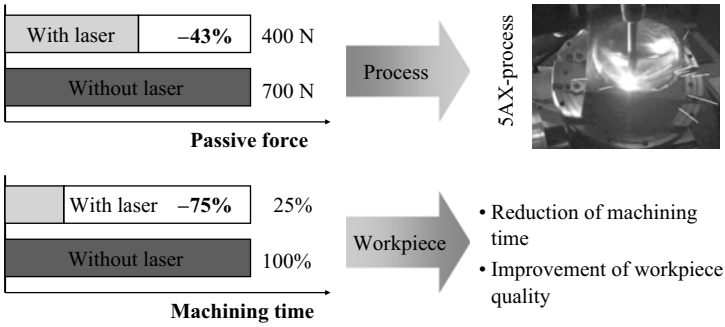

FIGURE 7.149. Results of laser-assisted milling in comparison to conventional milling (without laser) of stellite

On a long-term basis the machining also of ceramic materials for the production of wear-resistant tool inserts in die and mould making industry is possible. Beyond that the integration of modular diode lasers into a machine tool enables a flexible, local hardening within the production sequence directly following the machining and hence creates new possibilities for the design of process chains with reduced production times and costs.

Laser-Assisted Milling of Stellite

Research for laser-assisted milling of Stellites yielded that cutting speeds can be increased by a factor of approximately 4 while maintaining almost identical tool wear rates. This reduces the machining time by 75%, which in turn brings about excellent cost-saving potential (Fig. 7.149).

To summarize, it has been established that the laser-assisted machining of difficult to machine materials such as ceramics and cobalt-based alloys presents a significant technological, economic, and ecological improvement over conventional manufacturing strategies. Further development of this technology has the potential to bring about a critical competitive advantage in the future.

7.3. Surface Treatment

7.3.1. Introduction

R. Polzin

Surface treatment is the youngest laser technology in industrial manufacturing. Two introductory examples show the vast range of laser surface treatment applications from laser surface hardening to laser cladding.

The first example (Fig. 7.150) shows the hardening of a torsion spring using two high-power diode lasers. The use of two lasers allows hardening of a circular section on the half circumference. The arrangement of the two lasers is as such

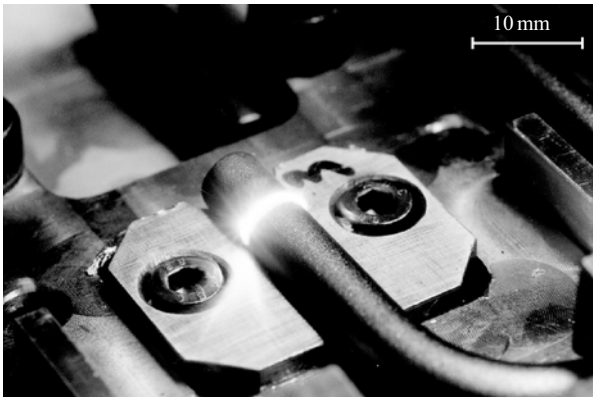

FIGURE 7.150. Local laser hardening of the edge layer of a torsion spring using two high-power diode lasers (courtesy of Muhr & Bender KG, Germany)

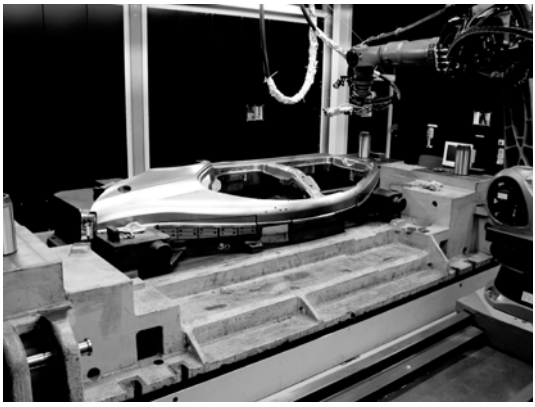

FIGURE 7.151. Plant for repairing of stamping tools

that reduction of the hardness penetration in the overlap of the two laser beams due to annealing effects is avoided. In a plant especially designed for this application, every year about 7 million torsion springs are hardened.

The second example (Fig. 7.151) is a plant for local repairing of stamping tools. The plant serves the local modification of the design and also the repairing of abrasion areas. The main advantages to using this plant are the minimized heat distortion and the accuracy.

An economic examination [7.50] shows for the laser-hardening process a cost and cycle-time saving of about 60% compared to flame hardening as well as better quality.

Among the advantages of using laser radiation for surface treatment, are the possibility of local use and good automation. As the laser beam works only locally

and the treatment zone is restricted to a defined area, there is, in comparison to other surface treatment methods, only minimal heat input into the component and as a consequence only a reduced thermal distortion. The good automation guarantees a constant quality of the process. Furthermore, because of the higher rates of cooling, the hardness results to be obtained are normally better than the results of the other surface treatment methods. For the same reason the structure is very fine-grained when laser radiation is used for cladding. A further and important advantage is possible process control. Surface treatment with laser radiation is an expanding field.

The section is divided into a discussion of laser beam hardening and layer deposition for generation and repair, using different high-power diode laser systems. Moreover the effects of different physical conditions and process parameters of the surface treatment will be described.

7.3.2. Laser Hardening

7.3.2.1. Process Principles and Equipment

Absorption of Laser Radiation

K. Wissenbach, G. Vitr

Optical Properties of Materials. In surface treatment with laser radiation, the treatment result depends largely on the energy coupling into the workpiece. The absorbed optical energy leads to a heating of and to phase changes in the material, which could change the material properties in the boundary layer. The proportion of the power absorbed P_A, the power reflected P_R, and the power transmitted P_T to the incident laser power P_L, is described as absorptance A, reflectance R, and transmittance T.

$$A = \frac{P_A}{P_L};\quad R = \frac{P_R}{P_L};\quad T = \frac{P_T}{P_L} \tag{7.7}$$

The conservation of energy results in the following power balance:

$$P_L = P_A + P_R + P_T \tag{7.8}$$

These equations provide the connection

$$A + R + T = 1 \tag{7.9}$$

With metals, the optical penetration depth of the laser radiation, caused by the 1/e reduction of the incident power density, amounts in the sub-micrometer range for the wavelengths used in surface treatment with laser radiation (CO_2 laser:10.6 μm, Nd:YAG laser: 1.06 μm, diode laser: ≈ 800–950 nm, excimer laser: approx. 200–400 nm).

The absorptance depends on [7.51]

- the optical constants of the material (refractive index n, absorption index k),
- the physical properties of the laser radiation (wavelength, polarization state, power density distribution),
- the chemical composition of the surface (surface layers such as oxides, nitrides, graphite, etc.),
- the topography of the surface (roughness), and
- their dynamic changes during surface treatment in dependence on the temperature and the state of aggregation (solid, liquid, gaseous) in the surface or in its environment.

Absorption in Materials. The optical constants determine the penetration depth of the laser radiation. With thermal surface treatment using laser radiation, only the absorbed optical energy is converted into thermal energy causing a temperature distribution in the material and resulting in changes of the surface properties [7.52]. The temperature distribution is dynamically changed through a diffusive and convective energy transport in a solid and liquid state.

In regard to a plane electromagnetic wave hitting the infinitely extensive, ideally plane surface of a material, Fresnel's formulas describe reflection as a function of the angle of incidence and the polarizing state.

Using Fresnel's formulas, a vertical beam incidence results in the following reflectance R [7.51]:

$$R = \frac{(n-1)+k_A^2}{(n+1)+k_A^2} \tag{7.10}$$

The absorptance for metals of adequate thickness

$$d \geq \frac{\lambda}{2\,\pi\,k_A} \tag{7.11}$$

with negligible transmittance is described by

$$A = 1 - R \tag{7.12}$$

That is to say, the absorptance of metals ensues directly from the reflectance. The absorptance can be determined by measuring the incident and the reflecting optical energy or by measuring the incident optical energy while simultaneously measuring the temperature in case of known temperature-dependent thermal properties of the material.

Absorption and Properties of Laser Radiation. Figure 7.152 shows the calorimetrically measured absorptance as a function of the angle of incidence for laser radiation polarized parallel to the incident plane. An angle of around 80° results in a marked maximum of absorption. The absorptance, and thus, the energy coupling, can be changed by altering the angle of incidence and the state of polarization [7.52, 7.53].

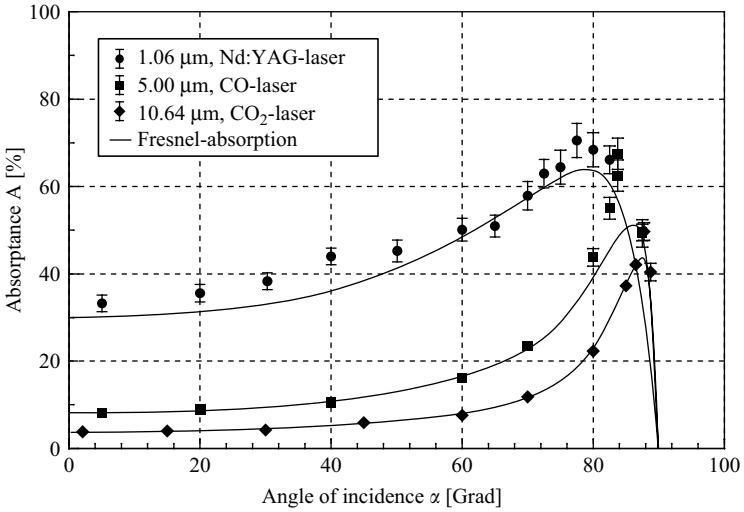

FIGURE 7.152. Absorptance as a function of the angle of incidence for p-polarized laser radiation [7.53]

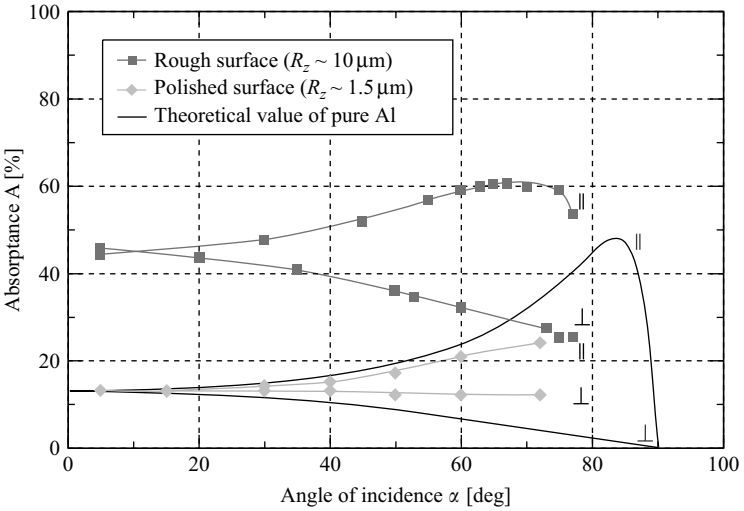

FIGURE 7.153. Absorptance as a function of the angle of incidence for s- and p-polarized laser radiation [7.54]

Figure 7.153 shows the calorimetrically measured absorptance on rough and polished $AlMg_5Mn$ surfaces and the theoretical value for pure Al as function of the angle of incidence for high-power diode laser radiation polarized parallel and vertical to the incident plane [7.54].

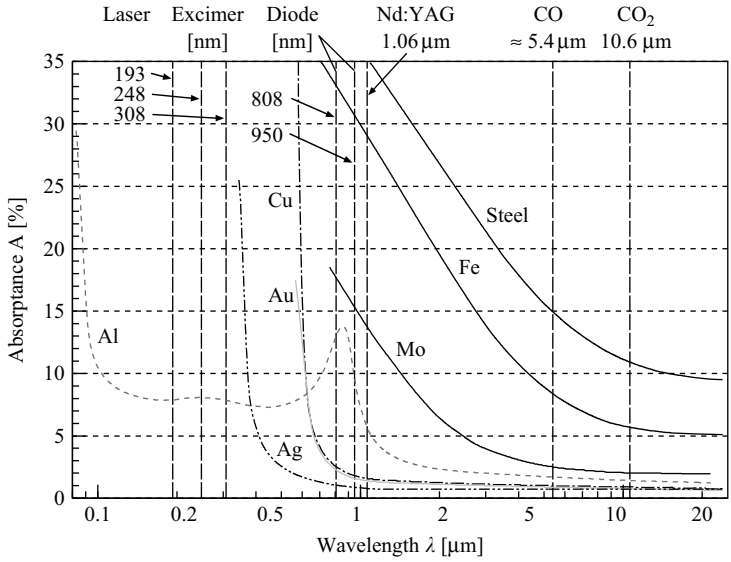

FIGURE 7.154. Absorptance of various metals as a function of the wavelength [7.55]

Figure 7.154 shows the dependence of the absorptance on the wavelength for various metals [7.55]. The absorptance decreases with the wavelength, so that the absorption is lowest for CO_2 laser radiation.

The coupling of the optical energy is influenced by the topography of the material surface. The absorptance increases with an increasing arithmetic average of roughness R_a (Fig. 7.155). A maximum absorption is ensured with a surface roughness of the dimension of the laser wavelength.

Absorption and Chemical Composition of the Surface. The coupling of optical energy is also influenced by the chemical composition of the material surface. Reflection-reducing surface layers decrease the reflectance and increase the absorptance and/or the transmittance. Depending on the type and thickness of the surface layer applied to metals of adequate thickness with negligible transmittance, this results in a changed energy coupling with increased absorptance (Fig. 7.156) [7.56, 7.57]. The required thermal and chemical stability of the surface layers decides on the application in surface processing of materials with laser radiation, since the physical, thermal, and metallurgical processes can be influenced.

Absorption and Material Changes. At the start-up phase of surface processing, the optical constants statically determine the energy coupling of laser radiation into the material. During the treatment process, these constants could change so that the energy coupling of laser radiation into the material becomes dynamic.

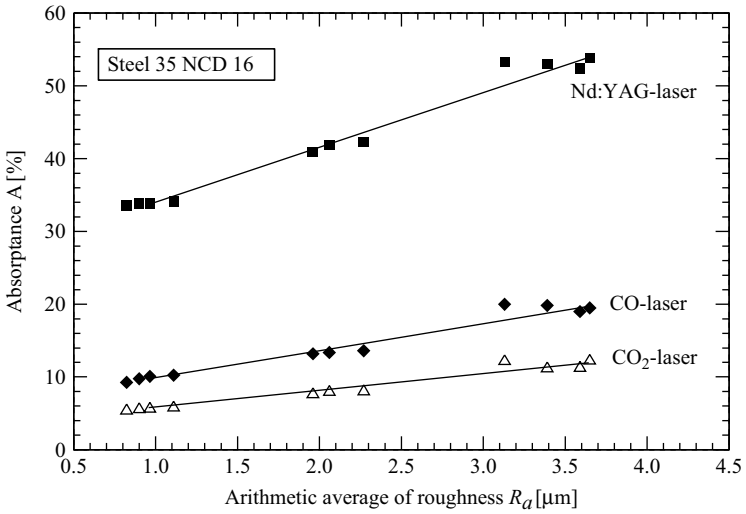

FIGURE 7.155. Absorptance as a function of the arithmetic average of roughness for various wavelengths

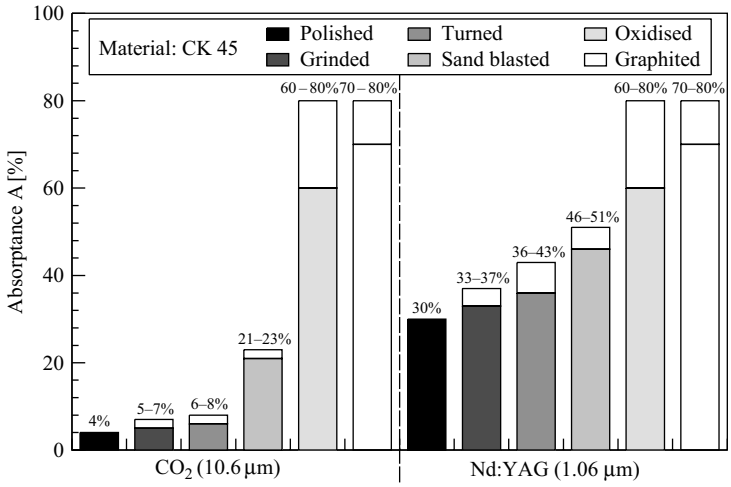

FIGURE 7.156. Absorptance in dependence on the type of the surface layers

The occurring changes in temperature, the phase transitions, the chemical reactions, and the surface morphology facilitate an improved energy coupling.

Depending on the material, the temperature dependence of the optical constants changes the reflectance, absorptance, and transmittance. With phase transitions (solid–liquid, liquid–gaseous), the changes of the optical constants through

changes of the dielectric function are particularly distinct. Chemical reactions of the materials with the ambient atmosphere or with process gases (working or inert gas) influence the chemical composition in the interaction zone of the laser radiation.

Microstructural Changes During Hardening

S. Bonss

Hardening of steel means, in general formation, of a martensitic structure by heat treatment in solid state. This structure has higher strength but less ductility and is more resistant against a lot of kinds of wear. At room temperature pure iron consists of ferrite with a body-centered cubic (bcc) structure, also called α-iron. At 0.9% carbon, steel consists of perlite. This is an eutectoid mixture of ferrite and zementite (Fe_3C). Perlite forms grains which consist of lamellar ferrite and zementite. With carbon content below 0.9%, steel is a mixture of ferrite and perlite. At higher carbon between 0.9% and 1.7%, secondary zementite and perlite are structural components of steel. At room temperature ferrite can dissolve only little amounts of carbon. Between the temperatures Ac_1 and Ac_3 the transformation of ferrite into austenite with a face-centered cubic (fcc) structure occurs. Ac_3 is 906°C for pure iron and 721°C for steel with 0.9% carbon. Austenite can dissolve up to 1.7% carbon. Holding steel at a temperature above Ac_3 leads to diffusion of carbon into Austenite. At slow cooling the carbon diffuses back and austenite transforms to perlite. But quenching the steel keeps the carbon in the austenite structure and the lattice transformation from face-centered cubic to body-centered cubic cannot occur completely. The result is the so-called martensitic structure and some remained austenite. Martensite is very hard and needle-like in cross sections. At less abrupt quenching nevertheless a certain portion of perlite is formed. Alloying elements have a considerable influence on the above-mentioned transformations. They form, for instance, carbides, which are less soluble and reduce the critical quenching rate. In general it can be said that higher-alloyed steels need more time and temperature for complete austenite formation, carbon solution, and diffusion. On the other hand, alloying elements are often an agent that martensite forms even at lower quenching rates. It is important to know that at some steels the martensitic transformation is not completed at room temperature. Sometimes liquid nitrogen cooling is applied. More details on structural changes and transformation behavior are given in [7.61]. The characteristic behavior of the different types of steel during cooling from austenite is described in time-temperature-transformation charts. But these charts are developed for classical heat treatment. For laser short-time processes these charts are a good estimation but have to be applied creatively. The main difference is the much higher surface temperature compared to classical heat treatment. The transformation and diffusion processes must be accelerated by higher temperatures because the interaction time of the laser at a given position is very short. Typical surface temperatures at laser beam hardening are, depending on the material, in the range of 1100–1400°C.

Laser Hardening Compared to Other Heat-Inducing Hardening Methods

S. Bonss

During flame hardening, the surface of the workpiece is heated up to austenitizing temperature by a hydrocarbon-oxygen flame and quenched by water flow or water, oil, or salt bath before the heat is conducted to the core. Martensitic transformations only occur in the heated surface layer. Case depth is determined by flame temperature, heating time, and heat conductivity of the steel.

Induction hardening is conducted by heating up a surface layer in a high-frequency coil by induced current to austenitizing temperature and quenched most commonly by water flow. With rising frequency of the alternating current, the depth of the heated layer decreases by skin effect. Depending on the frequency, deeper contours are heated up by lower frequencies, protruding outlines by higher ones. Simultaneous or sequential dual-frequency induction heating is applied to obtain uniform case depths, e.g., for gears and sprockets wheels.

Induction and flame hardening are common transformation-hardening processes, but the power density is not as high as it is with laser application (cf. Table 7.12). Because the energy implemented in the workpiece cannot be as concentrated as in case of laser beam induction, hardening and flame hardening are used for bigger parts with larger areas to be hardened. Induction and flame hardening can be incorporated in a manufacturing line but in contrast to laser transformation hardening, external quenching, machining, and purifying and the associated environmental behavior of the liquids has to be considered.

Process Principles of Laser Hardening and Remelting

U. Haag

Laser Transformation Hardening. Laser transformation hardening provides a hard and wear-resistant skin in combination with a ductile core. Due to forming favorable compressive residual stress, strength and fatigue behavior is improved.

During laser transformation hardening the laser radiation impinging on the workpiece nearly instantaneously causes a heat flow proportional to the surface temperature. A thin layer is heated above Ac_1 transformation temperature. The absorptivity is strongly influenced by the surface finish, e.g., grinded, phosphated (see Fig. 7.156). During this process the surface temperature is measured with a

TABLE 7.12. Comparison of power densities of different sources of energy

Source of energy	Density of energy (W/cm^2)
Laser	$10^3 \ldots 10^5$
Induction	$10^3 \ldots 10^4$
Flame	$10^3 \ldots 10^5$
Oven (convection)	0.5

pyrometer, and accordingly the output power is controlled to achieve a constant surface temperature shortly below the melting point. The maximum temperature always appears at the end of the laser spot, with increasing temperature from the beginning of the spot. Holding time of a specific volume element is determined by the time between the point when the temperature increases above Ac_1 and the second point when it decreases below this temperature. The heat is rapidly conducted into the bulk material and the layer effectively self-quenches ($\sim 10^4$ K/s) above critical cooling rate. No external cooling is required for martensitic transformation.

Because of the short interaction time the so-called short time austenitizing needs a suitable carbon distribution inside the microstructure of the starting material for homogeneous martensitically transformed structure. To dissolve carbides and achieve suitable carbon distribution, preheating treatments like tempering or annealing are applied.

Carbon concentration above 0.6% formation of retained austenite is expected, which lowers the hardness. A few percent of the alloying elements Mn, Cr, Ni, V, and Mo correspond with transformation behavior and cause an improved hardenability of carbon steels. Hardness of heat-treated areas shows a plateau-like shape and a rapid decrease toward the values of the substrate within a narrow transition zone. Dimensional and form shape stability are high because of the concentrated energy feed to a limited surface layer. Overlapping of hardening tracks should be avoided because of annealing effects. A solid-state process in inert atmosphere and low distortion saves costs for after work.

Laser transformation hardening can be incorporated in a manufacturing line because in contrast to thermochemical case hardening, e.g., carburizing, nitriding, carbonitriding, nitrocarburizing, continuous and not batchwise processing is carried out. The high degree of flexibility and the absence of external quenching media favors the laser process.

Remelting. In surface melting the laser is used successfully to melt a thin layer of a controlled area of the component surface. On rapid cooling due to heat conduction to the bulk solidification occurs which can produce structures and hence properties very different from the bulk slowly cooled material. Laser surface melting leads to the formation of a modified layer of crystals grown epitaxially from the underlying material.

The process result is dominated by the absorptivity, the heat flow, the melt pool geometry and dynamics, the process gas flow, and the rapid solidification process. Rapid quenching can produce extension of solubility to the solid state but more importantly the refinement of structure, metastable phases, or even the amorphous state. Remelting also results in a refinement and redistribution of inclusions.

The refinement not only increases the strength, hardness, and load-bearing capacity of the surface layer but also improves the resistance to adhesive wear. The process is mainly applied to cast iron and light metal alloys in as-cast conditions. To get oxide free surfaces with low roughness and to avoid oxidation of some elements with high affinity to oxygen, the process gas flow has to cover the whole melt pool during the remelting process. An alternative form is to cover the

melt with a reactive gas to produce a specific microstructure. The gas flow and the nozzle design must be adapted to the workpiece geometry. Substantial amounts of austenite structure may occur during subsequent laser passes due to reheating.

Advantages of laser remelting are the high degree of flexibility, the possibility of very local treatments, and the absence of external quenching media.

Process Simulation

N. Pirch, S. Bonss

The simulation of a hardening process using laser radiation includes model calculations to facilitate a prediction of the temperature distribution as a function of the process parameters while taking into account the temperature-dependent thermophysical data of the material. The temperature distribution is established by solving the heat equation using the finite-elements method since this shows the great flexibility of the various numerical processes in regard to complex component geometries. Due to the low proportion of optical to thermal penetration depths of metals, the thermalization of the optical energy can be mathematically modeled by using a surface source. To do so, the power density distribution of a laser module is established using a beam diagnostics device[2], discretized in a $128 * 128$ matrix, and edited for the FEM program to calculate the temperature field. With a deviation from a vertical alignment of the surface elements exposed to laser radiation to the direction of the beam propagation, its effect on the resulting reduction of local power density distribution must be taken into account.

The austenitized area and, from it, the volume percentage of the martensitic conversion can be determined on the basis of the temperature cycle time calculated in the volume elements. In the model calculations carried out for the austenitization, the volume areas exceeding an Ac_3 temperature dependent on the heating-up rate are assumed to be fully austenitically converted. The volume percentage of the martensitic conversion is calculated according to the Koistinen–Marburger equation [7.58, 7.59].

The calculation of the distortion is based on the thermoelastoplastic model equations [7.60]. The basis for the plastic deformation is a perfectly plastic-elastic material behavior with a temperature-dependent yield point. In the absence of material data, the transformation plasticity has to be left out of account in the model calculations.

In regard to their power density distribution, the high-capacity diode laser modules show certain tolerances toward each other that result in different temperature cycle times and heat penetration depths during material processing. For example, since linear safety rails during hardening must be worked using two-beam or four-beam technology to avoid a torsion of the rails, model calculations can be done beforehand to check the necessity of adjusting the laser power of two or four laser

[2] E.g., Primes Focus Monitor, Primes GmbH, Pfungstadt, Germany.

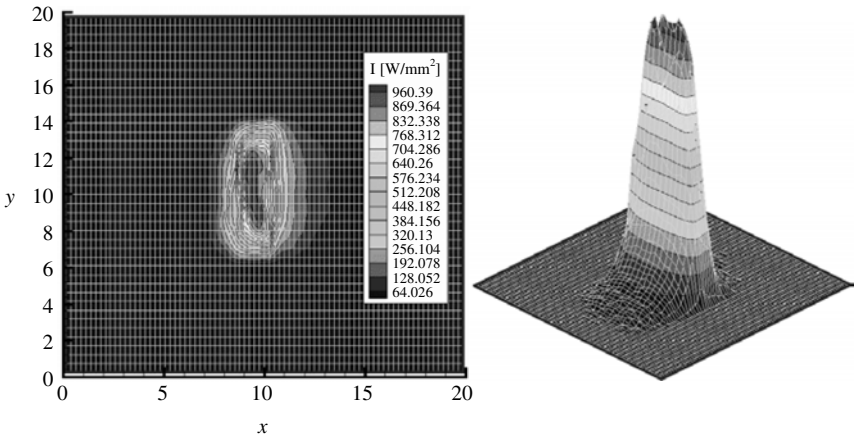

FIGURE 7.157. Power density distribution (PDD) and temperature field calculation for modules 03 and 08 ($v = 2$ m/min), PDD adjusted to 200W

modules each to generate roughly the same temperature cycle times and hardening depths.

Figure 7.157, for example, shows the power density distribution of two laser modules that are the same according to the manufacturer. The power density distributions differ by around 12.5% in regard to their maximum intensities. The resulting maximum temperatures, however, differ by around 130%.

The following refers to hardening of linear guiding rails discussed in section on "Hardening of Linear Guiding Rails". Since the laser hardening of the upper face of these rails is effected simultaneously at opposite bearing surfaces to avoid torsion, the temperature field calculation can be restricted to the area of the rail defined by the symmetry level $y = 0$ (Fig. 7.158). The area of the bore-hole and both ends of the rail experience a heat build-up that requires a calculated adjustment of the process parameters. This adjustment for these critical areas is to ensure a constant hardening depth and predict whether and to what extent the control temperature must be changed if the laser track passes an area in which there is a heat build-up. The martensite formation is initiated by the self-quenching. Due to the low material volume of the rail geometry, a process window must be determined in regard to the laser power and the velocity, in which the temperature in the cooling phase falls sufficiently below the martensite starting temperature, while assuming a specified hardening depth. When processing with four-beam technology, the temperature in the upper track, compared with the lower track, falls slightly below the martensite starting temperature in the cooling phase. According to the Koistinen–Marburger equation, this leads to a lower martensite volume percentage in the upper track. The possibility of heat dissipation in the area of the bore-hole is smaller than in an area further away. In this area, the temperature in the primary cooling phase does not fall below the martensite starting temperature. This is obvious from the martensite distribution. In the area of the bore-hole, the

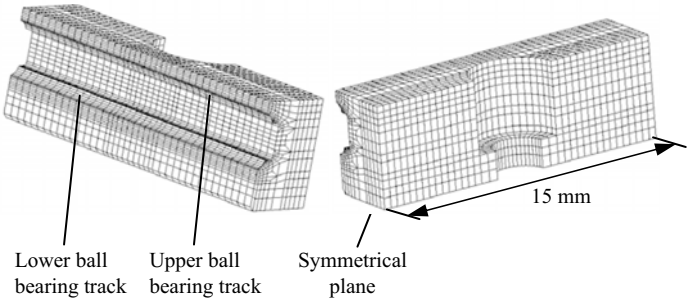

FIGURE 7.158. Networking of the rail geometry

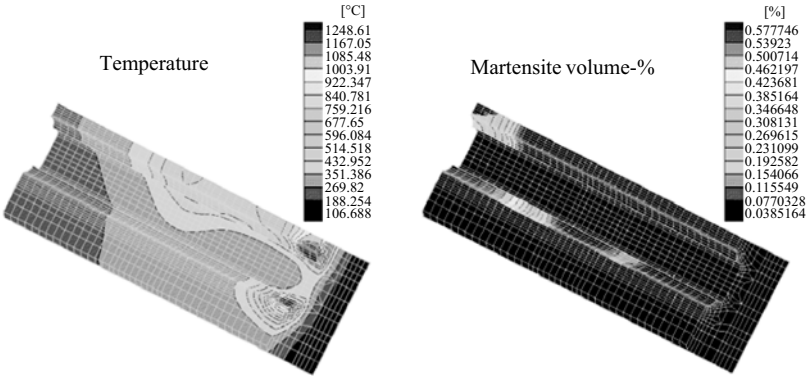

FIGURE 7.159. Temperature and martensite distribution in an isopleth representation ($P_L = 203$ W, $v = 1.2$ m/min, martensite starting temperature $T_M = 300°C$, austenitising temperature $T_A = 800°C$)

lower track shows an interruption of the martensite distribution (Fig. 7.159). To the right of the bore-hole, i.e., in traverse direction, the formation of new martensite can already be seen.

Using two-beam technology first of all leads to bending pointing the opposite way of the x-direction (Fig. 7.160). Following the temperature homogenization, the rail shows a lasting deformation opposite to it (Fig. 7.161). The reason for this lasting distortion is a plastic compression in traverse direction in the heat-affected boundary layer during thermal treatment (Fig. 7.162). The same hardening depths are possible by suitably adjusting the laser power while increasing the traverse rate. This increase in traverse rate leads to a greater degree of bending of the rail (Fig. 7.163).

With the proviso that the hardening depth remains constant, an increase in the traverse rate in detail leads to

- higher laser power,
- higher process temperature,

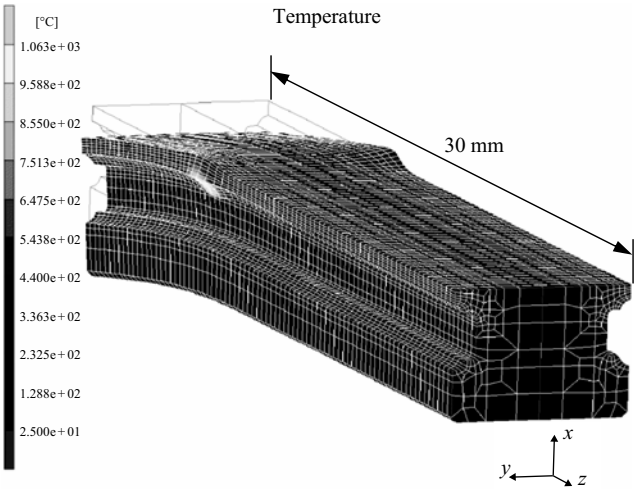

FIGURE 7.160. Temperature distribution in the deformed geometry (TKMD 12, Top Hat, $P_L = 1$ kW, $r_o = 1$ mm, $v_o = 1$ m/min, $t = 0.4$ s)

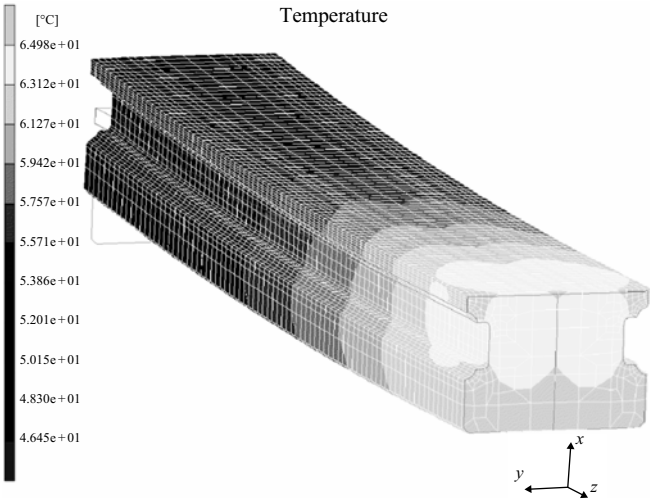

FIGURE 7.161. Temperature distribution in the deformed geometry (TKMD 12, Top Hat, $P_L = 1$ kW, $r_o = 1$ mm, $v_o = 1$ m/min, $t = 2$ s)

- lower thermal penetration depth,
- higher temperature gradients,
- lower maximum plastic compression in traverse direction, and
- greater expansion of the plastically compressed area.

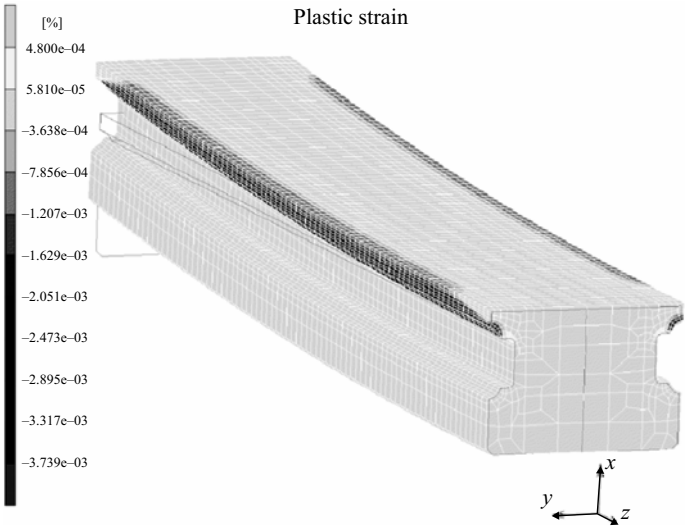

FIGURE 7.162. Component of the plastic expansion tensor in traverse direction in the deformed geometry (TKMD 12, Top Hat, $P_L = 1$ kW, $r_o = 1$ mm, $v_o = 1$ m/min, $t = 2$ s)

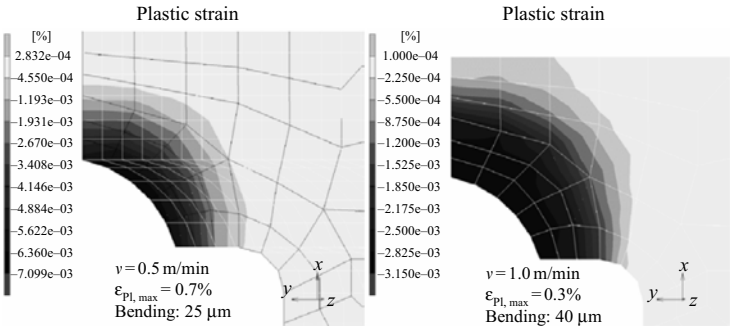

FIGURE 7.163. Component of the plastic expansion tensor in traverse direction in the cutting plane $z = 15$ mm for two different traverse rates (TKMD 12, top hat, $P_L = 1$ kW, $r_o = 1$ mm, $v_o = 1$ m/min)

The decisive factor for the greater degree of distortion with higher traverse rates and the same hardening depth seems to be the greater expansion in the depth of the plastically compressed area (Fig. 7.163).

For the purpose of predicting process parameters, dedicated software[3] exists that can calculate the results of a laser-beam-hardening process from input data

[3] E.g., Program system GEOPT, Fraunhofer IWS, Dresden, Germany [7.65].

like spot width, spot length, feed rate, and material, and vice versa: i.e., putting in the hardening zone geometry gives spot size and feed rate as the results.

Process Monitoring and Control

S. Bonss, R. Meyer, U. Haag, R. Polzin

Laser heat treatment for industrial applications needs to be a reliable process. Process monitoring or controlling are demands of most users. Laser heat treatment applications are executed with NC or mainly CNC machines. Because of this, feed rate and position of the laser spot are well defined by a particular program and controlled by the machine control unit. Spot geometry and applied spot size are given by laser optics and distance to the surface of the part. The surface temperature is the only process parameter which needs control. For laser heat treatment a certain material-dependent surface temperature or temperature range is required. Pure carbon steels have much free or loose bound carbon which dissolves in austenite pretty fast and at lower temperatures above austenitisation Ac_3. Alloyed steels or gray cast iron, in contrast, need to free the carbon of carbides and other hard soluble compounds. Those processes become possible and accelerate applying high temperatures close to the melting point. Roughly spoken the control task is keeping the surface temperature during laser beam hardening of steel within the laser spot at a certain level between temperature of austenitization and melting point. Adjusting laser power or feed rate are two principal ways to influence the surface temperature. A change of the feed rate at given spot size to keep the surface temperature constant changes the penetration of the hardening zone. It is recommended to optimize the feed rate following the required hardening zone geometry and fitting the laser power to the suitable surface temperature.

Fast and reliable measuring of the surface temperature during the laser process within the laser spot should be done without touching the surface. Optical methods are the preferred ones. Infrared thermometers, called pyrometers, or calibrated infrared camera systems, are suitable for that purpose. Infrared camera systems are very expensive and for most applications the information they give is more than a simple process control needs. In most cases the maximum surface temperature within the laser spot is needed as an input parameter for a laser power control. Infrared pyrometers give sufficient information. Pyrometer measurement is used because of following advantages: speed, economy, non-contact, wide measuring range, and measurability of moving objects.

Two types of infrared pyrometers are on the market. One type uses just one wavelength range and has to be calibrated to the emissivity of the surface. These are called radiation pyrometers. The other type measures at two wavelength ranges and calculates the ratio. This is called a two-color ratio pyrometer. It is independent on the emissivity of the surface or on the damping of the signal by a gray filter like steam or dust if the signal of both wavelengths is influenced similarly. But if the emissivity at the two wavelengths is different, the measure it is not independent from it. The radiation pyrometer gives a more reliable signal with lower noise. The emissivity at heat treatment of most steels is about 0.9 in the laser spot because

of the fast oxidation of the surface at elevated temperatures in the range of 1100–1400°C. Appropriate filters make the pyrometer work insensitive against radiation of diode, Nd:YAG and CO_2 lasers as well as daylight.

The feed rate of most laser heat treatment processes is in the range of 100 to 500 mm/min. A response time of the pyrometer of 10 ms is therefore suitable for those processes. High-speed pyrometers with 10–40 μs response time are necessary in some special cases. The spot-size question is another topic to discuss. Because of Stefan–Boltzmanns law temperature goes with the power of four into the radiation energy of an ideal black body [7.62].

$$E_r \propto T^4 \tag{7.13}$$

Higher temperatures have much more influence on the signal than lower temperatures. As a consequence, a field of observation larger than the laser spot can be used. But the measured value shows the risk to be much lower than the real temperature. If the proportion of the laser spot to cold areas in the observation spot changes because of misalignment or vibration the measured value fluctuates without a change of the real surface temperature. It is recommended to use a smaller observation field than the laser spot. The pyrometer spot has to be adjusted to the hottest area within the laser spot. In most cases this is done by experience or several tests. In more sophisticated systems the search for the hot spot is integrated and the pyrometer adjusts automatically, either by moving the pyrometer or by scanning the pyrometer spot [7.63, 7.64]. One option of lab systems as well as of commercially available high-power diode lasers is the coaxial measurement of the surface temperature by integrated pyrometer optics. By a semitransparent mirror the signal for the pyrometer is coupled out of the laser light path. For 3D-applications this is an advantage over external space consuming pyrometers. The disadvantage is the more difficult adjustment independently from the laser adjustment which is necessary because of the different wavelengths and spot sizes.

A control unit to adjust the laser power in dependence on the surface temperature can be established in different ways. One type is fully hardware-based systems with very short cycle times and high reliability but low flexibility. More common systems are software based. I/O-controllers in combination with a PC are used in combination with a much more flexible and user adapted software. Cycle times down to 20 μs are possible if I/O-controllers with a separate processor are used. A rough rule is to read and write about ten times faster than the signal changes. Those temperature-guide laser power controls can run separately or integrated in a CNC unit (Fig. 7.164).

Figure 7.165 shows the typical structure of the control loop. The electrical signal of the pyrometer is lead into a PID controller which modulates the laser output power to keep the temperature on the workpiece surface constant (Fig. 7.166). The control loop works just by comparing the set point of the temperature to the actual temperature of the measuring spot. Several technical implementations of this principle exist. The pyrometer can be coaxially integrated into the laser

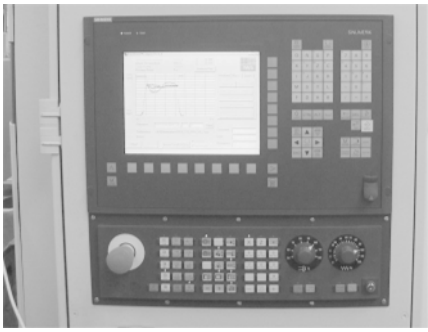

FIGURE 7.164. Laser power control "LompocPro" by Fraunhofer IWS integrated in a Siemens Sinumerik 840D with PCU50 and OP010 units

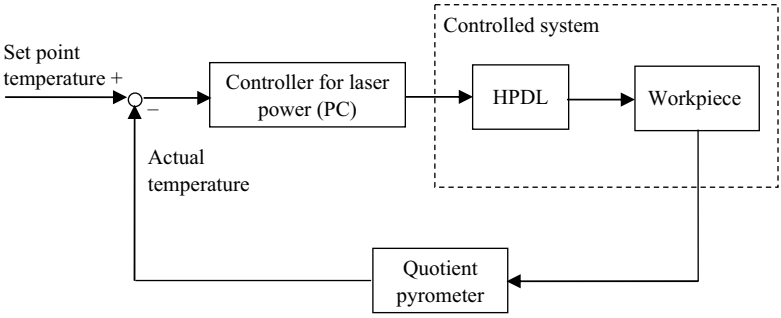

FIGURE 7.165. Block diagram of the control loop for temperature control of the laser power

head[4,5] as well as fiber-coupled to a front optic.[6] Figure 7.167 shows a setup with a pyrometer coaxial to the laser beam, integrated into the laser head. The sample position can be adjusted by a camera.

The efficiency of the closed-loop temperature control setup may be tested by hardening dummies of ^{100}Cr6, for example, with flat surfaces using a diode laser. The graphs in Fig. 7.168 show the temperature/laser power versus. time diagram and resulting hardness for this setup. It can be seen from the graphs that the closed control loop for the surface temperature leads to a reproducible hardening depth.

Figure 7.169 shows an example of a fiber-coupled temperature control system. The system consists of a ratio-pyrometer with front-optic, a high-speed computerized PID-controller, and an industrial PC with graphic user surface for operation and evaluation. Ratio-pyrometer, PID-controller, and industrial PC are in a single

4 System by Stiefelmayer GmbH & Co. KG, Denkendorf, Germany.
5 System by Robert Bosch GmbH, Stuttgart, Germany.
6 TCS (Temperature Control System), ThyssenKrupp Laser-Technik GmbH, Aachen, Germany.

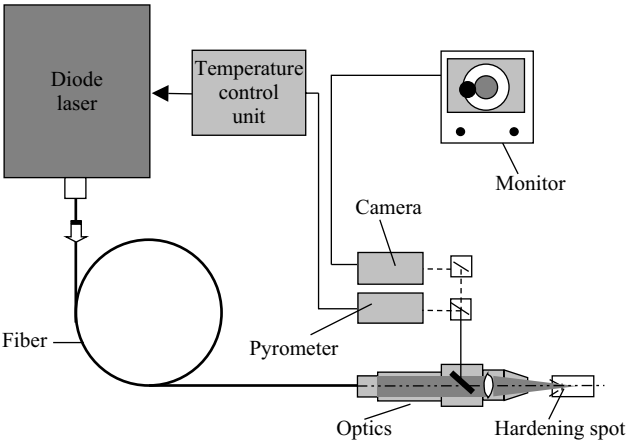

FIGURE 7.166. Principle of closed-loop temperature control

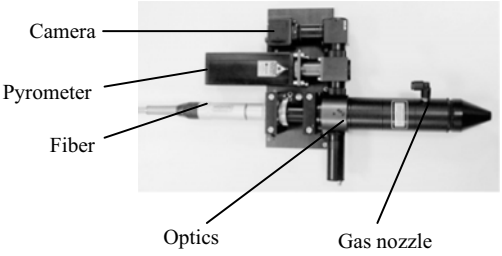

FIGURE 7.167. Experimental setup of working head

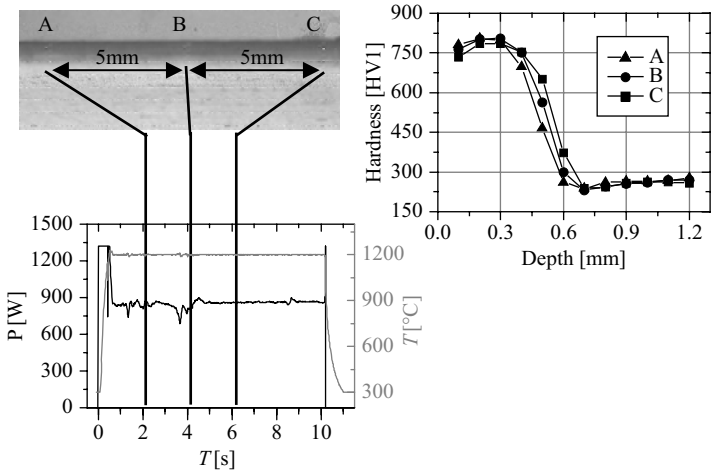

FIGURE 7.168. Testing of control loop

FIGURE 7.169. Example of a temperature control system

compact and portable housing. The front optic of the ratio-pyrometer is connected with the other components of the temperature control system by a flexible optical fiber. The measurable temperature of the shown system ranges from 600°C to 1600°C.

At the area, where the laser beam hits the component during the operation the surface of the component is heated up. The front optic of the ratio-pyrometer detects the heat radiation, which is emitted from this interaction zone and the ratio-pyrometer converts it into two signals. These signals correspond to the heat radiation at the two wavelengths $\lambda_1 = 1{,}200$ nm and $\lambda_2 = 1{,}700$ nm. From the ratio of these two temperature signals the so-called ratio-temperature is evaluated. The PID-controller uses this temperature as actual temperature and compares it with the nominal temperature, which is preset by the user. This variance comparison leads to an output of a correcting variable to the laser power control.

As the determined ratio temperature is independent of the spectral emission, an adjustment of the digital ratio-pyrometer to the material specific spectral emissivity ε is not necessary. The combination with the high-speed PID controller allows a temperature control by adjusting the laser power in 2.5 ms; this avoids undesirable effects like melting on the component surface.

The parameter sets of already realized hardening processes can be memorized. Also the measured values of the temperature adjustment can be memorized for a later check or evaluation.

The front optic, which detects the temperature can be mounted outside of the laser beam path or integrated into the beam path. When the laser is combined with a robot, integration into the beam path maintains the component accessibility of the robot. Thus, even when complex contours are treated the temperature can be controlled without problems. The front optic can be adjusted by means of a pilot light.

7.3.2.2. Peripheral Techniques

R. Meyer

To guarantee a wide dissemination of the diode laser technology throughout the industry, not only must the quality and efficiency of the laser beam be improved, but peripheral techniques supporting the application of diode lasers have to be provided as well. Besides a reliable temperature control (cf. "Process Monitoring and Control"), well-functioning peripheral components open reproducible qualities and high efficiencies of laser processing, justifying a wide use on an industrial scale.

Parameter Database

For a fast setup of laser hardening processes, a parameter database can be helpful. Its purpose is to meet the process requirements for hardening extremely manifold geometries of workpieces, e.g., tooth flanks and peaks, drillings, surfaces over hollows, etc. With an input of the desired hardness depth and the material, the database should deliver important process parameters like the required surface temperature or the time of interaction. Together with the online measuring of the surface temperature, these parameters determine the feeding speed and the emitted laser power. By providing the suitable parameters, the database helps to increase the productivity and to avoid standstills and the production of rejects.

The technical features of such a parameter database have to be

- collection of customer, trial, and evaluation data;
- recording of the processing data, e.g., feeding speed, temperature, etc.;
- fast retrieval of difficult processing geometries and materials;
- fast and simple searching for specific parameters and records;
- search for pictures of workpieces, experimental setups, cross cut specimens, clamping, etc.;
- supplement and support for users;
- user-friendly tool tips,
- administration of tables of process parameters, pyrometer diagrams, progression of the hardening processes; and
- documentation by reports.

A parameter database that meets these requirements can be realized as a graphical application.[7] It may comprise databases of common office software, one for pure material data (independent of the hardening process), and others containing customer specific, experimental and laser parameter sets. All databases should be integrated in a common user interface. One register (Experimental Data) should contain the name of a workpiece, the number of a drawing, number and name of a material, reachable hardness and depth, feed speed, temperature, shape and

[7] Database set up by Stiefelmayer GmbH & Co. KG, Denkendorf, Germany.

size of the laser beam, optics and focal length, customer specific data, etc. Even information on structural analysis of particle sizes and distributions may be filed. Another register (Evaluation) should contain pictures of workpieces, clamping, material structures, hardening processes, etc.

For easy application, the database should provide search masks allowing special data sets to be found. To search for a specific workpiece, AND/OR connections can be helpful. As another feature, the database should support the formulation of documentation or protocols. The database should be accessible by several clients in networks.

Fast Programming Strategies – CAD/CAM Coupling

Programming of tracking sophisticated hardness profiles may take several days and often requires teaching. A direct coupling between CAD data and CAM processing according to the geometry of the workpiece accelerates the process of generating CNC programs, leading to higher productivity of the laser unit. The generation of a CNC program can be comfortably realized as shown in the flow chart[8] (Fig. 7.170).

The basis is the CAD file of a workpiece to be hardened. The requirements for the hardening (e.g., hardness depth, material) are input to the parameter database

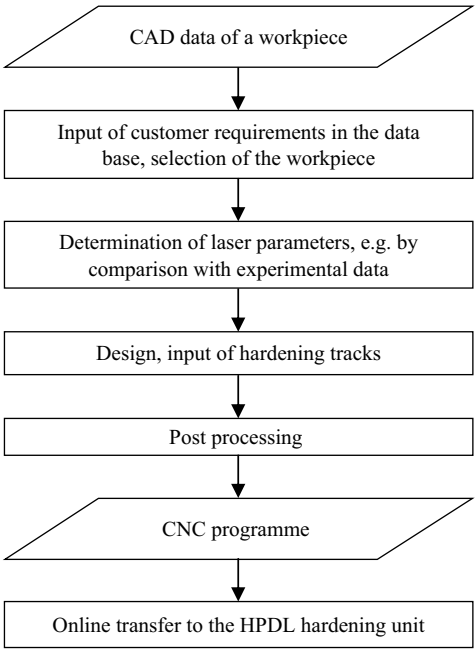

FIGURE 7.170. Flow chart of the CAD/CAM coupling together with the parameter database

[8] CAD/CAM coupling realized by Stiefelmayer GmbH & Co. KG, Denkendorf, Germany.

(cf. “Parameter Database”). By using a search function, workpieces with similar geometry or processed under similar conditions can be found. The laser parameters can then be determined directly or empirically from earlier processes. The desired hardness track is added in design to the CAD file. After a post processing of the data, generating a CNC file with modifiable parameters, the CNC program can be transferred to the handling unit and the laser control. Multi-head applications in parallel or in sequence are possible.

Modular Beam-Forming Optics

For high-power diode lasers, an increase of the emitted laser power is reached by arranging single diode laser bars on top of each other as stacks. However, the quality of the resulting beam suffers from deficiencies in precision and package density of the combined single beams. Therefore, the highly integrated packaging has to be combined with innovative concepts for the beam forming. In case of line shaped or flat geometries of beams, the laser power has to be adapted within the track to the beam geometry. This task can be accomplished by a scanner, realizing a variable profile of intensity synchronously to the temperature sensor.

A scanner concept of cylindrical lenses and rotating facette lenses mounted in bearings allows for flexible beam forming. A prototype of such a scanner unit[9] is shown in Fig. 7.171. The width of this scanner is foreseen to be 5 to 35 mm on

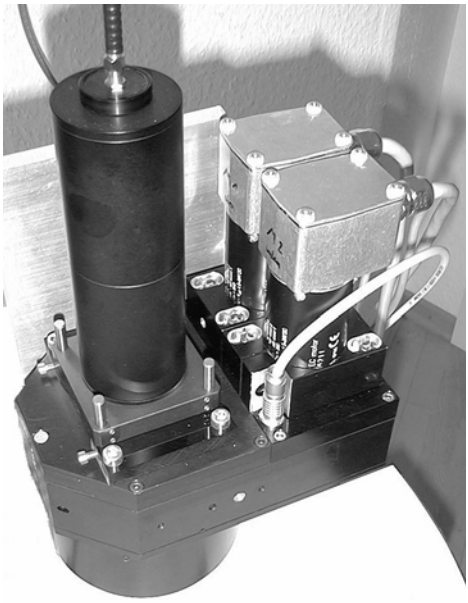

FIGURE 7.171. Scanner unit to form the beam of temperature controlled diode lasers

[9] Scanner unit developed by Stiefelmayer GmbH & Co. KG, Denkendorf, Germany.

the surface being adjusted by a motor control. Instead of the scanner unit, fixed optics can be used.

As an alternative to the scanner system for diode lasers, multi-head processing should be mentioned. The surface of a workpiece can be divided in several sectors and each sector can be processed by a single laser. The laser power within a sector can be controlled separately considering the respective geometry (see, e.g., Chapter 6.3.6).

7.3.2.3. Parameter Dependencies

Focus Alignment

R. Polzin

Using a high-power diode laser with modular construction, like the "modular hardening system" (described in Chapter 6.3.6), it is possible to influence the contour of the hardness profile. The gradient of the hardness profile depends on the arrangement of power density distributions of the single modules to each other. For example, it is possible to increase the power density distribution by positioning the focal points of the single modules on top of each other. The time of exposure to the laser beam can be increased by arranging the focal points in line. Figure 7.172 shows the influence of the focal points' distances on hardness results. The abscissa corresponds to the distance between the focal points. At zero the focal points are superimposed. This results in focusing of the maximum laser power on an area of $A_{\text{Focus}} = 2.0 \times 4.0$ mm^2. At a distance of $d_x = 2.5$ mm the focal points are arranged in line. In this example, the outer modules are run with a constant power $P_L = 150$ W. The beam power of the middle module is temperature controlled

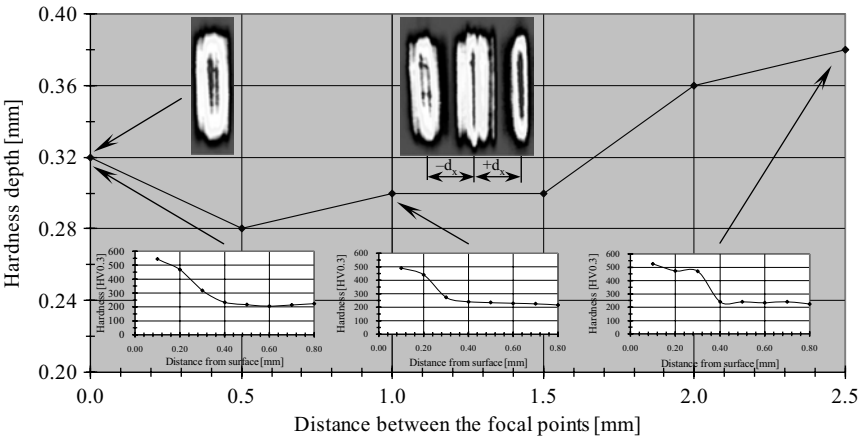

FIGURE 7.172. Changing of the hardness results caused by variation of the distance of the focal points

with a preset temperature of $T = 800°C$. Evidently, the hardness penetration depth increases with the duration of exposure to the laser beam.

The upper part of the diagram shows the intensity distributions on the working surfaces. The left figure in Fig. 7.172 shows the intensity distribution, when the three focal points are completely superimposed. The right figure in Fig. 7.172 shows the different intensity profiles of the single modules.

In the lower part of the diagram exemplary progressions of the hardening process at the focal distances $d_1 = 0.0$ mm, $d_2 = 1.0$ mm, and $d_3 = 2.5$ mm can be found. The hardness at the surface is approximately same for all shown focal distances and amounts to approximately 500 HV0.3. The hardness of the basic material is about 220 HV0.3. Clearly an enlargement of the focal point in the feeding direction, which is tantamount to increasing the duration of the laser beam exposure, leads to a distinct variation of the progressing of the hardening process. Therefore, the modular hardening system allows an increasing of the hardness penetration by increasing the time of exposure to the laser beam at constant feed rate.

Oxidation

R. Polzin, R. Meyer, S. Bonss

Often hardening is the final step in a process chain of a workpiece or product. This is especially valid for laser hardening, since in contrast to other hardening processes, the distortions are fewer and an after-treatment can be omitted. To keep this advantage, other process-dependent negative influences on the surface quality have to be avoided. However, during the hardening, surface heating beyond 1000°C occurs, leading to oxidation processes or scaling. Scaling particles on workpieces are rubbed off in the later use and cause abrasive wear or mix with lubricating liquids, for example, causing impairments of other processes. Therefore, a shielding with inert gases, e.g., nitrogen or argon, can be carried out during the hardening to prevent oxidation.

On the other hand, the oxidation offers advantages for the laser hardening as well. In the actual wavelength range about 30% to 40% of the laser light is absorbed from bare metal surfaces (see Fig. 7.154). The rest is reflected without effect (for comparison: 35% of the radiation of an Nd:YAG laser is absorbed and only 5% of a CO_2 laser, due to its longer wavelength). In contrast, if the surface is oxidized, up to 80% or 90% of the diode laser light are absorbed. Thus, an increase of the absorption is beneficial for a higher efficiency, e.g., reduction of the laser power or reaching faster feed speeds and higher track widths. Both of them offer economic advantages. This fact is illustrated in Fig. 7.173.

If forming gas is used as shielding gas, the hydrogen content leads to a reduction of the material surface and a light oxidation can be eliminated. In case of workpieces which are not allowed to show any oxidation or scaling, at least a tarnishing of the surface could be favorable. Often, a tarnished surface is admitted by the customer. Another possibility consists of controlling the oxidation during the hardening by a shielding gas, leading to a partial oxidation. Such a defined

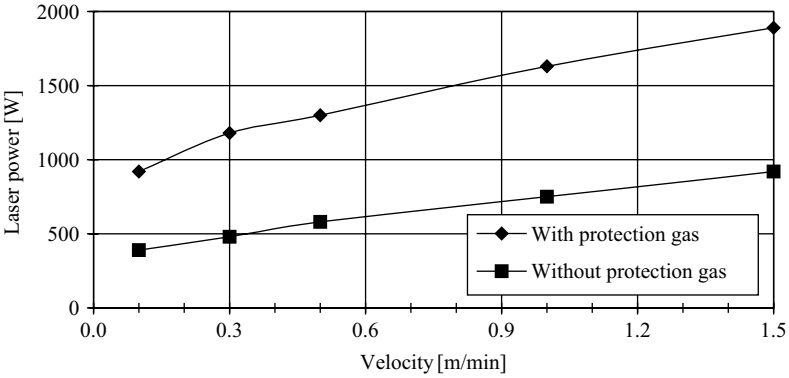

FIGURE 7.173. Dependency of the hardening results on the shielding gas

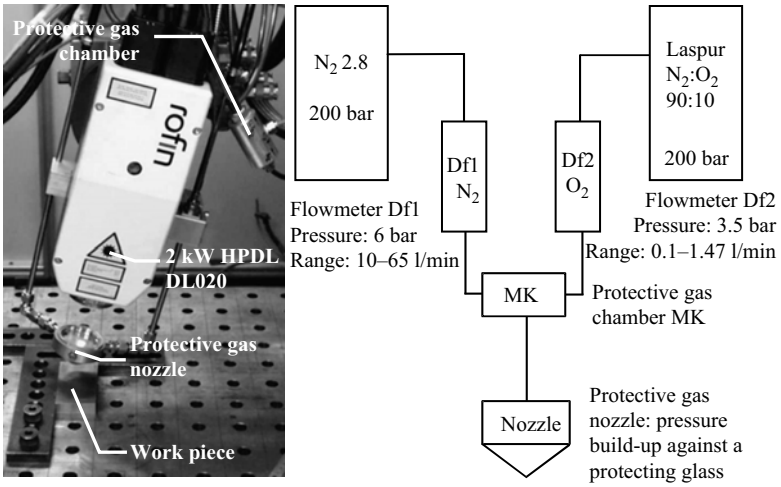

General:
Diode laser: DL020 Rofin Sinar, temperature control system: LASCON, internal
Beam angle: 15°, focal length: 125 mm, working distance: 129 mm (out of focus)
Track width at work piece: 11 mm, nozzle distance: 1.0 mm, dragging arrangement

FIGURE 7.174. Facility to realize defined levels of surface oxidation to optimize the surface absorption for laser hardening

oxidation of the surface can enhance the adsorption of the laser radiation effectively without generating impairing particles.

A suitable setup for creation of a defined surface oxidation is shown in Fig. 7.174. It comprises a standard diode laser ROFIN DL020 with a focal length of 125 mm, temperature control, nozzles of different forms integrated in the optical path, gas mixing station, etc. A piece of the material Ck45 with a planed surface serves as specimen. (Coarse and fine planed surfaces cause no big difference.)

Different oxidation levels aim at an optimized absorption in order to

- diminish the required power,
- avoid unfavorable reflections,
- decrease the load of beam forming and controlling devices,
- reach higher hardening depths with the same power,
- reach the same hardening depth with a higher feed speed, and
- optimize the use of shielding gas in terms of gas mixing ratio (N_2 and O_2), flow, nozzles, etc.

A comparison between a reference track under normal air (track 1), a reference track under N_2 (track 2), and several tracks under different shielding mixtures of N_2 and O_2, with an O_2 content ranging from 0.000083% (track 3) to 0.004% (track 20), demonstrates the effect. Different grades of oxidation arising from the use of different mixtures of shielding gas at a feed speed of 240 mm/min are shown in Fig. 7.175.

Examination of the hardened tracks renders the following:

- By the shown tarnish colors on the workpieces, no increased values of absorption can be reached. Higher grades of oxidation are supposed to be necessary, meaning higher contents of O_2 in the N_2/O_2 mixture. As a disadvantage, oxide particles may occur for higher O_2 contents.
- Evaluation of the hardness tracks (Fig. 7.176) reveals a nearly constant hardness for all mixtures and a slight tendency (track 20) toward higher hardness depths in case of higher oxidation.

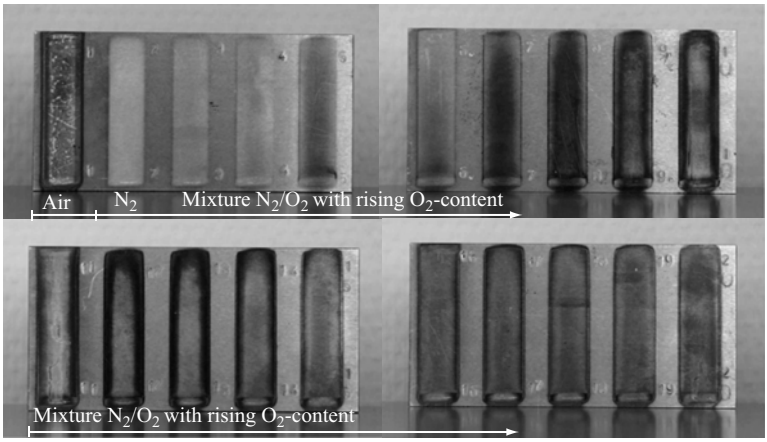

FIGURE 7.175. Grades of oxidation for different mixtures of shielding gas (tracks 1 to 20; rising O_2-content from track 2 to 20)

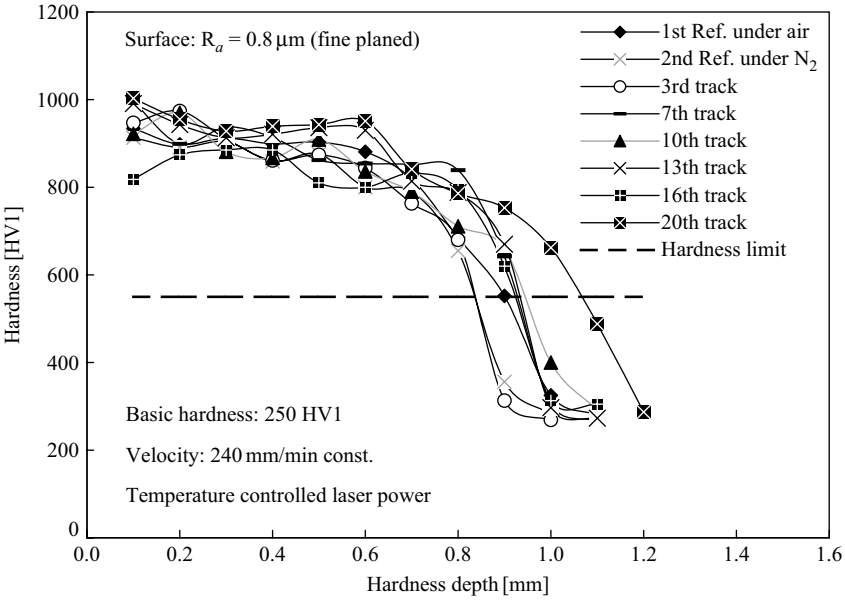

FIGURE 7.176. Grades of hardness depths for different mixtures of shielding gas (1st track under air, 2nd track under N_2, 3rd track lowest O_2 content (0.000083%), 20th track highest O_2 content (0.004%))

- Hardening under plain air requires much less laser power (track 1, P_L = 990 W) compared to hardening under a shielding atmosphere (other tracks, $P_L \geq$ 2,100 W).
- In case of subsequent treatments of the surface, e.g., galvanizing or phosphating, a gas shielding is necessary during laser hardening to avoid oxidation products on the surface.

During hardening, the following problems can arise:

- An appropriate flow is about 4–5 l/min, generating bare hardenings with pure N_2. The use of flow rates of about 20 l/min has a cooling effect, impairing the hardening.
- The shielding gas changes the characteristic of the optical path, turning the set point of the temperature control (e.g., from 1250°C without gas to 1450°C with gas). A calibration to the shielding gas gets necessary. The nozzle has to be water cooled to withstand the strong reflection of the laser radiation. Due to its location near to the surface of the workpiece, the nozzle is additionally charged by the hot surface temperature.
- The shielding gas flows into the area of the focused laser beam, receiving a strong thermal load which might destroy the gas. Therefore, the shielding gas has to be supplied from a certain distance to the hardening process.

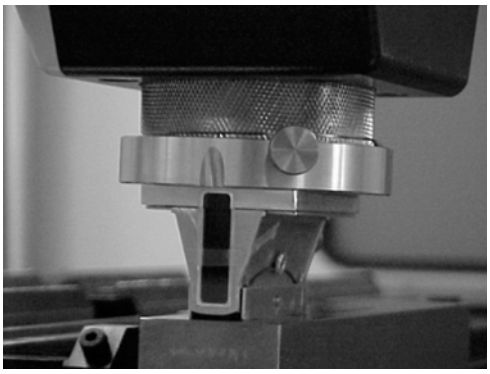

FIGURE 7.177. "Taylor-Nozzle" for laser heat treatment without surface oxidation

Laser beam hardening can be done in shielding gas atmosphere as well as in a vacuum chamber. In most cases shielding gas is cheaper and easier to integrate in automatic production lines than a vacuum chamber. All of the commonly available inert gases like argon or helium are suitable for use. But for brief heat treatments like laser beam hardening even much cheaper nitrogen can be used. Nitriding of the steel surface in those typical short interaction times of just several seconds or tenths of seconds has not been done so far. Simple gas nozzles are suitable for some applications, but it is more reliable to use small gas chambers with a continuous flow of shielding gas to avoid any discoloring. One example is the Taylor nozzle shown in Fig. 7.177 [7.68].

Surface Quality

R. Meyer

In Fig. 7.178, the hardness of differently processed surfaces of the material Ck45 is shown, obtained at a speed of 200 mm/min and by use of an Nd:YAG laser with a laser power of 600 W. The difference between the Nd:YAG laser wavelength of 1,064 nm and the diode laser wavelength of about 900 nm is supposed to be minor.

The material surfaces treated in Fig. 7.178 are as follows:

- milled and roughened,
- milled and planed,
- grinded, and
- polished.

The diagram shows an influence of the surface finish on the hardness depth. There is a tendency toward higher hardness depths for surfaces of higher quality. However, it is surprising that for the milled as well as for the polished surface the same hardness is achieved. As a reason, a kind of pre-oxidation is supposed, contributing to a uniform absorption.

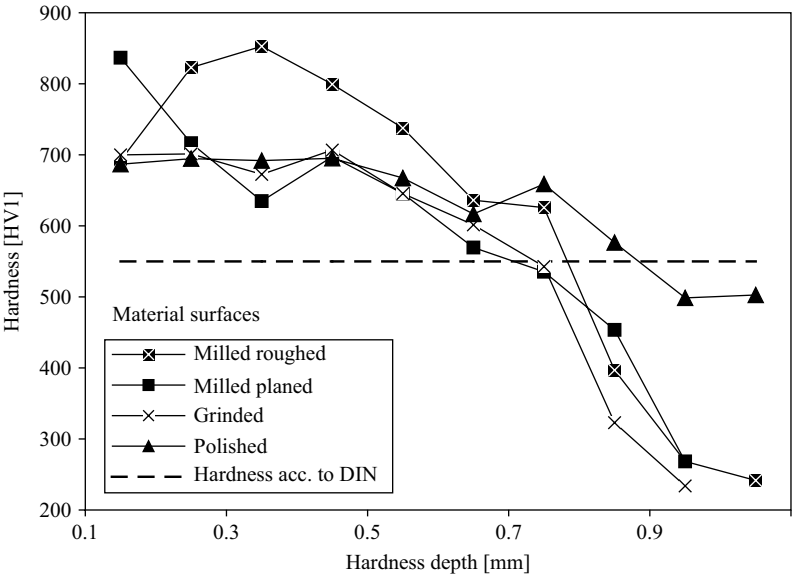

FIGURE 7.178. Relation of hardness depth to the surface finish for the material Ck45, speed of 200 mm/min, power of 600 W

Velocity

R. Meyer

If the temperature is held constant below the melting temperature while varying the feed speed, the following statements can be made:

- The hardness depth decreases after reaching an optimal speed if the speed is increased further.
- The surface temperature decreases in case of reaching the maximum power with increasing speed.

In Table 7.13, the optimal speed as well as the corresponding hardness depth is given for different materials at two temperatures. The minimum hardness depth required here is 0.1 mm.

With a sufficient reserve of the laser power, constantly high values of hardness and depths can be reached based on the temperature control even for higher feed speeds. This is of special interest for line-shaped foci as well.

Laser Power and Temperature

R. Polzin

A higher surface temperature results in a significantly higher hardening depth. Figure 7.179 shows hardness profiles obtained from different surface temperatures

TABLE 7.13. Relation between hardness depth and optimum speed for different materials

Material	Optimum speed [mm/min]	Hardening depth [mm]	Surface temperature [°C]	Remarks
Ck45	300	0.8–0.95	1350	Laser power 835 W
	150	0.6	1050	Laser power 542 W
90MnCrV8	200	0.9–1.0	1300	
	150	0.8	1050	
100Cr6	200	0.65–0.75	1450	
	450	0.3	1050	
42CrMo4	300	0.8–0.9	1350	
	200	0.6	1050	

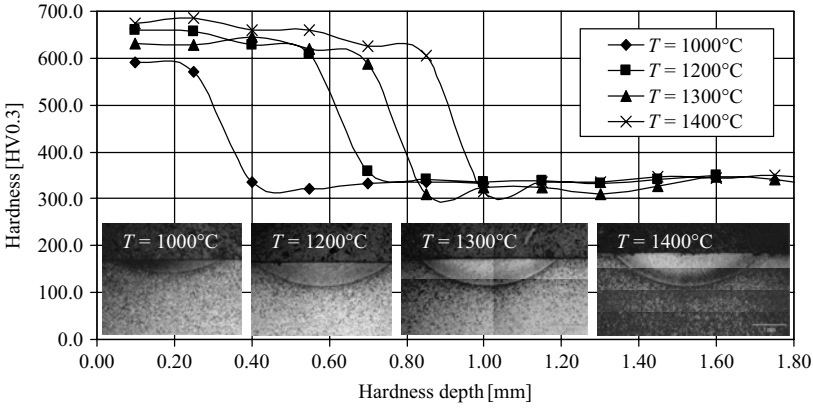

FIGURE 7.179. Hardness depth versus surface temperature

at a constant velocity and the use of Argon as shielding gas. For example, at a surface temperature of $T = 1400°C$, a hardening depth of $t = 0.9$ mm and a surface hardness of 680 HV0.3 can be reached without any melting of the surface.

The other way around, the hardening depth can be adjusted by varying the velocity. Figure 7.180 shows hardness profiles obtained at velocities in a range of $v_{S,min} = 0{,}05$ m/min to $v_{S,max} = 2{,}0$ m/min at a constant surface temperature and the use of argon as shielding gas. For example, at a velocity of $v_S = 0.05$ m/min a hardness depth of $t = 1.10$ mm and a surface hardness of 680 HV0.3 can be reached without any melting of the surface.

Microstructure and Chemical Composition

R. Polzin

The result of the laser hardening depends among others on the material to be hardened. Great influence has the microstructure and the chemical composition.

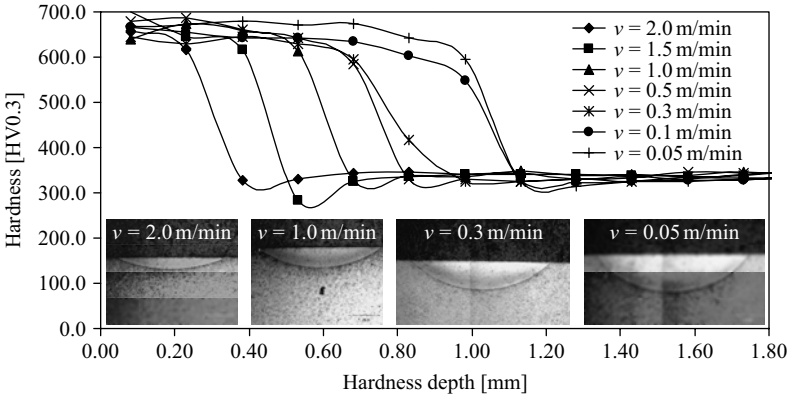

FIGURE 7.180. Hardness depth versus velocity ($T = 1300°C$)

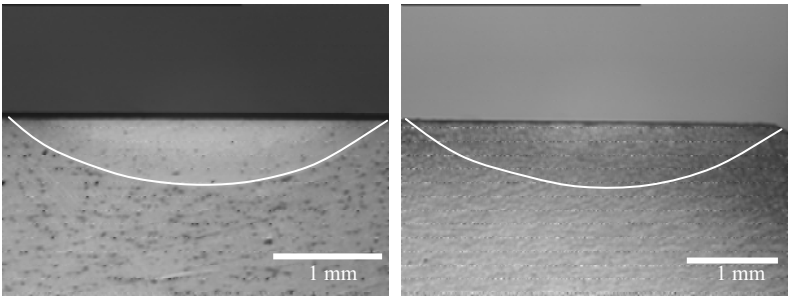

FIGURE 7.181. Cross sections of tool steels of different chemical composition (material: left 1.2738; right 1.2379)

The microstructures can be subdivided roughly into cast structure and forged structure.

The hardness to be obtained depends for both, the cast structures and the forged structures on the carbon content. If tool steel has to be hardened, the portions of the alloying elements are important.

Figure 7.181 shows, as an example, the cross sections of two tool steels which have different chemical compositions.

The materials have been hardened with a constant velocity of $v_s = 0.1$ m/min, the same laser power and the same dimension of the focus.

For the material 1.2738 a depth of the hardened lens of $t = 0.60$ mm and a width of the track of $b_{track} = 3.4$ mm with a maximum hardness of 735 HV0.3 can be realized. For the material 1.2379 the depth of the hardened lens is $t = 0.70$ mm, and the width of the track $b_{track} = 3.7$ mm. The maximum hardness is 540 HV0.3 and the basic hardness 245 HV0.3.

General Recommendations

R. Meyer

As a summary of the parameter considerations, the following recommendations can be given:

- The optimum surface temperature has to be selected, depending on the material, about 50°C below its melting temperature. The set point of the temperature control has to be set to this value since the control doesn't work correctly with smelt.
- Hardness and depth can be easily controlled by using a temperature control. Apart from the material to be processed, the surface temperature and the feed speed are important parameters. To keep the selected surface temperature with increasing speeds, reserves in the laser power are important.

7.3.2.4. Applications and Results

Hardening of Flat Samples with Transversal Drill-Holes

R. Polzin

As a simple example, hardening of flat samples of tool steel with transversal drill-holes underneath the surface is pictured in Fig. 7.182. The left picture shows a sketch of the component with the drill-holes. The three holes have a diameter of $d = 6$ mm and are at the distances of $h1 = 2.5$ mm, $h2 = 1.8$ mm, and $h3 = 0.7$ mm beneath the surface.

Figure 7.182, right, shows the temperature of the surface detected with a temperature control system (TCS, see Fig. 7.169) during the hardening process. The diagram shows that it is possible to hold the hardening temperature very constantly at $T = 1300$°C by the TCS. Even at the drill-hole 3 with the remaining wall thickness of only $h3 = 0.7$ mm a change of the temperature can be avoided. The output voltage signal can vary between $U_{\min} = 0$ V (:=0% $P_{\max}$) and $U_{\max} = 10$ V (:=100% $P_{\max}$). From the output voltage the activity of the control unit in the area

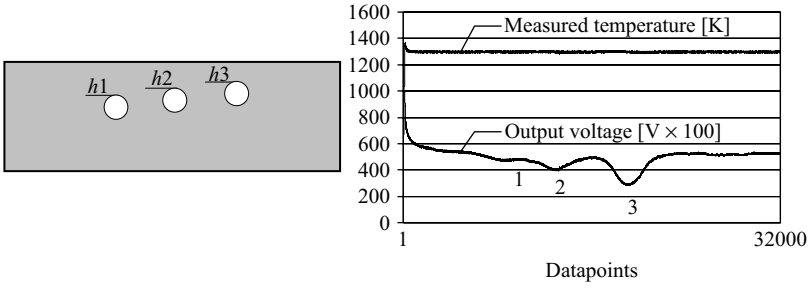

FIGURE 7.182. Left: Specimen with covered drill holes. Right: Measured temperature profile

FIGURE 7.183. Hardened component with covered drill holes

of the drill-holes can be seen very clearly. At hole 3 the beam power has been reduced from approx. 60% to only 30%.

Figure 7.183 shows the hardened component with covered drill-holes. There is no melting at the surface.

Edge Hardening with Multispots

R. Polzin

A modular high-power diode laser system, as for instance the modular hardening laser described in Chapter 6.3.6, offers the option of increasing the time of exposure to the laser beam at constant feed rate (cf. "Focus Alignment").

The angular arrangement of the single modules allows the simultaneous surface treatment of the two faces of an edge without risking an overheating of the edge. The left picture in Fig. 7.184 shows the laser surface treatment of an edge.

For hardening the edge, two laser-modules for each face of the edge are used. To increase the holding time the focal points of the two lasers have been arranged in line. The first module is run with constant laser-power and the second one is temperature controlled. The right part of Fig. 7.184 shows a cross section of the hardened edge, featuring a very homogeneous hardening result.

Using a conventional laser for the surface treatment, it would have been possible to either harden the two faces of the edge in succession, or to move the laser-beam along the edge with an angle of 135° to both faces. If the two flanks were hardened in succession, an annealing zone in the overlapping area of the hardened tracks would occur inevitably. On the other hand, moving the laser beam along the edge would include the risk of melting on the edge.

The hardness in the example shown amounts very constantly to 700 HV0.3 up to a depth of $t = 1.2$ mm, which is nearly the double basic hardness. The depth of the hardness lens is $t = 1.7$ mm. The visible phase in the cross section results from the preparation of the cross section.

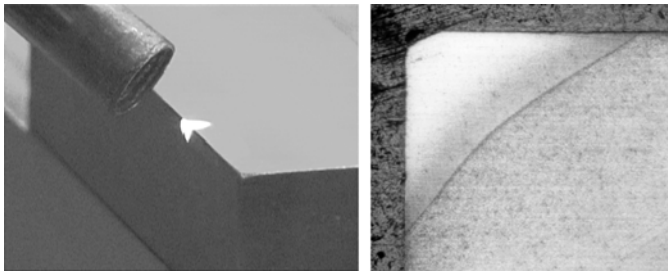

FIGURE 7.184. Left: Laser hardening of an edge. Right: Cross section

Hardening of Linear Guiding Rails

G. Vitr

Hardening of linear guiding rails with minimized warpage has been investigated by one of the following methods:

1. Processing with two Nd:YAG lasers for hardening and straightening using the two-beam method.
2. Processing using a dedicated high-power diode laser system.[10]
3. Processing using a dedicated high-power diode laser system[10] with homogenizers [7.67] and subsequent positioning of the modules (Fig. 7.185):
   - Processing with defocused beams and slow-axis direction of the beams parallel to the ball-bearing tracks (x-direction) with temperature control.
   - Processing with focused beams (same power density distributions [PDD] and same beam cross sections 0.8×6 mm^2, fast $\times$ slow) and slow-axis direction parallel to the ball-bearing tracks without and with temperature control.
   - Processing with focused beams and slow-axis direction vertical (y-direction) to the ball-bearing tracks with temperature control.
   - Processing with defocused beams and slow-axis direction vertical to the ball-bearing tracks with temperature control.

Hardening with Two Nd:YAG Lasers. Nd:YAG laser radiation[11] can be applied for minimized warpage hardening of linear guiding rails[12] using a two-beam method. The focusing lenses in the presented example have a focal length of $f = 140$ mm. The lenses have to be adjusted using different processing distances to produce the same beam diameters of 4.5 mm and the same PDD on the surface of the tracks. The processing strategy for hardening and straightening using the two-beam method

[10] For example, process-controlling modular diode laser system (PMDS) [7.66].
[11] For example, LAY 2006 and HL 3006, Trumpf GmbH, Ditzingen, Germany.
[12] For example, TKVD 15 (material: 58 CrMoV 4) from INA-Lineartechnik, Herzogenaurach, Germany.

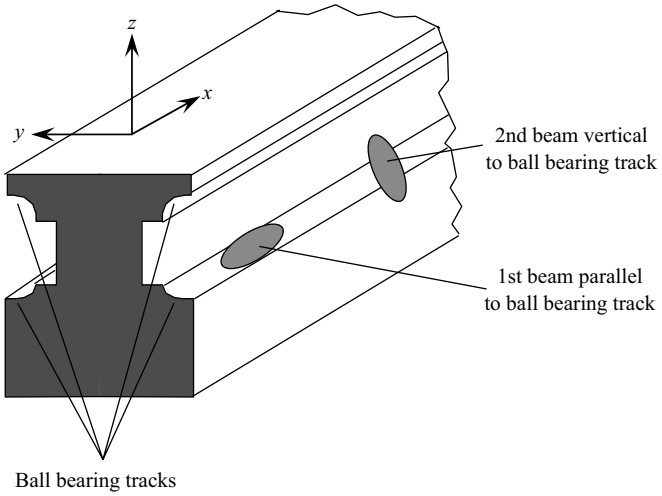

FIGURE 7.185. Scheme of the positioning of the beam orientation (slow axis parallel or vertical to the ball-bearing tracks)

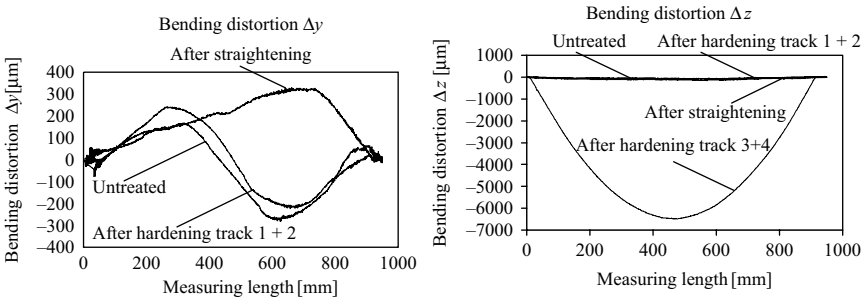

FIGURE 7.186. Distortion measurement of a linear guide rail TKVD 15 hardened and straightened using the two-beam method ($P_L = 1{,}150$ W, $v = 1.4$ m/min)

is shown in Fig. 7.186. Using the same laser power of $P_W = 1{,}150$ W and the same PDD, first the two lower ball-bearing tracks on the guide rails are hardened simultaneously. Turning the rail, the two upper ball-bearing tracks are hardened afterwards. The process speed is varied from $v = 1{,}300$ to 1,700 mm/min. The hardening depths achieved is 0.2–0.27 mm; the hardness is around 900 HV0.3, which meets the requirements of this specific example. Figure 7.187 shows the cross section of a rail processed with a speed of $v = 1,400$ mm/min.

Prior to the processing of the rails and after each processing stage, the bending distortion of the rail Δz has to be measured in the x-z-plane and Δy in the x-y-plane (Fig. 7.188). The bending distortion of the rails after processing should be of the same magnitude as their as-cast state (approx. 50–200 µm/m each for Δz and

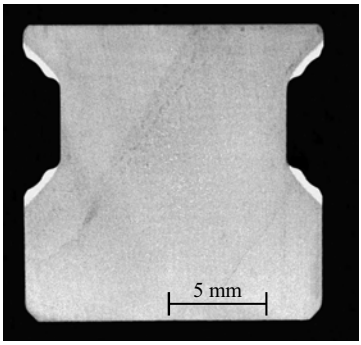

FIGURE 7.187. Cross section of a linear guide rail TKVD 15 hardened and straightened using the two-beam method (P_L = 1,150 W, v = 1.4 m/min; effective hardening depth HD = 0.23 mm; hardness 900 HV0.3)

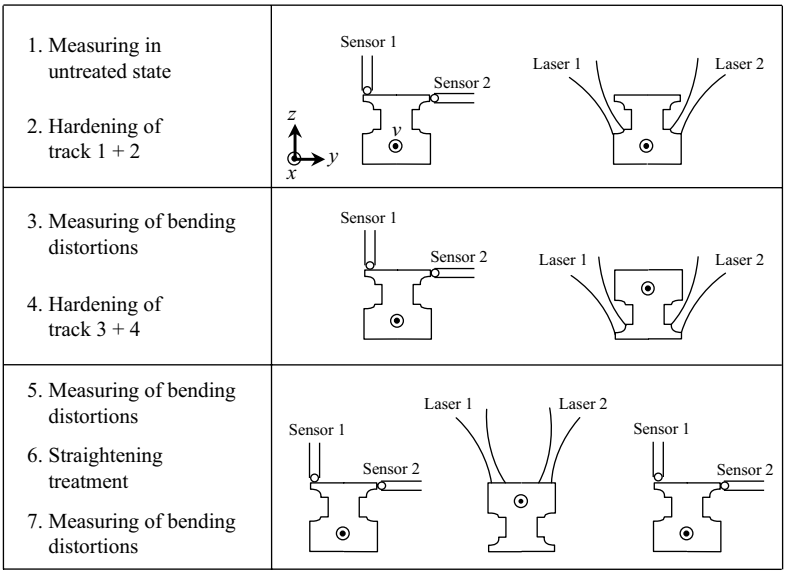

FIGURE 7.188. Processing strategy for the hardening and straightening of linear guiding rails using the two-beam method

Δy). The warp can be measured using suitable sensors[13] with a measuring range of ± 1 mm (Δy) and $\pm$ 5 mm (Δz).

To compensate for the bending distortion induced during hardening, the guide rails can be straightened at the back of the rail using the two-beam method by

[13] For example, Millitron, Mahr GmbH, Göttingen, Germany.

positioning each beam between the bore holes and the outer edge, keeping a distance to the outer edge of around 2 mm. Straightening of the rails can be effected using the same laser power of $P_W = 1{,}150$ W as during hardening, and a process speed of $v = 900$ mm/min. Doing so, the maximum permissible deflection of the rail of around 50–200 μm/m (as-cast state) will be maintained after the hardening and straightening process (Fig. 7.186). The linear guiding rails of this example, hardened and straightened using the two-beam method, pass required endurance tests.[14]

Hardening with a Dedicated High-Power Diode Laser System. The aim of hardening linear guiding rails using a dedicated high-power diode laser system as, for instance, the process-controlling modular diode laser system (PMDS) [7.66] is a further reduction of the warpage by simultaneously hardening all four ball-bearing tracks. Figures 7.189 and 7.190 show a scheme and the process of hardening linear guiding rails using the four-beam method with eight modules. Each module has a maximum output of around 400 W. To reach high processing speeds (reduction of the warpage), two modules are positioned simultaneously on one bearing tracks. One module is operated with constant laser power, the other with temperature control. The surface temperature in the example presented is varied between 750–900°C in 50°C increments. The process speeds applied are 500, 750, and 1000 mm/min.

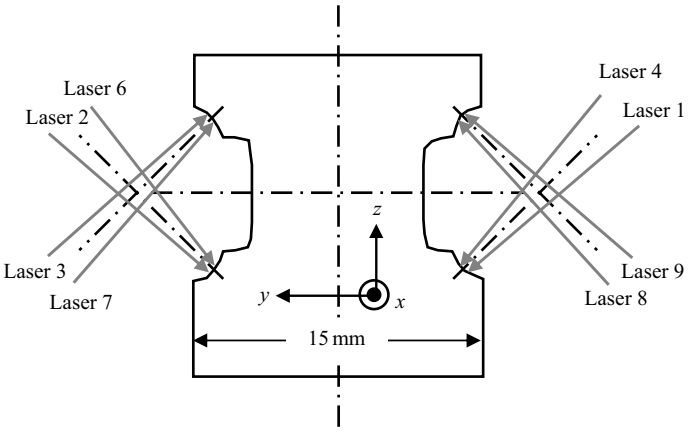

FIGURE 7.189. Scheme of the hardening of linear guiding rails using the four-beam method with eight diode laser modules (PMDS)

[14] A defined load is moved back and forth over the rails for a defined length (stroke length = 0.7 m) with a defined speed of $v = 1.5$ m/s, covering a total distance of 6,400 km. After this, the linear guiding rails show no changes on the surface topography. The surface roughness and the track geometry (osculation and track distance) are impaired only insignificantly. The tracks have an osculation of 51.7–53.2% (nominal: 51.8–52.3%), their roughness being $R_z = 0.22$–0.38 μm (nominal: 0.5 μm).

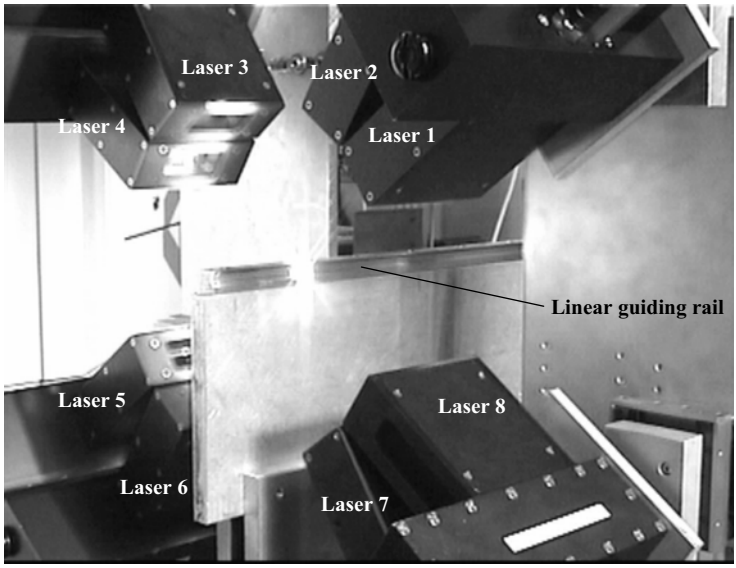

FIGURE 7.190. Hardening of linear guiding rails using the four-beam method with eight diode laser modules (PMDS)

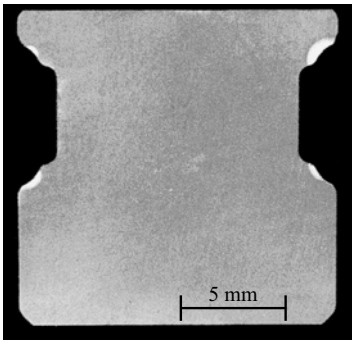

FIGURE 7.191. Cross section of a linear guiding rail TKVD 15 hardened and straightened using the four-beam method (PMDS modules 1, 3, 6, 8: $P_L = 400$ W, modules 2, 4, 7, 9: $T_R = 800°C$, $v = 750$ m/min)

Figure 7.191 shows that differences in the power density distributions of the diode laser modules produce individual hardening geometries for the four ball-bearing tracks. With $\Delta y > 1$ mm/m, the resulting bending distortions and torsional distortions are well above the as-cast state.

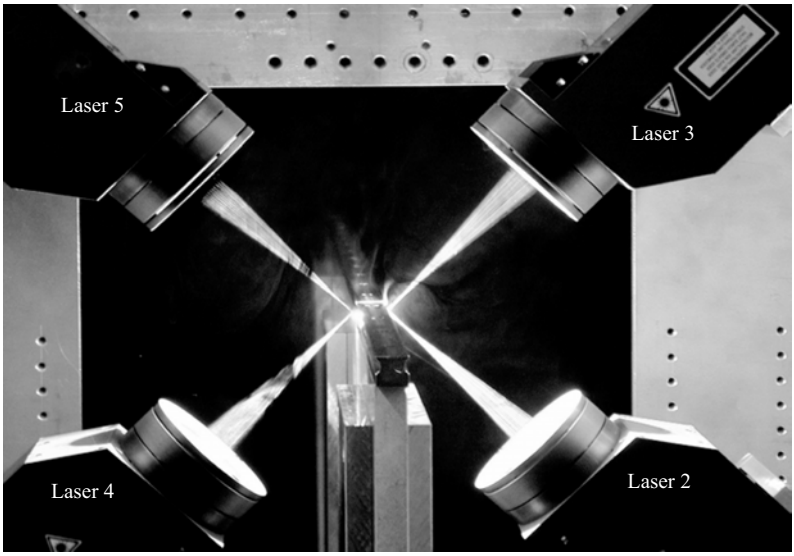

FIGURE 7.192. Hardening of linear guiding rails using the four-beam method with four homogenizer modules

A redesign of the diode laser modules with the power density distribution (PDD) being homogenized in the focus in slow-axis direction by means of waveguides [7.67] can improve the hardening results.

To harden the entire width of ball-bearing tracks of linear guiding rails[15] using the four-beam method, the beam cross sections of the individual beams have to be adjusted to each other by defocusing. For the diode laser modules used in this example, defocusing of around 10 mm yields roughly identical beam cross sections of 3 × 6.2 mm^2, fast × slow. Positioning of the slow-axis (x-direction: 6.2 mm) parallel to the ball-bearing tracks leads to a long interaction time between the laser beam and the ball-bearing tracks, and, as a result, to a great effective hardening depth (HD) of around 0.25–0.4 mm on the ball-bearing tracks. Figure 7.192 shows the hardening process using the four-beam method with the homogenizer modules. In the example presented, the processing is carried out with temperature control (control temperature T_R = 850–1000°C; 50°C increments) and process speeds of v = 200–300 mm/min in 50 mm/min increments. Differences in the hardening geometries in all four ball-bearing tracks as shown in Fig. 7.193, resulting in warpage Δy of about 1 mm/m exceeding the as-cast state of the rails, may be again due to different PDD and beam cross sections of the single modules as well as errors in the temperature measurements of the pyrometers used. The hardening

[15] For example, TKVD 15 (material: 58 CrMoV 4) and TKVD 15 VA (material: X65Cr13), INA-Lineartechnik, Herzogenaurach, Germany.

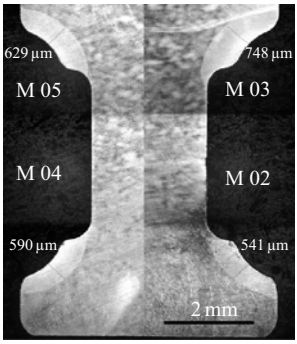

FIGURE 7.193. Cross section of a linear guiding rail TKVD 15 hardened with the homogenizer modules using the four-beam method (defocused; slow-axis parallel to the ball-bearing tracks; $T_R = 950°C$, $v = 200$ mm/min)

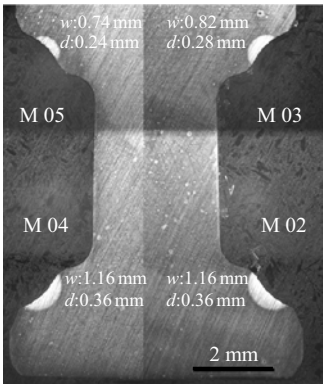

FIGURE 7.194. Cross section of a linear guiding rail TKVD 15 hardened with the homogenizer modules using the four-beam method (focused; slow-axis parallel to the ball-bearing tracks; $T_R = 950°C$, $v = 200$ mm/min)

depth of the rails is around 0.25 mm (required: around 0.22 mm), with hardening values of around 500–580 HV0.3 (required: around 550–600 HV0.3).

To narrow down the possible causes mentioned, rail segments can be processed using a four-beam method with focused beams, continuing with the slow axis parallel to the ball-bearing tracks. However, due to this strategy, only part of the ball-bearing tracks will be hardened (Fig. 7.194). To avoid possible errors in temperature measurements, the segments have to be processed using the same laser power without temperature control at all 4 modules. The hardening geometries obtained in this example with a laser power of $P_L = 350$ W are the same (Fig. 7.194). However, the recorded temperatures of the pyrometers may show different temperatures for modules 2–5 (e.g., module 2: $T = 1230°C$; 3: $T = 1080°C$; 4: $T = 1050°C$; 5: $T = 1350°C$).

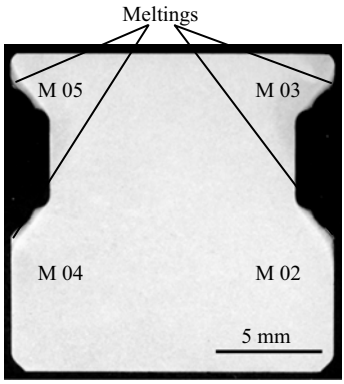

FIGURE 7.195. Cross section of a linear guiding rail TKVD 15 hardened with the homogenizer modules using the four-beam method (focused; slow-axis vertical to the ball-bearing tracks; $P_L = 300$ W, $v = 300$ mm/min)

As a consequence the rail segments should then be processed with temperature control, with the nominal temperature for each module being adjusted individually. The process speed in the example is varied from 200 to 600 mm/min (100 mm/min increments). This processing strategy makes it possible to achieve the same hardening geometries for each ball-bearing track (Fig. 7.194) and warpage Δy of the same magnitude as the as-cast state of the rails.

An alternative would be processing rail segments with focused beams and the slow-axis direction vertical to the ball-bearing tracks, using a fixed process speed of, e.g., $v = 300$ mm/min and a variation of the laser power of $P_L = 225$–300 W in 25 W increments, operating all modules at the same laser power. Depending on the process speed, the small beam cross sections in x-direction of $d_X \approx 0.8$ mm and the resulting little interaction time in the example presented here, either lead to an effective hardening depth <0.2 mm (required: >0.2 mm) or local meltings at the radiuses of the ball-bearing tracks (Fig. 7.195).

As a remedy, the linear guiding rails can be processed by positioning the slow-axis direction of the beams vertically to the ball-bearing tracks and by defocusing the beams (e.g., 1.1×6.2 mm^2, fast $\times$ slow). The defocused beam cross section prevents a melting at the radiuses of the ball-bearing tracks.

For the linear guiding rails in the example presented here, further processing with temperature control (adjusted temperatures of $T_R = 1050$–1250°C; laser power of $P_W \approx 275$–300 W) and variation of the process speed from $v = 200$–300 mm/min (50 mm/min increments) is appropriate. The attainable effective hardening depths are HD ≈ 0.2–0.23 mm, with hardening values of around 550–720 HV0.3 (required: around 550–600 HV0.3). Figure 7.196 shows the cross section of a rail hardened using this strategy. The distortion measurements on fully processed rails prove the importance of identical PDDs and beam cross sections of the diode laser modules even with this strategy. Measured distortions of $\Delta y \approx$ 500–700 μm/m are still too much.

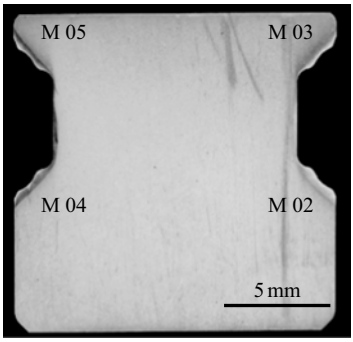

FIGURE 7.196. Cross section of a linear guiding rail TKVD 15 hardened with the homogenizer modules using the four-beam method (defocused; slow-axis vertical to the ball-bearing tracks; modules 2–5: $T_R = 1050$–1250°C adjusted, $v = 300$ mm/min)

The comparison of the results achieved with Nd:YAG laser radiation using the two-beam method (circular beam cross section with the same PDD) and with the PMDS and homogenizer modules using the four-beam method show

- For the minimized warpage hardening of linear guiding rails lasers with the same PDD have to be used.
- The beam cross sections of the lasers must have an adapted width (around 3–4 mm for the linear guiding rails treated as an example).
- With a top-hat-shaped PDD, the beam cross sections should be homogeneous (maximum deviation of medium intensity around ±10%).

Hardening of Valve Seats of Gasoline Injection Valves

K. Spennemann

In the field of automotive components distortion plays an important role for quality and function. As any process involving heat input inevitably leads to thermally induced tension and therefore distortion, application-adapted process management in laser hardening can help to achieve good machining results and save costs. To demonstrate the influence of different process parameters on distortion the valve seat of a gasoline injection valve, as shown in Fig. 7.197, is chosen as a demonstrator.

To clarify the impact of distortion, the basic functionality of the valve shall briefly be explained. The valve is sealed by pressing a ball into the cone-shaped valve seat with a spring. To open the valve and inject gasoline into the suction pipe the ball is pulled back via magnetic transmission of force. On the one hand, the constant load on the valve seat surface in the operation mode caused by the ball requires a high level of hardness in the valve seat material. On the other hand, leakage has to be avoided in the sealed state of the valve which demands a very good roundness of the valve seat. This again means working with a hardening

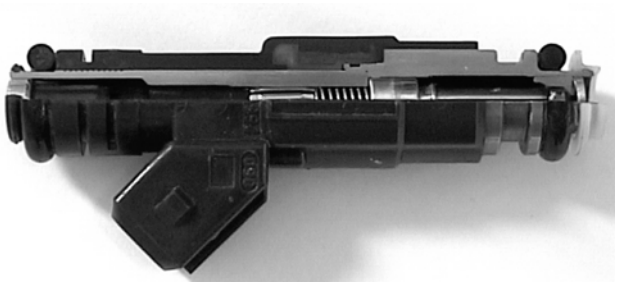

FIGURE 7.197. Gasoline injection valve

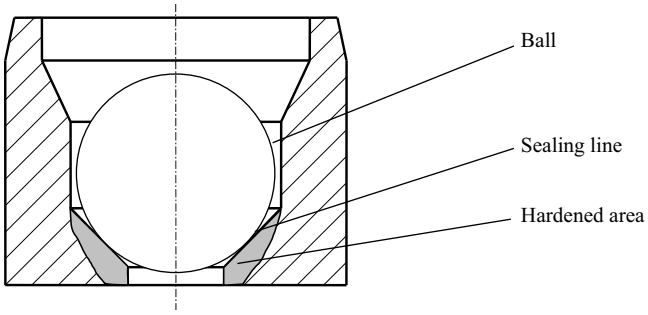

FIGURE 7.198. Section drawing of valve seat

process causing minimum distortion or implementing a second production step, e.g., grinding after hardening.

To guaranty an acceptable wear over the valve lifetime a hardness of 650 HV0.1 with a hardening depth of 0.3 mm has to be achieved (Fig. 7.198).

The hardening results are influenced by many parameters, which can be divided into beam parameters, material parameters, and parameters of application, as shown in Fig. 7.199.

With a given material and geometry the parameters that can be varied are beam parameters and application parameters. For the given application the following equipment is appropriate:

- direct-beam diode laser: wavelength: 808 nm; maximum output power: 1,440 W; focus dimensions: 1.6×4.4 mm^2,
- fiber-coupled diode laser, fiber core diameter, 600 μm; wavelength: 808, 940, and 980 nm; maximum output power: 900 W; focus diameter: 1.5 mm or 4.5 mm, respectively.

Three different focus shapes, as shown in Fig. 7.200, are compared. The large and the small circular focus can be created with a fiber-coupled laser with different optical setups, while the line focus is the generic focus shape of direct-beam diode lasers.

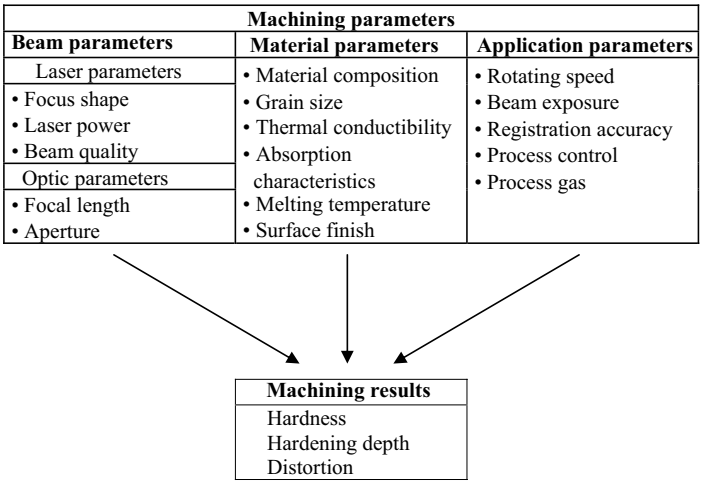

FIGURE 7.199. Parameters influencing the hardening result

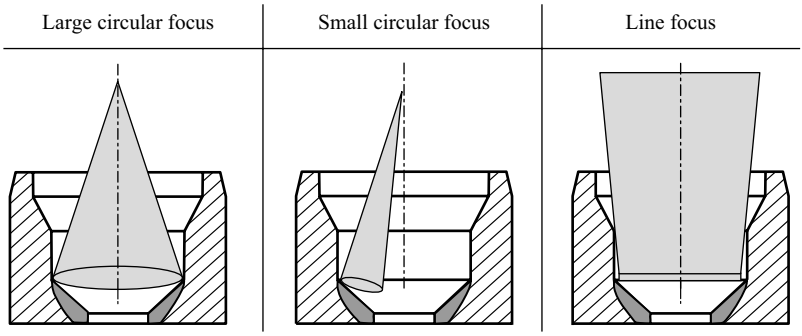

FIGURE 7.200. Focus shapes used for investigation

The overlap of the focus and the hardening area is shown in Fig. 7.201.

A hardness profile of the laser hardened seat area can be recorded by a microhardness tester and the roundness can be measured by a tactile roundness meter.

The roundness difference before and after hardening can be calculated by subtracting each deviation from ideal roundness.

To verify circumferential hardness distribution of the seat, concentric hardness measurements on sealing level 0.1 mm underneath surface can be carried out in 10° divisions.

Generally, the energy supplied to the workpiece increases with greater beam power and process duration. Therefore the resulting depths of hardness as well as the distortion correlate with these two parameters. Furthermore the intensity distribution of the laser focus on the workpiece as well as the process speed have a significant influence on the result (cf. Table 7.14).

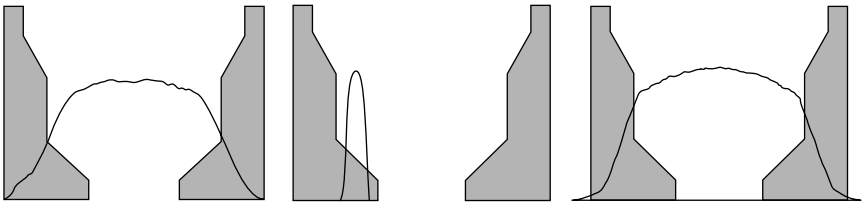

FIGURE 7.201. Overlap of laser intensity and hardening area

TABLE 7.14. Hardening results at different focus shapes

Focus shape	Large circ. focus	Small circ. focus	Line focus
t (s)	1.8	10	10
ω (U/s)	–	1	1
Energy applied (J)	1188	2700	850
Depth of hardness (mm)	0.39	0.30	0.34
Hardness HV0.1	708	701	620
Average distortion (μm)	0.6	0.7	1.7

The comparison of the different focus shapes reveals the following dependencies. The two focus shapes that require rotation of the workpiece during the hardening process, lead to a much higher distortion and demand a longer process time to achieve the specified depth of hardness. The high level of distortion mainly results from the inevitable overlap of the irradiated area which does not exist in the case of the large circular focus where the process is run without movement between laser beam and workpiece. Only with relatively slow rotational speed the required depth of hardness can be achieved due to the fact that the conversion temperature necessary for the structural change is reached only in areas very close to the surface at higher speeds. As the irradiated area is much smaller for the line focus and the small circular focus compared to the large circular focus, the maximum laser power that can be applied without melting the surface is a lot less for the line and the small circular focus. Therefore the minimum process time to achieve the specified results is a lot shorter for the large circular focus. With all focus shapes, a constant laser power is applied during the hardening process.

The advantage of the large circular focus is that it covers the whole hardening area. By a single shot the whole seat can be hardened without any relative motion between workpiece and beam. Due to hardening without a rotary axis there is no overlapping area with annealing problems.

If remachining is saved due to the minimum distortion caused by laser, laser transformation hardening will be economically interesting.

In contrast to conventional hardening laser hardening with beam duration of approximately one second is feasible for in-line production and quality assurance can be carried out by pyrometric temperature control.

Hardening of Folding Matrices

R. Meyer

Folding matrices (see Fig. 7.202, left picture) are generally induction hardened in the area of the bending radius. The problems occurring are a high distortion beyond of tolerances, the danger of hardening cracks and an intensive after treatment.

Besides of reaching the desired hardness depth and keeping a constant hardness track of a defined width over the whole matrix length, the following ameliorations shall be attained by means of laser hardening:

- distortions <0.1 mm,
- shortening the passing through time,
- no hardening tracks,
- lowering of the rate of rejects.

A suitable setup for hardening folding matrices is shown in Fig. 7.202, right picture. Temperature sensors are integrated into the optical path. Reflections back into the laser can be avoided by an incident angle of 15°. The axes of the handling system are lined-up with the workpieces. In the example shown, high hardness depths >1.0 mm in the area of the bending radius and a hardening profile according to Fig. 7.203 are required.

With the diode laser ROFIN DL020, equipped with a focal length of 120 mm, a surface temperature of 1150°C and a feed speed of 180 mm/min are adequate. As a strategy to prevent distortion, two counter tracks, so-called guide tracks, are driven on the bottom of the matrices before the processing. If a single beam technique is used, the dimensions of the beam have to be chosen broad enough to harden the upper side and the flank in one track. As a result, different incident angles occur, causing different absorptions of the laser radiation. The alternative is dividing the

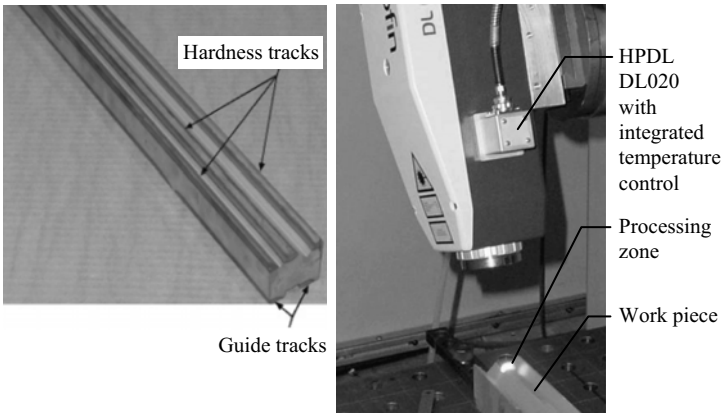

FIGURE 7.202. Left: Folding matrix (material 42CrMo4). Right: Suitable setup for hardening folding matrices

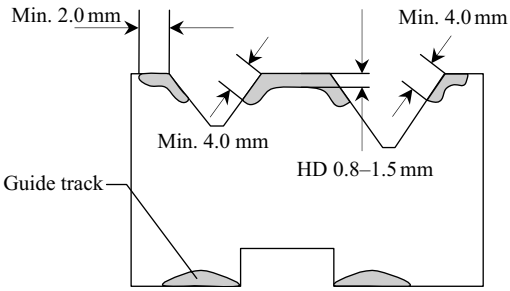

FIGURE 7.203. Required hardening profile of the folding matrices (HD = effective hardening depth)

track in the middle into three tracks (rising flank, flat area, and falling flank) which will cause tempering.

Hardness measurements on cross cuts of specimens reveal what can be achieved with the single beam technique on the sample application:

- The required hardness depths in the area of the radius can be reached.
- The hardness depth in the flanks is too low.
- The hardness area along the flanks is not sufficient.
- The required track positions are not reached.

Though the strategy with the guide tracks can help preventing distortion, the other requirements can not be met with single beam technique. The single beam technology cannot compensate different volumes of the workpiece as well as different incident angles.

In contrast, a multi-head technique would allow for processing of the flanks with more favorable angles and without causing tempering of the middle part.

Hardening of Shank Housings

R. Meyer

Shank housings as shown in Fig. 7.204 are generally equipped with an internal hard ring which causes additional costs for the extra part and assembly effort. Induction hardening can not be applied since it requires costly after-treatment. Laser hardening shall overcome the need for further treatment, generating hardness tracks of high quality and low distortion of the workpiece.

Hardening of the internal wear area of shank housings is an application which requires the laser beam to be tilted, resulting in a beam spot of increased size. The processing has to compensate for the spot size to achieve constant hardness and hardness depth.

Using a diode laser ROFIN DL020 with a focal length of 125 mm and a line shaped beam, a feed speed of 400 mm/min is appropriate while the workpiece and the laser have to rotate to each other over several axes. For a controlled temperature of 1050°C, a laser power of about 1450–1600 W will be necessary. Beside of low

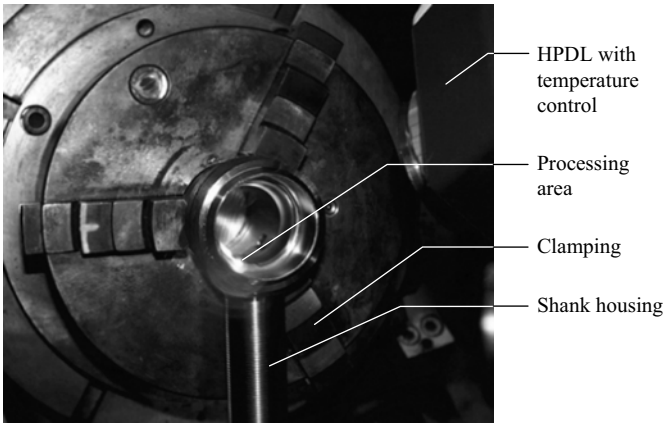

Figure 7.204. Internal hardening of shank housings

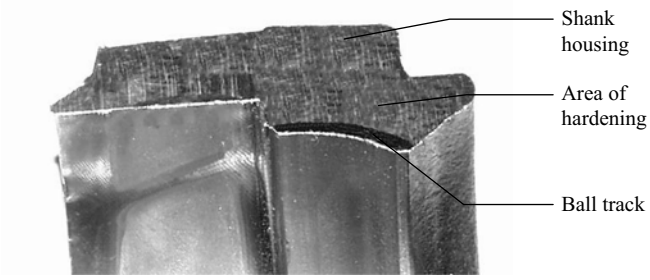

Figure 7.205. Cross cut of the shank housing

distortions, the application requires a hardness depth of 0.5 mm with a constant hardness over the internal circumference.

With the process described, a hardness depth of 0.6 mm with a hardness of 60 HRC can be reached. As shown by the cross cut of the shank housing in Fig. 7.205, the track position meets the requirements. The distortions within the groove can be kept within the tolerances. For the true running, the distortions are only 0.004 mm. Nevertheless, the setup of the track position causes a considerable effort to process the complete area under the same incident angle. But the effort will be rewarded since no negative influences of the tilted beam will occur.

Inductive Assisted Laser Beam Hardening

S. Bonss

Heating of steel with induction is an established method since more than 40 years [7.69]. Depending on the frequency the penetration of the heating varies from some tenths of a millimeter applying high frequency to many millimeters applying radio frequency or commercial frequency [7.70]. Surface hardening of shafts and gears

are the main application field of inductive hardening. Ring-shaped induction coils are most effective injecting electrical energy for steel heating.

In the applications discussed in the previous sections, induction hardening was either to be replaced (cf. "Hardening of Folding Matrices") or not appropriate at all (cf. "Hardening of Shank Housings"). In the example presented in the current section, induction will be used as additional energy source during laser beam hardening.

Inductive preheating below the austenite formation temperature range reduces the necessary laser power for heating the surface region in the transformation temperature range. The feed rate at inductive-assisted laser beam hardening is up to ten times higher at given laser power. In contrast to induction hardening, this combined process in general needs no additional quenching media like water or water-based solutions. The advantage of the inductive-assisted laser beam hardening over induction hardening is the more exact positioning of the hardened areas at corners, edges and other critical contours where inductive energy is injected unintentionally. At localized 3D-hardening, the higher flexibility of, for instance, a scanned and power controlled laser beam can be used at very high process feed rates. In contrast to the pure laser beam hardening, the feasibility is reduced because of the shape-fixed and inflexible induction coils and the strong dependence of the injected inductive energy on the coil gap. The penetration of the laser-hardened zone can be enlarged using inductive preheating at higher alloyed steels, which form martensite even at classical heat treatment being left in air.

Figure 7.206 shows a prototype of an integrated processing device,[16] consisting of two energy sources, a high-power diode laser and a radio frequency generator

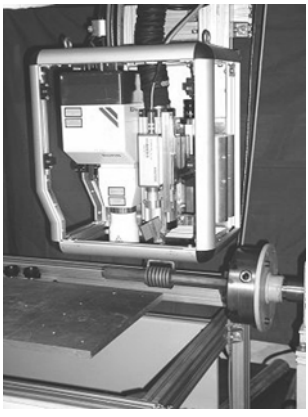

Figure 7.206. Prototype of an integrated processing device developed at Fraunhofer IWS, 2.5 kW high-power diode laser by Rofin (DL025S) and 60 kW radio frequency generator (MINAC 60 DUAL, 9-12 kHz or 16-15 kHz) by EFD Induction

16 Fraunhofer IWS, Dresden, Germany.

with external resonant circuit and coil. The effective range of those two energies on the part can be adjusted by three compact linear units. The frame of the device is designed in such a manner that even at high accelerations of the device at a robot the alignment of laser spot and coil varies less than 0.1 mm. This is important for a precise heat treatment of 3D areas where fast reorientation motions become necessary because of the large tool length. An infrared thermometer has been integrated for measuring the temperature of the preheated or laser treated surface. This information can be given to a laser power control (cf. “Process Monitoring and Control”).

The following examples shall show the effects at inductive-assisted laser beam hardening in detail. Cylindrical rods of C45 (0.46% Carbon) and 42CrMo4 (0.42% carbon, 1% chromium, 0.2% molybdenum) are treated. C45 is more quenching sensitive at hardening, whereas 42CrMo4 tolerates slower cooling because of the chromium content. on the other hand, the chromium forms carbides which need time to dissolve having all the available carbon content involved in the martensitic transformation. A ring shaped area is preheated inductively 0.5 s with different power. A laser spot of 7.5 × 7.5 mm^2 generates a circular hardening track. A maximum laser power of 1,500 W is controlled by a surface temperature guided laser power control system. The comparison of Figs. 7.207 and 7.208 gives an impression what influence inductive preheating at laser beam hardening has. The maximum surface hardness of the preheated samples is reduced slightly at the higher feed rates. It is similar to this of lower feed rates where the self-quenching at the surface is less effective because of heat accumulation. But the preheating causes a deeper transformation zone. Even at the high feed rate of 800 mm/min the laser energy is able to induce the martensitic transformation at similar depths like at 100 mm/min feed rate without preheating. Looking at 42CrMo4 the effects

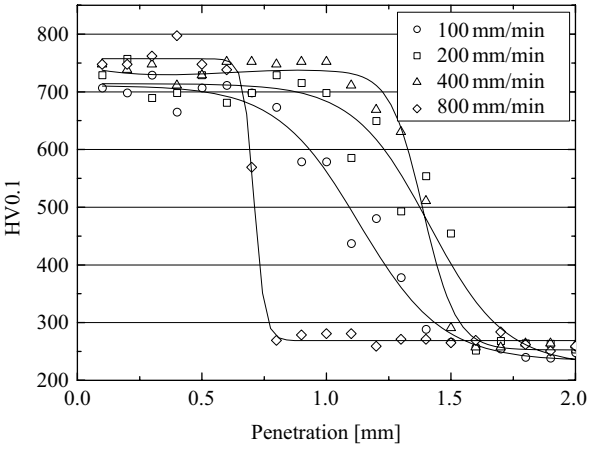

Figure 7.207. Hardness-depth profiles, C45, laser beam hardening without inductive preheating, surface temperature 1400°C, and different feed rates

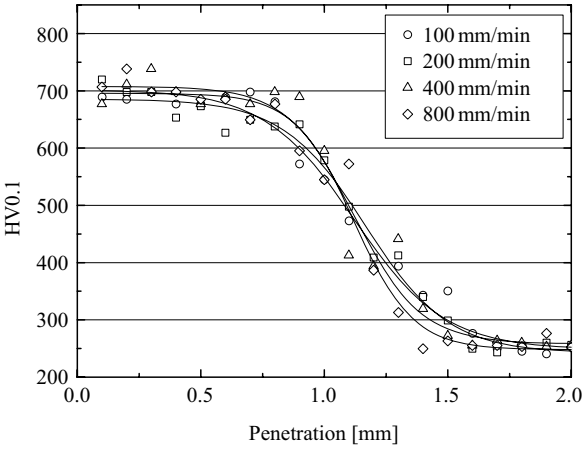

FIGURE 7.208. Hardness-depth profiles, C45, laser beam hardening with inductive preheating, preheating temperature 800°C, surface temperature 1400°C, different feed rates

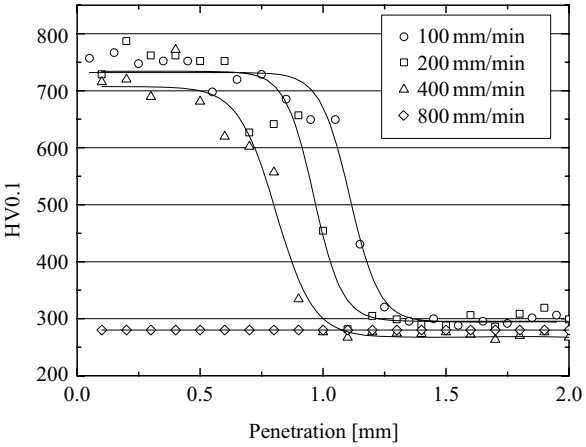

FIGURE 7.209. Hardness-depth profiles, 42CrMo4, laser beam hardening without inductive preheating, surface temperature 1300°C (except at 800 mm/min), different feed rates

are slightly different. A comparison of Figs. 7.209 and 7.210 with Figs. 7.207 and 7.208 shows the difference between the two steels. The 42CrMo4 samples are not hardenable with the used parameters and at 800 mm/min feed rate. The surface temperature does not reach the aimed value of 1300°C; the time of the surface area being at the necessary temperature range is too short for dissolving and diffusion of carbon and the resultant martensitic transformation. At lower feed rates the penetration is lower than at C45 because of the same reason. Inductive preheating at 800°C leads to a longer dwell time in the transformation temperature range.

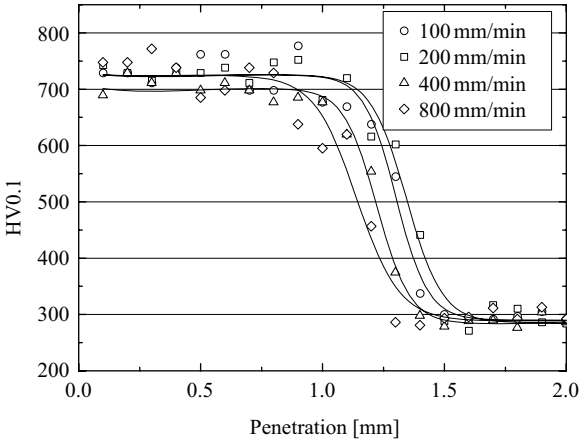

FIGURE 7.210. Hardness-depth profiles, 42CrMo4, laser beam hardening with inductive preheating, preheating temperature 800°C, surface temperature 1300°C, different feed rates

The result is a deeper transformation area. 42CrMo4 is less quenching sensitive than C45. Therefore austenite can transform to martensite in a thicker edge layer compared to C45. On the other hand it becomes possible to generate hard surface layers applying feed rates which are impossible for sheer laser beam hardening.

Integration of a High-Power Diode Laser into a Machine Tool

R. Meyer

The full efficiency of the diode laser technique can only be obtained from an adapted handling system. Conventional handling systems are not designed for processing laser hardening since either the flexibility and the precision are lacking or they are highly over dimensioned in bearing capacity and precision. For handling diode laser heads for hardening, rather, a compromise is useful, combining sufficient precision with the flexibility of a sixth axis for the tracking of lines. The axes cover a range of 1.5 m $\times$ 0.7 m $\times$ 0.8 m (height). The precision of the handling system amounts to $\pm$0.05 mm.

In alternative to handling systems, robots can be used to handle the high-power diode laser. However, the arrangement of their axes has the disadvantage that by a rotation of the laser head the parallel motion is lost which is necessary for realizing hardness tracks on workpieces.

For serial parts, a saving of time in the processing chain increases the productivity and lowers the costs. Therefore, the combination of hardening processes with metal cutting activities and automatic in- and output of workpieces is of special interest. This can be realized by integrating the high-power diode laser in a

FIGURE 7.211. Integration of high-power diode laser into a machine tool

conventional processing center available on the market as shown in Fig. 7.211.[17] Due to its compactness, the high-power diode laser can be easily integrated in machine tools or transfer lines, saving the working steps of channeling workpieces out for external hardening and in again. Combined with the direct processing, the in- and out-put of workpieces are automatized. The workpieces are transferred from a conveyer store by a multi-axial gripper into the spindle and taken out again after the processing.

Figure 7.212 shows a demonstrator providing integration of a high-power diode lasers into a handling system for hardening. The handling unit realizes the required movements of a linear processing by means of six axes, three for translation and three for rotation. The demonstrator is built as a stand, allowing sufficient accessibility. The arrangement of the axes is carried out according to the following principles:

- The carrier stand is screwed with the ground and carries the complete processing unit. Based on the assembled axes-stand, the further construction is carried out.
- The assembly of the X-axis is carried out on the axes-stand.
- The Z-axis is mounted via a highly stiff knee-connection on the X-axis.
- The Y-axis is designed as a cantilever for the processing head and the rotational axes, allowing high freedom of movement.

In the demonstrator shown here, high-power diode lasers of different power in the range of several kilowatts can be installed. The scopes of the translational axes are $X = 1{,}500$ mm, $Y = 730$ mm, $Z = 800$ mm. The maximum speed amounts to 10 m/min. A precision in positioning reaches ± 0.1 mm.

[17] Stiefelmayer GmbH & Co. KG, Denkendorf, Germany.

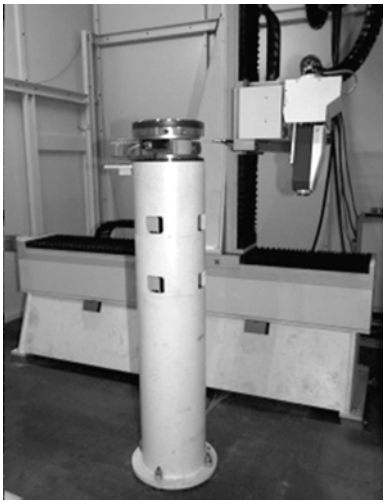

FIGURE 7.212. Demonstrator: Handling system for high-power diode laser hardening

Integration of a High-Power Diode Laser into a Robot

R. Polzin

In a variety of laser-applications three-dimensional problems have to be solved, especially in the surface treatment, when local areas of forming tools or injection molding tools shall be hardened or coated. This requires plants with component accessibility that is as unrestricted as possible.

Robot systems provide optimal component accessibility and an unrestricted utilization of the working area. Especially, articulated arm robots are very versatile and their initial costs are low. Due to their low weight articulated arm robots can even be placed in an overhead position, which facilitates the positioning of large components.

Figure 7.213 shows the combination of a fiber-coupled diode laser and an articulated arm robot[18].

The fiber-coupling has the advantage that only the fiber has to be lead to the robot and not, as in case of a direct-treatment, a bundle of cooling water hoses and electrical wires. A further advantage is that behind the fiber the intensity distribution is homogeneous and rotationally symmetrical. Therefore a module for a tangential tracking of the elliptical intensity distribution at 2D or 3D treatment is not necessary.

The fiber is fixed at a collimating module inside the robot‘s arm. This reduces the mechanical stresses of the fiber, which is advantageous especially when

[18] Robot system from Reis Robotics, Obernburg, Germany.

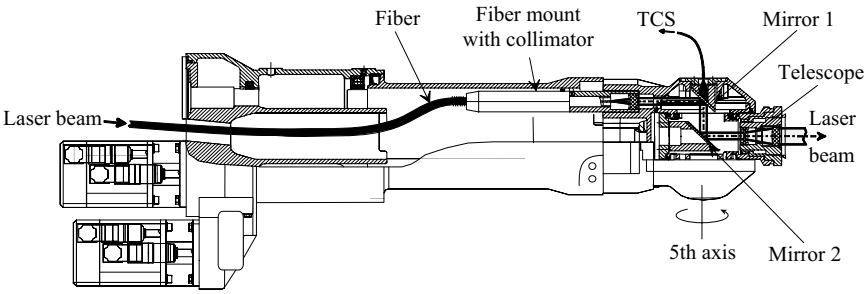

FIGURE 7.213. Combination of a fiber-coupled diode laser and an articulated arm robot

fibers of higher diameters are used. Because of the beam guiding inside of the robot's arm, the beam leaves the robot's hand on-axis, which allows a simple programming. The space needed for the beam guiding and the focusing unit can be minimized. Using small working optics further optimizes the component accessibility.

Quality and Economic Considerations

R. Meyer

The quality and economic considerations can begin with a comparison to conventional induction hardening: In induction hardening, distortion and cracks occur. Therefore, workpieces have to be after-treated. Induction hardening requires an immense energy input and the necessary cooling causes environmental impacts. Coolants have to be disposed of, which is costly. The cooling process is carried out externally, causing the workpiece to contract, and cracking occurs. Partial hardening or the drawing of a hardness track is not possible in thermal hardening, but it is possible when the laser is used as a very precise and flexible processing tool.

The principle of laser hardening consists of a short-term local heating of the material beyond the austenitic temperature but below melting, a short-term holding of the temperature for diffusion to the desired depth, and finally a rapid cooling in solid phase. During the cooling, the effect of self-quenching by a heat flow to the inside of the workpiece is used. Due to this short-term and local treatment with a small heating load, only small distortions occur. The surface quality can mostly be kept as it is. In case of diode laser hardening, an after-treatment to correct distortion or oxidation can be omitted. Therefore, diode laser hardening can often be the final step in a process chain and workpieces can be directly put in use. Laser hardening can be applied for numerous materials. It has become a very precise and reliable process. Partial hardening is possible, e.g., in track widths for functional areas of 3–16 mm with a depth of 0.1–1.5 mm. Hardening can be carried out very precisely along edges, guide ways, grooves or free-shaped areas of tools and moulds. A big advantage is the hardening of tooth flanks with a multi-head assembly, processing

both flanks in parallel and avoiding the annealing of already hardened areas which might occur in single-head processing.

Economic considerations must include the efficiency. At first sight, the process of diode laser hardening in isolation is not in any case cost saving, compared to conventional hardening, especially for mass-produced parts, because of the rather high investment costs. However, an analysis of the efficiency has to comprise the whole process chain. Time becomes a more and more a critical factor in the production. In this context, the handling of workpieces plays an important role. If diode laser hardening is integrated in the in-house process chain, not only can the after-treatment be omitted, but also the conventional external hardening as well as the reintroduction of the externally hardened parts in the internal processes. Often, this reintroduction has to handle a big amount of parts, while an internal hardening can keep a continuous process flow. In this complete context, laser hardening reaches a higher efficiency. With regard to partial hardening, the process can even be considered isolated. If only 10–15% of a surface has to be hardened, laser hardening is directly cheaper than the conventional thermal hardening of the complete workpiece.

The process efficiency can even be increased if the diode laser is integrated in machine tools for metal cutting. The input and output of workpieces can be automated and the workpieces are transferred from a conveyer store by a multi-axial gripper into the spindle. By such integration, the laser hardening can be looked at as part of a normal machine tool or processing center.

The option of partial hardening shall be illustrated by a real part. For example, sintered components for gears which can be produced cheaper than steel parts couldn't be hardened conventionally due to distortions of their thin shape. By means of diode laser hardening, tooth flanks, gullets, and other fine structures can be specifically hardened in a reproducible process. The distortion remains less than 0.05 mm. The sintered and laser-hardened gear components are cheaper than conventionally hardened steel parts.

Besides conventional hardening, further considerations will be given to a direct comparison between the use of Nd:YAG lasers and high-power diode lasers (cf. Table 7.15) specifically laser units of about 2 kW for metal hardening.

Compared to CO_2 lasers, which have similar investment costs, diode lasers face a higher surface absorption due to their shorter wavelength. The beam delivery of CO_2 lasers is rather complex, relying on mirrors which might cause adjustment problems.

Finally, the essential advantages of laser hardening against conventional processes can be summarized as follows:

- Possibility of hardening areas of low accessibility.
- Locally limited hardenings can be carried out.
- Laser hardening causes low distortions.
- The processing times are low.
- Due to the self-quenching, no cooling media are necessary which might cause disposal problems.

Table 7.15. Comparison between conventional Nd:YAG lasers and high-power diode laser (laser units of about 2 kW for metal hardening)

Comparison	Nd:YAG laser	HPDL
Laser beam quality	High	Sufficient for laser hardening
Beam geometry	Emission of a circular beam; to obtain a rectangular spot, further optics are necessary	Emission of a rectangular spot which is especially suited for hardening
Efficiency (referring to mains power)	3% (driven by flash lamps)	Upto 50%
Focus range	Large focus range due to the availability of more flexible optics; higher beam quality allows higher working distances being beneficial against reflections	Limited focus range due to fixed focal distances and optics with small flexibility; in practice, a relatively small distance to the workpiece has to be kept. However, an evolution toward higher focal depths (upto 200 mm) can be observed
Size of system	Higher	Upto 100 times smaller; flexible integration in production lines possible
Flexibility for applications	Limited to the application of one head due to the costs and size	Several heads can be combined either for faster processing or for the hardening of lines and areas
Investment costs	About €300,000 (diode driven)	About €130,000, depending on size, application, and required focus quality
Operating costs	Higher	Lower due to higher efficiency and lower energy consumption

7.3.3. Layer Deposition for Generation and Repair

R. Zieris, A. Weisheit, G. Habedank, S. Nowotny, M. Litmeyer, M. Brandner, H. Kohn

7.3.3.1. Process Principles and Equipment

Coating Techniques

R. Zieris

Different coating processes are used to protect surfaces. To apply a thick protection layer with a laser onto a substrate, laser beam alloying, laser beam dispersing, and laser beam cladding are used as the processes. The results of these processes are a high wear resistance of the surface and a protection against corrosion, depending

FIGURE 7.214. Laser beam coating structure

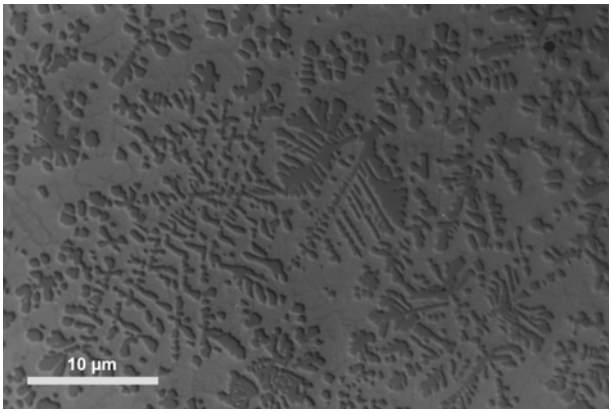

FIGURE 7.215. Laser beam alloying structure

on the material. To understand the difference between these three processes, the definitions for laser surface treatment with additional material are given.

Laser beam cladding is the deposition of a coating material onto a substrate with metallurgical bonding but preferably low mixing of both material components. The maximal base material mixing with the coating material is 5%. The used materials are metals, light metals and their alloys, ceramics, and also carbides. With these processes the coating materials build up a dense coating to generate or repair. A typical coating structure is shown in Fig. 7.214.

Laser beam alloying is predominantly used for metals and their alloys. Laser beam alloying is the injection of alloying elements into a thin, molten surface zone with a preferably complete dissociation in the melted base material (Fig. 7.215). During solidification, crystals accrue from the melting zone in the coating.

Laser beam dispersing, also named laser injection, is often used for carbides. With this method the coating material is completely distributed in the melting zone of the base material. But the coating material is not dissociated or dissolving.

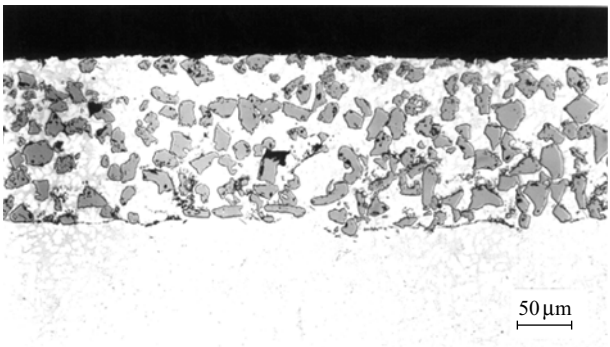

FIGURE 7.216. Laser beam dispersing (laser beam injection) structure

After solidification the hard material particles are evenly distributed in the coating (Fig. 7.216).

Solidification Process

A. Weisheit

During laser cladding, the filler material (wire or powder) and a thin layer of the substrate is molten. The surface tension gradient on the melt pool surface arising from a temperature gradient leads to convection (Marangoni convection [7.73]) within the melt pool. The velocity of the melt is 2 to 3 orders of magnitude higher than typical velocities of the sample movement (0.3–2 m/min). When the laser beam or the workpiece moves on solidification starts. The morphology of the solidified material can be planar, cellular, or dendritic (see Fig. 7.217). A cellular structure occurs when the growth of secondary arms is suppressed. The process parameters relevant for the microstructure morphology are the temperature gradient

$$G = \partial T/\partial x, \tag{7.14}$$

the solidification rate

$$v_s = \partial x/\partial t \tag{7.15}$$

and the cooling rate

$$\dot{T} = \partial T/\partial t. \tag{7.16}$$

The three parameters are correlated as follows:

$$\dot{T} = v_s \cdot G. \tag{7.17}$$

Figure 7.217 shows the correlation between G and v_s. The limits of cellular and dendritic growth are determined by the constitutional undercooling and the absolute stability [7.74].

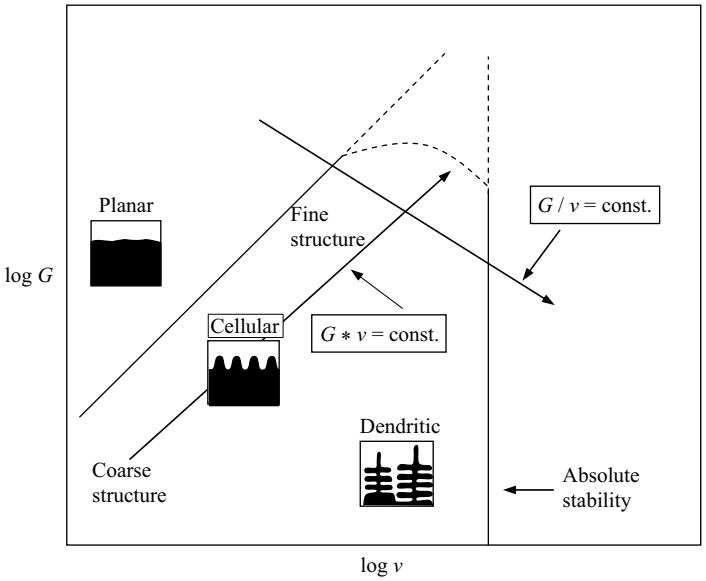

FIGURE 7.217. Solidification morphology as a function of temperature gradient and solidification rate

The fineness of the microstructure is mainly determined by the heat flow volume dissipated per time. The time for the growth of the cells or dendrites decreases with increasing heat flow resulting in a finer structure. The morphology is determined mainly by the ratio G/v_s.

Normally, the volume of the melt pool is small compared to the volume of the whole workpiece and after the irradiation the heat flows rapidly into the cold volume (self-cooling effect); and thus, the melt solidifies at high cooling rates (10^2–10^7 K/s). The cooling rate is determined by the process parameters, the thermophysical properties of the material, and the geometry of the workpiece.

Powder-feed Nozzles

A. Weisheit

In laser cladding, the supply of the filler material is one of the key factors controlling the process [7.75]. If the filler material is used as powder, three different concepts of powder injection can be applied:

- off-axis powder injection (a single powder stream is fed laterally into the laser beam; see Fig. 7.218),
- continuous coaxial powder injection (a powder stream cone is produced which encloses the laser beam, see Fig. 7.219), or
- discontinuous coaxial powder injection (three or more powder streams are fed coaxial to the laser beam, see Fig. 7.220).

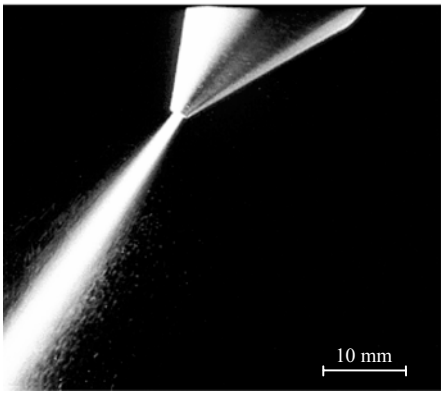

FIGURE 7.218. Powder stream of an off-axis powder injection nozzle

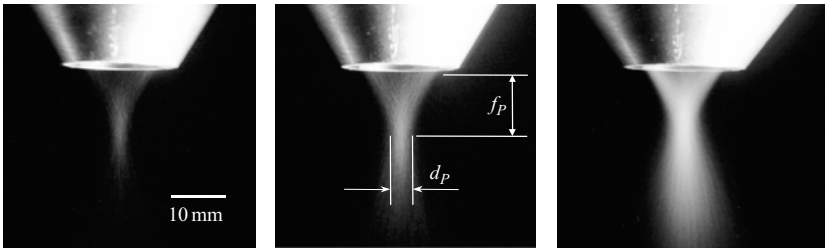

Slit size: 0.7 mm
$d_P \approx 2$ mm
$f_P \approx 11$ mm

Slit size: 1.4 mm
$d_P \approx 2.7$ mm
$f_P \approx 11$ mm

Slit size: 2.1 mm
$d_P \approx 3.5$ mm
$f_P \approx 11$ mm

FIGURE 7.219. Continuous coaxial powder stream for different slit sizes

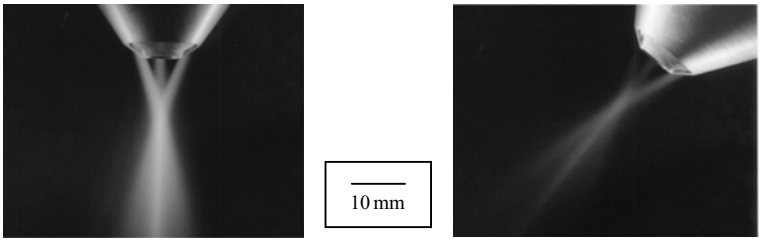

Tilt angle 0º

Tilt angle 45º

FIGURE 7.220. Powder stream of a three way nozzle for tilt angles of 0° and 45°

Off-axis powder injection is suited for the cladding of broad tracks. For track widths between 0.5 and 5 mm, a circular cross section of the opening with a diameter of 1.5 to 3.5 mm is adequate. Cladding of wider tracks (5–25 mm) requires a rectangular cross section of the opening (e.g., 1.5 × 15 mm^2). Furthermore,

off-axis powder injection is suitable for the cladding of areas difficult to access. Since in off-axis powder injection the nozzle is positioned lateral to the laser beam, it is not suitable for 3D-cladding.

In continuous coaxial powder injection a powder stream cone encloses the laser beam. The powder stream is specified by the core diameter d_p of the powder stream focus and the distance f_p between nozzle tip and focus point, these values are determined by the slit size, the carrier gas flow, the powder-feed rate, and the powder particle size. As shown in Fig. 7.220, d_p increases significantly with increasing slit size. The same effect is observed when the powder-feed rate is increased. Reducing the particle size leads to a smaller powder stream focus diameter. The typical powder stream focus diameter of a continuous coaxial powder injection nozzle lies in the range of 1 to 3 mm.

The major advantage of continuous coaxial powder injection compared to off-axis powder injection is the potential for 3D-cladding. However, tilting of the nozzle is restricted. Since the homogeneity of the powder stream cone depends on the powder distribution inside the expansion chamber of the nozzle, gravity will affect the powder stream when the nozzle is tilted. Experiments have shown that a maximum tilt angle of approx. 20° can be accepted without significant effects on the geometry of the cladded layer.

In discontinuous coaxial powder injection three or more individual powder streams are distributed around the laser beam, thus forming a powder stream focus (Fig. 7.219). The typical core diameter of the powder stream focus lies in the range of 2.5 to 4 mm. The major advantage of discontinuous coaxial powder injection is the potential for 3D-cladding, including the option to tilt the nozzle while retaining a uniform powder focus. Figure 7.220 shows the powder stream for tilt angles of 0 and 45°. The powder stream focus is only slightly affected. The tilt angles tested successfully range from 0 to 180°.

Crack Formation

G. Habedank

During powder-feed laser beam cladding the powder and partially the substrate material are melted and solidify rapidly as described in “Solidification Process.” The shrinking and the high cooling rates impose formation of tensile stress. The tensile stress can exceed the yield strength during the cooling down, causing plastic deformation or crack formation.

A method for measuring the residual stress is described in “Measurement of The Residual Stress.”

7.3.3.2. Special Techniques

Laser Hybrid Coating Technologies

R. Zieris, S. Nowotny

For coating processes, which use thermal spray technologies, such as plasma spraying, flame spraying, and high-velocity oxygen fuel spraying, numerous

technical applications have been discovered hitherto. Plasma spraying techniques carried out under plain atmosphere are referred to as Atmospheric plasma spraying (APS).

One of the few drawbacks is the relatively low bonding strength between coating and substrate due to the bonding mechanism of physical adhesion. Another disadvantage is the need for pre-treatment procedures for the substrate, such as grit blasting. If the substrate is pre-heated, the bonding strength will be higher because of some physical and chemical interaction between the coating and the substrate. Furthermore, porosity, which is found mainly in plasma sprayed coatings, can lead to problems in use.

Laser cladding is one example of a laser technology that has been successfully applied in production. The advantages of this technology are the metallurgical bonding of the coating to the substrate and the high precision of the coating material build-up on the substrate surface, whereas the low coating rate of laser cladding is rather a hindrance for its broader industrial use.

As a consequence, hybrid technologies were developed in order to improve the coating properties and increase the productivity of coating processes. Several studies deal with the integration of laser beam and thermal spray processes with regard to CO_2 laser radiation [7.76, 7.77] as well as Nd:YAG laser radiation [7.78]. A laser beam can also be used for surface cleaning immediately before spraying[19] [7.79].

Laser-assisted atmospheric plasma spraying (LAAPS) is a hybrid technique developed in order to eliminate the particular drawbacks both of the APS and of the laser cladding processes. LAAPS is a one-step coating process performed in the atmosphere in which the laser beam interacts simultaneously with the plasma torch on the substrate or deposited coating surface while generating the coating [7.80]. The general advantages, compared to traditional APS coatings, are the high productivity of the process, the metallurgical bonding of the coating to the substrate, and the decreased porosity.

The special equipment required for LAAPS is described in "Equipment for the Mobile Use of Laser-Assisted Atmospheric Plasma Spraying (LAAPS)."

Laser Cladding with Wire

M. Litmeyer

Although laser cladding is predominantly performed using metal powder, it is not restricted to this technique. Laser cladding with wire is an alternative technique avoiding the handling specifics of the powder and providing 100% material efficiency. On the other hand, there are certain limitations in matters of 3D applicability and range of available materials.

[19] This process is commercially known as the Protal® process of Sulzer Metco.

For a more detailed comparison between laser cladding with wire and laser cladding with metal powder, see "Comparison of Laser Cladding with Wire and with Metal Powder."

7.3.3.3. Parameter Dependencies

The quality of the coating is mainly determined by mechanical characteristics like coating height and width, hardness, wear resistance, bond strength between coating and substrate, and by metallographic characteristics like microstructure, dimensions of the dilution zone compared to the dimensions of the layer, occurrence of pores in the coating, occurrence of cracks in the coating or in the substrate.

The following sections deal with the influence of procedural parameters ("Laser Power" through "Dilution and Hardness") and material parameters ("Cladding Material" and "Compatibility of Base Material and Cladding Material") on these characteristics.

Laser Power

A. Weisheit, M. Brandner

Figure 7.221 shows the principle of the cladding process with an off-axis powder-feed nozzle using a 2 kW fiber-coupled diode laser. As an example flat samples (thickness 10 mm) of carbon steel C45 are used as substrate. Prior to cladding the samples are sand blasted to remove oxide layers and any kind of contamination. Stellite F is chosen as coating material. Stellite F (particle size $\sim 45 + 22.5\ \mu m$) is a cobalt-based alloy used for wear applications at elevated temperatures (e.g., valve seats).

During alteration of powder-feed rate (m_P), velocity (v), and laser power, (P) the process parameters noted in Table 7.16 are held constant.

If the cladded tracks are cut perpendicular to the clad direction (cross section) track height (h), track width (b), and melt depth (t) can be measured using

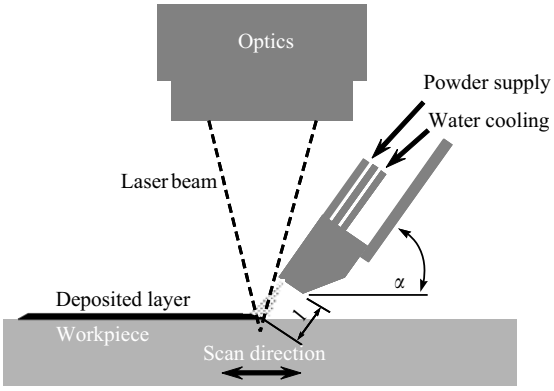

Figure 7.221. Principle of laser cladding using an off-axis powder-feed nozzle

Table 7.16. Sample parameters

Focal spot size of the laser beam	3 mm
Distance between powder nozzle tip and sample (L)	10 mm
Angle between powder nozzle and sample (α)	60°
Carrier gas flow rate for powder-feeding	3 L/min
Powder-feeding direction	dragging
Carrier gas	Ar

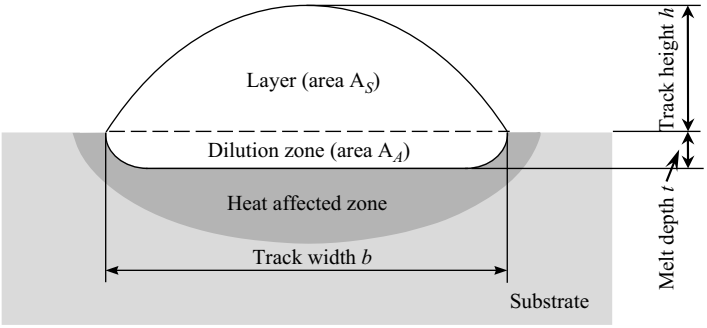

Figure 7.222. Schematic drawing of a cross section; h: track height, t: melt depth, b: track width, A_S: area of cladded layer, A_A: area of dilution zone

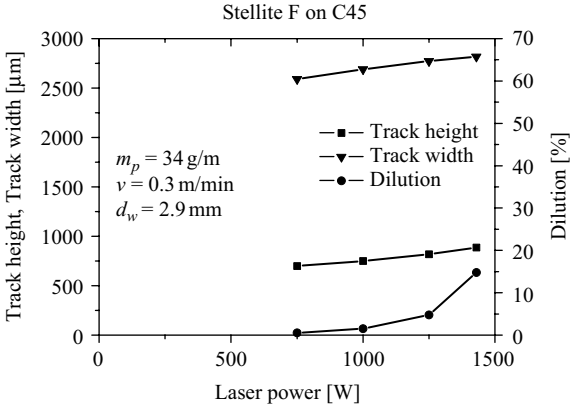

Figure 7.223. Track height, track width and dilution as a function of laser power for Stellite 6 on C45

optical microscopy (see Fig. 7.222). Furthermore, the dilution is determined as $D = A_A / A_S \times 100$ [%].

Figure 7.223 shows track height, track width, and dilution as a function of the laser power for Stellite F on C45. The velocity and the powder-feed rate are

held constant. Increasing the laser power leads to an increase of the track height because more powder is melted. Track width and melt depth (not shown) increase too, because more power is absorbed in the substrate. However, since the powder-feed rate is constant, the track height increases less than the melt depth, which leads to a significant increase of the dilution.

Figure 7.224 shows the influence of the laser power on the coating geometry for coatings of Höganäs M2 on different types of tool steel. At higher power, coating height and dilution increase. On the one hand, more powder is melted, i.e., the rate of powder utilization increases. On the other hand, more energy is coupled into the substrate. The laser power is limited to 800 W, since higher laser powers lead to excessively high dilution (Fig. 7.225**)** ($P = 1{,}200$ W). The differences in the dilution with the different alloys will be found in their different melting temperatures.

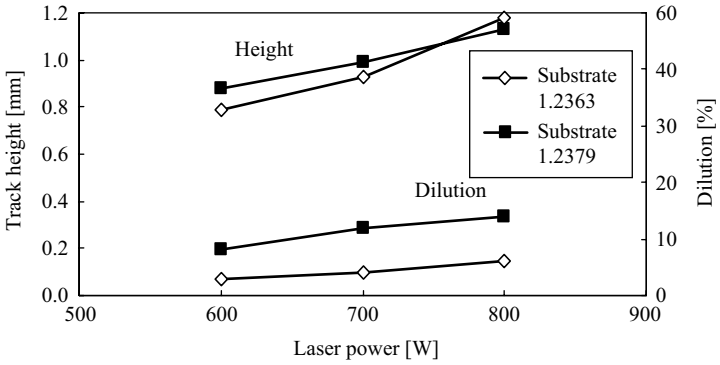

FIGURE 7.224. Influence of laser power on track height and dilution for Höganäs M2 ($v = 0.3$ m/min; $m_{fm} = 5$ g/min)

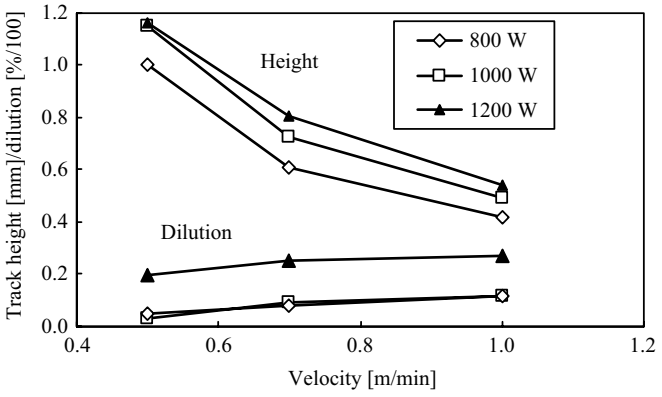

FIGURE 7.225. Influence of velocity on track height and dilution for 1.3344 layers on C45 ($m_P = 10$ g/min)

Single Focus

G. Habedank

The beam intensity is one of the main points of influence on the process windows. Generally the top-hat intensity distribution appearing on fiber-coupled diode lasers is suitable for the cladding process. Because of this intensity distribution, it is possible to get a small dilution, relatively even distributed over the whole width of the cladded track. Using low feed rates, the process windows are limited by the dilution of <5%, the formation of pores greater than 100 μm and the formation of cracks. Using high feed rates, the limit is lack of connection between cladded layer and substrate. With respect to the powder-feed rate the process limits are also high dilution and lack of connection. Figure 7.226 shows that in the given range of parameters the usage of higher beam intensities leads to an increasing maximum speed and an extension of the process window. A further extension of the process window is possible using preheating with the segmented intensity distribution [7.84], mentioned in "Segmented Focus."

The effect of defocusing on the cladding result is shown in Fig. 7.227a, b. One effect of defocusing is the decreasing of the intensity; the second effect is the change of the top-hat beam intensity distribution to a Gauss-shaped intensity distribution. So the intensity decreases on the rim of the spot, and it becomes too low to melt the powder in this region. Hence the consequence is nearly not increasing, but in the case of strong defocusing, a decreasing of the width of the cladded track.

The above mentioned effects are demonstrated by comparison of Fig. 7.227a, b. Each picture shows a three-layered cladding consisting of eight overlapping tracks. The geometry of the claddings is similar, but the feed rate during the process is 1.2 m/min using the focused beam and only 0.3 m/min using the defocused beam. Therefore, one can say that the defocusing has no advantages regarding the width of the cladded tracks and the feed rate.

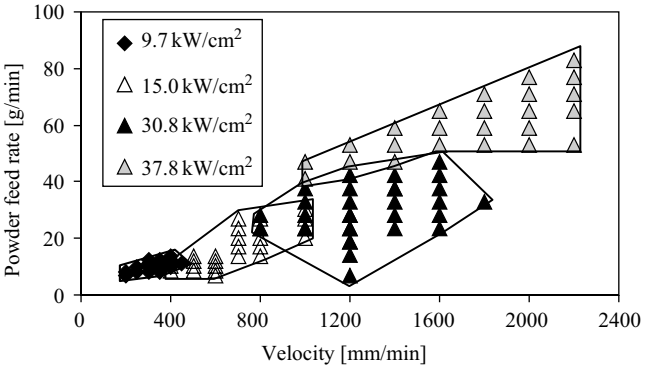

FIGURE 7.226. Process windows for different beam intensities, Stellite 21 and Stellite 6 on steel 1.3563

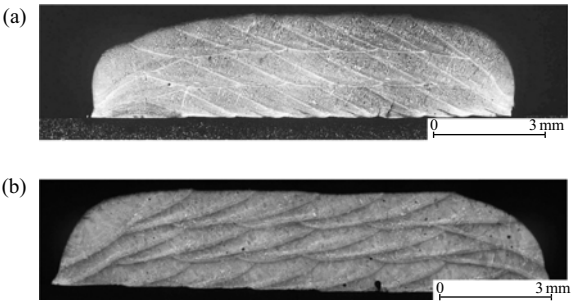

FIGURE 7.227. Three-layered cladding of eight tracks, base material steel 1.3563 (a) Cladded with Stellite 21, focused beam, feed rate $v = 1.2$ m/min. (b) Cladded with Stellite 6, defocused beam, defocusing 20 mm, feed rate $v = 0.3$ m/min

Segmented Focus

G. Habedank

During the process of powder-feed laser cladding the heating of the total workpiece is low. Due to the point-shaped heat source, the temperature distribution on the surface and in the rim zone is very inhomogeneous. There occur high peak values and gradients of the temperature. This causes the development of tensile residual stresses in the cladding and on the interface to the substrate material, particularly when a phase transformation occurs in the substrate.

To lower the peak temperature during the cladding process and to possibly improve the residual stress situation the intensity distribution of the laser beam can be segmented. The segmentation of the intensity distribution is in principle possible [7.71]. Instead of a diode laser with a segmented intensity distribution, a segmented intensity distribution can be simulated by a diode laser beam used for the cladding process and an additional Nd:YAG laser beam for pre- and post-heating with a variable distance between the foci (Fig. 7.228). The focal spot diameters of the two lasers should match.

Preheating or postheating (Fig. 7.228) influences not only the peak temperature but also the height of the cladded tracks. One can see in Fig. 7.229 that at each of the given feed rates the preheating in a distance of 1–2 mm causes an increasing of ca. 0.1 mm of the height of the cladded tracks. On the other hand, postheating causes a decreasing of the height of the cladded tracks. This effect is probably caused by flowing of the molten material in the width direction.

Absorption of Laser Radiation

G. Habedank

Regarding the absorption of the laser beam in the substrate material and consequently the height of the cladded layer, there are no remarkable differences between

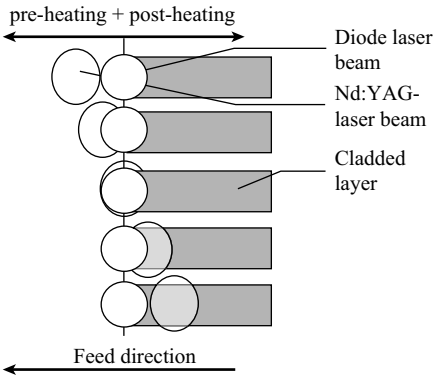

FIGURE 7.228. Principle of the simulation of the segmented intensity distribution with Nd:YAG and diode lasers

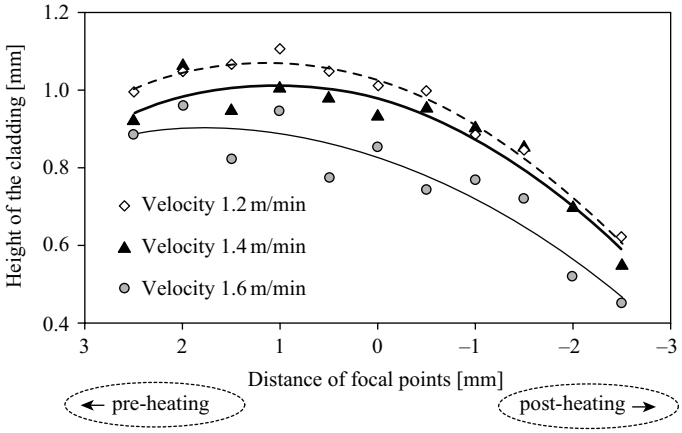

FIGURE 7.229. Height of the cladding in dependence on pre- or post-heating, Stellite 21 on steel 1.3563

the substrate materials construction steel, tool steel (1.3563), and a Ni-based alloy (Nimonic 80 A), when cladded with high-power diode lasers.

A further factor that might influence the height of the cladding is the absorption of the laser beam in the powder. However, as experiments have shown, the height of the cladded layer is not remarkably different with the use of different powders (Stellite 6, Stellite 21, NiCrBSi, NiBSi, CrNi 50:50) at comparable laser parameters.

Standard wavelengths of diode lasers are 808, 880, and 940 nm. Radiation of these short wavelengths will be absorbed well on steel surfaces and other heavy metal surfaces like Ni and Cr. Regarding the powder-feed laser beam cladding, there are advantages of the diode laser over the CO_2 laser ($\lambda = 10.6\ \mu m$) due to

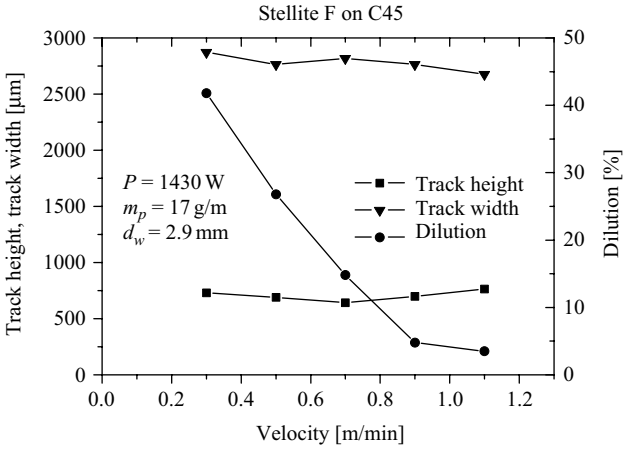

FIGURE 7.230. Track height, track width, and dilution as a function of the velocity for Stellite 6

the shorter wavelength. Compared to the Nd:YAG laser, which has a marginally higher wavelength of 1.06 µm, there is no explicit advantage of the diode lasers regarding the absorption and the cladding results on steel surfaces.

Feed Speed

M. Brandner, A. Weisheit

The influence of the traverse speed on coating height and dilution is shown in Fig. 7.225 using the powder 1.3344 and the base material C45 at a constant powder-supply rate as an example. The coating height decreases with increasing speed since the mass per distance drops. At the same time, the dilution increases, since a greater percentage of the energy is coupled in the substrate. A variation in the speed does not make sense for the cold-working steels. In this case, there is an increase in crack formation at speeds above 0.3 m/min.

Figure 7.230 shows track height, track width, and dilution as a function of the velocity for Stellite F. Laser power and powder-feed per unit length are held constant.[20] Increasing the velocity in the range of 0.3–1.1 m/min has no significant effect on track height and width. The dilution decreases rapidly due to the decreasing interaction time.

Powder-Feed Rate

A. Weisheit, M. Litmeyer

Figure 7.231 shows track height, track width, and dilution as a function of powder-feed rate for Stellite F. Laser power and velocity are held constant.[20] Increasing

[20] The complete set of parameters used in this example is given in "Laser Power."

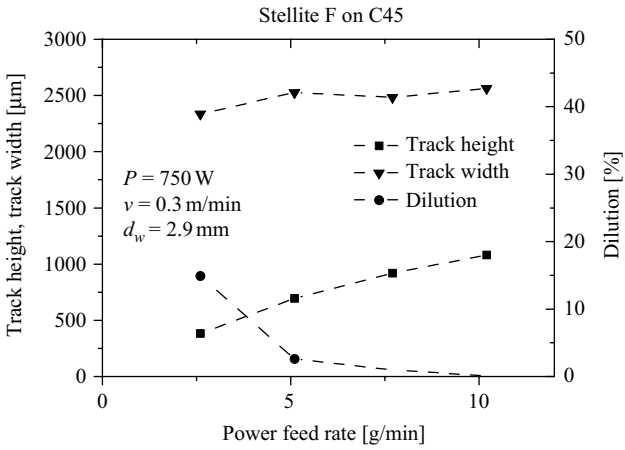

FIGURE 7.231. Track height, track width, and dilution as a function of the powder-feed rate for Stellite 6

the powder-feed rate has only a minor effect on the track width. The track height increases significantly whereas the melt depth (not shown) decreases. Both effects are due to the increasing absorption of the laser beam power in the powder stream. According to the increasing ratio of track height and melt depth the dilution decreases.

Figure 7.232 shows the dependencies of laser power and powder-flow rate (PFR) on layer height, melt depth, and hardness depth. It shows that the layer height increases with higher powder flow, the same way the melt depth decreases. But with higher powder flow the risk of misconnection at the border areas of the cladding rises. Layer heights of $t_{layer} = 0.55$ mm to $t_{layer} = 0.80$ mm can be reached at a laser power of $P_L = 780$ W. Figure 7.232 additionally shows that an increase of the laser power without increasing the powder flow doesn't increase the layer height. It only causes a higher melt and hardness depth. A further increase of the layer height can be reached by increasing the powder flow together with the laser power.

Angle of Incidence of Powder Stream

A. Weisheit, M. Brandner

It is known that the absorption of the laser beam depends on the angle of incidence. The highest absorption is achieved at 90°. Lower values lead to a decrease of absorption. Considering cladding of 3D geometry (e.g., tools) it is important to know which angle of incidence can be tolerated without a significant change of the quality of the cladded track, holding all other process parameters constant.

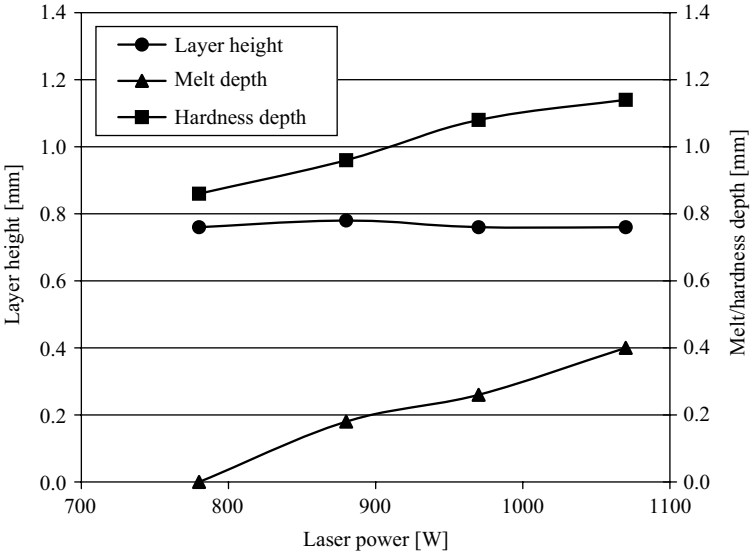

FIGURE 7.232. Laser power vs. layer height, melt depth, and hardness depth at laser cladding with powder

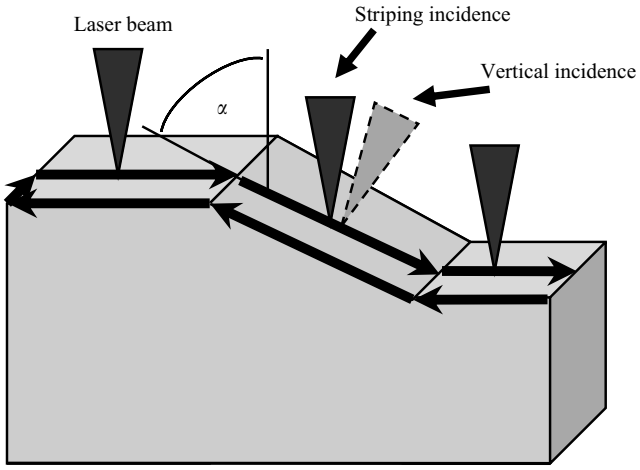

FIGURE 7.233. Process strategy for the cladding of an inclined plane; $\alpha = 10°$, $30°$, and $50°$

The track height on a test sample (Fig. 7.233) shows no significant differences for striping incidences of 80° and 60° (Fig. 7.234) as well as for striping incidence of 40° (not shown) compared to perpendicular incidence. This means that the decrease of absorption is of no importance.

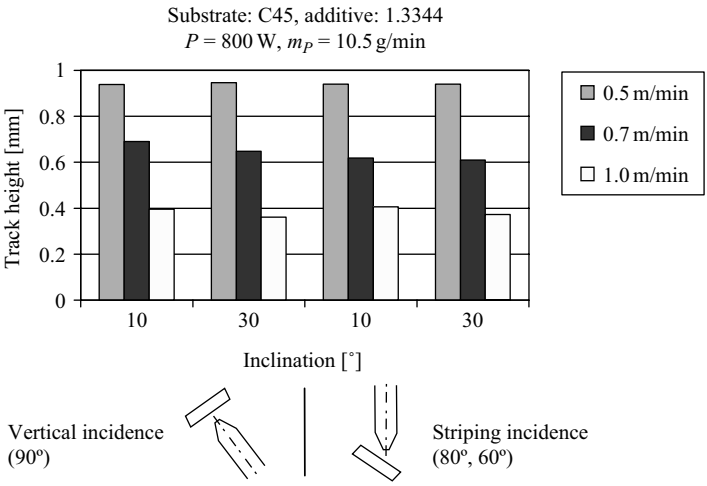

FIGURE 7.234. Track height as a function of the inclination for vertical and striping incidence

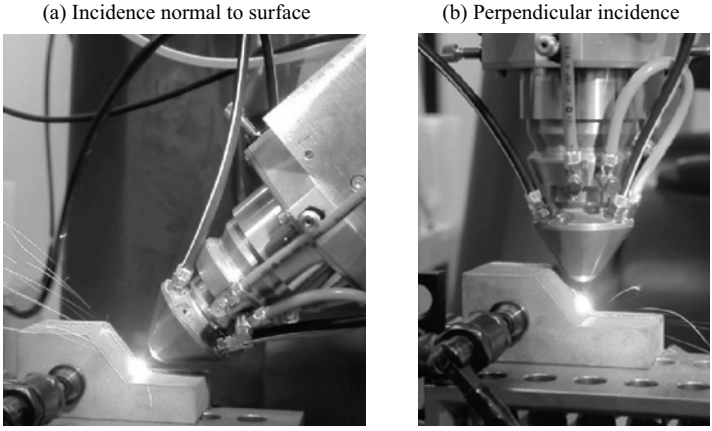

FIGURE 7.235. Process strategy for cladding of 3D contours – cladding of an inclined plane

Figure 7.235 shows another model geometry with transitions (sloping plane with pitch angle $\alpha = 10/30/50°$). The coating strategies pursued are again:

- powder stream incidence perpendicular to path – tipping of the nozzle depending on the angle (a),
- grazing powder stream incidence – alignment perpendicular to the nozzle (b).

The result remains the same, Fig. 7.236 shows that the coating height along the path remains constant. Noticeable differences cannot be recognized, neither along the coating paths nor between the two coating strategies.

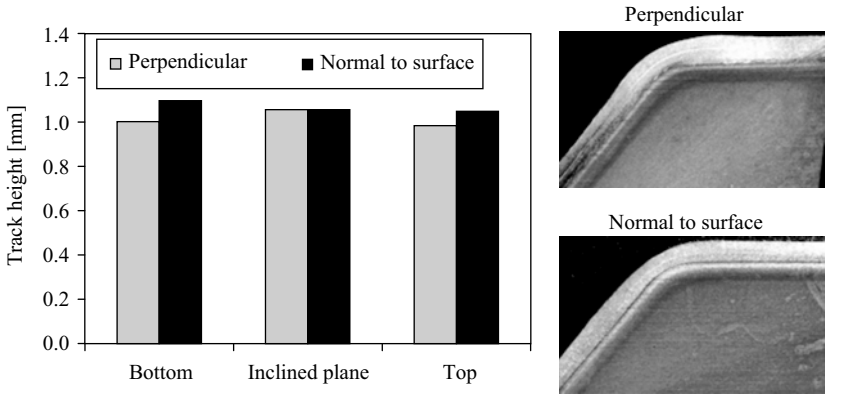

FIGURE 7.236. Track height and longitudinal section in dependence of position along the path and process strategy (Metco42 C on steel 1.2379; $P_L = 1{,}000$ W; $v = 0.3$ m/min; $m_{fm} = 6$ g/min)

As a consequence of this result programming of a complex 3D geometry can be simplified since a striping angle of incidence can be tolerated. Motions of a robot axis can be optimized instead of preserving a perpendicular incidence of the powder stream.

Dilution and Hardness

A. Weisheit, G. Habedank, M. Brandner

The quality of a laser cladded coating is significantly determined by the dilution, provided that substrate and filler material have a different composition. The dilution is necessary to ensure the metallurgical bonding to the substrate. However, to preserve the properties of the coating it should be kept at a minimum. Therefore a dilution (as defined in section "Laser Power") of 5–10% should be achieved. Lower values can lead to local bonding defects; higher values can lead to a decrease of the coating properties due to a significant change of the composition.

Figure 7.237 shows parameter combinations of laser power, velocity, and powder-feed rate partly drawn from Figs. 7.223, 7.230, and 7.231. Bright columns mark the areas where the dilution is higher than 10%, dark columns mark the areas where the dilution is lower than 10%. The diagram shows that in a wide range of parameter combinations coatings with an acceptable dilution can be produced.

Figure 7.238a, b shows typical cross sections with high and low dilution. Figure 7.238c shows the dendritic microstructure of Stellite F. Figure 7.239 shows a typical hardness profile.

The hardness of the cladded tracks is strongly influenced by the dilution. Figure 7.240 shows single tracks of Stellite 6 with high (a) and low (b) dilution cladded with variable feed rates. One can see the heat-affected zones (HAZ) in the quenched and tempered substrate material. The hardness depending on

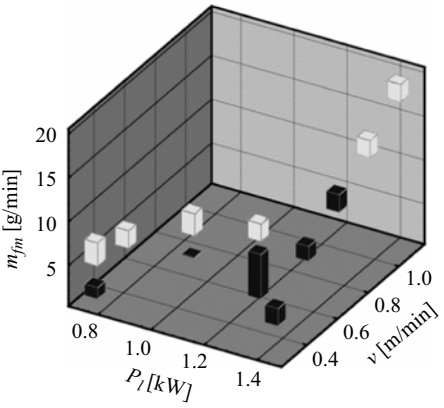

FIGURE 7.237. Parameter combinations of laser power, velocity, and powder-feed rate; dark columns: dilution <10%, bright columns: dilution >10%

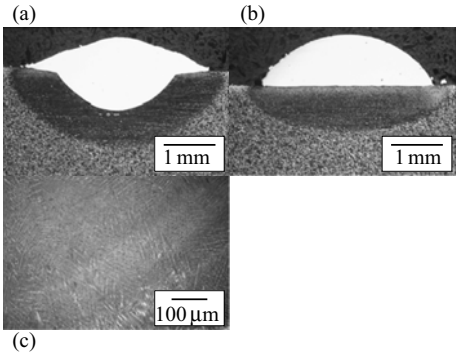

FIGURE 7.238. Cross sections of Stellite 6 layers on C 45. (a) $P = 1,000$ W, $v = 0.3$ m/min, $m_{fm} = 4.6$ g/min, $D = 56\%$. (b) $P = 1250$ W, $v = 0.3$ m/min, $m_{fm} = 6.9$ g/min, D = 2%. (c) dendritic microstructure

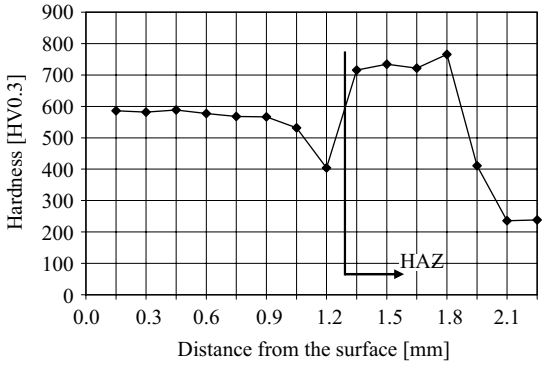

FIGURE 7.239. Hardness of a Stellite F cladding on C 45

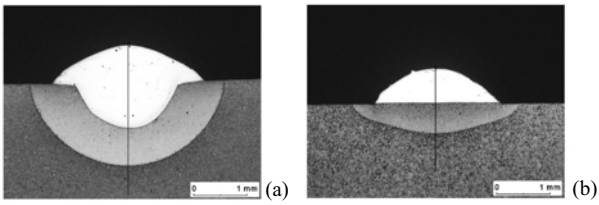

FIGURE 7.240. Cross section of cladded layers of Stellite 6 on the substrate of 1.3563 with different dilutions (a) $v = 0.4$ m/min, powder-feed rate 6.7 g/min. (b) $v = 1.2$ m/min, powder-feed rate 30.4 g/min

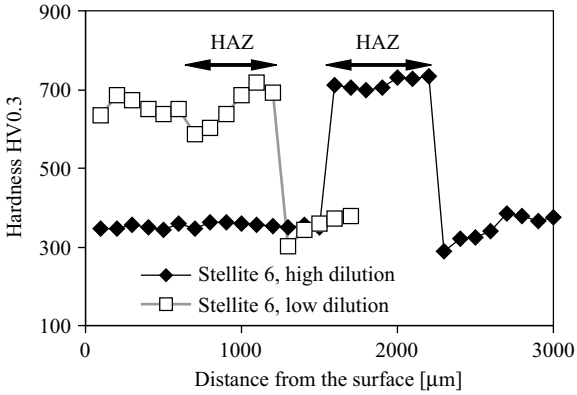

FIGURE 7.241. Hardness of cladded layers of Fig. 7.240

the distance from the surface shows Fig. 7.241. The lines drawn in Fig. 7.240 characterize the paths of the hardness measurements. Both specimens show high hardness values in the martensitic-transformed heat-affected zones. However, the desired high hardness of the Stellite 6 cladding is only obtained in the case of the cladded track with low dilution (Fig. 7.240b). Owing to the diffusion of iron out of the substrate into the cladding, the high dilution (Fig. 7.240a) causes a strong decreasing of the hardness of the whole cladding (Fig. 7.241).

Figure 7.242 shows a typical cross section with good bonding and low dilution. Because of the rapid cooling during laser cladding, the microstructure of the coating applied is extremely fine. In the case shown, it consists of martensite and austenite with dendritically arranged carbide network. Figures 7.243 and 7.244 show typical hardness curves for the different steel alloys. For both steel alloys, a characteristic behavior can be observed in the heat-affected zone, which can be attributed to changes in the microstructure. At first, there is a drop in hardness below the melting zone. The cause of this is residual austenite percentages in the microstructure. In contrast, in deeper zones, the microstructure consists of

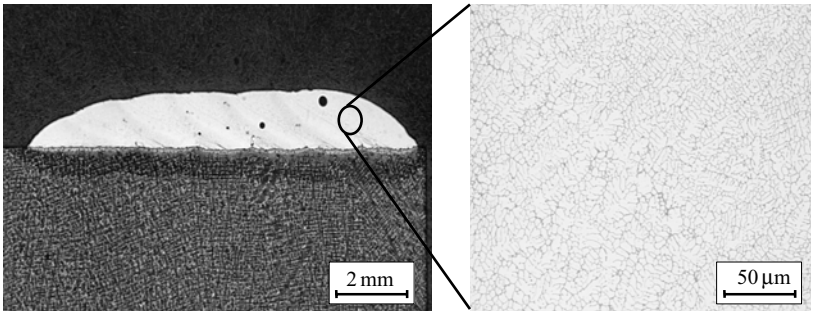

Figure 7.242. Typical cross section of M2 layers on 1.2382 with corresponding dendritic microstructure

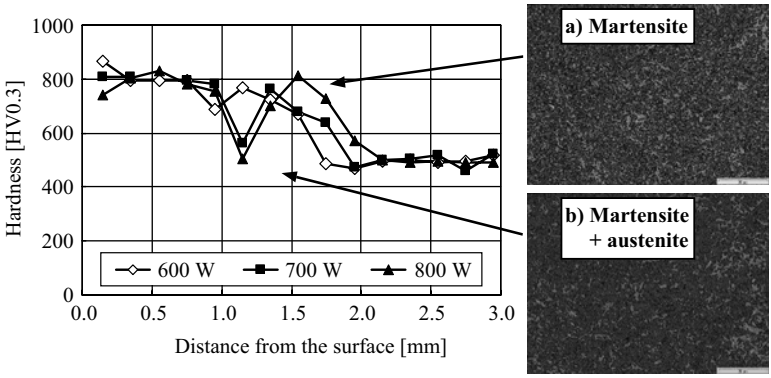

Figure 7.243. Typical hardness profile of a 1.3344 cladding on 1.2363 and the characteristic microstructure in the heat-affected zone ($v = 0.3$ m/min; $m_{fm} = 5$ g/min)

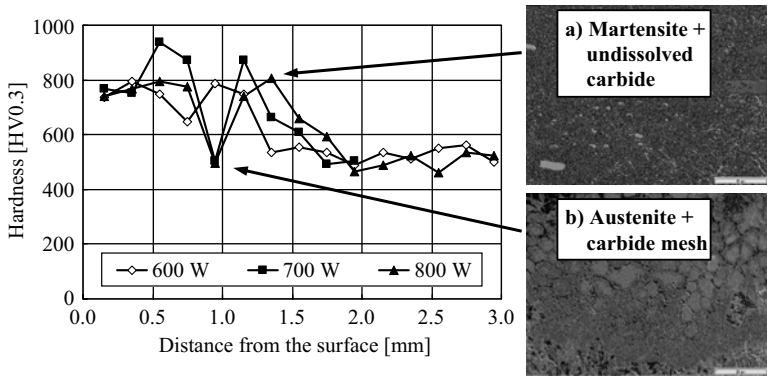

Figure 7.244. Typical hardness profile of a M2 cladding on 1.2379 and the characteristic microstructure in the heat-affected zone ($v = 0.3$ m/min; $m_{fm} = 5$ g/min)

martensite (in case of 1.2363 as the substrate) and/or martensite and carbides (in case of 1.2379 as the substrate), so the hardness increases to values of 800 HV0.3 again.

Cladding Material

R. Zieris, St. Nowotny, G. Habedank

The field for possible applications is limited by the availability of suitable coating materials. Generally these suitable materials are used for tribological and chemical resistance. For instance, Inconel is very often used in the chemical industry to coat components against chemical corrosion. Depending on the coating process, there are some problems. In some cases the bond strength of APS-sprayed coatings is not sufficient. The APS sprayed self-fluxing NiCrBSi, for example, needs a secondary step, which is remelting, to obtain the best properties.

Pure metals and other metal alloys can be used for their classical function. Which advantage is used, higher deposition ratio, better coating properties, higher bond strength, or less work for pre-treatment, depends on the material and the application.

There are differences between the process windows of different powders (Stellite 6, Stellite 21, NiCrBSi, NiBSi, CrNi 50:50) regarding the quality of the cladded layers. These differences are caused by the different powders' material properties and to a minor degree by a different absorption (cf. "Absorption of Laser Radiation"). For example, Stellite 6 has a stronger tendency to crack formation and the CrNi-50:50 alloy has a stronger tendency to pores and oxidation in comparison with Stellite 21.

Compatibility of Base Material and Cladding Material

M. Brandner, M. Litmeyer

The selection of suitable deposition materials plays a role in coating of tools. Depending on the application, there can be different requirements for the coatings created. For coating forming tools, this basically includes

- a hardness of 60 HRC,
- coating application free of cracks, and
- precision coats with high contour accuracy with minimum dilution.

For high-quality laser beam cladding of deep drawing, forming, or casting tools with metal powder or wire, a cladding material optimized for the base material and application used is necessary. There is a huge variety of cladding materials available and in common use, e.g., Co-, Ni- or Fe-base materials. The base materials cast iron and tool steel are typical materials for deep drawing tools, forming tools, or casting tools.

For cladding with metal powder, mainly gas-atomized materials are used. Water-atomized metal powder affects a higher porosity in the layer, caused by remaining hydrogen.

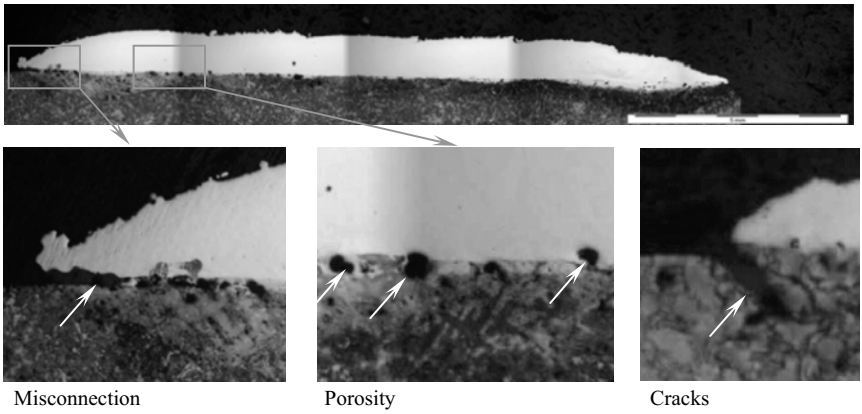

FIGURE 7.245. Cross section of GG25 coated with Stellite 6

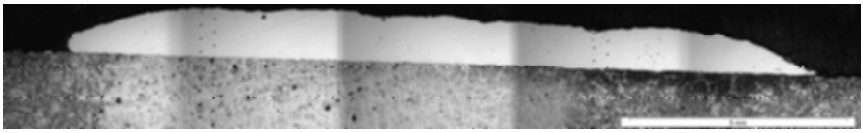

FIGURE 7.246. Cross section of GG25 coated with Ni-based alloy

Using the cast iron materials GG25 and GGG70 for laser beam cladding, a tendency to crack initiation into the base material can be observed (see Fig. 7.245). The cracks are running into the base material at the border of the hardened zone. Additionally a higher porosity in the interface area and misconnection at the layer border can be detected.

Cladding of cast iron with a Ni-based alloy shows much better results than cladding with the Co-based Stellite 6. With the Ni-based alloy, a good connection to the base material and a low porosity can be observed (see Fig. 7.246). But on the other side, the used Ni-base alloy offers a lower hardness. A reduction of the tendency to porosity can be achieved by previous cleaning the surface by sand blasting.

The tool steel materials 1.1438, 1.2738, and 1.2379 in general show a low porosity and a low error tendency. Table 7.17 gives a survey of the characteristics of coatings for numerous metal powders used on different base materials.[21]

[21] Coatings applied using a three-stream coaxial powder nozzle and a fiber-coupled high-power diode laser with a maximum power of $P_L = 2{,}000$ W at the workpiece.

Table 7.17. Combinations of base materials and cladding materials

	Fe-based alloy	Co-based alloy (Stellite 6)	Co-based alloy (Stellite 21)	Ni-based alloy
GG25	✓ Good connection × Porosity × Cracks in base material	× Misconnection at the border area ✓ Low porosity × Cracks in base material at multi-line cladding	–	× Good connection × No porosity
GGG70	× Good connection ✓ Porosity × Cracks in base material at multi-line cladding	× Misconnection at the border area ✓ No porosity	–	–
1.1438	✓ Good connection ✓ no porosity	✓ Sometimes misconnection at the border area ✓ No porosity	–	–
1.2738	✓ Good connection ✓ No porosity	✓ Sometimes misconnection at the border area ✓ no porosity	–	–
1.2379	✓ Good connection ✓ No porosity	✓ Sometimes misconnection at the border area ✓ No porosity	✓ Sometimes misconnectin at the border area ✓ No porosity	–

7.3.3.4. Temperature Distribution and Residual Stress

Numerical Computation of the Temperature Distribution

G. Habedank

The distribution of the temperature during the process can be simulated with the aid of FEM-software.[22] The example presented here refers to the segmented focus described in "Segmented Focus."

One can see in Fig. 7.247 the effect of preheating using different distances between the centers of the beam spots. Using the preheating with a second laser beam, it is possible to reduce the peak value of the temperature in the middle of the beam spot on the surface. The peak value of the temperature decreases about 400 K at preheating with a distance of 4 mm between the spots compared to overlaid beam spots.

[22] For example, ANSYS, ANSYS, Inc., Canonsburg, USA.

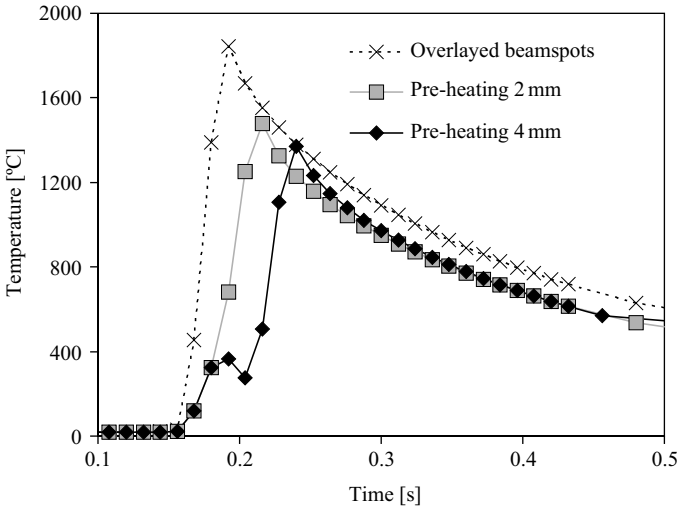

FIGURE 7.247. Simulated temperature in the middle of the laser spot of a diode laser on the surface of the workpiece; for laser powder cladding with diode laser (2,100 W) and Nd:YAG-Laser (1,200 W) for variable preheating distance of the Nd:YAG-Laser, material: Stellite 21 on substrate of steel 1.3563, feed rate 5 m/min, powder-feed rate 102 g/min, diameter of the focus 3 mm

Numerical Computation of the Residual Stress

G. Habedank

The residual stress developing during the powder-feed laser beam cladding can also be simulated by means of FEM-software. The model used as an illustration is a quarter of a valve of a ship engine (Fig. 7.248). The cladding of the valve seats for repairing is a process used in the industry already in some cases (cf. "Cladding of Valve Seats"). Due to the geometry of the valve that causes a heat accumulation the risk of crack formation is high. A further negative component is in many cases a residual old cladding that cannot be removed because of the very deep groove that would be generated in this case.

The aim of the simulation is to compare residual stresses of the two cladding possibilities: with top hat intensity distribution (cf. "Single Focus") and with segmented intensity distribution (cf. "Segmented Focus"). The maximum tensile residual stress in the case of the laser cladding occurs at the interface between the cladding and the substrate [7.72]. Therefore at nine nodes along the interface between cladding and substrate the residual stress is simulated (Fig. 7.248). The computed residual stress in z-direction after a cooling time of 18 min in the nine nodes is shown in Fig. 7.249. The z-direction is equivalent to the longitudinal direction of the cladded tracks at the vertical section represented in Fig. 7.248.

The cladding starts on the internal rim of the valve seat (node 1) and runs spirally to the outer rim (node 9). In both cases (Fig. 7.249a, b) the same overall

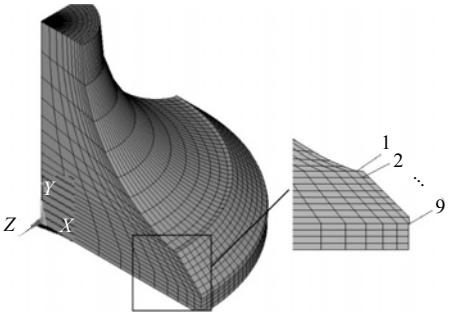

FIGURE 7.248. FEM-model for the simulation of the residual stress after powder-feed laser beam cladding of a valve of the motor of a ship with marking of the calculated nodes

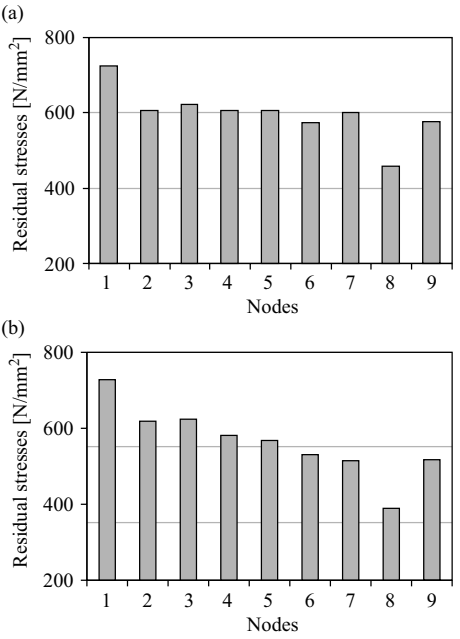

FIGURE 7.249. Calculated residual stress on the nine marked nodes in Fig. 7.248; substrate material Nimonic 80 A, cladded with Stellite 6, $v = 10$ mm/s. (a) $P = 800$ W. (b) $P = 400$ W for the cladding + 400 W for preheating, distance of the focal spot for preheating 1.5 mm, diameter of both focal points: 1 mm

power output of the laser of 800 W is used. In Fig. 7.249b the segmented intensity distribution is used. The cladding is carried out with 400 W and the preheating also with 400 W.

One can see in both cases very high tensile residual stress in the first track and the following two or three tracks. This high tensile residual stress causes the risk of

cracks on the real valve cladding. The cracks from the first tracks could propagate through the following tracks, thus disabling the valve.

So it is clear for the cladding of valve seats that a segmented intensity distribution leads to a slight lowering of the peak temperature and therefore a slight lowering of the tensile residual stresses, especially for the tracks six to nine. However, the risk of crack formation cannot be completely overcome because of the unfavorable heat distribution in the rim of the valve.

Measurement of the Residual Stress

G. Habedank

To study the size and the distribution of the residual stresses X-ray measurements can be carried out.

The X-ray measurement yields analyzable results only on a planar surface. Therefore the cladded specimens have to be grinded, removing 20–30 μm from the surface. The grinding causes residual stress itself. Due to this, a further 20–30 μm of the original surface has to be removed electrolytically at further 20–30 μm. So the first, X-ray measurement can be carried out at a depth of 50–60 μm. Further measurements can be carried out after stepwise electrolytic removal of the cladding in steps of 100–150 μm. With Co-based alloys (e.g., Stellite 6) the residual stresses can be measured in the Co-phase due to the high percentage of this phase (e.g., 65% in case of Stellite 6). However, the X-ray measurement yields only the order of magnitude of the residual stress because of the dendritic microstructure of the cladded layer. This dendritic microstructure causes spreading of the measured residual stress values.

Figure 7.250 shows the development of the residual stresses in the longitudinal direction of cladded tracks.[23] One can see the tensile residual stresses with an average value of ca. 200 N/mm^2 and compressive stresses at the depth of 200–400 μm. In the case of the "one focus" cladding (cf. "Single Focus") occurs locally higher tensile stress (upto ca. 500 N/mm^2) and higher stress gradients than at the cladding with preheating (cf. "Segmented Focus"). One can say for the cladded flat specimens that in the case of preheating the risk of the formation of cracks is marginally lower.

7.3.3.5. Special Equipment

Robot with External Axis

M. Brandner

During laser-coating of tools, the system concept plays an important role with respect to processing quality and process efficiency. In particular, complex 3D contours (e.g., forming tools) set higher demands of system technology. In addition

[23] Size of the specimen: 160 × 60 × 10 mm; substrate construction steel, cladding Stellite 6; experimental setup with off-axis powder nozzle cf. [7.85].

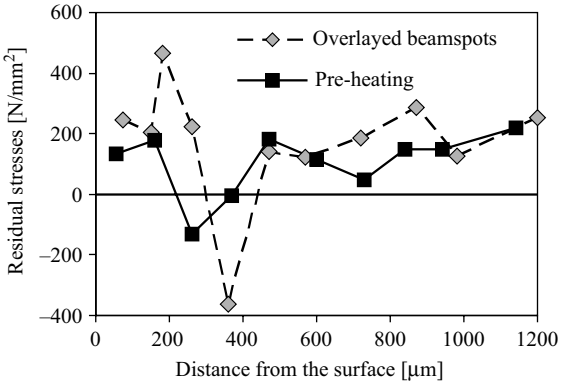

FIGURE 7.250. Residual stress in longitudinal direction in the cladding consisting of Stellite 6, parameters: $v = 400$ mm/min, $P_{\text{diode laser}} = 400$ W, $P_{Nd:YAG\text{-laser}} = 400$ W, diameter of both focal points: 1 mm, "one focus" = 100% overlapping focal points, "pre-heating" = distance of the focal points 1.5 mm

to the coaxial supply of the powdered filler material (cf. powder-feed nozzles in "Solidification Process"), the workpiece and tool handling are also decisive for high coating quality. Usually, industrial robots are used for coating tools. In view of the high weights and/or large dimensions the tools may have, the robot assumes the task of tool handling, i.e., it moves the coating head relative to the fixed clamped workpiece. This results in various disadvantages, especially with 3D contours:

- Reclamping of the workpieces becomes necessary for coating application at different locations (e.g., side and top surface in the area of an edge).
- When there are complex contours, extensive reorientations of the robot hand lead to a decrease in accuracy of path and thus, to more poor processing quality.
- Processing in constrained position – good trough position is not always possible.

In this context, the use of external axes that are coupled to the robot control offers advantages (e.g., turn-tip positioner). In this way, the sequence of coating head motions can be optimized relative to the component surface. The accuracy of the path can be increased by minimizing and/or optimizing the axis motions. It is better to process in trough position, depending on the powder nozzle design. In addition, processing of complex geometry can be carried out with one clamping operation. Figure 7.251 compares the two variations, using a demonstrator component as an example.

Robot-Based Mobile Cladding System

M. Litmeyer

Deep drawing and forming tools are often of very big size and weight with dimensions of more than $4.0 \times 3.0 \times 0.7$ m^3 ($l \times w \times h$) and a weight of more than

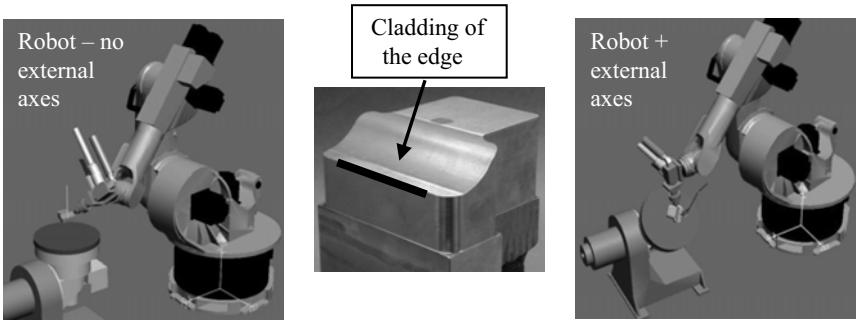

FIGURE 7.251. Cladding of a forming tool – Comparison of cladding equipment with/without external axis regarding machining plane (angle of incidence), position of robot axes

40 tons. These kinds of tools are very difficult to carry. In some cases a transportation of the tools is even not possible. In these cases a mobile cladding system would be very useful. Because of the big size and weight of conventional high-power laser sources like Nd:YAG- or CO_2-lasers, it is normally impossible to carry the laser cladding system to the workpiece. With high-power diode lasers, which are of small size and low weight and available with an optical power of $P_L > 2{,}000$ W, it is possible to build up a compact mobile cladding system. Another point of interest of a mobile laser cladding system is the possibility of equipment sharing to optimize the efficiency and reduce the investment.

The handling system shown in Fig. 7.252 is based on an industrial articulated robot with an integrated beam guiding system and a fiber-coupled high-power diode laser with a maximum laser power of $P_{L,max.} = 2{,}000$ W at the workpiece. To increase the accessibility, the robot is placed in overhead position on a rotatable arm, so that the workpiece can be placed under the system. To increase the work area of the system the rotation axis with the robot is placed on a linear axis of $l = 2.5$ m. Both additional axes are fully integrated in the system control of the robot. The whole system provides a total working area of $2.5 \times 2.5 \times 1.1$ m^3 ($l \times w \times h$). The whole cladding system, including laser source, handling system and all necessary utilities, is based on a stable platform. The total size of the system is $4.0 \times 2.4 \times 2.4$ m^3 ($l \times w \times h$) at a total weight of 4,000 kg. With its dimensions it is designed for transportation by a standard truck. Because of the low weight of the system the loading and unloading is possible by the most indoor cranes.

The beam guiding system of the fiber-coupled diode laser is integrated in the working head of the robot, so that the laser beam is provided axial to the sixth axis of the robot. This provides a simple programming of the robot and an increased accessibility at the workpiece because of the possibility to use compact processing optics.

FIGURE 7.252. Mobile laser cladding system

Cartesian Mobile Cladding System

A. Weisheit

Normally parts to be repaired by laser cladding are dismounted and transported to the laser job shop. However, there are applications where a mobile laser cladding system makes sense. If dismounting is time consuming (e.g., steam turbine component) or the handling of the part needs large equipment (e.g., crankshafts for ship engines) it might be cost-effective to move the cladding system to the customer.

Diode lasers are particularly suitable for mobile use because they are small, robust and need only little maintenance.

Figure 7.253 shows the constituents of a mobile laser cladding system based on a Cartesian handling. The handling unit has three linear and two rotary axes. The unit weighs approx. 1,600 kg and needs a space of 2×3 m^2. The laser is a fiber-coupled diode laser with an output power of 2 kW. The laser beam is guided through the rotary axes by mirrors. Thus the fiber is not twisted during operation. The cladding head is a three-way nozzle suitable for 3D applications. Additionally the mobile system is equipped with a chiller for the laser and the optics. The supplies needed on-site are electric current and compressed air.

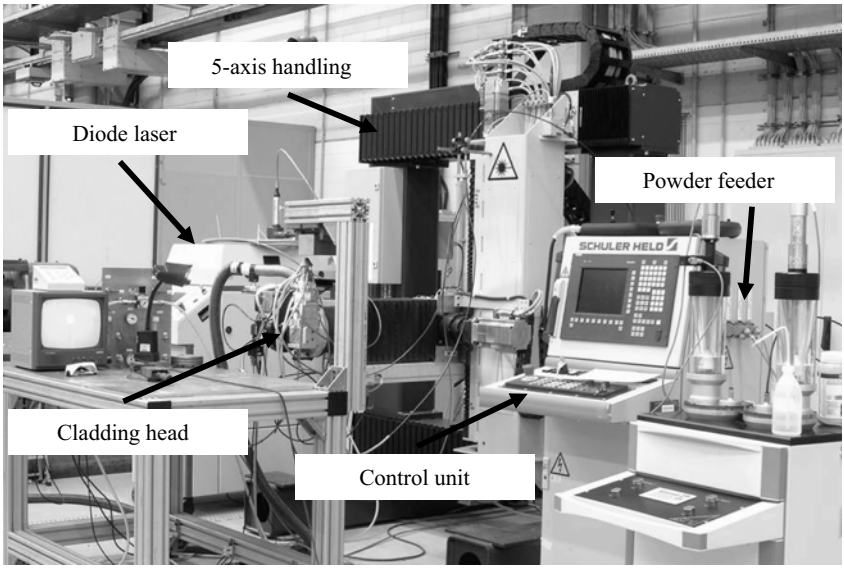

FIGURE 7.253. Constituents of the mobile laser cladding system

Equipment for the Mobile Use of the Laser Assisted Atmospheric Plasma Spraying (LAAPS)

R. Zieris, S. Nowotny

In general, for the hybrid process LAAPS described in "Laser Hybrid Coating Technologies" any commercial APS system can be used, provided that

- the laser system can be moved to the APS system,
- the hybrid gun can be implemented in the APS systems, and
- the system controls of the APS and the laser system can be linked.

Commercial plasma systems can often be combined with plasma guns with a power ranging from 6 kW upto 60 kW.

The equipment shown in Fig. 7.254 is built in a noise barrier with an air off take due to employment protection. It consists of a robot system with an external turning tilting table and a powder-feed system, all controlled by a single computer.

Two hybrid cladding units are shown in Fig. 7.255. In the following text they are referred to as hybrid gun 1 and hybrid gun 2. They are designed for use with a fiber-coupled high-power diode laser or a fiber-coupled Nd:YAG laser.

Hybrid gun 1 is shown on the left-hand side of Fig. 7.255. It consists of an F6 plasma gun (maximum power of 60 kW), combined with the fiber-coupled kilowatt laser system ($P_L = 2.2$ kW) presented in Chapter 6.2.3. This hybrid gun has a 23° off-axis laser beam. The laser beam can be arranged in front, in the middle, or behind the plasma torch.

FIGURE 7.254. The complete used system: plasma gun, robot system, and control panel in a noise barrier

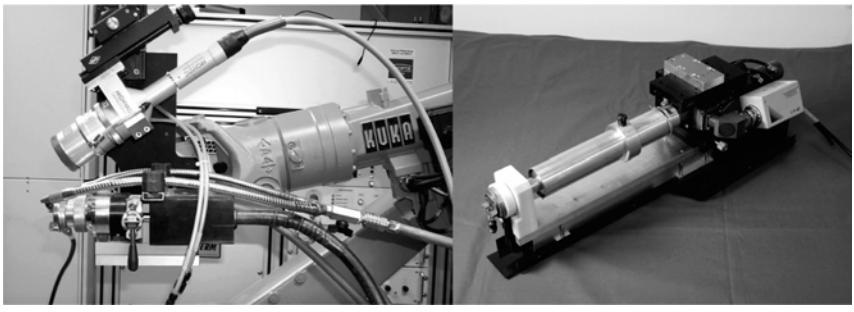

FIGURE 7.255. Two designed and built laser-plasma-cladding-units. Left: Commercial F6 plasma gun with a optic for the 2.2 kW high-power diode laser. Right: Modified F1 plasma gun with a hole in the cathode and a 3 kW Nd:YAG laser optic

Hybrid gun 2 – a further development – is shown on the right-hand side of Fig. 7.255. This hybrid gun is used with an Nd:YAG laser system ($P_L = 3$ kW). It has a concentrically arranged laser beam. In this configuration the cathode of the plasma gun has a hole in the middle allowing for laser beam passing. The used commercial F1 plasma gun (maximum power of 25 kW) had to be modified for a regular function. In this case the hybrid gun can be moved non-directionally, while the laser beam hits the surface always in the middle of the plasma spot.

The principle of the hybrid gun 2 with a coaxially arranged laser beam is presented in Fig. 7.256. The laser is already in interaction with the plasma torch and the spray particles. The plasma-particle torch is transparent for the laser beam upto 99.8% which has been shown by theoretical and practical investigations [7.81–7.83].

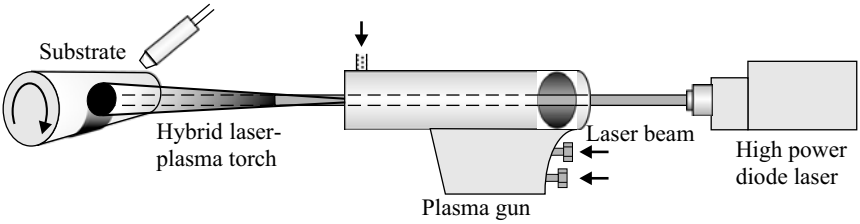

FIGURE 7.256. Principle of the coaxially arranged laser beam

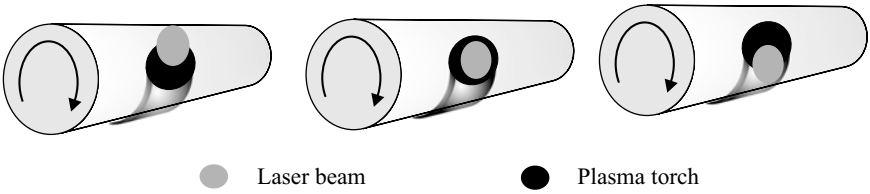

FIGURE 7.257. Possible arrangements of laser beam and plasma torch

As demonstrated in Fig. 7.257 several possible arrangements of the laser beam and plasma torch exist during the coating process. In all cases the laser beam is round and always in interaction with the plasma torch. In Fig. 7.257, left-hand side, the laser is in front of the plasma torch. In this arrangement the substrate is pre-treated and the laser is fusing the surface. Subsequently the liquid particles come into the weld pool, and the coating is built up. In the middle of Fig. 7.257, the laser is in the center of the plasma torch. In this arrangement the effect of heat conduction welding is used. There, where the laser beam hits the surface, there are already particles. The result is a simultaneous treatment of the surface and the coating. In the third case a post treatment takes place, while the laser is arranged behind the plasma torch. In some cases there is also a heat-conduction welding.

More flexibility and possibilities are feasible with the hybrid gun 1, but there are also some disadvantages. At first there is the optical imaging of the laser beam on the surface. Depending on the off axis angle, an ellipse is imaging. Across this area it has not the same intensity distribution. This can have an effect on the coating results. Another disadvantage is the short interaction time between the laser and the liquid particles from the plasma torch. Furthermore the use of the hybrid gun 1 has a directionality dependence of the cladding process.

7.3.3.6. Applications and Results

Laser-Assisted Atmospheric Plasma Spraying (LAAPS)

R. Zieris, S. Nowotny

NiCrBSi and AlSi 30 as coating materials are representatives for metal, light metal, and their alloys [7.90, 7.91].

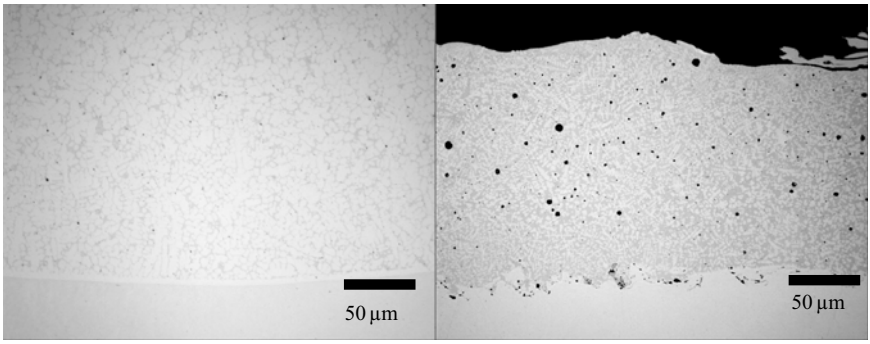

FIGURE 7.258. Left: NiCrBSi coatings deposited by the LAAPS process – substrate surface prepared by turning ($R_z = 15$ µm). Right: Substrate surface prepared by grit blasting with corundum ($R_z = 50$ µm)

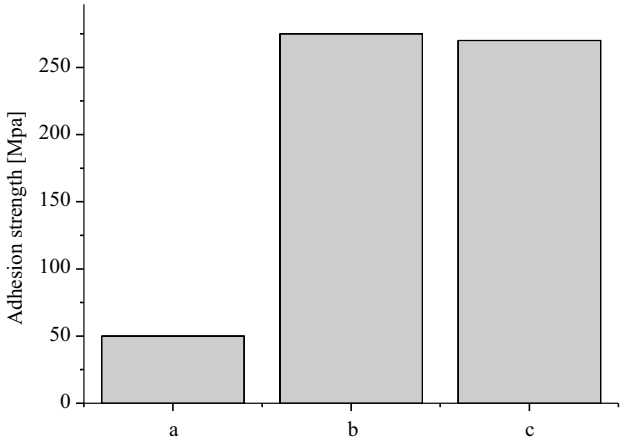

FIGURE 7.259. Results of bond strength tests for the NiCrBSi coatings: column a – APS coating, with substrate turned and grit blasted; column b – LAAPS (diode laser), with substrate turned and grit blasted; and column c – LAAPS (diode laser), with substrate turned

Examples of NiCrBSi coatings on mild steel substrates deposited by the LAAPS process are shown in Fig. 7.258. Substrate surface preparation can be performed in different ways, i.e., by traditional grit blasting or by just turning, resulting in different coating roughness. Independent of the surface preparation, the coatings show a metallurgical bonding to the substrate and a dendritic coating structure.

Figure 7.259 presents results of bond strength tests for NiCrBSi coatings. The results demonstrate the significant increase in the bond strength of LAAPS coatings (made by using the diode laser) (columns b and c) compared to the coating

TABLE 7.18. Test results (hardness and parameters from the oscillating wear test) for APS and LAAPS NiCrBSi coatings

Properties	APS	LAAPS
Hardness HV0.3	320	282
Coefficient of friction	0.85	0.7
Volumetric wear (mm^3)	0.003	0.00041
Ball wear (μm)	490	610

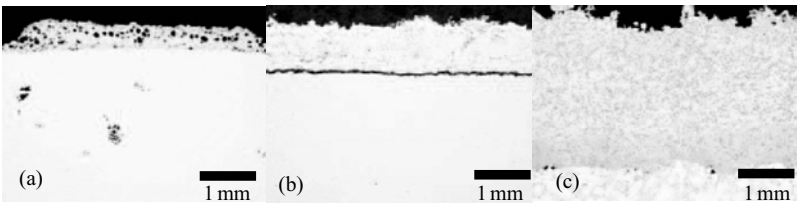

FIGURE 7.260. AlSi 30 coating deposited by the LAAPS process, substrate surface prepared by turning ($R_z = 30$ μm): (a) sprayed with a concentric arranged laser beam, laser power 2 kW, (b) with a low porosity but without a bonding at the interface, (c) cross section sprayed by LAAPS with optimize parameters, surface speed was 4 m/min, feed motion 4 mm

prepared by APS (column a). Surface treatment by grit blasting (column b) shows no advantages compared to pure turning (column c). The absolute values of bond strength are not comparable with those obtained by the traditional glue resin test because of the differences in the test procedures involved.

Results of hardness measurements and wear tests of NiCrBSi coatings are compiled in Table 7.18. Test results (hardness and parameters from the oscillating wear test) for APS and LAAPS NiCrBSi coatings. The volumetric wear is given for a load of 10 N, an amplitude of oscillation of 1 mm, and a duration of 10^5 cycles. Despite its lower coating hardness compared to that of the APS coating, the LAAPS coating has a volumetric wear that is an order of magnitude lower than that of the APS coating. Simultaneously, the wear rate of the test body is slightly higher. The LAAPS coating also shows a lower coefficient of friction.

Some examples of an AlSi 30 coating on an AlMg 10 substrate, deposited by the LAAPS process, are shown in Fig. 7.260. For the coating process a pretreatment is necessary to eliminate the reaction-inactive oxide film. In this example, the substrate is turned before coating. After the turning the roughness of the substrate is $R_z = 30$ μm. A better bonding results in an additional pre heating of the substrate. The thickness of a single layer with optimized parameters ranges between 300 and 400 μm. There is a considerable influence of the process parameters on the coating properties. Parameters which are slightly out of the optimized process window lead to porosity (Fig. 7.260c) or bonding defects (Fig. 7.260b). In contrast, optimized parameters and a precise adjustment of the laser beam to the plasma

torch guarantee a flawless coating reliably. Figure 7.260c shows a cross section of such a non-porous and well-bonded coating. Depending of the measuring point, the micro hardness ranges from 250 up to 298 HV0.3. The bond strength ranges between 25 up to 30 MPa. The wear resistance as the result of the oscillating sliding wear test is as good as APS-sprayed or laser-clad coatings [7.92].

Coating of Punching Dies

M. Brandner

The topic here is coating of components in the course of a design change and/or repairing contours damaged as a result of the appearance of wear. Generally, partial coatings with small thickness are applied here. The requirement in this process is low thermal influence on the workpiece (avoidance of straightening scopes).

Figures 7.261 and 7.262 show sample results from coating of punching dies made of cold-working steel (1.2382) with 3D contours. In both cases, a coating is applied on the cutting surface by overlapping approx. 30 individual tracks in two layers. The process strategy is varied here. In the first case, the cladding head is adjusted perpendicular to the surface (see Fig. 7.263). In the second case, the processing is carried out with vertical orientation of the head, i.e., different grazing angles of incidence depending on the contour. The coatings do not exhibit any notable differences in coating height and thus confirm the statements made earlier (see chapter "Angle of Incidence of Powder Stream"). The coating quality is good on both tools. The microstructure exhibits no pores or cracks and has a hardness of 750 HV0.3.

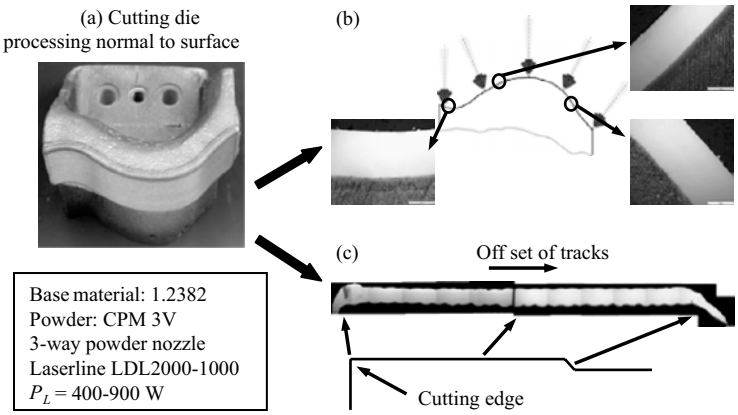

FIGURE 7.261. Cladding of a punching die – processing normal to surface: (a) coated tool; (b) process strategy; (c) cross section of the layer

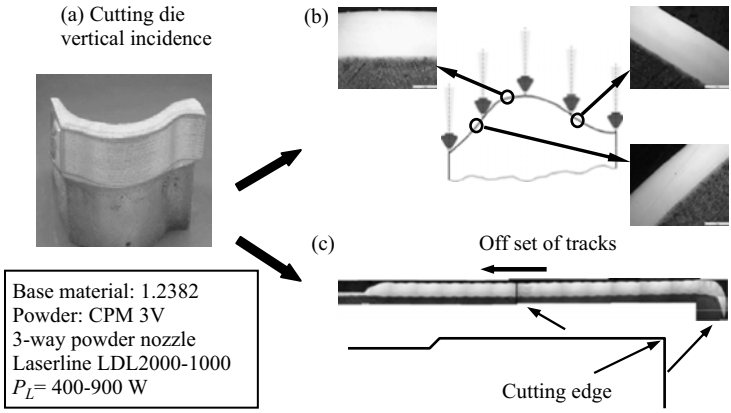

FIGURE 7.262. Cladding of a punching die – processing with vertical incidence: (a) coated tool; (b) process strategy; (c) cross section of the layer

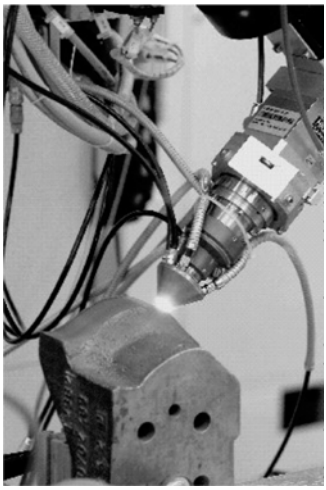

FIGURE 7.263. Cladding process – processing normal to surface

Cladding of Valve Seats

A. Weisheit, G. Habedank, H. Kohn

The cladding of valve seats for gas engines of a block heat and power plant is demonstrated. The valves are made from CrNiMn steel. The process is shown in Fig. 7.264a, b. For powder-feeding an off-axis nozzle is used. The valve is tilted by 30°. The cladding of a single track with a width of 3 mm and approx. 0.8 mm height is sufficient for this application. A cross section of the layer is shown in

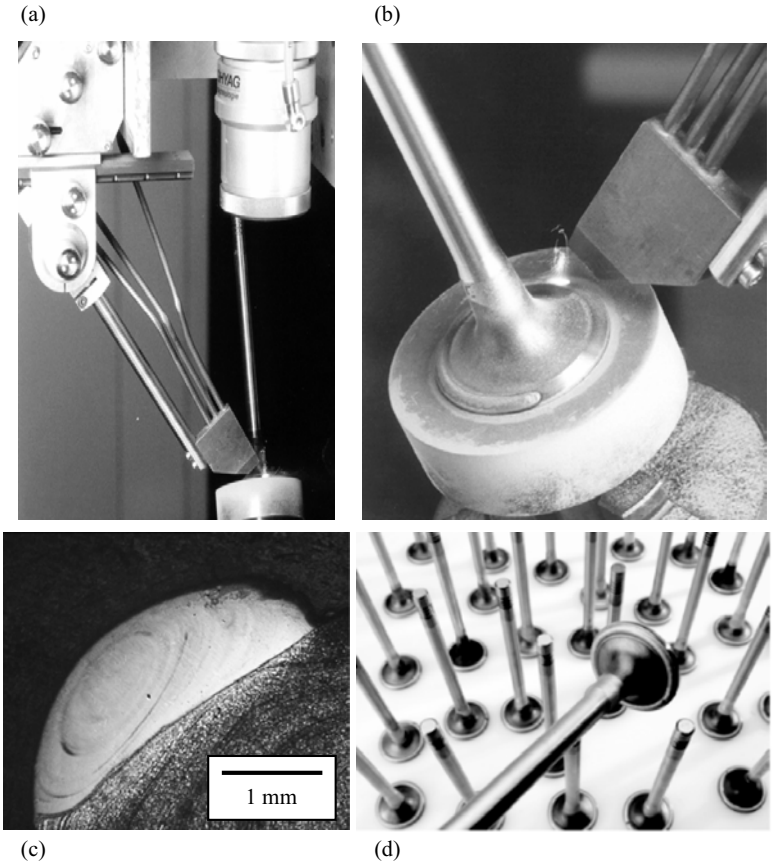

FIGURE 7.264. Cladding of valve seats using a fiber-coupled diode laser; filler material Stellite F, $P = 1{,}100$ W, $v = 0.5$ m/min, $m_{fm} = 15$ g/min. (a), (b) process; (c) cross section; (d) cladded valves

Fig. 7.264c. The microstructure is free of pores and cracks and no bonding defects occur. Figure 7.264d shows the cladded valves.

A further example of application is the cladding of seats of valves for diesel engines of ships with the fiber-coupled kilowatt laser (Chapter 6.2.3). The simulation of the process is already explained in chapter "Numerical Computation of the Residual Stress". The valves consisting of Nimonic 80A are cladded with Stellite 6. On the left side of the Fig. 7.265 the cladding process is to be seen. The valve is fixed at a rotary table so that the laser beam is perpendicular to the valve seat. The cladding begins on the internal rim with direction outwards spirally. An off-axis powder nozzle with inclination angle of 45° is used in dragging direction. The laser output power is $P = 700$ W at a feed rate of 20 mm/s and a powder-feed rate of 3.8 g/min. As noted in chapter "Numerical Computation of the Residual Stress",

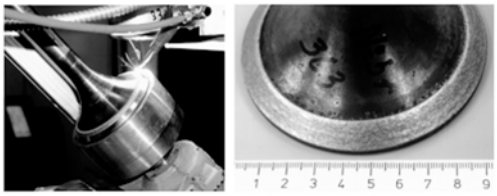

FIGURE 7.265. Cladding process of the seat of valves of a diesel engine of a ship and the completely cladded component

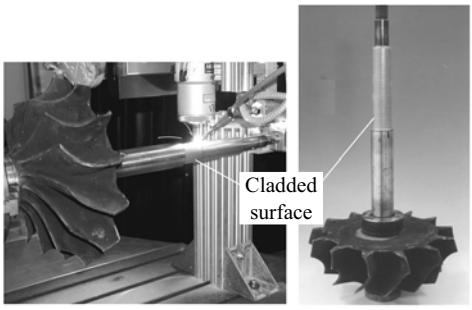

FIGURE 7.266. Cladding process of the shaft of a turbo charger and the completely cladded component

the cladding of the valve seats is sensitive to cracks and the process window is small because of this. Cladded valves without cracks are finished by grinding and after this, implemented in an engine of the power supply of a container ship. It is very important to get completely crack free claddings because of the risk of a damage of the engine.

Repair of a Shaft of a Turbo Charger

G. Habedank, H. Kohn

Another example for the application of the powder-feed laser beam cladding with a diode laser is the repairing of the shaft of a turbo charger (Fig. 7.266). For this purpose the turbo charger is pivoted and cladded with the fiber-coupled kilowatt diode laser presented in Chapter 6.2.3 and an off-axis powder nozzle with an inclination angle of 45°. The cladding direction is dragging. The cladding is carried out two-layered with Stellite 21 with a laser output power of $P = 700$ W, a feed rate of 20 mm/s and a powder-feed rate of 6.2 g/min. By these parameters it is possible to generate a crack-free cladding with a thickness of 1.2 mm.

Three-Dimensional Applications

M. Litmeyer

In most cases cladding contours are not flat or symmetric; they are mostly free-formed surfaces. To handle these cases an articulated robot system with integrated beam guiding system for fiber-coupled diode lasers (cf. "Integration of a High-Power Diode Laser into a Robot") can be used in combination with a three-stream powder-nozzle, providing fully three-dimensional operation. In Figs. 7.267–7.269 some three-dimensional samples are displayed.

In Fig. 7.267 the cladding process and the repaired workpiece of a deep drawing tool for an engine mount are shown. A Fe-based alloy is used as layer material. At a process speed of $v_S = 0.3$ m/min and a laser power of $P_L = 2{,}000$ W at the workpiece a layer height of $t_{\text{layer}} = 1.0$ mm can be reached.

Figure 7.268 shows the cladding process and the coated sample of a perpendicular cladding. Cross sections across the perpendicular sections, across the radius and the top sections show no porosity and a low melt-deep. With a process speed

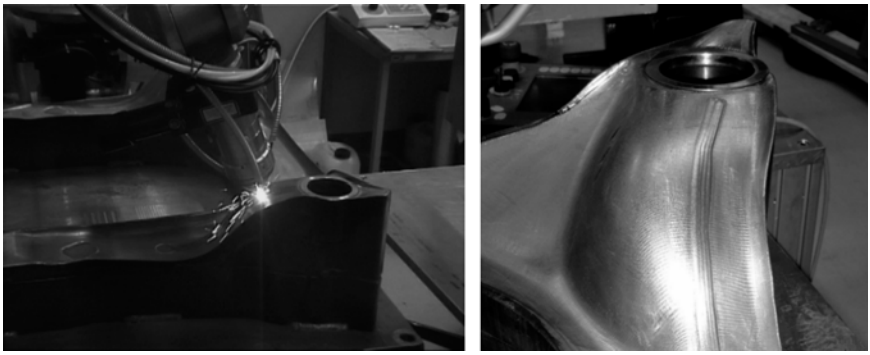

FIGURE 7.267. Repairing of a deep drawing tool for an engine mount

FIGURE 7.268. Cladding of a 180° sample

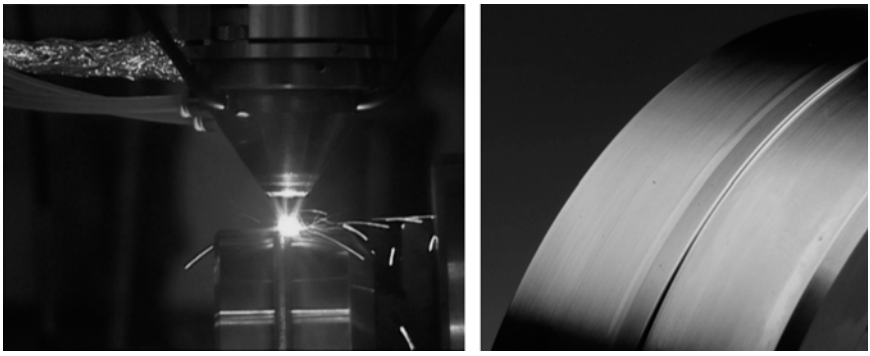

FIGURE 7.269. Regeneration of the profile on a pressing roll

of $v_S = 0.5$ m/min and laser power at the workpiece of $P_L = 2{,}000$ W a layer height of $t_{layer} = 1.0$ mm can be reached.

Another sample is shown in Fig. 7.269, where a regeneration process of the profile on a pressing roll is displayed.

Comparison between Atmospheric Plasma Spraying and Laser-Assisted Atmospheric Plasma Spraying

R. Zieris, St. Nowotny

Some of the material groups listed in Table 7.19 are more suitable[24] for the LAAPS process, as for instance the metals, metal alloys, light metals and light metal alloys. In contrast, the carbides and ceramic coatings have problems with regard to the process, or the coating properties do not have the required performance.

The coating structure has a very high porosity and the carbon rates are very low. This cannot be eliminated by a variation of the parameters. The ceramic materials can be deposited on the substrate without bondcoats. The coating structure is dense, but there are some vertical cracks. The coatings can be tested by the sliding wear test, the adhesive strength test for thermal spray coatings [7.88] and additionally by a thermal alternate strength test, because the ceramic is often used for thermal barrier coatings. At room temperature, the mechanical test results are as good as APS-sprayed coatings. The adhesive strength for the hybrid sprayed coatings (32 MPa) is less than for APS-sprayed coatings with bondcoats (43 MPa) [7.89]. After a few cycles of the thermal alternate strength test, the hybrid deposited ceramic coatings break down. The APS sprayed coatings with bondcoats are not destroyed after 30 test cycles. The ceramic coatings can be deposited by the LAAPS process without bondcoats, but they are not suitable for thermal strain.

[24] The adhesive strength, generally measured by the tensile bond strength test using a resin [7.86], is significantly higher for LAAPS coatings than for thermally sprayed coatings. For this reason, a test originally developed for weld overlays and widely applied for coatings obtained by laser cladding [7.87] is more suitable.

Comparison of Laser Cladding with Wire and with Metal Powder

M. Litmeyer

Besides the typical laser cladding with metal powder coatings can be applied by laser cladding with wire. Figure 7.270 shows a setup for laser beam cladding with wire. For wire feeding, a two-roll drive with a programmable control unit is used. To prevent movement of the wire at the workpiece a special adjustment line is installed. The wire and the shielding gas supply are mounted in dragging position. The laser beam is working in stinging position to prevent reflection of scattered laser light into the focusing optic. To minimize the soiling of the focusing optics a protection glass and an "Air-Knife" cross-jet are used.

Laser cladding with wire shows similar dependencies of laser-power on layer height, melt depth, and hardness depth as powder cladding (see Fig. 7.271). Higher laser power causes an increase in melt depth and hardness depth. But in contrast to cladding with metal powder, the layer height decreases a little as laser power rises. This depends on an increasing transversal flow of the molten wire, so that an increase of the layer width results.

With a laser power ranging from $P_L = 1{,}300$ W to $P_L = 1{,}500$ W, a layer of the hard material Stellite 6 with a thickness of $t_{layer} = 0.6$ mm can be produced on the typical tool steel 1.2738 (see Fig. 7.272).

Laser cladding with powder and laser cladding with wire are showing assets and drawbacks on either side (see Table 7.20). Main advantages of cladding with wire are a material efficiency of nearly 100% and a low health risk. The main advantages of powder cladding are good 3D applicability, good process stability and wide range of available materials.

Coating Strategy Based on a CAX Data Chain

M. Brandner

The goal of the strategy developed for coating tools is fast and cost-effective creation of defined coatings on 3D contours that are complex in some cases. In addition to a suitable system design (see chapter "Robot with External Axis"), an important component is a continuous CAX data chain, which allows a short cycle

Table 7.19. Applicability of coating materials on various substrate materials, classified in material groups

Substrate material	Coating material	Applicability
Metal, metal alloys	NiCrBSi	Applicable
Light metal, light metal alloys	AlSi30, AlSi45, AlSi60	Applicable
Metal, metal alloys, Light metal, light metal alloys	Al_2O_3, Al_2O_3 $3TiO_2$, ZrO_2 $3Y_2O_3$	Conditionally applicable
Metal, metal alloys	Inconel 625, Molybdenum	Conditionally applicable
Metal, metal alloys	Carbides	Not applicable

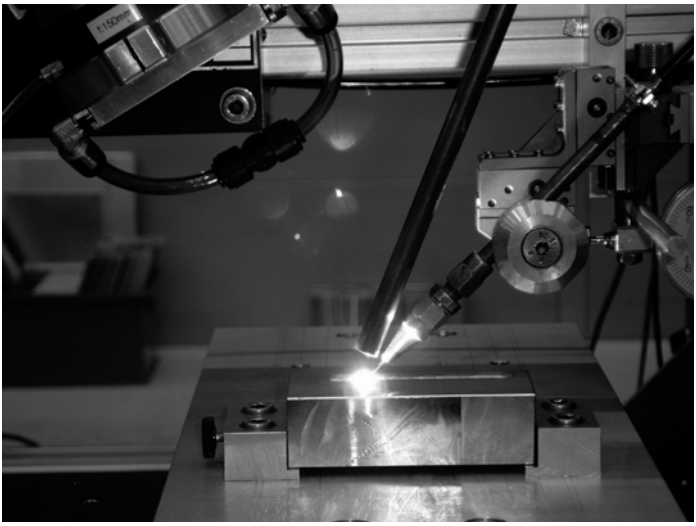

FIGURE 7.270. Laser cladding with wire

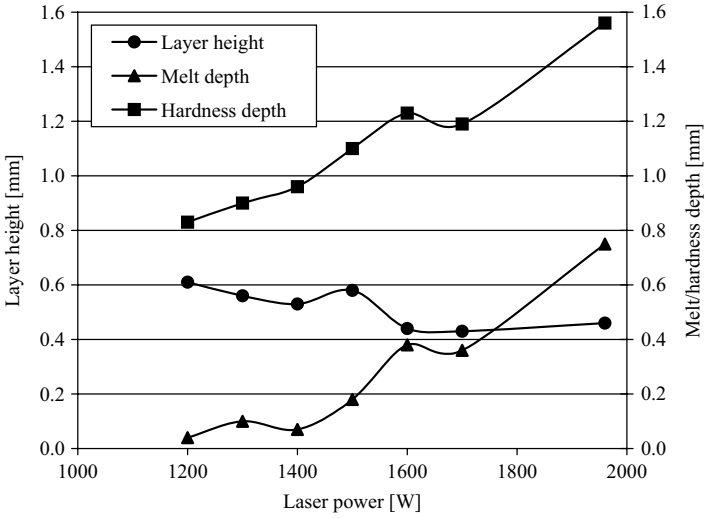

FIGURE 7.271. Laser-power versus layer height, melt depth and hardness depth at laser cladding with wire

time with 3D contours. The basic requirement for successful implementation is the availability of CAD data for the component. Figure 7.273 shows the coating strategy on the basis of the CAX chain, using a tool segment as an example. The central point of the strategy being pursued is the use of an offline programming

Table 7.20. Comparison of powder cladding and wire cladding

	Powder cladding	Wire cladding
Alloying rate of cladding material and base material	Low	Middle
Material efficiency	60%–80%	100%
Material range	High	Limited
Health risk	High	Low
3D applicability	Good	Limited
Process stability	High	Low
Surface roughness	Low	Higher than powder clad

system.[25] This offline programming system allows path planning on the CAD model, simulation of the robot kinematics, including a collision check between component and moving system components (robot + cladding head) and the output of the robot program using a post-processor adapted to the system. Parameters like path speed, laser power, or powder-mass flow rates are included in the robot program directly using software macros. The advantage of offline programming lies in the clear reduction in programming effort in comparison to the previous teach-in method, especially with complex geometries. In addition, the system is not blocked during programming.

Strategy for the Prevention of Cracks

M. Brandner

During coating of tool steels, increased crack formation in the substrate occurs, in addition to transverse cracks in the coating. Cracks in the coating are attributed to the high carbon content contained in the coating and the high percentage of carbide formers; they mainly occur in multi-layer coatings. High carbon content in the tool steels and the carbides they contain should be considered as the cause of the cracks

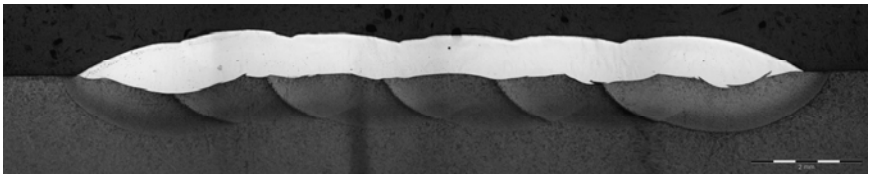

Figure 7.272. Cross section of 1.2738 coated with Stellite 6

[25] For example, TopLas3D®, ERLAS Erlanger Lasertechnik GmbH.

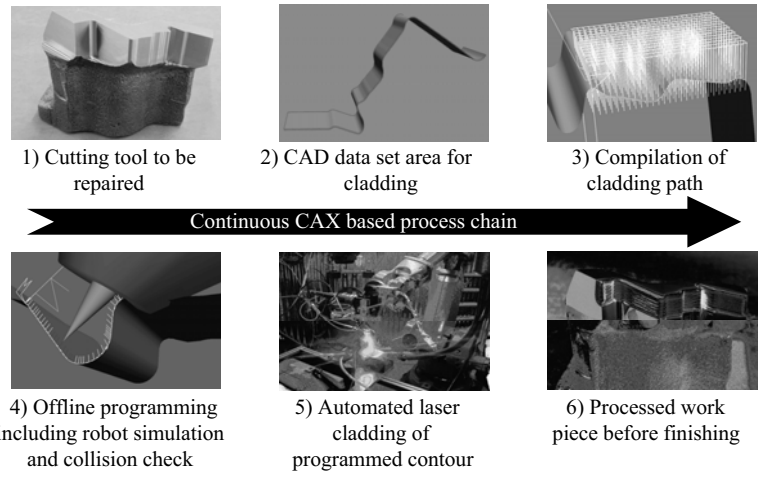

FIGURE 7.273. Layer deposition for repair of tools-process strategy and CAX process chain

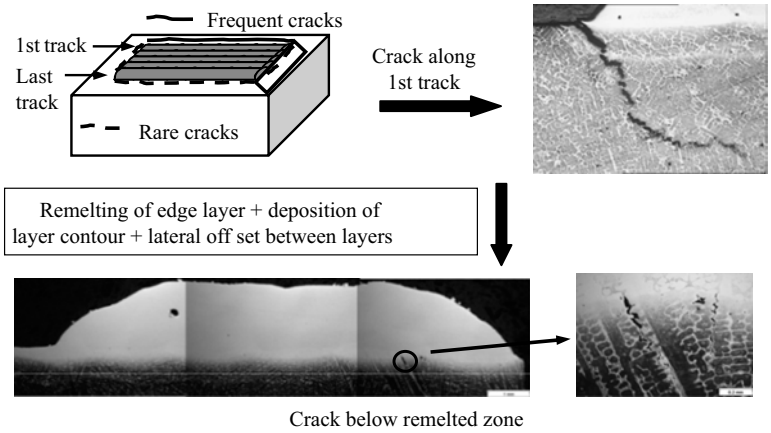

FIGURE 7.274. Prevention of cracks by adapted process management

that are initiated in the substrate itself. Due to differences in the microstructure various forms of cracks emerge. On two-dimensional coatings, these cracks run parallel to the edges of the coating. Cracks develop most frequently along the first track. With materials 1.2379 and 1.2382, individual cracks parallel to the face surface and along the last track also occur (see Fig. 7.274).

If the traverse speed is limited to 0.3 m/min, a reduction in crack formation can be achieved, especially transverse cracks in the coating. Suppression of cracks in the base material requires further adaptation of the process management. In the first step, the edge layer is melted in the area of the surface to be coated. Refinement of the microstructure and reduction in the hardness will counteract crack formation.

In this way, mainly cracks that develop below the coating in the substrate can be stopped in the melting zone. In the second step, the surface to be coated is surrounded using a track with low height and then filled. Because of this, the edge angle of the coating is reduced, and thus the notch effect is as well. The application of additional layers is carried out according to the same scheme with additional offset toward the inside. This results in a more flat edge and lower porosity in the overlap area. The interaction of the measures explained above leads to a clear reduction in crack formation along the side edges. Starting with an illustration of the cracking problems, Figure 7.274 shows results of a coating created with the adapted strategy. The cross section shows an example of a crack in the base material that ends in the melt zone.

Economic Considerations

A. Weisheit

For many applications laser cladding has to compete with conventional cladding technologies. Table 7.21 lists various cladding techniques regarding investment costs, cladding rate and dilution. A main feature of laser cladding is the low dilution due to the fact that the laser beam can be focused very well. Only flame spray welding leads to a lower dilution, but this is a two-step process where first the coating is sprayed on the substrate and than fused. Compared to the other techniques the cladding rate is low which means that laser cladding is most competitive when small areas and thin layers (<2 mm) have to be cladded. The investment costs are highest for laser technology. However, an economical evaluation has to consider the whole process chain which includes pre-treatment and post-treatment of the part. The amount for post-treatment especially can be reduced significantly when using laser cladding due to high precision coatings and minimum distortion (low heat input). Furthermore the microstructure of laser cladded layers is finer than that of those produced by other technologies (due to higher cooling rate) which leads to an increase in hardness and ductility. A finer structure improves corrosion and wear properties.

Table 7.21. Comparison of various cladding techniques regarding cladding rate, dilution and investment [7.93]

Technique	Cladding rate (kg/h)	Dilution (%)	Costs
Laser cladding	0.1–2.5	<5	Highest
Plasma powder welding	2.5–6.5	5–10	
Submerged arc welding	5–28	8–20	
Tungsten inert gas welding	0.5–3.5	10	
Metal inert gas welding	2.3–11	15	
Flame spray welding	0.2 2–5	1	Lowest

Comparing high-power diode lasers with CO_2 and Nd:YAG lasers, also suitable for cladding, the diode lasers exhibit significant advantages regarding the running costs. This is mainly due to their high efficiency (∼40% and ∼25% with fiber coupling, Nd:YAG, ∼3%; CO_2, ∼12%) which reduces the electric power consumption and the cooling capacity necessary to remove the lost heat. Furthermore diode lasers need only a little maintenance. Considering the overall low operating costs, the use of a diode laser can be a significant cost-saving factor compared to other lasers.

References

[7.1] Petring D, Benter C, Poprawe R (October 2001) Fundamentals and Applications of Diode Laser Welding. ICALEO 2001, Jacksonville, FL, USA.
[7.2] Gillner A, Loosen P, Petring D, Wissenbach K, Poprawe R (November 1999) Industrial Applications of High Power Diode Lasers. ICALEO 1999, San Diego, CA, USA, LIA, 87, A12–A22.
[7.3] Petring D (September 1999) Tiefschweissen mit Hochleistungs-Diodenlasern. Laser Magazin, S. 3.
[7.4] Petring D (December 1999) Deep-penetration welding with diode lasers. Industrial Laser Solutions, p. 3.
[7.5] Michel J, Niessen M, Kostrykin V, Schulz W, Zimmermann C, Petring D (1999) LaserWeld 3D, Software package, Fraunhofer-Institute for Laser Technology, Aachen, Germany.
[7.6] Modulare Diodenlaser Strahlwerkzeuge (MDS), funded by the Federal Ministry of Education and Research, Germany.
[7.7] DaimlerChrysler AG (2003), Sindelfingen, Germany.
[7.8] Developed at DaimlerChrysler AG, Sindelfingen, Germany.
[7.9] Brandner M, Seibold G, Chang C, Dausinger F, Hügel H (2000) Soldering with solid state and diode lasers: Energy coupling, temperature rise, process window. Journal of Laser Applications 12, 194–199.
[7.10] Bohmann CF (1974) The Laser and Microsoldering. SME: Technical Paper, No. AD74-810, pp. 1–19.
[7.11] Haag M (1997) Assessment of different high power diode lasers for material processing, Lasers in Material Processing. Proceedings of the SPIE 3097, 583–591.
[7.12] Ringle H, Vayhinger HU, Laser lötet räumliche Lötstellen. Feinwerktechnik & Messtechnik, Carl Hanser Verlag, Ausgabe 11.
[7.13] van Veen NJA, Laser Löttechnologie. VDI Berichte Band 966, 39–52.
[7.14] Horneff P, Treusch HG, Beyer E, Herziger G, Knödler D, Möller W (1990) Temperaturgeregeltes Lasermikrolöten. DVS-Berichte Band 129, 62–65.
[7.15] Nakahara S, Kamata T, Yoneda N, Hisada S, Fujita T (2000) Micro soldering using a YAG laser – on lead-free solder: First International Symposium on Laser Precision Microfabrication. Proceedings of the SPIE, 4088, 276–279.
[7.16] Kerbow G (2001) High-temperature environments create new SMT challenges. Surface Mounted Technology September, 66–71.
[7.17] Liedke V (2001) Lasersysteme für selektives Löten. Messeinformation der SEHO Seitz & Hohnerlein GmbH, Kreuzwertheim. LASER'01, München.
[7.18] Hierl S, Geiger M (1999) Simultaneous laser soldering for SMDS on 3D-MIDS. Proceedings of Surface Mount Technology 440–445.

[7.19] Bosse L, Schildecker A, Gillner A, Poprawe R (2002) High quality laser beam soldering. Microsystem Technologies 7, 215–219.
[7.20] Bosse L, Gillner A, Poprawe R (2001) Adapted time-power profile for laser beam soldering with solder paste. Proceedings of the SPIE 4406, 76–81.
[7.21] Herrmann G, Egerer KA (1991) Handbuch der Leiterplattentechnik, Band. 2 Neue Verfahren neue Technologien. Leuze Verlag.
[7.22] Hacke HJ (1987) Montage Integierter Schaltungen. Springer Verlag, Berlin.
[7.23] Hanreich G, Wolter KJ, Nicolics J (2001) Rework of Flip-Chip populated PCBs by laser desoldering. Proceedings of the 24th International Spring Seminar on Electronics Technology, May 5–9, 63–67.
[7.24] Sommerfeld P, Jendritza D, Hell S (1999) Advanced packaging and interconnection technologies for automotive microelectronic modules. Advanced Microsystems for Automotive Applications 99, 111–119.
[7.25] Engbring J, Jendritza D (1998) Gehäusemontage von Keramikhybriden mit Hilfe eines Flammlötprozesses, VTE 3, 130–135.
[7.26] Chang DU (1986) Experimental investigation of laser beam soldering. Welding Journal October, 33–41.
[7.27] Klein RM (1990) Bearbeitung von Polymerwerkstoffen mit infraroter Laserstrahlung. PhD Thesis RWTH Aachen, Fraunhofer-Institut für Lasertechnik ILT, Germany.
[7.28] Duley WW, Mueller RE (1992) CO_2 laser welding of polymers. Polymer Engineering and Science, Mid-May 1992, 32(9), 582–585.
[7.29] Atanasov PA (1995) Laser welding of plastics – theory and experiment. Optical Engineering 34/10, pp. 2976–2980.
[7.30] Nonhof CJ (1994) Laser welding of polymers, Optical Engineering SCI 34/20, pp. 1547–1549.
[7.31] Hänsch D (2001) Die optischen Eigenschaften von Polymeren und ihre Bedeutung für das Durchstrahlschweißen mit Diodenlaser. PhD Thesis RWTH Aachen. Fraunhofer-Institut für Lasertechnik ILT, Germany.
[7.32] Bachmann FG, Russek UA (2002) Laser welding of polymers using high power diode lasers. Proceedings Photonics West.
[7.33] Russek UA et al., (2003) Laser beam welding of thermoplastics, Proceedings of the LASE 2003, San Jose, CA, USA. Conference 4977 B, Laser-Based Packaging in Microelectronics and Photonics, San Jose, CA, USA, pp. 458–472.
[7.34] Brune J (2000) Thermoplastische Kunststoffe schweissen. Laser Praxis 51, Juni.
[7.35] Russek UA, Otto G, Poggel M (2001) Verbindliche Nähte – Automatisiertes Fügen von Kunststoffen mit Hochleistungs-Diodenlasern. Laser Praxis 1/2001, 14–16.
[7.36] Haferkamp H, von Busse A, Hudstedt M, Haberstroh E, Lützeler R (2002) Bestimmung der Laserschweißeignung von Kunststoffen mit einem thermographischen Verfahren. Der Praktiker, 10.
[7.37] Menges G, Haberstroh E, Michaeli W, Schmachtenberg E, Werkstoffkunde Kunststoffe, 5. Auflage. Chapter 12. Carl Hanser Verlag, München Wien.
[7.38] Saechtling H, Kunststoff Taschenbuch, 27. Ausgabe, Tab. 5.6. Carl Hanser Verlag, München Wien.
[7.39] Kaplan AFH (2002) Theoretical Analysis of Laser Beam Cutting. Berichte aus der Fertigungstechnik. Shaker Verlag, Aachen.

[7.40] Petring D (2001) Basic description of laser cutting. In JF Ready and DF Farson (eds.): LIA Handbook of Laser Materials Processing. Laser Institute of America and Magnolia Publishing, Orlando.
[7.41] Petring D (1995) Anwendungsorientierte Modellierung des Laserstrahlschneidens zur rechnergestützten Prozessoptimierung. Doctor Thesis. RWTH Aachen 1994. Shaker Verlag, Aachen.
[7.42] Knitsch A, Seme B, Hoffmann D, Petring D, Loosen P, Iffländer R, Poprawe R (2003) Diode Laser Systems for Cutting Applications of Thin Materials. ICALEO 2003. Jacksonville, FL, USA.
[7.43] Petring D (2005) Computer simulation of laser cutting for the limiting-value-oriented development of robust processes. Welding and Cutting 4(1), 37–42.
[7.44] Michel J, Niessen M, Kostrykin V, Schulz W, Zimmermann C, Petring D (1999) LaserWeld3D. ILT Software-Paket.
[7.45] Franke JW (1994) Modellierung und Optimierung des Laserstrahlbrennschneidens niedriglegierter Stähle. Dissertation RWTH Aachen, DVS-Berichte, Band 161.
[7.46] Franke J, Schulz W, Herziger G (1993) Abbrandstabilisiertes Laserstrahlbrennschneiden – ein neues Verfahren. Schweißen und Schneiden 45, Heft 9, S, 490–493.
[7.47] Arata Y et al. (1979) Dynamic behavior in laser gas cutting of mild steel. Transaction of JWRI, 8 S, 15–25.
[7.48] Bausch S, Groll K (2003) Perspektiven für die laserunterstützte Zerspanung – Wirtschaftliche Bearbeitung schwerzerspanbarer Werkstoffe. WT Werkstattstechnik Online 06/2003.
[7.49] Klocke F, Bausch S (2001) Integration of high power diode laser in machine tools. Proceedings of 1st International WLT-Conference on Lasers in Manufacturing. Munich, Germany, June 2001, 8–21.
[7.50] Nagel J (2004) Laserhärten und Laser-Pulver-Auftragschweißen von Umformwerkzeugen. Aachener Kolloquium für Lasertechnik AKL'04, 28.–30.04.2004, Tagungsband, pp. 295–305.
[7.51] Bergmann L, Schäfer C (1987) Lehrbuch der Experimentalphysik. Volume III Optik. Walter de Gryter, Berlin, New York.
[7.52] Gasser A, Kreutz EW, Wissenbach K (1988) Physical aspects of surface processing with laser radiation. SPIE Proceedings Series 1020.
[7.53] Dausinger F (1990) Laser with different wavelength – implications for various applications. Proceeding of the ECLAT'90, 1.
[7.54] Brandner M, Seibold G, Haag M, Dausinger F, Hügel H (1999) Effektive Umsetzung der spezifischen Strahleigenschaften von HLDL zur Materialbearbeitung. LaserOpto 31, 1/1999.
[7.55] Beyer E, Wissenbach K (1998) Oberflächenbehandlung mit Laserstrahlung. Springer Verlag, Berlin, Heidelberg, New York, Barcelona, Budapest, Hong Kong, London, Mailand, Paris, Santa Clara, Singapur, Tokyo, p. 50.
[7.56] Stern G (1990) Absorptivity of cw CO_2, CO and YAG laser beams by different metallic alloys. Proceeding EKLAT'90 1, 25.
[7.57] Wissenbach K (1985) Umwandlungshärten mit CO_2-Laserstrahlung. Ph.D. Thesis. Darmstadt.
[7.58] Koistinen DP, Marburger RE (1959) A general equation prescribing the extent of the austenite–martensite transformation in pure iron–carbon alloy and plaine carbon steels. Acta Metal 7, 59–60.

[7.59] Hougardy HP (1984) Darstellung der Umwandlungen für Technische Anwendungen und Möglichkeiten ihrer Beeinflussung. Werkstoffkunde Stahl, volume 1. Grundlagen. Springer Verlag, Berlin, Heidelberg, New York, Tokyo, Verl. Stahleisen Düsseldorf, pp. 198–231.
[7.60] Sluzalec A (1992) Introduction to Nonlinear Thermomechanics. Springer Verlag, Berlin, Heidelberg, New York, Tokyo, Hong Kong, Barcelona, Budapest, pp. 73–78.
[7.61] Eckstein HJ (1969) Wärmebehandlung von Stahl. Metallkundliche Grundlagen. VEB Deutscher Verlag für Grundstoffindustrie, Leipzig.
[7.62] Grimsehl (1985) Lehrbuch der Physik, volume 3. Optik. BSB B.G. Teubner Verlagsgesellschaft, Leipzig, p. 225.
[7.63] Bonss S, Goebel G, Seifert M, Brenner B, Beyer E (2003) Fast and Innovative Determination of Parameters for Steel Hardening with High Power Diode Lasers. 1st International Symposium on High-Power Laser Macroprocessing. Proceedings of the SPIE 4831, 53–58.
[7.64] Schwarz T, Morgenthal L, Pollak D, Quitzow A (1998) Verfahren zur lokal gezielten Wärmebehandlung von Werkstückoberflächen. Patent DE 198 53 733 C1.
[7.65] Lepski D, Reitzenstein W (1991) Computergestützte Prozessoptimierung bei der Laser-Umwandlungshärtung von Eisenwerkstoffen. Härterei-Technische Mitteilungen, volume 46, issue 3. Carl Hanser Verlag, München Wien, pp. 178–183.
[7.66] Drenker A, Baumann M, Pirch N, Plum H-D, Sommer J, Vitr G, Kaierle S, Wissenbach K, Poprawe R (2003) An example for modular diode laser systems: Minimizing warpage during transformation hardening of linear guiding rails. Proceedings of the Second International WLT-Conference on Laser in Manufacturing, June 2003, Munich, Germany, p. 33.
[7.67] Traub M, Plum H-D, Hoffmann H-D, Loosen P, Poprawe R (2003) Homogenised high power diode laser systems for material processing and illumination. Proceedings of the Second International WLT-Conference on Laser in Manufacturing, June 2003, Munich, Germany, p. 29.
[7.68] Bonss S, Seifert M, Brenner B, Beyer E (2000) Innovations in heat treatment with high power diode lasers. 19th Congress on Applications of Lasers and Electro-Optics, ICALEO 2000. Proceedings of the LIA 91, D19–D27.
[7.69] Brown GH, Hoyler CN, Bierwith RA (1948) Theory and Application of Radio-Frequency Heating. D. Van Nostrand Co., Toronto, New York, London.
[7.70] Benkowsky G (1990) Induktionserwärmung: Härten, Glühen, Schmelzen, Löten, Schweißen. Verlag Technik GmbH, Berlin.
[7.71] Schubert E, Seefeld T, Zerner I, Grupp M, Sepold G (1999) Hochleistungsdiodenlaser in der Oberflächen- und Fügetechnik. In Laser Opto 31, Heft 1, pp. 75–77.
[7.72] de Deus AM, Mazumder J (1996) Two-dimensional thermo-mechanical finite element model for laser cladding. Proceedings of the ICALEO, LIA volume 81, LIA, Orlando, USA, pp. 174–183.
[7.73] Pirch N, Kreutz EW (1998) 3D modelling of heat, momentum and solute transport in laser surface alloying. Conference Modelling of Casting, Welding and Advanced Solidification Processes VIII, 8.–12.06.1998. San Diego, CA.
[7.74] Kurz W, Fisher DJ (1989) Fundamentals of Solidification. Trans Tech Pub, Switzerland.
[7.75] Weisheit A, Backes G, Stromeyer R, Gasser A, Wissenbach K, Poprawe R (2001) Powder injection: The key to reconditioning and generating of components using laser cladding. Proceedings of the Materials Week 2001, 1.–4.10.2001, Munich.

[7.76] Hiraga H, Inoue T, Shimura H, Matsunawa A (1998) Cavitation Erosion Resistant Coating of NiTi Made by Laser Plasma Hybrid Spraying. Proceedings of the ICALEO 1998, Laser Material Processing, volume 85, part 2. Laser Institute of America, Orlando, FL, Section D, pp. 113–120.
[7.77] Sasaki S (1997) Tribological properties of coating films synthesised by laser assisted plasma spraying. Surface Engineering 13(3), 238–242.
[7.78] Ohmori, Zhou Z, Eguchi N (1997) Hybrid spraying of zirconia thermal barrier coating with YAG laser combined plasma beam. Transactions of the JWRI 26(1), 99–107.
[7.79] Coddet C, Marchione T (1993) Process for the Preparation and Coating of a Surface. EP 580534, B1, filed: 21.07.1993, published: 23.04.1997; US 5688564, published: 18.11.1997.
[7.80] Beyer E, Nowotny S (1998) Method for Applying a Coating by Means of Plasma Spraying While Simultaneously Applying a Continuous Laser Beam. EP 903423, A2, A3, filed: 10.09.1998, published: A2 24.03.1999, A3 09.05.2001; US 6,197,386, B1, published: 06.03.2001.
[7.81] Beyer E, Nowotny St, Bonß St, Zieris R (2001) 3. Zwischenbericht zum FuE-Vorhaben 13N7357/6, Modulare Diodenlaser-Strahlwerkzeuge, Teilvorhaben:Hybridtechniken zum Beschichten und Härten. Fraunhofer IWS (Fraunhofer Institute for Material and Beam Technology), Dresden.
[7.82] Shen J (1994) Optimierung von verfahren der laseroberflächenbehandlung bei gleichzeitiger pulverzufuhr. Forschungsberichte IFSW. B.G.Teubner Stuttgart, ISBN 3-519-06214-3.
[7.83] Gasser A (1993) Oberflächenbehandlung metallischer Werkstoffe mit CO_2 Laserstrahlung in flüssiger Phase. Wissenschaftsverlag Mainz, ISBN 3-930085-11-9.
[7.84] Habedank G, Theiler C, Grupp M, Kohn H, Sepold G, Vollertsen F (2003) Laser beam cladding of steel with High Power Diode Lasers. Proceedings of the 2nd International WLT-Conference on Lasers in Manufacturing June 2003, Munich, pp. 45–49.
[7.85] Habedank G, Theiler C, Seefeld T, Vollertsen F (2003) Beschichten mit Hochleistungslasern. Tagungsband zur 5. Industriefachtagung "Oberflächen- und Wärmebehandlungstechnik" und zum 6. Werkstofftechnischen Kolloquium, Sept. 2003. Eigen verlag, TU Chemnitz, pp. 160–165.
[7.86] Pawlowski L (1995) The Science and Engineering of thermal spray coatings. John Wiley & Sons, Chichester, etc., pp. 183–185.
[7.87] Nowotny S, Richter A, Tangermann K, (1999) Surface protection of light metals by one-step laser cladding with oxide ceramics. Journal of Thermal Spray Technology 8(2), 258–262.
[7.88] DIN EN 582, 10.1993.
[7.89] Beyer E, Nowotny St, Bonß St, Zieris R (2001) 4. Zwischenbericht zum FuE-Vorhaben 13N7357/6, Modulare Diodenlaser-Strahlwerkzeuge, Teilvorhaben: Hybridtechniken zum Beschichten und Härten. Fraunhofer IWS (Fraunhofer Institute for Material and Beam Technology), Dresden.
[7.90] Zieris R, Naumann T, Nowotny St, Eckart G, Füssel U, Beyer E (2000) Neuheiten beim laser-plasma-hybridspritzen. Tagungsband VIII, Workshop Plasmatechnik, Ilmenau 2000. IISLE-Verlag, pp. 50–56.
[7.91] Zieris R (2003) Neues aus der Forschung, Laserunterstütztes Plasmaspritzen. Galvanotechnik Heft 4 2003, Jahrgang 94. Eugen G. Leunze Verlag, ISSN 0016-4232, pp. 937–938.

[7.92] Zieris R, Langner G, Berger L-M, Nowotny St (2004) Investigation of AlSi coatings prepared by laser-assisted atmospheric plasma spray on internal diameters of tubes. ITSC 2004, 10.–12.05.2004, Osaka.

[7.93] Bieler H-W (1995) Oberflächenbehandlung mit CO_2-Hochleistungslasern, Angewandte Lasertechnik – Systeme, Werkstoffe, Verfahren. Sonderheft Techn. Rundschau.

8
Summary and Outlook

Reinhart Poprawe

Wilhelm von Humboldt (1767–1835) recognized the necessity of the coherence of research and education about 200 years ago. Today we see a third component coming in simultaneously: *innovation*. Not that this third aspect gained key importance only recently, but the demands for handling the increasing complexity of innovation have grown dramatically. Innovations need vertically structured processes, i.e., from simultaneous consideration of the product definition, the market, and recognition of relevant technologies all the way to the related fundamental research. The deeper the consideration, the greater the sustainability of the innovation. By definition, an innovation is first of all something new. There is still no scale to measure innovation, but it seems reasonable to define an innovation as any new process, technology, or product that leads to a quantitative economical benefit.

The project described in this book[1] is a unique example in this sense. The value of its results has been recognized and confirmed by all partners, including the funding and administrating authorities. The results are extremely interdependent and interdisciplinary. Thus, they only could be achieved in a well-structured and continuously coordinated process. The study was a challenge, at times a tremendously difficult and complex one. The interests of at least three levels of society had to be balanced: the individual, the organization, and the national. Every single individual participating had to recognize and accept this three-level thinking. The nature of the process had to be accepted as well as the opportunity to differentiate skills, potential, and effectiveness of the competing groups in the participating R& D network.

As a result of the project, a number of industrial applications – e.g., hardening, laser generating, heat conduction metal welding, polymer welding and annealing – have already benefitted because demands on beam quality are reduced. However, in the big markets the demand for high power and higher beam quality still requires diode-pumped solid state lasers (DPSSLs). The entropy-converting active

[1] The official name of the project is Modular Diode Laser Systems (MDS), and it was run under the funding of the German Ministry of Education and Research (BMBF) from 1998 to 2003.

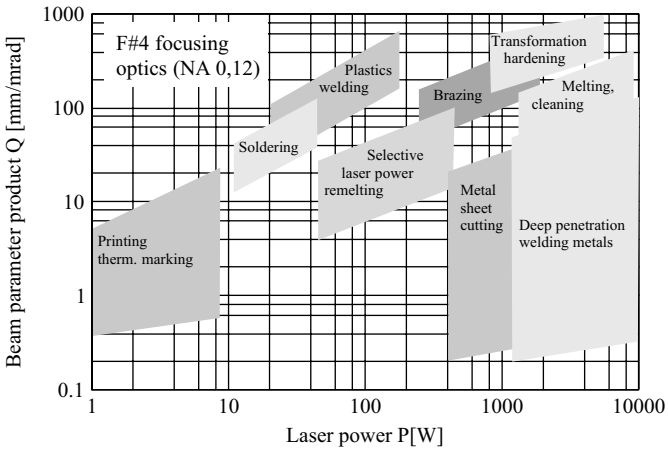

FIGURE 8.1. In this diagram, industrial laser applications are classified according to the typically required laser power and beam parameter product. The power density on the workpiece increases from the top left to the bottom right corner

medium is absolutely necessary, because the present beam quality of industrial high power diode lasers (HPDL) is not sufficient for the traditional laser applications like cutting and deep-penetration welding (Fig. 8.1), which make up the lion's share of today's laser market in the industrial materials processing area.

The question for the future is: Will there be ways to build high-power diode lasers for direct application in these yet unreachable markets? Three factors have to be considered and improved simultaneously for that goal to be achieved:

1. Power
   Scaling of the power can be achieved, on the one hand, by increasing the power of the single bar. Today powers of more than 500 W have been achieved for short times, demonstrating the potential of laser medium itself [8.1]. Higher power level for the single bar will reduce the number of bars required in stacked kW systems and also increase the quality.
2. Lifetime
   The lifetime of the laser diodes depends mainly on the power level of operation. With the use of laser diodes as pump sources for DPSSLs as well as for direct application in HPDLs, the influence of the mode of operation became obvious. At high modulation rates above 100 Hz, the performance is similar to continuous operation, because the time constant is too small for the system to react thermally. However, in the range around 1 Hz the thermo-mechanical load is about maximum and life is reduced significantly. As a consequence, the diodes can be operated only upto power levels of about 50 W in this mode with lifetimes up to 10,000 h.

3. Beam Quality
   Here is the most challenging factor from the systems point of view. Several concepts are being investigated presently to couple diode emitters coherently in one bar: direct injection [8.2], diffraction, or reflection structures inside the chip itself like distributed feedback or total reflection ("Z-laser" [8.3]) or external resonators [8.4, 8.5]. The goal is to reduce the beam parameter product of a 100-W bar from today 10 mm * mrad ($M^2 = 30$) to less than 0.5 mm * mrad corresponding to $M^2 < 2$. Integrated MOPA-designs like the "tapered laser" [8.6] do work nicely, however, for the time being they seem to lack scalability to the necessary power densities.

   Besides the coherent coupling strategies mentioned above, incoherent, i.e., polarization and especially wavelength coupling, which are described in the book in detail, are the most promising avenues for increasing the brightness. With the advent of volume reflectors (holographic or Bragg), the line width of a bar can be reduced to less than 0.3 nm. Consequently about 50–100 bars could be superimposed by wavelength multiplexing to give a theoretical output power of 5 kW at a beam parameter product less than 10 mm * mrad – a fascinating scenario.

The potential exists for high-power diode lasers with characteristics fulfilling the demands of high-power laser application in terms of spatial and modulation quality. Whether the scientific and technical challenges can be solved is an open question. Whether the concepts will be realized economically enough to be practicable remains to be seen. Exactly when these developments will lead to mature products that compare favorably with the alternative lasers serving the markets today, especially the existing diode-pumped solid state lasers, is not known. However, one thing is for sure: There is a chance for a positive answer to all the foregoing questions, and that is why the future of high power diode lasers has just begun.

References

[8.1] Lichtenstein N (2005) 325 W from 1-cm wide 9xx laser bars for DPSSL- and FL-applications. Proceeding of SPIE 5711, 1–11.
[8.2] Lücke B, Hergenhang G, Brauch U, Giesen A (2001) Phase tuning of injection-locked VCSELs http://www.dlr.de/lido/EN-TP/2001/1827412001.html. Photonics Technology Letters, 13(2), 100–102,
[8.3] Boucke K, Rogg J, Poprawe R (2003) Development of high-brightness diode lasers, the Z-laser. Proceedings of SPIE 4831, 21–25.
[8.4] Xin G, Zheng V, et al. (2004) Effective suppression of beam divergence for a high power laser diode bar by an external cavity technique. Optics Letters, 29(4).
[8.5] Raab V, Menzel R (2002) External resonator design for high-power diodes that yields 400 mW of TEM_{00} power. Optics Letters, 27(3).
[8.6] Kelemen M, Weber J, Mikulla M, Weimann G (2005) High-power high-brightness tapered diode lasers and amplifiers. Proceedings of SPIE, 5723, 198–208.

Index

2D-light-section sensor, 299–301
3D-light-section sensor, 301–302
16MnCr5, 307, 308, 309
III/V compound semiconductors, 7

ABCD matrix, 186
Aberration, 194
Absorptance, 427
Absorption, 287, 338, 389, 391, 394, 427, 449, 469, 493
  of aluminum, 304
  of polymers, 363, 364, 370, 375, 376
  of steel, 303–304
Absorption coefficient, 378
Absorptivity, 390, 391, 403
Acceleration factor, 53
Accessibility, 330
Accuracy, 388
Activation energy, 86
Additives, 363, 375
Aeronautical applications, 333–334
Air knife, 291, 418
Alloying, 432, 456, 482, 483
  elements, 287
AlMg5, 397
Aluminum, 304, 305, 313, 322–323, 324, 339, 391, 397
  alloys, 321, 322
  fittings, 333
Aluminum oxide, 105
Amorphous thermoplastics, 376
Angle of incidence, 318, 319, 391, 428, 496, 517
Annealing, 426, 434, 459, 470, 481
Annular diode laser beam, 268–272, 314–315, 320, 388, 406, 407, 408, 409, 412
Anti-reflection coating, 61, 66
Aperture filling, 149
Argon, 310, 312, 453
Arrhenius relationship, 207
Aspect ratio, 288, 289, 306, 307, 308, 309, 312, 315
Assist gas jet, 389, 391, 393–394
Assist gas pressure, 393
Astigmatism, 58–59, 67–68, 190–195, 233
  measurement, 59, 233
Atmospheric plasma spraying (APS), 503, 522
AuSn, 80, 95
Austenite, 314
Autogenous cutting, 405, 406, 408, 409, 410, 411
  cutting speeds, 406
Automotive applications, 324–333
Axial annular welds, 321
Axle carrier, 330

Ball grid arrays. *See* BGA
Band gap, 5–10
Band material, 400
Band-pass filter, 146
Band-stop filter, 146
Band structure, 6, 7, 10, 43
Band tension, 401–405
Batch process, 79
Bead-on-plate welding, 303–306
Beam caustic, 200
Beam characteristics, 181
Beam-director, 168
Beam divergence angle, 37
Beam-guiding system, 399
Beam homogenization, 400
Beam intensity, 389, 416
Beam intensity distribution, 310
Beam parameter product (BPP), 121, 159, 166, 175, 181, 193, 389, 391, 393
Beam patterns, 405
Beam positional stability, 204–205
Beam propagation, 183–186, 379, 394
Beam propagation parameter (M^2), 56, 65, 66, 67
Beam propagation ratio (M^2), 182, 193, 196, 203–204
Beam properties, 394
Beam quality, 63–66, 121, 152–153, 388, 389, 391, 409, 416

Beam radius, 122
Beam shaping, 162, 386
Beam splitter, 145
Beam-splitter cubes, 142
Beam symmetrization, 162
Beam width, 182
Bearing cross section, 318
Bending radius, 418
Beryllia (BeO), 105, 357
BGAs (ball grid arrays), 355, 356
Biological contamination, 101
Birefringent crystals, 142
Boundary feeding rates (BFR), 304
Boundary layer, 406
Brazing, 285, 342, 343, 344, 345, 346, 347–349
  alloys, 346–347
  filler, 342, 343, 344, 348
  head, 345
  seam, 346–347
  system, 347
  velocity, 346
Bridged gap, 383
Bridge formation, 343
Brightness, 56, 63–66, 67, 122, 182
Broad area emitters and arrays, 47–55
Broad area lasers, 15
Bumps, 355, 356
Burning front, 406
Burning proportion, 406
Burnoff-stabilization, 412
Burnoff-stabilized cutting, 411
Burnoff-stabilized laser beam oxygen cutting, 405, 407, 409, 410
Burr, 398, 404
  formation, 393, 398
Burst pressure, 374, 383, 384, 385
Butt joint, 322, 323, 363, 364
“By-emitter” analysis, 41–45

Camera systems, 196–197
CAN-bus, 256, 276
Car body, 328
Carbon black concentration (cbc), 378, 383, 385
Catastrophic optical mirror damage (COMD), 48, 56, 206
Ceramics, 389, 413, 425
  materials, 425
Characteristic temperature, 19
Chip formation, 413, 419
Chip section, 421
Circular spot welds, 320
Cladding, 427, 482, 483
Cladding rate, 527
Cladding with wire, 488
Clamping, 345
  device, 363–364
  wheels, 294, 295
CO_2, 313
CO_2 laser, 326, 332, 370, 388, 399, 407, 409, 410, 411
Coating, 346–347, 482, 499, 508, 522
Coaxial shielding gas nozzle, 293, 294
Cobalt-based alloys, 413, 423, 425
Coefficient of thermal expansion (CTE), 104, 107
Coherence, 183, 194
Coherent coupling, 175–177
Coil material, 388
Cold forming tool steels, 419
Collimation lens, 130, 136
Collision, 330
Color additives, 376
Combustion, 406
Complex optical index, 57
Composites, 413
Compressively strained, 10, 11
Conduction band, 6
Conduction cooling, 87–92
Confinement factor, 13, 64
Conical nozzle, 407
Connection length, 318, 319, 346
Constructional laser-adapted design of joining partners, 374
Contact conditions, 415
Contact sensors, 297
Contour cuts, 396, 398, 399, 410, 411
Contour welding, 365–366, 371, 382–383, 385, 387
Convection-cooled heat sinks, 94, 95, 96
Conventional finishing, 423
Conventional machining, 412
Conventional milling, 423
Conversion efficiency, 18
Cooling fluid, 96
Copper, 337, 390
Corrected far-field, 58–59, 67–68
Corrosion, 98, 99
Costs, 336, 399, 400
Cotton fabric, 396, 397, 398
Crack, 471, 504, 520, 525
Cross member, 331
Cross section, 307, 308, 311, 312, 315, 316, 322, 323, 326, 339, 346–349, 404, 405

Cross-jet, 291, 292
  nozzle, 291, 292, 407
Cross-talk, 253
Crystalline growth, 26
Crystalline quality, 27
Crystalline thermoplastics, 376
Crystallinity, 375
CTE matching, 102
CTE measurement, 114
$CuAl_5Ni_2$, 346–347
$CuSi_3$, 346–347
Cut edge, 389, 398, 403, 404, 406, 410, 411, 412
  roughness, 407
Cut geometry, 388
Cut kerf, 389, 411
  width, 398, 407, 410
Cut quality, 410
Cutting, 387, 390, 391
  depth, 423
  force, 419
  front, 390, 391, 406
  gas jet, 394
  head, 391, 393
  length, 401
  model, 394
  nozzle, 393, 406, 407
  process, 388
  speed, 388, 390, 393, 394, 407, 410, 413, 420, 421, 425
  time, 401, 402, 403, 422
  track, 401
Cutting-to-length, 388
CVD diamond, 102

Decomposition, 384
  temperature, 371, 376
Deep-penetration welding, 286, 288, 289, 290, 312, 315, 324, 326, 340–341
Defocusing, 322
Degradation, 54, 63, 80, 86, 132, 163, 164, 170, 206, 207
  mechanism, 86
  process, 86
Degree of absorption, 338, 363
Degree of crystallinity, 376
Degree of reflection, 363
Dendrite formation, 289
Dendrites, 308
Deposition, 482, 503
  of dielectrics, 29–31
Depth of cut, 420, 421, 424
Design aspects, 48
Design parameters, 49
Determination, of optical properties, 378
DI (de-ionized) water, 100
Diamond, 106
Diamond heat spreaders, 101–104
Diamond substrate, 113
Difficult to machine materials, 424, 425
Diffraction, 194
Diffusion, 406
Dilution, 489, 490, 527
Diode laser cutting plotter, 392
Diode lasers, 1, 10, 122, 125, 127, 128–130, 136, 142, 206, 209–210
  application, 285, 537
  bars, packaging of, 75, 150
  beam quality, 162–177
  broad area emitters and arrays, 47–55
  chip characterization methods/measurements, 33–47
  high-brightness emitters and arrays, 55–70
  homogeneization, of high power diode-lasers, 138–141
  manufacturing technology, 25–33
  principles, of operation, 5
  stacking, 147–162
  system, 215, 388
Direct application, 417
Direct integration, 418
Distortion, 290, 328, 329, 340, 341, 342
Distributed-feedback (DFB) lasers, 56
Divergence angle, 38, 40, 129–133
Double-wheel system, 294–295
Dyes, 375

Economic efficiency, 399
Edge-tracking sensors, 296, 299–302
Effective thermal conductivity, 107
Efficiency, 34
Efficiency model, 19
Electric characteristics, of diode lasers, 49–53
Electric field, 183
Electric steel, 396, 397, 398, 401, 402, 403, 404
Electrochemical corrosion, 100–101
Electroluminescence, 43
Electro-lumiscence spectroscopy, 112
Electromigration, 80
Electronic packaging, 349
Electro-optical characterization, 34–37, 61–63
Emission spectrum, 50–51

Energy bands, 5, 111
Energy input per unit length, 377, 383, 384, 420
Epitaxy, 26
Erosion, 99
Etching, 29
Evaporation, 288, 390
Excessive melting, 408
Exothermal reaction, 388, 391
Expansion-matching, 102, 104, 105, 106, 117

Fabry–Perot resonators, 16
Facet reflectivity, 66
Far-field, 14, 37–40, 52, 59, 130, 193, 194, 266
  astigmatism, 58–59, 67–69
  corrected, 58, 67–68
  divergence angle, 122
  intensity distribution, 37, 39, 138–141, 176
  measurement, 37, 201
  power density distribution, 187, 201
Fast-axis, 37, 53, 306, 309, 316, 318, 323
Fast axis collimation, 128–131
Ferrite, 313
Fiber coupling, 152, 162, 325, 331, 332–333, 334–335, 388, 417, 418
Fiber-reinforced
  ceramics, 423
  metals, 413
  polymers, 251, 362
Filamentation, 57
Filler metal, 345
Fillet weld, 320, 328, 329, 330, 346
  at lap joint, 318, 319
Filling factor, 123, 136, 137, 147–149, 227, 252, 257, 279
Five-axes milling, 415
Five-axes machining, 416
Fixed costs, 399
Flame cutting, 272, 405, 412
Flame hardening, 426, 433
Flame retardants, 376
Flexible beam guiding, 405
Flexprints, 355
Flip-chips, 355, 356
Flow rate, 98, 311
Flux, 358
F-number, 392, 393, 409
Focal diameter, 335, 353, 389, 392, 409
Focal length, 37, 131, 136, 149, 163, 305, 306, 328, 331, 393, 407
Focal position, 310, 316, 317, 393
Focal spot position, 420
Focusability, 388
Focusing, 400
Focusing optics, 392, 408
“Foot point,” 310
Force/elongation diagram, 360
Forming tools, 479, 503, 509, 510
Free-form surfaces, 415
Fresnel absorption, 391
Frictional heat, 421
F-Theta lens, 353, 367
Full penetration, 315, 316, 317
Fume, 291
Fusing time, 403
Fusion cutting, 389

Galvanization, 328, 329
Galvanized steel, 333
Galvanometer scanner, 353
Galvanometric scanning mirrors, 367
Gap, 326, 345, 377
Gap bridging, 316, 320, 322–323, 331, 372, 377, 378
  capabilities, 383, 385
Gap width, 323
Gas foot point, 311, 312
Gas jet, 407, 408
Gas nozzle, 311
Gas pressure, 391, 407
Gaussian beam, 181, 187, 193
  profile, 273
General astigmatic, 190
Glass, 399
Glass fiber concentration, 379
Grade of crystallisation, 379
Graphical user interface, 272, 278
Graphite, 389
Guiding rails, 459

Handling system, 391, 399
Hardening, 425
Hardness, 313
  gradient, 423
  profile, 313, 314
Hartmann sensor, 205
Heat-affected zone, 313, 314
Heat capacity, 390
Heat conduction, 87, 304, 394, 406
  equation, 338
  losses, 390, 395
  welding, 286, 288, 321, 324, 333, 334, 338, 339

Heat conductivity, 338, 390
of polymers, 376
Heating, 390, 403, 413, 419
Heat load, 389
Heat radiation, 371, 374
Heat sink, 19–24, 61–69, 79–82, 87–91, 94–105, 150
Heat source, 338, 341, 406, 412, 413
Heat spreading, 88, 106
Heat transfer coefficient, 88, 89, 90, 92
Height profile, 300
Helium, 310, 312, 322
Hem flange, 342, 343
High carbon steel, 335
High-brightness, 55
arrays, 69–70
emitters, 55
systems, 233–245
High-power laser diode. *See* Diode lasers
High-strength steel, 313, 315
High-temperature-resistant steel, 412
Holmium-YAG laser, 370
Holographic interferometry, 107
Homogeneity, 34
Beam quality, 236, 265, 269, 275, 374, 410
intensity, 162, 164, 235, 262
powder stream, 487
wavelength, 41, 50
waver growth, 26, 27
Homogenization, 138–141, 164, 266
Homogenizer, 262
Hot forming tool steels, 419
Hot machining, 413
Hot-melt adhesive, 381–382
Hot-zinc-dipped mild steel, 398
Hybrid, 487
Hybrid circuits, 357
Hybrid process, 405
LAAPS, 512

Ignition temperature, 391, 406, 408
Image processing, 352, 374
with IR-camera, 373
Incidence angle, 345
Inclination angle, 345
Incoherent beam superposition
basics, 125–128
collimation, 128–141
combination techniques, 142–149
quality, 121–125, 175–177
stacking techniques, 150–162
symmetrization and fiber coupling, 162–174
Indium, 80, 103
Indium solder, 112
Induction, 473
hardening, 433, 472, 480
Industrial applications, 387, 400
Inert gas cutting, 389, 393–394
Inert gas jet, 389
Inert gas nozzle, 345
Influence of geometry, 380
Injection, 483
Injection valve, 334, 467
Integrating sphere, 34
Intensities, 389
Intensity distribution, 374, 379
Interaction zone, 390
Internal loss, 17
International standards, 121, 122, 181–183, 203, 204, 210–211
IEC 60825-1, 209
ISO 306, 380
ISO 11146, 64, 67, 130, 211, 212
ISO 17526, 206
Intrinsic general astigmatic, 191
Intrinsic optical parameters, 22
Ion-assisted-deposition (IAD), 144
Ion beam sputtering (IBS), 144
IR-camera, 352, 374
Iron, 406, 432, 501
Iron combustion, 406, 407
Iron oxide, 406
Irradiation time, 321, 360

Joining of plastic to metal, 381
Joining technologies, 285, 286
Joint gap, 344
Joint geometries, 363
Joint interface, 318
Joints, 323
Joint tracking, 300

Kerf cross section, 390
Kerf volume, 390, 394, 406
Kerf width, 389, 390, 406
Keyhole, 289
Kramers–Kronig relation, 15

Lap joint, 324, 330, 326, 336
Large optical cavity (LOC), 14, 48
Large-scale production, 27

Laser-assisted atmospheric plasma spraying (LAAPS), 488, 512
Laser-assisted machining, 278, 283, 388, 413, 416, 419, 421, 423, 425
  of metallic materials, 423
Laser-assisted milling, 413, 414, 416, 420, 421, 425
  of steel, 424
  of Stellites, 425
Laser-assisted roughing, 423
Laser-assisted turning, 413, 423
Laser beam oxygen cutting, 405, 406, 411
Laser beam soldering, 349, 359, 360
Laser beam welding, of thermoplastics, 361, 362, 386, 387
Laser brazing, 342
Laser cutting, 389, 392
Laser cutting systems, 388
Laser fusion cutting, 390
Laser hardening, 272, 426, 427
Laser light pattern, 290
Laser operation, principle of, 5–25
Laser power, 306, 391, 395, 396, 397, 408, 409, 421, 422
  at workpiece, 394
Laser processing, 27–31
Laser protective window, 418
Laser punching, 401, 405
Laser reflection polarimetry, 109, 115
Laser soldering system, 353
Laser-spot orientation, 316
Laser spot position, 320
Laser triangulation, 298
Laser vaporization cutting, 390
Laser wavelength, 391
Laser welding, 286
Latent heat, 389, 390
Lateral waveguide, 15–16
Laval nozzle, 272, 407, 409
Leading nozzle, 311
Leather, 396, 397, 398
Length of cut, 422
Lifetime, 53–55, 63, 86, 98–101, 206–209
Light pipe, 139
Linear guiding rails, 436, 459–467
Linear optical systems, 185–186
Linear polarization, 396
Line current density, 21
Line series resistance, 22
Line-shaped laser beam, 350, 400
Linewidth enhancement factor, 57, 58
Longitudinal mode, 16
Long-term stability, 204
Losses, 48

Machine tool, 414
  design, 416
Machining, 388, 413
  properties, 413
  strategies, 423
  time, 424, 425
  zone, 414
Manufacturing technology, of semiconductor laser, 25–33
Marangoni effect, 313
Martensite, 313, 314, 474, 501
Martensitic structure, 432
Mask welding, 366–367
Mass density, 390
Material, 388
  gain, 11
  parameter, 49
  removal, 389
  removal rate, 412, 421, 424
  strength, 388, 413
  thickness, 390
Maximum cutting speed, 393, 394, 395, 396, 397, 408, 410
Maximum permissible exposure, 209
Maximum welding depth, 287
Maxwell equations, 183
Mean-time-to-failure (MTTF), 86
Mechanical processes, 405
Medium-term stability, 204
Melt, 324, 389
Melt burr, 381
Melt ejection, 393, 394
Melt flow, 394
Melt front, 403
Melting, 376, 388, 390, 394, 402
Melting point, 324, 338
  of solder for heat sink, 77, 95, 102
Melting temperature, 380, 390, 403
Melting volume, 403
Melt pool, 286, 287, 288–289
Metal cutting, 388
Metallization, 31
Metrology, 181–212
Microchannel cooler, 150
Microchannel heat sinks, 94–101
Micro-lenses, 131
Micro-optic mounting, 155–158
Micro-optics, 117–118
Microstructure, 313, 314, 434, 484, 499, 517

Microtome cuts, 363, 377, 383, 384, 386
Micro-welding, 336–338
Mild steel, 288, 304, 305, 306, 314, 320, 328, 339, 388, 393, 394, 396, 397, 398, 405, 406, 408, 409, 410, 411
Milling machine, 414
Milling path, 422
Milling tool, 415, 419, 420, 422
Mirror coating, 31–32
Mobile cladding system, 509
Modal optical gain, 10
Modular hardening system, 272, 448
Modular setup, 245
Moiré fringe analysis, 107
MOPAs (master-oscillator power amplifiers), 56
Morphous polymers, 379
Mounting process, 77, 102
Moving knife-edge, 197
Moving pinhole, 198–200
Moving slit, 197
Multi-reflection, 289
Mutual coherence, 183–184

Nd:YAG laser, 326, 330, 332–333, 334–335, 370, 388, 399
Near-field profile, 59, 65
Near-net-shape, 423
Nickel-based alloys, 413
Nitrogen, 389, 394, 395, 396, 397
Nitrogen-assisted cutting, 395, 398
Nitrogen cuts, 398
Nominal ocular hazard distance (NOHD), 209
Non-contact sensors, 298
Non-metals, 391, 397, 399
Notch effect, 527
Nozzle, 328, 391, 393–394, 407, 408
Nozzle angle, 310
Nozzle's orientation, 310
Nozzle parameters, 311
Nozzle stand-off distance, 393, 408
Numerical aperture, 128

Offline programming, 330
Offset, 322–323
On-line process control, 374
Operation temperature, 35, 36
Optical characteristics, 49–53
Optical gain, 7–11
Optical losses, 58
Optical-path rotating devices, 168
Optical penetration depth, 363, 364, 375, 376, 383, 385
Optical power, 34
Optical power density, 20
Optical properties, 375, 376
Optical resonator, 11–12
Optical stacking, 149
Optimization, of wall plug efficiency, 23
Organic coating, 346
Organic materials, 396
Out-gassing gap, 327
Output power, 391
Overheating, 377
Overlap joint, 346, 363, 364, 383
Overlap welding, 335, 378, 381
Oxidation, 311, 312, 389, 441, 449, 480, 503
Oxide layer, 323, 324
Oxides, 323, 389, 391
Oxygen, 388, 391, 394, 396, 398, 405, 406, 407, 408
Oxygen cutting, 389, 398
  applications, 407
  variants, 405
Oxygen jet, 406, 407
Oxygen pressure, 408, 410
Oxygen purity, 408

PA (Polyamide), 382, 383, 385, 386
Packaging-induced stress, 43
Packaging process, 75
Pack of fibers, 386
Paper, 389, 396, 397, 398
Parameter extraction, 22
Partially crystalline polymers, 379
Particle-reinforced metals, 413
Passivating scales, 406
Pasteboard, 396, 397, 398, 403, 404
Patterning, 29
PC (Polycarbonate), 373, 383
Peclet number, 390
Peltier module, 92, 93
Perlite, 432
Phase steel, 313
Phase transition, 389, 400–401
Photocurrent spectroscopy (PCS), 42, 112, 115
Photo-elastic measurement method, 113
Photo-elastic stress measurement, 109–111
Photolithography, 28–29
Photo-luminescence spectroscopy (PLS), 112

Photoresists, 28
P-I-characteristics (power vs. current), 49–50, 61, 69
Pitch, 69, 137, 222, 227, 237, 252
Plastics, 389, 391, 397, 399
Plastification, 362, 363, 364
Plate thickness, 405, 406, 407, 410
Plumb, 342
p-n-junction, 8
Polarization, 51–52
  coupling, 217, 225, 239
  multiplexing, 126, 142–145
Polyamide. *See* PA
Polycarbonate. *See* PC
Polypropylene. *See* PP
Polymer welding, 258, 285, 375
Positioning, of laser focal spot, 419
Position sensors, 296
Powder-feed, 490, 506
  nozzles, 485
Power balance, for laser cutting, 390
Power demand, 391
Power density, 285, 388
Power density distribution, 186–188, 196–204, 338, 340
PP (Polypropylene), 383
PPJ (pick, place and join) process, 79, 80
Precision parts, 334
Preheating, 388, 406, 407, 434, 474, 492, 505
Pressure measurement, 373
Pressure drop, 98
Pressure-wheel system, 294
Prism stacks, 149, 224
Process control, 427, 440, 462
Process control system, 272–278
Process diagnostic systems, 174
Process forces, 419, 420, 421, 424
Process gas, 312
Processing center, 478
Process monitoring, 371, 373, 440
Process regimes, 287, 288
Process temperature, 353, 390, 416
Process tolerances, 316, 322–323
Propagation, of beam widths, 188, 192–196
Protective glass window, 418
p-side-down assembly, 60
p-side-up assembly, 253
Pulsing, 391
Pyrometer, 272, 275, 350, 416, 440, 464
Pyrometer measurement, 372
  of working temperature, 371
Pyrometric signal, 354
Pyrometry, 371

Quality control, 371
Quantum well, 9, 13, 15
  compressively strained, 10–12, 52
  tensile strained, 10–13
Quasi-simultaneous welding, 367–368

Radial annular welds, 321
Raw beam diameter, 393
Rayleigh length, 192, 389, 392, 393, 400, 409
Reaction, 389
Reaction power, 390, 391, 406
Rearrangement, of beam shape, 386
Reflectance, 381, 427
Reflectivity, 61
Reflow process, 79
Reinforcement materials, 376
Reliability, 53–55, 63, 64, 70
Remelting, 433, 434, 503, 526
Removal rate, 413
Residual stress, 433, 493, 505, 506, 508
Ridge waveguide structure, 16
Ring-shaped laser, 278–283
Robot, 388, 444, 475, 508
Robot systems, 479
Rollover, 20, 35
Roof bow, 328–329
Roof header, 328, 329, 330, 348, 349
Rosenthal solution, 402–403
Rough-down process, 415
Roughing, 424
Roughness, 398, 430, 434, 462, 515
Running costs, 399

Safety, 209–210
Scanner, 405
Scanning, 367–368
Scattering, 375, 376, 378, 379
Scheimpflug condition, 298–299
Schematic, of tapered diode laser, 57
Seam cross-section, 346
Seam strength versus energy input per unit length, 377
Segmented mirrors, 149
Self-focusing, 57
Self-quenching, 434, 475, 480
Separation, 402
Separation process, 401
Series resistance, 34

Shack–Hartmann sensor, 205
Sheet thickness, 392, 394, 395
Shielding gas, 293, 310, 311, 312, 314
Short-term stability, 204
Shrinkage, 376
Silicon, 355, 356
Simple astigmatic, 190
Simulation, 338, 340, 402, 403
Simultaneous tacking, 384
Simultaneous welding, 257, 258, 368–370, 372, 373, 384–385, 386, 387
Single-shot cutting, 388
Single-shot cutting-to-length, 400, 401, 402, 404, 405
Single-shot welding, 290, 314–315
Single-wheel system, 295
Slit-shaped nozzle, 401
Slope efficiency, 17, 34, 85
Slow-axis, 37, 53, 306, 309, 316, 318, 323
Slow-axis collimation, 135–138
Smile, 79, 103, 131, 133, 135, 159, 220, 257
Softening, 419
Softening zone, 380, 381
Solder depot, 359
Soldering, 78, 246, 257, 285, 349, 350, 352, 353, 355, 356, 357, 358, 360
Solder interface, 83
Solder joint, 360
Solder pad, 354, 357, 358, 359
Solder thickness, 82
Solidification, 355
Spatial coupling, 147–149, 223, 239
Spatial emission pattern, 52–53
Spatial multiplexing, 125
Spatters, 291, 292, 327, 328, 329
Speckle pattern interferometry, 108
Spectral broadening, 35
Spherulites, 376
Spindle, 417
Spot, 389
Spot orientation, 309, 317, 318, 319
Spot welds, 314
Square butt joints, 315
Square butt welding, 316, 317
Stacking, 121–178, 218, 262, 310
  faults, 150, 153, 154, 170, 172
  techniques of, 150–162
Stainless steel, 286, 290, 304, 305, 306, 307, 309, 311, 312, 314, 315, 317, 319, 320, 321, 322–323, 339, 341, 389, 394, 395, 396, 398, 401, 402, 403, 404, 405
Standard characterization methods, 33–40
Standards, 181, 210–211
Stellite, 421, 423
  machining, 422
  materials, 416
Step mirrors, 168, 218
Stigmatic, 190
Strength, of joint, 318
Stress, 82, 104, 105, 109, 111, 113, 114
Stress distribution, 110
Sublimation cutting, 389, 398
Surface preparation, 382
Surface temperature, 390, 432, 440
Symmetric beam, 152
Symmetrization, 162, 174

Tactile seam tracking, 302–303
Tailored blanks, 331, 332, 333
Tapered devices, 56, 59–61
Tapered diode laser, 56, 58, 62, 64, 65, 66, 67, 69, 164, 172, 233, 235–245
  astigmatism of, 68
  fabrication of, 59–61, 245
  lifetime of, 63
  reliability of, 63, 70
Tapered diode laser bars, 233
TE polarization, 51
Tearing process, 402
Tearing-up, 401
Temperature distribution, 338, 339, 341, 350, 359, 413
Temperature field, 419, 421
Temperature measurement, 350
Temperature profile, 354, 376, 413
Tensile shear stress, 360, 361
Tensile-strained QWs, 10, 11
Tensile strength, 401, 402
Terminal lead, 353, 354–355, 357, 358, 359, 360
Thermal conductivity, 107, 287, 396
Thermal diffusivity, 338, 390
Thermal expansion coefficients, of thermoplastics, 376
Thermal expansion measurements, 114
Thermal power, 84
Thermal properties, of thermoplastics, 376
Thermal resistance, 36, 84, 87, 88, 90, 97, 98, 101
Thermal wavelength drift factor, 36
Thermo-electric cooling, 87, 92
Thermo-mechanical stress cycles, 55
Thermoplastics, 362
Thick-film, 357

Thin film polarizers, 142, 143, 144
Thin metal sheets, 399
Three-dimensional cutting, 388
Threshold current, 18, 34, 85
Threshold current density, 17, 19
Titanium, 391, 421
TM polarization, 51
Tool contact, 419
  conditions, 420
Tool diameter, 415
Tool inserts, 425
Tool length, 415
Tool life, 412
Tool materials, 422
Tool service life, 420
Tool wear, 412, 421, 422, 424, 425
Top-hat distribution, 230, 225, 266, 273
Total contact, 420
Trailing nozzle, 311
Transformation, 124, 390
Transformation hardening, 272
Transmission, 378, 379
Transmission welding, 285
Transmissive soldering, 355
Transmittance, 427
Transparency, 370
Transparency current density, 19
Transverse electric (TE), 12
Transverse magnetic (TM), 12
Triangulation, 299, 300
Tube joints, 321
Tubes, 333
Tube-sheet joints, 320
Turbo charger, 520

Undercut, 315, 327
Unsoldering, 355
UV curable adhesives, 118
UV curable glue, 156

Valence bond, 6
Valve seats, 467, 506, 518
Vapor capillary, 288, 289, 340
Vapor gradient, 394
Vaporization, 394
Vaporization cutting, 389, 391
Vaporization temperature, 338
Vaporizing, 388
Vapor plume, 288, 289, 311, 312, 315, 326
Vertical waveguide structure, 12–14
Vicat softening temperature, 380
Viscosity of plastified (molten) thermoplastics, 376
Voltage, 34

Wall plug efficiency, 20, 24, 25, 49–50, 61, 69
Wavefront, 194
  of laser beam, 205
Waveguide, 12, 164
Wavelength coupling, 225, 235, 238, 239, 279
Wavelength distribution, 51
Wavelength multiplexing, 126, 145–147
Wavelength spectrum, 35
Weibull analysis, 207
Welding, 285
  of aluminum, 287
  depth, 304, 305, 306, 307, 308, 309, 312, 322
  head, 294, 295
  sequence, 328, 329
  strength, 385
  structure, 313–314
Wetting, 346, 354–355
Wetting angle, 342
Wetting temperature, 354
Widths, of power density distribution, 187, 188, 201–203
Wigner distribution, 184–185
Wire, 337, 338
Wire cladding, 408, 489, 525
Wire feeder, 345
Wire feed rate, 346
Woehler diagram, 208
Wood, 389, 399
Working area, 418
Working distance, 291, 292, 316, 322, 325, 353
Working-spot size, 388

Young's modulus, 104

Zementite, 432
Zinc-coating, 327, 329, 342
  of steel, 292, 296
Zinced mild steel, 397

Springer Series in
OPTICAL SCIENCES

Volume 1

1 **Solid-State Laser Engineering**
By W. Koechner, 5th revised and updated ed. 1999, 472 figs., 55 tabs., XII, 746 pages

Published titles since Volume 85

85 **Sensing with Terahertz Radiation**
By D. Mittleman (Ed.), 2003, 207 figs., 14 tabs., XVI, 337 pages

86 **Progress in Nano-Electro-Optics I**
Basics and Theory of Near-Field Optics
By M. Ohtsu (Ed.), 2003, 118 figs., XIV, 161 pages

87 **Optical Imaging and Microscopy**
Techniques and Advanced Systems
By P. Török, F.-J. Kao (Eds.), 2003, 260 figs., XVII, 395 pages

88 **Optical Interference Coatings**
By N. Kaiser, H.K. Pulker (Eds.), 2003, 203 figs., 50 tabs., XVI, 504 pages

89 **Progress in Nano-Electro-Optics II**
Novel Devices and Atom Manipulation
By M. Ohtsu (Ed.), 2003, 115 figs., XIII, 188 pages

90/1 **Raman Amplifiers for Telecommunications 1**
Physical Principles
By M.N. Islam (Ed.), 2004, 488 figs., XXVIII, 328 pages

90/2 **Raman Amplifiers for Telecommunications 2**
Sub-Systems and Systems
By M.N. Islam (Ed.), 2004, 278 figs., XXVIII, 420 pages

91 **Optical Super Resolution**
By Z. Zalevsky, D. Mendlovic, 2004, 164 figs., XVIII, 232 pages

92 **UV-Visible Reflection Spectroscopy of Liquids**
By J.A. Räty, K.-E. Peiponen, T. Asakura, 2004, 131 figs., XII, 219 pages

93 **Fundamentals of Semiconductor Lasers**
By T. Numai, 2004, 166 figs., XII, 264 pages

94 **Photonic Crystals**
Physics, Fabrication and Applications
By K. Inoue, K. Ohtaka (Eds.), 2004, 209 figs., XV, 320 pages

95 **Ultrafast Optics IV**
Selected Contributions to the 4th International Conference on Ultrafast Optics, Vienna, Austria
By F. Krausz, G. Korn, P. Corkum, I.A. Walmsley (Eds.), 2004, 281 figs., XIV, 506 pages

96 **Progress in Nano-Electro Optics III**
Industrial Applications and Dynamics of the Nano-Optical System
By M. Ohtsu (Ed.), 2004, 186 figs., 8 tabs., XIV, 224 pages

97 **Microoptics**
From Technology to Applications
By J. Jahns, K.-H. Brenner, 2004, 303 figs., XI, 335 pages

98 **X-Ray Optics**
High-Energy-Resolution Applications
By Y. Shvyd'ko, 2004, 181 figs., XIV, 404 pages

99 **Mono-Cycle Photonis and Optical Scanning Tunneling Microscopy**
Route to Femtosecond Ångstrom Technology
By M. Yamashita, H. Shigekawa, R. Morita (Eds.) 2005, 241 figs., XX, 393 pages

100 **Quantum Interference and Coherence**
Theory and Experiments
By Z. Ficek and S. Swain, 2005, 178 figs., XV, 418 pages

101 **Polarization Optics in Telecommunications**
By J. Damask, 2005, 110 figs., XVI, 528 pages

102 **Lidar**
Range-Resolved Optical Remote Sensing of the Atmosphere
By C. Weitkamp (Ed.), 161 figs., XX, 416 pages

103 **Optical Fiber Fusion Splicing**
By A.D. Yablon, 2005, 137 figs., XIII, 306 pages

104 **Optoelectronics of Molecules and Polymers**
By A. Moliton, 2005, 229 figs., 592 pages

105 **Solid-State Random Lasers**
By M. Noginov, 2005, 131 figs., XII, 238 pages

106 **Coherent Sources of XUV Radiation**
Soft X-Ray Lasers and High-Order Harmonic Generation
By P. Jaeglé, 2005, 150 figs., approx. 264 pages

107 **Optical Frequency-Modulated Continuous-Wave (FMCW) Interferometry**
By J. Zheng, 2005, 137 figs., XVIII, 254 pages

108 **Laser Resonators and Beam Propagation**
Fundamentals, Advanced Concepts and Applications
By N. Hodgson and H. Weber, 2005, 497 figs., approx. 790 pages

109 **Progress in Nano-Electro Optics IV**
Characterization of Nano-Optical Materials and Optical Near-Field Interactions
By M. Ohtsu (Ed.), 2005, 123 figs., XIV, 206 pages

110 **Kramers-Kronig Relations in Optical Materials Research**
By V. Lucarini, J.J. Saarinen, K.-E. Peiponen, E.M. Vartiainen, 2005,
37 figs., X, 162 pages

111 **Semiconductor Lasers**
Stability, Instability and Chaos
By J. Ohtsubo, 2005, 169 figs., XII, 438 pages

112 **Photovoltaic Solar Energy Generation**
By A. Goetzberger and V.U. Hoffmann, 2005, 139 figs., XII, 234 pages

113 **Photorefractive Materials and Their Applications 1**
Basic Effects
By P. Günter and J.P. Huignard, 2005, 169 figs., approx. XII, 300 pages

114 **Photorefractive Materials and Their Applications 2**
Materials
By P. Günter and J.P. Huignard, 2005, 100 figs., approx. XII, 300 pages

115 **Photorefractive Materials and Their Applications 3**
Applications
By P. Günter and J.P. Huignard, 2005, 100 figs., approx. XII, 300 pages

116 **Spatial Filtering Velocimetry**
Fundamentals and Applications
By Y. Aizu and T. Asaikura, 2006, 112 figs., approx. XII, 220 pages

117 **Progress in Nano-Electro-Optics V**
Nanophotonic Fabrications, Devices, Systems, and Their Theoretical Bases
By Motoichi Ohtsu, 2006, 122 figs., 3 tables, approx. 193 pages

118 **Mid-infrared Semiconductor Optoelectronics**
By A. Krier, 2006, 443 figs., approx. 776 pages

119 **Optical Interconnects**
The Silicon Approach
By L. Pavesi and G. Guillot, 2006, 265 figs., approx. 410 pages

120 **Relativistic Nonlinear Electrodynamics**
Interaction of Charged Particles with Strong and Super Strong Laser Fields
By H.K. Avetissian, 2006, 23 figs., XIII, approx. 333 pages

121 **Thermal Processes Using Attosecond Laser Pulses**
When Time Matters
By M. Kozlowski and J. Marciak-Kozlowska, 2006, 46 figs., XII, approx. 232 pages

122 **Modeling and Analysis of Transient Processes in Open Resonant Structures**
New Methods and Techniques
By Y.K. Sirenko, Nataliya P. Yashina, S. Ström, 2006, 110 figs., approx. X, 390 pages

123 **Wavelength Filters in Fibre Optics**
By H. Venghaus, 2006, 210 figs., XXIV, approx. 451 pages

124 **Light Scattering by Systems of Particles**
Null-Field Method with Discrete Sources - Theory and Programs
By A. Doicu, T. Wriedt and Y.A. Eremin, 2006, 98 figs., XIII, approx. 318 pages

125 **Electromagnetic and Optical Pulse Propagation 1**
Spectral Representations in Temporally Dispersive Media
By K.E. Oughstun, 2006, 50 figs., IV, approx. 250 pages

126 **Quantum Well Infrared Photodetectors**
Physics and Applications
By H. Schneider, 2006, 153 figs., XVI, 254 pages

127 **Physics of Thin-Film Photovoltaics and Related Systems**
By V. Karpov, 2006, 50 figs., 304 pages

128 **High Power Diode Lasers**
Technology and Applications
By F. Bachmann, P. Loosen, and R. Poprawe, 2006, 535 figs., VI, 548 pages

129 **Laser Ablation and its Applications**
By C. Phipps, 2007, 300 figs., XX, 588 pages

130 **Concentrator Photovoltaics**
By A. Luque and V. Andreev, 2007, 242 figs., XV, approx. 298 pages

131 **Surface Plasmon Nanophotonics**
By M.L. Brongersma and P.G. Kik, 2007, X, approx. 290 pages

132 **Ultrafast Optics V**
By S. Watanabe and K. Midorikawa, 2007, 303 figs., approx. 520 pages